Università degli Studi di Cagliari

Facoltà di Scienze

Dipartimento di Scienze Chimiche e Geologiche

Dottorato di ricerca in Scienze e Tecnologie Chimiche

XXVIII Ciclo

Metal complexes with biological activity

SSD CHIM/01

PhD Thesis of: **Elisa Valletta**

Coordinator: Prof. Mariano Casu

Supervisor: Dr. Tiziana Pivetta

Final Exam A.A. 2014-2015

Abstract

Cancer is a group a diseases that involves abnormal cell growth with potential to invade or spread to other parts of the body, and it represents the second leading cause of death in developed countries.

Cisplatin is one of the most chemotherapeutic drug. In spite of its great efficacy, it shows several side effects and most patients develop a resistance to cisplatin. To overcome the cisplatin resistance, drugs are often administered in combination in order to exploit the drug synergy. After discovery of cisplatin, the research focused on metal complexes less toxic, more effective and that exploit synergistic effect when used in combination.

In this work I studied new copper, zinc and vanadium complexes with biological activity. I tested *in vitro* the studied compounds alone and in combination with drug currently in use against a panel of wild type tumour cell lines and their cisplatin-resistant sublines. I applied chemometric tools such as experimental design (ED) and artificial neural networks (ANNs) to the biochemical data collected. Finally, I used the artificial neural networks to evaluate the cell culture cross-contamination.

I selected a new family of copper(II) complexes with 1,10-phenanthroline (**phen**), 1,10-phenanthrolin-5,6-dione (**phendione**), and 1,10-phenanthrolin-5,6-diol (**phendiol**) for the synthesis of new antiproliferative agents. Considering that the DNA is an important target for several cytotoxic metal complexes, I studied the interaction of these Cu(II) complexes with DNA. I tested the ligands and complexes against normal and tumour derived human cell lines.

I tested combinations of the studied complexes and cisplatin for their potential synergistic effect against a panel of wild type tumour cell lines and their cisplatin-resistant sublines. I evaluated the selectivity of drug combinations testing the compounds also against ex vivo cultures of human

normal cell lines. Considering that the synergy may arise from a chemical reaction among the drugs, I studied the possible formation of new adducts between cisplatin, copper(II) complexes and glutathione.

I studied the phospholipid profile of wild type human cancer cell lines and their cisplatin-resistant sublines, given that changes in lipid composition and distribution on the cell membranes have been observed in cancer cells.

The in vitro cultured cell lines are widely used as model in biomedical research and the cross-contamination of cell lines represents a highly relevant problem. The ex-post discovery of erroneous results and conclusions led to paper retraction and many high-impact journals started to adopt a zero-tolerance policy requiring confirmation of cell line identity as prerequisite for publication. On the base of these considerations, I decided to develop and validate a method for evaluation of cell culture cross-contamination.

I also studied zinc and vanadium complexes. Zinc is an essential metal ion involved in a wide variety of biological processes and several proteins bind zinc for their proper functioning. I studied zinc complexes with the drug methimazole (**MeImHS**) and its anion (**MeImS**) in order to provide information for the structure prediction and reactivity of Zn-metalloproteins and -metalloenzymes.

Vanadium plays a number of roles in biological systems and vanadocene dichloride was the first discovered vanadium species with antitumour activity. Considering that the mechanism of the anticancer agent vanadocene dichloride is closely related to the biotransformation in the blood plasma, I studied the speciation of vanadocene dichloride in the plasma under physiological conditions.

In order to prepare new metal complexes, I also synthesized and characterized a new group of Schiff base ligands derived from salicyladehyde and six natural amino acids.

For the analysis of the collected data, I used the ED to set up the experiments for the evaluation of the synergistic effect of drug combinations, and for the study of the possible formation of new adducts between cisplatin, glutathione and studied complexes. I used ANNs for predict and quantify the synergism of drugs, and for the evaluation of cell culture cross-contamination levels.

List of publications

Parts of the results of this thesis have been published as follows:

I. T. Pivetta, F. Trudu, **E. Valletta**, F. Isaia, C. Castellano, F. Demartin, R. Tuveri, S.Vascellari, and A. Pani. *Novel copper(II) complexes as new promising antitumour agents. A crystal structure of [Cu(1,10-phenanthroline-5,6-dione)$_2$(OH$_2$)(OClO$_3$)](ClO$_4$).* Journal of Inorganic Biochemistry (2014) 141, 103-113. DOI: 10.1016/j.jinorgbio.2014.08.011

II. T. Pivetta, V. Lallai, **E. Valletta**, F. Trudu, F. Isaia, D. Perra, E. Pinna, A. Pani. *Mixed copper-platinum complex formation could explain synergistic antiproliferative effect exhibited by binary mixtures of cisplatin and copper-1,10-phenanthroline compounds: An ESI-MS study.* Journal of Inorganic Biochemistry (2015) 151, 107-114. DOI: 10.1016/j.jinorgbio.2015.05.004

III. **E. Valletta**, L. Kučera, L. Prokeš, F. Amato, T. Pivetta, A. Hampl, J. Havel, P. Vaňhara. *Multivariate calibration approach for quantitative determination of cell-line cross contamination by intact cell mass spectrometry and artificial neural networks.* PLoS ONE 11(1): e0147414. DOI:10.1371/journal.pone.0147414

IV. F. Isaia, M. C. Aragoni, M. Arca, A. Bettoschi, C.Caltagirone, C. Castellano, F. Demartin, V. Lippolis, T. Pivetta and **E. Valletta**. *Zinc(II)-methimazole complexes: synthesis and reactivity.* Dalton Transactions (2015) 44, 9805-9814. DOI: 10.1039/c5dt00917k

V. D. Sanna, V. Ugone, G. Micera, T. Pivetta, **E. Valletta**, E. Garribba. *Speciation of the potential antitumor agent vanadocene dichloride in the blood plasma and model systems.* Inorganic chemistry (2015) *54* (17), 8237-8250. DOI: 10.1021/acs.inorgchem.5b01277

VI. E. Valletta, E. Pinna, S. Vascellari, G. Caddeo, E. Cadoni, F. Isaia, A. Pani, T. Pivetta. *Identification of specific phospholipids to differentiate cisplatin-resistant and wild type cells in leukemic (CCRF-CEM) and ovarian cancer (A2780).* (PLoS ONE - Submitted)

Abbreviation list

1 L-Salicylidenealanine

2 L-Salicylidenevaline

3 L-Salicylidenecysteine

4 L-Salicylideneserine

5 L-Salicylidenearginine

6 L-Salicylidenehistidine

A2780 Human ovarian carcinoma

A2780-res Cisplatin-resistant subline of human ovarian carcinoma

A2780-wt Wild type human ovarian carcinoma

AE Addictive effect

ANNs Artificial neural networks

ATR-IR Attenuated Total Reflectance Infrared Spectroscopy

C0 $[Cu(phen)_2(H_2O)](ClO_4)_2$

C1 $[Cu(phen)_2(H_2dit)](ClO_4)_2$

C10 $[Cu(phen)(H_2O)_2(ClO_4)_2]$

CCRF-CEM Human acute T-lymphoblastic leukemia

CCRF-CEM-res Cisplatin-resistant subline of human acute T-lymphoblastic leukemia

CCRF-CEM-wt Wild type human acute T-lymphoblastic leukemia

CCRF-SB Human acute B-lymphoblastic leukemia

CDDP Cisplatin or cis-diammineplatinum(II) dichloride

ct-DNA Calf thymus DNA

DMSO Dimethyl sulfoxide

DMSO-d_6 Hexadeuterodimethyl sulfoxide

DU-145 Human prostate carcinoma

E^0 Electrode standard potential

ED Experimental design

ESI-MS Electro-Spray Ionisation at Atmospheric-Pressure Mass Spectrometry

GSH Gluthathione

GSSG Gluthathione disulfide

H_2dit Imidazolidine-2-thione

hCtr1 Human copper transport protein

Hep-G2 Human hepatocellular carcinoma

hESCs Human embryonic stem cells

His Histidine

HLA Human leukocyte antigen

hOCT2 Human organic cation transporter 2

HTFA Trifluoroacetic acid

I1 $[Cu(phendiol)(H_2O)_2(ClO_4)_2]$

I2 $[Cu(phendiol)_2(H_2O)](ClO_4)_2$

IC_{50} Concentration of compound required to reduce the viability of the tested cells by 50%

K1 $[Cu(phendione)(H_2O)_2(ClO_4)_2]$

K2 $[Cu(phendione)_2(H_2O)(OClO_3)](ClO_4)$

K_b Binding constant

MDT Multidrug therapy

mEFs Mouse embryonic fibroblasts cells

MeImHS Methimazole (1-methyl-3H-imidazole-2-thione)

mESCs mouse embryonic stem cells

mp Melting points

MTT 3-(4,5-dimethylthiazol-2-yl)-2,5-diphenyl-tetrazolium bromide

NAAE Non-algebraic additive effect

NMDEI Net multi-drug effect index

NMR Nuclear Magnetic Resonance

phen 1,10-phenanthroline

phendione 1,10-phenanthrolin-5,6-dione

phendiol 1,10-phenanthrolin-5,6-diol

PIPES 1,4-piperazinediethanesulfonic acid

pK_w Water ionic product

PL phospholipid

RMS Root mean square

ROS Reactive oxygen species

SK-MES-1 Human squamous cell lung carcinoma

SPE Solid phase extraction

STR Short tandem repeat

UV-vis Ultraviolet-visible

VDC or [Cp_2VCl_2] Vanadocene dichloride

Index

Part I

Introduction

Essential metal ions

The study of the metal ions in biological systems represents a link between chemistry and living world (Figure 1). Given the importance of this topic, a programme on "the Chemistry of Metals in Biological Systems" was founded by the European Science Foundation in the 1990s.[1] Some metal ions are essential since they are involved in vital functions like respiration, circulation, reproduction, and are integral part of metabolic and biochemical enzymatic processes. The human body provides a complex series of homeostatic mechanisms that increase or decrease metal uptake and excretion in order to maintain its concentrations in physiological levels. In fact, at high concentration also essential metal ions can became toxic.

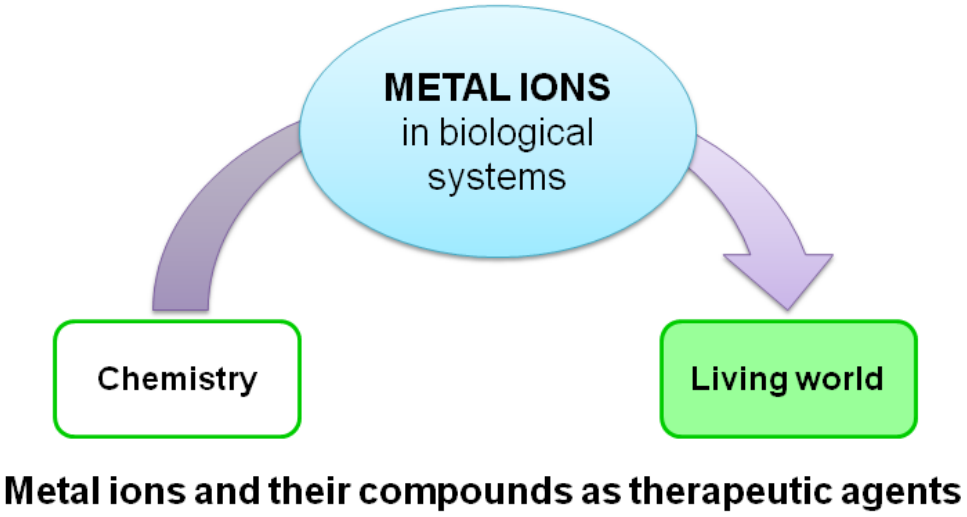

Figure 1. Metal ions as connection between chemistry and living world.

Metals in medicine

Metal ions and their compounds play an important role in medicine as therapeutic agents. Metals have been used to treat different human diseases since antiquity. Nowadays the number of metal-based drugs is in continuous growing, involving a broad spectrum of metals. For example, several

platinum compounds are used to treat various types of cancers; zinc compounds are used as chelating agents; silver and its compounds are used as antimicrobial agents; and finally various gold compounds and lithium salts are used in the treatment of rheumatoid arthritis and bipolar disorder, respectively.

Antitumor chemotherapy

Cancer is a group of diseases that involves abnormal cell growth with the potential to invade or spread to other parts of the body. This disease represents the second leading cause of death in developed countries. Chemotherapy, surgery, radiation, hormonal and immune-therapy represent the most used treatments for cancer, depending on type, location, severity, and person's health. The chemotherapy is the treatment of cancer with one or more cytotoxic anti-neoplastic drugs able to kill cancer cells or to inhibit their proliferation. The antitumor properties of cis-diammineplatinum(II) dichloride, cisplatin or CDDP (Figure 2), were discovered fortuitously in 1965 by Rosenberg and colleagues[1]. [2]

Figure 2. Cisplatin (cis-diammineplatinum(II) dichloride or CDDP) was introduce in clinical practice in 1978.

[1] The "accidental" discovery of cisplatin was made when Barnett Rosenberg used platinum electrodes to apply an alternating electric field across a chamber in which bacteria *E. coli* were growing. Although bacterial cell growth continued, cell division was arrested. Additional studies were required to understand that the effective agent in blocking cell division in the bacteria was a platinum complex in solution, the cisplatin, electrolytically formed by the applied electric field.

In 1978, with the introduction of cisplatin in clinical practice, the real use of metal complexes in cancer therapy actually started. Many complexes with metal ions, such as ruthenium, gold, copper, silver or vanadium, have been designed, synthesized and tested in order to develop effective and not toxic drugs.[3]

Cytotoxic activity of a drug

In order to experimentally estimate the cytotoxic activity of a drug, the percentage of living cells after drug treatment is measured for each solution with respect to the control (untreated cells). This value represents the vitality but usually the data are expressed as mortality, i.e. 100% minus vitality. To compare the antiproliferative activities of different drugs, the concentration required to inhibit cell proliferation by 50%, with respect to untreated cells, is used (IC_{50}). The IC_{50} values are determined from the dose-response curve by non-linear regression of the mortality % as a function of the drug concentration (Figure 3).

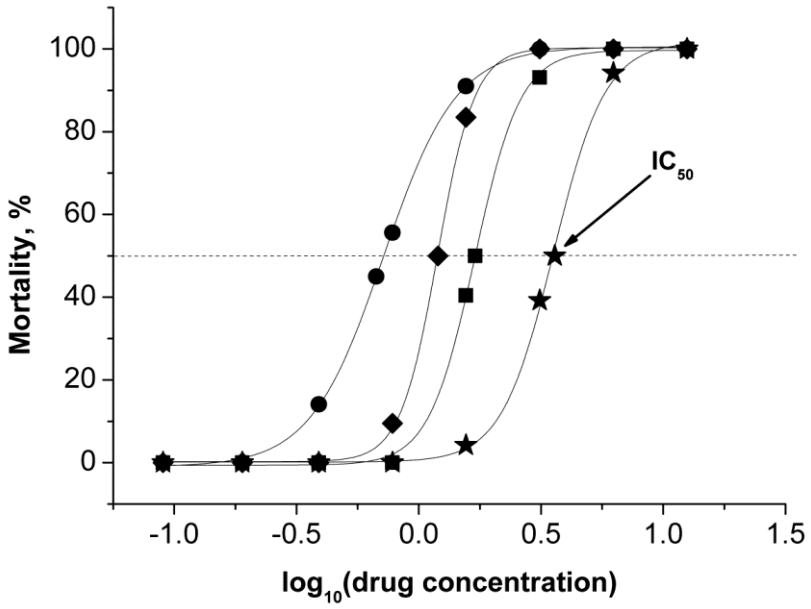

Figure 3. Example of dose-response curves.

Cisplatin

Cisplatin is one of the most powerful metal based chemotherapeutic agent, used alone or in combination for the treatment of several cancers, including testicular, ovarian, bladder, head and neck, esophageal, small and non-small cell lung, breast, cervical, stomach, and prostate cancers.[4] Cisplatin is administered intravenously due to its low chemical stability. It interacts with plasma proteins and 1 day after administration, is bound for 95% to different plasmatic proteins containing thiolic groups, thanks to the great affinity of platinum for the sulfur atom.[5]–[7] The molecules of cisplatin enter the cells by passive diffusion and by active protein-mediated transport systems, in particular by human copper transport protein (hCtr1) and human organic cation transporter 2 (hOCT2).[8],[9] In cytoplasm, one chloride ligand is displaced by a water molecule to form the $[Pt(Cl)(H_2O)(NH_3)_2]^+$, this species interacts with DNA in the N7 position of guanine and adenine and in the N3 of cytosine, and forms the monofunctional adduct $[Pt(Cl)(DNA)(NH_3)_2]^+$ (Figure 4). This last can hydrolyze to form the species $[Pt(H_2O)(DNA)(NH_3)_2]^+$. Both the monofunctional adduct and its hydrated form may re-interact with DNA by crosslinking forming the bifunctional adduct $[Pt(NH_3)_2DNA]^+$. This last acts triggering cellular apoptosis.[10] Cisplatin can interact with DNA in several modes: 1,2-intrastrand cross-linking with two adjacent guanines (1,2-d(GpG)); 1,2-intrastrand cross-linking with an adenine and an adjacent guanine (1,2-d(ApG)); 1,3-intrastrand cross-linking with nonadjacent guanines, and finally by interstrand adducts.

Despite the great efficacy of cisplatin, it shows high cytotoxicity also for normal tissues and causes several side-effects, as nausea and vomiting, neuro- and nephrotoxicity.[11] Moreover, the efficacy of cisplatin therapy is often limited by the development of drug resistance. In fact, cancer cells may show an inherited or acquired resistance, and, in order to reach the therapeutic effectiveness, higher doses of the drug are required with a higher incidence of the side effects related to the doses. Among the main identified mechanisms of cisplatin resistance there are:

reduced cisplatin influx due to decreased levels of hCtr1[12]; an increased cisplatin efflux due to overexpression of copper-transporting protein ATP7B or multidrug resistance protein MRP-2[13],[14]; a higher deactivation by thiol-containing biomolecules, as glutathione (GSH) or thioredoxin[15]–[17]; and an increased capacity of DNA repair or inhibition of the apoptotic pathway.[18]

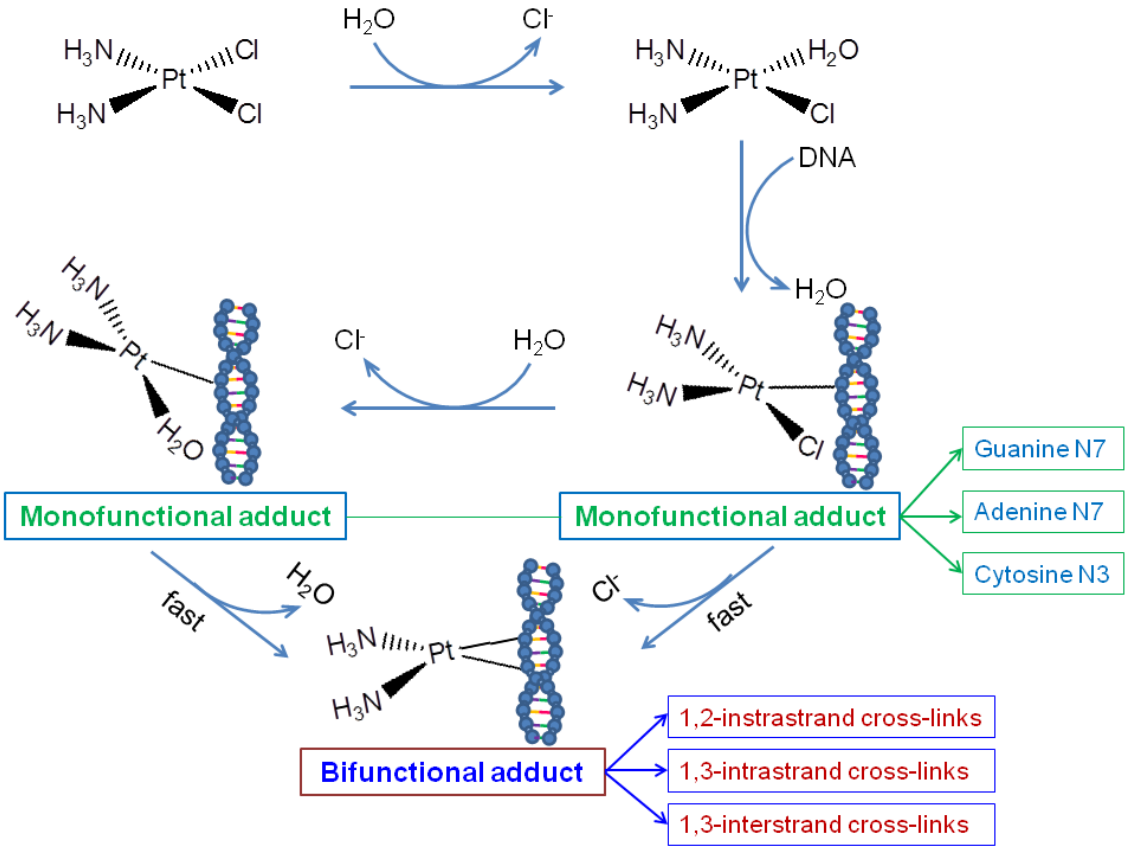

Figure 4. Interaction of cisplatin with DNA.

Glutathione

One of the most abundant thiol-containing molecules in the human body is the glutathione, a tripeptide of the sequence γ-Glu-Cys-Gly. GSH is ubiquitous in biological fluids and prevents cellular damage caused by reactive oxygen species (ROS). GSH is in equilibrium with its oxidized

form (GSSG) formed by two glutathione molecules bound with a disulfide bridge between the cysteine residuals (Scheme 1).

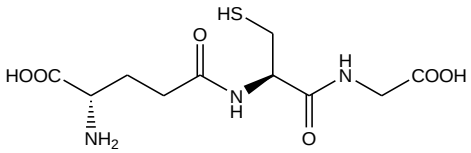

GSH

(2S)-2-amino-4-{[(1R)-1-[(carboxymethyl)carbamoyl]-2-sulfanylethyl]carbamoyl}butanoic acid

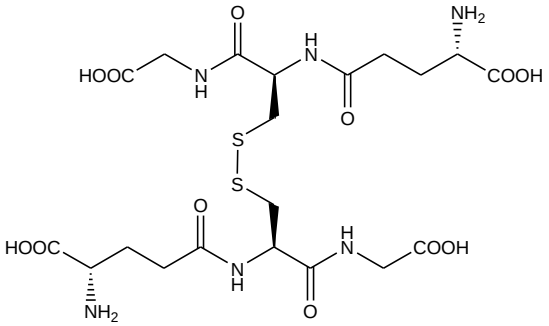

GSSG

(2S)-2-amino-5-[[(2R)-3-[(2R)-2-[[(4S)-4-amino-5-hydroxy-5-oxopentanoyl]amino]-3-(carboxymethylamino)-3-oxopropyl]disulfanyl-1-(carboxymethylamino)-1-oxopropan-2-yl]amino]-5-oxopentanoic acid

Scheme 1. Formula and acronyms of glutathione (GSH) and its oxidized form (GSSG).

In physiological conditions, the intracellular concentrations of GSSG is 1/10 of that of GSH. The GSSG is reduced to GSH by glutathione reductase. The glutathione depletion, i.e. the decrease of the normal ratio GSH/GSSG, is often correlated with cancer. It has been shown that in some kinds of cancer the level of GSH is lower than the physiological one.[4] GSH is involved also in the elimination of xenobiotics and in the intra-, inter- and extracellular metal ion transport. GSH presents eight coordination sites (two carboxyls, one thiol, one amino and two pairs of carbonyls and amide donors within the peptide chain), and having N, O and S donor atoms, it is able to interact with both soft and hard metal ions.[19] Since Pt(II) is a soft ion, it has more affinity towards a soft donor such as the sulfur atom of GSH than toward a hard one such as the nitrogen atoms of DNA bases. The cisplatin can react with GSH, resulting deactivated as drug.[4] Actually, CDDP

forms with GSH the bis-(glutathionato)-platinum $[Pt(GS)_2]$[20], however the formation of adducts with GSH is a controversial issue in literature.[21] Since the increasing of GSH level is not associated to a decreasing in Pt(II)-DNA adducts in the tumor cells, it has been supposed that GSH plays a role in apoptotic regulatory pathways.[22] Moreover, the increase of the GSH level inside the cells could enhance the sensibility of cancer cells to the CDDP, by increasing the number of copper transporters and then the drug uptake within the cell.[23]

Copper complexes

Copper-based complexes have been selected for the synthesis of new antitumour agents on the assumption that complexes with essential metal ions may be less toxic for normal cells than toward cancer ones.[24] In human, copper concentration is regulated by the homeostatic system and in blood stream, it is transported by ceruloplasmin as Cu(I) and Cu(II) or by albumins and small molecules like histidine. Copper enters the cells via the hCtr1 (the same carrier protein exploited by cisplatin[25],[26]), and, inside the cell, copper is bound to a variety of ligands[27] that prevent the interaction of the free copper ion with DNA, proteins or cellular membranes. Actually, the concentration of free Cu is kept $< 10^{-18}$ M. The majority of the copper is complexed by GSH as Cu(I). The complex Cu(I)-GSH can donate copper to proteins such as metallothionein (proteins involved in metal detoxification) or chaperones (molecules involved in copper delivery).

The study of Cu(II) complexes with nitrogen-containing ligands, such as 1,10-phenanthroline (phen) and 2,2'-bipyridine, started with the discovery of the antitumour properties of the $[Cu(phen)_2]^{2+}$ complex.[28] This complex is able to cleave DNA and has been tested against several tumour cell lines.[29],[30] Several copper-phen complexes have been then tested *in vitro* and *in vivo*, showing cytotoxic[31], genotoxic[32] and antitumoural activity.[33] In the research group where I

prepared my PhD thesis, several copper(II) complexes containing two phenanthrolinic units and N,N'-substituted imidalidine-2-thione as auxiliary ligands, have been studied.[30],[34] The studied complexes exhibit IC_{50} values in the μM range against human acute T-lymphoblastic leukemia (CCRF-CEM), human acute B-lymphoblastic leukemia (CCRF-SB), human squamous cell lung carcinoma (SK-MES-1), and human prostate carcinoma (DU-145). For the SK-MES-1 cell line these copper complexes are more toxic than cisplatin, while for the other cell lines they are almost equally cytotoxic as cisplatin. It has been found a correlation between the polarity of the complexes and their citotoxic activity toward solid or liquid tumors. In fact, complexes with higher dipole moments resulted more active against the hematological cancer cells, while complexes with lower dipole moments, were more active against solid cancer cells. These results lead us also to assess that cultured cancer cells may reflect the physiological environment of the original organ from which they are derived.

Multidrug therapy

The multidrug therapy (MDT) was introduced as a modern approach in order to defeat the drug resistance, reduce the required dose and therefore the side effects. In MDT, two or more drugs are administered simultaneously to exploit their synergism. The combined drugs might show equal or different effects with respect to those of the individual drugs (addictive effect, AE). When the therapeutic effect of the drug combination is enhanced, the drugs act synergistically, when the overall effect is decreased, the drugs act antagonistically. The final effect of MDT depends on the kind of drugs and on their doses. The AE of two drugs was described at first by Webb and Bliss as algebraic summation of drug activities and a third term that takes into account the sequence of drugs.[35][36] A new definition of AE, that is the non-algebraic additive effect (NAAE), was

introduced in 2013.[37] The NAAE is a operational definition of the additive effect, not related to the number of drugs or to the action mechanism. The occurrence of synergism or antagonism of drugs is defined by the Net Multi-drug Effect Index (NMDEI). When the NMDEI assumes positive values, the net multidrug effect is synergistic. Otherwise, when the NMDEI assumes negative values, the net multidrug effect is antagonistic. The NMDEI can be also equal to zero, in this case the experimental activity of the multidrug mixture is equal to NAAE.

Artificial neural network

Artificial neural networks (ANNs) represent a robust and versatile mathematical tool for many applications in various fields. ANNs mimic the structure of the human brain as well as its "*learning*" and "*generalization*" ability. The basic units of ANNs are called "*nodes*" or "*neurons*". They are organized in one "*input"* layer, in one or more "*hidden"* layers, and in one "*output"* layer. The *i*-th neuron in a layer is linked to all the *j*-th neurons in the next layer. Each connection is weighted with a weight w_{ij}. The ANN architecture is usually written as (**a**, **b**, **c**), where **a**, **b**, and **c** represent the number of neurons in the *input*, *hidden*, and *output* layer, respectively. An example of ANN architecture is given in Figure 5.

The role of the neurons in the *input* layer is to receive the input data and transfer them to the neurons in the *hidden* layer through the weighed connections. The neurons in the *hidden* layer(s) perform mathematical operations on the incoming data (summation, addition of a "*bias*" term and transformation by a suitable mathematical function). The result is then transferred to the neurons in the *output* layer where the ANN output is calculated.

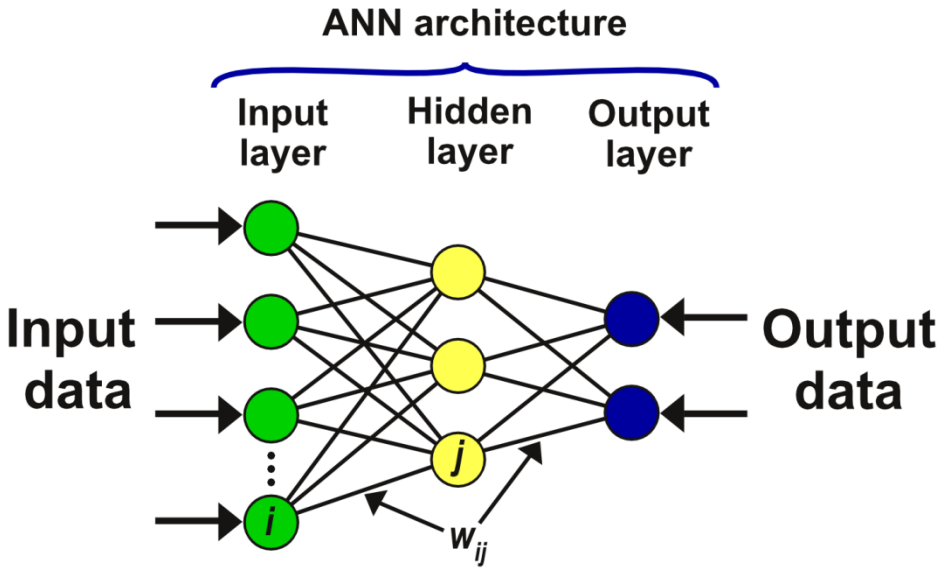

Figure 5. Example of ANN architecture (1 *input* layer, 1 *hidden* layer with three neurons, and 1 *output* layer). The w_{ij} are weights assigned to each connection between the nodes (neurons).

The ANN "*learning*" is achieved by adjusting iteratively the values of connection weights in order to minimize the difference between ANN calculated output value (o^*_{pk}) and the experimental one (o_{pk}). This is done using a suitable mathematical rule called "*training algorithm"*. After each iteration, the root mean square of the sum of $(o_{pk} - o^*_{pk})^2$ residuals (RMS) is calculated. The weights are altered in order to minimize the RMS value (for a given ANN architecture). However, also the optimal ANN architecture must be searched for. It means that the optimal number of *hidden* layers and that of neurons therein have to be found too. The most common approach to find the optimal ANN architecture is to plot the RMS value *vs*. the number of neurons in the *hidden* layer(s). At first, as the number of neurons increases, the RMS value decreases. However, when an "optimal" number of neurons is reached, the RMS value is reduced and further increase of the number of neurons has no or little effect on it.

The "*generalization*" ability of the network is its ability to predict the correct value of the output for input data not used for training. Such ability should be checked performing the so called

"*verification*" step. Most of the modern software tools allow to perform training and verification steps simultaneously. The "*verification*" step is stopped when acceptably low RMS value for the verification set is achieved. Afterwards, the network can be used for "*predict*" the response for "unknown" data sets.

In order to obtain good results, the choice of the experimental data is fundamental. Besides, for practical reasons, the number of experiments should be as low as possible while providing a high content of information. Experimental design (ED) techniques can be useful for this purpose.[38]

Aim of the work

The aim of the present work was to prepare and study new metal complexes with biological activity. In particular, I synthesized and characterized new copper, zinc and vanadium complexes. I tested *in vitro* the studied compounds alone and in combination with drug currently in use against a panel of tumour cell lines. I applied chemometric tools such as experimental design and artificial neural networks to the biochemical data achieved in the previous steps. Moreover, I used the artificial neural networks to evaluate the cell culture cross-contamination.

I selected a new family of copper(II) complexes with 1,10-phenanthroline (**phen**), 1,10-phenanthrolin-5,6-dione (**phendione**), and 1,10-phenanthrolin-5,6-diol (**phendiol**) for the synthesis of new antitumour agents. I studied the interaction of these Cu(II) complexes with DNA given that the DNA is an important target for several cytotoxic metal complexes. I tested the ligands and complexes against normal and cancer derived human cell lines.

I tested combinations of the studied complexes and chemotherapeutic drugs currently in use for their potential synergistic effect against a panel of wild type cancer cell lines and their cisplatin-resistant sublines. I evaluated the selectivity of drug combinations testing the compounds also against human normal cell lines. I studied the possible formation of new adducts between cisplatin, copper(II) complexes and glutathione given that the synergy may arise from a chemical reaction among the drugs.

Considering that changes in lipid composition and distribution on the cell membranes have been observed in cancer cells, I studied the phospholipid profile of wild type human cancer cell lines and their cisplatin-resistant sublines.

Cross-contamination of cell lines represents a highly relevant problem in biomedical research. After the ex-post discovery of erroneous results and conclusions that led to paper retraction, many

high-impact journals started to adopt a zero-tolerance policy requiring confirmation of cell line identity as prerequisite for publication. On the base of these considerations, I decided to develop a rapid and routinely applicable method for evaluation of cell culture cross contamination.

I studied complexes of zinc and vanadium. Zinc is an essential metal ion involved in a wide variety of biological processes, and several proteins bind zinc for their proper functioning. In order to provide information for the structure prediction and reactivity of Zn-metalloproteins and -metalloenzymes, I studied zinc complexes with (N,S)-donor molecules.

Vanadium plays a number of roles in biological systems and vanadocene dichloride was the first discovered vanadium species with anticancer activity. I studied the speciation of vanadocene dichloride in the plasma under physiological conditions because the mechanism of the antitumour agent vanadocene dichloride is closely related to the biotransformation in the blood plasma.

In order to prepare new metal complexes, I also synthesized and characterized a new group of Schiff base ligands derived from salicyladehyde and six natural amino acids.

For the analysis of the acquired data, I used many chemometric tools. In particular I used the ED to set up the experiments for the determination of the synergistic effect of drug combinations, and for the study of the possible formation of new adducts between cisplatin, glutathione and studied complexes. I used ANNs for predict and quantify the synergism of drugs, and for the evaluation of cell culture cross-contamination levels.

References

1. Crichton, R. R. *Biological Inorganic Chemistry: An Introduction*. (Elsevier Science Publishing Company, 2008).
2. Rosenberg, B. Some biological effects of platinum compounds. *Platin. Met. Rev.* **15,** 42–51 (1971).
3. Trudu, F., Amato, F., Vaňhara, P., Pivetta, T., Peña-Méndez, E. M. & Havel, J. Coordination compounds in cancer: Past, present and perspectives. *J. Appl. Biomed.* **13,** 79–103 (2015).
4. Florea, A.-M. & Büsselberg, D. Cisplatin as an anti-tumor drug: cellular mechanisms of activity, drug resistance and induced side effects. *Cancers (Basel).* **3,** 1351–71 (2011).
5. Rudnev, A. V, Aleksenko, S. S., Semenova, O., Hartinger, C. G., Timerbaev, A. R. & Keppler, B. K. Determination of binding constants and stoichiometries for platinum anticancer drugs and serum transport proteins by capillary electrophoresis using the Hummel-Dreyer method. *J. Sep. Sci.* **28,** 121–7 (2005).
6. Sooriyaarachchi, M., Narendran, A. & Gailer, J. Comparative hydrolysis and plasma protein binding of cis-platin and carboplatin in human plasma in vitro. *Metallomics* **3,** 49–55 (2011).
7. Ivanov, a I., Christodoulou, J., Parkinson, J. a, Barnham, K. J., Tucker, a, Woodrow, J. & Sadler, P. J. Cisplatin binding sites on human albumin. *J. Biol. Chem.* **273,** 14721–14730 (1998).
8. Ishida, S., Lee, J., Thiele, D. J. & Herskowitz, I. Uptake of the anticancer drug cisplatin mediated by the copper transporter Ctr1 in yeast and mammals. *Proc. Natl. Acad. Sci. U. S. A.* **99,** 14298–302 (2002).
9. Burger, H., Zoumaro-Djayoon, A., Boersma, A. W. M., Helleman, J., Berns, E. M. J. J., Mathijssen, R. H. J., Loos, W. J. & Wiemer, E. A. C. Differential transport of platinum compounds by the human organic cation transporter hOCT2 (hSLC22A2). *Br. J. Pharmacol.* **159,** 898–908 (2010).
10. Alderden, R. A., Hall, M. D. & Hambley, T. W. The Discovery and Development of Cisplatin. *J. Chem. Educ.* **83,** 728 (2006).
11. Boulikas, T., Pantos, A., Bellis, E. & Christofis, P. Designing platinum compounds in cancer: structures and mechanisms. **5,** (2007).
12. Kuo, M. T., Fu, S., Savaraj, N. & Chen, H. H. W. Role of the human high-affinity copper transporter in copper homeostasis regulation and cisplatin sensitivity in cancer chemotherapy. *Cancer Res.* **72,** 4616–21 (2012).
13. Leslie, E. M., Deeley, R. G. & Cole, S. P. C. Multidrug resistance proteins: role of P-glycoprotein, MRP1, MRP2, and BCRP (ABCG2) in tissue defense. *Toxicol. Appl. Pharmacol.* **204,** 216–37 (2005).
14. Komatsu, M., Sumizawa, T., Mutoh, M., Chen, Z. S., Terada, K., Furukawa, T., Yang, X. L., Gao, H., Miura, N., Sugiyama, T. & Akiyama, S. Copper-transporting P-type adenosine triphosphatase (ATP7B) is associated with cisplatin resistance. *Cancer Res.* **60,** 1312–6 (2000).

15. Niedermeyer, T. H. J. & Strohalm, M. mMass as a software tool for the annotation of cyclic peptide tandem mass spectra. *PLoS One* **7,** e44913 (2012).

16. Schebb, N. H., Faber, H., Maul, R., Heus, F., Kool, J., Irth, H. & Karst, U. Analysis of glutathione adducts of patulin by means of liquid chromatography (HPLC) with biochemical detection (BCD) and electrospray ionization tandem mass spectrometry (ESI-MS/MS). *Anal. Bioanal. Chem.* **394,** 1361–73 (2009).

17. Sasada, T., Nakamura, H., Ueda, S., Sato, N., Kitaoka, Y., Gon, Y., Takabayashi, A., Spyrou, G., Holmgren, A. & Yodoi, J. Possible involvement of thioredoxin reductase as well as thioredoxin in cellular sensitivity to cis-diamminedichloroplatinum (II). *Free Radic. Biol. Med.* **27,** 504–14 (1999).

18. Kartalou, M. & Essigmann, J. M. Mechanisms of resistance to cisplatin. *Mutat. Res.* **478,** 23–43 (2001).

19. Krezel, A. & Bal, W. Coordination chemistry of glutathione. *Acta Biochim. Pol.* **46,** 567–80 (1999).

20. Ishikawa, T. & Ali-Osman, F. Glutathione-associated cis-diamminedichloroplatinum(II) metabolism and ATP-dependent efflux from leukemia cells. Molecular characterization of glutathione-platinum complex and its biological significance. *J. Biol. Chem.* **268,** 20116–20125 (1993).

21. Kasherman, Y., Sturup, S. & Gibson, D. Is glutathione the major cellular target of cisplatin? A study of the interactions of cisplatin with cancer cell extracts. *J. Med. Chem.* **52,** 4319–28 (2009).

22. Circu, M. L. & Aw, T. Y. Glutathione and modulation of cell apoptosis. *Biochim. Biophys. Acta* **1823,** 1767–77 (2012).

23. Kuo, M. T., Chen, H. H. W., Song, I.-S., Savaraj, N. & Ishikawa, T. The roles of copper transporters in cisplatin resistance. *Cancer Metastasis Rev.* **26,** 71–83 (2007).

24. Santini, C., Pellei, M., Gandin, V., Porchia, M., Tisato, F. & Marzano, C. Advances in copper complexes as anticancer agents. *Chem. Rev.* **114,** 815–62 (2014).

25. Holzer, A. K., Manorek, G. H. & Howell, S. B. Contribution of the Major Copper Influx Transporter CTR1 to the Cellular Accumulation of Cisplatin, Carboplatin, and Oxaliplatin. *Mol. Pharmacol.* **70,** 1390–1394 (2006).

26. Wang, X., Du, X., Li, H., Chan, D. S.-B. & Sun, H. The effect of the extracellular domain of human copper transporter (hCTR1) on cisplatin activation. *Angew. Chem. Int. Ed. Engl.* **50,** 2706–11 (2011).

27. Marzano, C., Pellei, M., Tisato, F. & Santini, C. Copper complexes as anticancer agents. *Anticancer. Agents Med. Chem.* **9,** 185–211 (2009).

28. Sigman, D. S., Graham, D. R., D'Aurora, V. & Stern, A. M. Oxygen-dependent cleavage of DNA by the 1,10-phenanthroline . cuprous complex. Inhibition of Escherichia coli DNA polymerase I. *J. Biol. Chem.* **254,** 12269–72 (1979).

29. Cai, X., Pan, N. & Zou, G. Copper-1,10-phenanthroline-induced apoptosis in liver carcinoma Bel-7402 cells associates with copper overload, reactive oxygen species production, glutathione depletion and oxidative DNA damage. *Biometals* **20,** 1–11 (2007).

30. Pivetta, T., Isaia, F., Verani, G., Cannas, C., Serra, L., Castellano, C., Demartin, F., Pilla, F., Manca, M. & Pani, A. Mixed-1,10-phenanthroline-Cu(II) complexes: synthesis, cytotoxic activity versus hematological and solid tumor cells and complex formation equilibria with glutathione. *J. Inorg. Biochem.* **114,** 28–37 (2012).

31. Gracia-Mora, I., Ruiz-Ramírez, L., Gómez-Ruiz, C., Tinoco-Méndez, M., Márquez-Quiñones, A., Lira, L. R., Marín-Hernández, A., Macías-Rosales, L. & Bravo-Gómez, M. E. Knigth's Move in the Periodic Table, From Copper to Platinum, Novel Antitumor Mixed Chelate Copper Compounds, Casiopeinas, Evaluated by an in Vitro Human and Murine Cancer Cell Line Panel. *Met. Based. Drugs* **8,** 19–28 (2001).

32. Alemón-Medina, R., Breña-Valle, M., Muñoz-Sánchez, J. L., Gracia-Mora, M. I. & Ruiz-Azuara, L. Induction of oxidative damage by copper-based antineoplastic drugs (Casiopeínas). *Cancer Chemother. Pharmacol.* **60,** 219–28 (2007).

33. Carvallo-Chaigneau, F., Trejo-Solís, C., Gómez-Ruiz, C., Rodríguez-Aguilera, E., Macías-Rosales, L., Cortés-Barberena, E., Cedillo-Peláez, C., Gracia-Mora, I., Ruiz-Azuara, L., Madrid-Marina, V. & Constantino-Casas, F. Casiopeina III-ia induces apoptosis in HCT-15 cells in vitro through caspase-dependent mechanisms and has antitumor effect in vivo. *Biometals* **21,** 17–28 (2008).

34. Pivetta, T., Cannas, M. D., Demartin, F., Castellano, C., Vascellari, S., Verani, G. & Isaia, F. Synthesis, structural characterization, formation constants and in vitro cytotoxicity of phenanthroline and imidazolidine-2-thione copper(II) complexes. *J. Inorg. Biochem.* **105,** 329–38 (2011).

35. BLISS, C. I. THE TOXICITY OF POISONS APPLIED JOINTLY1. *Ann. Appl. Biol.* **26,** 585–615 (1939).

36. Webb, J. L. *Effect of more than one inhibitor*. *Enzymes and Metabolic Inhibitors* (Academic Press, 1961).

37. Pivetta, T., Isaia, F., Trudu, F., Pani, A., Manca, M., Perra, D., Amato, F. & Havel, J. Development and validation of a general approach to predict and quantify the synergism of anti-cancer drugs using experimental design and artificial neural networks. *Talanta* **115,** 84–93 (2013).

38. Massart, D. L., Vandeginste, B. G., Buydens, L. M. C., Lewi, P. J., Smeyers-Verbeke, J. & Jong, S. De. *Handbook of Chemometrics and Qualimetrics: Part A*. (Elsevier Science Inc., 1997).

Part II

Results and discussion

Chapter 1

Novel copper(II) complexes as new promising antitumour agents. A crystal structure of [Cu(1,10-phenanthroline-5,6-dione)$_2$(OH$_2$)(OClO$_3$)](ClO$_4$)

Journal of Inorganic Biochemistry 141 (2014) 103–113

Contents lists available at ScienceDirect

Journal of Inorganic Biochemistry

journal homepage: www.elsevier.com/locate/jinorgbio

Novel copper(II) complexes as new promising antitumour agents. A crystal structure of [Cu(1,10-phenanthroline-5,6-dione)$_2$(OH$_2$)(OClO$_3$)](ClO$_4$)

Tiziana Pivetta [a,*], Federica Trudu [a], Elisa Valletta [a], Francesco Isaia [a], Carlo Castellano [b], Francesco Demartin [b], Rossana Tuveri [c], Sarah Vascellari [c], Alessandra Pani [c]

[a] Dipartimento di Scienze Chimiche e Geologiche, University of Cagliari, Cittadella Universitaria, 09042 Monserrato, CA, Italy
[b] Dipartimento di Chimica, University of Milano, Via C. Golgi, 19-20133 Milano, Italy
[c] Dipartimento di Scienze Biomediche, University of Cagliari, Cittadella Universitaria, 09042 Monserrato, CA, Italy

ARTICLE INFO

Article history:
Received 13 May 2014
Received in revised form 22 August 2014
Accepted 24 August 2014
Available online 4 September 2014

Keywords:
Copper complexes
Cytotoxicity
Solution equilibria
Crystal structure
DNA binding

ABSTRACT

The cytotoxic properties of copper(II) complexes with 1,10-phenanthroline (phen) can be modified by substitution in the phen backbone. For this purpose, Cu(II) complexes with phen, 1,10-phenanthrolin-5,6-dione (phendione) and 1,10-phenanthrolin-5,6-diol (phendiol) have been synthesised and characterised. The crystal structure of [Cu(phendione)$_2$(OH$_2$)(OClO$_3$)](ClO$_4$) is discussed. The complex formation equilibria between Cu(II) and phen or phendione were studied by potentiometric measurements at 25 and 37 °C in 0.1 M ionic strength (NaCl). The antitumour activity of the compounds has been tested *in vitro* against a panel of tumour (DU-145, HEP-G2, SK-MES-1, CCRF-CEM, CCRF-SB) and normal (CRL-7065) human cell lines. The studied compounds generally present an antiproliferative effect greater than that of cisplatin. The phen and phendione ligands present a similar antiproliferative effect against all the tested cells. Phendiol presents an antiproliferative effect 1.3 to 18 times greater than that of phen or phendione for leukemic, lung, prostatic and fibroblast cells, while it presents less activity towards hepatic cells. Complexes with two ligands are more cytotoxic towards all the tested cell lines than complexes with one ligand and are generally more cytotoxic than the ligand alone. Complexes [Cu(phendiol)$_2$(OH$_2$)](ClO$_4$)$_2$ and [Cu(phendione)$_2$(OH$_2$)(OClO$_3$)](ClO$_4$) appear to be the most active compounds for the treatment of SK-MES-1 and HEP-G2 cells, respectively, being at least 18 times more cytotoxic than cisplatin. The studied Cu(II) complexes are characterised by a strong DNA affinity and were found to interact with DNA mainly by groove binding or electrostatic interactions. The complexes appear to act on cells with a mechanism different from that of cisplatin.

1. Introduction

Copper is a metal ion essential for aerobic microorganisms, plants and animals. It binds molecular oxygen in oxygen-transport proteins and participates in electron transport [1]. In the human body the copper concentration level is regulated by the homeostatic system. Copper has been selected for the synthesis of new antitumour drugs since complexes containing essential metal ions, thanks to the homeostatic regulatory system, may produce less systemic toxicity than complexes with exogenous metal ions. Copper(II) complexes with nitrogen ligands such as 1,10-phenanthroline (phen) show cytotoxic activity against a panel of human tumour cell lines [2–4]. Also complexes of 1,10-phenanthroline-5,6-dione (phendione) with copper(II) show interesting cytotoxic activity against human kidney adenocarcinoma and human hepatocellular carcinoma cell lines [5,6]. Many other phen derivatives, alone or in complexes, have been tested for antitumour activity towards human ovarian carcinoma, melanoma and breast, colon, ovarian, renal and non-small-cell lung cancers [7–10].

Being the DNA an important target for several cytotoxic agents, the interaction of metal complexes containing phenanthroline derivatives with DNA has also been studied. In fact, DNA offers multiple binding sites and modes for covalent and non-covalent interactions. Cisplatin binds covalently DNA [11], but most of the metal complexes bind DNA by non-covalent interactions, i.e. by intercalation, groove bindings, electrostatic forces and hydrogen bonds [12,13]. Some ruthenium complexes with phenanthroline ligands cleave DNA via a proton-coupled electron transfer mechanism [14]. The DNA-interaction modes can be studied by UV–visible (UV–vis) absorption study as the intercalation is associated with hypochromism and red shifting of the DNA adduct absorption bands, while groove binding and electrostatic interactions are associated with hyperchromism [15]. The cytotoxic properties and the DNA binding of copper(II) complexes with phen may be influenced also by the substituents eventually present on the phen backbone.

In this work, a new family of copper(II) complexes with phendione and 1,10-phenanthroline-5,6-diol (phendiol) has been synthesised

* Corresponding author. Tel./fax: +39 0706754473.
E-mail address: tpivetta@unica.it (T. Pivetta).

http://dx.doi.org/10.1016/j.jinorgbio.2014.08.011
0162-0134/

Abstract

Copper-based complexes have been selected for the synthesis of new antitumour agents on the assumption that complexes with essential metal ions, thanks to the homeostatic regulatory system, may be less toxic for normal cells than toward cancer cells. Copper(II) complexes containing 1,10-phenanthroline (**phen**) and its derivatives show antitumour activity against several human derived tumour cell lines. The antiproliferative activity and the DNA binding of these complexes can be also modified by substitution in the phen backbone. From these considerations and results, I decided to study the antitumour activity and the DNA affinity of a new family of copper(II) complexes with **phen**, 1,10-phenanthrolin-5,6-dione (**phendione**), and 1,10-phenanthrolin-5,6-diol (**phendiol**). This study is reported in Chapter 1 - Article I. The formulas, names and abbreviations of the studied ligands and complexes are reported in Figure 6 and Table 1.

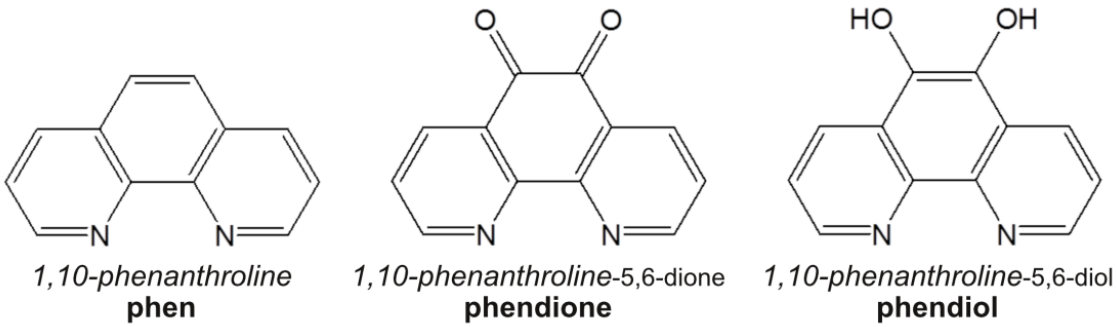

Figure 6. Formulas, names and abbreviations of the studied ligands.

The cytotoxic activity of the studied ligands and complexes have been tested[1] *in vitro* against a panel of tumour and normal human cell lines. It was found that the studied compounds present antitumour activity higher than that of cisplatin towards the human hepatocellular carcinoma

[1] In collaboration with professor Alessandra Pani (Dipartimento di Scienze Biomediche, Università degli Studi di Cagliari).

(HEP-G2), squamous cell lung carcinoma (SK-MES-1), human acute T-lymphoblastic leukaemia (CCRF-CEM), and human acute B-lymphoblastic leukaemia (CCRF-SB). In particular, **C0** and **K2** are promising for the treatment of SK-MES-1 and HEP-G2 cell line, respectively. These two complexes, in fact, show an IC_{50} value 37 and 18 times lower than that of cisplatin (Figure 7).

Compound	Abbreviations
$[Cu(phen)(OH_2)_2(OClO_3)_2]$	**C10**
$[Cu(phen)_2(OH_2)](ClO_4)_2$	**C0**
$[Cu(phendione)(OH_2)_2(ClO_4)_2]$	**K1**
$[Cu(phendione)_2(OH_2)(OClO_3)](ClO_4)$	**K2**
$[Cu(phendiol)(OH_2)_2(ClO_4)_2]$	**I1**
$[Cu(phendiol)_2(OH_2)](ClO_4)_2$	**I2**

Table 1. Formulas and abbreviations of the studied complexes.

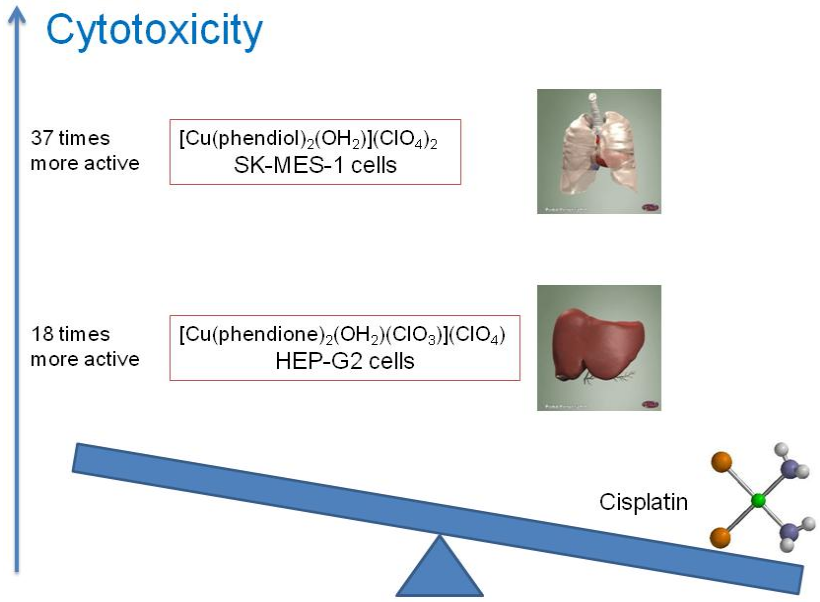

Figure 7. Comparison of the cytotoxic activity of $[Cu(phendiol)_2(OH_2)](ClO_4)_2$ (**I2**), $[Cu(phendione)_2(OH_2)(ClO_3)](ClO_4)$ (**K2**) and cisplatin against SK-MES-1 and HEP-G2 cell line.

The ligand cytotoxicity, although measured *in vitro*, appears related to the cellular microenvironment of the original organ, i.e. its lipophilicity or hydrophilicity. To discriminate the polarity and lipophilicity/hydrophilicity of the ligands, dipole moments in aqueous medium were calculated by quantomechanical calculations. It has been found that **phendiol**, the less lipophilic ligand, appears as the most active on cells surrounded by an hydrophilic environment, while **phendione,** the most lipophilic, is more effective against cells in a lipophilic environment (Figure 8).

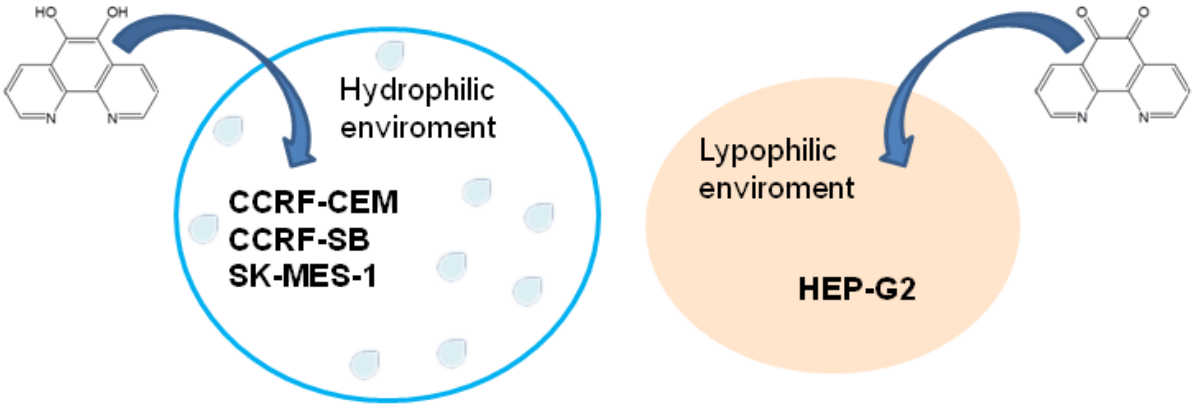

Figure 8. Relation between ligand cytotoxicity measured *in vitro* and cellular microenvironment (lipophilicity or hydrophilicity) of the original organ.

Considering that the DNA is an important target for several cytotoxic metal complexes, that can bind DNA by covalent or non-covalent interactions, the reactivity of Cu(II) complexes towards DNA has been studied by UV-vis spectroscopy. It has been found that the prepared complexes interact with DNA by groove binding or electrostatic interactions. The most important result was that the DNA binding constants resulted directly correlated with IC_{50} values and then inversely correlated with the antitumour activity (Figure 9). In fact, the complexes with the highest DNA affinity show the lowest antitumour activity. In particular, **C10**, that presents the highest DNA

binding constant, shows the lowest cytotoxicity, while **I2**, that presents the lowest DNA binding constant, shows the highest antitumour activity. This behavior can be explained assuming that the copper complexes exhibit their antiproliferative activity with mechanisms different from the DNA binding.

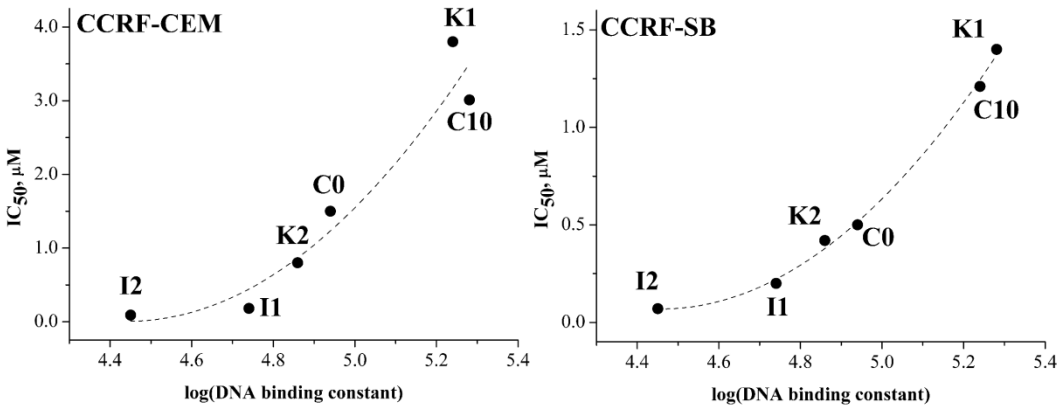

Figure 9. Trend of IC_{50} versus logarithm of the DNA-binding constant for CCRF-CEM (left) and CCRF-SB (right) cell lines.

Article I

Novel copper(II) complexes as new promising antitumour agents. A crystal structure of [Cu(1,10-phenanthroline-5,6-dione)$_2$(OH_2)($OClO_3$)](ClO_4)

Tiziana Pivetta, Federica Trudu, Elisa Valletta, Francesco Isaia, Carlo Castellano, Francesco Demartin, Rossana Tuveri, Sarah Vascellari, Alessandra Pani

Citation: Journal of Inorganic Biochemistry 141 (2014) 103–113

Cite this: DOI: 10.1016/j.jinorgbio.2014.08.011

Published by Elsevier

Journal of Inorganic Biochemistry 141 (2014) 103–113

Contents lists available at ScienceDirect

Journal of Inorganic Biochemistry

journal homepage: www.elsevier.com/locate/jinorgbio

Novel copper(II) complexes as new promising antitumour agents. A crystal structure of [Cu(1,10-phenanthroline-5,6-dione)$_2$(OH_2)($OClO_3$)](ClO_4)

Tiziana Pivetta [a,*], Federica Trudu [a], Elisa Valletta [a], Francesco Isaia [a], Carlo Castellano [b], Francesco Demartin [b], Rossana Tuveri [c], Sarah Vascellari [c], Alessandra Pani [c]

[a] Dipartimento di Scienze Chimiche e Geologiche, University of Cagliari, Cittadella Universitaria, 09042 Monserrato, CA, Italy
[b] Dipartimento di Chimica, University of Milano, Via C. Golgi, 19-20133 Milano, Italy
[c] Dipartimento di Scienze Biomediche, University of Cagliari, Cittadella Universitaria, 09042 Monserrato, CA, Italy

ARTICLE INFO

Article history:
Received 13 May 2014
Received in revised form 22 August 2014
Accepted 24 August 2014
Available online 4 September 2014

Keywords:
Copper complexes
Cytotoxicity
Solution equilibria
Crystal structure
DNA binding

ABSTRACT

The cytotoxic properties of copper(II) complexes with 1,10-phenanthroline (phen) can be modified by substitution in the phen backbone. For this purpose, Cu(II) complexes with phen, 1,10-phenanthrolin-5,6-dione (phendione) and 1,10-phenanthrolin-5,6-diol (phendiol) have been synthesised and characterised. The crystal structure of [Cu(phendione)$_2$(OH_2)($OClO_3$)](ClO_4) is discussed. The complex formation equilibria between Cu(II) and phen or phendione were studied by potentiometric measurements at 25 and 37 °C in 0.1 M ionic strength (NaCl). The antitumour activity of the compounds has been tested *in vitro* against a panel of tumour (DU-145, HEP-G2, SK-MES-1, CCRF-CEM, CCRF-SB) and normal (CRL-7065) human cell lines. The studied compounds generally present an antiproliferative effect greater than that of cisplatin. The phen and phendione ligands present a similar antiproliferative effect against all the tested cells. Phendiol presents an antiproliferative effect 1.3 to 18 times greater than that of phen or phendione for leukemic, lung, prostatic and fibroblast cells, while it presents less activity towards hepatic cells. Complexes with two ligands are more cytotoxic towards all the tested cell lines than complexes with one ligand and are generally more cytotoxic than the ligand alone. Complexes [Cu(phendiol)$_2$(OH_2)](ClO_4)$_2$ and [Cu(phendione)$_2$(OH_2)($OClO_3$)](ClO_4) appear to be the most active compounds for the treatment of SK-MES-1 and HEP-G2 cells, respectively, being at least 18 times more cytotoxic than cisplatin. The studied Cu(II) complexes are characterised by a strong DNA affinity and were found to interact with DNA mainly by groove binding or electrostatic interactions. The complexes appear to act on cells with a mechanism different from that of cisplatin.

1. Introduction

Copper is a metal ion essential for aerobic microorganisms, plants and animals. It binds molecular oxygen in oxygen-transport proteins and participates in electron transport [1]. In the human body the copper concentration level is regulated by the homeostatic system. Copper has been selected for the synthesis of new antitumour drugs since complexes containing essential metal ions, thanks to the homeostatic regulatory system, may produce less systemic toxicity than complexes with exogenous metal ions. Copper(II) complexes with nitrogen ligands such as 1,10-phenanthroline (phen) show cytotoxic activity against a panel of human tumour cell lines [2–4]. Also complexes of 1,10-phenanthroline-5,6-dione (phendione) with copper(II) show interesting cytotoxic activity against human kidney adenocarcinoma and human hepatocellular carcinoma cell lines [5,6]. Many other phen derivatives, alone or in complexes, have been tested for antitumour activity towards human ovarian carcinoma, melanoma and breast, colon, ovarian, renal and non-small-cell lung cancers [7–10].

Being the DNA an important target for several cytotoxic agents, the interaction of metal complexes containing phenanthroline derivatives with DNA has also been studied. In fact, DNA offers multiple binding sites and modes for covalent and non-covalent interactions. Cisplatin binds covalently DNA [11], but most of the metal complexes bind DNA by non-covalent interactions, i.e. by intercalation, groove bindings, electrostatic forces and hydrogen bonds [12,13]. Some ruthenium complexes with phenanthroline ligands cleave DNA via a proton-coupled electron transfer mechanism [14]. The DNA-interaction modes can be studied by UV–visible (UV–vis) absorption study as the intercalation is associated with hypochromism and red shifting of the DNA adduct absorption bands, while groove binding and electrostatic interactions are associated with hyperchromism [15]. The cytotoxic properties and the DNA binding of copper(II) complexes with phen may be influenced also by the substituents eventually present on the phen backbone.

In this work, a new family of copper(II) complexes with phendione and 1,10-phenanthroline-5,6-diol (phendiol) has been synthesised

* Corresponding author. Tel./fax: +39 0706754473.
E-mail address: tpivetta@unica.it (T. Pivetta).

http://dx.doi.org/10.1016/j.jinorgbio.2014.08.011
0162-0134/

and characterised by determining their chemical speciation in aqueous media, as well as their cytotoxicity and their DNA binding properties. Analogue series of complexes with phen was also prepared and studied for comparison.

2. Experimental section

2.1. Reagents

Calf thymus DNA sodium salt, chloridric acid standard solutions, copper(II) carbonate basic ($Cu_2(CO_3)(OH)_2$), copper(II) chloride, dichloromethane, dimethyl sulphoxyde (DMSO), dithiooxamide, ethanol, ethyl ether, ethylenediaminetetraacetic acid, isopropanol, nitric acid, petroleum ether, perchloric acid, 1,10-phenanthroline monohydrate, 1,4-piperazinediethanesulfonic acid (PIPES), potassium bromide, potassium hydroxide, sodium chloride, sodium hydroxide, sodium perchlorate, sodium sulphate anhydrous and sulphuric acid were purchased from Sigma-Aldrich and used without any further purification. Caution: perchlorate complexes are potentially explosive. Handle these compounds in small quantities with care.

2.2. Synthesis

2.2.1. Preparation of 1,10-phenanthroline-5,6-dione (phendione)

An ice-cold solution of concentrated HNO_3 (18 mL) and H_2SO_4 (35 mL) was added drop-wise to a mixture of phen (3.6 g, 18 mmol) and KBr (3.2 g, 27 mmol) in an ice bath (Scheme 1). The mixture was then refluxed until dark-red vapours disappeared (approx. 4 h). The light yellow solution was poured over 200 mL of ice and then neutralized by addition of a saturated solution of KOH. The presence of a white precipitate of inorganic salts was observed depending on solution concentration. The solids were filtered off and repeatedly washed with CH_2Cl_2. The desired product was extracted from the aqueous solution with fresh CH_2Cl_2. The extracted phases were combined with the portions of CH_2Cl_2 used for washing. The remaining water was removed with anhydrous Na_2SO_4. The yellow product phendione was recovered by solvent evaporation under vacuum. Yield 82%. I.R. selected bands (cm^{-1}): 2959, 2927, 2874 C–H stretching (broad, medium strong); 1688 C═O stretching (sharp, medium); 1567, 1461, 1415 C═C stretching (sharp, medium strong); and 813, 739, 623 C═C–H bending (sharp, medium). Elemental analysis: calc. C% 68.57, H% 2.88, N% 13.33, found C% 68.65, H% 2.92, and N% 13.36.

2.2.2. Preparation of 1,10-phenanthroline-5,6-diol (phendiol)

An ethanol solution (15 mL) of phendione (0.1 g, 0.48 mmol) and dithiooxamide (0.58 g, 0.48 mmol) was refluxed for 16 h. The resulting yellow solid was recovered by filtration, washed in sequence with ethanol, CH_2Cl_2 and petroleum ether and air dried. Yield 82%. I.R. selected bands (cm^{-1}): 2966, 2927, 2718, 2622 C–H stretching (broad, strong); 1575, 1497, 1426 C═C stretching (sharp, medium strong); and 806, 739, 629 C═C–H bending (sharp, medium). Elemental analysis: calc. C% 67.92, H% 3.80, N% 13.20, found C% 67.54, H% 3.84, N% 13.18.

2.2.3. Preparation of $Cu(phendione)(OH_2)_2(ClO_4)_2$ (K1)

Concentrated perchloric acid was added to an isopropanolic suspension of $Cu_2(CO_3)(OH)_2$ (0.110 g, 0.50 mmol of copper, 10 mL) warming under stirring till the complete dissolution of the salt was achieved. The light blue solution was cooled at room temperature and an isopropanolic solution of phendione (0.050 g, 0.24 mmol, 10 mL) was added drop-wise under stirring. The resulting light blue solution was left at room temperature and a light blue product was recovered after solvent evaporation. Yield 79%. I.R. selected bands (cm^{-1}): 3400 O–H stretching (broad, weak); 2955, 2927, 2853 C–H stretching (broad, weak); 1585, 1521, 1418 C═C stretching (sharp, medium strong); 1146, 1111, 1086 Cl–O stretching of coordinating perchlorate group (broad, very strong); 852, 717 C═C–H bending (sharp, medium strong), 627 C═C–H bending and OClO deforming (sharp, medium strong). Elemental analysis: calc. C% 28.33, H% 1.98, N% 5.51, found C% 29.22, H% 2.01, and N% 5.48.

2.2.4. Preparation of $[Cu(phendione)_2(OH_2)(OClO_3)](ClO_4)$ (K2)

Concentrated perchloric acid was added to an isopropanolic suspension of $Cu_2(CO_3)(OH)_2$ (0.044 g, 0.20 mmol of copper, 10 mL) warming under stirring till the complete dissolution of the salt was achieved. The light blue solution was cooled at room temperature and an isopropanolic solution of phendione (0.084 g, 0.40 mmol, 10 mL) was added drop-wise under stirring. The green precipitate of **K2** was filtered, washed with isopropanol and dried under vacuum. The solid was dissolved in ethanol and allowed to crystallise at room temperature. After four days green crystals suitable for X-ray analysis were recovered. Yield 81%. I.R. selected bands (cm^{-1}): 3450 O–H stretching (broad, weak); 2923, 2856 C–H

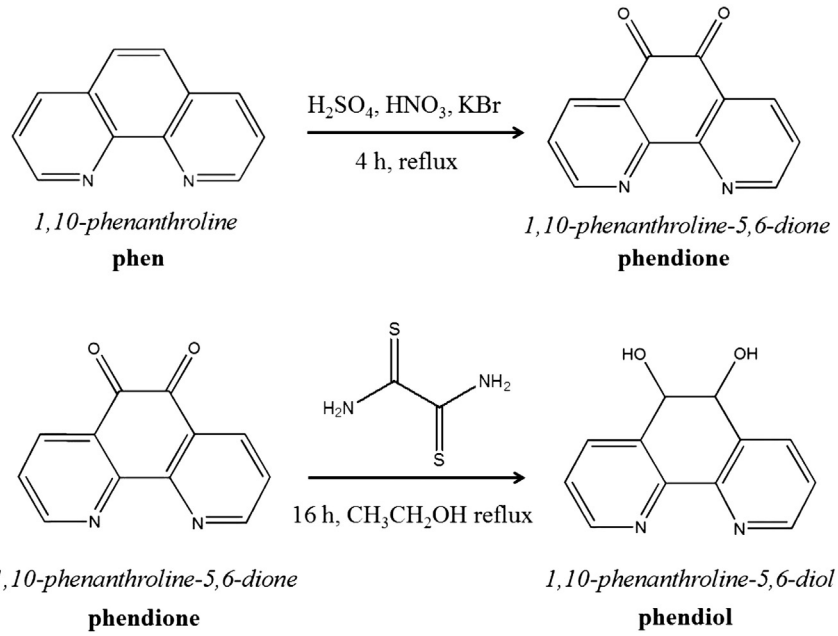

Scheme 1. Synthetic route for the preparation of 1,10-phenanthroline-5,6-dione (phendione) and 1,10-phenanthroline-5,6-diol (phendiol).

stretching (broad, weak); 1585, 1521, 1425 C═C stretching (sharp, medium); 1146, 1093 Cl – O stretching non coordinating perchlorate group (broad, very strong); 856, 725 C═C – H bending (sharp, medium strong), 625 C═C – H bending and OClO deforming (sharp, medium strong). Elemental analysis: calc. C% 41.13, H% 2.01, N% 7.99, found C% 41.44, H% 2.04, and N% 7.95.

2.2.5. Preparation of Cu(phendiol)$(OH_2)_2(ClO_4)_2$ (I1)

Concentrated perchloric acid was added to an isopropanolic suspension of $Cu_2(CO_3)(OH)_2$ (0.104 g, 0.47 mmol of copper, 10 mL) warming under stirring till the complete dissolution of the salt was achieved. The light blue solution was cooled at room temperature and an ethanolic suspension of phendiol (0.100 g, 0.47 mmol, 10 mL) was added. The dark green solution was refluxed for half an hour and cooled at room temperature. The dark green precipitate of **I1** was filtered under vacuum, washed with isopropanol and petroleum ether and air dried. Yield 46%. I.R. selected bands (cm^{-1}): 3400 O – H stretching (broad, strong); 3079, 2923, 2852 C – H stretching (broad, weak); 1086, 1070 Cl – O stretching of coordinating perchlorate group (broad, very strong); 834, 809, 718 C═C – H bending (sharp, medium strong), 626 C═C – H bending and OClO deforming (sharp, medium strong). Elemental analysis: calc. C% 28.22, H% 2.37, N% 5.49, found C% 28.78, H% 2.22, and N% 5.42.

2.2.6. Preparation of Cu(phendiol)$_2(OH_2)(ClO_4)_2$ (I2)

Concentrated perchloric acid was added to an isopropanolic suspension of $Cu_2(CO_3)(OH)_2$ (0.051 g, 0.23 mmol of copper, 10 mL) warming under stirring till the complete dissolution of the salt was achieved. The light blue solution was cooled at room temperature and an isopropanolic suspension of phendiol (0.098 g, 0.46 mmol, 10 mL) was added drop wise under stirring. The dark green product obtained was filtered under vacuum, washed with isopropanol, and air dried. Yield 75%. I.R. selected bands (cm^{-1}): 2958, 2930, 2874 C – H stretching (broad, medium); 1606, 1514, 1432 C═C stretching (medium broad, medium); 1117, 1090 Cl – O stretching non coordinating perchlorate group (broad, very strong); 820, 728 C═C – H bending (sharp, medium strong), 628 C═C – H bending and OClO deforming (sharp, medium strong). Elemental analysis: calc. C% 40.90, H% 2.57, N% 7.95, found C% 41.25, H% 2.66, and N% 7.99.

2.2.7. Preparation of [Cu(phen)$_2(OH_2)](ClO_4)_2$ (C0) and [Cu(phen)$(OH_2)_2(OClO_3)_2$] (C10)

The synthesis of **C0** and **C10** were previously reported [2].

2.3. Determination of the crystal structure of K2

$C_{24}H_{14}Cl_2CuN_4O_{13}$, M = 700.83 g/mol, orthorhombic, $a = 14.174(3)$, $b = 16.440(3)$, $c = 22.350(5)$ Å, $U = 5208(2)$ Å^3, $T = 293$ K, space group *Pbca* (no. 61), Z = 8, μ = (Mo–Kα) 1.125 mm^{-1}. 52,523 reflections (8383 unique; $R_{int} = 0.0282$) were collected at room temperature in the range $3.64° < 2\vartheta < 63.30°$, employing a $0.30 \times 0.15 \times 0.12$ mm crystal mounted on a Bruker APEX II CCD diffractometer and using graphite-monochromatized Mo–Kα radiation (λ = 0.71073 Å). Final *R1* [*wR2*] values are 0.0584 [0.2055] on $I > 2\sigma(I)$ (all data). Datasets were corrected for Lorentz polarization effects and for absorption (SADABS, Siemens Area-Detector ABSorption correction program, Bruker AXS Inc. Madison, WI, USA 2000). The structure was solved by direct methods [16] and was completed by iterative cycles of full-matrix least squares refinement on F_o^2 and ΔF synthesis using the SHELXL-97 [17,18]. Hydrogen atoms, with the exception of those of the water molecule, were located on the ΔF maps and allowed to ride on the carbon atoms of the phendione ligand. Crystallographic data for compound **K2** (excluding structure factors) have been deposited with the Cambridge Crystallographic Data Centre as supplementary publication no. CCDC-977445. These data can be obtained free of charge via www.ccdc.cam.ac.uk/conts/retrieving.html.

2.4. Biological assays

2.4.1. Compounds

Stock solutions of test compounds were prepared in DMSO at 100 mM and stored at 4 °C in the dark. For evaluation of the cytotoxicity, stocks were serially diluted in the growth media specific for each cell line. In all experiments, the highest concentration of DMSO on cells was 0.1%, corresponding to the maximum non-toxic dose of DMSO for all cell lines.

2.4.2. Cell lines

All cell lines used in this study were purchased from the American Type Culture Collection (ATCC, USA), and were stored in aliquots in liquid nitrogen between the third to the fourth passage in culture. Cell lines derived from human lung squamous carcinoma (SK-MES-1), human prostate carcinoma (DU-145), and human hepatocellular carcinoma (Hep-G2), were used as representative cells of solid cancers. Human acute T-lymphoblastic leukaemia (CCRF-CEM) and human acute B-lymphoblastic leukaemia (CCRF-SB) cell lines were used as representative cells of hematologic tumours. A cell line established from human normal skin fibroblasts (CRL-7065) was used as a control cell line to determine the degree of selectivity of each compound towards neoplastic cells. All cell lines were cultured at 37 °C in a 5% CO_2 atmosphere in their specific media according to ATCC instructions, with 5–10% foetal bovine serum (FBS), antibiotic, and, unless otherwise indicated, sodium pyruvate. Cell cultures were maintained in exponential growth by periodically (one to two times/week) diluting high density non-adherent cells (i.e. 10^6 cell/mL), or when monolayers of adherent cells reached sub-confluency (70–90% confluence). All cell lines were replaced every three–four months by freshly thawed cells from liquid nitrogen collections. The absence of mycoplasma contamination was checked periodically by the Hoechst staining method [19].

2.4.3. Cytotoxic assays

The cytotoxic effect of test compounds was evaluated in exponentially growing cells. For adherent cells (i.e. SK-MES, DU-145, Hep-G2, CRL-7065), 100 μL of cell suspensions at a density of 5×10^4 cells/mL was seeded in each well of 96-well flat bottomed plates. Cell cultures were incubated overnight before the addition of 100 μL of growth medium (controls) or of 2× the final concentrations of test compounds (four replicates/concentration). For non-adherent cells (i.e. CCRF-CEM and CCRF-SB), 100 μL of cell suspensions at a density of 1×10^5 cells/mL was seeded in 96-well flat bottomed plates, and equal volumes of growth medium (controls) or of 2× the final concentrations of each compound (four replicates/concentration) were immediately added. Cell viability was determined after 96 h (approximately three to four cell divisions) of incubation at 37 °C, 5% CO_2, by the 3-(4,5-dimethylthiazol-2-yl)-2,5-diphenyl-tetrazolium bromide (MTT) method as previously described [20]. Cisplatin was used as reference drug [21–23]. The extent of cell viability at each drug concentration tested was expressed as percentage of untreated controls. Dose–response curves and concentrations resulting in 50% of cell viability of cells, compared to the controls, were determined for each compound by non-linear curve fitting. All data reported represent the mean values ± SD of three to four independent experiments.

2.5. DNA binding

The binding constants (K_b) between ct-DNA and the phen, phendione and Cu(II) complexes were determined at 25 °C by spectrophotometric titrations with ct-DNA, in PIPES buffer 0.01 M at pH 7.0. The UV–vis measurements were carried out on an Agilent Cary 60 spectrometer equipped with a fibre optic dip probe (1 cm path length). A stock solution of ct-DNA in 0.01 M PIPES buffer at pH 7.0 was stored at 4 °C and used within four days. The concentration of DNA per nucleotide was determined by UV absorption at 260 nm using its molar absorption

coefficient (6600 M^{-1} cm^{-1}) [24]. The purity of the DNA was checked by monitoring the ratio of the absorbance at 260 nm to that at 280 nm. A ratio higher than 1.8 indicated a DNA sufficiently protein-free [25].

Two sets of solutions were prepared: i) thirty solutions containing a fixed amount of ligand or metal complex (ranging from $\approx 1.5 \times 10^{-6}$ to $\approx 8 \times 10^{-5}$ mmol, according to compound absorptivity) and variable amounts of DNA (ranging from 4.5×10^{-5} to 2.4×10^{-4} mmol, DNA/complex molar ratio from 0 to 3); ii) twenty solutions containing a fixed amount of ligand or metal complex (ranging from $\approx 6.5 \times 10^{-6}$ to $\approx 3.6 \times 10^{-5}$ mmol, according to compound absorptivity) and variable amounts of DNA (ranging from 6.5×10^{-5} to 3.6×10^{-4} mmol, DNA/complex molar ratio from 0 to 10). All the solutions were stored in the dark at room temperature. The hydrolysis of the copper complexes as well as the interaction between DNA and ligands were slow processes. Therefore, spectra in the 200–400 nm range were recorded after equilibration was reached. This was checked spectrophotometrically, by determining the time after which further changes in UV–vis spectra were not observed (≈15 h).

The number of linearly independent absorbing species was obtained by applying the eigenvalues analysis on the absorbance data matrix [26,27]. Binding constants were obtained by using the Hyperquad 2003 program [28].

2.6. Potentiometric study

Potentiometric titrations were carried out in a thermostatted vessel with a Mettler-Toledo Seven Compact pH/Ion-meter equipped with a Mettler-Toledo InLab Micro Pro combined glass electrode with an integrated temperature probe. Potentiometric titrations were performed at 25 and 37 °C in 0.1 M ionic strength (NaCl) under N_2 atmosphere. The glass electrode was calibrated daily by titration of a known amount of HCl with carbonate-free NaOH solution prepared according to Albert [29]. Electrode standard potential (E^0), water ionic product (pK_w), electrode response and carbonate content of the titrant solution were checked with Gran's procedure [30] using the Glee program [31].

The copper(II) stock solution was prepared by dissolving the proper amount of $CuCl_2$ salt in 0.01 M HCl aqueous solution (pH ≈ 2, copper(II) concentration $\approx 5 \times 10^{-3}$ M). The metal content was determined by titration with EDTA [32]. A solution of phendione was prepared daily by dissolving the proper amount of the compound in freshly distilled water (concentration of phendione $\approx 4 \times 10^{-3}$ M). Due to its low water solubility, phen (≈0.03 g) was dissolved in 20 μL of DMSO. The resulting solution was diluted with freshly distilled water up to 20 mL. The mixing of the two solvents was favoured by gentle shaking and heating (avoiding sonication to prevent emulsion formation). For the potentiometric titration, approx. 3 mL of this stock solution was diluted up to 20 mL with aqueous solution, so that the DMSO content in the titration vessel was never higher than 0.015% (final concentration of phen $\approx 5 \times 10^{-3}$ M).

Ligand protonation constants were determined by titrating solutions containing a known amount of ligand and three (for phen) or five (for phendione) equivalents of HCl per mole of ligand. Complex formation constants between phen or phendione with Cu(II) were determined by titrating solutions with 3:1, 2:1 and 1:1 ligand:metal molar ratios. The hydrolysis of the metal ion was studied at 1.0×10^{-3} M, 5.0×10^{-4} M and 3.3×10^{-4} M concentrations. The reversibility of all the studied equilibria was checked by back-titration with standard HCl. The overall stability constants were determined with the Hyperquad2003 program [28].

2.7. Computation

The quantomechanical calculations were performed on a dual core INTEL i-7 CPU with the "SPARTAN'06" program for Windows (Wavefunction Inc); geometries were optimized using ab-initio methods with 6–31G^{++} Gaussian basis sets [33,34]; dipole moments were calculated using semi-empirical methods with AM1/SM2 basis sets [35].

3. Results and discussion

3.1. Synthesis

The ligands phendione and phendiol were synthesised (Scheme 1) by slight modifications of previously reported syntheses [36,37]. A less toxic solvent was preferred for the extraction and washing steps. Compound phendiol is slightly soluble in the most common solvents such as CH_3CN, CH_2Cl_2, DMSO, dimethylformamide, ethanol, isopropanol, petroleum ether and water. Despite the presence of two hydroxyl groups, its solubility in polar solvents is reduced due to the formation of polymers. Phendiol is water soluble at basic pH but is rapidly and irreversibly oxidised.

Complexes Cu(phen)$(OH_2)_2(ClO_4)_2$ (**K1**), [Cu(phendione)$_2(OH_2)(OClO_3)](ClO_4)$ (**K2**), Cu(phendione)$(OH_2)_2(ClO_4)_2$ (**I1**), and Cu(phendione)$_2(OH_2)(ClO_4)_2$ (**I2**) are novel. No polynuclear complexes with phendione or phendiol were obtained, not even in an excess of Cu(II) salt. All the complexes are stable in the solid state at room temperature. Suspensions of **I1** and **I2** are stable in the dark at 4 °C for one week. In compounds **K1** and **I1**, one ligand is present like in **C10**, while two ligands are present in compound **I2**, as in **C0**. The I.R. spectra of **K1** and **I1** show the signals of coordinating perchlorate groups, while the I.R. spectrum of **I2** shows the signals of uncoordinated perchlorate groups. By analogy with the reported structures of **C10** and **C0** [2], the molecular formulas [Cu(phendione)$(OH_2)_2(OClO_3)_2$], [Cu(phendiol)$(OH_2)_2(OClO_3)_2$] and [Cu(phendiol)$_2(OH_2)](ClO_4)_2$ for **K1**, **I1** and **I2** are proposed.

3.2. Crystal structure

The asymmetric unit of **K2** contains Cu(phendione)$_2(OH_2)(OClO_3)^+$ cations with the copper atoms in a distorted tetragonal bypiramidal coordination and an additional perchlorate anion (Fig. 1). Selected bond lengths and angles are reported in Table 1. The Cu – O_2 distance in the perchlorate coordinated at the apical position is longer than typical Cu – O bond lengths of about 1.95 Å, but lies in the 2.3–2.8 Å range observed for complexes with Jahn–Teller distortion (mean axial Cu – O bond lengths for Jahn–Teller distorted complexes are about 2.48 Å). The axially-coordinated perchlorate displays an additional intramolecular hydrogen bond with the equatorial water molecule [O4···Ow 3.076(9) Å]. The other perchlorate interacts with the water molecule only through an intramolecular hydrogen bond O8···Ow of 2.698(8) Å. No other interactions below the sum of the van der Waals radii are observed. One of the two phendione ligands occupies two equatorial positions of the octahedron with atoms N1 and N2, whereas the other one is coordinated at one equatorial position through N4 and at one apical position through N3. The copper atom is about 0.20 Å displaced from the average coordination plane defined by atoms N1, N2, N4 and Ow, towards the apical position N3. The dihedral angle between the two nitrogen ligands is 78.6°. A comparison can be done with the structure of the similar complex [Cu(phen)$_2(H_2O)](ClO_4)_2$ [2,38], where instead the coordination of the copper ion is closer to a trigonal bipyramidal geometry and no perchlorate anion interacts with the metal ion. With respect to this compound the Cu – Ow distance is definitely shorter in our case (2.026(3) Å vs. 2.245(4) Å), whereas the Cu – N distances are larger [range 2.003(2)–2.187(3) 1.993(2) Å vs. 1.980(4)–2.032(3) Å)]. A structure similar to that of **K2** was reported for [Co(phendione)$_2Cl_2$]Cl where the central Co(III) ion is hexacoordinated with distorted octahedral geometry. The mean Co – N bond length is 1.944(3) Å which is shorter than the Cu – N bond length in **K2** [39]. Differently, in the crystal structures of [Cu(phendione)$_2(NO_3)]NO_3 \cdot CH_3CN$ or [Cu(phendione)$_2$Br]Br$\cdot 2CH_3CN$, the copper ion is coordinated by two phendione

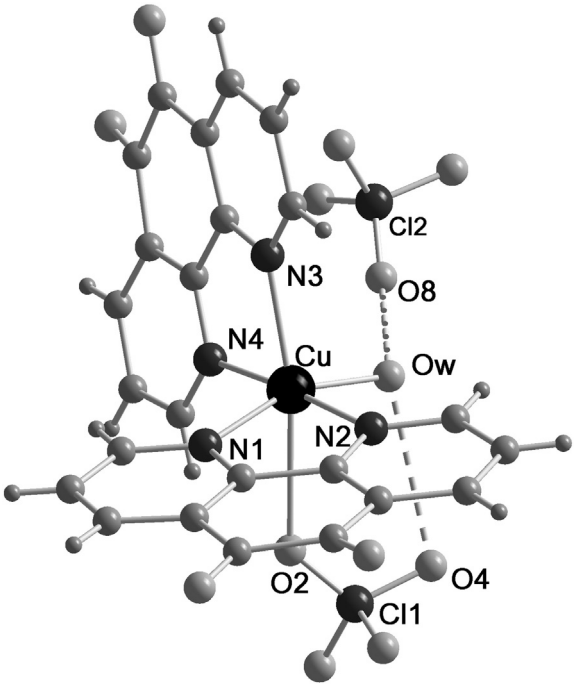

Fig. 1. Crystal structure of **K2** complex.

molecules and a nitrate or a bromide ligand in a distorted trigonal bipyramidal geometry [40]. An example of crystal structure of a metal complex with phendiol is [(di-tert-butylbipyridine)$_2$Ru(phendiol)Pt(di-tert-butylbipyridine)](PF$_6$)$_2$, where phendiol molecule acts as a linker between Ru(di-tert-butylbipyridine)$_2$- and Pt(di-tert-butylbipyridine)-units [37].

3.3. Dipole moments of ligands

The low water solubility of phendiol prevents accurate determination of its octanol/water partition coefficient. Thus, to discriminate the polarity and lipophilicity/hydrophilicity of the ligands, dipole moments in aqueous medium were calculated by quantum mechanical calculations. The calculated dipole moments for the three ligands are in the following order: phendiol (3.52 Debye) > phen (3.42 Debye) > phendione (3.11 Debye).

Table 1
Selected bond lengths (Å) and angles (deg) for **K2**. In parenthesis the standard deviation on the last significant figure is reported.

Atom1	Atom2	Length
Cu	N1	2.040 (2)
Cu	N2	2.003 (2)
Cu	N3	2.187 (3)
Cu	N4	2.019 (2)
Cu	OW	2.026 (3)
Cu	O2	2.667 (4)

Atom1	Atom2	Atom3	Angle
N1	Cu	N2	81.6 (1)
N1	Cu	N3	101.28 (9)
N1	Cu	N4	97.7 (1)
N1	Cu	OW	160.2 (1)
N1	Cu	O2	77.0 (1)
N2	Cu	N3	106.11 (9)
N2	Cu	N4	175.4 (1)
N2	Cu	OW	89.9 (1)
N2	Cu	O2	85.9 (1)
N3	Cu	N4	78.5 (1)
N3	Cu	OW	98.2 (1)
N3	Cu	O2	167.6 (1)
N4	Cu	OW	89.3 (1)
N4	Cu	O2	89.5 (1)
OW	Cu	O2	84.6 (1)

Table 2
Antiproliferative activity of the test compounds against six different cell lines. The standard deviation on the last significant figure is given in parentheses.

Compound	IC$_{50}$[a] (μM)					
	CRL-7065[b]	DU-145[c]	HEP-G2[d]	SK-MES-1[e]	CCRF-CEM[f]	CCRF-SB[g]
Phen	2.3 (1)	2.30 (5)	1.7 (2)	2.60 (4)	2.70 (2)	1.20 (1)
Phendione	1.90 (2)	2.16 (2)	1.60 (2)	1.90 (1)	2.90 (1)	0.95 (1)
Phendiol	1.80 (2)	0.79 (1)	2.90 (1)	0.47 (1)	0.15 (1)	0.145 (4)
C10	>5	2.6[i]	2.90 (3)	1.9[j]	3.2[j]	1.4[i]
K1	6.30 (1)	4.10 (1)	1.70 (2)	3.10 (1)	3.80 (2)	1.21 (1)
I1	3.10 (1)	4.00 (2)	3.60 (1)	2.25 (2)	0.18 (1)	0.20 (1)
C0	2.20 (3)	1.6[i]	1.05 (1)	0.93[i]	1.25[i]	0.50[i]
K2	2.47 (2)	1.16 (2)	0.67 (2)	1.20 (1)	0.80 (2)	0.42 (1)
I2	1.34 (3)	0.93 (1)	1.20 (1)	0.54 (1)	0.090 (4)	0.070 (3)
6-MP[h]	–	2.0 (1)	–	> 100	2.0 (2)	0.70 (8)
Cisplatin	–	2.0[k]	12.0[l]	20.0[m]	0.95	1.38

[a] compound concentration required to reduce the viability by 50%, as determined by the MTT method.
[b] CRL-7065 skin fibroblasts.
[c] DU-145 human prostate carcinoma.
[d] HEP-G2 human hepatocellular carcinoma.
[e] SK-MES-1 squamous cell lung carcinoma.
[f] CCRF-CEM human acute T-lymphoblastic leukaemia.
[g] CCRF-SB human acute B-lymphoblastic leukaemia.
[h] 6-MP 6-mercaptopurine.
[i] From Ref. [2].
[j] From Ref. [4].
[k] from Ref. [21].
[l] From Ref. [22].
[m] From Ref. [23]. Values represent the mean ± SD of at least three independent experiments.

3.4. Cytotoxic activities

The antiproliferative activities of the studied ligands and complexes are expressed as IC$_{50}$, i.e. the concentration of compound required to reduce the viability of the tested cells by 50% (Table 2).

3.4.1. Phen, phendione and phendiol ligands

The phen and phendione ligands present very similar antiproliferative effects against all the tested cells (Fig. 2). For phen the IC$_{50}$ value ranges from 1.20 to 2.70 μM, while for phendione it ranges from 0.95 to 2.90 μM. Both compounds are more active against CCRF-SB leukemic cells. The phendiol compound presents an antiproliferative effect from 1.3 to 18 times greater than that of phen or phendione for leukemic, lung, prostatic and fibroblast cells, while it presents less activity towards hepatic cells. The cellular microenvironment appears related to the cytotoxicity shown by the ligands. In fact, their different activities on solid and/or haematological cancer cells can be explained in terms of the lipophilicity or hydrophilicity of the compound and the target cells.

The tested cells are derived from human organs characterised by different physical–chemical conditions. In prostate, blood and lungs the microenvironment is mainly hydrophilic while in liver and fibroblasts it is mainly lipophilic.[1] However, the phenotype, metabolic reactions and

[1] Prostatic cells produce a slightly acidic solution containing citric acid, spermine and spermidine, acid phosphatase, protease serum, prostate-specific antigen, calcium, zinc, sodium and dihydrotestosterone. Liver is involved with carbohydrate and lipid metabolism, cholesterol synthesis and triglyceride production. Plasma (55 % of blood fluid) contains water, dissipated proteins, glucose, mineral ions, hormones, and blood cells themselves. Lungs, involved in the CO_2/O_2 exchange, contain blood and aqueous vapour. Fibroblasts produce collagen, glycosaminoglycan, fibres and glycoproteins that are constituents of the extracellular material.

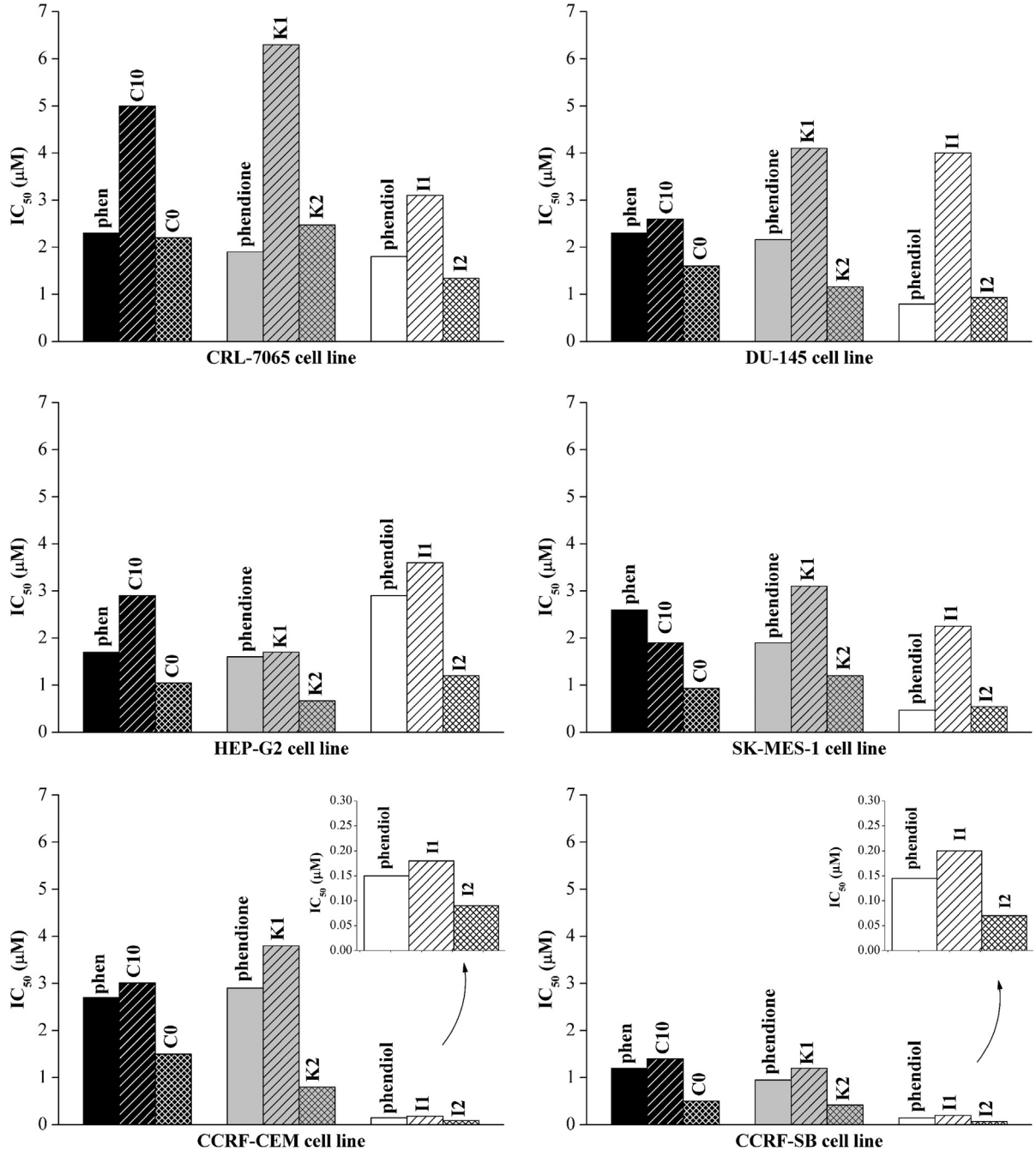

Fig. 2. Doses (IC_{50} values, μM) of the studied complexes required to reduce the viability by 50%, as determined by the MTT method. CRL-7065 skin fibroblasts; DU-145 human prostate carcinoma; HEP-G2 human hepatocellular carcinoma; SK-MES-1 squamous cell lung carcinoma; CCRF-CEM human acute T-lymphoblastic leukaemia; CCRF-SB: human acute B-lymphoblastic leukaemia.

gene expression patterns of the original organ may not be preserved in cultured cells. In our case, the experimental results, i.e. the different activities shown by the ligands, indicate that microenvironmental conditions in the cell lines reflect those of the original organ from which they were derived. This phenomenon has also been observed in other studies, for example in terms of pH and vacuolar-H-ATPase expression [41]. The less lipophilic ligand, phendiol, is preferentially active against cells in a hydrophilic environment, while the most lipophilic ligand phendione is more effective than phendiol against cells in a lipophilic one.

3.4.2. Copper(II) complexes

The cytotoxicity of the studied copper(II) complexes (Fig. 2) is mainly due to the presence of the nitrogen containing ligands, the metal ion being devoid of relevant antiproliferative activity (IC_{50} > 100 μM). Complexes with one ligand (**C10**, **K1** and **I1**) exhibit an antiproliferative activity generally lower than that of the ligand alone (phen, phendione and phendiol, respectively) on all tested cell lines. The **C10**, **K1** and **I1** compounds present the highest cytotoxic activity against CCRF-SB cells and the lowest towards CRL-7065 and DU-145 cells. Complexes with two ligands (**C0**, **K2** and **I2**) are more cytotoxic towards all the tested cell lines than the related complexes with one ligand (**C10**, **K1** and **I1**, respectively) and are generally more cytotoxic than the ligand alone (phen, phendione and phendiol, respectively). The **C0**, **K2** and **I2** compounds present the highest cytotoxic activity against CCRF-SB and the lowest towards CRL-7065 cells.

Although it is not possible to make a direct comparison between the antiproliferative activities against normal and cancerous cells that belong to different lineages, the parallel could be useful in estimating the possible selectivity of a compound, i.e. the ability of the drug to discriminate between normal and cancerous cells. The potential selectivity, calculated with respect to the normal fibroblasts, varies from 1.7 to 3.6 for **C10**, from 1.4 to 4.4 for **C0**, from 1.5 to 5.2 for **K1**, from 2.1 to 5.9 for **K2**, from 0.78 to 17.2 for **I1** and from 1.1 to 19.1 for **I2**. From all these results **I2** appears as the most active compound for the treatment of leukemic (CCRF-CEM and CCRF-SB), lung (SK-MES-1) and prostatic (DU-145) cancer cells, while **K2** is eligible for the treatment of hepatic (HEP-G2) ones.

3.5. DNA binding constants

The intrinsic binding constants of the adducts formed by ct-DNA and the studied compounds were evaluated by spectrophotometric titrations. The binding constants of phendiol were not studied because of the poor solubility of the ligand in PIPES. The UV–vis spectra of the synthesised copper(II) complexes exhibit bands at ≈800 nm (d–d transitions, $\varepsilon \approx 100\ M^{-1}\ cm^{-1}$) and at ≈270 nm (ligand-to-metal charge transfer (LMCT) transitions, $\varepsilon \approx 50{,}000\ M^{-1}\ cm^{-1}$). Due to the low absorption at 800 nm, only the changes in the LMCT bands were followed during the titrations with DNA. In the absorbance spectra of **C10**, **K1** and **C0** two peaks (at ≈ 225 and 275 nm) and a shoulder (at ≈ 295 nm) are present. In the spectrum of **K2** two pairs of overlapping peaks (at 260 and 272 nm and at 226 and 232 nm) and a shoulder (at 295 nm) are evident.

In the absorbance spectrum of **I1** a wide band is present at 267 nm and, finally, in the spectrum of **I2** two partially overlapping bands are present at 258 and 280 nm. The UV spectra of phen and phendione show peaks at 266 nm and 254 nm, respectively.

By titrating the ligands and Cu(II) compounds with DNA, the following trends were shown:

- the absorbance increases without a significant shift in the maximum wavelength for phen and phendione;
- for DNA:Cu(II) molar ratios in 0–3 range:
  - o the absorbance increases without a significant shift in the maximum wavelength for **C10**, **K1**, **K2** and **I2**;
  - o the absorbance increases with a significant shift in the maximum wavelength for **I1** (from 267 to 259 nm);
  - o the absorbance decreases without a significant shift in the maximum wavelength for **C0**;
- for Cu(II):DNA molar ratios > 3:
  - o the absorbance increases with a significant shift in the maximum wavelength for all the complexes (from ≈270 to 260 nm).

Selected spectra recorded during the titrations are reported in Supporting Information (Fig. S1).

For the studied systems, hyperchromism is evident for all the compounds except for **C0**. However, the extent of the hyperchromism/hypochromism noted and the shift towards higher wavelengths is affected by the presence of excess DNA, whose spectrum is characterised by a wide band centred at 260 nm. For this reason direct inspection of the experimental spectra to determine if hyper- or hypochromism is really present may lead to inaccurate results. Therefore, to assign the correct interaction mode, the pure spectra of the involved species were compared.

From eigenvalue analysis of spectrophotometric data, three significant eigenvalues were found. These can be interpreted as the number of linearly independent absorbing species [27]. In our case, such species are the free DNA, the free ligand or copper complex, and the related DNA adduct. The absorbance data were fitted supposing a model taking into account the 1:1 DNA:ligand or DNA:copper complex adduct, and the pure spectra of all the absorbing species were calculated (Fig. 3). The obtained absorptivity spectra show hyperchromism in all the titrations, suggesting that ligands and complexes interact with DNA principally by groove binding or electrostatic interaction. A blue shift in the absorbance maximum is revealed for **K2** (from 272 nm to 261 nm), while for the other complexes no significant shift is evident (Table 3).

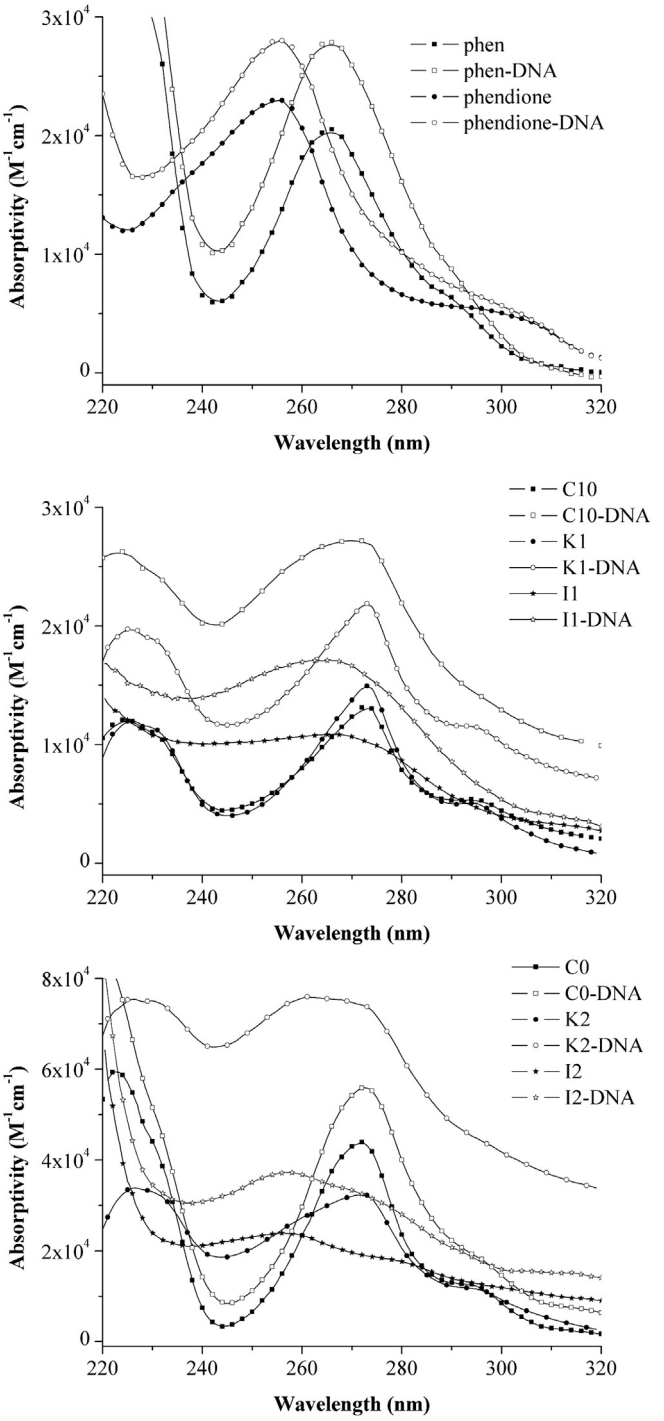

Fig. 3. Absorptivity spectra of adducts formed between DNA and the studied compounds (25 °C, 0.01 M PIPES buffer, pH = 7.0).

The extent of the hyperchromism is related to the kind of DNA interaction [42,43] and varies along the series: **K2**–DNA (135%) > **C10**–DNA (108%) > **I1**–DNA (58%) ≈ **I2**–DNA (56%) > **K1**–DNA (47%) > phen (36%) > **C0**–DNA (28%) > phendione (22%). In particular, **K2** and **C10** present the highest DNA affinity through groove binding or electrostatic interaction, while **I2**, **K1** and **I1** exhibit lower affinities. The high

Table 3
DNA binding constants and spectral data for the studied compounds (25 °C, in PIPES buffer 0.01 M, pH = 7.0).

Compound	DNA binding constants (M^{-1})	λ_{max} (nm)	ε_{max} (M^{-1} L^{-1})	Ref.
Phen	–	266	20,524	This work
Phen–DNA	2.29 (1) × 10^6	266	27,861	"
Phendione	–	256	22,975	"
phendione–DNA	7.76 (1) × 10^4	256	28,019	"
C10	–	272	13,114	"
C10–DNA	1.9 (1) × 10^5	270	27,236	"
K1	–	273	14,943	"
K1–DNA	1.8 (2) × 10^5	273	21,902	"
I1	–	267	10,876	"
I1–DNA	5.5 (1) × 10^4	263	17,145	"
C0	–	273	43,916	"
C0–DNA	8.3 (1) × 10^4	273	56,432	"
K2	–	272	32,373	"
K2–DNA	7.2 (1) × 10^4	261	75,980	"
I2	–	256	23,901	"
I2–DNA	2.8 (1) × 10^4	258	37,329	"
$[Cu(phen)_2$(branched polyethyleneimine)$]Cl_2 4H_2O$	5.95 × 10^5	–	–	[49]
$Cu(phen)_2Cl_2$	2.75 × 10^3	–	–	[50]
$Cu_2(phen)_2Cl_4$	4.79 × 10^4	–	–	[51]
[Cu(L-phenylalanine) (phen)$(H_2O)](NO_3)$	3.6 (1) × 10^5	–	–	[52]

hyperchromism shown by **C10** and **K2** suggests that these complexes do not intercalate or intercalate just partially. This is in agreement with the results reported by Chikira and co-workers [44] for **C10**. The low percentage of hyperchromism shown for phen and phendione is due to their ability to intercalate. The low hyperchromism shown by **C0** could be due to a possible partial DNA intercalation. In fact, it has been reported that bis(1,10-phenanthroline) copper(II) complexes apparently bind to DNA by intercalation but the correct binding mode is still controversial [45,46]. Furthermore, in the copper(I) complex $[Cu(phen)_2]^+$ the phen ligands are roughly perpendicular to each other, so complete intercalation of the phen ring between a set of adjacent base pairs is sterically impossible, but some type of partial intercalation involving one of the ligands can be presumed [47]. Similar considerations may also be proposed for **C0**, $[Cu(phen)_2(OH_2)]^{2+}$, where a trigonal bypiramidal coordination around Cu(II) is present. It is worthwhile remarking that the action of the $[Cu(phen)_2(OH_2)]^{2+}$ complex on DNA, besides intercalation, is due to an oxidative attack on the deoxyribose units that cleaves the DNA strand leading to cell death [48].

The magnitude of the DNA binding constants is related to the strength of the interaction, independently of the binding mode. The calculated constants (Table 3) vary along the series: **C10**–DNA ≈ **K1**–DNA > **I1**–DNA > **C0**–DNA > **K2**–DNA > **I2**–DNA. The obtained values are in agreement with binding constants reported in the literature for similar compounds [49–52].

The DNA binding constants for the studied copper(II) complexes appear directly correlated with the IC_{50} values and then inversely correlated to the cytotoxic activity. This behaviour is particularly relevant on the CCRF-CEM and CCRF-SB cell lines (Fig. 4). As can be seen, **C10** presents the highest DNA binding constant but the lowest antiproliferative activity, while **I2** presents the lowest binding constant and the highest biological activity. These results indicate that different reaction mechanisms with respect to DNA-binding are responsible for the anticancer activities of these complexes.

3.6. Potentiometric measurements

The protonation constants of phendiol and the complex formation constants of the phendiol-copper(II) system were not studied because of the poor solubility of the ligand in water or in water-DMSO solution (less than 1 × 10^{-5} M).

3.6.1. Protonation constants of phen and phendione

At acidic pH all the nitrogen and oxygen atoms of the ligands may hypothetically be protonated. Actually, in the 2–11 pH range only one protonation equilibrium was in evidence during the potentiometric titration. The protonation of the second nitrogen atom of phen and phendione and also that of the oxygen atoms of phendione should happen at more acidic pH, outside the working range of the glass electrode. The calculated log β and the related log K values are reported in Table 4. For both ligands the log K value decreases with temperature, and the difference is double in the case of phendione (0.31 and 0.15 log K units for phendione and phen, respectively). Besides the presence in phendione of the two oxygen atoms that exert a negative inductive effect, no significant differences between the log K values of the two ligands are evident.

3.6.2. Copper(II) hydrolysis

The formation constants of copper(II) hydrolysed species were determined by titrating several solutions containing Cu(II) at three different molar concentrations (1 × 10^{-3} M, 5.0 × 10^{-4} M and 3.3 × 10^{-4} M). The copper(II) concentration was varied to verify the presence of polynuclear species. All the solutions titrated with NaOH were back-titrated with HCl. The overlapping of the acidic and basic titration curves indicates the reversibility of the involved equilibria although it is slow to be reached. In fact, the time delay between additions necessary to reach equilibrium ranged from 1 to 30 min. A colloidal phase occurred after pH ≈ 6 or after pH ≈ 5 at 25 and 37 °C, respectively. At the end of the basic titrations (pH > 10) the solutions appeared slightly turbid. The potentiometric data for all the titrations carried out at the same temperature were fitted simultaneously. At the studied temperatures the formations of the $Cu(OH)_2$, $[Cu(OH)_3]^-$ and the polynuclear $[Cu_2(OH)]^{3+}$ species were evident.

The hydrolysis equilibria of copper(II) have been studied by several authors but under different experimental conditions, mainly at 25 °C and in the presence of nitrate or perchlorate ions as the background electrolyte [53–56]. The $[Cu(OH)]^+$, $[Cu_2(OH)_2]^{2+}$, $[Cu_2(OH)]^{3+}$ and $[Cu_3(OH)_4]^{2+}$ species were observed. A direct comparison between our data and those reported in the literature is problematic since most of the stability constants are expressed using different definitions and conventions. However, we observe that, after proper conversion, our values are slightly lower. These

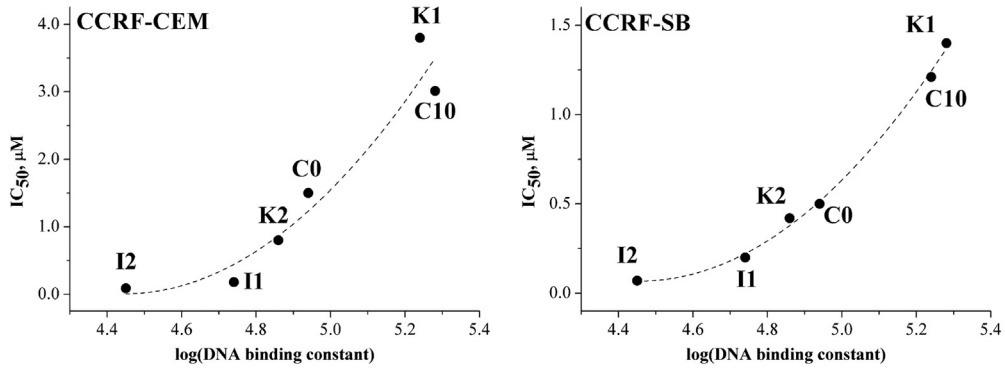

Fig. 4. Trend of IC_{50} versus logarithm of the DNA-binding constant. ($y = 4.99x^2 - 44.29x + 98.22$, $r^2 = 0.9332$ for CCRF-CEM; $y = 1.92x^2 - 17.14x + 38.28$, $r^2 = 0.9970$ for CCRF-SB; DNA binding constants were determined at 25 °C in 0.01 M PIPES buffer, pH 7.0).

differences may be due to the chosen experimental conditions. The $[Cu(OH)]^+$, $[Cu_2(OH)_2]^{2+}$ and $[Cu_3(OH)_4]^{2+}$ species were not found suitable to fit our experimental data. The calculated stability constants of hydroxo-complexes of Cu(II) are reported in Table 4.

3.6.3. Cu(II)–phen system

Complex formation equilibria between Cu(II) and the phen ligand were studied by potentiometric titrations. It was not possible to simultaneously record the UV–vis spectrum due to the absorption being too low in the visible region (d–d bands, $\varepsilon < 100\ M^{-1}\ cm^{-1}$) and too high in the UV region (charge transfer bands, $\varepsilon > 100{,}000\ M^{-1}\ cm^{-1}$). In fact, molar concentrations of complexes equal to 10^{-2} M or 10^{-5} M, not suitable for potentiometric measurements, had to be used. Some titration curves for phen:Cu(II) at molar ratios of 1:0, 3:1, 2:1 and 1:1 are reported in the Supplementary Materials (Fig. S2A and S2B). At a 3:1 ligand:metal molar ratio, variously protonated CuL_2 and CuL_3 complexes are formed. At pH < 4 the species $[CuL_3H]^{3+}$ is present. In this complex, the nitrogen atom of one ligand is still protonated and does not coordinate the metal ion. At a 2:1 phen:Cu(II) molar ratio, variously protonated CuL_2 and CuL forms are present. At a 1:1 molar ratio, CuL is the predominant species. At every molar ratio, the neutral CuL_2H_{-2} species is formed beyond pH = 10 (the term H_{-i} means that *i* water molecules coordinated to the metal ion have lost a proton). A colourless colloidal species is present after pH = 10 at a 1:1 molar ratio, probably due to the formation of the CuH_{-2} species.

The complex formation constants are reported in Table 4. In all the complexes the coordination sphere is completed by water molecules. Taking into account the solid state structures for $Cu(phen)(OH_2)_2(OClO_3)_2$ and $[Cu(phen)_2(OH_2)](ClO_4)_2$, and their visible absorption spectra [3], the hypothesised structures in solution for $[Cu(phen)_2]^{2+}$, $Cu(phen)_2H_{-2}$, and $[Cu(phen)_3H]^{3+}$ are reported in Fig. 5. The distribution curves at 25 and 37 °C are shown in Fig. S3. The complex formation constants obtained in this work are higher than those reported in the literature for this system [57–60]. However, in most of the previous studies, the constants were determined under different experimental conditions, and no protonated species were considered for fitting the experimental data.

Table 4
Overall stability constants for the studied systems, in 0.1 M ionic strength (NaCl) at 25 °C and 37 °C temperatures (the standard deviations on the last significant figure are reported in parentheses).

System	Species	Overall stability constants			
		25 °C		37 °C	
		Log β	Log K	Log β	Log K
phen	HL^+	5.08 (1)	5.08	4.93 (1)	4.93
phendione	HL^+	5.14 (1)	5.14	4.83 (1)	4.83
Cu(II)	$Cu(OH)_2$	−8.42 (1)	–	−7.08 (2)	–
	$[Cu(OH)_3]^-$	−19.07 (3)	10.65	−17.27 (3)	10.19
	$[Cu_2(OH)]^{3+}$	4.92 (3)	–	5.39 (4)	–
Cu(II)–phen	$[CuL_3H]^{3+}$	36.7 (1)	–	36.5 (1)	–
	$[CuL_3]^{2+}$	32.3 (1)	4.4	32.7 (1)	3.8
	$[CuL_2]^{2+}$	25.5 (1)	–	27.58 (4)	–
	$[CuL_2H_{-1}]^+$	17.72 (5)	7.78	19.41 (4)	8.17
	CuL_2H_{-2}	7.54 (4)	10.18	8.6 (1)	10.8
	$[CuL]^{2+}$	16.98 (2)	–	17.24 (2)	–
	$[CuLH_{-1}]^+$	10.20 (2)	6.78	10.33 (5)	6.91
	$[CuLH_{-3}]^-$	–	–	−9.3 (1)	9.8
Cu(II)–phendione	$[CuL_3H]^{3+}$	34.3 (1)	–	35.0 (1)	–
	$[CuL_3]^{2+}$	29.6 (1)	4.7	30.84 (5)	4.2
	$[CuL_2H]^{3+}$	28.0 (1)	–	30.2 (1)	–
	$[CuL_2]^{2+}$	24.0 (1)	4.0	24.34 (3)	5.9
	$[CuL_2H_{-1}]^+$	13.9 (1)	10.1	–	–
	$[CuL_2H_{-3}]^-$	–	–	−2.85 (4)	9.1
	$[CuL]^{2+}$	15.51 (2)	–	15.71 (3)	–
	$[CuLH_{-1}]^+$	8.54 (2)	6.97	8.8 (1)	6.9
	$CuLH_{-2}$	–	–	1.19 (2)	7.6
	$[CuLH_{-3}]^-$	−13.40 (1)	10.97	−8.91 (4)	10.10

3.6.4. Cu(II)–phendione system

As for the phen–Cu(II) system, complex formation equilibria between Cu(II) and the phendione ligand were studied by potentiometric titrations. Titration curves for 1:0, 3:1, 2:1 and 1:1 phendione:Cu(II) molar ratios are reported in Fig. S2C and S2D. Similarly to phen, phendione forms variously protonated CuL, CuL_2 and CuL_3 complexes with Cu(II). At a 3:1 ligand:metal molar ratio, CuL_2 and CuL_3 complexes are the predominant species. At pH < 4 the protonated species $[CuL_3H]^{3+}$ and $[CuL_2H]^{3+}$ are present. In these complexes, the nitrogen atom of one ligand is still protonated, and does not coordinate the metal ion. At a 2:1 phendione:Cu(II) molar ratio, CuL_2 and CuL are present. At a 1:1 molar ratio the predominant species is CuL. Unlike the phen–Cu(II) system, the neutral CuL_2H_{-2} species is formed only at 37 °C and 1:1 molar ratio. A colourless colloidal species is present after pH = 10 at 1:1 molar ratio, probably due to the formation of the CuH_{-2} species.

The complex formation constants are reported in Table 4. In all the complexes the coordination sphere is completed by water molecules. Taking into account the solid state structure for $[Cu(phendione)_2(OH_2)(OClO_3)](ClO_4)$ and on the basis of the visible absorption spectra, the hypothesised structures in solution for $[Cu(phendione)_2]^{2+}$ and $[Cu(phendione)_3]^{2+}$ are reported in Fig. 5. The distribution curves for the phendione–Cu(II) system at 25 and 37 °C are shown in Fig. S4.

3.6.5. Stability of the copper(II) complexes

The complex formation constants depend on ligand protonation constants and on metal hydrolysis; therefore, they cannot be directly compared to evaluate the relative complex stability. Then, in order to properly compare the stabilities of the formed complexes, the minus logarithm of the equilibrium concentration of the free metal ion ($-\log [Me_{free}] = pMe$), in a solution at specified pH, total metal and total ligand concentrations, might be calculated. In this way, a smaller free metal ion concentration, i.e. a larger pMe, indicates a more effective

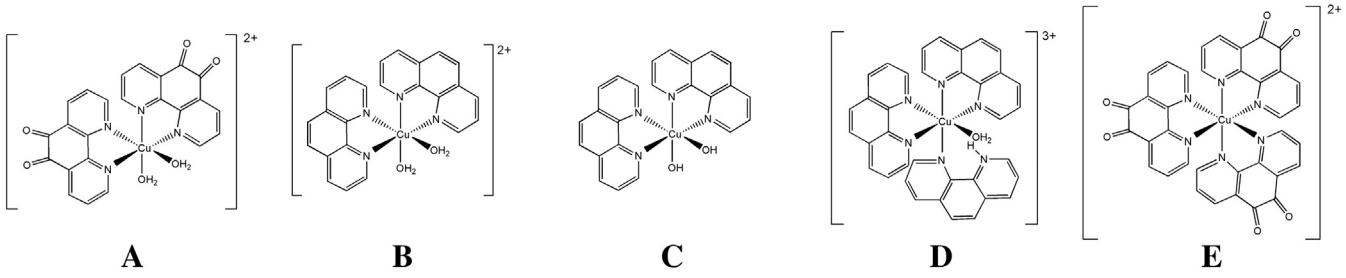

Fig. 5. Hypothesised structures for $[Cu(phendione)_2]^{2+}$ (A), $[Cu(phen)_2]^{2+}$ (B), $Cu(phen)_2H_{-2}$ (C), $[Cu(phen)_3H]^{3+}$ (D) and $[Cu(phendione)_3]^{2+}$ (E).

ligand towards that metal [61]. The pMe value depends on all the involved equilibria, and can be directly compared to state definitely which ligand forms the most stable complex under the chosen experimental conditions. The pCu(II) values for the phen–Cu(II) system are 22.8 (25 °C) and 23.7 (37 °C), while for the phendione–Cu(II) system they are 20.3 (25 °C) and 21.4 (37 °C), respectively. From these results it is evident that the formed complexes are more stable at physiological temperature and the complexes formed with phen are the most stable at both temperatures.

A direct correlation between the results obtained through potentiometric measurements and DNA binding study, could be misleading because of the different experimental conditions such as ionic strength, pH, temperature, and, in particular, concentration range. However some information could be translated. From the potentiometric study, it results that the predominant species, at pH 7.0 and 25 °C, are (L = phen or phendione): i) $[CuL_3]^{2+}$ when ligand and metal are present in 3:1 molar ratio; ii) $[CuL_2(OH_2)_2]^{2+}$ when ligand and metal are present in 2:1 molar ratio; iii) $[CuL(OH_2)(OH)]^{+}$ when ligand and metal are present 1:1 in molar ratio; and iv) L when only ligand is present. Then, dissolving **C10**, **C0**, **K1** and **K2** in PIPES buffer, the species in solution that react with DNA are supposed to be $[CuL(OH_2)(OH)]^{+}$ for **C10** and **K1**, $[CuL_2(OH_2)_2]^{2+}$ for **C0** and **K2**. Regarding **I1** and **I2**, in the absence of potentiometric data, it is possible to suppose a behaviour similar to that shown by the other complexes. Then the species in solution supposed to react with DNA, are $[CuL(OH_2)(OH)]^{+}$ for **I1** and $[CuL_2(OH_2)_2]^{2+}$ for **I2**. Among the species present in solution, only L for phen and phendione and $[Cu(phen)_2(OH_2)_2]^{2+}$ are able to partially intercalate.

4. Conclusion

Copper(II) form with 1,10-phenanthroline, 1,10-phenanthrolin-5,6-dione, and 1,10-phenanthrolin-5,6-diol, complexes with 1:1, 2:1 and 3:1 ligand:metal stoichiometry.

The studied ligands and complexes generally present a higher antiproliferative effect than that of cisplatin. Complexes with two ligands are more cytotoxic towards all the tested cell lines than the related complexes with one ligand and are generally more cytotoxic than the ligand alone. The $[Cu(1,10\text{-phenanthrolin-5,6-diol})_2(OH_2)](ClO_4)_2$ complex appears as the most active compound for the treatment of CCRF-CEM, CCRF-SB, SK-MES-1 and DU-145 human tumour cell lines. In particular this compound is very promising for the treatment of SK-MES-1, having a IC_{50} value 37 times lower than that of cisplatin. The $[Cu(1,10\text{-phenanthrolin-5,6-dione})_2(OH_2)(OClO_3)](ClO_4)$ complex is eligible for treatment of the HEP-G2 cell line, having a IC_{50} value 18 times lower than that of cisplatin. The cytotoxic activity of the ligands was found to be correlated to the cellular microenvironment. Compound 1,10-phenanthrolin-5,6-diol appears the most active ligand on cells surrounded by a hydrophilic environment.

The studied copper(II) complexes are characterised by a DNA affinity in the range 3×10^4–2×10^5 M^{-1}, and were found to interact with DNA mainly by groove binding or electrostatic interactions. The DNA complexes formed with $[Cu(1,10\text{-phenanthrolin-5,6-dione})(OH_2)_2(OClO_3)_2]$ or $[Cu(1,10\text{-phenanthroline})(OH_2)_2(OClO_3)_2]$ are characterised by greater DNA binding constants than the analogous ones formed with $[Cu(1,10\text{-phenanthrolin-5,6-dione})_2(OH_2)(OClO_3)](ClO_4)$ or $[Cu(1,10\text{-phenanthroline})_2(OH_2)(OClO_3)](ClO_4)$. The lower stability of these latter complexes may be due to the steric hindrance of two ligand molecules. It is interesting to notice that the Cu(II) complexes that present the highest DNA affinity show also the lowest cytotoxicity. The correlation found between cytotoxicity and DNA binding constants for copper complexes shows that DNA affinity cannot be considered a reliable universal indicator of the cytotoxic activity of a drug, giving only a suggestion of the involved action mechanism. Our complexes appear to act via a mechanism different from that of cisplatin. Therefore, they might be exploited for the treatment of cisplatin resistant cancer cells. Concluding, the results provide valuable information for the development of novel copper(II) complexes, as anticancer drugs with wider spectrum of action.

Acknowledgements

Federica Trudu gratefully acknowledges Sardinia Regional Government, for the financial support of her PhD scholarship (P.O.R. Sardegna F.S.E. Operational Programme of the Autonomous Region of Sardinia, European Social Fund 2007–2013 — Axis IV Human Resources, Objective l.3, Line of Activity l.3.1.)

Appendix A. Supplementary data

Supplementary data to this article can be found online at http://dx.doi.org/10.1016/j.jinorgbio.2014.08.011. These data include MOL files and InChiKeys of the most important compounds described in this article.

References

[1] N.B. Terwilliger, J. Exp. Biol. 201 (1998) 1085–1098.
[2] T. Pivetta, M.D. Cannas, F. Demartin, C. Castellano, S. Vascellari, G. Verani, F. Isaia, J. Inorg. Biochem. 105 (2011) 329–338.
[3] T. Pivetta, F. Isaia, G. Verani, C. Cannas, L. Serra, C. Castellano, F. Demartin, F. Pilla, M. Manca, A. Pani, J. Inorg. Biochem. 114 (2012) 28–37.
[4] T. Pivetta, F. Isaia, F. Trudu, A. Pani, M. Manca, D. Perra, F. Amato, J. Havel, Talanta 115 (2013) 84–93.
[5] C. Deegan, B. Coyle, M. McCann, M. Devereux, D. Egan, Chem. Biol. Interact. 164 (2006) 115–125.
[6] M. McCann, A.L.S. Santos, B.A. Da Silva, M.T.V. Romanos, A.S. Pyrrho, M. Devereux, K. Kavanagh, I. Fichtner, A. Kellett, Toxicol. Res. 1 (2012) 47–54 (Cambridge, U. K.).
[7] S. Roy, K.D. Hagen, P.U. Maheswari, M. Lutz, A.L. Spek, J. Reedijk, G.P. Van Wezel, Chem. Med. Chem. 3 (2008) 1427–1434.
[8] S. Betanzos-Lara, O. Novakova, R.J. Deeth, A.M. Pizarro, G.J. Clarkson, B. Liskova, V. Brabec, P.J. Sadler, A. Habtemariam, J. Biol. Inorg. Chem. 17 (2012) 1033–1051.
[9] A.N. Wein, A.T. Stockhausen, K.I. Hardcastle, M.R. Saadein, S.B. Peng, D. Wang, D.M. Shin, Z.G. Chen, J.F. Eichler, J. Inorg. Biochem. 105 (2011) 663–668.
[10] D.V. Luís, J. Silva, A.I. Tomaz, R.F.M. de Almeida, M. Larguinho, P.V. Baptista, L.M.D.R. S. Martins, T.F.S. Silva, P.M. Borralho, C.M.P. Rodrigues, A.S. Rodrigues, A.J.L. Pombeiro, A.R. Fernandes, J. Biol. Inorg. Chem. (2014), http://dx.doi.org/10.1007/s00775-014-1110-0.
[11] R.A. Alderden, M.D. Hall, T.W. Hambley, J. Chem. Educ. 83 (2006) 728–734.
[12] S. Kashanian, M.M. Khodaei, H. Roshanfekr, H. Peyman, Spectrochim. Acta A Mol. Biomol. Spectrosc. 114 (2013) 642–649.
[13] M. Kaplanis, G. Stamatakis, V.D. Papakonstantinou, M. Paravatou-Petsotas, C.A. Demopoulos, C.A. Mitsopoulou, J. Inorg. Biochem. 135 (2014) 1–9.

[14] S. Poteet, M. Majewski, Z.S. Breitbach, C.A. Griffith, S. Singh, D.W. Armstrong, M.O. Wolf, F.M. MacDonnell, J. Am. Chem. Soc. 135 (2013) 2419–2422.
[15] V.A. Bloomfield, D.M. Crothers, I. Tinocco Jr., Physical Chemistry of Nucleic Acids, Harper & Row, New York, 1974. 432.
[16] A. Altomare, M.C. Burla, M. Camalli, G.L. Cascarano, C. Giacovazzo, A. Guagliardi, A.G.G. Moliterni, G. Polidori, R. Spagna, J. Appl. Crystallogr. 32 (1999) 115–119.
[17] G.M. Sheldrick, Acta Crystallogr. 64A (2008) 112–122.
[18] L.J. Farrugia, J. Appl. Crystallogr. 32 (1999) 837–838.
[19] S.A. Latt, G. Stetten, L.A. Juergens, H.F. Willard, C.D. Scher, J. Histochem. Cytochem. 23 (1975) 493–505.
[20] R. Pauwels, J. Balzarini, M. Baba, R. Snoeck, D. Schols, P. Herdewijn, J. Desmyter, E. De Clercq, J. Virol. Methods 20 (1988) 309–321.
[21] S. Dhanalakshmi, P. Agarwal, L.M. Glode, R. Agarwal, Int. J. Cancer 106 (2003) 699–705.
[22] M. Okamura, K. Hashimoto, J. Shimada, H. Sakagami, Anticancer Res. 24 (2004) 655–662.
[23] P. Ceppi, M. Papotti, V. Monica, M. Lo Iacono, S. Saviozzi, M. Pautasso, S. Novello, S. Mussino, E. Bracco, M. Volante, G.V. Scagliotti, Mol. Cancer Ther. 8 (2009) 3066–3074.
[24] M.E. Reichmann, S.A. Rice, C.A. Thomas, P. Doty, J. Am. Chem. Soc. 76 (1954) 3047–3053.
[25] J. Murmur, J. Mol. Biol. 3 (1961) 208–218.
[26] M. Meloun, J. Čapek, P. Mikšík, R.G. Brereton, Anal. Chim. Acta. 423 (2000) 51–68.
[27] E.R. Malinowski, Factor Analysis in Chemistry, third ed. Wiley-Interscience, New York, 2002.
[28] P. Gans, A. Sabatini, A. Vacca, Talanta 43 (1996) 1739–1753.
[29] A. Albert, E.P. Serjant, The Determination of Ionization Constants, Chapman & Hall, London, 1984.
[30] G. Gran, Analyst 77 (1952) 661–671.
[31] P. Gans, B. O'Sullivan, Talanta 51 (2000) 33–37.
[32] J. Bassett, R.C. Denney, G.H. Jeffrey, J. Mendham, Vogel's Textbook of Quantitative Inorganic Analysis, The ELBS and Longman, London, 1989. 326.
[33] C.C.J. Roothaan, Rev. Mod. Phys. 23 (1951) 69–89.
[34] G.G. Hall, Proc. R. Soc. A 205 (1951) 541–552.
[35] J.A. Pople, D.A. Beveridge, Approximate Molecular Orbital Theory, McGraw-Hill, New York, 1970.
[36] K. Ocakoglu, C. Zafer, B. Cetinkaya, S. Icli, Dyes Pigments 75 (2007) 385–394.
[37] W. Paw, R. Eisenberg, Inorg. Chem. 36 (1997) 2287–2293.
[38] A.W. Addison, T.N. Rao, J. Reedijk, J. Van Rijn, G.C. Verschoor, J. Chem. Soc. Dalton Trans. (1984) 1349–1356.
[39] S. Ghosh, A.C. Barve, A.A. Kumbhar, A.S. Kumbhar, V.G. Puranik, P.A. Datar, U.B. Sonawane, R.R. Joshi, J. Inorg. Biochem. 100 (2006) 331–343.
[40] M.D. Stephenson, M.J. Hardie, Dalton Trans. (2006) 3407–3417.
[41] F. Luciani, M. Spada, A. De Milito, A. Molinari, L. Rivoltini, A. Montinaro, M. Marra, L. Lugini, M. Logozzi, F. Lozupone, C. Federici, E. Iessi, G. Parmiani, G. Arancia, F. Belardelli, S. Fais, JNCI J. Natl. Cancer Inst. 96 (2004) 1702–1713.
[42] M.S.S. Babu, K.H. Reddy, P.G. Krishna, Polyhedron 26 (2007) 572–580.
[43] Y. Sun, Y.J. Hou, Q.X. Zhou, W.H. Lei, J.R. Chen, X.S. Wang, B.W. Zhang, Inorg. Chem. 49 (2010) 10108–10116.
[44] M. Chikira, Y. Tomizawa, D. Fukita, T. Sugizaki, N. Sugawara, T. Yamazaki, A. Sasano, H. Shindo, M. Palaniandavar, W.E. Antholine, J. Inorg. Biochem. 89 (2002) 163–173.
[45] O. Zelenko, J. Gallagher, D.S. Sigman, Angew. Chem. Int. Ed. Engl. 36 (1997) 2776–2778.
[46] J.M. Veal, R.L. Rill, Biochemistry 30 (1991) 1132–1140.
[47] G.S. Manning, Q. Rev. Biophys. 11 (1978) 179–246.
[48] C. Marzano, M. Pellei, F. Tisato, C. Santini, Anti Cancer Agents Med. Chem. 9 (2009) 185–211.
[49] R.S. Kumar, S. Arunachalam, V.S. Periasamy, C.P. Preethy, A. Riyasdeen, M.A. Akbarsha, Eur. J. Med. Chem. 43 (2008) 2082–2091.
[50] T. Gupta, S. Dhar, M. Nethaji, A.R. Chakravarty, Dalton Trans. (2004) 1896–1900.
[51] Q.G. Zhang, F. Zhang, W.G. Wang, X.L. Wang, J. Inorg. Biochem. 100 (2006) 1344–1352.
[52] A.K. Patra, T. Bhowmick, S. Ramakumar, M. Nethaji, A.R. Chakravarty, Dalton Trans. (2008) 6966–6976.
[53] M. Whitfield, J. Chem. Eng. Data 17 (1972) 124–128.
[54] A. Vacca, A. Sabatini, L. Bologni, J. Chem. Soc. Dalton Trans. (1981) 1246–1250.
[55] S. Sjoberg, Y. Hagglund, A. Nordin, N. Ingri, Mar. Chem. 13 (1983) 35–44.
[56] J. Nordin, P. Persson, A. Nordin, S. Sjoberg, Langmuir 14 (1998) 3655–3662.
[57] T. Kohzuma, A. Odani, Y. Morita, M. Takani, O. Yamauchi, Inorg. Chem. 27 (1998) 3854–3858.
[58] G. Nakagawa, H. Wada, T. Sako, Bull. Chem. Soc. Jpn. 53 (1980) 1303–1307.
[59] M. Mohan, D. Bancroft, E. Abbott, Inorg. Chem. 18 (1979) 2468–2472.
[60] H. Irving, D. Mellor, J. Chem. Soc. (1962) 5222–5237.
[61] W.R. Harris, C.J. Carrano, S.D.R. Cooper, S.R. Sofen, A.E. Avdeef, J.V. Mc Ardle, K.N. Raymond, J. Am. Chem. Soc. 101 (1979) 6097–6104.

SUPPLEMENTARY MATERIALS

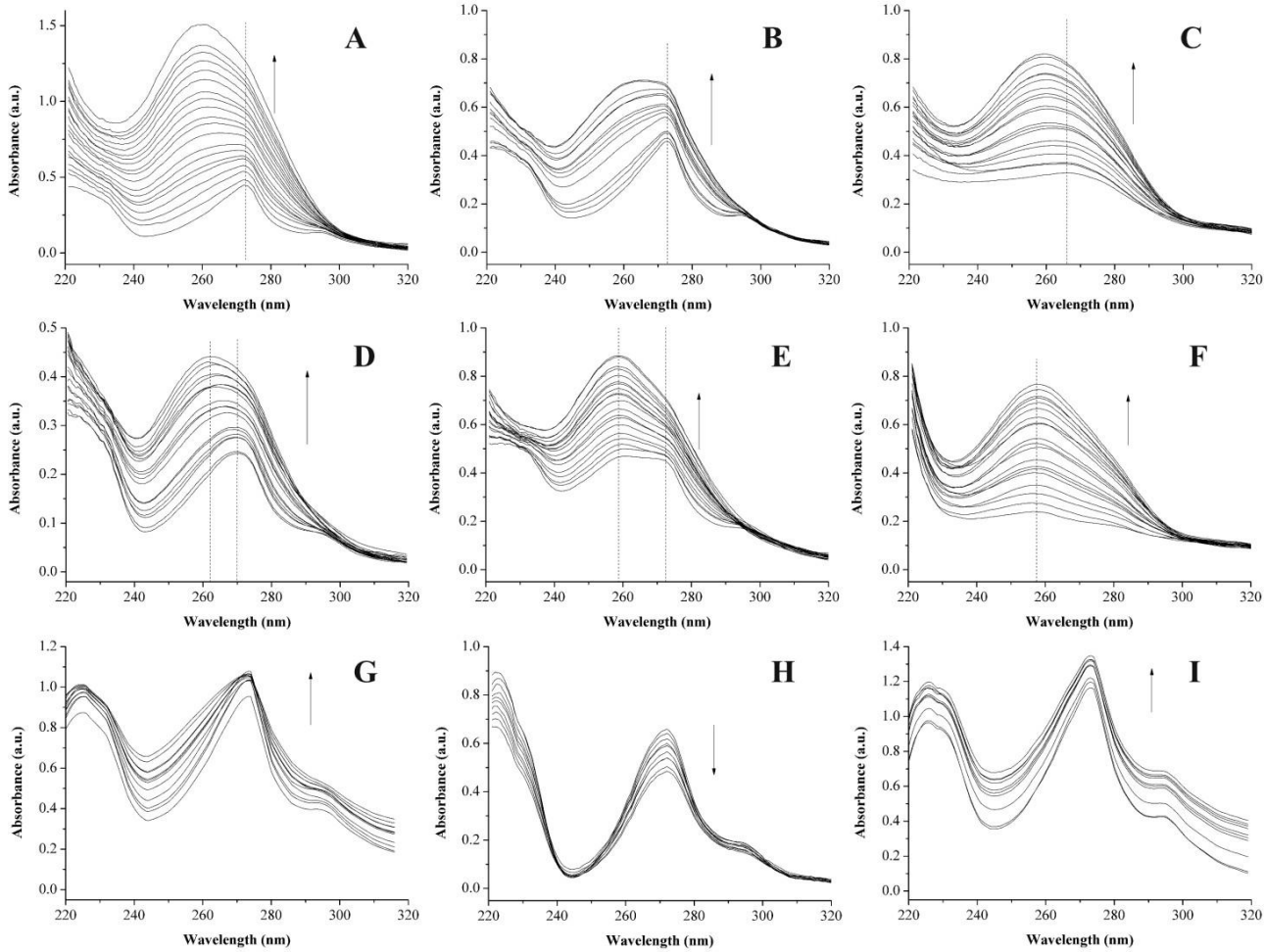

Fig. S1. Selected UV-Vis spectra recorded during titration with at least 10 equivalents of DNA and 2.65 x 10^{-5} mmoles of **C10** (A), 3.04 x 10^{-5} mmoles of **K1** (B), 3.61 x 10^{-5} mmoles of **I1** (C), 6.54 x 10^{-6} mmoles of **C0** (D), 1.69 x 10^{-5} mmoles of **K2** (E) and 1.20 x 10^{-5} mmoles of **I2** (F), and with, at maximum 3 equivalents of DNA of 3.5 x 10^{-5} mmoles of **C10** (G), 1.5 x 10^{-5} mmoles of **C0** (H), 7.8 x 10^{-5} mmoles of **K1** (I); at 25 °C, 0.01 M PIPES buffer, pH = 7.0, 1 cm optical path length.

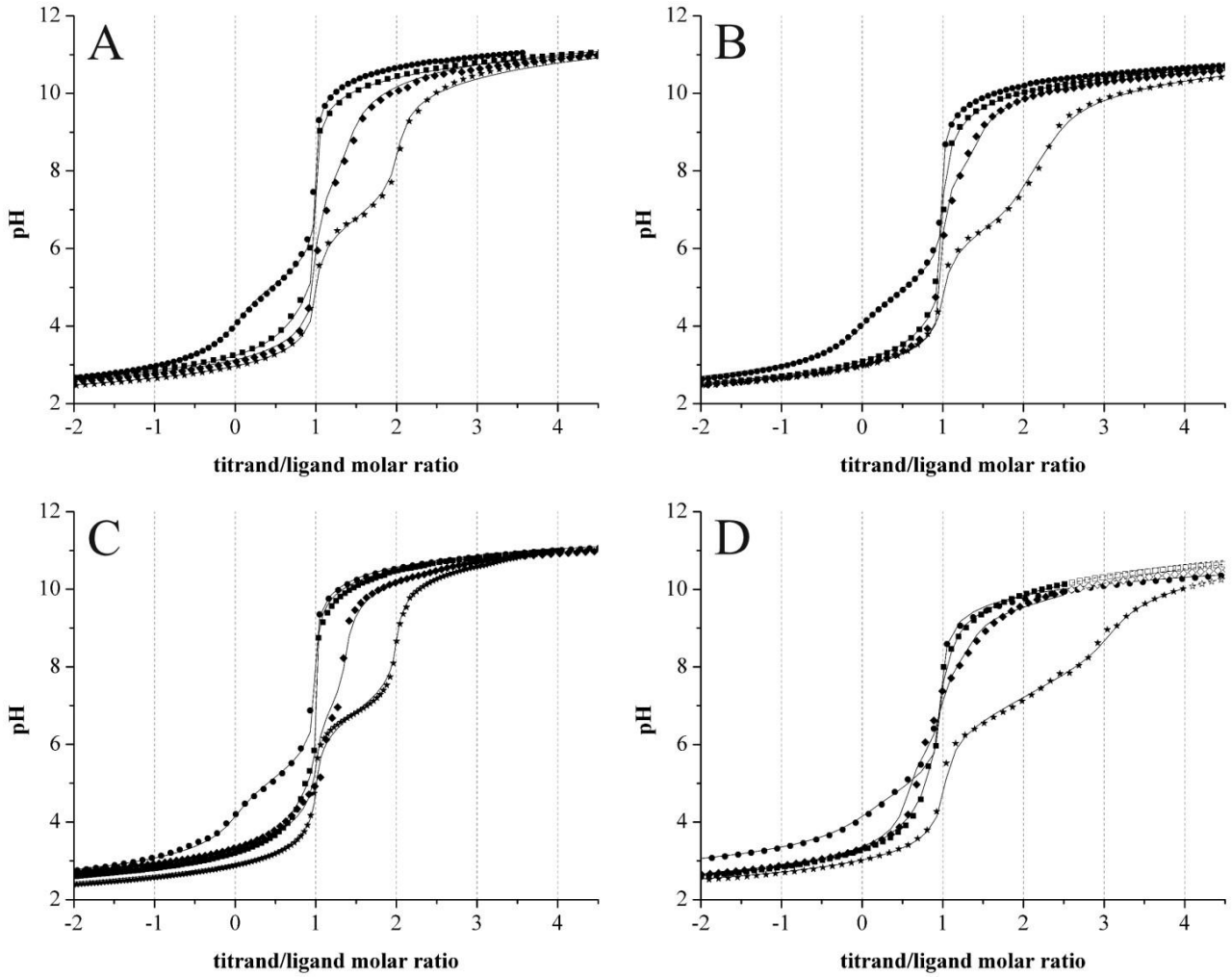

Fig. S2.Titration curves for Cu(II)-phen at 25 (A) and 37 °C (B), Cu(II)-phendione at 25 (C) and 37 °C (D); 1:0 (•), 3:1 (■), 2:1 (◆) and 1:1 (★) ligand:Cu(II) molar ratios, ligand concentration ≈ 1 mM, 0.1 M NaCl ionic strength, NaOH ≈ 0.1 M.

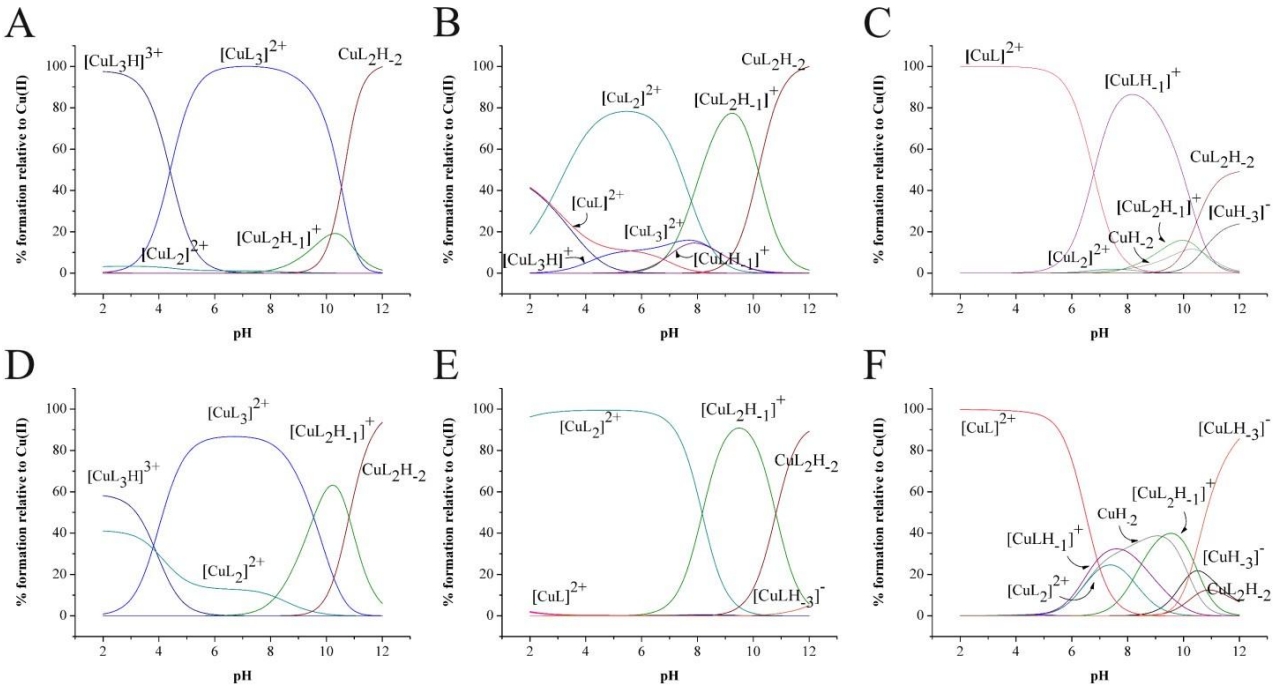

Fig. S3. Distribution curves at 0.1 M NaCl ionic strength and 25 °C (upper) and 37 °C (bottom) for 3:1 (A and D), 2:1 (B and E) and 1:1 (C and F) 1,10-phenanthroline:Cu(II) molar ratios.

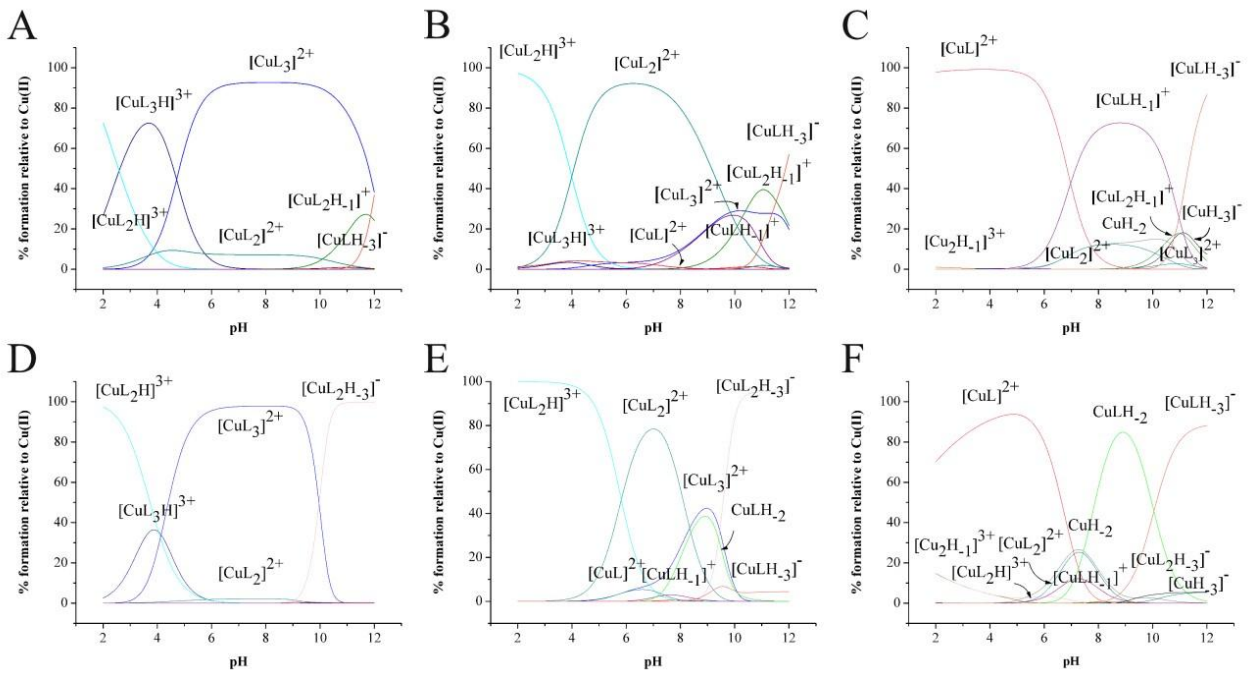

Fig. S4. Distribution curves at 0.1 M NaCl ionic strength and 25 °C (upper) and 37 °C (bottom) for 3:1 (A and D), 2:1 (B and E) and 1:1 (C and F) 1,10-phenanthroline-5,6-dione:Cu(II) molar ratios.

Chapter 2

Mixed copper-platinum complex formation could explain synergistic antiproliferative effect exhibited by binary mixtures of cisplatin and copper-1,10-phenanthroline: An ESI-MS study

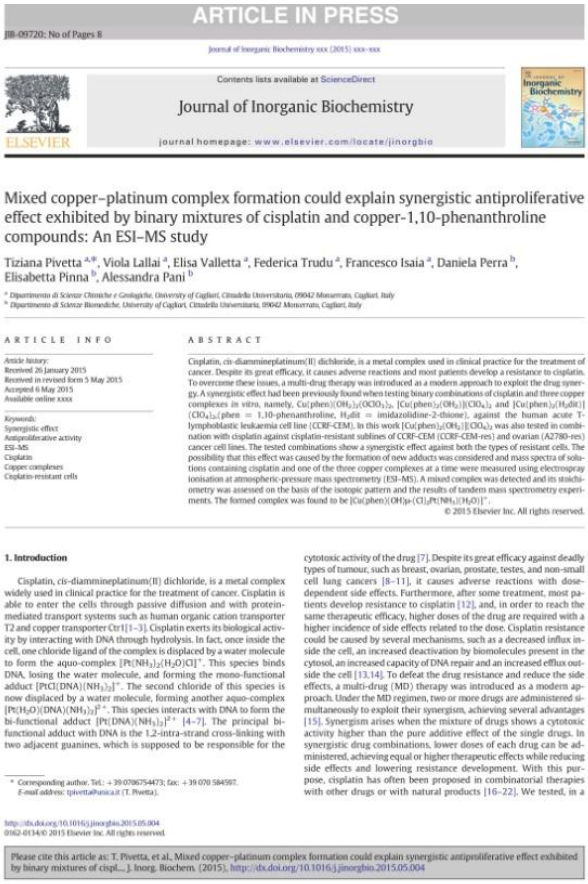

ARTICLE IN PRESS

JIB-09720; No of Pages 8

Journal of Inorganic Biochemistry xxx (2015) xxx–xxx

Contents lists available at ScienceDirect

Journal of Inorganic Biochemistry

journal homepage: www.elsevier.com/locate/jinorgbio

Mixed copper–platinum complex formation could explain synergistic antiproliferative effect exhibited by binary mixtures of cisplatin and copper-1,10-phenanthroline compounds: An ESI–MS study

Tiziana Pivetta [a,*], Viola Lallai [a], Elisa Valletta [a], Federica Trudu [a], Francesco Isaia [a], Daniela Perra [b], Elisabetta Pinna [b], Alessandra Pani [b]

[a] Dipartimento di Scienze Chimiche e Geologiche, University of Cagliari, Cittadella Universitaria, 09042 Monserrato, Cagliari, Italy
[b] Dipartimento di Scienze Biomediche, University of Cagliari, Cittadella Universitaria, 09042 Monserrato, Cagliari, Italy

ARTICLE INFO

Article history:
Received 26 January 2015
Received in revised form 5 May 2015
Accepted 6 May 2015
Available online xxxx

Keywords:
Synergistic effect
Antiproliferative activity
ESI-MS
Cisplatin
Copper complexes
Cisplatin-resistant cells

ABSTRACT

Cisplatin, *cis*-diammineplatinum(II) dichloride, is a metal complex used in clinical practice for the treatment of cancer. Despite its great efficacy, it causes adverse reactions and most patients develop a resistance to cisplatin. To overcome these issues, a multi-drug therapy was introduced as a modern approach to exploit the drug synergy. A synergistic effect had been previously found when testing binary combinations of cisplatin and three copper complexes *in vitro*, namely, $Cu(phen)(OH_2)_2(OClO_3)_2$, $[Cu(phen)_2(OH_2)](ClO_4)_2$ and $[Cu(phen)_2(H_2dit)](ClO_4)_2$ (phen = 1,10-phenanthroline, H_2dit = imidazolidine-2-thione), against the human acute T-lymphoblastic leukaemia cell line (CCRF-CEM). In this work $[Cu(phen)_2(OH_2)](ClO_4)_2$ was also tested in combination with cisplatin against cisplatin-resistant sublines of CCRF-CEM (CCRF-CEM-res) and ovarian (A2780-res) cancer cell lines. The tested combinations show a synergistic effect against both the types of resistant cells. The possibility that this effect was caused by the formation of new adducts was considered and mass spectra of solutions containing cisplatin and one of the three copper complexes at a time were measured using electrospray ionisation at atmospheric-pressure mass spectrometry (ESI–MS). A mixed complex was detected and its stoichiometry was assessed on the basis of the isotopic pattern and the results of tandem mass spectrometry experiments. The formed complex was found to be $[Cu(phen)(OH)\mu\text{-}(Cl)_2Pt(NH_3)(H_2O)]^+$.

1. Introduction

Cisplatin, *cis*-diammineplatinum(II) dichloride, is a metal complex widely used in clinical practice for the treatment of cancer. Cisplatin is able to enter the cells through passive diffusion and with protein-mediated transport systems such as human organic cation transporter T2 and copper transporter Ctr1 [1–3]. Cisplatin exerts its biological activity by interacting with DNA through hydrolysis. In fact, once inside the cell, one chloride ligand of the complex is displaced by a water molecule to form the aquo-complex $[Pt(NH_3)_2(H_2O)Cl]^+$. This species binds DNA, losing the water molecule, and forming the mono-functional adduct $[PtCl\{DNA\}(NH_3)_2]^+$. The second chloride of this species is now displaced by a water molecule, forming another aquo-complex $[Pt(H_2O)\{DNA\}(NH_3)_2]^{2+}$. This species interacts with DNA to form the bi-functional adduct $[Pt\{DNA\}_2(NH_3)_2]^{2+}$ [4–7]. The principal bi-functional adduct with DNA is the 1,2-intra-strand cross-linking with two adjacent guanines, which is supposed to be responsible for the cytotoxic activity of the drug [7]. Despite its great efficacy against deadly types of tumour, such as breast, ovarian, prostate, testes, and non-small cell lung cancers [8–11], it causes adverse reactions with dose-dependent side effects. Furthermore, after some treatment, most patients develop resistance to cisplatin [12], and, in order to reach the same therapeutic efficacy, higher doses of the drug are required with a higher incidence of side effects related to the dose. Cisplatin resistance could be caused by several mechanisms, such as a decreased influx inside the cell, an increased deactivation by biomolecules present in the cytosol, an increased capacity of DNA repair and an increased efflux outside the cell [13,14]. To defeat the drug resistance and reduce the side effects, a multi-drug (MD) therapy was introduced as a modern approach. Under the MD regimen, two or more drugs are administered simultaneously to exploit their synergism, achieving several advantages [15]. Synergism arises when the mixture of drugs shows a cytotoxic activity higher than the pure additive effect of the single drugs. In synergistic drug combinations, lower doses of each drug can be administered, achieving equal or higher therapeutic effects while reducing side effects and lowering resistance development. With this purpose, cisplatin has often been proposed in combinatorial therapies with other drugs or with natural products [16–22]. We tested, in a

* Corresponding author. Tel.: +39 0706754473; fax: +39 070 584597.
E-mail address: tpivetta@unica.it (T. Pivetta).

http://dx.doi.org/10.1016/j.jinorgbio.2015.05.004
0162-0134/

Please cite this article as: T. Pivetta, et al., Mixed copper–platinum complex formation could explain synergistic antiproliferative effect exhibited by binary mixtures of cispl..., J. Inorg. Biochem. (2015), http://dx.doi.org/10.1016/j.jinorgbio.2015.05.004

Abstract

Cisplatin is one of the most powerful chemotherapeutic drug. In spite of the great efficacy of this drug, it shows several side effects and most patients develop a resistance to cisplatin. To overcome the cisplatin resistance, drugs are often administered in combination (multi-drug therapy) in order to exploit the drug synergy. In the research group where I prepared my PhD thesis, it has been found that binary combinations of cisplatin and three copper complexes, $[Cu(phen)(OH_2)_2(OClO_3)_2]$ (**C10**), $[Cu(phen)_2(OH_2)](ClO_4)_2$ (**C0**), and $[Cu(phen)_2(H_2dit)](ClO_4)_2$ (**C1**) (**phen** = 1,10-phenanthroline, **H_2dit** = imidazolidine-2-thione) (Figure 10), present *in vitro* a synergistic effect against the wild type human acute T-lymphoblastic leukaemia cell line (CCRF-CEM-wt). From these results, I decided to study the cytotoxic activity of cisplatin in combination with **C0** against the cisplatin-resistant sublines of CCRF-CEM (CCRF-CEM-res) and ovarian (A2780-res) cancer cell lines.

The three copper complexes have been re-synthesized using new synthetic route with less-toxic solvent and/or with higher yields. In particular, the new synthesis method of **C10** led to a crystalline product with higher purity (≥95%) and yield. In the synthesis method of **C1**, the solvent H_2O was used instead of CH_3CN.

The cytotoxic activity of **C0** and cisplatin, both alone and in binary combinations, were evaluated against cisplatin-resistant sublines of leukemic and ovarian cancer cell lines[1]. Copper complex **C0** showed an IC_{50} values of 0.75 and 0.24 μM in CCRF-CEM-res and A2780-res, respectively. Cisplatin showed an IC_{50} values of 6.98 and 5.3 μM in CCRF-CEM-res and A2780-res, respectively. The combinatorial treatment against cisplatin-resistant cell lines, gave rise to a synergistic antiproliferative effect between cisplatin and the studied copper complex *in vitro*.

[1] In collaboration with professor Alessandra Pani (Dipartimento di Scienze Biomediche, Università degli Studi di Cagliari).

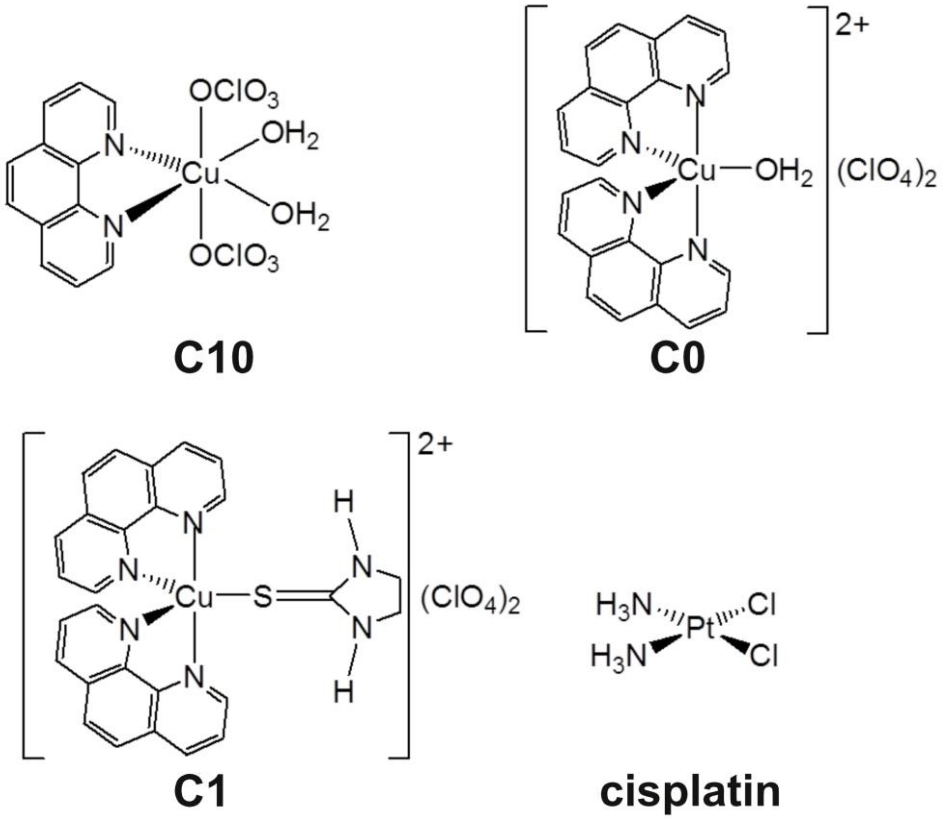

Figure 10. Formulas and acronyms of the studied molecules. Complex **C10** is $Cu(phen)(OH_2)_2(OClO_3)_2$, **C0** is $[Cu(phen)_2(OH_2)](ClO_4)_2$, **C1** is $[Cu(phen)_2(H_2dit)](ClO_4)_2$, and cisplatin is cis-diammineplatinum(II) dichloride (**phen** = 1,10-phenanthroline, **H_2dit** = imidazolidine-2-thione).

Considering that the synergy may arise from the interaction of the drugs with different targets, from the shielding effect or from a chemical reaction among the drugs, I decided to study the possible formation of new adducts between cisplatin and copper(II) complexes by mass spectrometry. This study is reported in Chapter 2- Article II.

A mixed complex containing copper and platinum with a stoichiometry of $[Cu(phen)(OH)\mu\text{-}(Cl)_2Pt(NH_3)(H_2O)]^+$ was detected (Figure 11) regardless of the copper complex used.

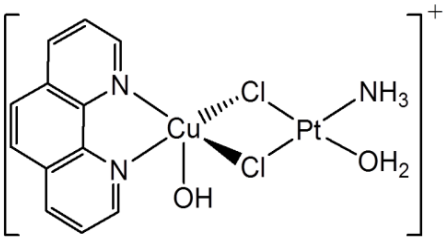

Figure 11. Formula of the detected mixed copper-platinum complex.

The detected mixed complex is able to hydrolyze to form $[Cu(phen)(OH)\mu\text{-}(Cl)_2Pt(H_2O)_2]^+$, species that could be responsible of the synergistic effect shown by the studied mixtures and it is likely to interfere with one or more of the mechanisms that lead to cisplatin resistance. Given that the determining step in the interaction of cisplatin with DNA are the slow hydrolysis processes and considering that the hydrolyzed complexes $[Cu(phen)(OH)\mu\text{-}(Cl)_2Pt(NH_3)(H_2O)]^+$ and $[Cu(phen)(OH)\mu\text{-}(Cl)_2Pt(H_2O)_2]^+$ are formed within a few minutes, this mixed copper-platinum complex is supposed to be able to react with DNA more readily than cisplatin (Figure 12).

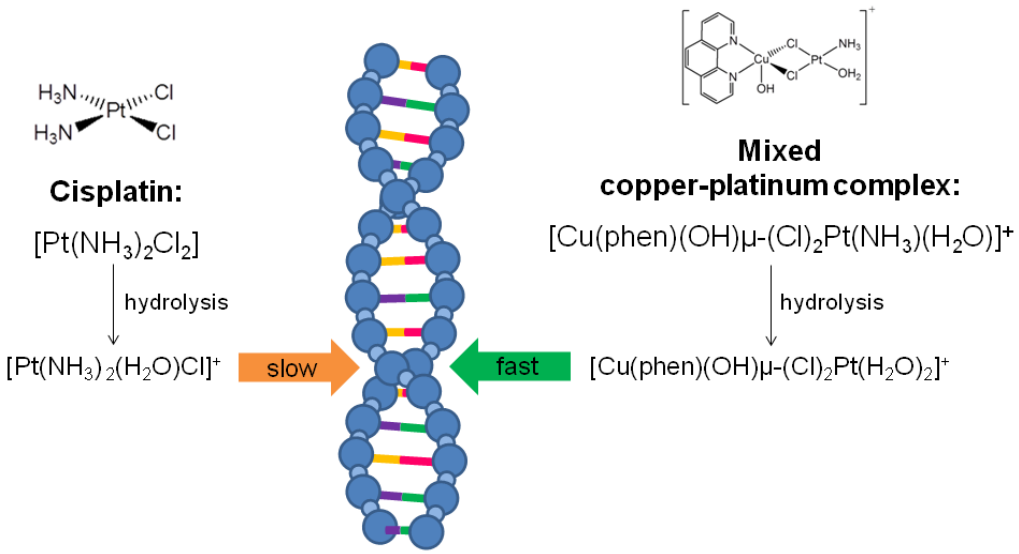

Figure 12. Comparison between the determining step in the interaction of cisplatin with DNA and that hypothesized for the mixed complex $[Cu(phen)(OH)\mu\text{-}(Cl)_2Pt(NH_3)(H_2O)]^+$, species that could be responsible of the synergistic effect shown by studied mixtures.

Article II

Mixed copper-platinum complex formation could explain synergistic antiproliferative effect exhibited by binary mixtures of cisplatino and copper-1,10-phenanthroline: An ESI-MS study

Tiziana Pivetta, Viola Lallai, Elisa Valletta, Federica Trudu, Francesco Isaia, Daniela Perra, Elisabetta Pinna, Alessandra Pani

Citation: Journal of Inorganic Biochemistry (2015) 151, 107-114

Cite this: DOI: 10.1016/j.jinorgbio.2015.05.004

Published by Elsevier

Journal of Inorganic Biochemistry 151 (2015) 107–114

Contents lists available at ScienceDirect

Journal of Inorganic Biochemistry

journal homepage: www.elsevier.com/locate/jinorgbio

Mixed copper–platinum complex formation could explain synergistic antiproliferative effect exhibited by binary mixtures of cisplatin and copper-1,10-phenanthroline compounds: An ESI–MS study

Tiziana Pivetta [a,*], Viola Lallai [a], Elisa Valletta [a], Federica Trudu [a], Francesco Isaia [a], Daniela Perra [b], Elisabetta Pinna [b], Alessandra Pani [b]

[a] Dipartimento di Scienze Chimiche e Geologiche, University of Cagliari, Cittadella Universitaria, 09042 Monserrato, Cagliari, Italy
[b] Dipartimento di Scienze Biomediche, University of Cagliari, Cittadella Universitaria, 09042 Monserrato, Cagliari, Italy

ARTICLE INFO

Article history:
Received 26 January 2015
Received in revised form 5 May 2015
Accepted 6 May 2015
Available online 14 May 2015

Keywords:
Synergistic effect
Antiproliferative activity
ESI–MS
Cisplatin
Copper complexes
Cisplatin-resistant cells

ABSTRACT

Cisplatin, *cis*-diammineplatinum(II) dichloride, is a metal complex used in clinical practice for the treatment of cancer. Despite its great efficacy, it causes adverse reactions and most patients develop a resistance to cisplatin. To overcome these issues, a multi-drug therapy was introduced as a modern approach to exploit the drug synergy. A synergistic effect had been previously found when testing binary combinations of cisplatin and three copper complexes *in vitro*, namely, $Cu(phen)(OH_2)_2(OClO_3)_2$, $[Cu(phen)_2(OH_2)](ClO_4)_2$ and $[Cu(phen)_2(H_2dit)](ClO_4)_2$,(phen = 1,10-phenanthroline, H_2dit = imidazolidine-2-thione), against the human acute T-lymphoblastic leukaemia cell line (CCRF-CEM). In this work $[Cu(phen)_2(OH_2)](ClO_4)_2$ was also tested in combination with cisplatin against cisplatin-resistant sublines of CCRF-CEM (CCRF-CEM-res) and ovarian (A2780-res) cancer cell lines. The tested combinations show a synergistic effect against both the types of resistant cells. The possibility that this effect was caused by the formation of new adducts was considered and mass spectra of solutions containing cisplatin and one of the three copper complexes at a time were measured using electrospray ionisation at atmospheric-pressure mass spectrometry (ESI–MS). A mixed complex was detected and its stoichiometry was assessed on the basis of the isotopic pattern and the results of tandem mass spectrometry experiments. The formed complex was found to be $[Cu(phen)(OH)\mu\text{-}(Cl)_2Pt(NH_3)(H_2O)]^+$.

1. Introduction

Cisplatin, *cis*-diammineplatinum(II) dichloride, is a metal complex widely used in clinical practice for the treatment of cancer. Cisplatin is able to enter the cells through passive diffusion and with protein-mediated transport systems such as human organic cation transporter T2 and copper transporter Ctr1[1–3]. Cisplatin exerts its biological activity by interacting with DNA through hydrolysis. In fact, once inside the cell, one chloride ligand of the complex is displaced by a water molecule to form the aquo-complex $[Pt(NH_3)_2(H_2O)Cl]^+$. This species binds DNA, losing the water molecule, and forming the mono-functional adduct $[PtCl(DNA)(NH_3)_2]^+$. The second chloride of this species is now displaced by a water molecule, forming another aquo-complex $[Pt(H_2O)(DNA)(NH_3)_2]^{2+}$. This species interacts with DNA to form the bi-functional adduct $[Pt(DNA)(NH_3)_2]^{2+}$ [4–7]. The principal bi-functional adduct with DNA is the 1,2-intra-strand cross-linking with two adjacent guanines, which is supposed to be responsible for the cytotoxic activity of the drug [7]. Despite its great efficacy against deadly types of tumour, such as breast, ovarian, prostate, testes, and non-small cell lung cancers [8–11], it causes adverse reactions with dose-dependent side effects. Furthermore, after some treatment, most patients develop resistance to cisplatin [12], and, in order to reach the same therapeutic efficacy, higher doses of the drug are required with a higher incidence of side effects related to the dose. Cisplatin resistance could be caused by several mechanisms, such as a decreased influx inside the cell, an increased deactivation by biomolecules present in the cytosol, an increased capacity of DNA repair and an increased efflux outside the cell [13,14]. To defeat the drug resistance and reduce the side effects, a multi-drug (MD) therapy was introduced as a modern approach. Under the MD regimen, two or more drugs are administered simultaneously to exploit their synergism, achieving several advantages [15]. Synergism arises when the mixture of drugs shows a cytotoxic activity higher than the pure additive effect of the single drugs. In synergistic drug combinations, lower doses of each drug can be administered, achieving equal or higher therapeutic effects while reducing side effects and lowering resistance development. With this purpose, cisplatin has often been proposed in combinatorial therapies with other drugs or with natural products [16–22]. We tested, in a

* Corresponding author. Tel.: +39 0706754473; fax: +39 070 584597.
E-mail address: tpivetta@unica.it (T. Pivetta).

http://dx.doi.org/10.1016/j.jinorgbio.2015.05.004
0162-0134/

previous study, several binary combinations of cisplatin with $[Cu(phen)(OH_2)_2(OClO_3)_2]$ (**1**), $[Cu(phen)_2(OH_2)](ClO_4)_2$ (**2**) and $[Cu(phen)_2(H_2dit)](ClO_4)_2$ (**C1**) (phen = 1,10-phenanthroline, H_2dit = imidazolidine-2-thione) *in vitro* against the wild type human acute T-lymphoblastic leukaemia cell line (CCRF-CEM-wt), finding a synergistic effect. Especially, the maximum of synergistic effect was observed for particular combinations of copper complexes and cisplatin, i.e. 5:1 for **1** and cisplatin, 1:1 for **2** and cisplatin and 1:2 for **C1** and cisplatin [15]. In this work, we extended the study of the cytotoxic activity of the most promising copper complex **2** as a leader compound, on cisplatin-resistant sublines of leukemic (CCRF-CEM-res) and ovarian (A2780-res) cancer cell lines. The CCRF-CEM-res cells were purposely selected in order to verify whether the synergistic effect shown by **2** and cisplatin in the CCRF-CEM-wt cell line [15] was maintained in a cisplatin-resistant counterpart, even if cisplatin is not used in the chemotherapic treatment of leukaemia. The A2780-res cells were selected since they are derived from the ovarian cancer for which cisplatin is still now one of the chemotherapic agent of choice. This kind of cancer is actually sensitive to cisplatin but becomes resistant to this drug during chemotherapy cycles or in recurrences [23].

Copper(II) complexes are supposed to act against cancer cells in different ways with respect to cisplatin, but the real mechanisms are not completely clarified to date [24]. Furthermore, as both copper(I) and copper(II) are involved in several biological functions, it is not universally accepted that the cytotoxic properties of copper complexes are related to a specific oxidation state of the metal ion. In most studies, cell apoptosis and enzyme inhibition (proteasome, topoisomerase I and II, tyrosin protein kinase) are involved [25,26], whereas DNA appears to be the target of copper complexes containing nitrogen chelators, such as phen [27]. The synergistic effect shown by cisplatin and our copper complexes containing one or two phen molecules may then arise from several mechanisms, that is, simultaneous involvement of the same or different targets, such as DNA, proteins, enzymes, biomolecules, but also through the formation of new adducts. According to the Pearson acid–base concept [28], platinum(II) and copper(I) are both soft ions, whereas copper(II) has a hard–soft intermediate character. These ions present an affinity for the same ligands, which may lead to the formation of polynuclear complexes containing both platinum and copper. Starting from the above considerations, we decided to verify the formation of mixed complexes, acquiring mass spectra of solutions containing cisplatin and copper complexes, using electrospray ionisation in atmospheric-pressure mass (ESI–MS). This ionisation system limits fragmentation processes, allowing the additional detection of complexes that fragment readily. The ESI–MS technique is, in fact, suitable for the study of various complexes [29] and was successfully applied for the study of copper and platinum complexes [30–36]. Preliminary measurements made using stronger ionisation systems, such as laser desorption ionisation (LDI) or matrix-assisted laser desorption ionisation (MALDI), only showed evidence of signals deriving from the platinum ion and from copper–phen complexes [15]. Instead, using ESI–MS, polynuclear complexes containing copper and platinum were found, and their stoichiometry was assessed on the basis of isotopic patterns and fragmentation results of tandem mass spectrometry (MS–MS). The molecules studied in this work are reported in Fig. 1.

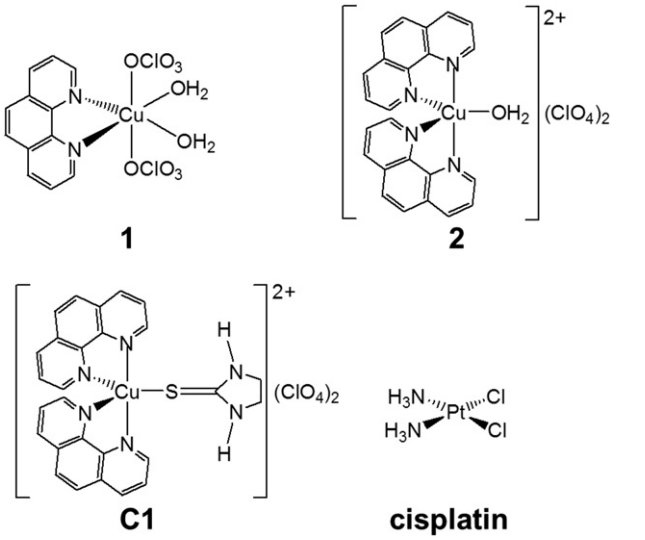

Fig. 1. Formulas and acronyms of the molecules studied in this work. Complex **1** is $Cu(phen)(OH_2)_2(OClO_3)_2$, **2** is $[Cu(phen)_2(OH_2)](ClO_4)_2$, **C1** is $[Cu(phen)_2(H_2dit)](ClO_4)_2$ and cisplatin is *cis*-diammineplatinum(II) dichloride (phen = 1,10-phenanthroline, H_2dit = the imidazolidine-2-thione).

2. Experimental section

2.1. Reagents and apparatus

Methanol (CH_3OH), propanol ($CH_3(CH_2)_2OH$), isopropanol ($(CH_3)_2CHOH$), CH_3CN, DMSO, H_2dit, phen and trifluoroacetic acid (HTFA) were purchased from Sigma-Aldrich. *Cis*-diammineplatinum(II) dichloride (cisplatin) was purchased from Alfa-Aesar. The commercial reagents were used as received, without any further purification. Ultrapure water obtained with MilliQ Millipore was used for all experiments. Mass spectra in positive-ion mode were obtained on a triple quadruple QqQ Varian 310-MS mass spectrometer using the atmospheric-pressure ESI technique. The sample solutions were infused directly into the ESI source using a programmable syringe pump at a flow rate of 1.50 ml/h. A dwell time of 14 s was used and the spectra were accumulated for at least 10 min in order to increase the signal-to-noise ratio. Tandem MS–MS experiments were performed with argon as the collision gas (1.8 PSI) using a needle voltage of 6000 V, shield voltage of 800 V, housing temperature of 60 °C, drying gas temperature of 120 °C, nebuliser gas pressure of 40 PSI, drying gas pressure of 20 PSI and a detector voltage of 2000 V. The collision energy was varied from 2 to 45 V. The isotopic patterns of the measured peaks in the mass spectra were analysed using mMass 5.5.0 software package [37–39]. The assignments were based on the copper-63 and platinum-195 isotopes.

2.2. Preparation of *1*, *2* and *C1*

The synthesis methods for **1**, **2** and **C1** have previously been reported [40,41]. However, in this work, we report new synthetic routes with less-toxic solvents and/or with higher yields.

$[Cu(phen)(OH_2)_2(OClO_3)_2]$ **(1):** The basic carbonate of copper(II) $Cu_2(CO_3)(OH)_2$ (1.0 g, 4.54 mmol) was suspended in isopropanol (50 ml), and the suspension was warmed to boiling point. Concentrated perchloric acid was slowly added to the suspension, whilst stirring, until a clear-blue solution was obtained. The solution was boiled for 10 min to remove all carbon dioxide that was formed, and then it was cooled to room temperature. An isopropanolic solution of phen (0.4 g, 2.22 mmol) was slowly added drop-wise whilst stirring. In presence of opalescence, the addition of phen was interrupted and the solution was left stirring until the precipitate disappeared, and phen addition was then resumed. The entire process required 3 h. The resulting blue solution was filtered, concentrated under vacuum (10 ml) and left to crystallise. Blue crystals were obtained after 12 h. The percentage yield was 95% (calculated on the basis of the amount of phen). The product was re-crystallised from CH_3CN. The final yield was 98%. Anal. Calcd. for $Cu(phen)(OH_2)_2(ClO_4)_2$: C 30.11, H 2.53, N 5.85, found: C 30.87, H 2.66, N 5.79.

$[Cu(phen)_2(OH_2)](ClO_4)_2$ **(2)**: The basic carbonate of copper(II) $Cu_2(CO_3)(OH)_2$ (1.0 g, 2.22 mmol) was suspended in isopropanol (50 ml) and the suspension was warmed to boiling point. Concentrated perchloric acid was slowly added to the suspension, whilst stirring, until a clear-blue solution was obtained. The solution was boiled for 10 min to

remove all carbon dioxide that was formed, and then it was cooled to room temperature and an isopropanolic solution of phen (1.64 g, 4.44 mmol) was slowly added. The resulting turquoise precipitate was filtered off under vacuum, washed with isopropanol and dried at room temperature. The percentage yield was 88%. The product was re-crystallised from CH_3CN. The final yield was 99%. Anal. Calcd. for $Cu(phen)_2(OH_2)(ClO_4)_2$: C 44.98, H 2.84, N 8.74, found: C 44.30, H 2.96, N 8.91.

$[Cu(phen)_2(H_2dit)](ClO_4)_2$ **(C1)**: A portion of **2** (0.30 g, 0.41 mmol) and H_2dit (0.048 g, colourless) were suspended in distilled water (50 ml). The suspension was stirred for 12 h at room temperature, after which a green powder was recovered by filtration under vacuum. The product was washed with water and dried at room temperature. Yield: 80%. The product was re-crystallised from CH_3CN. The final yield was 97%. Anal. Calcd. for $Cu(phen)_2(H_2dit)(ClO_4)_2$: C 44.73, H 3.06, N 11.59, found: C 45.01, H 2.98, N 11.30.

2.3. ESI–MS measurements

2.3.1. Copper complexes

A solution of **1** was prepared by dissolving an appropriate amount of the compound in water containing 0.05% of HTFA (v/v). Solutions of **2** and **C1**, which are both insoluble in water, were prepared by dissolving an appropriate amount of the compounds in DMSO (100 μl) and diluting to 50 ml with water containing 0.05% of HTFA (v/v). The stability of the compounds in DMSO or in DMSO/water/HTFA solutions was checked by measuring the UV–visible (UV–Vis) absorbance of the resulting solutions during the time. No changes in the UV–Vis absorbance were evidenced in 14 days.

All sample solutions were mixed with methanol in 1:1 H_2O/CH_3OH volume ratio immediately before the mass measurements in order to improve the quality of the spectra. Mass spectra of **1**, **2** and **C1** were recorded in the *m/z* range 100–1000 at a final concentration of 0.5 mM. The same experimental conditions were used for the three compounds (needle voltage 4500 V, shield voltage 600 V, housing temperature 60 °C, drying gas temperature 120 °C, nebuliser gas pressure 40 PSI, drying gas pressure 20 PSI, and detector voltage 1450 V).

2.3.2. Cisplatin

A solution of cisplatin was prepared by dissolving an appropriate amount of the compound in water containing 0.05% of HTFA (v/v). The solution was mixed with methanol in 1:1 H_2O/CH_3OH volume ratio immediately before the mass measurements in order to improve the quality of the spectra. The mass spectrum of cisplatin was recorded in the *m/z* range 100–1000 at a final concentration of 0.5 mM. The experimental conditions were: needle voltage 6000 V, shield voltage 600 V, housing temperature 60 °C, drying gas temperature 120 °C, nebuliser gas pressure 40 PSI, drying gas pressure 20 PSI, and detector voltage 2000 V.

2.3.3. Binary combinations

Solutions containing a copper complex and cisplatin in 10:1, 5:1 and 1:1 Pt/Cu molar ratios were prepared, keeping the cisplatin concentration constant (1.0 mM). Sample solutions were mixed with methanol in 1:1 H_2O/CH_3OH volume ratio in order to improve the quality of the spectra. So as not to alter the complex formation equilibria, methanol was added immediately before the mass spectra were recorded. Solutions containing cisplatin and the copper complex were analysed at 4500, 600 and 1500 V as needle, shield and detector voltages, respectively, for studying masses in the *m/z* range 100–450, and at 6000, 800 and 2000 V as needle, shield and detector voltages, respectively, for studying masses in the *m/z* range 450–1000. All other parameters were kept constant during the experiments (housing temperature 60 °C, drying gas temperature 120 °C, nebuliser gas pressure 40 PSI, and drying gas pressure 20 PSI).

2.4. Biological assays

2.4.1. Cell lines

The cisplatin-resistant subline of human acute T-lymphoblastic leukaemia (CCRF-CEM-res) and cisplatin-resistant subline of human ovarian carcinoma (A2780-res) were used in the study. The CCRF-CEM-res subline was obtained by us (see Section 2.4.2); the cell line was maintained in culture between 1×10^5 cells/ml and 1×10^6 cells/ml in RPMI medium 10% foetal bovine serum (FBS) with 1% kanamycin (growth medium). To the growth medium for CCRF-CEM-res cell cultures, we also added cisplatin (5 μM). A2780-res cells were a generous gift by Dr. Eva Fischer (Tumor Biology Laboratory, The Ion Chiricuta Oncology Institute, Cluj-Napoca, Romania) and were grown in RPMI medium with 2 mM glutamine and 10% FBS. Cell monolayers were sub-cultivated when they reached 70% confluency (every 3–4 days) by a 1:3 ratio. In order to keep the cisplatin resistance, A2780-res were cultured in the presence of 1 μM cisplatin every two to three passages. All cell lines were periodically checked for micoplasma contamination. For the experiments, each cell line was replaced every 3 months with freshly-towed cells from the cell stores in liquid nitrogen.

2.4.2. Selection of the cisplatin-resistant CCRF-CEM subline

A CCRF-CEM subline able to grow at the same extent in the absence and in the presence of 5 μM cisplatin (CCRF-CEM-res) was obtained by serial passages of wild-type cells in the presence of increasing cisplatin concentrations, starting from a sub-inhibitory concentration (0.5 μM). At each cell passage (every 3–4 days), the number of viable cells of cisplatin-treated cultures was compared to that of duplicate untreated cultures. The cisplatin concentration was increased at each cell passage up to 1.50 μM; from then on, cisplatin-treated cultures grew poorly and much slower than their untreated counterparts and had to be kept (5–10 passages) at the same cisplatin concentration until the cell population had regained original growth timing and viability. At intervals during the selection process, the level of cisplatin resistance was checked by the 3-(4,5-dimethylthiazol-2-yl)-2,5-diphenyl-tetrazolium bromide (MTT) method in cells that had grown without the drug for one passage; doxorubicin was used as a reference compound to evaluate the cisplatin-resistance specificity. Given that cell cultures never survived at concentrations over 5 μM, the cell population was stabilised by 15 further passages at 5 μM cisplatin, and then grown without the drug for one passage, checked for the level of resistance as described above, and finally stored in aliquots in liquid nitrogen for further use.

2.4.3. Cytotoxic assays

Stock solutions of the copper complexes were prepared in DMSO (1 mM) and stored at 4 °C in the dark. The biological stability of these solutions was checked verifying the cytotoxic activity measured by using the same solutions over more than 6 months. The tested compounds maintained the same IC50 (concentration required to inhibit cell proliferation by 50% with respect to untreated cells) in all the performed experiments. The DMSO solutions of cisplatin (1000× of the highest concentration to be used on the cell culture), being stable only for few hours and showing a decreasing of the cytotoxic potency during the time, were prepared in DMSO and diluted to the necessary concentration each time immediately before the experiments.

Dilutions of the drug stocks for biologic investigations were made in RPMI medium at 2× the final concentration for single drug evaluations, or at 4× the final concentration for evaluation of dual drug combinations. The concentration of DMSO in the cells was never higher than 0.1%. The effects of the drugs and drug combinations were evaluated in cultures of exponentially growing cells; for experiments in cisplatin-resistant cell cultures, both CCRF-CEM-res and A2780-res cells were allowed to grow in the absence of the drug for 1 passage. CCRF-CEM-res cells were seeded at a density of 1×10^5 cells/ml of growth medium in flat-bottomed 96-well plates and simultaneously exposed to the drugs or drug combinations. A2780-res cells were seeded

at 5×10^3 cells/well of flat-bottomed 96-well plates and allowed to adhere overnight before of the addition of the drugs or the drug combinations. Cell growth in the absence and presence of drugs was determined after 96 h of incubation at 37 °C and 5% CO_2 (corresponding to three to four duplication rounds of untreated cells), through both the viable cell counting, with the trypan blue exclusion method, and the MTT method [42,43]. Values obtained in drug-treated samples were expressed as percentages of those of their respective controls. Dose–response curves for each drug were determined and the IC50s of single drugs and drug combinations were calculated.

3. Results and discussion

3.1. Synthesis

The synthesised compounds were characterised, in addition to elemental analysis, by infrared (IR) and UV–Vis spectroscopy, finding results in agreement with the previously reported data [40,41]. The new synthesis method of **1** led to a crystalline product with a higher purity (≥95%) and yield. The obtained compound, which must be stored under vacuum, is hygroscopic and deliquescent. It is stable for a number of months at room temperature in a desiccator, but if warmed, its colour changes from blue to turquoise. The turquoise product was characterised by elemental analysis and IR spectroscopy and it resulted to be **2**. In the synthesis method of **C1**, the previously used solvent CH_3CN was changed to H_2O.

3.2. Cytotoxicity measurements

The cytotoxic activities of **2** and cisplatin, both alone and in dual drug combinations, were evaluated against CCFR-CEM-res and A2780-res human cell lines. Dose–response curves for **2** and cisplatin were obtained, and the IC50 values were determined. Copper complex **2** showed IC50 values of 0.75 and 0.24 μM in CCFR-CEM-res and A2780-res cells, respectively. Cisplatin showed IC50 values of 6.98 and 5.3 μM for CCFR-CEM-res and A2780-res cells, respectively. Dose–response curves of **2** and cisplatin in cisplatin-resistant cell lines are reported in the Supplementary Information (Fig. S1). The effects of single drugs and dual drug combinations on the tested cell lines are reported in Table 1 as a percentage of the untreated controls. In all cases, combinatorial treatment gave rise to a synergistic interaction between cisplatin and the studied copper complex. In particular, it is worth mentioning the synergistic effect shown by combinatorial treatments against cisplatin-resistant cell lines, which has evident potential in the clinic of cisplatin-resistant cancers.

Table 1
Antiproliferative activity (%) against cisplatin-resistant leukemic cancer cells (CCRF-CEM-res), cisplatin-resistant ovarian cancer cells (A2780-res) exhibited by copper complex **2**, cisplatin and their binary combinations.

2 (μM)	Cisplatin (μM)	Antiproliferative activity (%)	Cell line	Effect	Index of synergy*
0.67		40.0	CCRF-CEM-res		
	5.0	28.2			
0.67	5.0	88.0		synergism	31%
0.60		24.0			
	4.0	17.5			
0.60	4.0	59.5		synergism	22%
0.20		32.7	A2780-res		
	4.0	6.0			
0.20	4.0	58.4		synergism	22%
0.10		6.0			
0.10	4.0	20.0		synergism	8%

* Calculated as in Ref. [15].

3.3. ESI–MS results

3.3.1. Copper complexes

In the mass spectra of **1**, **2** and **C1**, only mono-charged species containing copper(II) or copper(I) were evidenced. Reduction of Cu(II) to Cu(I) is commonly observed in the ESI phase for solutions of Cu(II) salts [44]. Characteristic isotopic peaks for copper- and copper–chlorine-containing ions were clearly seen, and the isotopic patterns of these peaks confirmed the elemental composition of the observed ions. The most relevant peaks are assigned in the shown spectra (Fig. 2), whereas calculated and experimental isotopic patterns for selected peaks are reported in the Supplementary Information (Fig. S2). In the spectrum of **1** (Fig. 2A), the most important signals correspond to $[Cu^{(II)}(phen)(ClO_4)]^+$ (*m/z* 342), $[Cu^{(II)}(phen)Cl]^+$ (*m/z* 278) and $[Cu^{(I)}(phen)]^+$ (*m/z* 243) species. The last two species derive from fragmentation–recombination reactions occurring during the MS–MS of the parent compound $[Cu^{(II)}(phen)(ClO_4)]^+$. In the insert the peaks falling in the *m/z* range 340–350 are reported. Also other complexes were recognised, but they were identified as adducts with TFA or as the products of exchange reactions with fluorine carried out by the TFA. These complexes were $[Cu^{(II)}(phen)(TFA)]^+$ (*m/z* 356), $[Cu^{(II)}(phen)F]^+$ (*m/z* 262), and $[Cu^{(II)}(phen)_2(TFA)]^+$ (*m/z* 536). In the spectrum of **2** (Fig. 2B), some species observed in the spectrum of **1** are present ($[Cu^{(II)}(phen)Cl]^+$ (*m/z* 278), $[Cu^{(II)}(phen)(TFA)]^+$ (*m/z* 356), $[Cu^{(II)}(phen)_2(TFA)]^+$ (*m/z* 536)) together with $[phen+H]^+$ (*m/z* 181), $[Cu^{(I)}(phen)_2]^+$ (*m/z* 423), $[Cu^{(II)}(phen)_2Cl]^+$ (*m/z* 458), and $[Cu^{(II)}(phen)_2(ClO_4)]^+$ (*m/z* 522). The species $[phen+H]^+$, $[Cu^{(I)}(phen)_2]^+$ and $[Cu^{(II)}(phen)_2Cl]^+$ are fragmentation products of the parent compound $[Cu^{(II)}(phen)_2(ClO_4)]^+$. In the spectrum of **C1** (Fig. 2C), some species observed in the spectrum of **1** and **2** are

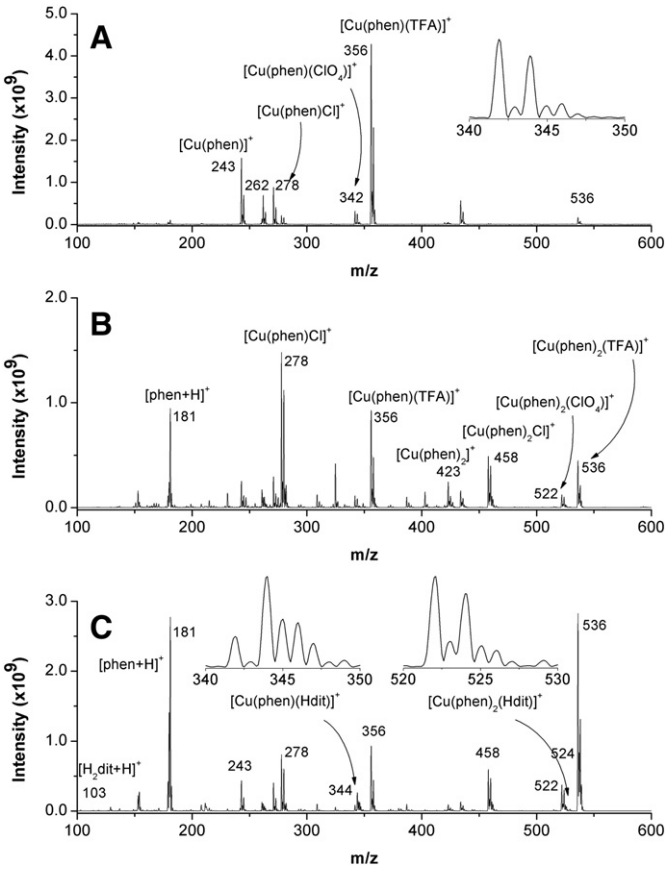

Fig. 2. ESI mass spectra (+) of **1** (A), **2** (B) and **C1** (C); 0.5 mM, 50:50 methanol/water with 0.05% of trifluroacetic acid (phen = 1,10-phenanthroline, H_2dit = the imidazolidine-2-thione, TFA = trifluroacetate ion).

present ($[phen+H]^+$ (*m/z* 181), $[Cu^{(I)}(phen)]^+$ (*m/z* 243), $[Cu^{(II)}(phen)Cl]^+$ (*m/z* 278), $[Cu^{(II)}(phen)(TFA)]^+$ (*m/z* 356), $[Cu^{(II)}(phen)_2Cl]^+$ (*m/z* 458), $[Cu^{(II)}(phen)_2(ClO_4)]^+$ (*m/z* 522), $[Cu^{(II)}(phen)_2(TFA)]^+$ (*m/z* 536)) together with species containing the thionic ligand H_2dit, that is, $[Cu^{(II)}(phen)_2(Hdit)]^+$ (*m/z* 524), $[Cu^{(II)}(phen)(Hdit)]^+$ (*m/z* 344), and $[H_2dit+H]^+$ (*m/z* 103). In the inserts are reported the peaks falling in the *m/z* ranges 340–350 and 520–530. The presence of the $[phen+H]^+$ signal in the spectra of **2** and **C1**, is due to the fragmentation of the Cu–phen complexes. The species $[Cu^{(I)}(phen)]^+$, $[Cu^{(II)}(phen)Cl]^+$, $[Cu^{(II)}(phen)(TFA)]^+$, $[Cu^{(II)}(phen)_2(TFA)]^+$ are detectable in all the spectra, as fragmentation products of the parent compounds. The species $[Cu^{(II)}(phen)(Hdit)]^+$ and $[H_2dit+H]^+$ are fragmentation products of the parent compound $[Cu^{(II)}(phen)_2(Hdit)]^+$. The occurrence of $[Cu(phen)_2(TFA)]^+$ also in the spectrum of **1**, is due to a reaction in ESI phase between the monochelate complex Cu–phen and the freed phen (the intensity of the related signal at *m/z* 536, lowers directly with the needle potential). All the fragmentation processes were studied by tandem MS-MS. The assignments are tabulated with calculated *m/z* values in Table 2 (rows 1–18).

It is interesting to remark that, although the copper complexes have been measured at the same molar concentration, their mass spectra presented different intensities, from 4.5×10^9 (for **1**) to 1.75×10^9 a.u. (for **2**).

3.3.2. Cisplatin

The ESI–MS spectrum of cisplatin is reported from *m/z* 200 to 315 in Fig. 3 and from 300 to 600 in Fig. S3. Due to the number of the isotopic peaks of the metal ion and to the limited resolving power of the instrument, the peaks in the spectrum appear broad. The signal related to the protonated cisplatin, $[Pt(NH_3)_2Cl_2+H]^+$, appears at *m/z* 300. Other signals related to $[Pt(NH_3)_2Cl]^+$, $[Pt(NH_3)Cl]^+$ and $[Pt(NH_2)]^+$ are present at *m/z* 264, 247, and 211, respectively. A signal interpreted as a mixture of $[Pt(NH_3)_3(H_2O)_2Cl]^+$ (78%) and $[Pt(NH_3)_2(H_2O)_3Cl]^+$ (22%) is present at *m/z* 317-318. At *m/z* 546 and 563, signals of the di-nuclear complexes $[Pt_2(NH_3)_3Cl_3]^+$ and $[Pt_2(NH_3)_4Cl_3]^+$ can be seen. Calculated and experimental isotopic patterns for selected peaks are reported in the Supplementary Information (Fig. S4). In the species containing platinum and NH_2^-, a double bond between platinum and nitrogen ion is present, which has already been reported [36,45]. It is important to remark that the mass-spectral profile of cisplatin solutions begins to change 1 h after preparation, as the compound undergoes hydrolysis. In fact, the signals at *m/z* 300, 264 and 247 decrease in intensity and adducts with water and methanol are formed. The assignments are tabulated with calculated *m/z* values in Table 2 (rows 19–26).

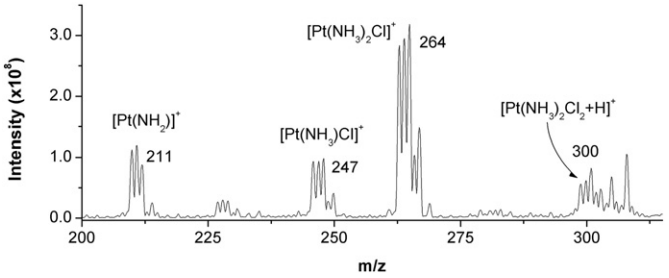

Fig. 3. ESI–MS (+) spectrum of cisplatin in the *m/z* 200–315 range; 0.5 mM, 50:50 methanol/water with 0.05% of trifluroacetic acid.

3.3.3. Binary combinations

Several binary mixtures of cisplatin and copper complexes were prepared and their mass spectra were acquired in order to verify the formation of a mixed complex.

3.3.3.1. Cisplatin and copper complexes. The number and the aspect of the signals present in the spectra are strongly dependent on the chosen experimental conditions of needle, shield and detector voltages. Generally, increasing the voltage of the needle, shield and detectors causes the fragmentation processes to increase. The fragmentations are helpful, as they are characteristic of the molecule and provide structural information. However, as the fragments themselves can undergo to a further fragmentation, the resulting spectra could become difficult to understand. On the other hand, a voltage that is too low determines a fall in the overall ion current, leading to a reduction in the ionisation efficiency. These issues could determine non-reliable signals [46].

The mass spectra of the binary combinations were collected by varying the voltage values in order to find the optimal conditions. In all the experiments, signals with isotopic pattern characteristic of species containing both copper and platinum were observed. However, at needle, shield, and detector voltages of 4500, 600, and 1500 V, respectively, the signals with reliable intensities (10^9 magnitude) were characteristic of species containing only copper as the metal ion. In particular, signals of the species $[Cu^{(II)}(phen)(TFA)]^+$ (*m/z* 356), $[Cu^{(I)}(phen)(H_2O)]^+$ (*m/z* 261), and $[Cu^{(I)}(phen)]^+$ (*m/z* 243) were present. To observe signals of the other ions with sufficient intensity, needle, shield, and detector voltages of 6000, 800, and 2000 V, respectively, were used. The binary combinations were tested at 1:1, 5:1 and 10:1 platinum/copper molar ratios. In the spectra of the equimolar mixtures, the signals originating from the copper complexes were more intense than those originating from cisplatin. The measured mass spectra of the solutions containing cisplatin and **2** at the three different molar ratios are reported as an example in Fig. S5. The signals of the mixed complexes containing both copper and platinum appeared at all molar ratios for all of the studied systems; however, at 1:1 platinum/copper, the more intense signals (marked with "*" in Fig. S5) were attributed to mono- and polynuclear copper complexes. The stoichiometry of these complexes were identified from the *m/z* value and from the isotopic pattern as $[Cu^{(II)}{}_2(phen)_2(TFA)Cl_2]^+$ (*m/z* 669), $[Cu^{(I)}{}_3(phen)_2(TFA)(OH)(H_2O)_2]^+$

Table 2
Species identified from the ESI–MS studies.

Row	Ion	Composition	Exp. *m/z**	Calc. *m/z**
1	$[Cu_2(phen)_2(TFA)_2(ClO_4)]^+$	$C_{28}H_{16}ClCu_2F_6N_4O_8$	810.94	810.91
2	$[Cu_2(phen)_2(TFA)_2Cl]^+$	$C_{28}H_{16}ClCu_2F_6N_4O_4$	746.90	746.94
3	$[Cu_3(phen)_2(TFA)(OH)(H_2O)_2]^+$	$C_{26}H_{21}Cu_3F_3N_4O_5$	714.86	714.93
4	$[Cu_2(phen)_2(TFA)Cl_2]^+$	$C_{26}H_{16}Cl_2Cu_2F_3N_4O_2$	668.87	668.92
5	$[Cu(phen)_2(TFA)]^+$	$C_{26}H_{16}CuF_3N_4O_2$	536.11	536.05
6	$[Cu(phen)_2(Hdit)]^+$	$C_{27}H_{21}CuN_6S$	522.02	524.08
7	$[Cu(phen)_2(ClO_4)]^+$	$C_{24}H_{16}ClCuN_4O_4$	521.95	522.01
8	$[Cu(phen)_2Cl]^+$	$C_{24}H_{16}ClCuN_4$	458.03	458.04
9	$[Cu(phen)_2]^+$	$C_{24}H_{16}CuN_4$	423.05	423.07
10	$[Cu(phen)(TFA)]^+$	$C_{14}H_8CuF_3N_2O_2$	355.94	355.98
11	$[Cu(phen)(Hdit)]^+$	$C_{15}H_{13}CuN_4S$	343.99	344.02
12	$[Cu(phen)(ClO_4)]^+$	$C_{12}H_8ClCuN_2O_4$	341.88	341.95
13	$[Cu(phen)Cl]^+$	$C_{12}H_8ClCuN_2$	277.92	277.97
14	$[Cu(phen)F]^+$	$C_{12}H_8CuFN_2$	261.95	262.00
15	$[Cu(phen)(H_2O)]^+$	$C_{12}H_{10}CuN_2O$	260.94	261.01
16	$[Cu(phen)]^+$	$C_{12}H_8CuN_2$	242.96	243.00
17	$[phen+H]^+$	$C_{12}H_9N_2$	181.05	181.08
18	$[H_2dit+H]^+$	$C_3H_7N_2S$	102.99	103.03
19	$[Pt_2(NH_3)_4Cl_3]^+$	$H_{12}Cl_3N_4Pt_2$	562.79	562.94
20	$[Pt_2(NH_3)_3Cl_3]^+$	$H_9Cl_3N_3Pt_2$	545.80	545.92
21	$[Pt(NH_3)_2(H_2O)_3Cl]^+$	$H_{12}ClN_2O_3Pt$	318.88	318.02
22	$[Pt(NH_3)_3(H_2O)_2Cl]^+$	$H_{13}ClN_3O_2Pt$	317.84	317.03
23	$[Pt(NH_3)_2Cl_2+H]^+$	$H_7Cl_2N_2Pt$	300.84	299.96
24	$[Pt(NH_3)_2Cl]^+$	H_6ClN_2Pt	263.88	263.99
25	$[Pt(NH_3)Cl]^+$	H_3ClNPt	246.85	246.96
26	$[Pt(NH_2)]^+$	H_2NPt	210.88	210.98
27	$[CuPt(phen)(H_2O)_2(OH)Cl_2]^+$	$C_{12}H_{13}Cl_2CuN_2O_3Pt$	560.90	560.92
28	$[CuPt(phen)(H_2O)(NH_3)(OH)Cl_2]^+$	$C_{12}H_{14}Cl_2CuN_3O_2Pt$	559.90	559.94
29	$[CuPt(phen)(H_2O)_2Cl_2]^+$	$C_{12}H_{12}Cl_2CuN_2O_2Pt$	543.95	543.92

* The experimental and calculated *m/z* values refer to the peak representative of the monoisotopic mass.

(m/z 715), $[Cu^{(II)}_2(phen)_2(TFA)_2Cl]^+$ (m/z 747) and $[Cu^{(II)}_2(phen)_2(TFA)_2(ClO_4)]^+$ (m/z 811).

At 10:1 platinum/copper molar ratio, together with signals of copper and mixed copper–platinum complexes, signals of poly-nuclear complexes containing two or more platinum ions and a variable number of chlorine, ammonia and water molecules, were present in the m/z range 800–1000. The lack of a good pattern resolution prevented the determination of their exact stoichiometry. From these results, it followed that the combination at 5:1 platinum/copper molar ratio was the best one to study mixed platinum–copper complexes.

In Fig. 4, the mass spectra of solutions containing cisplatin and **1**, cisplatin and **2** as well as cisplatin and **C1**, at 5:1 platinum/copper molar ratio, are reported (signals from the copper complexes are marked with "*"). As can be seen, the mass spectra of all systems present a similar profile, even if they have different intensities, indicating that the same mixed complexes were formed. In particular, the signals with the isotopic pattern typical of mixed platinum–copper complexes fall in the m/z range 540–660. As for the copper complexes, the stoichiometry of these mixed complexes was identified from the m/z value and from the isotopic pattern. In many cases, convoluted signals were observed, owing to the simultaneous presence of complexes with similar masses. In this case, the experimental pattern was attributed to a weighted combination of the isotopic pattern of the different molecules. The weights, that is, the percentage in which each molecule was present, were obtained by multivariate regression analysis of the experimental data. An example of this treatment is reported in Fig. S6, in which the experimental pattern can be compared to the theoretical one, calculated as a contribution of four molecules.

From the analysis of the spectra, we identified three principal complexes, all mono-charged with the following stoichiometries: **I**) $[CuPt(phen)(H_2O)_2(OH)Cl_2]^+$ (m/z 561), **II**) $[CuPt(phen)(H_2O)(NH_3)(OH)Cl_2]^+$ (m/z 560), and **III**) $[CuPt(phen)(H_2O)_2Cl_2]^+$ (m/z 544). Together with **I–III**, nine other complexes were identified, but they turned out to be adducts with TFA or products of exchange reactions with the fluorine carried out by the TFA. These nine complexes could be thought as by-products (the complete list of these complexes is reported in the Supplementary, Table S1). The assignments are tabulated with calculated m/z values in Table 2 (rows 27–29).

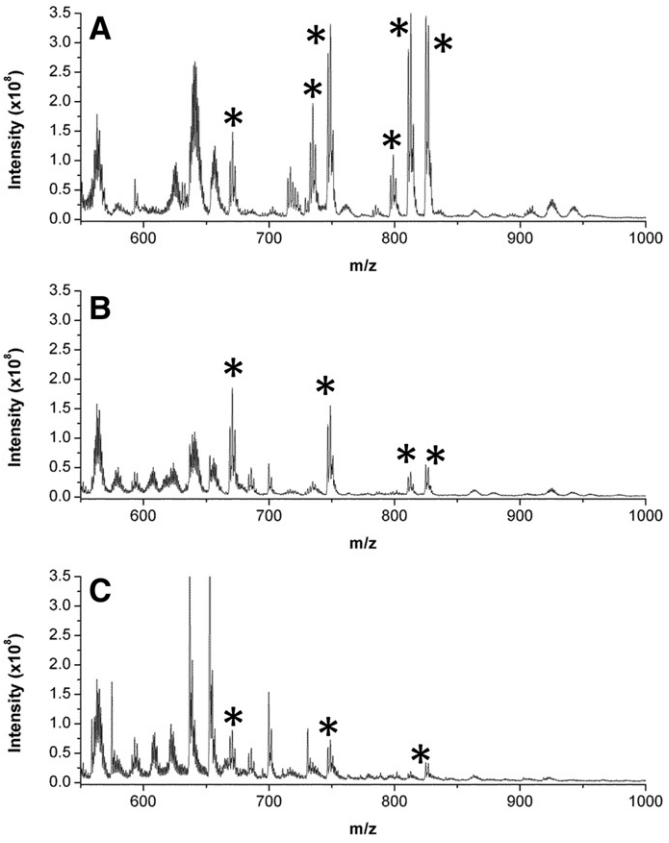

Fig. 4. ESI mass (+) spectra of cisplatin and **1** (A), cisplatin and **2** (B), cisplatin and **C1** (C) (cisplatin 0.5 mM, copper complex 0.1 mM, 50:50 methanol/water with 0.05% of trifluroacetic acid). In the spectra, copper complexes are marked with "*".

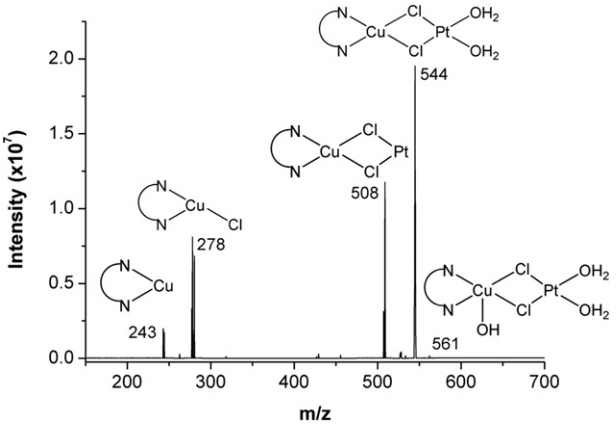

Fig. 5. Tandem MS–MS spectrum of the signals at m/z 561. The isotopic pattern was partially lost for the low signal intensity and for the little range of m/z isolated (collision energy 20 V, charges are omitted for clarity, the two nitrogen connected by a curved line represent the phen molecule).

3.3.3.2. Tandem MS–MS. Tandem mass spectrometry was essential to confirm the proposed stoichiometry and to hypothesise the structure of the formed complexes. A brief description of this technique is reported in the caption of the Fig. S7.

The fragmentation profiles obtained for compounds **I–III** are reported in Figs. 5–7. As can be seen in Fig. 5 for **I**, species with stoichiometries $[Cu(phen)]^+$ (m/z 243), $[Cu(phen)Cl]^+$ (m/z 278), and $[CuPt(phen)Cl_2]^+$ (m/z 508) were visible as fragments of the parent compound $[CuPt(phen)(H_2O)_2(OH)Cl_2]^+$ (m/z 561). The structures of the $[Cu(phen)]^+$, $[Cu(phen)Cl]^+$ and $[CuPt(phen)Cl_2]^+$ ions were easily proposed, as shown in the figure. To define the structure of the fragment at m/z 544, it was convenient to consider it as (m/z 508 + m/z 2 × 18). Three possibilities were considered as two water molecules linked to the copper (case *i*) or to the platinum (case *ii*) or one water molecule linked to the copper and one to the platinum (case *iii*). If one or two water molecules were linked to the copper, the resulting

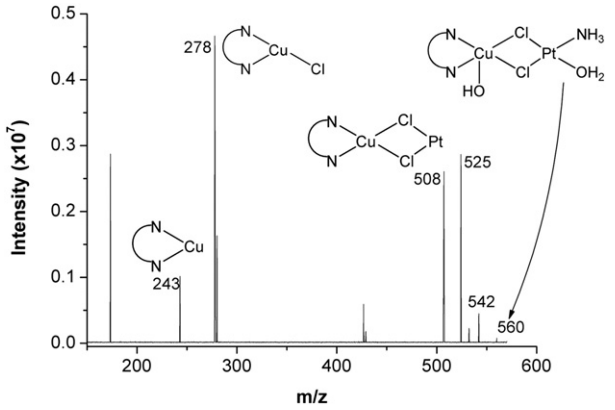

Fig. 6. Tandem MS–MS spectrum of the signals at m/z 560. The isotopic pattern was partially lost for the low signal intensity and for the little range of m/z isolated (collision energy 20 V, charges are omitted for clarity, the two nitrogen connected by a curved line represent the phen molecule).

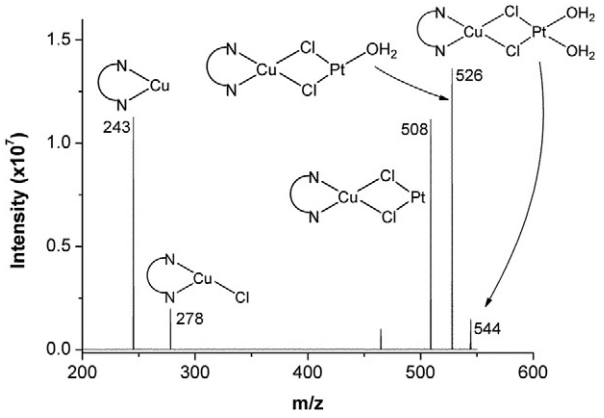

Fig. 7. Tandem MS–MS spectrum of the signals at *m/z* 544. The isotopic pattern was partially lost for the low signal intensity and for the little range of *m/z* isolated (collision energy 20 V, charges are omitted for clarity, the two nitrogen connected by a curved line represent the phen molecule).

complex should have had a +2 charge, while, if the water molecules were linked to the platinum the charge of the complex should have been +1 (note that when copper is tetra-coordinated its oxidation number is +1, if it is penta- or esa-coordinated its oxidation number is +2). The fragment was mono-charged, then only the case *ii* was considered. To define the structure of the parent compound at *m/z* 561, it was convenient to consider it as (*m/z* 544 + *m/z* 17). Ammonia and hydroxide ions have an *m/z* of 17; therefore, the two possibilities were considered as hydroxide or ammonia linked to the copper. If OH^- was linked to the copper, the resulting complex should have had a +1 charge, whereas, if ammonia was present, the charge of the complex should have been +2. The fragment was mono-charged, then only the OH^- ion was considered. Therefore, the structure of the parent ion was proposed as reported in the figure, that is, $[Cu(phen)(OH)\mu\text{-}(Cl)_2Pt(H_2O)_2]^+$.

The study of compound **II** appeared more complicated. As for **I**, the structures of the $[Cu(phen)]^+$, $[Cu(phen)Cl]^+$, and $[CuPt(phen)Cl_2]^+$ were easily proposed, as shown in Fig. 6. As for the fragment at *m/z* 525, it was considered as (*m/z* 508 + *m/z* 17). Then, four possibilities were considered, that is, hydroxide linked to platinum (*i*) or to copper (*ii*) and ammonia linked to platinum (*iii*) or to copper (*iv*). If OH^- or NH_3 were linked to platinum, the resulting complexes (cases *i* and *iii*) should have had 0 or +1 as the charge, respectively. If OH^- or NH_3 were linked to copper, the resulting complexes (cases *ii* and *iv*) should have had a +1 or +2 charge, respectively. As the fragment was mono-charged, only cases *ii* and *iii* were considered. With regards to the fragment at *m/z* 542, as before, it was considered as (*m/z* 525 + *m/z* 17). Then, six possibilities were taken into account, starting from the previous cases *ii* and *iii*, that is, *ii* + OH^- or NH_3 linked to platinum (cases *v* and *vi*), *iii* + OH^- or NH_3 linked to copper (cases *vi* and *ix*), *iii* + OH^- or NH_3 linked to platinum (cases *vii* and *viii*). As the fragments are mono-charged, the only possibilities that were considered were *vi* and *viii*. The last fragment was considered as (*m/z* 525 + *m/z* 18), and a water molecule was added to *vi* and *viii*, to obtain *x* (with +1 charge) and *xi* (with +2 charge). Then, the most probable structure of the parent ion was that of *x*, that is, $[Cu(phen)(OH)\mu\text{-}(Cl)_2Pt(NH_3)(H_2O)]^+$. The entire route is shown in Fig. S7. As far as compound **III** is concerned, similar considerations were made to obtain as the most probable structure, $[Cu(phen)\mu\text{-}(Cl)_2Pt(H_2O)_2]^+$, as shown in the Fig. 7. All of the reported fragmentations were obtained with a CE of 20 V. To fragment the $[Cu(phen)]^+$ complex, a collision energy of 45 V was necessary, but at this energy value, the other fragments were no longer observable.

Compound **III** can be considered as a fragment of **I**, which itself can be considered as a hydrolysis product of **II**. A precursor with the formula $[Cu(phen)(OH)\mu\text{-}(Cl)_2Pt(NH_3)_2)]^+$ can be hypothesised in solution; however, this species was not detected in our experiments. The proposed reaction between copper complexes and cisplatin is finally resumed in Scheme 1. As can be seen, the same complex is formed, regardless of the copper complex (**1**, **2** or **C1**) involved. In the reaction of **2** or **C1** with cisplatin, one phen unit is released; in the case of **C2**, a H_2dit unit is also released. In the formed complex, copper and platinum are linked by two bridging chlorides and the coordination spheres of copper is completed by a phen and a hydroxide ion, and that of platinum is completed by ammonia and water molecules. From the mass spectral evidence, the mixed copper–platinum complex was formed in aqueous solution a few minutes after the mixing of the reagents, and it was stable for at least 1 week. The same reaction carried out in water–acetonitrile required 3 weeks to be completed.

4. Conclusions

Binary combinations of cisplatin and the copper complex $[Cu(phen)_2(OH_2)](ClO_4)_2$ present a synergistic antiproliferative effect against the cisplatin-resistant sublines of leukemic (CCRF-CEM-res) and ovarian (A2780-res) cancer cells *in vitro*. Considering that the synergy may arise from a chemical reaction between the two metal complexes, solutions containing cisplatin and the copper complex $Cu(phen)(OH_2)_2(OClO_3)_2$, $[Cu(phen)_2(OH_2)](ClO_4)_2$ or $[Cu(phen)_2(H_2dit)](ClO_4)_2$ were studied by ESI–MS and tandem MS–MS. A mixed complex containing copper and platinum with a stoichiometry of $[Cu(phen)(OH)\mu\text{-}(Cl)_2Pt(NH_3)(H_2O)]^+$ was detected. This complex was able to hydrolyse to form $[Cu(phen)(OH)\mu\text{-}(Cl)_2Pt(H_2O)_2]^+$ that was actually detected. Both the complexes were formed, regardless of the copper complex used; then, in the reaction of $[Cu(phen)_2(OH_2)](ClO_4)_2$ and $[Cu(phen)_2(H_2dit)](ClO_4)_2$ with cisplatin, one phen and/or one H_2dit was released. Phen presents itself an IC50 value of approximately 2 μM towards the tested cell lines, and it can contribute to the overall cytotoxic activity shown by the mixtures, unlike H_2dit, which is devoid of any biological activity against the tested cells. The formation of the mixed copper–platinum complex could be related to the synergistic effect of the combination of the studied copper complexes with cisplatin shown towards the tested cell line. Given that the synergy was also observed against cisplatin-resistant cells, the formed copper–platinum complex is likely to interfere with one or more of the mechanisms that lead to cisplatin resistance. Furthermore, considerations about the reactivity can be made. In fact, it is accepted that the determining steps in the interaction of cisplatin with DNA are the hydrolysis processes that are slow in saline solutions. Complexes $[Cu(phen)(OH)\mu\text{-}(Cl)_2Pt(NH_3)(H_2O)]^+$ and $[Cu(phen)(OH)\mu\text{-}(Cl)_2Pt(H_2O)_2]^+$ are formed within a few minutes and are already hydrolysed. They can then react with DNA more readily than cisplatin. More experiments

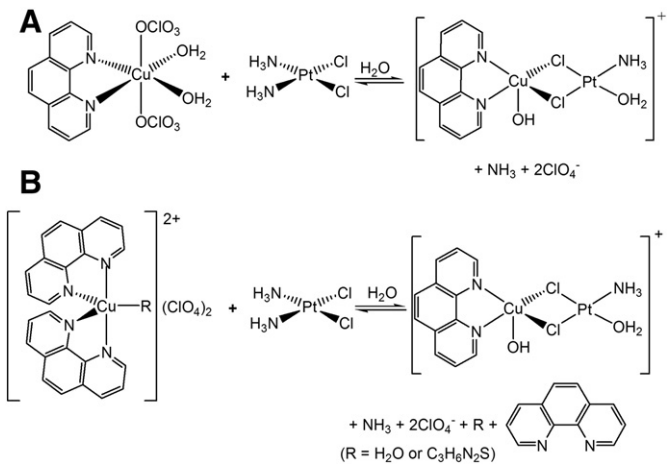

Scheme 1. Reaction mechanism between **1** and cisplatin (A) and **2** or **C1** and cisplatin (B).

have to be carried out in order to obtain more insights and possibly clarify the underlying molecular mechanism(s). In this regards, as a future perspective, we intend to extend these studies to other cisplatin-resistant cell lines.

From the reported results, the ESI–MS and tandem MS–MS appear as suitable tools for the study of the metal complexes formed in solution. Of course, in the transition process from the solution to gas phase, the structure of the complexes may be affected, and this is particularly relevant for large molecules such as metal complexes with biomolecules. In the case of the metal complexes, the electrochemical reactions occurring at the capillary may also modify the valence state of the metal ion inducing a structural change. Also the fragmentation products may recombine to form new species. Then, the species detected in ESI–MS not necessarily correspond to those actually present in the sample solution. Nevertheless, relevant information on the solution stability and reactivity of complexes that are not easily isolable in the solid state can indeed be obtained under several experimental conditions such as different media, pH values and ionic buffers.

Abbreviations

ESI–MS	electrospray ionisation mass spectroscopy
Phen	1,10-phenanthroline
CCRF-CEM	human acute T-lymphoblastic leukaemia
CCRF-CEM-res	cisplatin resistant human acute T-lymphoblastic leukaemia
A2780	ovarian cancer
A2780-res	cisplatin resistant ovarian cancer
MD	multi-drug
MALDI	matrix assisted laser desorption ionisation
LDI	laser desorption ionisation
HTFA	trifluoroacetic acid
TFA	trifluoroacetate
H_2dit	imidazolidone-2-thione
FBS	foetal bovine serum
MTT	3-(4,5-dimethylthiazol-2-yl)-2,5-diphenyl-tetrazolium bromide
IC50	concentration required to inhibit cell proliferation by 50% with respect to untreated cells
MS–MS	tandem mass spectrometry
CE	collision energy

Acknowledgements

Federica Trudu and Daniela Perra gratefully acknowledge the Sardinia Regional Government for the financial support of her PhD scholarship (P.O.R. Sardegna F.S.E. Operational Programme of the Autonomous Region of Sardinia, European Social Fund 2007-2013-Axis IV Human Resources, Objective l.3, Line of Activity l.3.1.).

Appendix A. Supplementary data

Supplementary data to this article can be found online at http://dx.doi.org/10.1016/j.jinorgbio.2015.05.004.

References

[1] S. Ishida, J. Lee, D.J. Thiele, I. Herskowitz, Proc. Natl. Acad. Sci. U. S. A. 99 (2002) 14298–14302.
[2] I. Song, N. Savaraj, Z.H. Siddik, P. Liu, Y. Wei, C.J. Wu, M.T. Kuo, Mol. Cancer Ther. 3 (2005) 1543–1549.
[3] H. Burger, a Zoumaro-Djayoon, a W.M. Boersma, J. Helleman, E.M.J.J. Berns, R.H.J. Mathijssen, W.J. Loos, E. a C. Wiemer, Br. J. Pharmacol. 159 (2010) 898–908.
[4] R.A. Alderden, M.D. Hall, T.W. Hambley, J. Chem. Educ. 83 (2006) 728–734.
[5] S. Trzaska, Chem. Eng. News 83 (2005) 52.
[6] E.R. Jamieson, S.J. Lippard, Chem. Rev. 99 (1999) 2467–2498.
[7] R.C. Todd, S.J. Lippard, Metallomics 1 (2009) 280–291.
[8] N. Eckstein, J. Exp. Clin. Cancer Res. 30 (2011) 91–102.
[9] S. Dhar, F.X. Gu, R. Langer, O.C. Farokhzad, S.J. Lippard, Proc. Natl. Acad. Sci. U. S. A. 105 (2008) 17356–17361.
[10] O. Rixe, W. Ortuzar, M. Alvarez, R. Parker, E. Reed, K. Paull, T. Fojo, Biochem. Pharmacol. 52 (1996) 1855–1865.
[11] J. Michels, I. Vitale, L. Galluzzi, J. Adam, K.A. Olaussen, O. Kepp, L. Senovilla, I. Talhaoui, J. Guegan, D.P. Enot, M. Talbot, A. Robin, P. Girard, C. Oréar, D. Lissa, A.Q. Sukkurwala, P. Garcia, P. Behnam-Motlagh, K. Kohno, G.S. Wu, C. Brenner, P. Dessen, M. Saparbaev, J.-C. Soria, M. Castedo, G. Kroemer, Cancer Res. 73 (2013) 2271–2280.
[12] B. Desoize, Anticancer Res. 24 (2004) 1529–1544.
[13] P.A. Andrews, S.B. Howell, Cancer Cells 2 (1990) 35–43.
[14] K.J. Scanlon, M. Kashani-Sabet, H. Miyachi, L.C. Sowers, J.J. Rossi, Anticancer Res. 9 (1989) 1301–1312.
[15] T. Pivetta, F. Isaia, F. Trudu, A. Pani, M. Manca, Talanta 115 (2013) 84–93.
[16] L. Huang, L.-M. Liao, A.-W. Liu, J.-B. Wu, X.-L. Cheng, J.-X. Lin, M. Zheng, BMC Cancer 14 (2014) 140.
[17] J. Ma, M. Maliepaard, K. Nooter, a W. Boersma, J. Verweij, G. Stoter, J.H. Schellens, Cancer Chemother. Pharmacol. 41 (1998) 307–316.
[18] B. Taylor-Harding, S. Orsulic, B.Y. Karlan, A.J. Li, Gynecol. Oncol. 119 (2010) 549–556.
[19] Y. Lin, M. Tsai, S. Weng, Y. Kuo, Y. Chiu, Mol. Pharmacol. 80 (2011) 136–146.
[20] E.E. Vokes, K.E. Choi, R.L. Schilsky, W.J. Moran, C.M. Guarnieri, R.R. Weichselbaum, W.R. Panje, J. Clin. Oncol. 6 (1988) 618–626.
[21] C. Andreadis, K. Vahtsevanos, T. Sidiras, I. Thomaidis, K. Antoniadis, D. Mouratidou, Oral Oncol. 39 (2003) 380–385.
[22] C. Faivre, P. Rougier, M. Ducreux, E. Mitry, A. Lusinchi, P. Lasser, D. Elias, F. Eschwege, Bull. Cancer 86 (1999) 861–865.
[23] N. Eckstein, J. Exp. Clin. Cancer Res. 30 (2011) 91.
[24] C. Santini, M. Pellei, V. Gandin, M. Porchia, F. Tisato, C. Marzano, Chem. Rev. 114 (2014) 815–862.
[25] L. Tripathi, P. Kumar, A.K. Singhai, Indian J. Cancer 44 (2007) 62–71.
[26] M.M. Cox, D.L. Nelson, Lehninger Principles of Biochemistry, 5th ed., 2008.
[27] D.S. Sigman, D.R. Graham, V.D. Aurora, A.M. Stern, J. Biol. Chem. 254 (1979) 12269–12272.
[28] R.G. Pearson, J. Am. Chem. Soc. 85 (1963) 3533–3539.
[29] V.B. Di Marco, G.G. Bombi, Mass Spectrom. Rev. 25 (2006) 347–379.
[30] R. Sekar, S.K. Kailasa, H.N. Abdelhamid, Y.-C. Chen, H.-F. Wu, Int. J. Mass Spectrom. 338 (2013) 23–29.
[31] P. Sgarbossa, S.M. Sbovata, R. Bertani, M. Mozzon, F. Benetollo, C. Marzano, V. Gandin, R. a Michelin, Inorg. Chem. 52 (2013) 5729–5741.
[32] P. Doležel, V. Kubáň, Chem. Pap. 56 (2002) 0–4.
[33] M.A. Telpoukhovskaia, C. Rodríguez-Rodríguez, L.E. Scott, B.D.G. Page, B.O. Patrick, C. Orvig, J. Inorg. Biochem. 132 (2013) 59–66.
[34] R. Franski, J. Mass Spectrom. 39 (2004) 272–276.
[35] R. Miao, G. Yang, Y. Miao, Y. Mei, J. Hong, C. Zhao, L. Zhu, Rapid Commun. Mass Spectrom. 19 (2005) 1031–1040.
[36] D. Esteban-Fernández, B. Cañas, I. Pizarro, M.a. Palacios, M.M. Gómez-Gómez, J. Anal. At. Spectrom. 22 (2007) 1113–1121.
[37] T.H.J. Niedermeyer, M. Strohalm, PLoS One 7 (2012) e44913.
[38] M. Strohalm, D. Kavan, P. Nova, M. Volny, Anal. Chem. 82 (2010) 4648–4651.
[39] M. Strohalm, M. Hassman, B. Kosata, M. Kodicek, Rapid Commun. Mass Spectrom. 22 (2008) 905–908.
[40] T. Pivetta, F. Isaia, G. Verani, C. Cannas, L. Serra, C. Castellano, F. Demartin, F. Pilla, M. Manca, A. Pani, J. Inorg. Biochem. 114 (2012) 28–37.
[41] T. Pivetta, M.D. Cannas, F. Demartin, C. Castellano, S. Vascellari, G. Verani, F. Isaia, J. Inorg. Biochem. 105 (2011) 329–338.
[42] W. Strober, Curr. Protoc. Immunol.John Wiley & Sons, Inc., 2001
[43] R. Pauwels, J. Balzarini, M. Baba, R. Snoeck, D. Schols, P. Herdewijn, J. Desmyter, E. De Clercq, J. Virol. Methods 20 (1988) 309–321.
[44] C. Hao, R.E. March, J. Mass Spectrom. 36 (2001) 509–521.
[45] M. Cui, Z. Mester, Rapid Commun. Mass Spectrom. 17 (2003) 1517–1527.
[46] W. Henderson, J.S. McIndoe, Mass Spectrometry of Inorganic, Coordination and Organometallic Compounds, John Wiley & Sons, Ltd, Chichester, UK, 2005.

Mixed copper–platinum complex formation could explain synergistic antiproliferative effect exhibited by binary mixtures of cisplatin and copper-1,10-phenanthroline compounds: An ESI–MS study

Tiziana Pivetta[*1], Viola Lallai[1], Elisa Valletta[1], Federica Trudu[1], Francesco Isaia[1], Daniela Perra[2], Elisabetta Pinna[2], Alessandra Pani[2]

[1]Dipartimento di Scienze Chimiche e Geologiche, [2]Dipartimento di Scienze Biomediche, University of Cagliari, Cittadella Universitaria, 09042 Monserrato – CA (ITALY)

[*]corresponding author:

Tiziana Pivetta

Dipartimento di Scienze Chimiche e Geologiche

University of Cagliari, Cittadella Universitaria, 09042 Monserrato – CA (ITALY)

Tel. +39 0706754473, fax +39 070 584597

mail: tpivetta@unica.it

KEYWORDS

Synergistic effect; antiproliferative activity; ESI-MS; cisplatin; copper complexes; cisplatin-resistant cells.

SUPPLEMENTARY INFORMATION

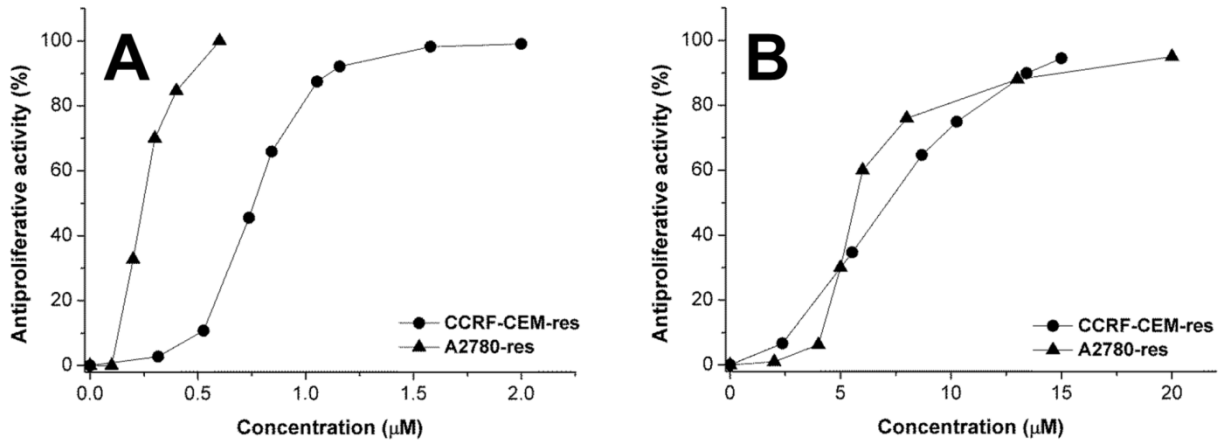

Fig. S1. Dose-response curves for **2** (**A**) and cisplatin (**B**) on leukemic cisplatin-resistant cancer cells (CCRF-CEM-res,●) and ovarian cisplatin-resistant cancer cells (A2780-res,▲). Antiproliferative effect is expressed as the percentage compared to untreated controls.

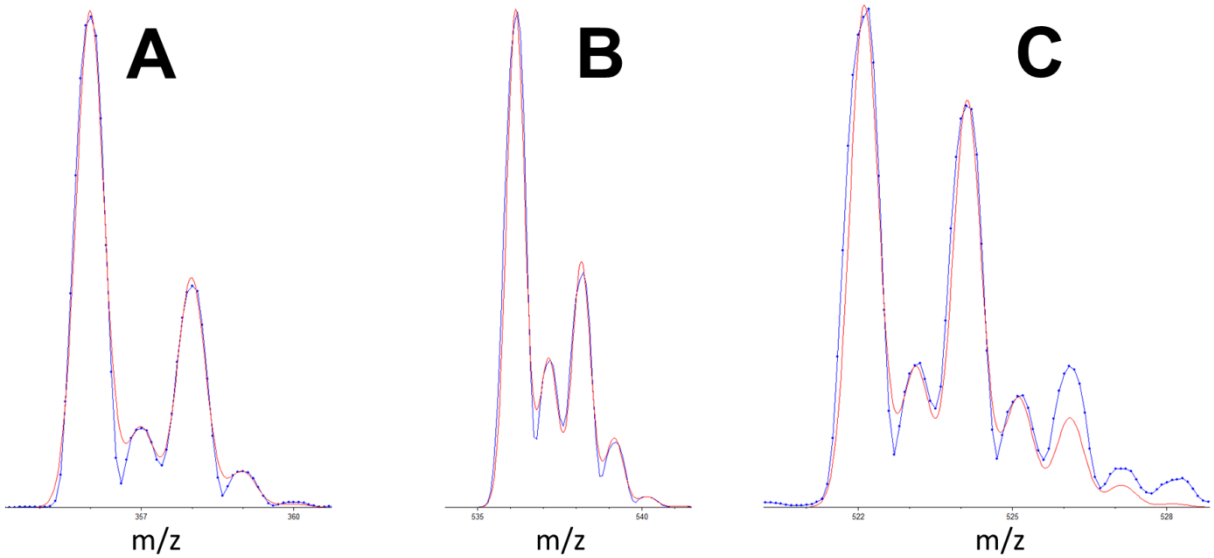

Fig. S2. Calculated (red line) and experimental (blue line) isotopic pattern for (**A**) $[Cu(phen)(TFA)]^+$ (*m/z* 356), (**B**) $[Cu(phen)_2(TFA)]^+$ (*m/z* 536), (**C**) $[Cu(phen)_2(ClO_4)]^+$ (*m/z* 522).

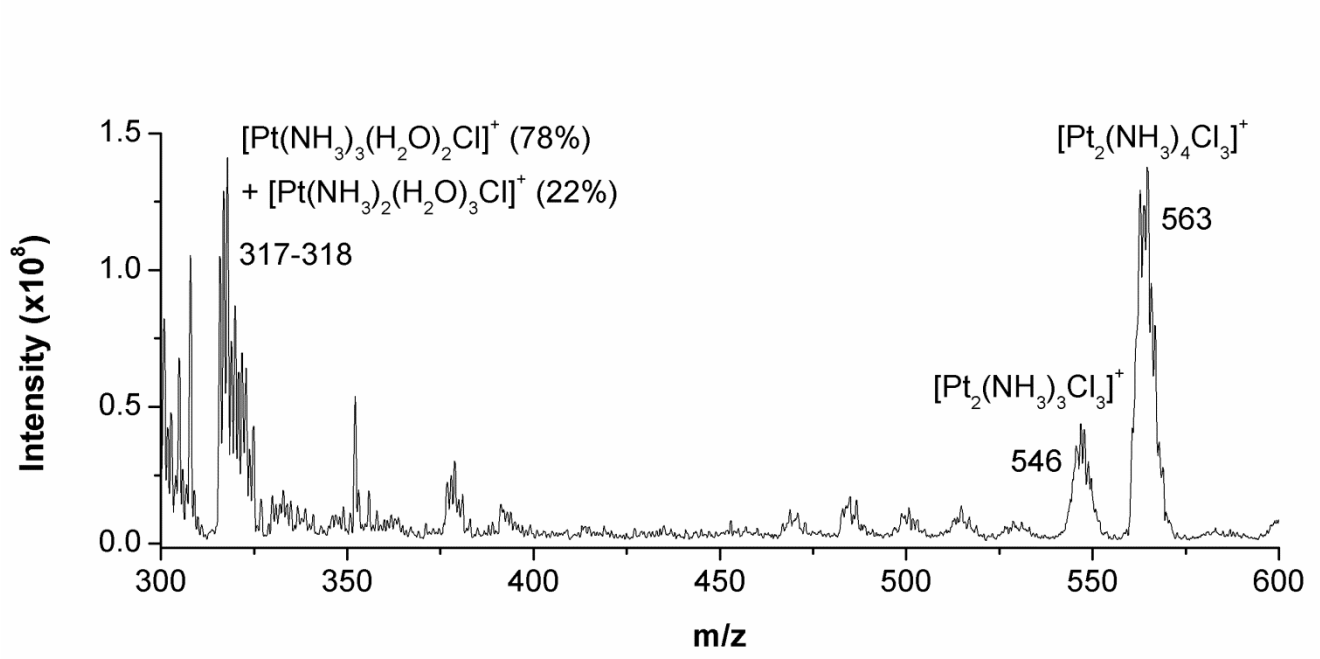

Fig. S3. ESI–MS (+) spectrum of cisplatin in the *m/z* 300-600 range; 0.5 mM, 50:50 methanol/water with 0.05% of trifluroacetic acid.

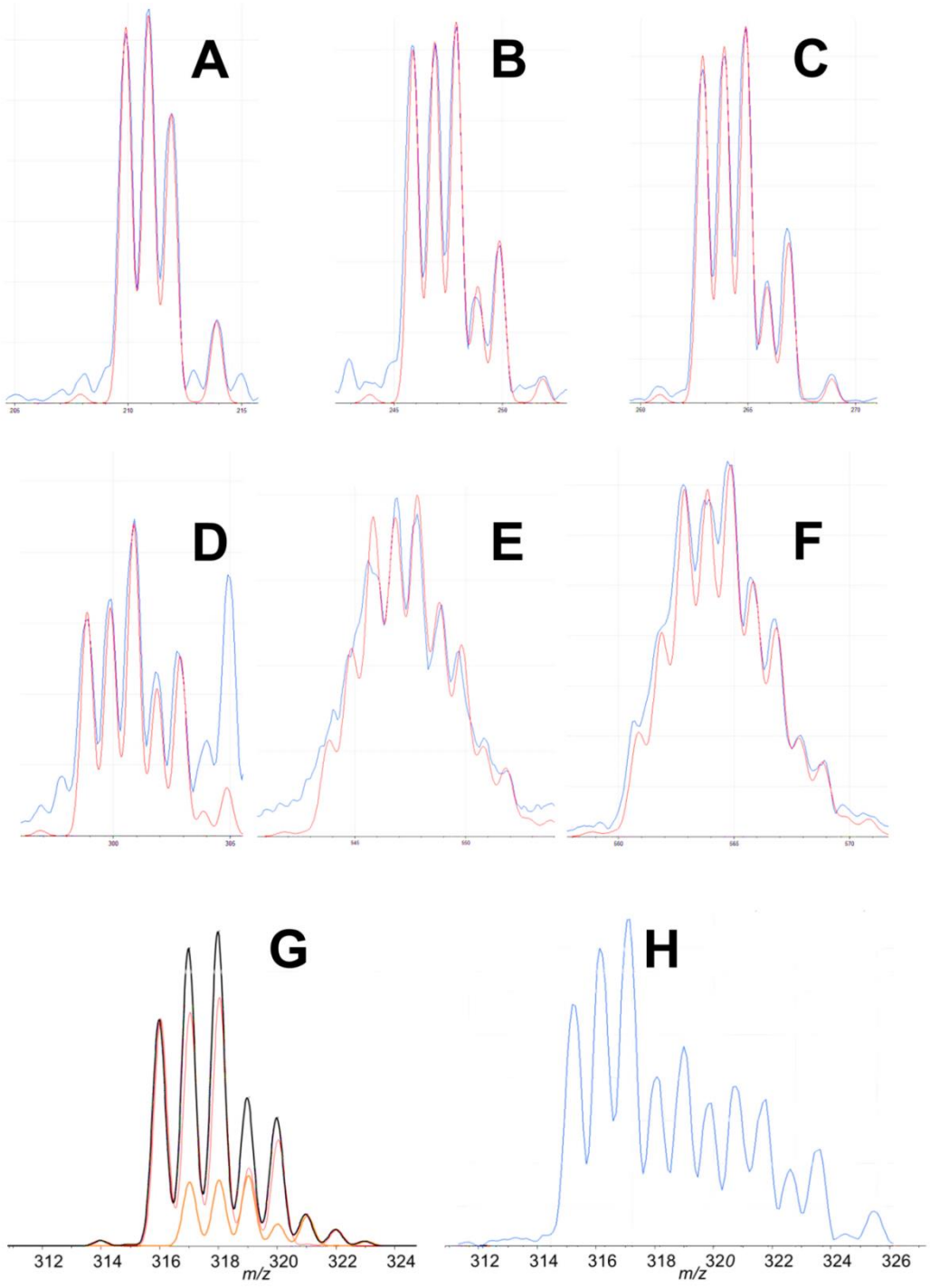

Fig. S4. Calculated (red line) and experimental (blue line) isotopic pattern for (**A**) $[Pt(NH_2)]^+$ (*m/z* 211), (**B**) $[Pt(NH_3)Cl]^+$ (*m/z* 247), (**C**) $[Pt(NH_3)_2Cl]^+$ (*m/z* 264), (**D**) $[Pt(NH_3)_2Cl_2+H]^+$ (*m/z* 300), (**E**) $[Pt_2(NH_3)_3Cl_3]^+$ (*m/z* 546), (**F**) $[Pt_2(NH_3)_4Cl_3]^+$ (*m/z* 563). Calculated pattern (**G**, black line) as a sum of $[Pt(NH_3)_3(H_2O)_2Cl]^+$ (78%, red line) and $[Pt(NH_3)_2(H_2O)_3Cl]^+$ (22%, orange line) and experimental data (**H**, blue line) in *m/z* range 314-320.

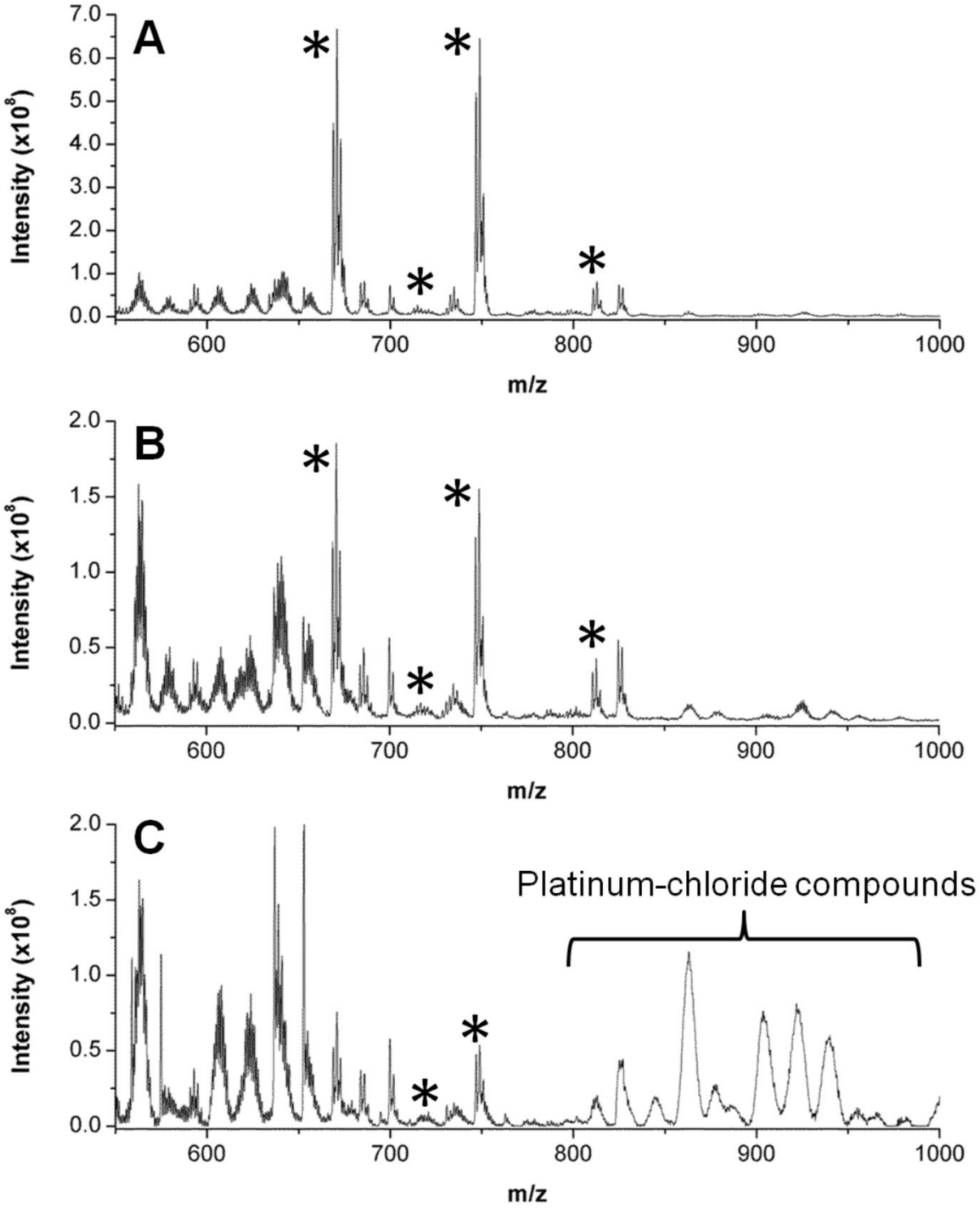

Fig. S5. ESI mass (+) spectra of cisplatin and **2** at 1:1 (**A**), 5:1 (**B**) and 10:1 (**C**) platinum/copper molar ratios (concentration of cisplatin is 0.5 mM, 50:50 methanol and water with 0.05% of trifluroacetic acid). In the spectra copper complexes are marked with "*****", polynuclear complexes containing two or more platinum ions and a variable number of chlorine, ammonia and water molecules are also pointed out.

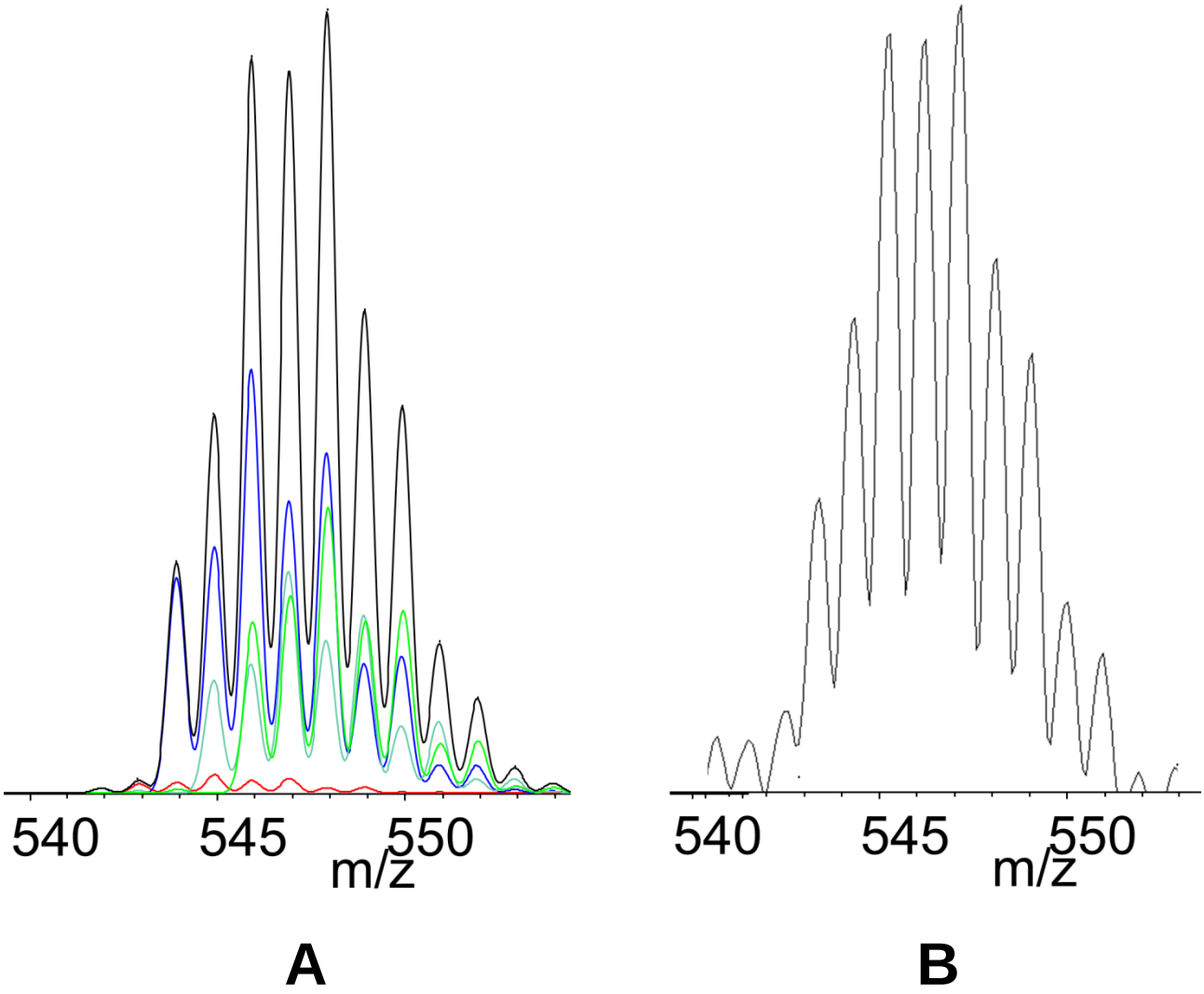

Fig. S6. Theoretical (**A**) and experimental (**B**) isotopic pattern for signal centred at *m/z* 547. The signal is due to a mixture of $[CuPt(phen)(H_2O)FCl_2]^+$ (46%, blue line), $[CuPt(phen)(H_2O)_2F_2Cl]^+$ (28%, green line), $[CuPt(phen)F_2Cl_2]^{*+}$ (24%, cyan line) and $[CuPt(phen)(H_2O)_2Cl_2]^+$ (2%, red line).

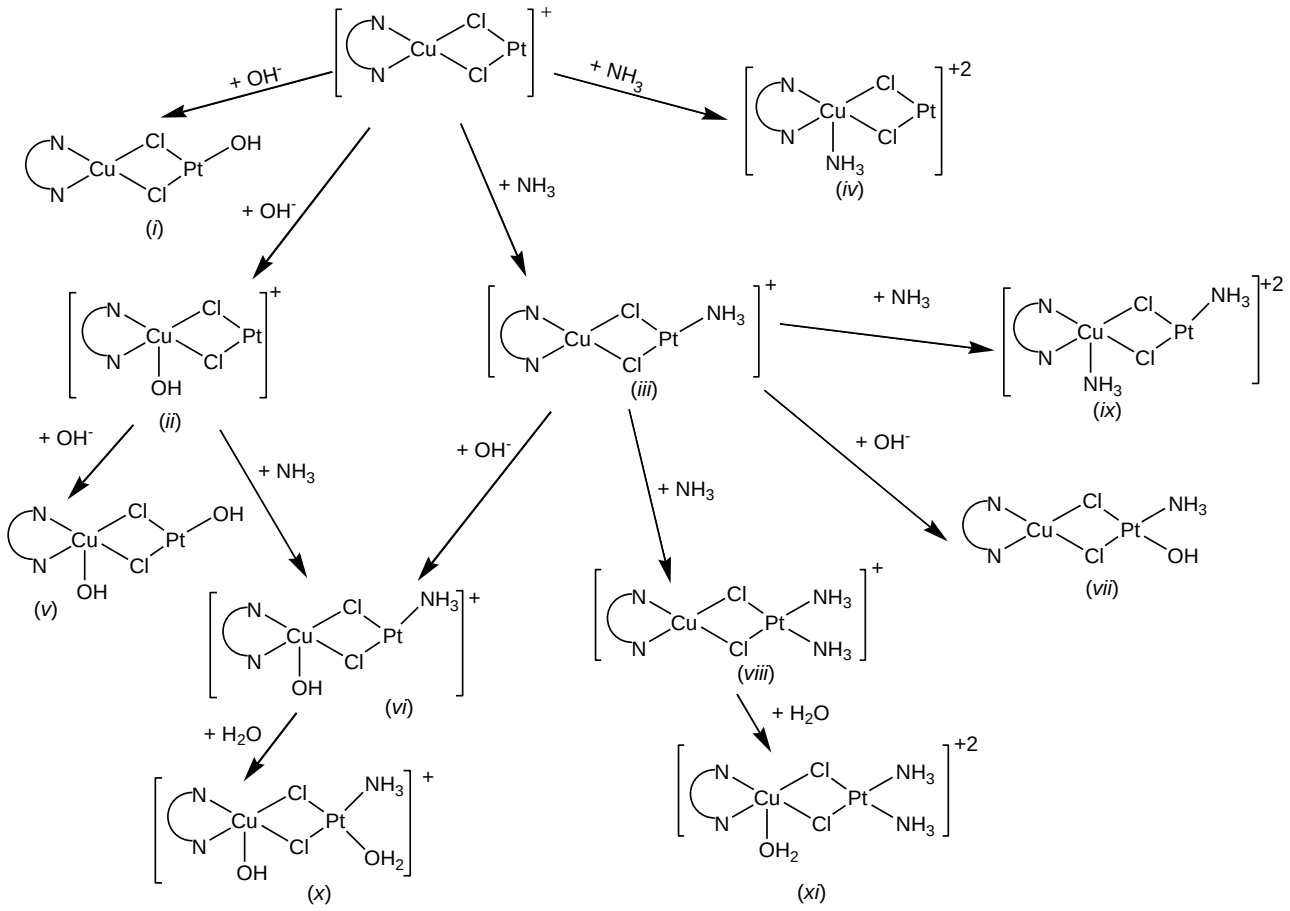

Fig. S7. A description of the possible structures as obtained from the tandem MS-MS experiments on the parent ion at *m/z* 560.

Tandem MS–MS consists of multiple steps of mass spectrometry selection, and between these steps, several fragmentation processes occur. On a triple quadrupole $Q_1q_2Q_3$ it is possible to select an ion of a certain mass (parent ion) in the first quadrupole Q_1 and send it in the second quadrupole q_2, which represents a collision cell. Here, the ion in the presence of an inert gas, such as Ar, He or N_2, is fragmented. The resulting fragments are passed within the third quadrupole Q_3, therein they are scanned and detected. The correct stoichiometry and structure of the parent ion can be deduced from the fragmentation profile. Furthermore, the energy required to fragment the ion gives information on its stability. In fact, when the MS–MS is applied to a metal complex, as in our case, the collision-induced dissociation determines the loss of neutral ligands such as water or ammonia at low collision energy (CE) (ca. 2–15 V), the breaking of bonds and aromatic-ring destruction at medium CE (ca. 15–30 V) and even the expulsion of the free metal ion at high CE (ca. 30–50 V). The necessary CE, which is strictly related to the strength of the bonds and the stability of the complex, is highly specific for each process and for each complex. Once obtained the fragmentation profile, the structure of the parent ion may be reconstructed, starting from the smallest fragments, whose structure could be easily hypothesised, as though the fragments were pieces of a puzzle. Of course, the fragment ions may rearrange in the gas phase, but this method generally leads to the most probable structure of the parent ion.

Table S1. Species containing copper and platinum as identified from the ESI-MS studies

N°	Ion	Composition	Exp. m/z*	Calc. m/z*
1	$[CuPt(phen)(H_2O)FCl_2]^+$	$C_{12}H_{10}Cl_2CuFN_2OPt$	544.96	544.91
2	$[CuPt(phen)F_2Cl_2]^+$	$C_{12}H_8Cl_2CuF_2N_2Pt$	545.93	545.90
3	$[CuPt(phen)(H_2O)_2F_2Cl]^+$	$C_{12}H_{12}ClCuF_2N_2O_2Pt$	546.93	546.95
4	$[CuPt(phen)(TFA)(HO)_3(H_2O)]^+$	$C_{14}H_{13}CuF_3N_2O_6Pt$	619.88	619.97
5	$[CuPt(phen)(TFA)(HO)_2(H_2O)_2]^+$	$C_{14}H_{14}CuF_3N_2O_6Pt$	620.99	620.97
6	$[CuPt(phen)(TFA)(HO)F(H_2O)_2]^+$	$C_{14}H_{13}CuF_4N_2O_5Pt$	622.90	622.97
7	$[CuPt(phen)(TFA)(H_2O)_2F_2]^+$	$C_{14}H_{12}CuF_5N_2O_4Pt$	624.87	624.97
8	$[CuPt(phen)(TFA)(H_2O)_3Cl]^+$	$C_{14}H_{14}ClCuF_3N_2O_5Pt$	639.92	639.95
9	$[CuPt(phen)(TFA)(H_2O)_2ClF]^+$	$C_{14}H_{12}ClCuF_4N_2O_4Pt$	640.91	640.94

* The experimental and calculated *m/z* values refer to the peak representative of the monoisotopic mass.

Chapter 3

Cisplatin, glutathione and the third wheel

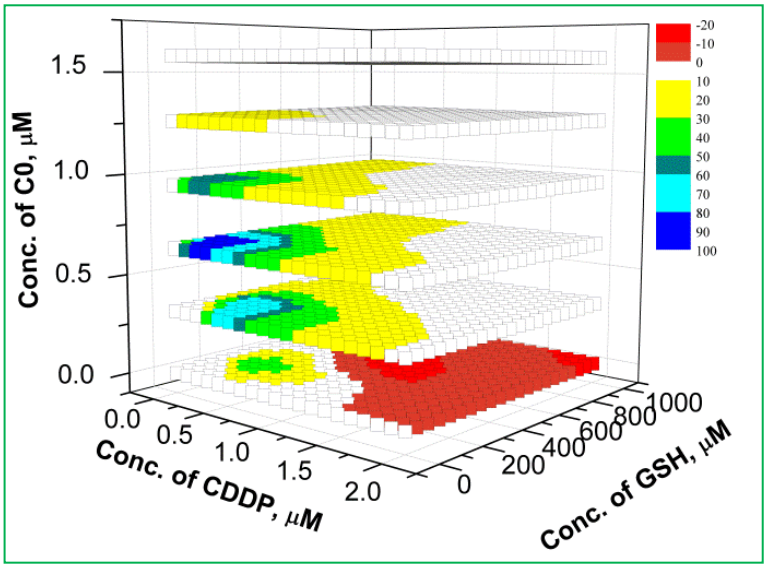

This chapter reports the study of the synergistic effect of binary mixtures of GSH with $[Cu(phen)(H_2O)_2(ClO_4)_2]$ or cisplatin, and ternary mixtures of GSH with $[Cu(phen)(H_2O)_2(ClO_4)_2]$ and cisplatin.

Abstract

The increase of intracellular levels of glutathione, able to bind cisplatin (CDDP) and deactivated it as drug, is one of the main mechanisms that cause the cisplatin-resistance. To overcome this issue, CDDP is often administered in combinations with other drugs, to exploit drug synergism.

In a previous work (Chapter 2 – Article II) the cytotoxic activity of $[Cu(phen)_2(OH_2)](ClO_4)_2$ (**C0)** and cisplatin, both alone and in binary combinations, were evaluate against cisplatin-resistant sublines of leukemic and ovarian cancer cell lines. Copper complex **C0** shown an IC_{50} values of 0.75 and 0.24 μM in CCRF-CEM-res and A2780-res, respectively, while CDDP shown values of 6.98 and 5.3 μM in the same lines. The combinatorial treatment with **C0** and CDDP against the cisplatin-resistant cell lines, gave rise to a synergistic effect *in vitro*.

Taking into account that the possible deactivation of the CDDP may be due to the presence of GSH, I decided to study the cytotoxic activity of binary mixtures of GSH with **C0** or CDDP and of ternary mixtures of GSH with **C0** and CDDP against the wild type leukemic (CCRF-CEM) cancer cell lines and its cisplatin-resistant subline (Chapter 3 – Manuscript I). For the evaluation of the cytotoxic effects of the mixtures, I applied a method based on the use of experimental design for the choice of the mixtures and on artificial neural network for the evaluation of the experimental results.

A synergistic effect was evidenced between **C0** and cisplatin or GSH, while an antagonistic effect was shown by CDDP and GSH, for both the cell lines. The calculated synergistic surfaces for the binary systems CDDP-GSH, **C0**-GSH, and **C0**-CDDP, for CCRF-CEM-wt cell line are reported in Figure 13.

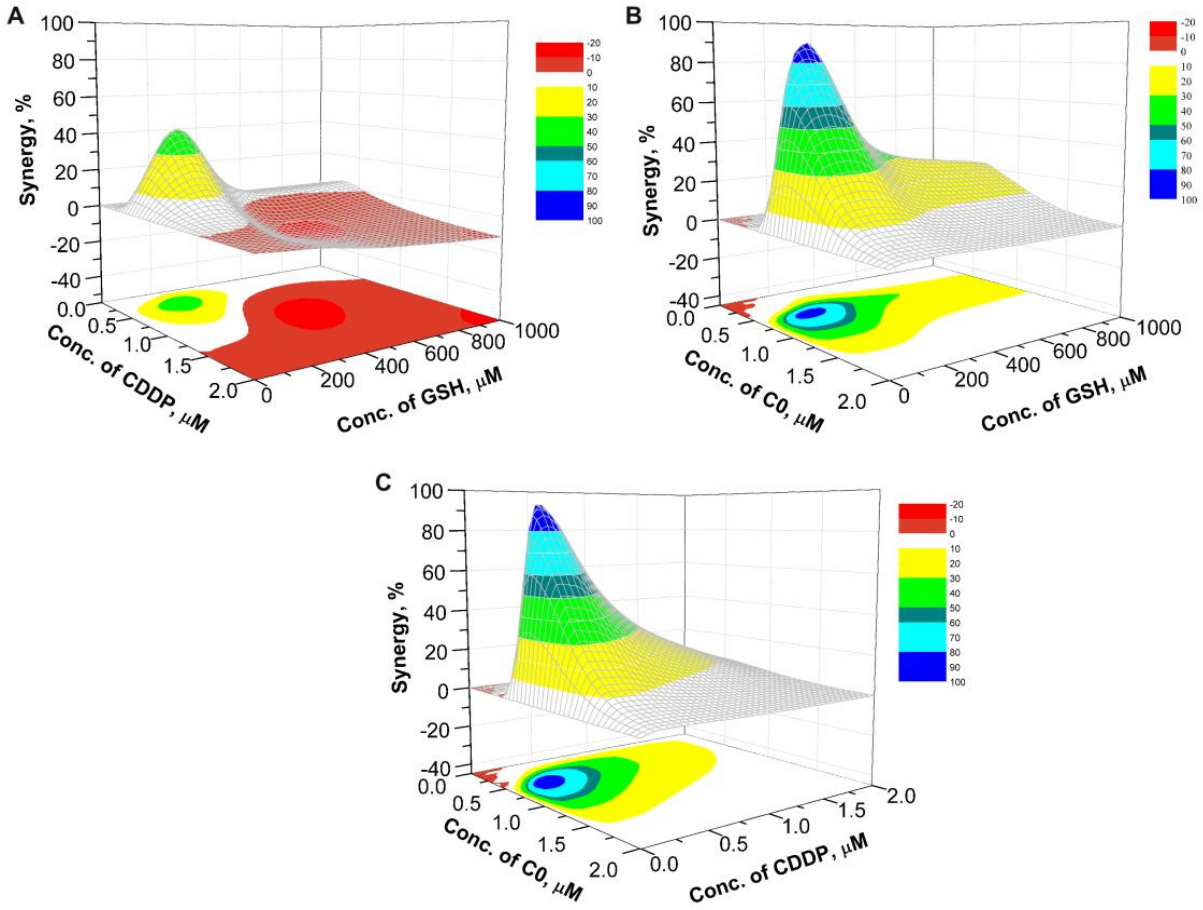

Figure 13. Synergistic surfaces for the binary systems of (**A**) CDDP and GSH, (**B**) **C0** and GSH, (**C**) **C0** and CDDP for CCRF-CEM-wt cell line. An antagonistic effect is shown by combinations of CDDP and GSH for concentration of GSH higher than 200 μM, a synergistic effect is shown by **C0** with CDDP and GSH for selected combinations.

For the ternary systems it was observed that in presence of **C0**, the sensitivity of the cells, wild type and/or resistant ones, towards CDDP in presence of GSH was restored, i.e. the antagonistic effect of the GSH versus CDDP was prevented. Furthermore, a synergistic effect was found for selected combinations. The plots showing the influence of the concentration of **C0** to the synergistic/antagonistic effect of mixtures CDDP-GSH for the CCRF-CEM-wt cells are reported in Figure 14.

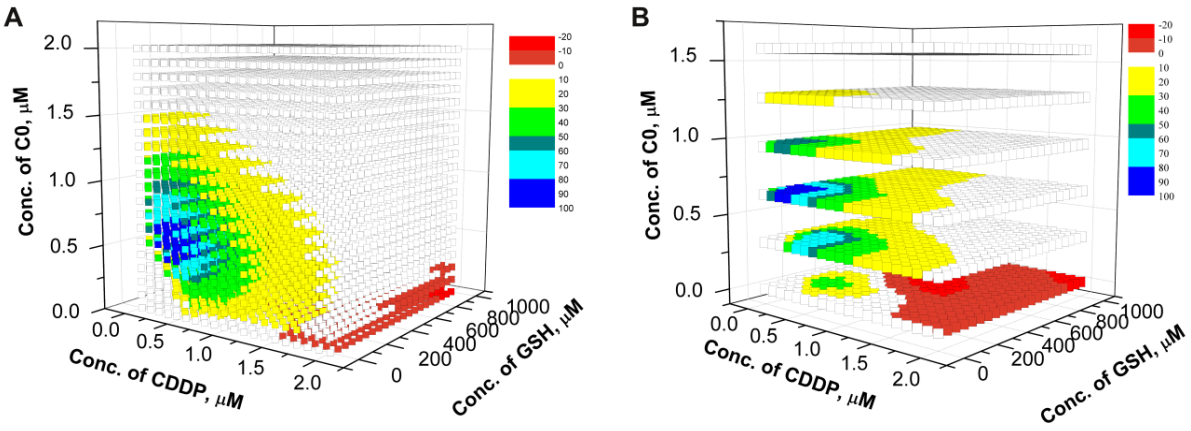

Figure 14. Three-dimensional solid showing the synergistic effect for the ternary systems CDDP-GSH-**C0** for CCRF-CEM-wt cell line (**A**), some selected planes of the solid (**B**); the color of the points is proportional to the synergistic effect, in particular red represents antagonistic effect, blue represents the synergistic effect, and white the additive effect).

The selectivity of these cocktails of drugs was evaluated testing the compounds also against *ex vivo* cultures of human Peripheral blood Lymphocytes (PBLs). The drug combination was totally devoid of cytotoxicity on the PBLs cells after 24 h, 48 h and 72 h of incubation. If we consider the effects of the ternary combination vs. the single-drug treatments in the PBLs, the drug cocktail always showed a degree of cytotoxicity comparable to that of the CDDP alone, whereas in the CCRF-CEM cells the toxic effect of the combination was 7 fold greater than that of CDDP alone.

Manuscript I

Cisplatin, Glutathione and the third wheel

Elisa Valletta, Elisabetta Pinna, Sarah Vascellari, Daniela Perra, Francesco Isaia, Alessandra Pani, Tiziana Pivetta

To be submitted

Cisplatin, Glutathione and the third wheel

Elisa Valletta[a*], Elisabetta Pinna[b*], Sarah Vascellari[b], Daniela Perra[b], Francesco Isaia[a], Alessandra Pani[b^], and Tiziana Pivetta[a^]

* Equal contribution

^Corresponding authors

[a]Dipartimento di Scienze Chimiche e Geologiche, [b]Dipartimento di Scienze e tecnologie biomediche, Università degli Studi di Cagliari, 09042 Monserrato (CA)-ITALY

keyword: cancer, drug combinations, copper complexes, cisplatin, glutathione, drug resistance, synergism, antagonism

Corresponding author:

Tiziana Pivetta, PhD

Dipartimento di Scienze Chimiche e Geologiche, Università degli Studi di Cagliari, Cittadella Universitaria, 09042 Monserrato (CA) - ITALY;

Tel. 0039 070 675 4473; Fax 0039 070 584597

e-mail tpivetta@unica.it

1. Introduction

Cisplatin, $[Pt(NH_3)_2Cl_2]$ (CDDP), is a cytotoxic agent currently used in the clinic for many types of cancer, i.e. ovary, testicle, head and neck, bones, brain, lymph node and skin cancers (1) (2). In the bloodstream CDDP binds different plasmatic thiol-containing proteins (3) (4) and only free CDDP molecules can enter the cell. As $[Pt(NH_3)_2(H_2O)Cl]^+$ species, it reacts with a DNA base (5) (6) (7) leading to DNA distortions that, depending on the extent of the damages, activate DNA repair pathways or trigger the apoptotic cascade (8) (9) (10). Beside of the total lack of selectivity towards cancer cells, the real CDDP effectiveness in monotherapy, as well as in multidrug protocols, is yet limited by the selection of CDDP-resistant cancer cell populations during cycles of chemotherapy. Claimed mechanisms of CDDP-resistance include i) over-expression of drug-efflux pumps, ii) increased ability to repair and/or to tolerate damaged DNA, and iii) increased intracellular levels of thiol-containing molecules, particularly of glutathione (GSH) (8) (9). Although some authors associated CDDP-resistance with the formation of CDDP / GSH adducts, i.e. bis-(glutathionato)-platinum $[Pt(GS)_2]$, preventing CDDP from binding DNA (11), others sustain that direct binding of Pt(II) of CDDP with GSH is not the most important cellular interaction (12). Actually, in some cases, CDDP-resistant cancer cells showed an increased intracellular levels of GSH (1), but given that higher GSH levels were not found to be correlated with lower Pt(II)-DNA adducts, it has been proposed that GSH might play a role in apoptotic regulatory pathways (13). Whatever is the mechanism(s) of CDDP resistance involving GSH, a reported feature of cancer cells is the presence of an increased ratio of the oxidized (GSSG) vs. the reduced (GSH) form of glutathione, which in physiologic conditions is maintained 1:10 by glutathione reductase (8) (9).

In previous works, we have shown in a wide range of hematologic and solid tumor cell lines, the cytotoxic effects of a novel class of complexes of copper(II) with 1,10-phenantroline (phen); the most potent being the complex $[Cu(phen)_2(OH_2)](ClO_4)_2$ **C0** (14) (15) (16). In one of these studies we also reported that GSH, known to reduce free Cu(II) to Cu(I) thus increasing GSSG formation, it is not able to reduce Cu(II) to Cu(I) in the complex **C0**, likely by virtue of the stabilizing effect of phen ligand towards the bivalent form of the metal ion, as we observed the formation of two complexes with one or two molecules of GSH per metal ion (15). Besides, in a more recent work we highlighted a strong synergic cytotoxic effect of **C0** in dual-drug combinations with CDDP against human T-leukemia CCRF-CEM cells (17). The potential clinical relevance of our findings coupled with the literature data calling GSH into play in cancer cells and / or in resistance to CDDP, prompted us to widen further our studies by investigating the cytotoxic activity of binary mixtures of GSH with **C0** or with CDDP, and of ternary mixtures of GSH, **C0**, and CDDP in populations of CCRF-CEM cells expressing phenotypes drug-sensitive, CEM wild type (CCRF-CEM-wt), or CDDP-resistant (CCRF-CEM-res). For the evaluation of types and degree of drug interactions in

both the binary and ternary combinations, we applied the method detailed in our previous work (17), which is based on the use of Experimental Design (ED) for the choice of the drug mixtures, and on Artificial Neural Network (ANN) for the evaluation of the experimental results. The toxic effect of ternary mixture was investigate on ex vivo cultures of human Peripheral blood Lymphocytes (PBLs).

2. Materials and Methods

2.1 Reagents

Copper(II) carbonate basic ($Cu_2(CO_3)(OH)_2$), 1,10-phenanthroline monohydrate, cisplatin, perchloric acid, ethanol, ethyl ether, dimethyl sulphoxyde (DMSO), glutathione (GSH), acetonitrile, trypan blue, Staurosporine and Doxorubicin were purchased from Sigma-Aldrich (Milan, Italy) and used without any further purification. Interleukin 2 was purchased from Roche. Foetal bovine serum (FBS), Phytohemagglutinin (PHA) and kanamycin sulphate were purchased by Gibco-Invitrogen (Milan, Italy) and used without any further purification. RPMI 1640 with stable L-glutamine was purchased by EuroClone. Stock solutions of compound **C0**, CDDP and Staurosporine were prepared in DMSO, at 1000× of the highest concentration to be used on the cell culture and stored at 4 °C in the dark. CDDP stock solution, being stable only for few hours and showing a decreasing of the cytotoxic potency during the time, was prepared fresh each time immediately before the experiments. GSH stock solution was prepared in RPMI medium and filtered.

2.2 Synthesis

The compound **C0** was prepared as previously reported (15) (16).

2.3 Cell lines

The human acute T-lymphoblastic leukemia cells (CCRF-CEM) with its respective cisplatin-resistant subline were used in the study. The CCRF-CEM human cell line was purchased from the American Type Culture Collection (ATCC-LGC; Milan, Italy). The CCRF-CEM-wt and CCRF-CEM-res cell lines were maintained in culture between 1×10^5 cells/ml and 1×10^6 cells/ml in RPMI medium 10% foetal bovine serum (FBS) with 1% kanamycin (growth medium). To the growth medium for CCRF-CEM-res cell cultures, we also added cisplatin (5 μM). The cells were periodically checked for micoplasma contamination. For the experiments, the cell line was replaced every 3 months with freshly-towed cells from the cell stores in liquid nitrogen.

2.4 Selection of the cisplatin-resistant CCRF-CEM subline

A CCRF-CEM subline able to grow at the same extent in the absence and in the presence of 5 μM cisplatin (CCRF-CEM-res) was obtained by serial passages of wild-type cells in the presence of increasing cisplatin concentrations, starting from a sub-inhibitory concentration (0.5 μM). At each cell passage (every 3–4 days), the number of viable cells of cisplatin-treated cultures was compared to that of duplicate untreated cultures.

Initially the CDDP concentration was increased by 0.25 μM at each cell passage up to 1.50 μM; from then on, cisplatin-treated cultures grew poorly and much slower than their untreated counterparts and had to be kept (5 consecutive passages) at the same CDDP concentration until the cell population had regained original growth timing and viability. After that the CDDP concentration was gradually increased. Given that cell cultures never survived at concentrations over 5 μM, the cell population was stabilised by 15 further passages at 5 μM CDDP. The number of viable cells was determined at each cell passage by the trypan blue exclusion method. At intervals during the selection process, the level of CDDP resistance was checked by the 3-(4,5-dimethylthiazol-2-yl)-2,5-diphenyl-tetrazolium bromide (MTT) method in cells that had grown without the drug for one passage. Resistance Index (RI) was calculated as ratio between IC_{50} in CCRF-CEM-res and CCRF-CEM-wt; Doxorubicin was used as a reference compound to evaluate the cisplatin-resistance specificity.

2.5 Cytotoxic assay

The biological stability of stocks solutions was checked verifying the cytotoxic activity measured by using the same solutions over more than 6 months. The tested compounds maintained the same IC_{50} (concentration of compound that reduce the viable cell by 50% with respect to untreated cells) in all the performed experiments. Dilutions of the drug stocks for biologic investigations were made in RPMI medium at 2x the final concentration for single drug evaluations, or at 4x the final concentration for evaluation of binary and ternary drug combinations. The concentration of DMSO in the cells was never higher than 0.1%. The effects of the drugs and drug combinations were evaluated in cultures of exponentially growing cells; for experiments in cisplatin-resistant cell cultures, were allowed to grow in the absence of the drug for 1 passage. CCRF-CEM-wt and CCRF-CEM-res cells were seeded at a density of 1×10^5 cells/well of growth medium in flat-bottomed 24-well plates and simultaneously exposed to the drugs or drug combinations. Cell growth in the absence and presence of drugs was determined after 96 h of incubation at 37 °C and 5% CO_2 (corresponding to three to four duplication rounds of untreated cells), through the viable cell counting with the trypan blue exclusion method. Values obtained in drug-treated samples were

expressed as percentages of those of their respective controls. All experiments were repeated three times.

2.6 Peripheral blood Lymphocytes (PBLs) separation

Peripheral blood Lymphocytes from healthy donors were obtained by method of gradient separation Lympholyte-H (Cedarlane). After extensive washing, cells were resuspended (1 x10^6 cells/ml) in RPMI-1640 with 10% FBS and incubated overnight.

For evaluations in resting PBLs, 1 x 10^5 cells/well were incubated in RPMI-1640 with 10% FBS in the absence or presence of the compounds at the indicate concentration in 24-well plat, at 37° C and 5% CO_2 , for 24 h, 48 h, 72 h.

For experiments with proliferating PBLs, 1 x 10^5 cells/well were incubated in RPMI-1640 with 10% FBS supplemented with PHA (2.5 μg/ml) or supplemented with PHA (2.5 μg/ml) and interleukin 2 (5 U/mL) in the absence or presence of the compounds at the indicate concentration in flat-bottomed 24-well plates, at 37° C and 5% CO_2.

Cell growth in the absence and presence of drugs was determined after 24 h, 48 h and 72 h of incubation at 37 °C and 5% CO_2 through the viable cell counting with the trypan blue exclusion method. Values obtained in drug-treated samples were expressed as percentages of those of their respective controls. All experiments were repeated three times using PBLs from three different healthy donors.

2.7 Procedures of the applied method

The used ED-ANNs method consists of the following steps:

1. Set-up of the ED for the choice of the combinations to be evaluated
2. Experimental determination of the cytotoxicity of the drugs alone and of the multidrug mixtures prepared according to the chosen ED
3. Training and verification of the artificial neural network to plan and set up the prediction ability of the network
4. Prediction of the response using the network according to a suitable grid that covers the whole working space
5. Calculation of the non-algebraic additive effect (*NAAE*) (17) for each point of the used grid, i.e. for each combinations of the drugs
6. Calculation of the Net Multi Drug Effect Index (*NMDEI*) (17) to determine the global effect (synergism, additive effect or antagonism)
7. Test of the obtained results.

2.8 Software

ANNs computation was performed using EasyNN-plus (Neural Planner Software Ltd, Cheadle Hulme, UK). All computations were performed on a standard PC computer with Microsoft Windows Vista as operating system.

3. Results and discussion

3.1 Set up of the ED

For the study of drug combinations, the concentrations of the drugs should be chosen in the range within 0 and twice the IC_{50} (the dose odf the drug which inhibits 50% of the cell proliferation). Then the knowledge of a simple estimation of IC_{50} is needed. To model the dose response curve of each drug and the cytotoxicity response surface an adequate number of experiments is required. A non-symmetrical experimental design has been used.

The **C0** and CDDP compounds were studied in the range of concentration of 0 - 2 μM while GSH in the interval 0 - 1000 μM.

We prepared for CCRF-CEM-wt i) 6 combinations of GSH and **C0**; ii) 6 combinations of GSH and CDDP; iii) 7 combinations of **C0** and CDDP; iv) 52 combinations of GSH, **C0** and CDDP; v) 10 solutions of CDDP alone, vi) 9 solutions of GSH alone and vii) 11 solutions of **C0** alone; for CCRF-CEM-res i) 9 combinations of GSH and **C0**; ii) 9 combinations of GSH and CDDP; iii) 9 combinations of **C0** and CDDP; iv) 27 combinations of GSH, **C0** and CDDP; v) 3 solutions of CDDP alone, vi) 3 solutions of GSH alone and vii) 3 solutions of **C0** alone.

Following the Experimental Design reported in Figures 1-2, solutions as i), vi) and vii) were used to study the binary system GSH-**C0** (Figures 1A, 2A); solutions as ii), v) and vi) were used to study the binary system GSH-CDDP (Figures 1B, 2B); solutions as iii), v) and vii) were used to study the binary system CDDP-**C0** (Figures 1C, 2C); solutions as iv), v), vi) and vii) were used to study the ternary system CDDP-GSH-**C0** (Figures 1D, 2D).

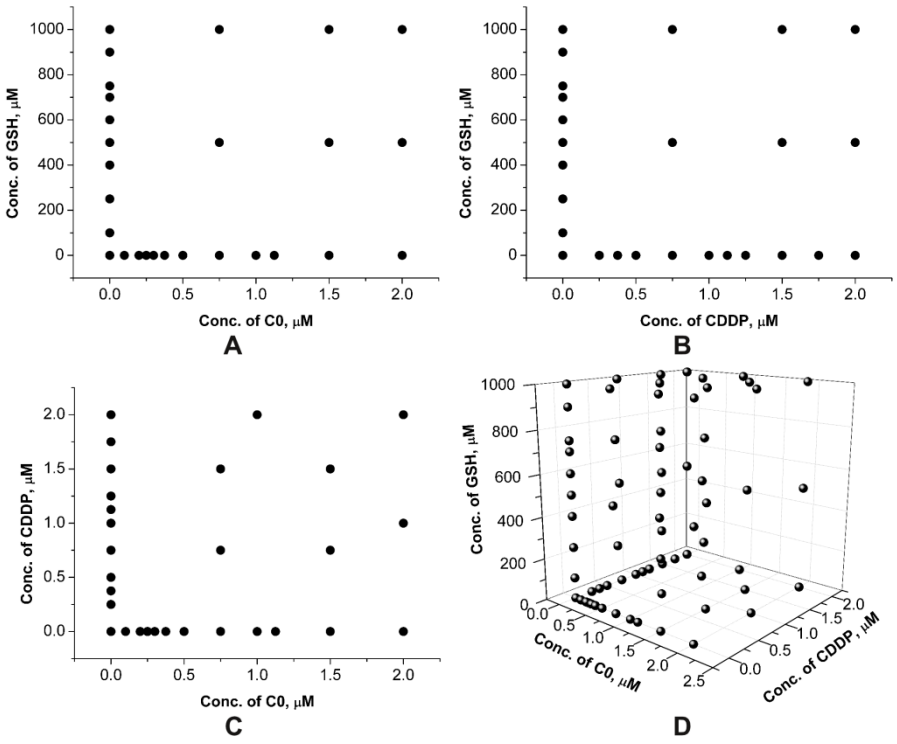

Figure 1. Concentration of combinations of (**A**) **GSH** and **C0**, (**B**) **GSH** and **CDDP**, (**C**) **CDDP** and **C0**, (**D**) **GSH**, **C0** and **CDDP** for CCRF-CEM-wt cell line.

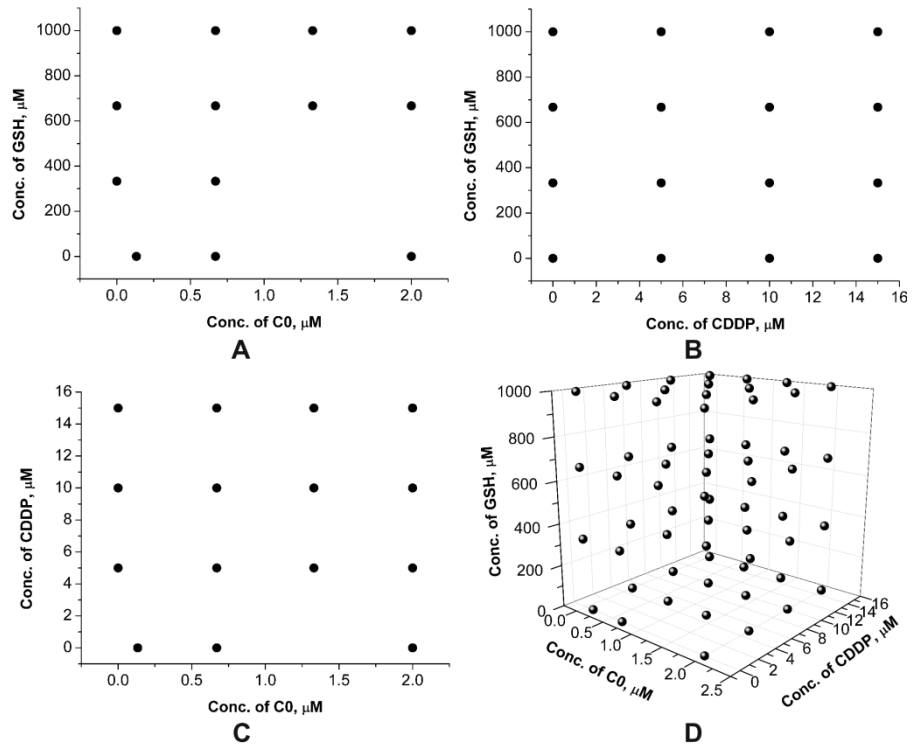

Figure 2. Concentration of combinations of (**A**) **GSH** and **C0**, (**B**) **GSH** and **CDDP**, (**C**) **CDDP** and **C0**, (**D**) **GSH**, **C0** and **CDDP** for CCRF-CEM-res cell line.

3.2 Determination of the cytotoxicity of the drugs

The experiments were carried out in three replicates. The vitality (% of living cells) after the treatment with the drugs was measured for each solution with respect to the control (untreated cells) and converted, for calculation purpose, into mortality (as 100% minus vitality).

3.3 Training and verification of the artificial neural network

The concentrations of drugs and the related mortality values were used to form the data matrix. Concentrations of drugs were used as input data and the experimental mortality as output ones. The standard back-propagation was used as training algorithm. The optimal neural network architecture was searched for using the criteria of lowest RMSE and it was found that a three layers structure with 4 (binary systems) and 5 (ternary system) neurons in the hidden layer was sufficient. The architecture of the network for the ternary system is shown in Figure 3.

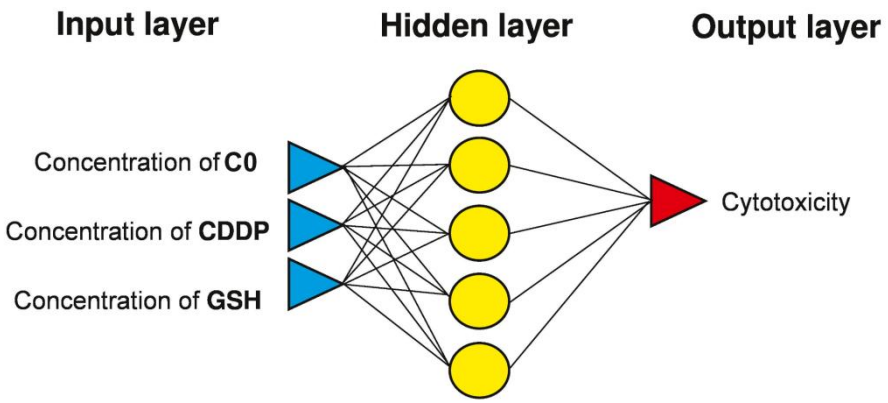

Figure 3. Architecture of the network used for the study of **C0-CDDP-GSH** ternary system.

The network was trained and verified using the training and validation sets. All points lying on the borders of the experimental design were included in the training set. Validation points were chosen randomly on the working space. Among the prepared 101 solutions for CCRF-CEM-wt, 80 were used as training set, 9 as validation set and 12 as test set, among the prepared 63 solutions for CCRF-CEM-res, 40 were used as training set, 11 as validation set and 12 as test set.

The generalization ability of the network was used to predict the cytotoxicity on the whole working space according to a bi-dimensional grid with 40 points per side for the binary systems and according to a cube with 20 points per side for the ternary system. At first, the data of binary systems were processed individually. Then, data of binary and ternary systems were processed together. The results for the binary systems obtained in the two processes were strictly comparable, proving the robustness and the reliability of the method. The agreement between calculated and experimental values for all the data for CCRF-CEM-wt cell line is shown in Figure 4 as example.

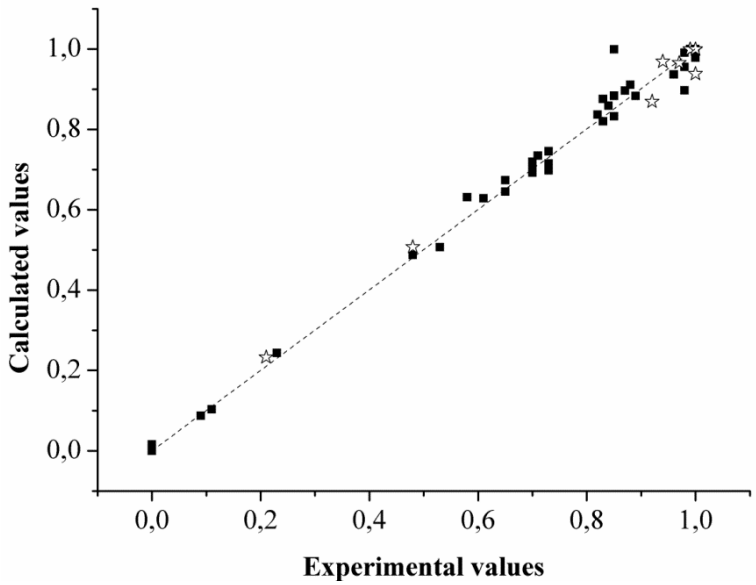

Figure 4. Comparison between experimental and calculated mortality values (■ training set, ☆ validation set) for the ternary systems **C0**-CDDP-GSH for CCRF-CEM-wt cell line(linear fitting parameters for the equation $y = mx+q$ are m = 0.9951, q = 0.007 with r = 0.9974 for training set, m = 0.9536, q = 0.0038 with r = 0.9947 for validation set, m = 0.9912, q = 0.0092 with r = 0.9974 for all the data).

3.4 CCRF-CEM-wt cell line

3.4.1 Prediction of the response (cytotoxicity surfaces)

The cytotoxicity of the mixtures and that of the drugs alone for the whole working space, were calculated by using the network. The dose-response curves for each compound and the cytotoxicity surface were then obtained.

The calculated dose-response curves together with the experimental points for CDDP, GSH and **C0** for CCRF-CEM-wt cell line are reported in Figure 5A,B,C, respectively.

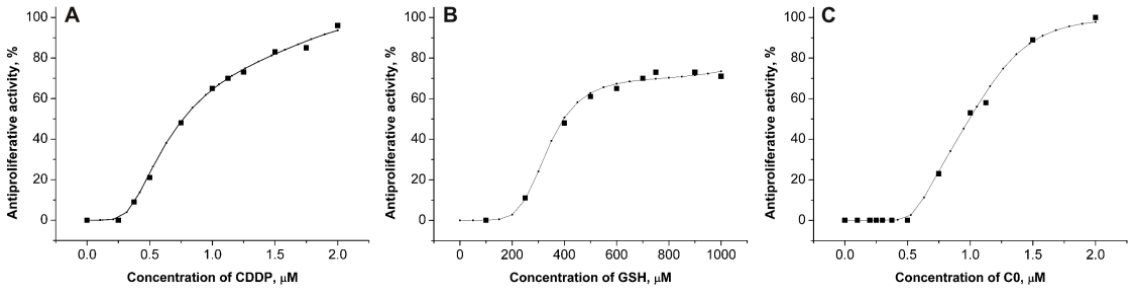

Figure 5: Calculated dose-response curve (-•-) and experimental points (■) for (**A**) CDDP, (**B**) GSH and (**C**) **C0**, for CCRF-CEM-wt cell line.

The different trends of the curves may suggest a different action mechanism inside the cells. The threshold doses (the minimum dose at which the drug presents an effect) for the three compounds are: 0.25 μM for CDDP, 150 μM for GSH and 0.5 μM for **C0**. The IC_{50} values are in the order CDDP (0.78 μM) < **C0**(1.05 μM) << GSH (332.1 μM).

The cytotoxicity of **C0** and CDDP are comparable. Also GSH presents a cytotoxic activity towards cancer cells.

3.4.1.1 Binary mixtures

The response surfaces calculated by the network (together with the experimental points) and the related contour plots for **C0**-CDDP, CDDP-GSH, and **C0**-GSH systems are shown in Figure 6A,B,C. The calculated values are in good agreement with the experimental ones. The mortality increases with the concentrations of the two drugs, having similar trend to that one of the dose-response curve.

The areas of cytotoxicity iso-values of the contour plot for the binary mixtures can be explored to discover the combination with desired cytotoxicity and the related dose of both drugs. For example, if a toxicity of 50% is searched for, instead of choosing **C0** alone at a concentration of 0.99 μM or CDDP alone at a concentration of 0.77 μM or GSH alone at a concentration of 403 μM, selected combination may be choosen, as:

- **C0** at 0.26 μM and CDDP at 0.40 μM (Figure 6A);
- CDDP at 0.32 μM and GSH at 200 μM (Figure 6B);
- **C0** at 0.42 μM and GSH at 200 μM (Figure 6C).

For a toxicity of 70%, instead of choosing **C0** alone at a concentration of 1.20 μM or CDDP alone at a concentration of 1.13 μM or GSH alone at a concentration of 769 μM, selected combination may be choosen, as:

- **C0** at 0.32 μM and CDDP at 0.40 μM (Figure 6A);
- CDDP at 0.63 μM and GSH at 240 μM (Figure 6B);
- **C0** at 0.47 μM and GSH at 200 μM (Figure 6C).

The possibility to reach the same effect but with lower doses of the drugs gives the chance to minimize the side effects related to the doses.

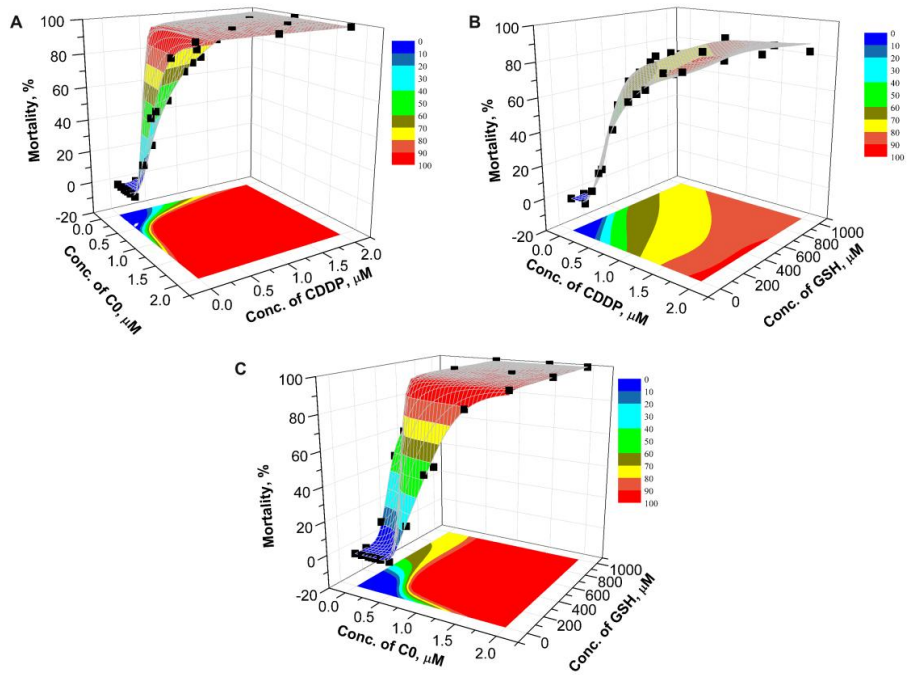

Figure 6. Calculated response surface and contour plot of cytotoxicity iso-values for the systems (**A**) **C0**-CDDP, (**B**) CDDP-GSH and (**C**) **C0**-GSH for CCRF-CEM-wt cell line; experimental points (■) are superimposed.

3.4.1.2 Ternary mixtures

The mortality surfaces calculated by the network for the ternary system CDDP-GSH-**C0** is shown in Figure 7A (colour is proportional to the cytotoxic activity of the mixtures). To simplify the interpretation of the graph and to appreciate the trend of the cytotoxicity also in the core of the cube, only seven planes along the z axis have been reported in Figure 7B.

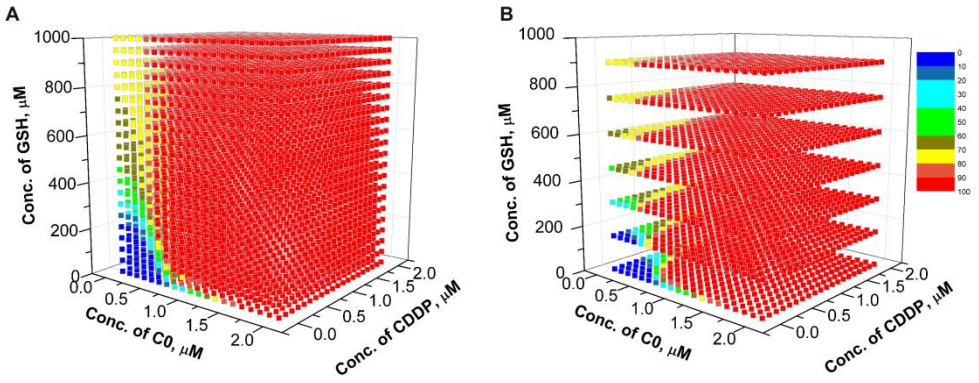

Figure 7. Full calculated response surface for the ternary systems CDDP-GSH-**C0** for CCRF-CEM-wt cell line (**A**), some selected planes are reported for clarity (**B**); the colour of the point is proportional to the cytotoxic activity.

As can be seen from the graph, a low value of cytotoxicity appears for low concentrations of all the compounds, while for concentration higher than 1 µM for **C0** or CDDP the activity reaches quickly the highest value of 100%. Several combinations with a cytotoxic activity of 50% or 70% may be chosen, as for example:

- **C0** at 0.11 µM, CDDP at 0.21 µM and GSH at 250 µM (mortality values of 50%)
- **C0** at 0.32 µM, CDDP at 0.11 µM and GSH at 200 µM (mortality values of 50%)
- **C0** at 0.11 µM, CDDP at 0.63 µM and GSH at 200 µM (mortality values of 70%)
- **C0** at 0.11 µM, CDDP at 0.11 µM and GSH at 650 µM (mortality values of 70%)
- **C0** at 0.11 µM, CDDP at 0.42 µM and GSH at 400 µM (mortality values of 70%)

3.4.2 Calculation of the non-additive effect and of the net multi drug effect index

The non-algebraic additive effect (NAEE) of the combined drugs was calculated according to the equation already presented (17). The synergistic/antagonistic effect was evaluated calculating the net multi drug effect index (NMDEI) (17) for all the points of the used grid. The calculated surfaces show (Figure 8 for the binary systems and Figure 9 for the ternary system) the possible interactions occurring between two or among three drugs, allowing to determine if there is a synergistic or an antagonistic effect.

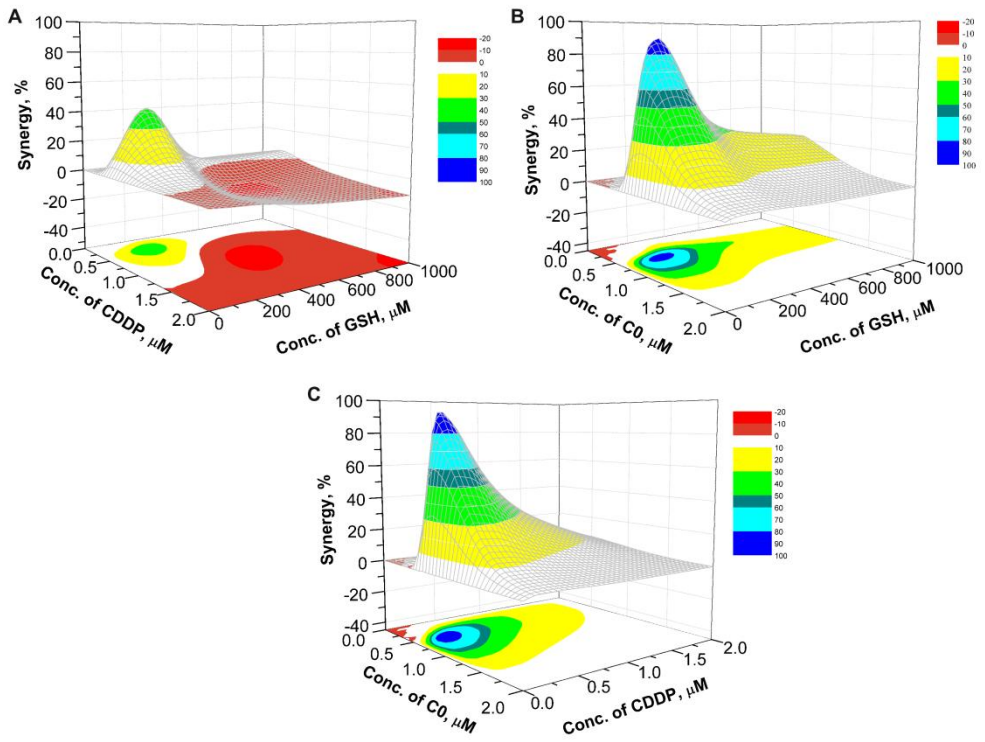

Figure 8. Synergistic surfaces for the binary systems of (**A**) CDDP and GSH, (**B**) **C0** and GSH, (**C**) **C0** and CDDP for CCRF-CEM-wt cell line.

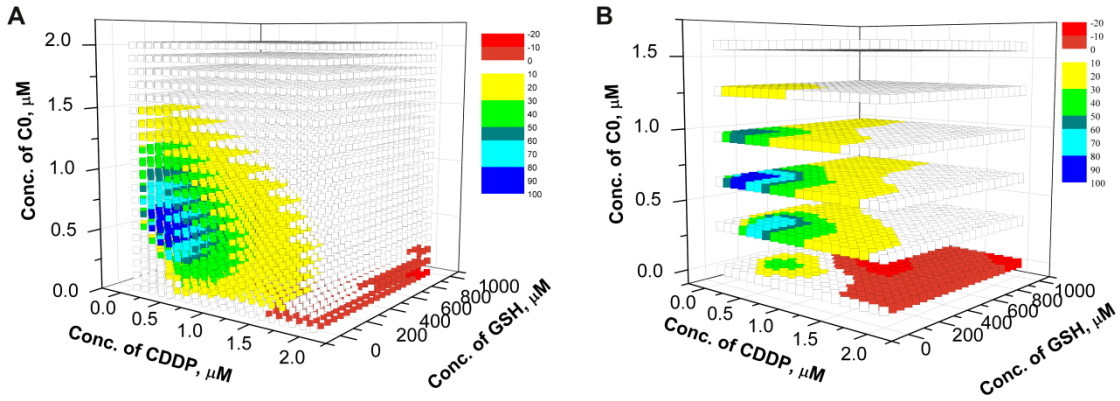

Figure 9. Synergistic surfaces for the ternary systems CDDP-GSH-**C0** for CCRF-CEM-wt cell line (**A**), some selected planes are reported for clarity (**B**); the color of the points is proportional to the synergistic effect.

3.4.2.1. Binary mixtures of CDDP and GSH

In the plot of the NMDEI as a function of CDDP and GSH concentrations (Figure 7A) a maximum (value is 42.0) is present for a concentration of CDDP 0.39 µM and of GSH 247 µM. At these concentrations both the two drugs, taken individually, present a mortality value of 10%, while their combination present a mortality value of 53.9% (Figure 6B). A synergistic effect is evident.

In the plot there is a wide area of negative values, in particular in the region where 0.76 µM ≤ CDDP ≤ 1.48 µM and 384 µM ≤ GSH ≤ 684 µM, with a minimum (value is -12.4) at CDDP 1.14 µM and GSH 533 µM. This combination presents a cytotoxicity value of 75.7% (Figure 6B), while the two drugs alone show at the same concentrations, a cytotoxicity of 69.6% and 65.0%, respectively. In this case an antagonistic effect is present.

3.4.2.2 Binary mixtures of C0 and CDDP

In Figure 8C is showed the plot of NMDEI as a function of the concentration of **C0** and CDDP. There is a wide positive area that indicates a synergistic effect between the two drugs. A maximum of NMDEI (value is 91.9) appears for CDDP 0.34 µM and **C0** 0.54 µM. This combination shows a cytotoxicity of 96.7% (Figure 6A) while the two compounds alone show at the same concentration of the combination, a cytotoxicity values of 3% and 6%, respectively. The synergistic effect between **C0** and CDDP is in agreement with my previous findings (17).

3.4.2.3 Binary mixtures of C0 and GSH

In Figure 8B is reported the plot of the NMDEI as a function of **C0** and GSH concentrations. A maximum (value is 89.2) is present for **C0** at 0.60 µM and GSH at 220 µM. At these concentrations

the two drugs, taken individually, present a mortality value of 8% and 6% respectively, while their combination present a mortality value of 95.7% (Figure 6C). A clear synergistic effect is evident.

3.4.2.4 Ternary mixtures of CDDP, GSH and C0

For the evaluation of the three-drugs system, cubic surface has been build up, representing the NMDEI value with the colour of the points (Figure 9A). For clarity only 6 planes were represented in Figure 9B. It shows the influence of the concentration of **C0** to the cytotoxicity of the mixtures. In absence of **C0** (first plane from the bottom)**,** for high concentrations of GSH, there is antagonism between CDDP and GSH. In presence of concentrations of **C0** higher than 0.5 μM the antagonism between CDDP and GSH disappears. There is synergism between **C0** and CDDP only at low concentration of GSH (for [C0]=[CDDP]= about 0.75 μM) (this could be explained by the formation of an adduct Pt-**C0** and high concentration of GSH interfere with this reaction).
Summarizing it's possible to see that:

- at low concentrations of **C0**, there is antagonism between GSH and CDDP**;**
- at low concentrations of GSH, there is a good synergy between **C0** and CDDP, for a combination in molar ration of about 1:1.

3.5 CCRF-CEM-res cell line

3.5.1 Selection of a cisplatin-resistant CCRF-CEM subline

Given the potential relevance of this finding for the clinic of cancer, it was of primary importance to investigate the effect of such drug combinations in sub-populations of the same cell line that showed a phenotype of resistance to CDDP (CCRF-CEM-res). To this end, a parallel culture of CCRF-CEM cells was serially passaged in the presence of increasing concentrations of CDDP. The selection of a CCRF-CEM subline with a stable phenotype of CDDP resistance was a long procedure that took about 7 months as cell cultivation in the presence of increasing drug doses had to be alternate with several passages at a constant concentration in order to avoid total cell death.
At first, cells were grown in the presence of a concentration of CDDP equal to 1/2 of the IC_{50}, i.e. 0.5 μM. This CDDP concentration was initially increased by 0.25 μM doses at each passage, but once the concentration of 1.50 μM was reached, it was necessary to dwell for 5 consecutive passages at the same concentration. If further increased, in fact, the cells started growing with difficulty, the percentage of viability dropped, and the few viable cells showed the tendency to form clusters, an unusual feature for this type of cells. After that, the CDDP concentration could be increased to 1.75 μM for 2 passages, to 2 μM for 12 passages, then to 2.50 μM for 14 passages, and finally to 5μM, the maximum drug concentration at which cells seemed able to multiply; in our hands, in fact, CCRF-CEM cells were not able to adapt to CDDP concentrations higher than 5μM.

The latter cell population was stabilized at 5μM CDDP by further 15 passages, then amplified, grown for one passage in the absence of the drug. Aliquots were stored in liquid nitrogen for experimental use.

At different times during the selection procedure, the sensitivity of cells to CDDP was determined and compared to that of the wild type CCRF-CEM cells by the MTT method. As can be seen (Table 1), only after 52 passages in the presence of CDDP it was possible to obtain a stable CCRF-CEM-res subline showing a Resistance Index (RI) of about 6.

It is worth mentioning that cell populations growing in the presence of CDDP, as well as the final one resistant to CDDP, never showed at any extent cross-resistance to the Cu(II) complex **C0**, indicating a different mechanism(s) of resistance of the two drugs, and thus also different molecular targets and modes of action. No modification in the cell sensitivity to the reference compound doxorubicin was ever observed.

Table 1. Citotoxicity of CDDP and **C0** against CCRF-CEM-wt and CCRF-CEM-res after 14, 26 and 52 passages in the presence of CDDP.

	CDDP	**C0**	**Doxorubicin**
CCRF-CEM-wt	± 1.12 μM	1 μM	0.02 μM
CCRF-CEM-res	2.6 μM	0.8 μM	0.02 μM
R.I.= 2.32 (14th passage)			
CCRF-CEM-wt	± 1.12 μM	1.1 μM	0.02 μM
CCRF-CEM-res	2.52 μM	0.8 μM	0.02 μM
R.I.= 2.25 (26th passage)			
CCRF-CEM-wt	± 1.12 μM	1 μM	0.02 μM
CCRF-CEM-res	6.98 μM	0.74μM	0.02 μM
R.I.= 6.23 (52th passage)			

Because cell resistance to CDDP has been reported to be multifactorial, i.e. reduced drug accumulation, increased drug inactivation, enhanced DNA-repair and increased DNA-damage tolerance, we deemed appropriate to obtain mechanistically homogenous cell clones from the mixed CDDP-resistant cell population in order to study them separately. However, despite of the several efforts made to grow cell clones by single-cell dilutions, an otherwise successful procedure to obtain cloned cell populations, in no case single-cell cultures were able to survive and multiply. Failed the separation of CDDP-resistant cells into different cloned populations, all studies implying CDDP-resistant CCRF-CEM cells had to be performed on the cell subline stabilized at 5μM CDDP.

3.5.2 Calculation of the non-additive effect and of the net multi drug effect index

The cytotoxicity of mixtures and drugs alone, together with the response surfaces, were calculated by using the network, for the case CCFR-CEM-res, following the same procedure adopted for the CCRF-CEM-wt. The calculated surfaces for the binary systems and that for the ternary system are reported in Figure 10 and Figure 11, respectively.

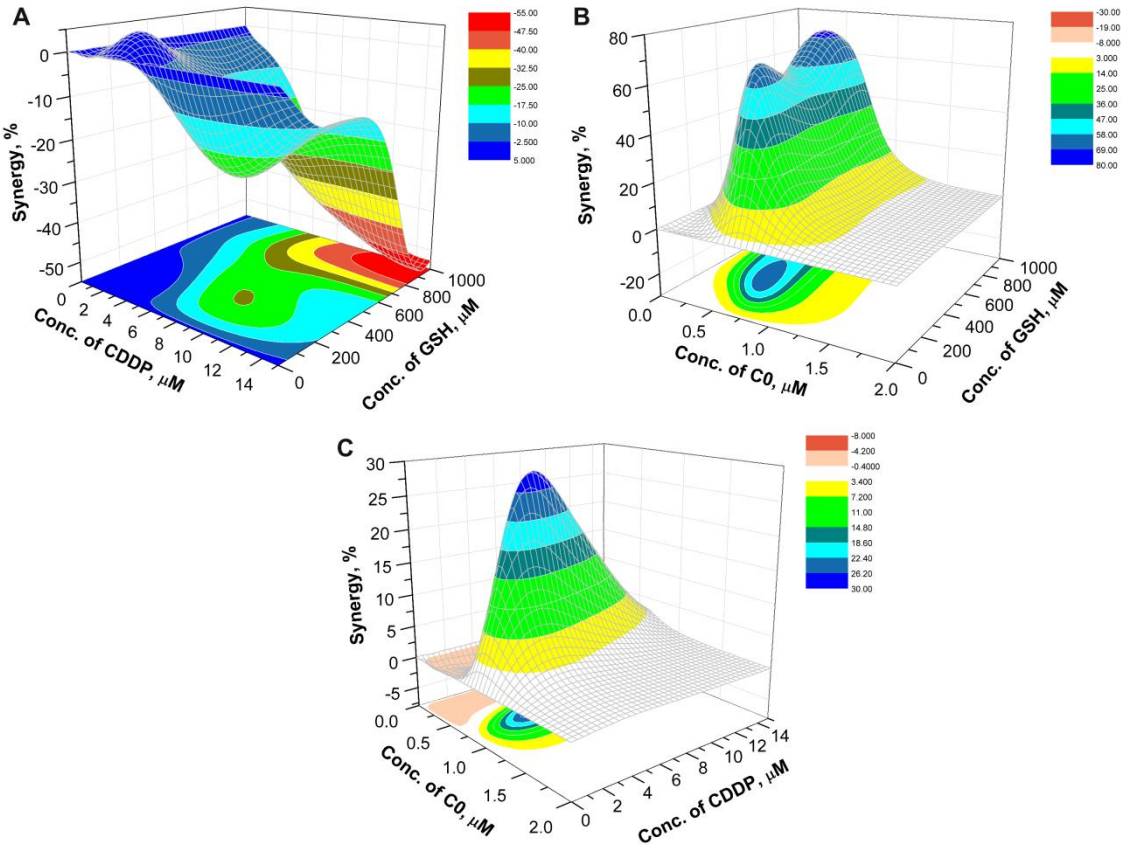

Figure 10. Synergistic surfaces for the binary systems of (**A**) CDDP and GSH, (**B**) **C0** and GSH, (**C**) **C0** and CDDP for CCRF-CEM-res cell line.

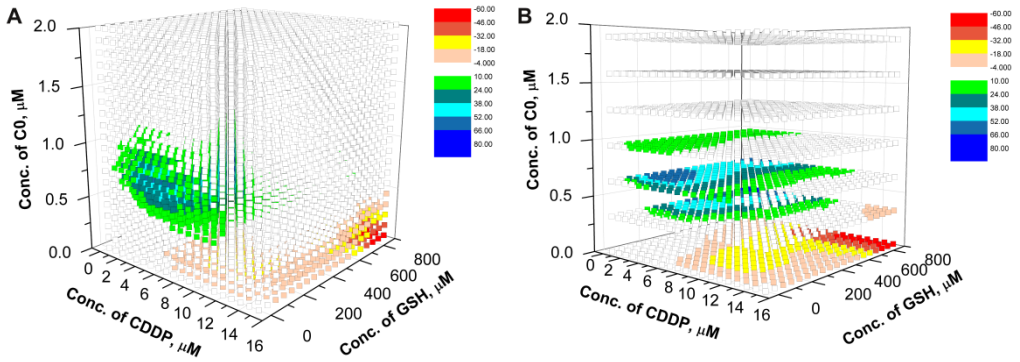

Figure 11. Synergistic surfaces for the ternary system CDDP-GSH-**C0** for CCRF-CEM-res cell line (**A**), some selected planes are reported for clarity (**B**); the color of the points is proportional to the synergistic effect.

3.5.2.1 Binary mixtures

In the plot of the NMDEI as a function of CDDP and GSH concentrations (Figure 10A), there is a wide negative area that indicates an antagonistic effect between the two drugs. A minimum of NMDEI (value is -53.8) appears for CDDP 15 μM and GSH 950 μM. This combination shows a cytotoxicity of 42 %, while the two drugs alone show at the same concentrations, a cytotoxicity of 94.4 % and 24.9 %, respectively. In the plot, there is a limited positive area, in particular in the region where 0.79 μM < CDDP < 3.95 μM and 50 μM < GSH < 300 μM, with a maximum of 4.1.

In Figure 10B, is reported the plot of NMDEI as a function of the concentration of **C0** and GSH. In all the studied region, a synergistic effect is evident. Two maximums (values are 70.9 and 65.4) appear for **C0** 0.42 μM and GSH 900 μM, and for **C0** 0.53 μM and GSH 350 μM. The second combination presents a cytotoxicity value of 95.6 %, while the two drugs alone show at the same concentrations, a cytotoxicity of 10.8 % and 21.8 %, respectively.

In Figure 10C, is showed the plot of the NMDEI as a function of **C0** and CDDP concentrations. The wide positive area indicates a synergistic effect between the two drugs. A maximum of NMDEI (value is 28.3) appears for **C0** 0.74 μM and CDDP 4.74 μM. This combination shows a cytotoxicity of 87.8 %, while the two compounds alone show at the same concentrations of the combination, a cytotoxicity values of 45.5 % and 25.7 %, respsectively. In the plot there is a limited negative area, in particular in the region where 0.11 μM < **C0** < 0.52 μM and 0.78 μM < CDDP < 8.68 μM, with a minimum of -2.9.

3.5.2.2 Ternary mixtures of CDDP, GSH and C0

In Figure 11, the plots show the influence of the concentration of C0 to the cytotoxicity of the mixtures CDDP-GSH. As for CCRF-CEM-wt, in absence of **C0** there is antagonism between CDDP and GSH. In presence of concentrations of **C0** higher than 0.4 μM the antagonism between CDDP and GSH disappears.

3.6 Test points

The most relevant combinations of drugs were chosen as test point and the mixture were prepared and the corresponding cytotoxicity measured, to compare the experimental values with the ones calculated by the network. The mortality values calculated with the network are in good agreement with the experimental ones, confirming the predicting abilities of the network.

3.7 Cytotoxic effects of the ternary drug combination in ex vivo cultures of human PBLs from healthy donors

On the basis of the strong cytotoxic synergism shown by the CDDP-**C0**-GSH combination in CCRF-CEM-wt and CCRF-CEM-res tumour cell lines, either drug-sensitive and CDDP-resistant, it was of critical importance to investigate their toxic effect on normal cells so as to have an estimate of the selectivity of action of these cocktails of drugs.

To this end, human peripheral blood lymphocytes (PBLs) freshly isolated from blood samples of healthy donors were seeded at the same cell density as such (i.e. resting PBLs), in the presence of the mitogen PHA (i.e. PHA-activated PBLs), or in the presence of both PHA and the growth factor Interleukin-2 (i.e. PHA/IL2-stimulated PBLs). Each of these cultures were then incubated in the presence of the most synergic three-drug combination in CCRF-CEM-wt cells and in the presence of the single drugs, each of them at the same concentrations present in the combination; i.e. 0.5µM CDDP, 0.5µM **C0**, and 300 µM GSH. The numbers of viable cells were determined by the trypan blue exclusion method and reported as percentage of untreated controls after 24 h (Figure 12A-C), 48 h (Figure 13A-C) and 72 h (Figure 14A-C) of incubation in comparison to those of CEM cells incubated in parallel under the same drug conditions (Figs 12D,13D,14D). It has to be mentioned that the PBL values in Figures 12,13,14 are the mean data of independent experiments with PBLs isolated from three different donors, whereas in Figure 15 PBL growth curves and viable cell counts of untreated vs. drug combination treated PBLs isolated from one single donor are shown.

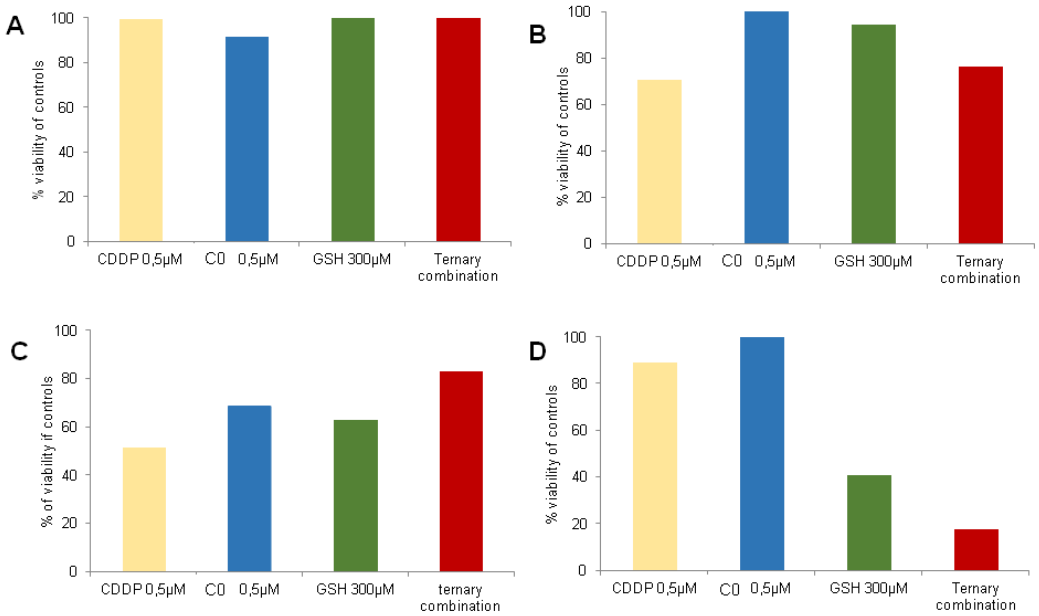

Figure 12. Cytotoxic activity of **C0**, CDDP, and GSH, alone and in ternary combinations, in freshly isolated human PBLs and in CCRF-CEM-wt cells after 24 h of treatment. (**A**) resting PBLs, (**B**) PHA-stimulated PBLs, (**C**) PHA+ IL2- stimulated PBLs, (**D**) CCRF-CEM-wt. Values obtained in drug-treated samples were expressed as percentages of their respective controls.

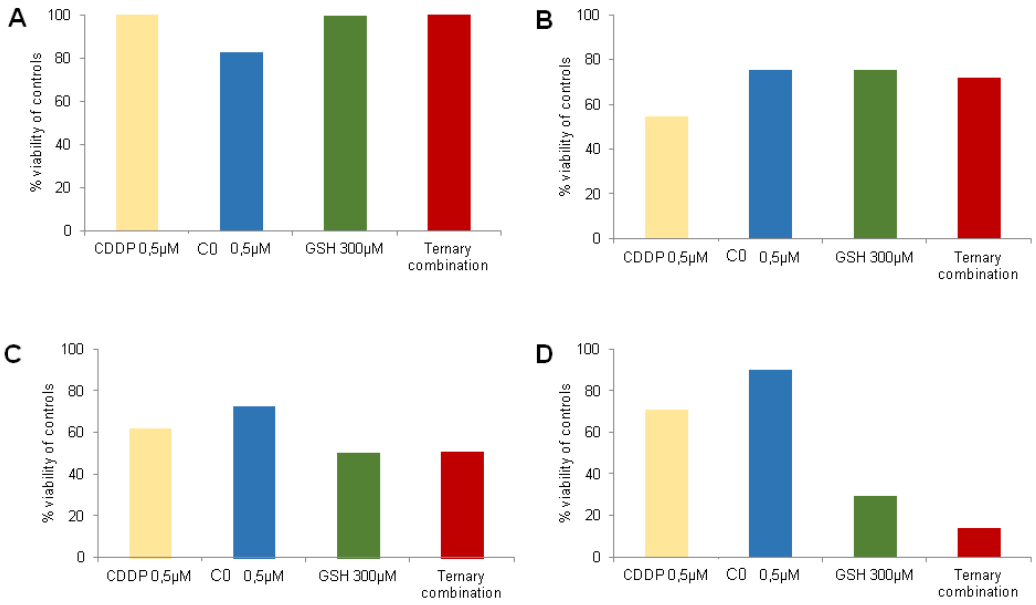

Figure 13. Cytotoxic activity of **C0**, CDDP and GSH, alone and in ternary combinations, in freshly isolated human PBLs and in CCRF-CEM cells after 48 hours of treatment. (**A**) resting PBLs, (**B**) PHA-stimulated PBLs, (**C**) PHA+ IL2- stimulated PBLs, (**D**) CCRF-CEM-wt. Values obtained in drug-treated samples were expressed as percentages of their respective controls.

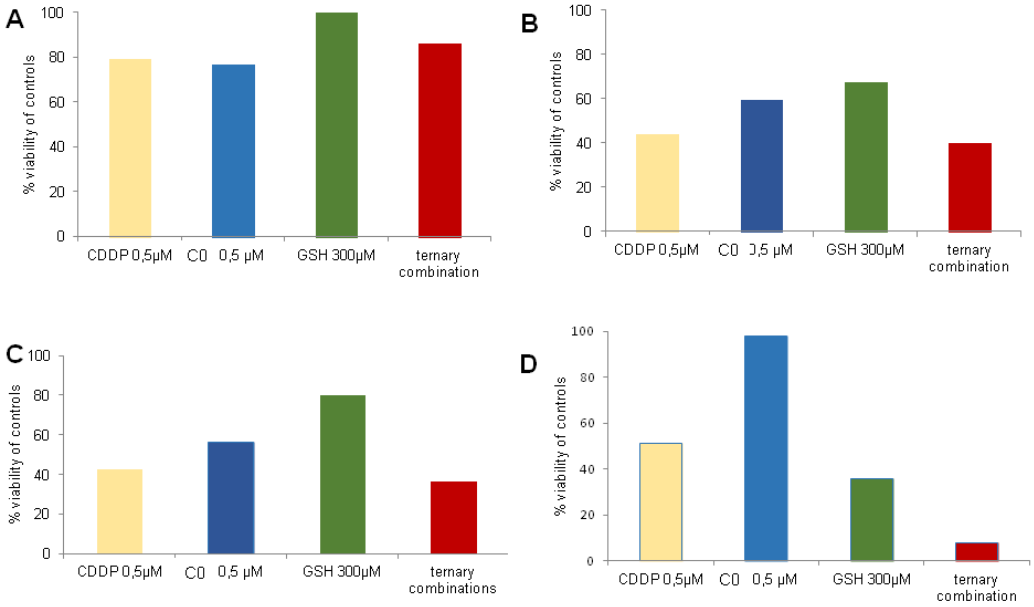

Figure 14. Cytotoxic activity of **C0**, CDDP and GSH, alone and in ternary combinations, in freshly isolated human PBLs and in CCRF-CEM-wt cells after 72 h of treatment. (**A**) Resting PBLs, (**B**) PHA-stimulated PBLs, (**C**) PHA+ IL2- stimulated PBLs, (**D**) CCRF-CEM-wt. Values obtained in drug-treated samples were expressed as percentages of their respective controls.

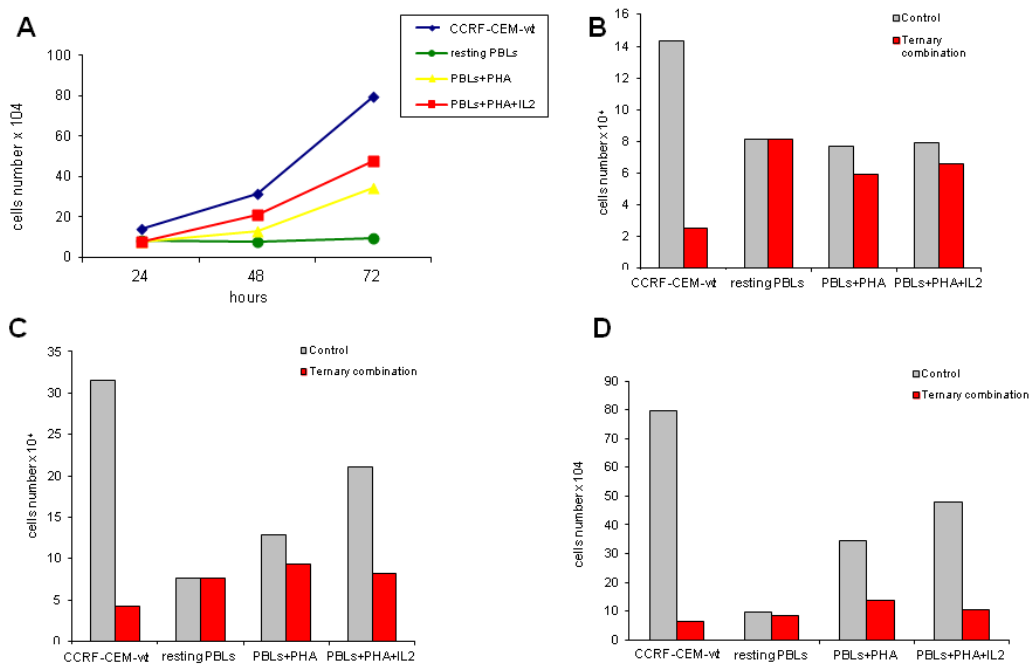

Figure 15. Growth curves and cell numbers of untreated vs. ternary combination-treated CEM and PBL cells. (**A**) Growth curves of CCRF-CEM-wt and PBLs. Viable cell numbers in untreated vs. ternary combination-treated CCRF-CEM-wt and PBLs after 24 h (**B**), 48 h (**C**), 72 h (**D**).

Single-drug treatments with 0.5µM CDDP showed a cytotoxic effect increasing over time only against active/proliferating cell cultures, i.e. against both PHA-activated and PHA/IL2-stimulated PBLs, and against CCRF-CEM cells, while, as expected, it had only negligible effects against non-activated/non-proliferating cells (i.e. resting-PBLs). After 72 h of incubation, the degree of cytotoxicity of CDDP was comparable in PBLs and CEM cells, with an average of 60%-70% cell viability with respect to their respective untreated controls. In the PBL cultures, however, the CDDP effect was more precocious (i.e. in PHA/IL2-stimulated at 24 h; in PHA-activated at 48 h) than in the CCRF-CEM cultures; viable CCRF-CEM cells being still over 80% of controls at 24 h, and over 70% of controls at 48 h.

The cytotoxic effect in PBLs of 0.5µM **C0** appeared to better correlate with the activation stage of the cells; the viability of PHA/IL2-stimolated PBLs was reduced by 30% already after 24 h, while that of the PHA-activated PBLs by 25%-30% only after 48 h. Differently from CDDP, **C0** seemed to affect the viability also of the resting PBLs as a slight toxic effect, i.e. a 10% to 20% mortality was observed in each PBL preparation of the three different donors. In CCRF-CEM cells, the cytotoxicity of **C0** appeared to be even lower, if any, than in the resting PBLs: the viability of treated CCRF-CEM cells being over 90% of controls at all time points considered.

Treatments with 300µM GSH were instead more toxic in CCRF-CEM cells than in PBLs, and among the latter, the PHA/IL2-stimulated were affected the most followed by the PHA-activated, whereas resting PBLs were not affected at all. Although GSH cytotoxicity was greater against the

CEM cells (60%-70% mortality) than against PHA/IL2-stimulated PBLs (50% mortality), in both types of cell cultures the maximum effect was reached after 48 h of exposure to GSH.

Compared to the single-drug treatments, in CCRF-CEM cells the drug cocktail confirmed the synergic effect showing a very strong toxic activity already in the first 24 h (over 80% mortality) which further increased at 48 h and 72 h with a mortality of 87% and 92%, respectively.

As for the PBLs, the PHA/IL2-stimulated were the most sensitive of all PBL cultures to the toxic effect of the drug combination that was, however, both less potent and more delayed with respect to that exerted in the CCRF-CEM cells, i.e. a 50% mortality only after 48 h, which did not increase further with time. The toxic effect against the PHA-activated PBLs was even slower than that shown in the PHA/IL2-stimulated, 20%- 30% mortality at the first two time points, and comparable only after 72 h. The drug cocktail was totally devoid of cytotoxicity on the resting PBLs at any time points considered.

Moreover, if we consider the effects of the ternary combination vs. the single-drug treatments in the PBLs, the drug cocktail always showed a degree of cytotoxicity comparable to that of the CDDP alone, whereas in the CCRF-CEM cells the toxic effect of the combination was 7 fold greater than that of CDDP alone.

Taken together, these findings are very promising given that the ternary combination showed a selective cytotoxic effect for T-leukemia CEM cells with respect to proliferating normal T-cells. Beside of being more potent against the leukemic CEM cells (8% viability after 72 h) than against PHA/IL2-stimulated PBLs (50% viability at 72 h), the effect of the ternary combination against CEM cells appeared to be also very precocious, i.e. only 17% viability left at 24 h, compared to 80% in the proliferating PBLs at the same time point.

4. Conclusions

CDDP was tested in combination with [Cu(phen)2(OH2)](ClO4)2 (**C0**) and GSH on wild type and cisplatin-resistant sublines of CCRF-CEM. A synergistic effect was evidenced between CDDP and **C0**, while an antagonistic effect was shown by CDDP and GSH. Combinations of **C0** and GSH shown synergistic effect, then ternary mixtures of CDDP, **C0** and GSH were tested. It was observed that in presence of **C0**, the sensitivity of the cells, wild type and/or resistant ones, towards CDDP in presence of GSH was restored, i.e. the antagonistic effect of the GSH versus CDDP was prevented. Furthermore, a synergistic effect was found for selected combinations.

On the basis of the strong cytotoxic synergism shown by the ternary mixtures of CDDP- **C0**-GSH combinations in CCRF-CEM-wt and CCRF-CEM-res tumour cell lines, their toxic effect was investigated also on normal cells so as to have an estimate of the selectivity of action of these cocktails of drugs. The drug cocktail was totally devoid of cytotoxicity on the resting human

peripheral blood lymphocytes (PBLs) at any time points considered. As for the PBLs, the PHA/IL2-stimulated, i.e. the PBLs in the presence of PHA and growth factor Interleukin-2, were the most sensitive of all PBL cultures to the toxic effect of the drug combination that was, however, both less potent and more delayed with respect to that exerted in the CCRF-CEM cells, i.e. a 50% mortality only after 48 h, which did not increase further with time. The toxic effect against the PHA-activated PBLs, i.e. PBLs in the presence of the mitogen PHA, was even slower than that shown in the PHA/IL2-stimulated, 20%- 30% mortality at the first two time points, and comparable only after 72 h. If we consider the effects of the ternary combination vs. the single-drug treatments in the PBLs, the drug cocktail always showed a degree of cytotoxicity comparable to that of the CDDP alone, whereas in the CCRF-CEM cells the toxic effect of the combination was 7 fold greater than that of CDDP alone.

References

1. **A.M. Florea, D. Busselberg.** Cisplatin as an Anti-Tumor Drug: Cellular Mechanism of Activity, Drug Resistance and Induced Side Effects. *Cancers.* 2011, Vol. 3, pp. 1351-1371.

2. **R.A. Alderden, M.D. Hall, T.W. Hambley.** The discovery and development of Cisplatin. *Journal of Chemical Education.* 2006, Vol. 83, pp. 728-734.

3. **A.I. Ivanov, J. Christodolou, J.A. Parkinson, K.J. Barnham, A. tucker, J. Woodrow, P.J. Sadler.** 1998, J. Biol. Chem., Vol. 273, pp. 14721-14730.

4. **Kratz, F.** [ed.] Germany VCH: Weinheim. *Metal Complexes in Cancer Chemotherapy.* s.l. : B.K. Keppler, 1993, pp. 391-429.

5. **Martin, R.B.** [ed.] Verlag Helvetica Chimica Acta: Zurich and Germay Wiley-VCH: Weinheim. *Cisplatin: Chemistry and Biochemistry of a Leading Anticancer Drug.* s.l. : B. Lippert, 1999, pp. 183-206.

6. **Arpalahti, J.** Cisplatin: Chemistry and Biochemistry of a Leading Anticancer Drug. [ed.] Verlag Helvetica Chimica Acta: Zurich and Germany Wiley-VCH: Weinheim. s.l. : B. Lippert, 1999, pp. 207-222.

7. **Legendre, F.** [ed.] Verlag Helvetica Chimica Acta: Zurich and Germany Wiley-VCH: Weinheim. *Cisplatin: Chemistry and Biochemistry of a Leading Anticancer Drug.* s.l. : B. Lippert, 1999, pp. 223-246.

8. **Z. guo, P.J. Sadler.** 2000, Adv. Inorg. Chem., Vol. 49, pp. 183-306.

9. **Hambley, T.W.** 2001, Dalton Trans., pp. 2711-2718.

10. **M.A. Fuertes, J. Castilla, C. Alonso, J.M. Perez.** 2002, Curr. Med. Chem. Anti-Cancer Agents, Vol. 2, pp. 539-551.

11. **T. Ishikawa, F. Ali-Osman.** Glutathione-associed cis-diamminedichloroplatinum (II) metabolism and ATP-dependent efflux from leukemia cells. Molecular characterization of glutathione-platinum complex and its biological significance. *Journal of Biological Chemistry.* 1993, Vol. 38, pp. 327-345.

12. **Y. Kasherman, S. Strurup, D. Gibson.** Is glutathione the major cellular target of cisplatin? A study of the interactions of cisplatin with cancer cell extracts. *Journal of Medicinal Chemistry.* 2009, Vol. 52, pp. 4319-4328.

13. **Siddik, Z.H.** Cisplatin: mode of cytotoxic action and molecular basis for resistance. *Oncogene.* 2003, Vol. 22, pp. 7265-7279.

14. **A.R. Chakravarty, P.A.N. Reddy, B.K. Santra, A.M. Thomas.** Copper Complexes as chemical nucleases. *Proc.Indian Acad. Sci.* 2002, Vol. 114, pp. 391-401.

15. **T. Pivetta, F. Isaia, G.Verani, C. Cannas, L. Serra, C. Castellano, F. Demartin, F. Pilla, M. Manca, A. Pani.** Mixed 1,10-phenantroline-Cu(II) complexes: Synthesis, cytotoxic activity versus heamtological and solid tumor cells and complex formation equilibria with glutathione. *Journal of Inorganic Biochemistry.* 2012, Vol. 104, pp. 28-37.

16. **T.Pivetta, M.D. Cannas, C. Castellano, F. Demartin, S. Vascellari, G. Verani, F. Isaia.** Synthesis, structural characterization, formation constants and in vitro cytotoxicity of phenantroline and iminazolidine-2-thione copper(II) complexes. *Journal of Inorganic Biochemistry.* 2011, Vol. 105, pp. 329-338.

17. **T. Pivetta, F. Isaia, F. Trudu, A. Pani, M. Manca, D. Perra, F. Amato, J. Havel.** Development and validation of a general approach to predict and quantify the synergism of anti-cancer drugs using experimental design and artificial neural networks. *Talanta* 2013, Vol. 115, pp. 84–93.

Chapter 4

Glutathione, cisplatin and copper-phenanthroline compounds: reactivity and complexation study

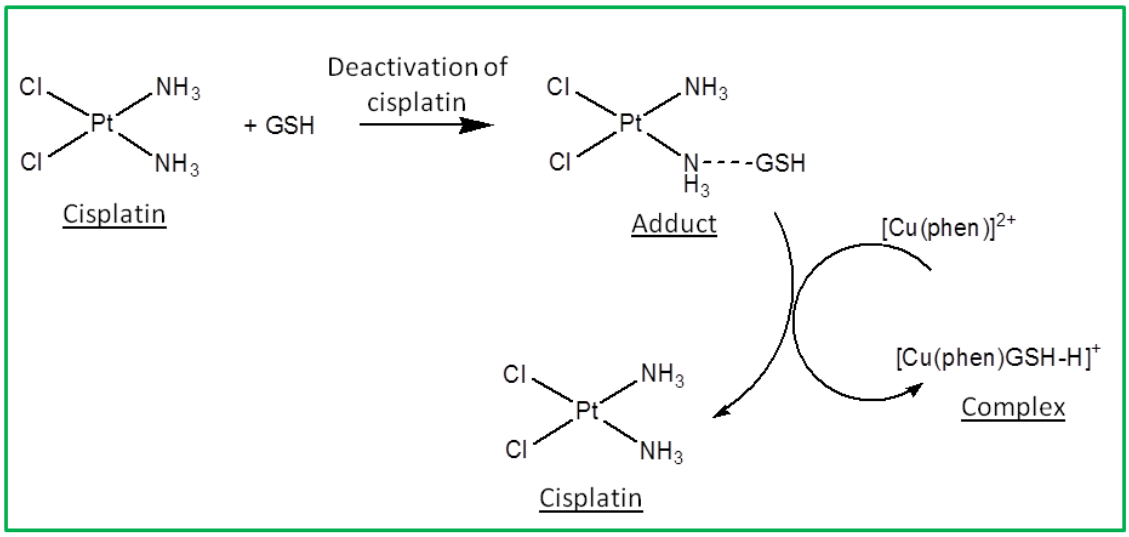

This chapter reports the study of the reactivity of cisplatin, $[Cu(phen)_2(H_2O)](ClO_4)_2$, $[Cu(phen)(H_2O)_2(ClO_4)_2]$, GSH and GSSG, in binary and ternary mixtures.

Abstract

In previous studies, CDDP was tested *in vitro* with the copper complex $[Cu(phen)_2(H_2O)](ClO_4)_2$ (**C0**) showing a synergistic effect not only towards the wild type leukemic (CCRF-CEM) and ovarian (A2780) cancer cell lines but also towards their cisplatin-resistant sublines (Chapter 2-Article II). Considering that the cisplatin-resistance could be due to a reaction between CDDP and GSH and that in presence of **C0** the sensibility of the resistant cell lines to CDDP is restored, I decided to study the reactivity of CDDP and **C0** with GSH or GSSG with the aim to identify and characterize the possible formation of mixed complexes. I extended these studies also to GSSG, since it is in equilibrium with GSH, and to $[Cu(phen)(H_2O)_2(ClO_4)_2]$ (**C10**), a copper complex that shows an antiproliferative activity versus the CCRF-CEM cells similar to that of **C0** (Chapter 4 - Manuscript II). This study was carried out by Electro-Spray Ionisation at Atmospheric-Pressure Mass Spectrometry and tandem MS-MS of binary and ternary mixtures of the studied compounds. The formed complexes were identified by the fitting of the isotopic pattern and on the basis of the fragmentation pathways. The coordination mode around metal ions was assessed on the basis of the fragmentation pathways and quanto-mechanical calculations. In Figure 15 the formulas and acronyms of the molecules studied in this work are reported.

Although several authors studied the mass spectra of GSH and GSSG with ESI-MS, only selected peaks were identified and few fragmentation pathways were discussed. I studied in deep the mass spectra of GSH and GSSG in order to interpret the mass spectra of their metal complexes.

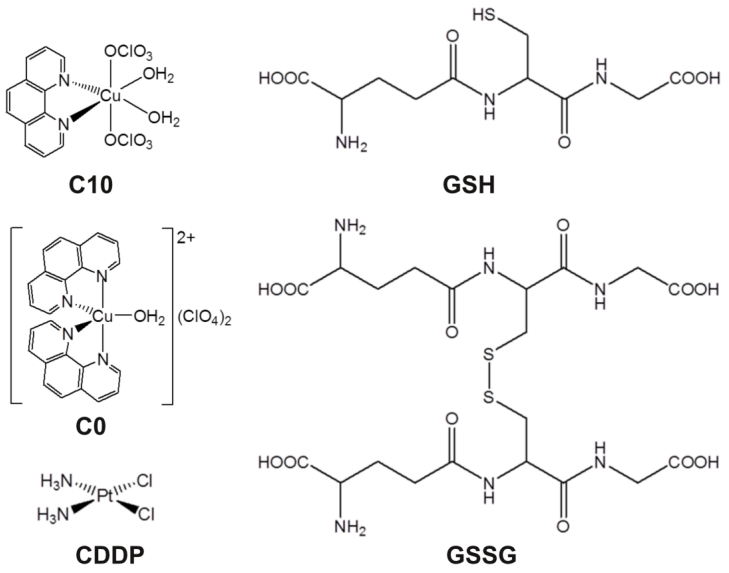

Figure 15. Formulas and acronyms of the molecules studied in this work.

CDDP reacts with GSH to form the complex $[Pt(NH_3)_2Cl_2(GSH+H)]^+$ (Figure 16), but with GSSG it forms the adduct $[Pt(NH_3)_2Cl_2+GSSG+H]^+$. Even in excess of thionic ligands, species containing more than one GSH or GSSG were not detected.

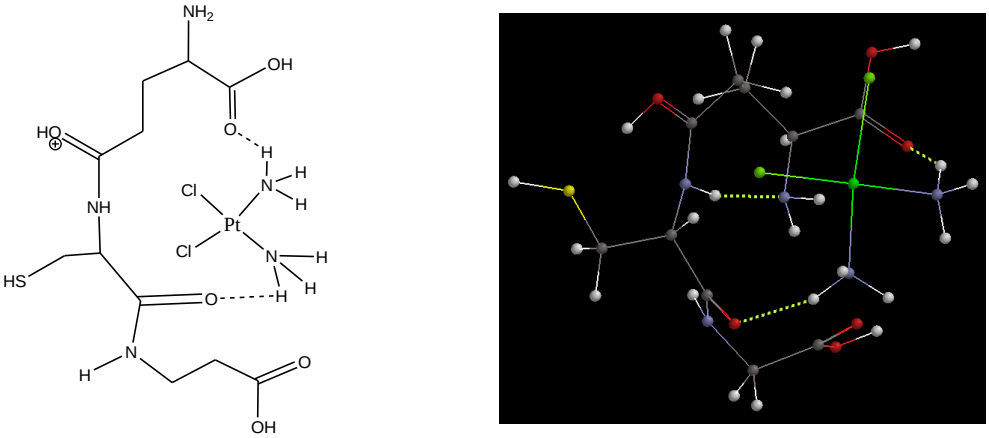

$[Pt(NH_3)_2Cl_2(GSH+H)]^+$, *m/z* 608

Figure 16. Coordination scheme (left) and optimized structure obtained by quanto-mechanical calculations (right) of $[Pt(NH_3)_2Cl_2(GSH+H)]^+$.

Copper complexes **C0** and **C10** react with GSH or GSSG to form complexes such as $[Cu(phen)(GSH)\text{-}H]^+$ and $[Cu(phen)(GSSG)(ClO_4)]^+$. The two copper complexes form with CDDP mixed complexes where the two metal centers are linked by two bridging chloride (Chapter 2 – Article II).

When the copper complexes were mixed with CDDP and GSH or GSSG, only copper-glutathione complexes were detected. No peaks relative to platinum- and copper-containing ions or to platinum- and sulphur-containing ions were detected.

Given that the cytotoxic activity of CDDP in presence of **C0** against cisplatin-resistance cells was restored, **C0** can be supposed to bind glutathione preventing in this way the deactivation of CDDP as anticancer agents.

Manuscript II

Glutathione, cisplatin and copper-phenanthroline compounds: reactivity and complexation study

Elisa Valletta, Enzo Cadoni, Graziano Caddeo, Sarah Vascellari, Francesco Isaia, Tiziana Pivetta

To be submitted

GLUTATHIONE, CISPLATIN AND COPPER-PHENANTHROLINE COMPOUNDS: REACTIVITY AND COMPLEXATION STUDY

Elisa Valletta[1], Enzo Cadoni[1], Graziano Caddeo[1], Sarah Vascellari[2], Francesco Isaia[1], Tiziana Pivetta[*1]

[1]Dipartimento di Scienze Chimiche e Geologiche, [2]Dipartimento di Scienze Biomediche, University of Cagliari, Cittadella Universitaria, 09042 Monserrato – CA (ITALY)

[*]corresponding author:

Tiziana Pivetta

Dipartimento di Scienze Chimiche e Geologiche

University of Cagliari, Cittadella Universitaria, 09042 Monserrato – CA (ITALY)

Tel. +39 0706754473

mail: tpivetta@unica.it

Keyword: cisplatin, glutathione, copper complexes, ESI-MS

ABSTRACT

A large number of cancers are treated with cisplatin (CDDP). The effectiveness of CDDP therapy is limited by the drug resistance, often related to the intracellular levels of thiol-containing molecules, such as glutathione (GSH). Up to now, the role of GSH in cisplatin-resistant cancer cells is still unclear. GSH may form adducts with CDDP that results deactivated as drug, and, actually, a high intracellular level of GSH was observed in some cisplatin-resistant cancers. On the other hand, the increase of the GSH levels inside the cells could enhance the CDDP uptake by increasing the number of copper transporters. CDDP is often administered in combination with one or more drugs in order to exploit a possible synergistic effect and overcome the drug resistance. In previous studies, it was observed that the sensibility of leukemic and ovarian cisplatin-resistant cancer cell lines to CDDP, was restored in presence of $[Cu(phen)_2(H_2O)](ClO_4)_2$ (**C0**) (phen is 1,10-phenathroline). In this work, the reactivity of CDDP, **C0** and GSH, in binary and ternary mixtures, was studied. The investigation was extended also to $[Cu(phen)(H_2O)_2(ClO_4)_2]$ (**C10**) and to GSSG, the oxidized form of GSH. It was observed that CDDP forms adducts with GSH or GSSG, but, in presence of **C0** or **C10**, only copper-glutathione complexes were detected, while no platinum-glutathione adducts were found. Glutathione shows towards copper(II) more affinity than towards platinum and the formation of mixed complexes between copper and platinum is discouraged in presence of glutathione. Then, it is possible to conclude that **C0** or **C10** are able to bind glutathione preventing the deactivation of CDDP as anticancer agent and restoring its cytotoxic activity also towards cisplatin-resistant cells.

1. INTRODUCTION

A large number of cancers in different organs like ovary, testicle, neck, head, bones, lymph nodes and skin are currently treated with *cis*-diammineplatinum(II) dichloride (cisplatin, CDDP) [1]–[5]. CDDP exerts its antitumor activity binding DNA and triggering cellular apoptosis. It is administered by injection and, once in the bloodstream, is bound to different plasmatic proteins containing thiol groups [6],[7]. The effectiveness of CDDP therapy is often limited by the development of resistance. Among the main identified mechanisms underneath this phenomenon, an important key role is played by the intracellular levels of thiol-containing molecules that, binding CDDP, form species without therapeutic efficacy [8],[9]. One of the most abundant thiol-containing molecule in the human body is the glutathione (GSH), a γ-Glu-Cys-Gly tripeptide [4],[10],[11] ubiquitous in biological fluids, with concentration ranging from 1 to 10 mM. GSH is in equilibrium with its oxidized form, GSSG, formed by two glutathione molecules bound by a disulfide bridge between the cysteine residuals. The GSSG is reduced to GSH by the glutathione reductase, so that

in physiological conditions the intracellular concentration of GSH is 1 to 10 of that of GSSG. When the ratio GSH/GSSG is lower than 10 the glutathione depletion, often correlated with cancer, arises. Pt(II) is a soft ion [12] and shows great affinity for the sulfur atom, then CDDP may form adducts with GSH, resulting deactivated as drug [13],[14]. Actually, a high intracellular level of GSH was observed in some cisplatin-resistant cancers [4], even if, according to some authors, the increase of the GSH levels inside the cancer cells could enhance the sensibility of the cells to CDDP by increasing the number of copper transporters and then the drug uptake [15],[16]. From these considerations, it appears evident that the role of GSH in cisplatin-resistant cancer cells is still unclear.

CDDP is often administered in combination with one or more drugs in order to exploit a possible synergistic effect and overcome slow down the drug resistance. Basically, a combination of drugs may exhibit an increased (synergism), equal (additive effect) or lowered (antagonism) therapeutic effect with respect to the sum of the effects of the single drugs. If two or more drugs act synergistically, the drugs can be administered in reduced doses, weakening the side effects related to the doses and reducing the development of the drug resistance [17],[18]. The synergism may arise from the simultaneous involvement of different targets or mechanisms, but also from a bio-chemical reaction among the combined drugs.

In previous studies, CDDP was tested *in vitro* with the copper complex $[Cu(phen)_2(H_2O)](ClO_4)_2$ (**C0**) showing a synergistic effect not only towards the wild type leukemic (CCRF-CEM) and ovarian (A2780) cancer cell lines but also towards their cisplatin-resistant sublines [19],[20]. Considering that the cisplatin-resistance could be due to a reaction between CDDP and GSH and that in presence of **C0** the sensibility of the resistant cell lines to CDDP is restored, we decided to study the reactivity of CDDP and C0 with GSH or GSSG with the aim to identify and characterize the possible formation of mixed complexes. We extended these studies also to GSSG, since it is in equilibrium with GSH, and to $[Cu(phen)(H_2O)_2(ClO_4)_2]$ (**C10**), a copper complex that shows an antiproliferative activity versus the CCRF-CEM cells similar to that of **C0** [21]. This study was carried out by Electro-Spray Ionisation at Atmospheric-Pressure Mass Spectrometry (ESI-MS) and tandem MS-MS of binary and ternary mixtures of the studied compounds. The formed complexes were identified by the fitting of the isotopic pattern and on the basis of the fragmentation pathways. In Fig. 1 formulas and acronyms of the molecules studied in this work are reported.

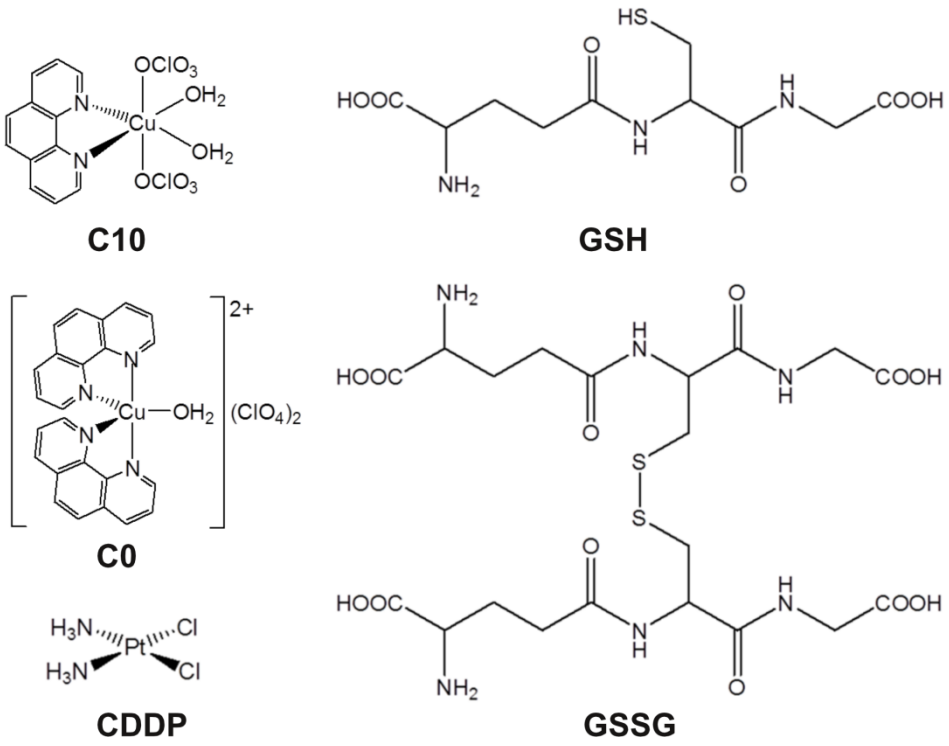

Fig. 1. Formulas and acronyms of the molecules studied in this work.

2. EXPERIMENTAL PART

2.1. Reagents

Methanol, oxidised glutathione (GSSG), *sodium hydroxide,* trifluoroacetic acid (HTFA) and reduced glutathione (GSH) were purchased from Sigma-Aldrich (Milan, Italy). *Cis*-diammineplatinum(II) dichloride (CDDP) was purchased from Alfa-Aesar (Heysham, United Kingdom). The commercial reagents were used as received, without any further purification. Ultra-pure water obtained with MilliQ Millipore was used for all the experiments. The copper complexes **C0** and **C10** were prepared as previously reported [21],[22].

2.2. Preparation of solutions for ESI-MS

Solutions containing CDDP, copper complexes, GSH, GSSG and the binary combinations of CDDP or copper complexes with GSH or GSSG in 1:0.5, 1:1, 1:2, 1:3, 1:4 and 1:100 metal:ligand molar ratios, were prepared by dissolving the appropriate amount of the compounds in water containing 0.05% of HTFA (v/v). The concentrations of the reagents in the ternary mixtures were chosen on the basis of an experimental design (ED). In an ED experiment [23], two or more process variables (called factors) are changed together in order to observe the mutual effect on one or more response variables. The ED is opposite to the classical procedure of changing one variable at time (OVAT method) and provides more effective and unbiased conclusions. The mixtures were prepared

according to a cubic factorial ED with three factors, i.e. the analytical concentrations of **C0**, CDDP and GSH or GSSG and three levels of concentration, i.e. 1.00 (a), 0.66 (b) and 0.33 (c) mM. The used concentrations were the 27 permutations with repetition of a, b and c. Sample solutions were mixed with methanol in 1:1 H_2O:CH_3OH volume ratio in order to improve the quality of the spectra. So as not to alter the complex formation equilibria, methanol was added immediately before the mass spectra were recorded.

2.3. Mass Spectrometry

Mass spectra were recorded on a triple quadruple QqQ Varian 310-MS mass spectrometer using the Atmospheric-Pressure Electro-Spray Ionisation (ESI) technique. The mass spectra were recorded in positive ion mode in the *m/z* 100–1000 range. The experimental conditions were: needle voltage 6000 V, shield voltage 800 V, housing temperature 60 °C, drying gas temperature 100 °C, nebuliser gas pressure 40 PSI, drying gas pressure 20 PSI, and detector voltage 2000 V. Tandem MS–MS experiments were performed with argon as the collision gas (1.8 PSI) using a needle voltage of 6000 V, shield voltage of 800 V, housing temperature of 60 °C, drying gas temperature of 100 °C, nebuliser gas pressure of 40 PSI, drying gas pressure of 20 PSI, and a detector voltage of 2000 V. The isotopic patterns of the measured peaks in the mass spectra were analysed using mMass 5.5.0 software package [24],[25]. The assignments were based on the copper-63 and platinum-195 isotopes. The sample solutions were infused directly into the ESI source using a programmable syringe pump at a flow rate of 1.50 mL/h. A dwell time of 14 s was used and the spectra were accumulated for 10 min in order to increase the signal-to-noise ratio.

2.4. Quantum chemical calculations

The theoretical calculations were performed on an INTEL-i7 processor based system with Spartan'06 program (SPARTAN'06 , Wavefunction, Inc). The complex geometries were optimised using semi-empirical methods with PM3 basis set [26]. Heat of formation, electron density surface, atomic, electrostatic [27],[28], natural [29] and Mulliken [30],[31] charges, HOMO and LUMO orbitals were obtained for each molecule, in order to evaluate the most stable conformers.

2.5. Synthesis of Cu(phen)(GSSG)(ClO4)2

A propanolic solution (15 mL) containing GSSG (0.0775 g, $1.27x10^{-4}$ mol) and NaOH (0.0102 g, $2.54x10^{-4}$ mol) was dropped into a propanolic solution of **C10** (0.0604 g, $1.27x10^{-4}$ mol). The resulting solution was refluxed for 3 h, during this time the color of the solution turned from blue to dark green. The green solution was concentrated under vacuum and a violet solid product was recovered by filtration. Percentage yield 65%. Soluble in CH_3OH and CH_3CN.

3. RESULTS AND DISCUSSION

3.1. ESI-MS experiments of pure compounds

The ESI-MS spectra of **C0**, **C10** and CDDP were previously discussed [20]. Regards GSH and GSSG, several authors studied their mass spectra with ESI-MS but only selected peaks were identified and few fragmentation pathways were discussed [32]–[37]. Since the full knowledge of the fragmentation of GSH and GSSG is necessary to interpret the mass spectra of their metal complexes and to determine their molecular structure, we studied in deep the mass spectra of GSH and GSSG (Fig. S1). We recognized five fragmentation pathways for GSH, from the parent peak at *m/z* 308 to 245, 233, 179, 144, 130; and nine for GSSG, from the parent peak at *m/z* 613 to 595, 538, 409, 355, 288, 231, 211, 177, 130. These fragmentation pathways are depicted in the Supporting (Scheme S1 for GSH and Scheme S2 for GSSG), while in Fig. 2 and 3 the most abundant fragments are shown for GSH and GSSG, respectively.

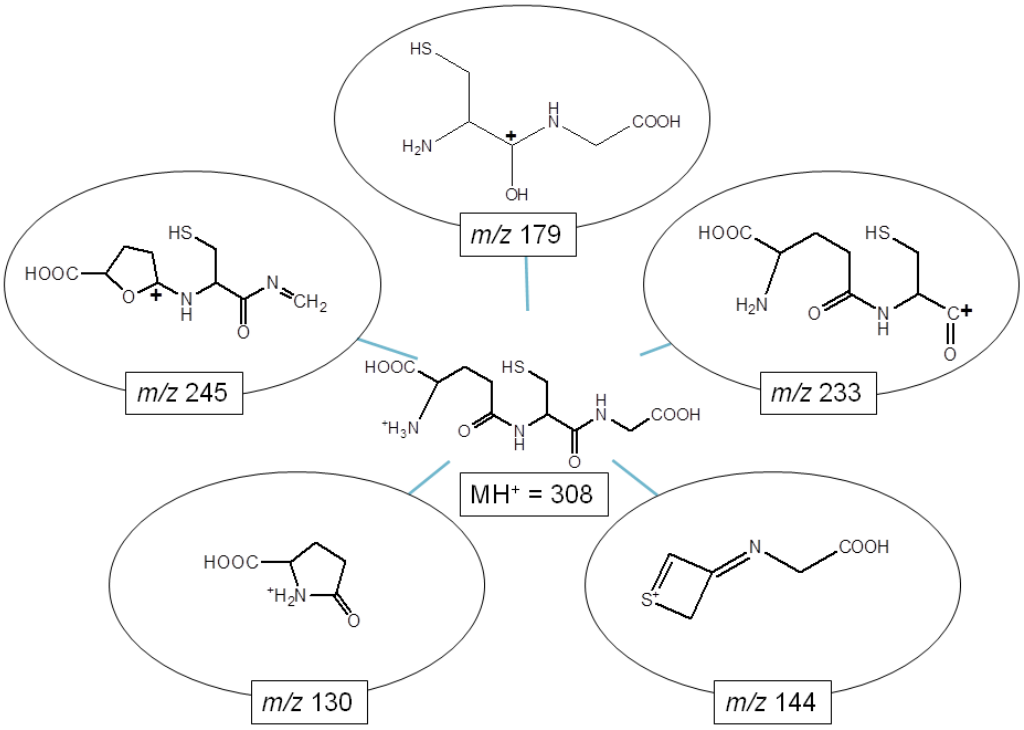

Fig. 2. The most abundant fragments of $[GSH+H]^+$ (*m/z* 308).

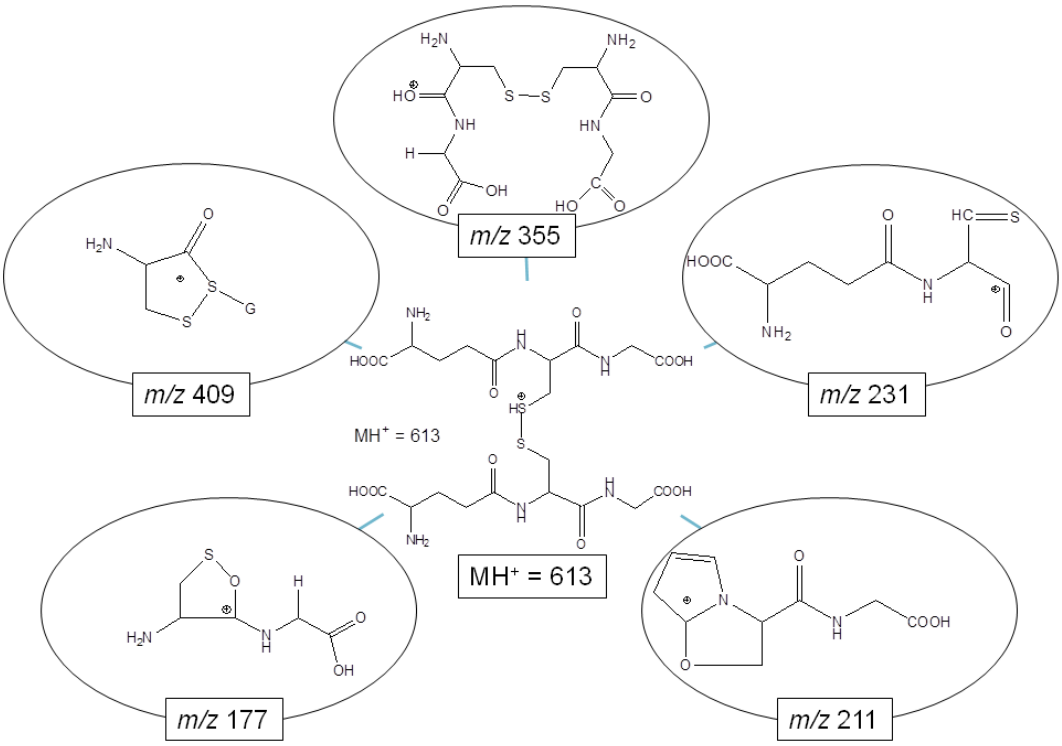

Fig. 3. The most abundant fragments of $[GSSG+H]^+$ (*m/z* 613) (G is $C_{10}H_{16}N_3O_6$).

3.2. ESI-MS experiments of binary systems

3.2.1. Copper complexes and GSH or GSSG

In the ESI-MS spectra of binary mixtures of **C0** or **C10** with GSH or GSSG, characteristic peaks of copper- and sulphur-containing ions were detected. Three peaks corresponding to $[Cu(phen)(GSH)-H]^+$ (*m/z* 549.10, **I**), $[Cu(GSSG)-H]^+$ (*m/z* 674.03, **II**), and $[Cu(phen)(GSSG)-H]^+$ (*m/z* 854.10, **III**) were common in all the systems, while two peaks corresponding to $[Cu_2(phen)(GSSG)-3H]^+$ (*m/z* 915.00, **IV**) and $[Cu(phen)(GSSG)(ClO_4)]^+$ (*m/z* 954.06, **V**) were observed in **C0**-GSH, **C0**-GSSG and **C10**-GSH systems. The assignments are tabulated in Table 1.

Reagents	Complex or adduct	Stoichiometry	Composition	Exp. *m/z**	Calc. *m/z**
C0 + GSH or GSSG, C10 + GSH or GSSG	**I**	$[Cu(phen)(GSH)-H]^+$	$C_{22}H_{24}CuN_5O_6S$	549.10	549.07
C0 + GSH or GSSG, C10 + GSH or GSSG, CDDP + GSH + C0	**II**	$[Cu(GSSG)-H]^+$	$C_{20}H_{31}CuN_6O_{12}S_2$	674.03	674.07
C0 + GSH or GSSG, C10 + GSH or GSSG, CDDP + GSH + C0	**III**	$[Cu(phen)(GSSG)-H]^+$	$C_{32}H_{39}CuN_8O_{12}S_2$	854.10	854.14
C0 + GSH or GSSG, C10 + GSH	**IV**	$[Cu_2(phen)(GSSG)-3H]^+$	$C_{32}H_{37}Cu_2N_8O_{12}S_2$	915.00	915.06
C0 + GSH or GSSG, C10 + GSH, CDDP + GSH + C0	**V**	$[Cu(phen)(GSSG)(ClO_4)]^+$	$C_{32}H_{40}ClCuN_8O_{16}S_2$	954.06	954.10
CDDP + GSH	**VI**	$[Pt(NH_3)_2Cl(GSH)]^+$	$C_{10}H_{23}ClN_5O_6PtS$	571.09	571.07
	VII	$[Pt(NH_3)_2Cl_2(GSH+H)]^+$	$C_{10}H_{24}Cl_2N_5O_6PtS$	608.04	607.05
CDDP + GSSG	**VIII**	$[Pt(NH_3)_2Cl_2+GSSG+2H]^{+2}$	$C_{20}H_{39}Cl_2N_8O_{12}PtS_2$	457.09	456.06
	IX	$[Pt(NH_3)_2Cl_2+GSSG+H]^+$	$C_{20}H_{39}Cl_2N_8O_{12}PtS_2$	912.98	912.11
CDDP + GSH + C0	**X**	$[Pt(NH_3)_2Cl]^+$	H_6ClN_2Pt	263.96	263.99
CDDP + C0 or C10	**XI****	$[CuPt(phen)(H_2O)_2(OH)Cl_2]^+$	$C_{12}H_{13}Cl_2CuN_2O_3Pt$	560.90	560.92
	XII**	$[CuPt(phen)(H_2O)(OH)(NH_3)Cl_2]^+$	$C_{12}H_{14}Cl_2CuN_3O_2Pt$	559.90	559.94.
	XIII**	$[CuPt(phen)(H_2O)_2Cl_2]^+$	$C_{12}H_{12}Cl_2CuN_2O_2Pt$	543.95	543.92

Table 1. Species identified from the ESI–MS studies. * The experimental *m/z* value is relative to the highest peak of the isotopic pattern while the calculated one refer to the monoisotopic mass, ** from ref. [20].

It is interesting to remark that **C0** and **C10** form the same complexes **I** (Scheme 1) and **III**, and that a phen molecule is lost in the reactions involving **C0**.

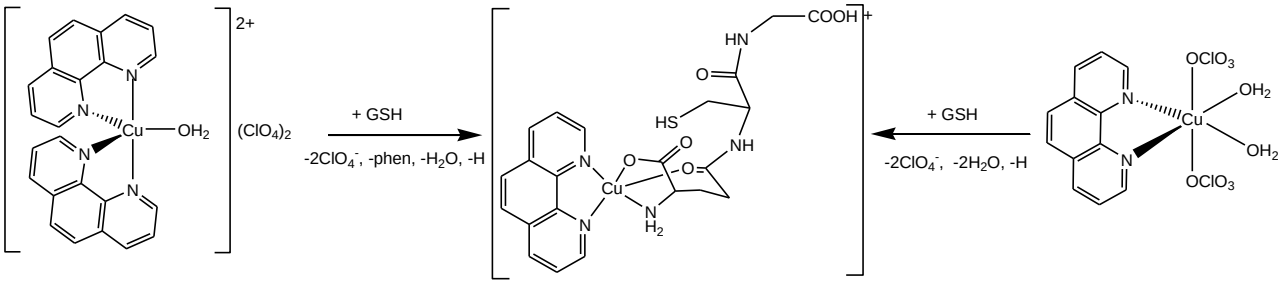

Scheme 1. Reaction mechanism between **C0** or **C10** with GSH to form $[Cu(phen)(GSH)\text{-}H]^+$, **I**.

In all the detected complexes the copper ion has +2 as oxidation number. The tandem MS-MS spectra confirmed the elemental composition proposed, for the observed ions, on the basis of the isotopic patterns. The mass spectra of the studied systems at 1:2 copper:ligand molar ratio are reported in the Supporting (Fig. S2). The calculated and experimental isotopic patterns for selected peaks, are shown in Fig. S3.

Species with more than one molecule of GSH or GSSG were not detected even in excess of the ligands. Species **I** and **III** were obtained also during fragmentation of **V**, species **II** was obtained also during fragmentation of **III** (Fig. 4).

The coordination mode of GSH or GSSG to copper(II) was assessed on the basis of the MS-MS fragmentation pathways, and the most probable geometry of the complexes was obtained by quanto-mechanical calculations. The hypothesized structures of **I**, **II**, **III** and **V** are shown in Fig. 5 while selected fragmentation pathways for **II**, **III** and **V** are shown in the Supporting (Schemes S3-S5).

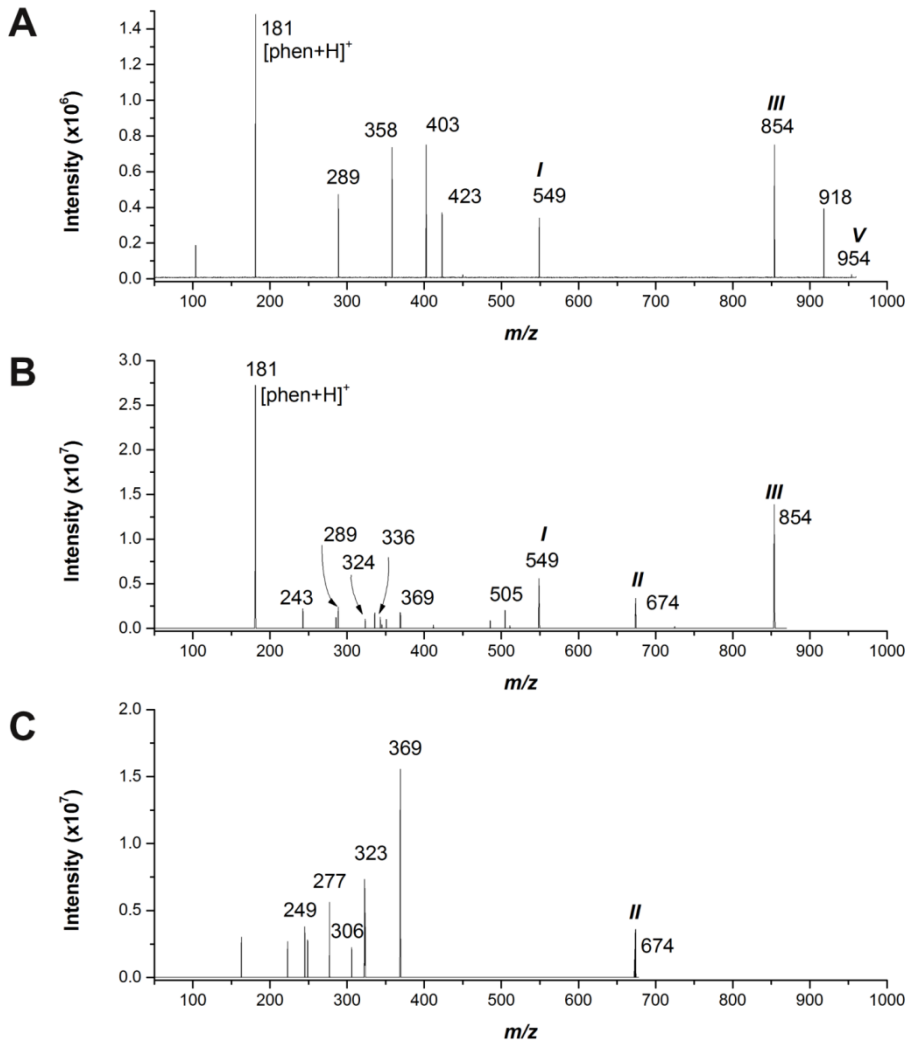

Fig. 4. MS-MS spectra of the signals at *m/z* 954 (**A**), 854 (**B**) and 674 (**C**) (collision energy 20 V, 1:2 C10:GSH, GSH 0.5 mM, 50:50 methanol/water with 0.05% of HTFA).

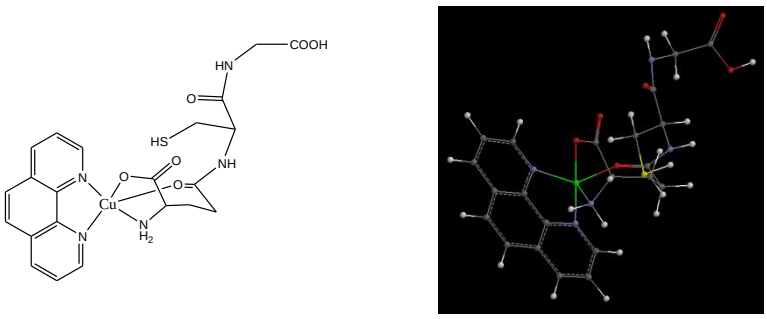

I, $[Cu(phen)(GSH)-H)]^+$ (E = -632.4 kJ/mol)

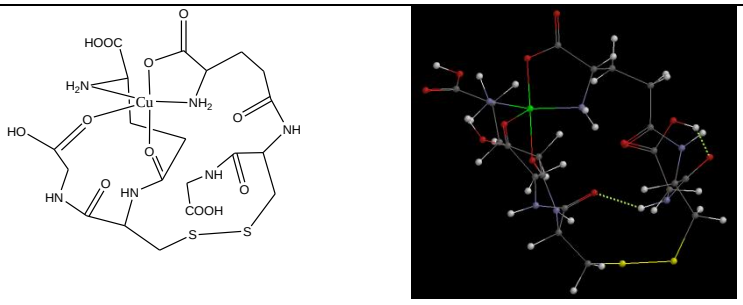

II, $[Cu(GSSG)-H]^+$ (E = -1880.3 kJ/mol)

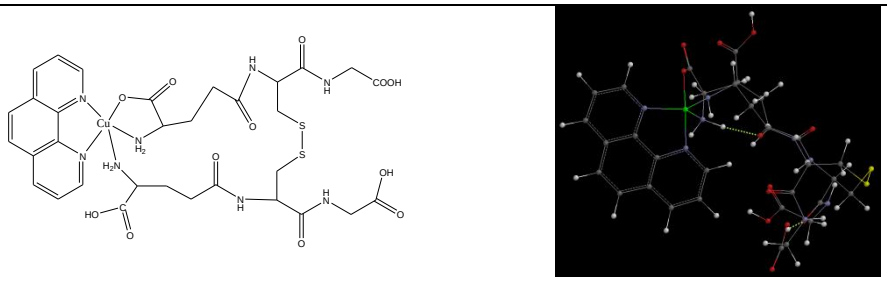

III, $[Cu(phen)(GSSG)-H)]^+$ (E = -1878.8 kJ/mol)

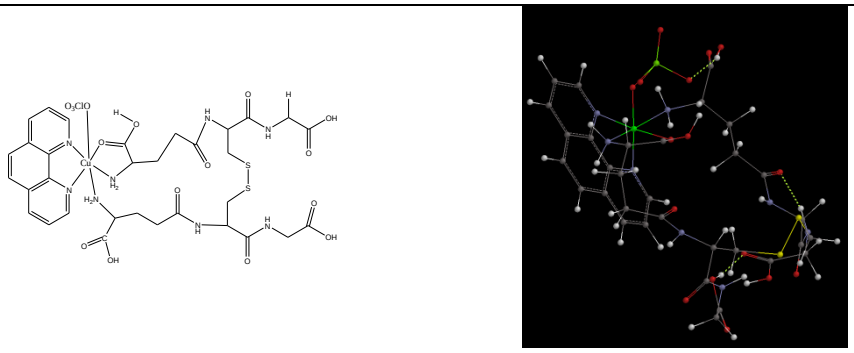

V, $[Cu(phen)(GSSG)(ClO_4)]^+$,

A conformer (E = -2194.958 kJ/mol)

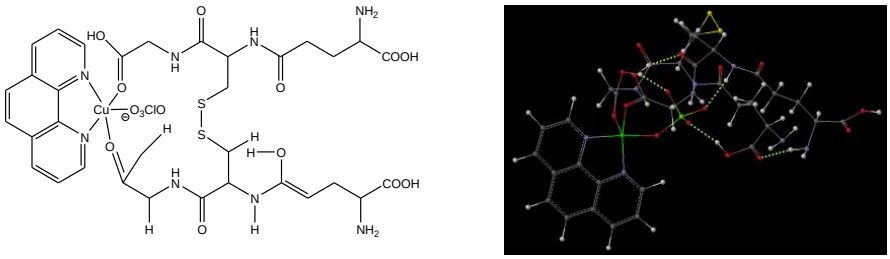

V, $[Cu(phen)(GSSG)(ClO_4)]^+$, B Conformer (E = - 2132.459 kJ/mol)

Fig. 5. Coordination scheme (left) and optimized structure obtained by quanto-mechanical calculations (right) of $[Cu(phen)(GSH)-H)]^+$ (**I**), $[Cu(GSSG)-H)]^+$ (**II**), $[Cu(phen)(GSSG)-H)]^+$ (**III**) and $[Cu(phen)(GSSG)(ClO_4)]^+$ (**V**).

The species **V** can exist in two different geometries, **A** and **B**, with similar formation enthalpies (kJ/mol -2195.0 and -2132.5 for **A** and **B**, respectively). In the first one, the metal ion is coordinated by the two phen nitrogen atoms, two aminic and one carboxylic groups of the glutamate residues, and a perchlorate anion. Three hydrogen bonds are present. In the second one, the copper(II) is coordinated, besides the two phen nitrogen atoms, by the two carboxylic groups of the glutamic residues and by the perchlorate anion. Five hydrogen bonds are present.

In the most stable structure of species **III**, copper(II) is coordinated by the two phen nitrogen atoms, the aminic groups of the GSSG glutamic residues and the carboxylate group of one glutamic residue; two hydrogen bonds are present. In **I**, the metal ion is coordinated, besides the two phen nitrogen atoms, by the aminic, carboxylic and chetonic groups of the glutamic residue. The presence of a fragment with *m/z* 336 that retains carboxylic and aminic groups but not the thiolic one, and the absence of fragments in which carboxylic and aminic groups are missing, leads us to consider the tholic group as not involved in coordination. The coordination of a second amino group to copper in **III** and **V**, is endorsed by the presence in the MS-MS spectrum of a peak at *m/z* 289 attributable to a unit of GSH which has lost one molecule of ammonia. The presence of the ion at *m/z* 181, due to the protonated phen, suggests that one carboxylic group of GSSG is involved in the coordination of copper in **III** and **V** or it is very close to phen to give it a proton. During collision, the species **V** gives **III** by losing perchloric acid and gives **I** by losing perchloric acid and a unit of GSH. The ion **I** is present also in the fragmentation of **III**. Species **III** results more stable than **I**, as shown by the greater abundance of the ion at *m/z* 549 compared to that at *m/z* 674. Moreover, species **I** is formed only at GSH:copper ratio $\geq$ 4:1.

Apart from the ion at *m/z* 181, attributable to the protonated phen, the fragmentation of **V** and **III** differ significantly. This can be explained by assuming that the fragments with low *m/z* ratios present in the MS-MS spectrum of **V**, derive directly from it. Both in the MS-MS spectra of **V** and **III**, the molecule of GSH, in fragments not containing the metal ion, lacks of carboxylic and aminic groups, suggesting that these groups are involved in coordination with the copper. Then a structure where copper ion is coordinated by carboxylic and aminic groups of the GSSG, the two phenanthrolinic nitrogen and the perchlorate anion, was supposed for **V**. The loss of perchloric acid from **V** leads to the more stable species **III**, which peak appears higher than that of **V**. **II** exists in ESI phase as a species and not only as a fragment of **III**. In fact, in the mass spectrum the intensity of the signal at *m/z* 674 appears not related with that of the signal at *m/z* 854. Moreover, the fragments of **II** are different from those of **III** for *m/z* lower than 674. Also in **II**, in fragments retaining copper, the metal ion is always bound to carboxylic and aminic groups, as shown by the

presence of the carboxylic/carboxylate groups in all the fragments, regardless of the applied collision energy.

During the reaction between **C0** and GSH or GSSG a phen molecule is lost, due to the steric hindrance and to the strength of the bonds formed with glutathione, greater than that with the phenanthrolinic nitrogen atoms.

3.2.2. Cisplatin and GSH

Mass spectra of solutions containing CDDP and GSH in 1:0.5, 1:1, 1:2, 1:3, 1:4 and 1:100 molar ratios were measured. The mass spectrum of solution containing CDDP and GSH at 1:2 platinum:GSH molar ratio, in the *m/z* 100-700 range is reported in Fig. 6 as an example.

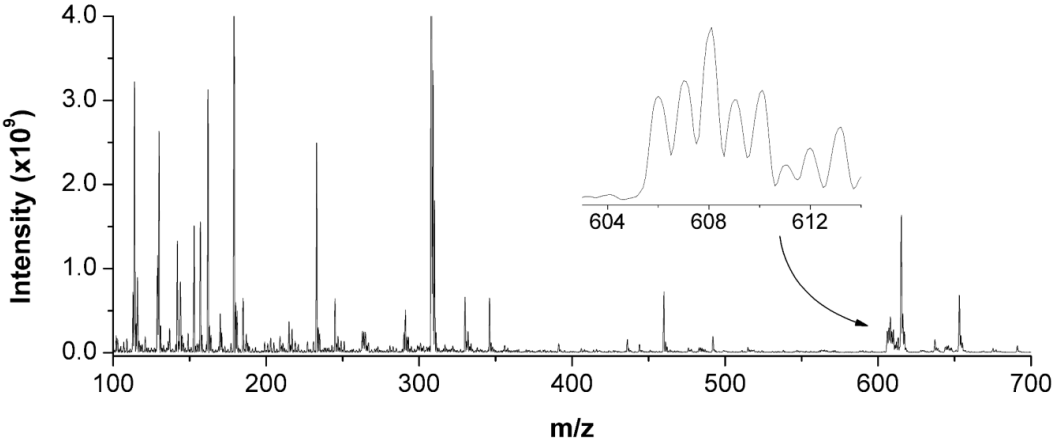

Fig. 6. ESI-MS (+) of solution containing CDDP (0.25 mM) and GSH (0.5 mM) (50:50 methanol/water with 0.05% of HTFA); in the inset the signal centered at *m/z* 608 is shown.

In all the recorded spectra, except in that of the 1:1 system, two signals centered at *m/z* 571 and 608 with an isotopic patterns characteristic of platinum- and sulphur-containing ions were detected. The stoichiometries of the species $[Pt(NH_3)_2Cl(GSH)]^+$ (*m/z* 571.09, **VI**) and $[Pt(NH_3)_2Cl_2(GSH+H)]^+$ (*m/z* 608.04, **VII**), were assigned on the basis of the isotopic patterns and the tandem MS-MS spectra (Fig. S4). The assignments are tabulated in Table 1.

The fragmentation of the peak at *m/z* 608 (Scheme S6) originates peaks at *m/z* 591 by loss of an ammonia molecule, at *m/z* 308 by loss of CDDP, at *m/z* 291, 233 and 179 by loss of CDDP and subsequent re-arrangement (note that the peak at *m/z* 608 could correspond to combinations of ^{196}Pt-^{35}Cl-^{35}Cl or ^{194}Pt-^{35}Cl-^{37}Cl).

On the basis of the fragmentation pathways and quanto-mechanical calculations the coordination mode around platinum ion was assessed. Basically, in **VII** two hydrogen bonds are formed between

i) an oxygen atom of the glycine residue and a proton of the ammonia of CDDP; ii) the oxygen atom of the carbonyl group of the glutamic residue and a proton of the second ammonia of CDDP. A third intramolecular hydrogen bond between the amino group of the glutamic residue and the cysteininc –NH group is also present. The hypothesized structures of **VII** is reported in Fig. 7.

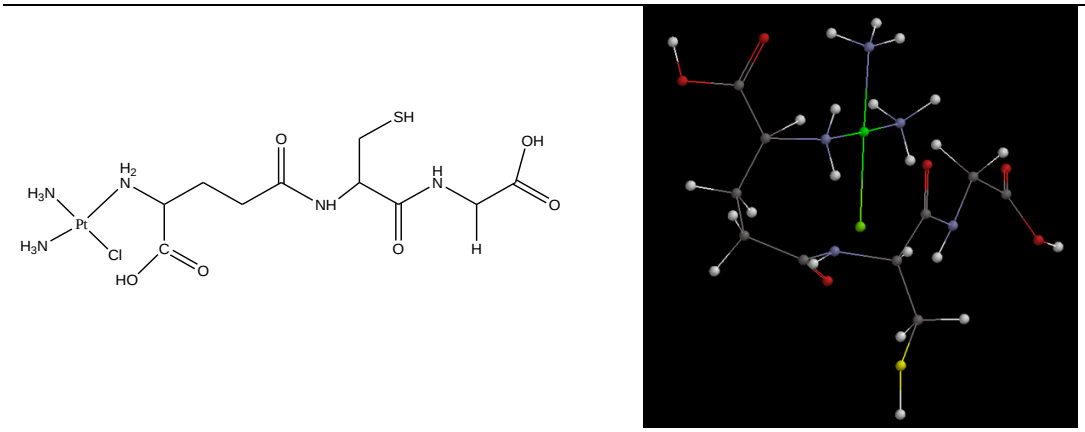

VI, $[Pt(NH_3)_2Cl(GSH)]^+$, *m/z* 571 (E = -2386.9 kJ/mol)

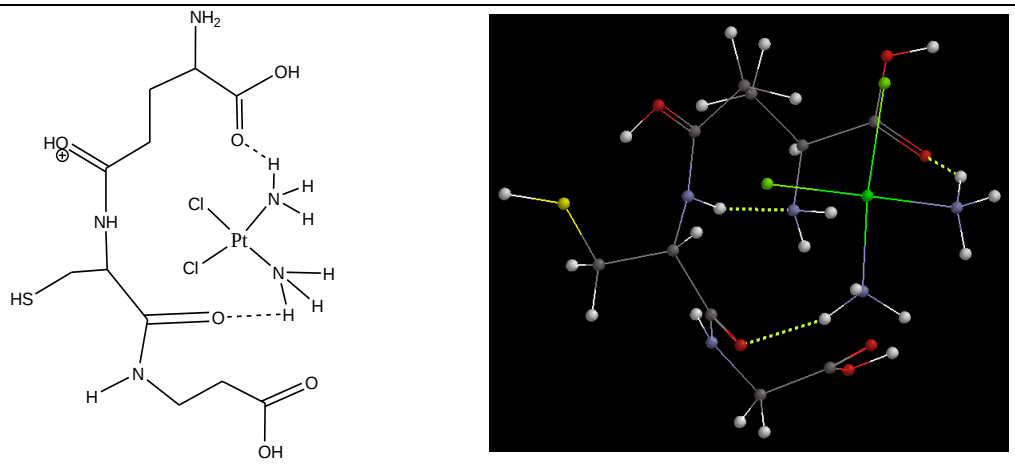

VII, $[Pt(NH_3)_2Cl_2(GSH+H)]^+$, *m/z* 608 (E = -2328.6 kJ/mol)

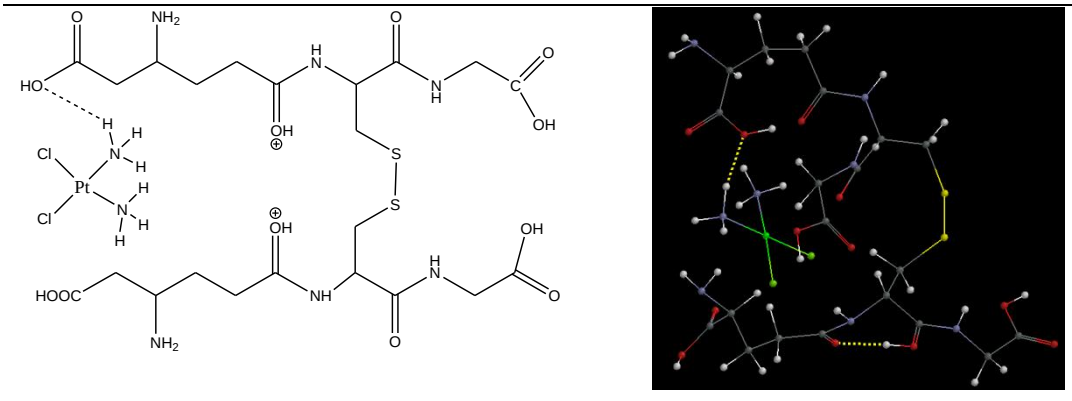

VIII, $[Pt(NH_3)_2Cl_2+GSSG+2H]^{2+}$, *m/z* 457 (E = -3554.6 kJ/mol)

Fig. 7. Coordination scheme (left) and optimized structure obtained by quanto-mechanical calculations (right) of $[Pt(NH_3)_2Cl(GSH)]^+$ (**VI**), $[Pt(NH_3)_2Cl_2(GSH+H)]^+$ (**VII**) and $[Pt(NH_3)_2Cl_2+GSSG+2H]^{2+}$ (**VIII**).

The CID of the peak at *m/z* 571 (Schemes S7) originates fragments at *m/z* 555, 554, 538, 479, 443, 425, 390, 388 and 272 (note that the peak at *m/z* 571 could correspond to combinations of ^{196}Pt-^{35}Cl or ^{194}Pt-^{37}Cl). In Fig. 7 the most probable structures of selected fragments originated by **VI** are reported. In **VI**, Platinum(II) ion is coordinated by the two ammonia molecules, one chloride and the amino group of the glutamic residue of the GSH.

Considering that a $Pt(GSH\text{-}H)_2$ complex was previously found [14], combinations of CDDP and GSH solutions in high excess of GSH (1:100 Pt/GSH) were prepared and analyzed but species containing more than one GSH molecule were not detected, neither after two days from the solution preparation. The different results may arise from the different experimental conditions used.

3.2.3. Cisplatin and GSSG

In the mass spectra of solutions containing cisplatin and GSSG, two peaks with characteristic isotopic pattern of platinum- and sulphur-containing ions were detected, the first at *m/z* 457 corresponding to the doubly-charged ion (**VIII**) $[Pt(NH_3)_2Cl_2+GSSG+2H]^{2+}$ (separation between adjacent peaks was *m/z* 0.5) and the second at *m/z* ≈ 912 corresponding to the mono-charged ion (**IX**) $[Pt(NH_3)_2Cl_2+GSSG+H]^{+}$. A so called GSSG-CDDP composite was previously reported.[38] The experimental and calculated isotopic patterns for these two peaks are shown in Fig. S5.

The assignments are tabulated with calculated and experimental *m/z* values in Table 1. On the basis of the fragmentation pathways (Scheme S8) and quanto-mechanical calculations, the most stable geometries for **VIII** was obtained (Fig. 7). In particular, since in the MS-MS spectra only fragments of GSSG not containing platinum were detected, the species **VIII** or **IX** can be considered as adducts between CDDP and GSSG, formed by hydrogen bonds.

Differently from **VIII** and **IX**, the most of the fragments of **VI** and **VII** contain platinum ion, than it is possible to conclude that a complex is formed by reaction of CDDP and GSH, while an adduct is originated by weak interactions between CDDP and GSSG.

3.2.4. Copper complexes and cisplatin

Compounds **C0** or **C10** form with CDDP the same complexes containing copper and platinum, i.e. $[CuPt(phen)(H_2O)_2(OH)Cl_2]^{+}$ (*m/z* 560.90, **XI**), $[CuPt(phen)(H_2O)(OH)(NH_3)Cl_2]^{+}$ (*m/z* 559.90, **XII**), and $[CuPt(phen)(H_2O)_2Cl_2]^{+}$ (*m/z* 543.95, **XIII**).[20]

3.3. ESI-MS experiments of ternary systems

Twenty-seven solutions containing **C0**, CDDP and GSH were prepared and analyzed. In all the spectra, peaks corresponding to the copper complexes **II**, **III** and **V** were detected together with a

peak relative to $[Pt(NH_3)_2Cl]^+$ (*m/z* 263.96, **X**). No peaks relative to platinum- and copper-containing ions or to platinum and sulphur-containing ions were detected.

3.4. Identification of $Cu(phen)(GSSG)(ClO_4)_2$

Considering that unexpected species may be detected as formed in ESI phase but not necessarily present in solution, I deemed interesting to verify if the $[Cu(phen)(GSSG)(ClO_4)]^+$ species could be formed. As a matter of fact, a mixed complex with stoichiometry $Cu(phen)(GSSG)(ClO_4)_2$ was actually synthesized by reaction between **C10** and the sodium salt of GSSG ($C_{20}H_{30}N_6\ Na_2O_{12}S_2$), confirming the possible formation of such species. The formation of a complex between **C0** and GSH with stoichiometry $[Cu(phen)_2(OH_2)(GSH)\text{-}H]^+$ has been previously discussed.[21]

4. CONCLUSIONS

CDDP reacts with GSH to form the complex $[Pt(NH_3)_2Cl_2(GSH+H)]^+$, but with GSSG it forms the adduct $[Pt(NH_3)_2Cl_2+GSSG+H]^+$. As shown by MS-MS experiments, glutathione and CDDP are kept together by hydrogen bonds. Even in excess of thionic ligands, only a 1:1 cisplatin:ligand adduct was detected.

Copper complexes **C0** and **C10** react with GSH or GSSG to form complexes such as $[Cu(phen)(GSH)\text{-}H]^+$ and $[Cu(phen)(GSSG)(ClO_4)]^+$. The complexes formed with GSSG are more stable than the counterparts formed with GSH. The two copper complexes form with CDDP mixed complexes where the two metal centers are linked by two bridging chloride.

When the studied copper complexes were mixed with CDDP and the thionic ligands, only copper-glutathione complexes were detected. No platinum-glutathione adducts or copper-platinum complexes were found. These results show that *i*) glutathione has towards copper(II) more affinity than towards platinum, *ii*) the formation of the mixed complexes between copper and platinum is not observed in presence of glutathione.

The previous cytotoxicity tests shown that the antiproliferative activity of CDDP in presence of **C0** against cisplatin-resistant cells was restored. **C0** can be supposed to bind glutathione preventing in this way the deactivation of CDDP as anticancer agent .

Bibliographic References

1. Martin, R. B. in *Cisplatin* 181–205 (Verlag Helvetica Chimica Acta, 1999). doi:10.1002/9783906390420.ch7
2. Arpalahti, J. in *Cisplatin* 207–221 (Verlag Helvetica Chimica Acta, 1999). doi:10.1002/9783906390420.ch8

3. Legendre, F. & Chottard, J.-C. in *Cisplatin* 223–245 (Verlag Helvetica Chimica Acta, 1999). doi:10.1002/9783906390420.ch9

4. Florea, A.-M. & Büsselberg, D. Cisplatin as an anti-tumor drug: cellular mechanisms of activity, drug resistance and induced side effects. *Cancers (Basel).* **3,** 1351–71 (2011).

5. Alderden, R. A., Hall, M. D. & Hambley, T. W. The Discovery and Development of Cisplatin. *J. Chem. Educ.* **83,** 728 (2006).

6. Ivanov, a I., Christodoulou, J., Parkinson, J. a, Barnham, K. J., Tucker, a, Woodrow, J. & Sadler, P. J. Cisplatin binding sites on human albumin. *J. Biol. Chem.* **273,** 14721–14730 (1998).

7. Kratzs, F., Hartmann, M., Keppler, B. & Messoriq, L. The Binding Properties of Two Antitumor Ruthenium (II1) Complexes to Apotransferrin ". 2581–2588 (1993).

8. Guo, Z. & Sadler, P.J. . 2000, Adv. Inorg. Chem., Vol. 49, p. 183-306. Z. guo, P.J. Sadler. 2000, Adv. Inorg. Chem., Vol. 49, p. 183-306. *Adv. Inorg. Chem.* **49,** 183–306 (2000).

9. Hambley, T. W. Platinum binding to DNA: structural controls and consequences. *J. Chem. Soc. Dalt. Trans.* 2711–2718 (2001). doi:10.1039/B105406F

10. Zimmermann, T. & Burda, J. V. Cisplatin interaction with amino acids cysteine and methionine from gas phase to solutions with constant pH. *Interdiscip. Sci. Comput. Life Sci.* **2,** 98–114 (2010).

11. Krężel, A. & Bal, W. Coordination chemistry of glutathione. *Acta Biochimica Polonica* **46,** 567–580 (1999).

12. Pearson, R. G. Hard and Soft Acids and Bases. *J. Am. Chem. Soc.* **85,** 3533–3539 (1963).

13. Kasherman, Y., Sturup, S. & Gibson, D. Is glutathione the major cellular target of cisplatin? A study of the interactions of cisplatin with cancer cell extracts. *J. Med. Chem.* **52,** 4319–28 (2009).

14. Ishikawas, Toshihisa, F. A.-O. Glutathione-associated cis-Diamminedichloroplatinum (I1) Metabolism and ATP-dependent Efflux from Leukemia Cells. *J. Biol. Chem.* **268,** 20116–20125 (1993).

15. Huang, S., Ye, J., Yu, J., Chen, L., Zhou, L., Wang, H., Li, Z. & Wang, C. The accumulation and efflux of lead partly depend on ATP-dependent efflux pump-multidrug resistance protein 1 and glutathione in testis Sertoli cells. *Toxicol. Lett.* **226,** 277–84 (2014).

16. Chen, H. H. W., Song, I.-S., Hossain, A., Choi, M.-K., Yamane, Y., Liang, Z. D., Lu, J., Wu, L. Y.-H., Siddik, Z. H., Klomp, L. W. J., Savaraj, N. & Tien, K. M. ELEVATED GLUTATHIONE LEVELS CONFER CELLULAR SENSITIZATION TO CISPLATIN TOXICITY BY UPREGULATION OF COPPER TRANSPORTER HCTR1. *Mol. Pharmacol.* **74,** 697–704 (2008).

17. Devita, V. T., Young, R. C. & Canellos, G. P. Combination versus single agent chemotherapy: A review of the basis for selection of drug treatment of cancer. *Cancer* **35,** 98–110 (1975).

18. Chou, T. Theoretical Basis , Experimental Design , and Computerized Simulation of Synergism and Antagonism in Drug Combination Studies □. *Pharmacol. Rev.* 621–681 (2007). doi:10.1124/pr.58.3.10.

19. Pivetta, T., Isaia, F., Trudu, F., Pani, A., Manca, M., Perra, D., Amato, F. & Havel, J. Development and validation of a general approach to predict and quantify the synergism of anti-cancer drugs using experimental design and artificial neural networks. *Talanta* **115,** 84–93 (2013).

20. Pivetta, T., Lallai, V., Valletta, E., Trudu, F., Isaia, F., Perra, D., Pinna, E. & Pani, A. Mixed copper–platinum complex formation could explain synergistic antiproliferative effect exhibited by binary mixtures of cisplatin and copper-1,10-phenanthroline compounds: An ESI–MS study. *J. Inorg. Biochem.* (2015). doi:10.1016/j.jinorgbio.2015.05.004

21. Pivetta, T., Isaia, F., Verani, G., Cannas, C., Serra, L., Castellano, C., Demartin, F., Pilla, F., Manca, M. & Pani, A. Mixed-1,10-phenanthroline-Cu(II) complexes: synthesis, cytotoxic activity versus hematological and solid tumor cells and complex formation equilibria with glutathione. *J. Inorg. Biochem.* **114,** 28–37 (2012).

22. Pivetta, T., Cannas, M. D., Demartin, F., Castellano, C., Vascellari, S., Verani, G. & Isaia, F. Synthesis, structural characterization, formation constants and in vitro cytotoxicity of phenanthroline and imidazolidine-2-thione copper(II) complexes. *J. Inorg. Biochem.* **105,** 329–38 (2011).

23. Vander Heyden, Y. Experimental design approaches in method optimization. *LC GC Eur.* **19,** 469–475 (2006).

24. Strohalm, M., Kavan, D., Nova, P. & Volny, M. mMass 3 : A Cross-Platform Software Environment for Precise Analysis of Mass Spectrometric Data. *Anal. Chem.* **82,** 4648–4651 (2010).

25. Niedermeyer, T. H. J. & Strohalm, M. mMass as a software tool for the annotation of cyclic peptide tandem mass spectra. *PLoS One* **7,** e44913 (2012).

26. Stewart, J. J. P. Optimization of parameters for semiempirical methods I. Method. *J. Comput. Chem.* **10,** 209–220 (1989).

27. Chirlian, L. E. & Francl, M. M. Atomic charges derived from electrostatic potentials: A detailed study. *J. Comput. Chem.* **8,** 894–905 (1987).

28. Breneman, C. M. & Wiberg, K. B. Determining atom-centered monopoles from molecular electrostatic potentials. The need for high sampling density in formamide conformational analysis. *J. Comput. Chem.* **11,** 361–373 (1990).

29. Reed, A. E., Weinstock, R. B. & Weinhold, F. Natural population analysis. *J. Chem. Phys. F. Full J. TitleJournal Chem. Phys.* **83,** 735–746 (1985).

30. Mulliken, R. S. Electronic Population Analysis on LCAO[Single Bond]MO Molecular Wave Functions. I. *J. Chem. Phys.* **23,** 1833 (1955).

31. Mulliken, R. S. Electronic Population Analysis on LCAO-MO Molecular Wave Functions. III. Effects of Hybridization on Overlap and Gross AO Populations. *J. Chem. Phys.* **23,** 2338 (1955).

32. Schebb, N. H., Faber, H., Maul, R., Heus, F., Kool, J., Irth, H. & Karst, U. Analysis of glutathione adducts of patulin by means of liquid chromatography (HPLC) with biochemical detection (BCD) and electrospray ionization tandem mass spectrometry (ESI-MS/MS). *Anal. Bioanal. Chem.* **394,** 1361–73 (2009).

33. Banu, L., Blagojevic, V. & Bohme, D. K. Dissociations of gas-phase complexes of deprotonated glutathione with Co2+, Ni2+, Cu2+ and Zn2+: The importance of metal ion reduction. *Int. J. Mass Spectrom.* **345-347,** 142–152 (2013).

34. Murphy, C. M., Fenselau, C. & Gutierrez, P. L. Fragmentation characteristic of glutathione conjugates activated by high-energy collisions. *J. Am. Soc. Mass Spectrom.* **3,** 815–22 (1992).

35. Camera, E., Rinaldi, M., Briganti, S., Picardo, M. & Fanali, S. Simultaneous determination of reduced and oxidized glutathione in peripheral blood mononuclear cells by liquid chromatography–electrospray mass spectrometry. *J. Chromatogr. B Biomed. Sci. Appl.* **757,** 69–78 (2001).

36. Hahn, H., Huck, C. W., Rainer, M., Najam-ul-Haq, M., Bakry, R., Abberger, T., Jennings, P., Pfaller, W. & Bonn, G. K. Analysis of glutathione in supernatants and lysates of a human proximal tubular cell line from perfusion culture upon intoxication with cadmium chloride by HPLC and LC-ESI-MS. *Anal. Bioanal. Chem.* **388,** 1763–9 (2007).

37. Thakur, S. S. & Balaram, P. Fragmentation of peptide disulfides under conditions of negative ion mass spectrometry: studies of oxidized glutathione and contryphan. *J. Am. Soc. Mass Spectrom.* **19,** 358–66 (2008).

38. Kozhemyakin, L. A. & Balasovski, M. B. Methods for production of the oxidized glutathione composite with cis-diamminedichloroplatinum and pharmaceutical compositions based thereof regulating metabolism, proliferation, differentiation and apoptotic mechanisms for normal and transformed cells. (2008).

SUPPLEMENTARY MATERIALS

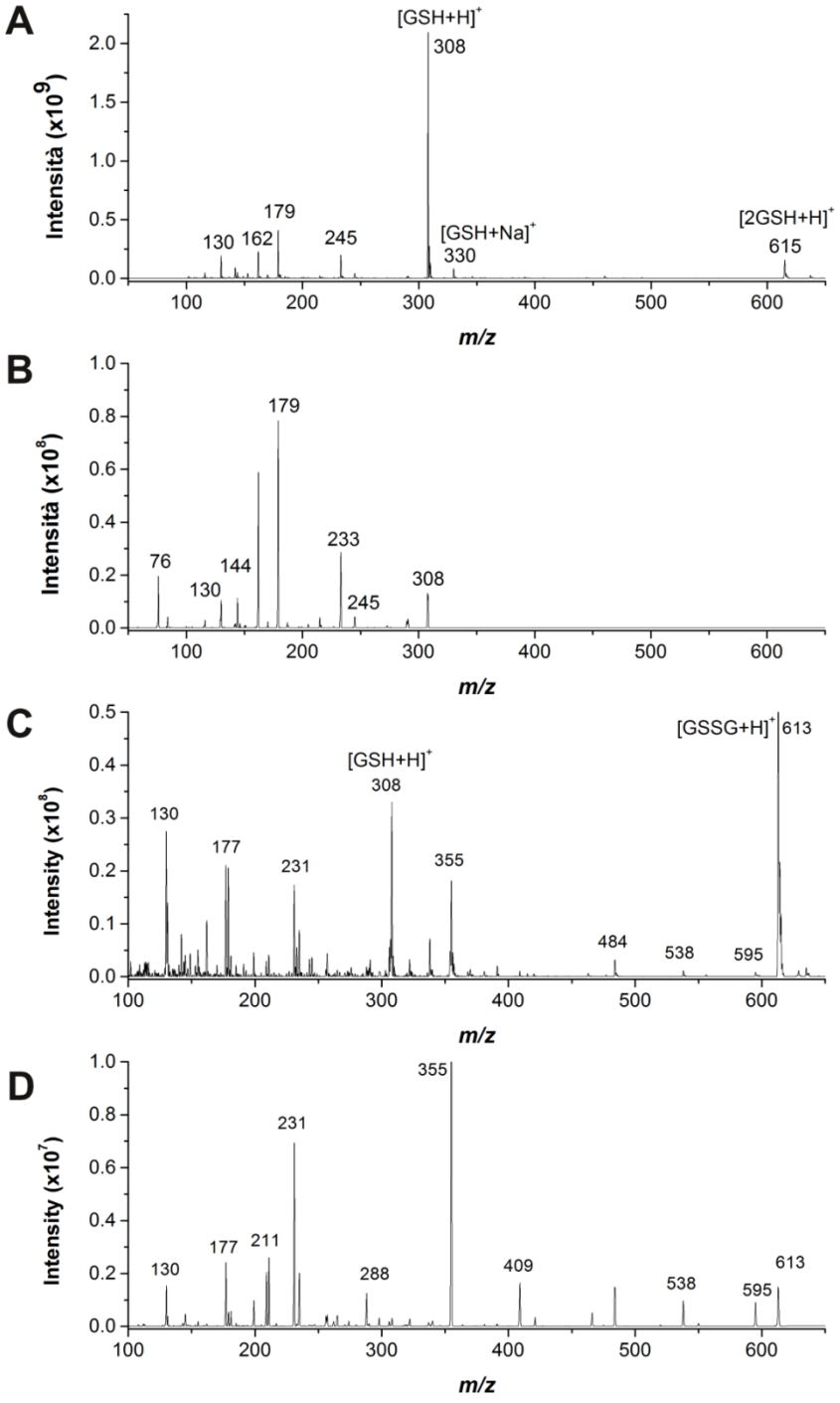

Fig. S1. ESI-MS (+) spectrum of GSH (**A**) and MS-MS spectrum of the parent peak at *m/z* 308 (**B**); ESI-MS (+) spectrum of GSSG (**C**) and MS-MS spectrum of the parent peak at *m/z* 613 (**D**) (0.5 mM, 50:50 methanol/water with 0.05% of HTFA; collision energy 20 V).

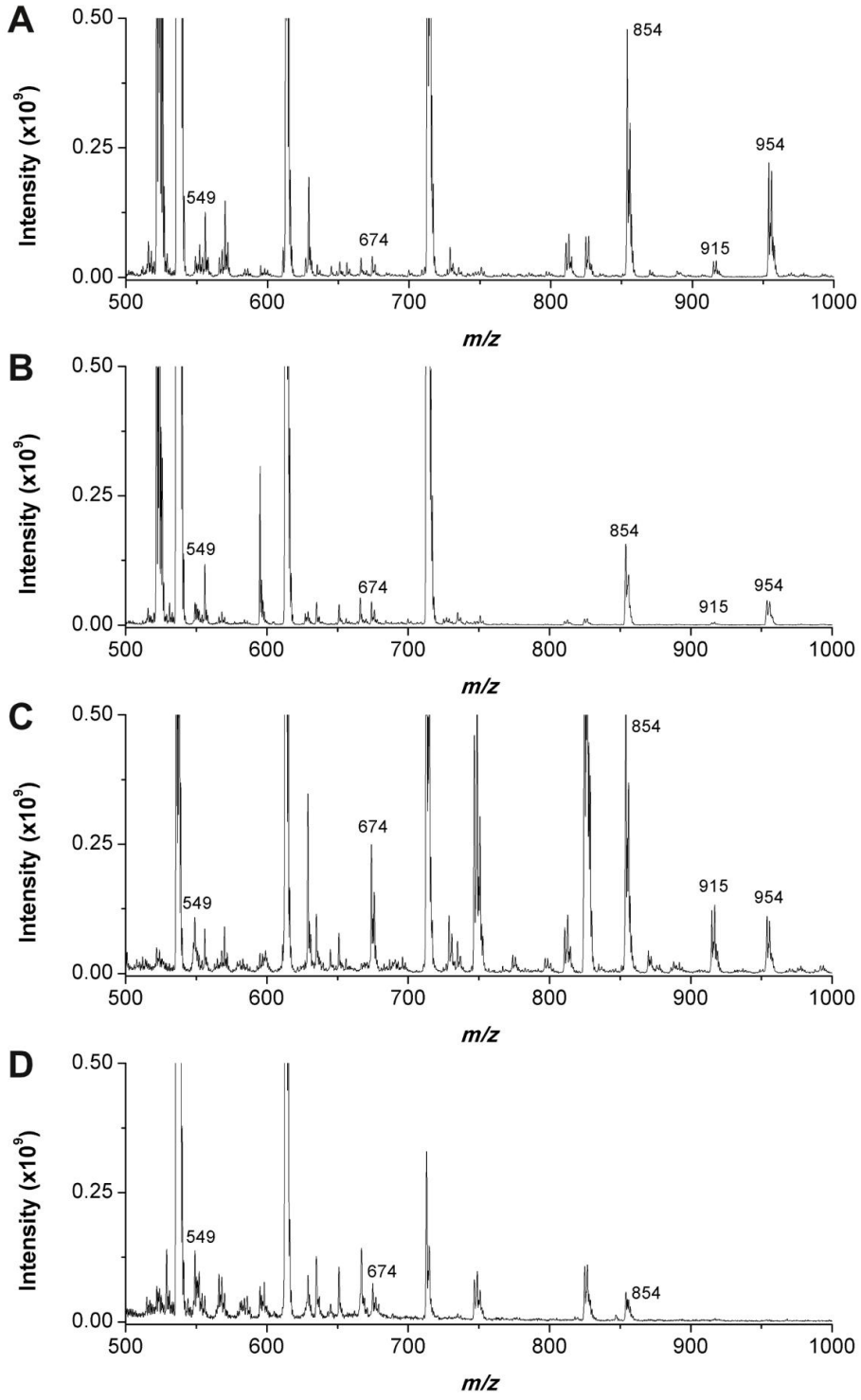

Fig. S2. ESI-MS (+) spectrum of solution containing (**A**) **C0** and GSH, (**B**) **C0** and GSSG, (**C**) **C10** and GSH, (**D**) **C10** and GSSG (1:2 copper/ligand molar ratio, ligand 0.5 mM, 50:50 methanol/water with 0.05% of HTFA).

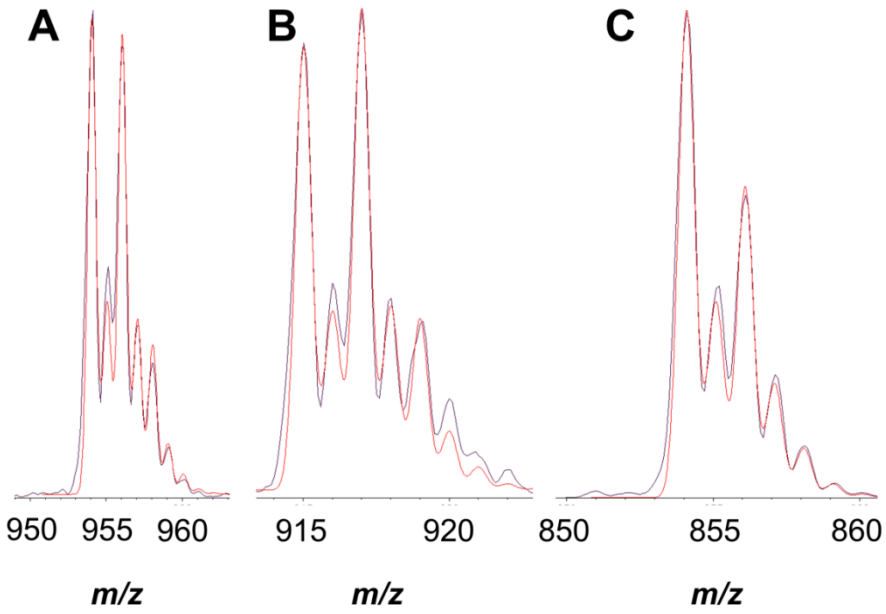

Fig. S3. Experimental (black line) and calculated (red line) isotopic patterns of the peaks at *m/z* 954 (**A**), 915 (**B**) and 854 (**C**) assigned to $[Cu(phen)(GSSG)(ClO_4)]^+$, $[Cu_2(phen)(GSSG)\text{-}3H]^+$ and $[Cu(phen)(GSSG)\text{-}H]^+$, respectively.

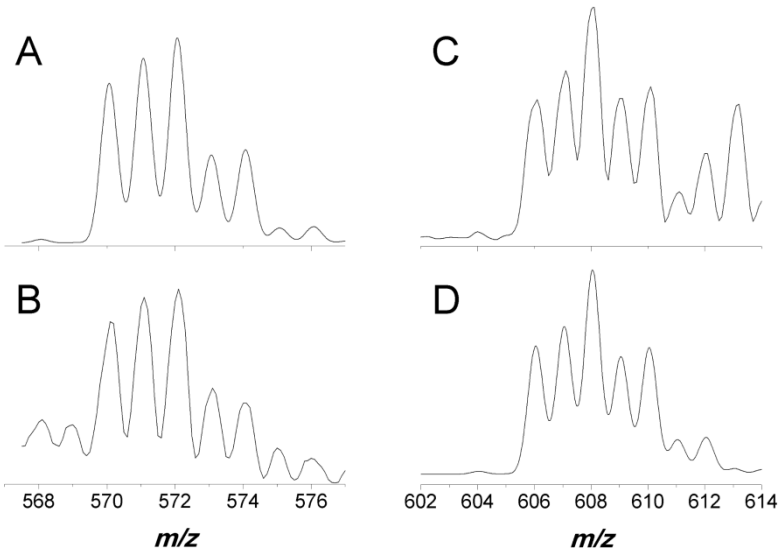

Fig. S4. Experimental (upper) and calculated (bottom) isotopic patterns of the peaks at *m/z* 571 (**A**, **B**) and 608 (**C**, **D**) for species with assigned stoichiometry $[Pt(NH_3)Cl_2+GSH]^+$ and $[Pt(NH_3)_2Cl_2+GSH+H]^+$.

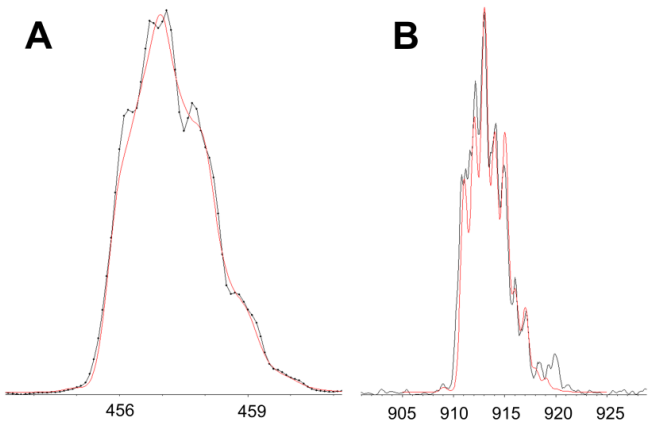

Fig. S5. Experimental (black line) and calculated (red line) isotopic patterns of the peaks at *m/z* 457 (**A**) and 912 (**B**) assigned to $[Pt(NH_3)_2Cl_2+GSSG+2H]^{+2}$ and $[Pt(NH_3)_2Cl_2+GSSG+H]^{+}$, respectively.

Scheme S1. GSH: fragmentation pathways from *m/z* 308 to 245 (*i*), 233 (*ii*), 179 (*iii*), 144 (*iv*) and 130 (*v*).

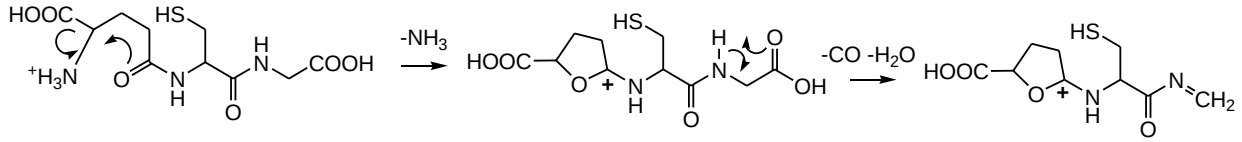

i) Fragmentation pathway (*i*) from *m/z* 308 (protonated GSH) to 245.

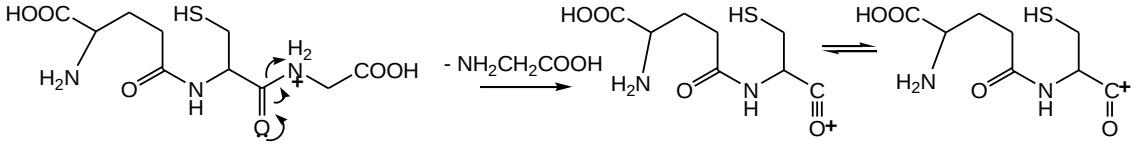

ii) Fragmentation pathway (*ii*) from *m/z* 308 (protonated GSH) to 233.

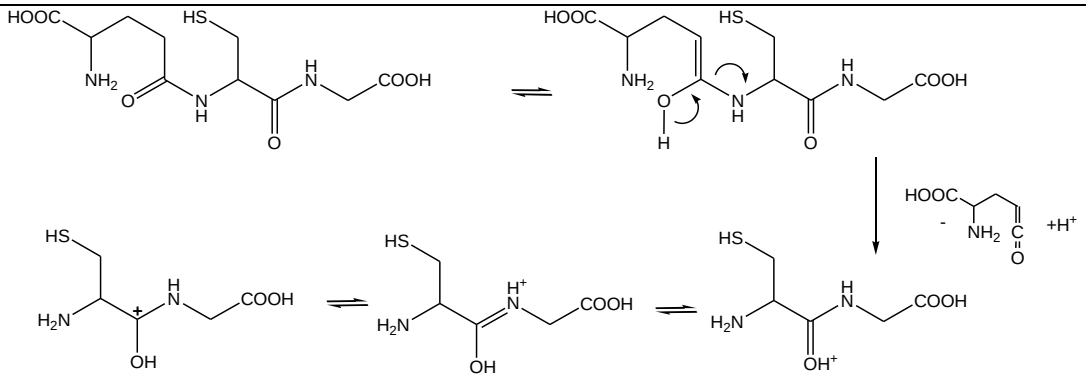

iii) Fragmentation pathway (*iii*) from *m/z* 308 (protonated GSH) to 179.

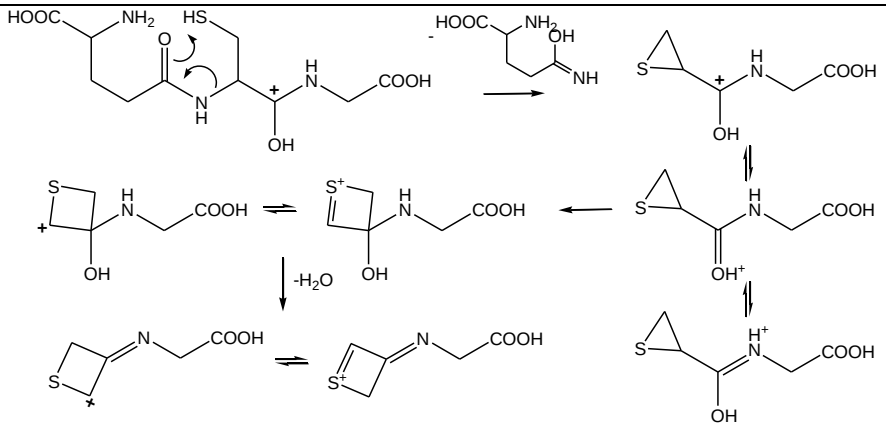

iv) Fragmentation pathway (*iv*) from *m/z* 308 (protonated GSH) to 144.

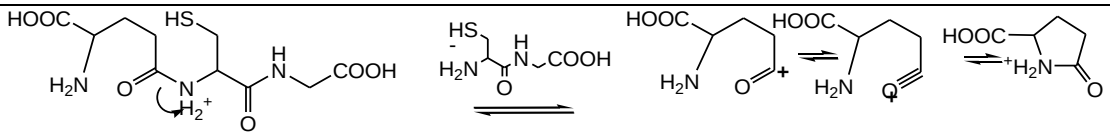

v) Fragmentation pathway (*v*) from *m/z* 308 (protonated GSH) to 130.

Scheme S2. GSSG: fragmentation pathways from *m/z* 613 to (*i*) 130, (*ii*) 177, (*iii*) 211, (*iv*) 231, (*v*) 288, (*vi*) 355, (*vii*) 409, (*viii*) 538 and (*ix)* 595.

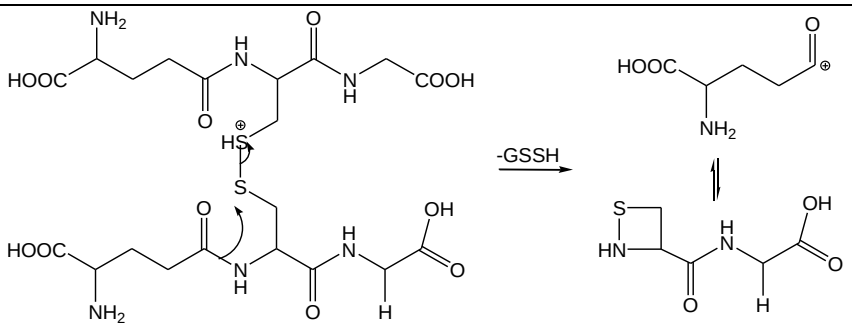

i) Fragmentation pathway (*i*) from *m/z* 613 (protonated GSSG) to 130.

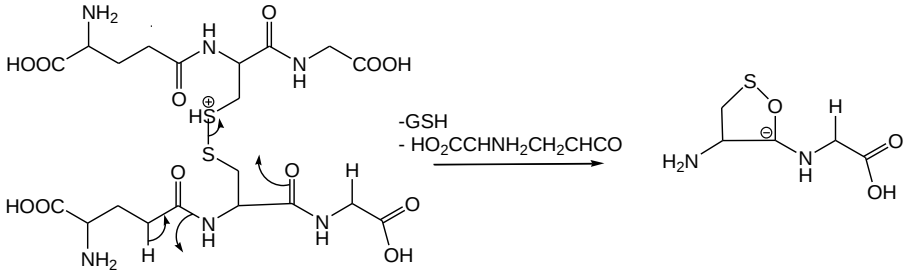

ii) Fragmentation pathway (*ii*) from *m/z* 613 (protonated GSSG) to 177.

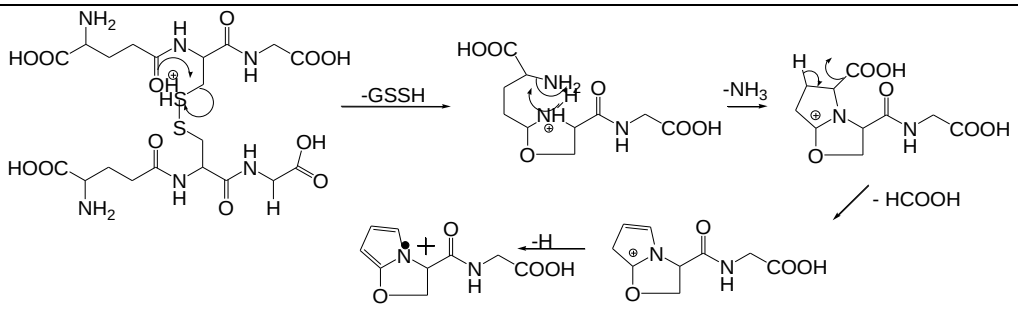

iii) Fragmentation pathway (*iii*) from *m/z* 613 (protonated GSSG) to 211.

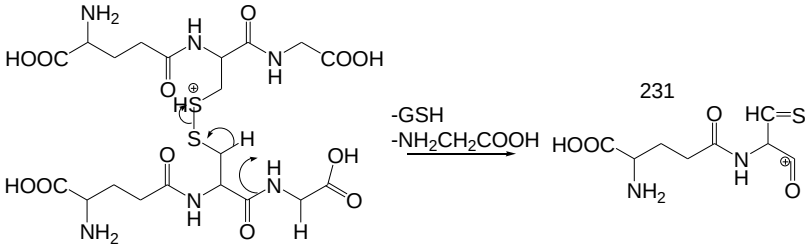

iv) Fragmentation pathway (*iv*) from *m/z* 613 (protonated GSSG) to 231.

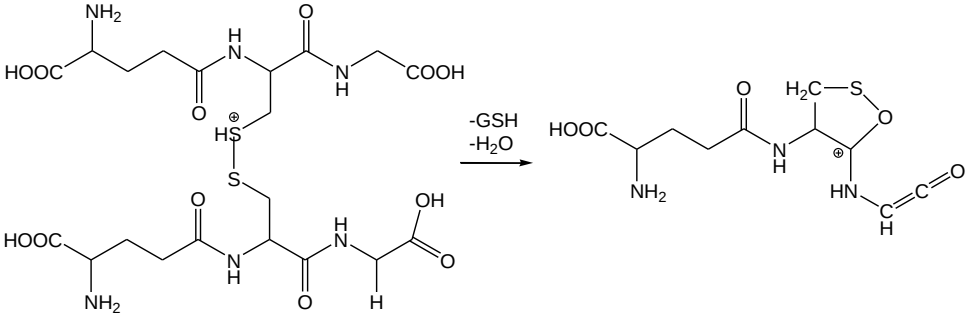

v) Fragmentation pathway (*v*) from *m/z* 613 (protonated GSSG) to 288.

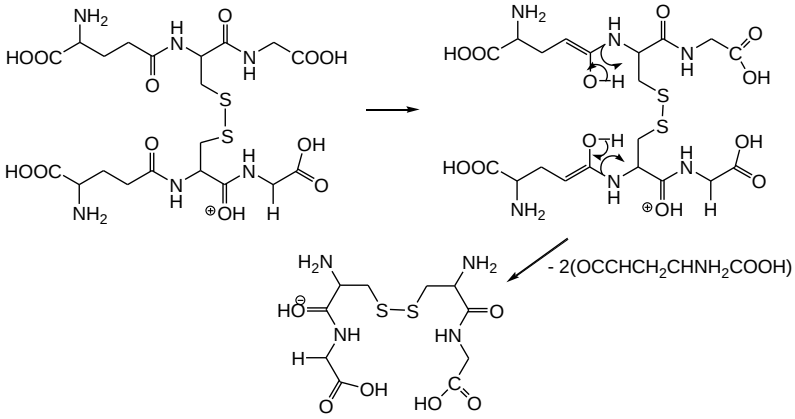

vi) Fragmentation pathway (*vi*) from *m/z* 613 (protonated GSSG) to 355.

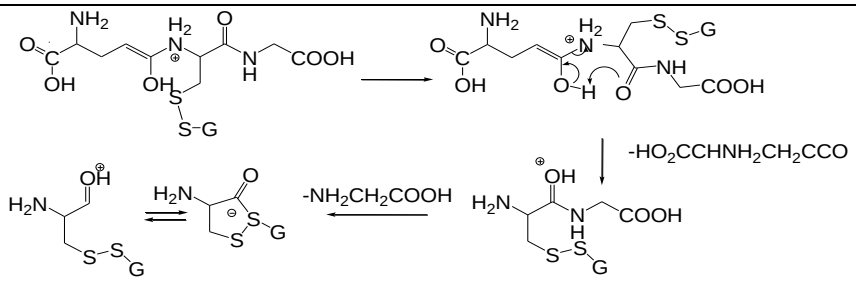

vii) Fragmentation pathway (*vii*) from *m/z* 613 (G is $C_{10}H_{16}N_3O_6$) to 409.

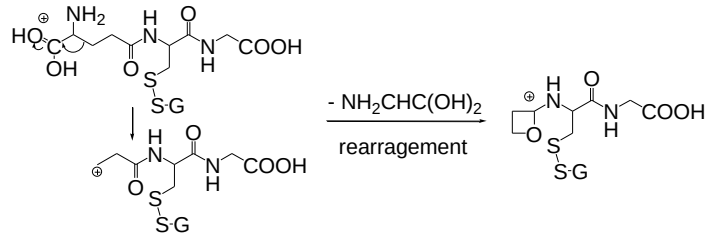

viii) Fragmentation pathway (*viii*) from *m/z* 613 (protonated GSSG) to 538 (G is $C_{10}H_{16}N_3O_6$).

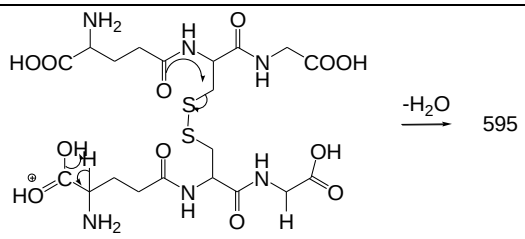

ix) Fragmentation pathway (*ix*) from *m/z* 613 (protonated GSSG) to 595.

Scheme S3. Selected fragmentation pathways of $[Cu(phen)(GSSG)(OClO_3)]^+$ (**V**, *m/z* 954).

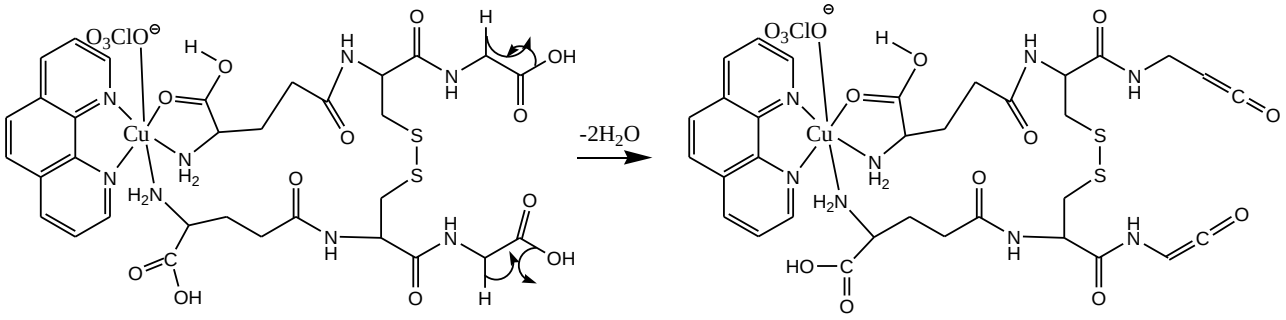

i) Fragmentation pathway from *m/z* 954 to 918.

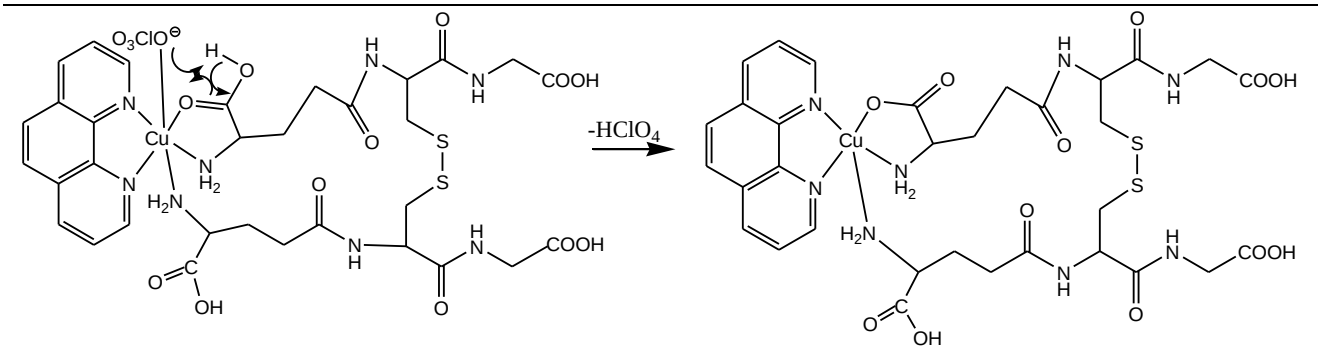

ii) Fragmentation pathway from *m/z* 954 to 854.

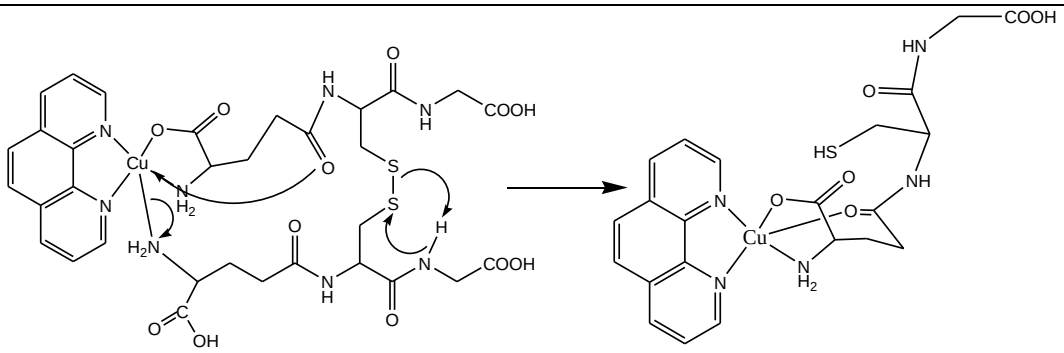

iii) Fragmentation pathway from *m/z* 854 to 549.

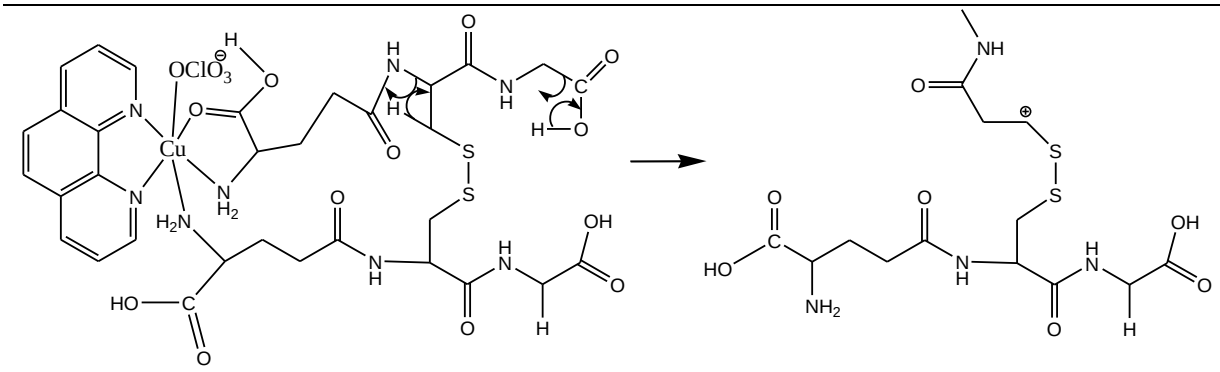

iv) Fragmentation pathway from *m/z* 954 to 423.

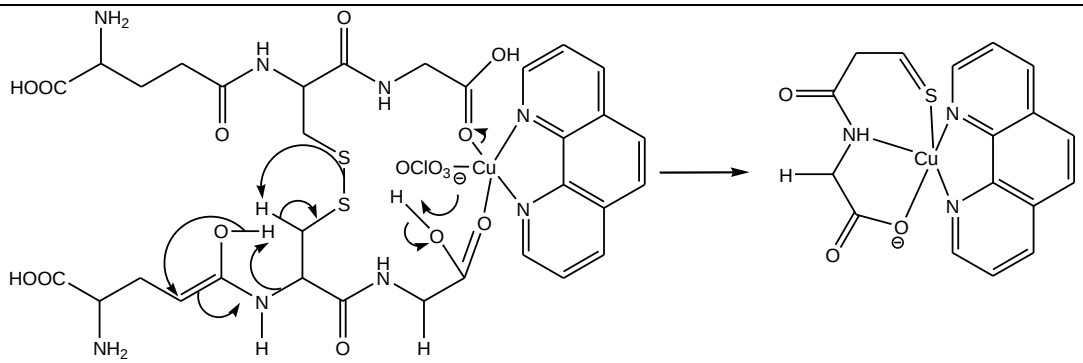

v) Fragmentation pathway from *m/z* 954 to 403.

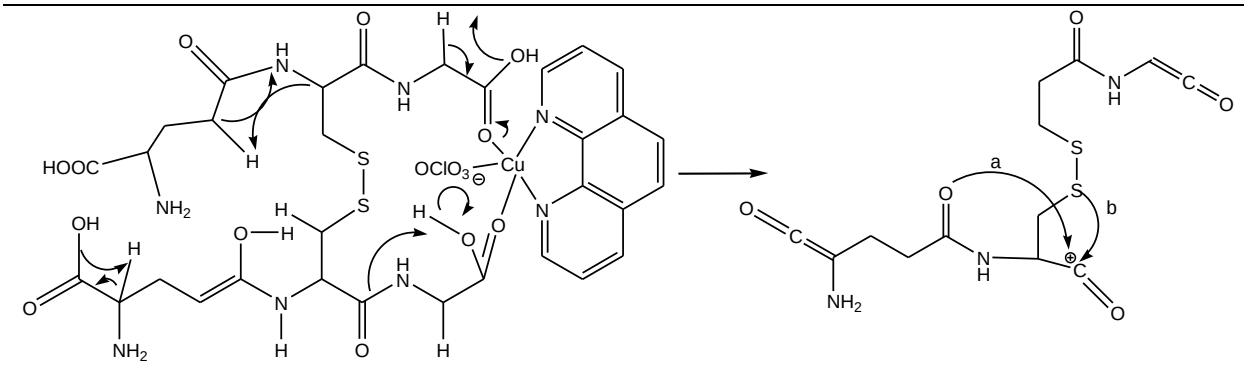

vi) Fragmentation pathway from *m/z* 954 to 358 (2 resonance structures could be written, pentatomic (a) and triatomic (b) cycles formation is also possible)

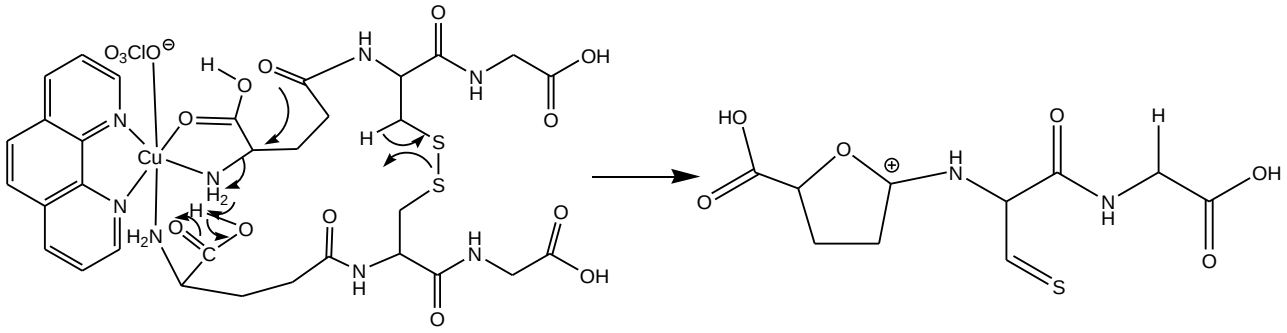

vii) Fragmentation pathway from *m/z* 954 to 289.

* All the fragments are monocharged (+1) even if not indicated.

Scheme S4. Selected fragmentation pathways of $[Cu(phen)(GSSG)-H)]^+$ (**III**, *m/z* 854)

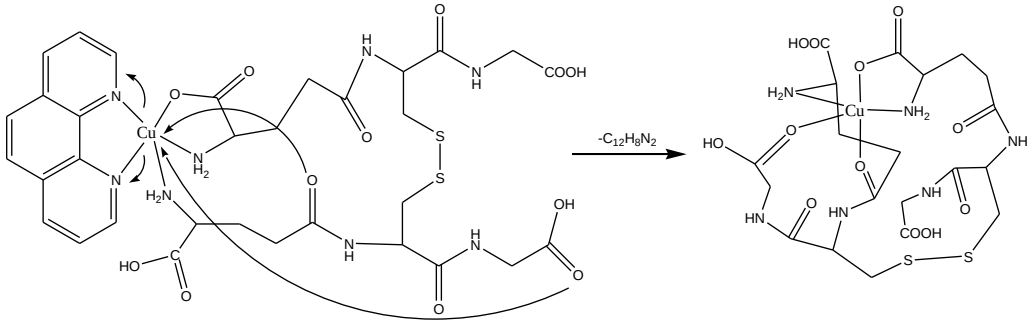

i) Fragmentation pathway from *m/z* 854 to 674.

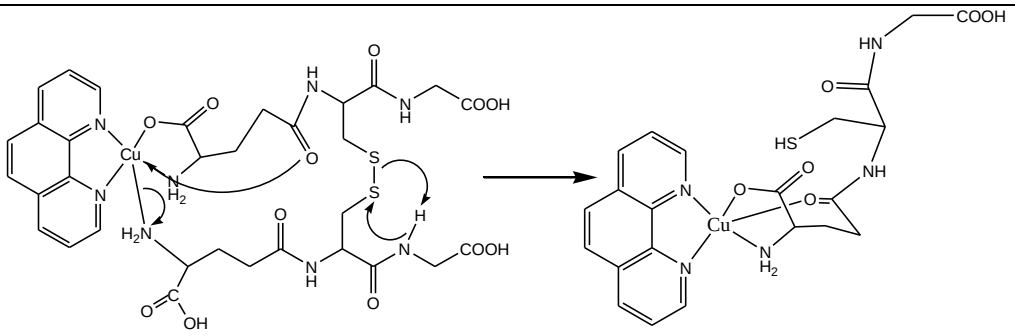

ii) Fragmentation pathway from *m/z* 854 to 549.

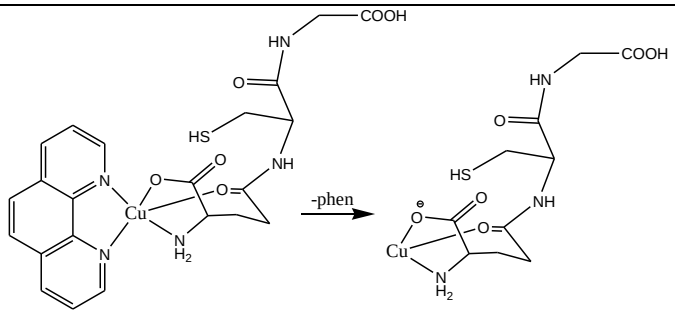

iii) Fragmentation pathway from *m/z* 549 to 369.

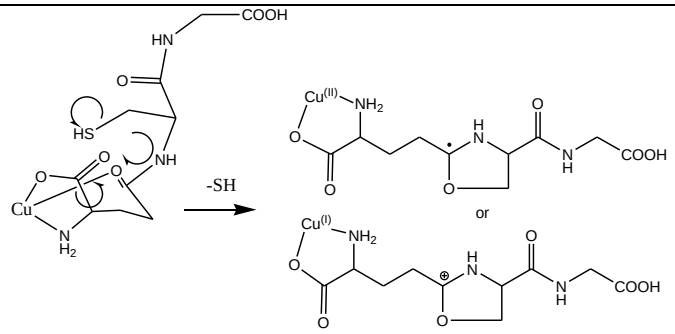

iv) Fragmentation pathway from *m/z* 369 to 336.

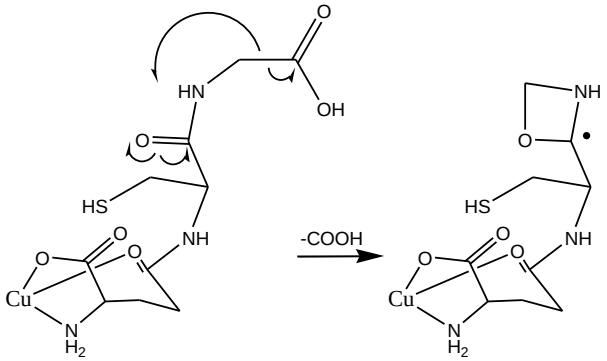

v) Fragmentation pathway from *m/z* 369 to 324.

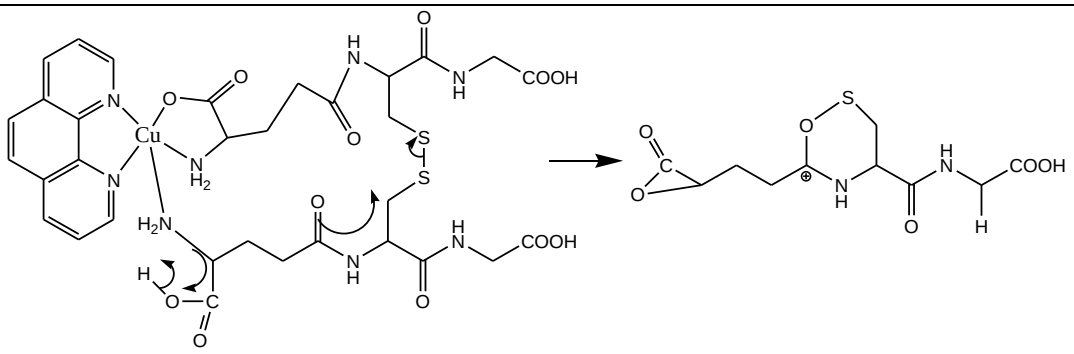

vi) Fragmentation pathway from *m/z* 854 to 289.

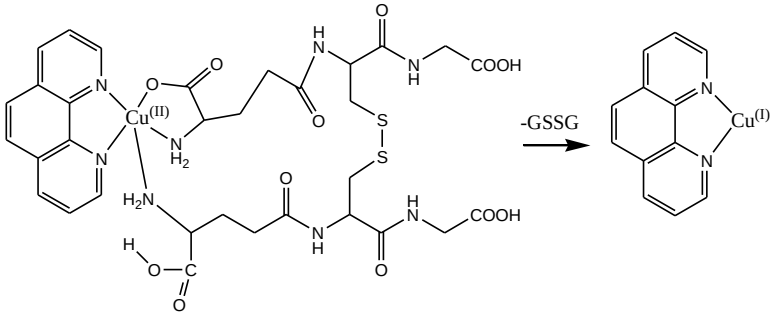

vii) Fragmentation pathway from *m/z* 854 to 243.

Scheme S5. Selected fragmentation pathways of $[Cu(GSSG)-H)]^{+}$ (**II**, *m/z* 674)

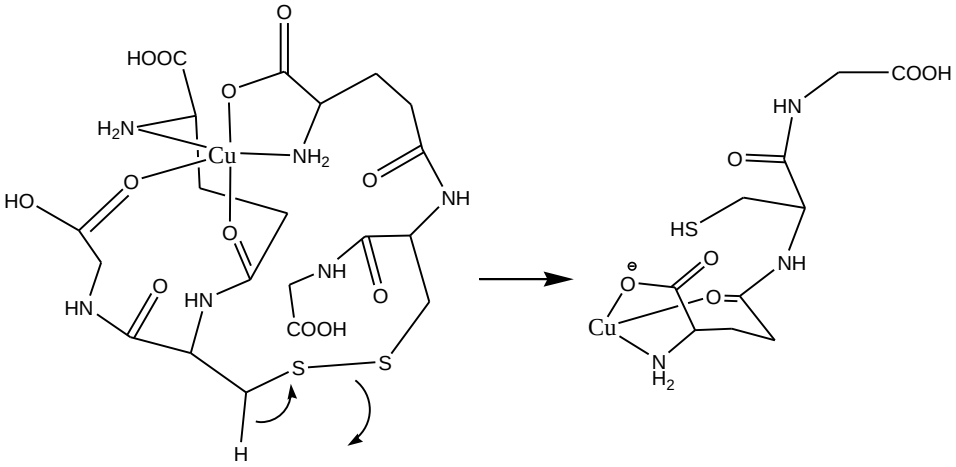

i) Fragmentation pathway from *m/z* 674 to 369.

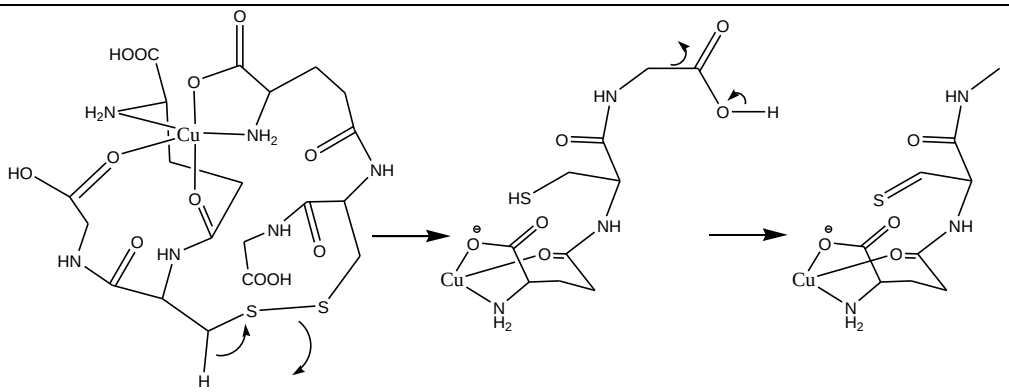

ii) Fragmentation pathway from *m/z* 674 to 323.

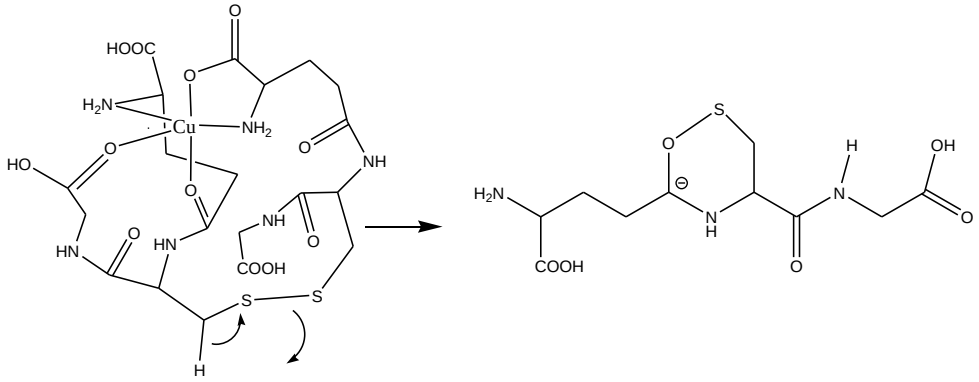

iii) Fragmentation pathway from *m/z* 674 to 306.

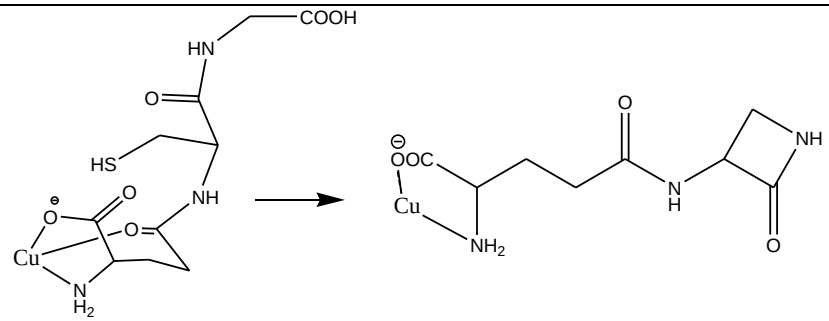

iv) Fragmentation pathway from *m/z* 369 to 277.

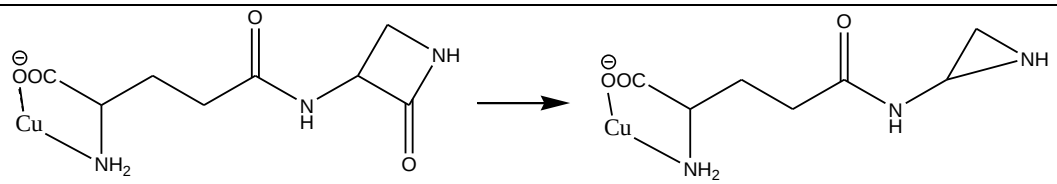

v) Fragmentation pathway from *m/z* 277 to 249.

Scheme S6. Fragments originated by the CID of the *m/z* 608 parent peak.

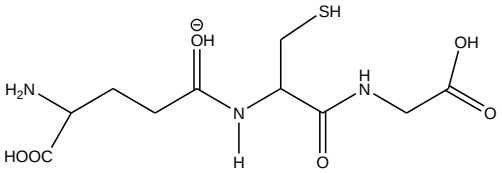

$[GSH+H]^+$, *m/z* 308*

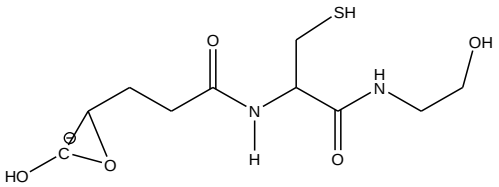

$[C_{10}H_{18}N_2O_4S]^+$, *m/z* 291*

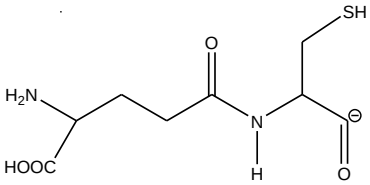

$[C_8H_{13}N_2O_4S]^+$, *m/z* 233**

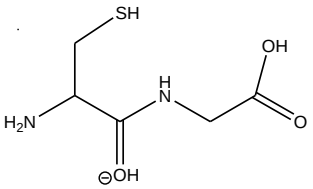

$[C_5H_{11}N_2OS]^+$, *m/z* 179*

* fragment containing ^{196}Pt-^{35}Cl-^{35}Cl, ** fragment containing ^{194}Pt-^{35}Cl-^{37}Cl.

Scheme S7. Fragments originated by the CID of the *m/z* 571 parent peak.

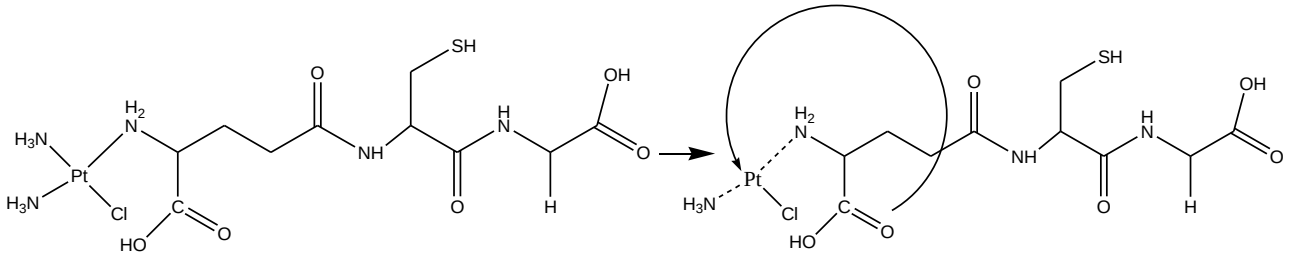

i) Fragmentation pathway from *m/z* 571 to 555 $[Pt(NH_3)Cl(GSH)]^+$

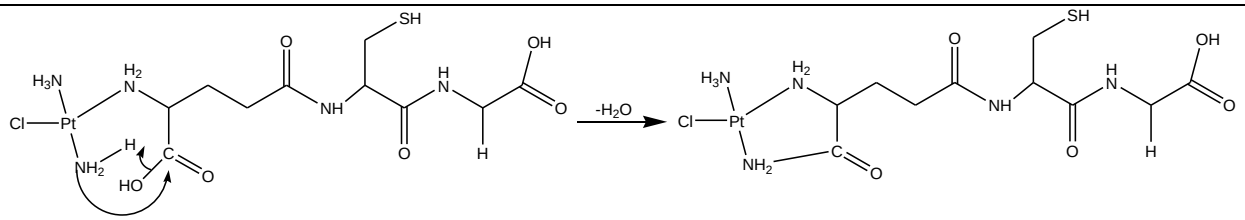

ii) Fragmentation pathway from *m/z* 571 to 554 $[PtC_{10}H_{21}N_5O_5ClS]^+$

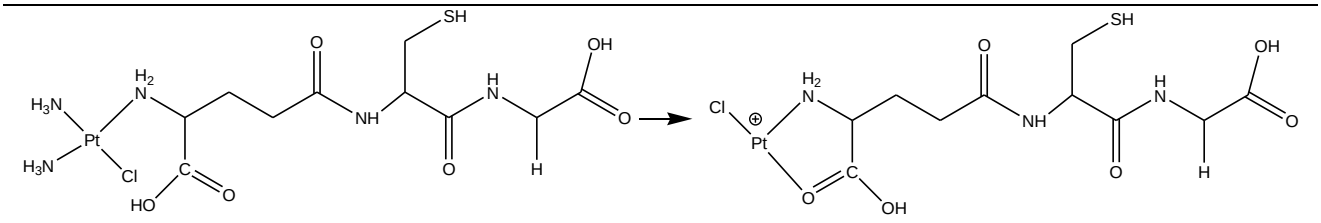

iii) Fragmentation pathway from *m/z* 571 to 538 $[PtC_{10}H_{17}N_3O_6ClS]^+$

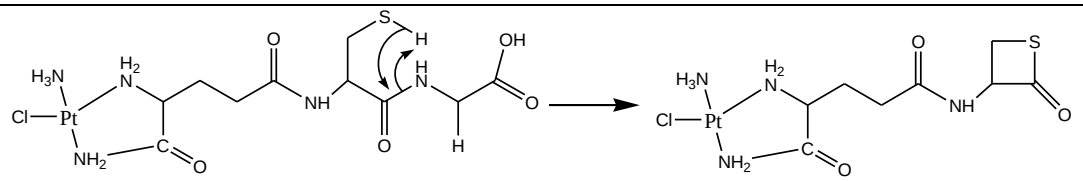

iv) Fragmentation pathway from *m/z* 554 to 479 $[PtC_8H_{16}N_4O_3ClS]^+$

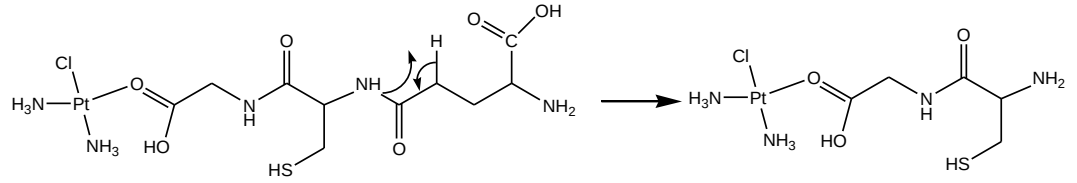

v) Fragmentation pathway from *m/z* 571 to 443 $[PtC_5H_{16}N_4O_3ClS]^+$

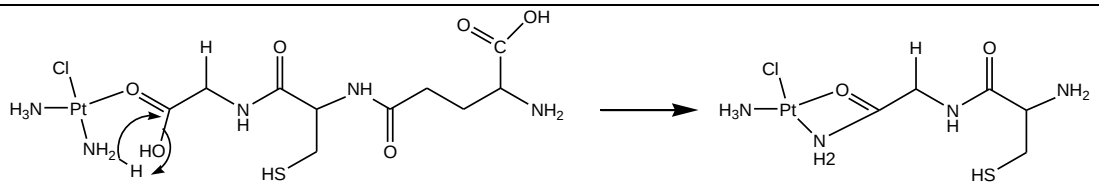

vi) Fragmentation pathway from *m/z* 571 to 425 $[PtC_5H_{14}N_4O_2ClS]^+$

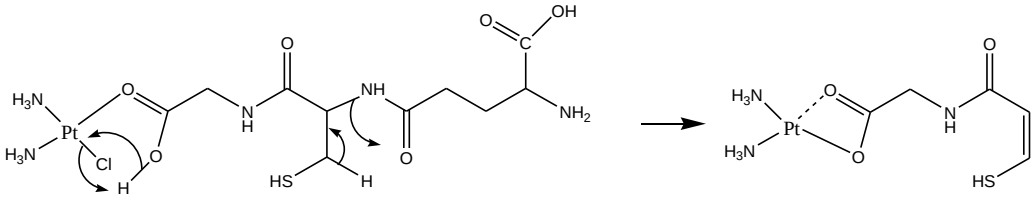

vii) Fragmentation pathway from *m/z* 571 to 390 $[PtC_5H_{12}N_3O_3S]^{+\,*}$

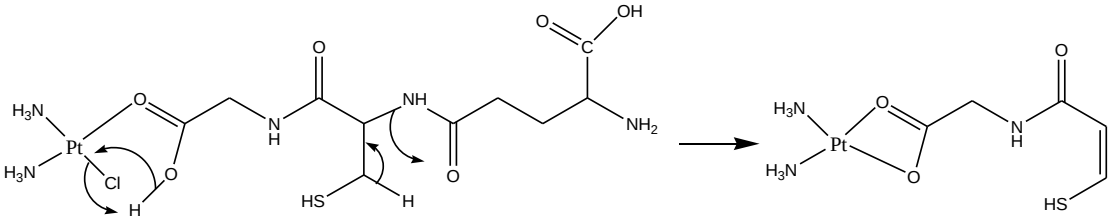

viii) Fragmentation pathway from *m/z* 571 to 388 $[PtC_5H_{12}N_3O_3S]^{+\,**}$

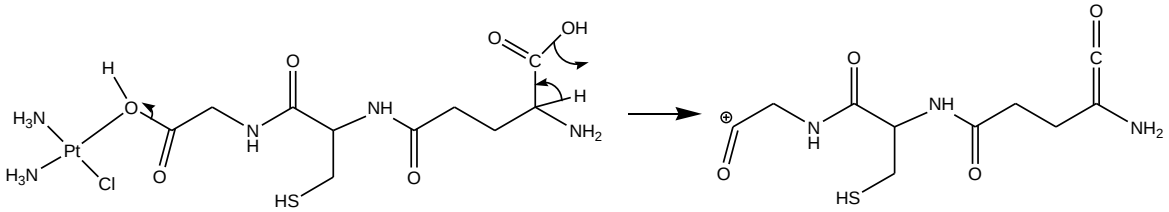

ix) Fragmentation pathway from *m/z* 571 to 272 $[C_{10}H_{14}N_3O_4S]^+$

* fragment containing ^{196}Pt, ^{35}Cl; ** fragment containing ^{194}Pt and ^{37}Cl.

Scheme S8. Fragments originated by the CID of the *m/z* 457 parent peak.

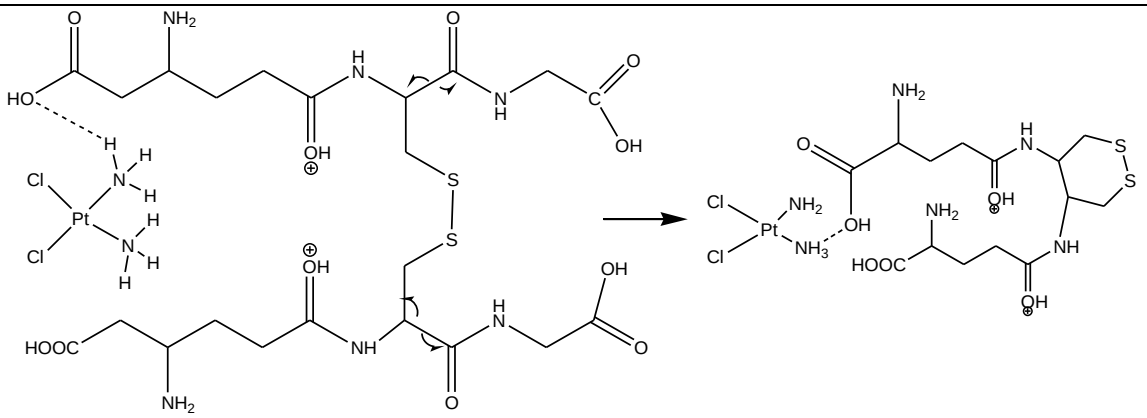

i) Fragmentation pathway from *m/z* 457 to 355*

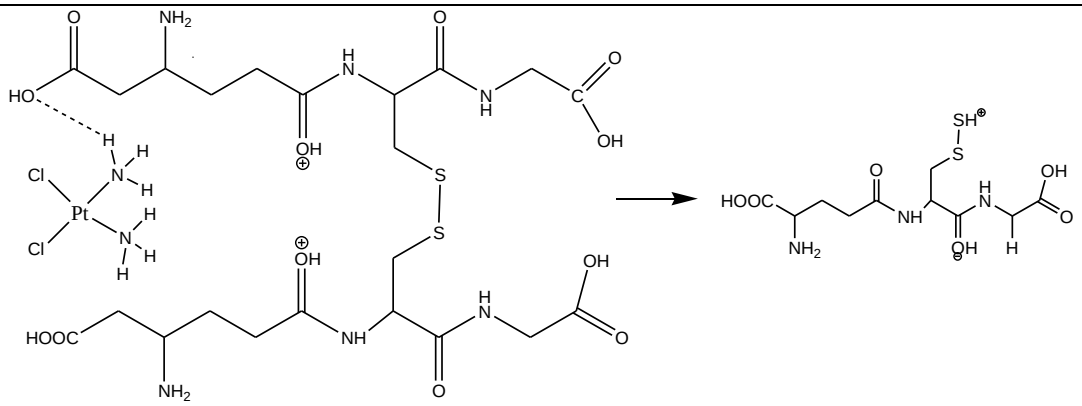

ii) Fragmentation pathway from *m/z* 457 to 340*

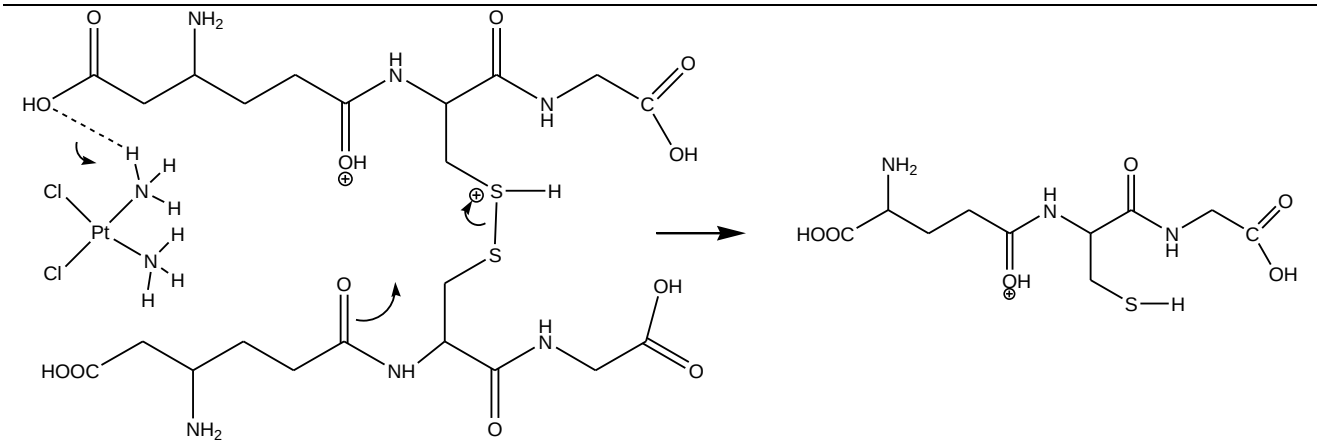

iii) Fragmentation pathway from *m/z* 457 to 308

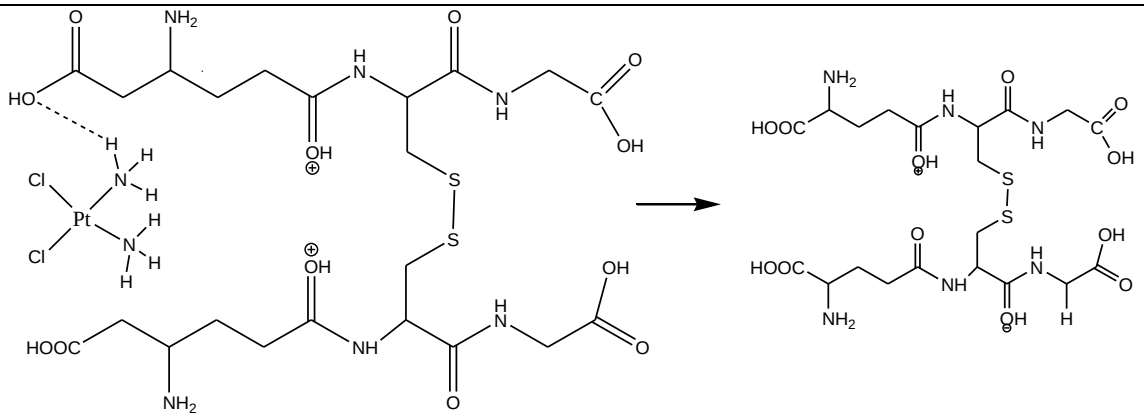

iv) Fragmentation pathway from *m/z* 457 to 307

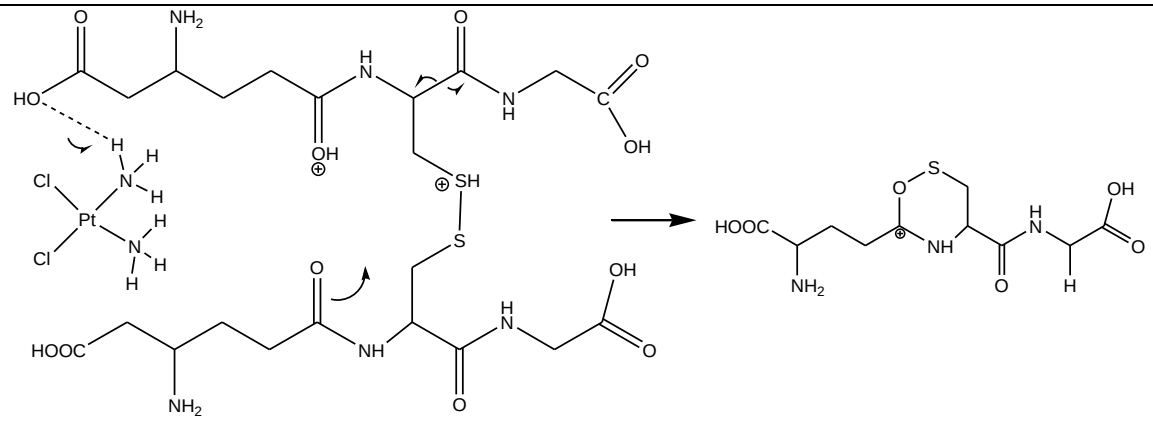

v) Fragmentation pathway from *m/z* 457 to 306

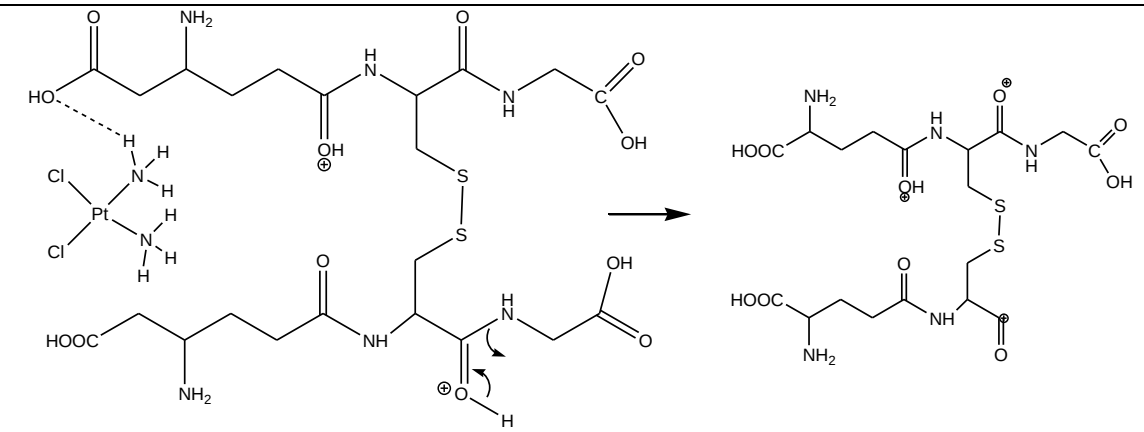

vi) Fragmentation pathway from *m/z* 457 to 269

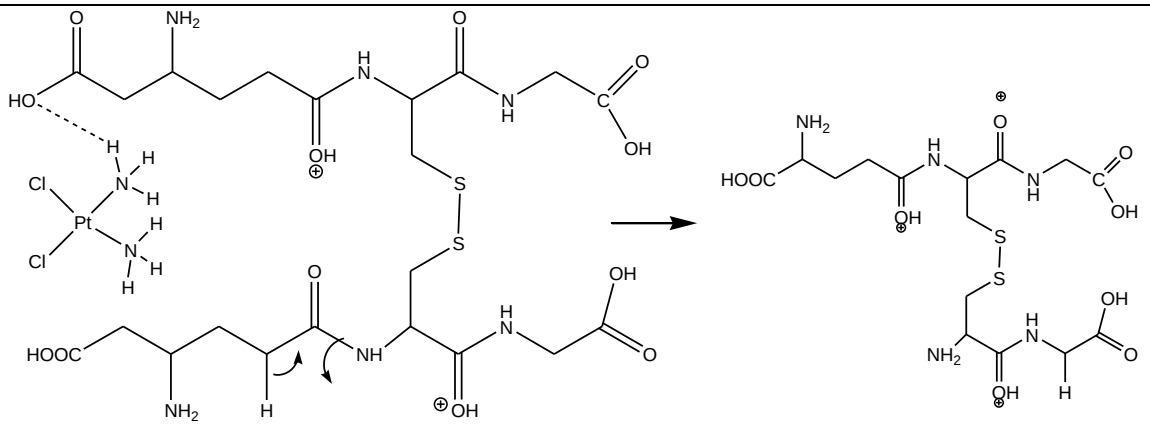

vii) Fragmentation pathway from *m/z* 457 to 242.5

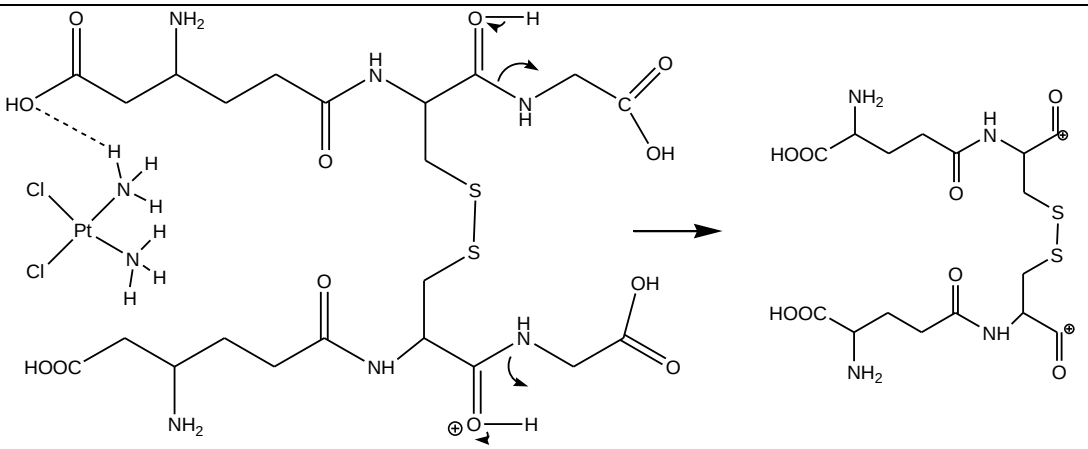

viii) Fragmentation pathway from *m/z* 457 to 231

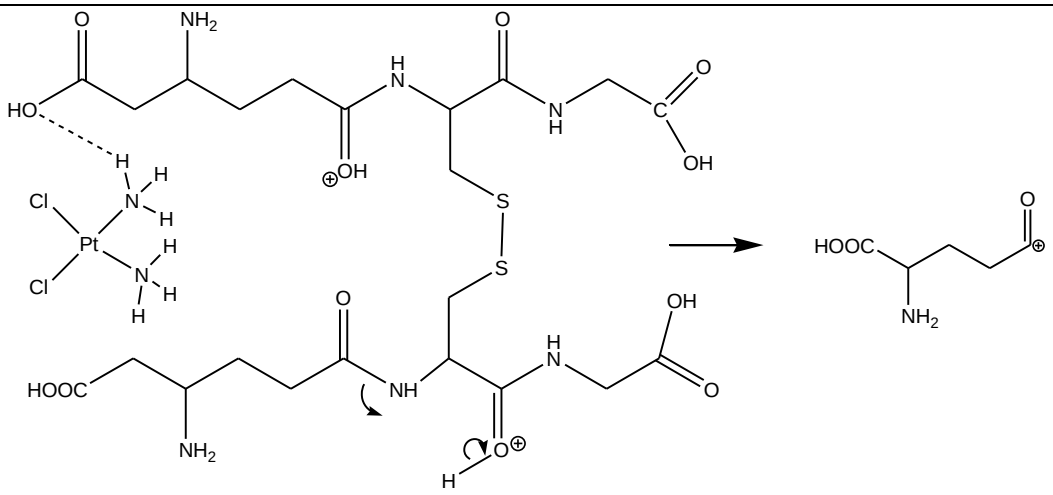

ix) Fragmentation pathway from *m/z* 457 to 130

Chapter 5

Identification of specific phospholipids to differentiate cisplatin-resistant and wild type cells in leukemic (CCRF-CEM) and ovarian cancer (A2780)

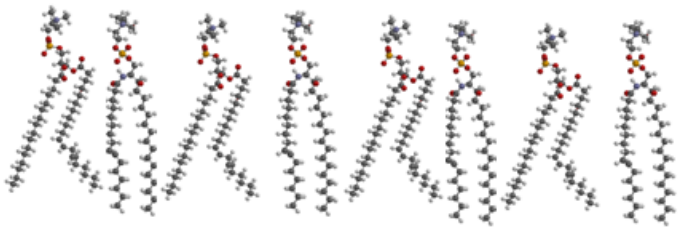

This chapter reports the study of the phospholipid profile of wild type and cisplatin-resistance lines of CCRF-CEM and A2780 cells.

Abstract

Some of the proposed mechanisms for cisplatin resistance are the reduced influx and the increased efflux of cisplatin across the membrane transporters. The structure and the function of the cells are dependent on the membranes that consist of a lipid bilayer with inserted proteins. Changes in lipid composition and distribution on the cell membranes have been observed in cancer cells, then the conformation of the cell membrane could directly or indirectly be related also with the cisplatin resistance. On the bases of these considerations, I decided to study the qualitative phospholipid (PL) profile of wild type and cisplatin-resistant lines of acute T-lymphoblastic leukaemia (CCRF-CEM) and ovarian carcinoma (A2780) cells, to highlight possible differences and identify some specific PLs (Chapter 5 – Submitted manuscript I). I proposed an analytical procedure based on solid phase extraction (SPE) and Electro-spray Ionization Mass Spectrometry (Figure 17), that allowed to study the PL profile of cell lysates, obtaining reliable and reproducible results, preventing peptide and metabolite interferences.

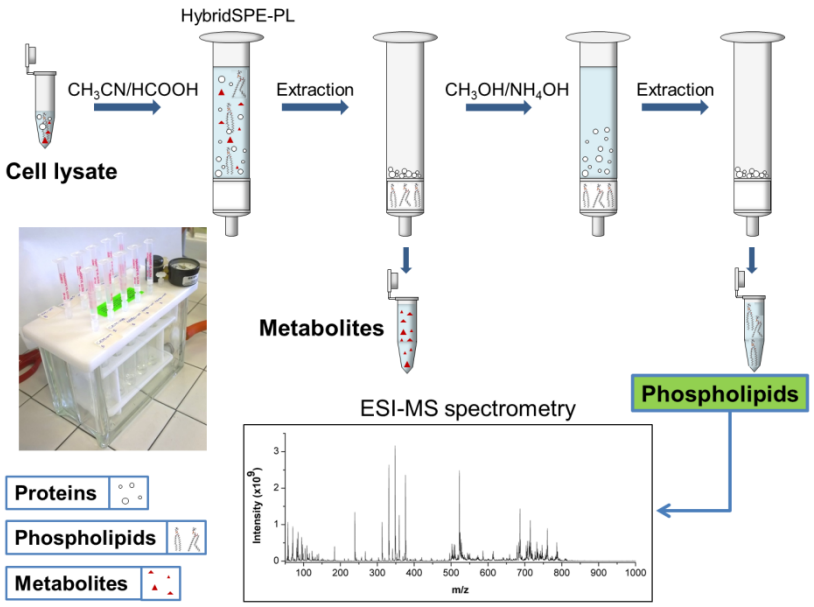

Figure 17. Experimental procedure to extract the PLs from the cell lysate.

From the analysis of supernatants and pellets fractions of cell lysate, a different PL profile was detected. These two fractions were taken into account simultaneously for a correct interpretation and a complete characterization of the PL profile. The PLs belonging to specific families were recognized and differentiate by the number of carbon atoms and double bonds. In some cases also the position of the double bonds was assigned (Figure 18).

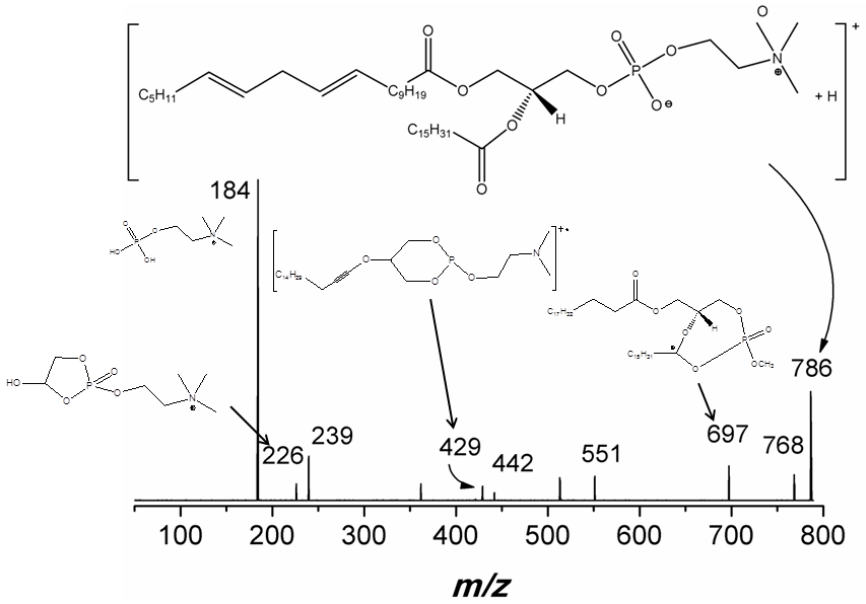

Figure 18. Tandem MS-MS(+) spectrum of *m/z* 786 peak (PC(20:2(11Z,14Z)/16:0)).

In Figure 19 the total PL content identified with ESI(+) for the wild type and cisplatin-resistant lines of CCRF-CEM and A2780 cells is reported. Some phospholipids were identified to be specific components, and can be considered as "markers" to distinguish between wild type and cisplatin-resistant cells. With respect to their parental counterparts, it was found that some glycerophosphocholines were strongly down-represented in the cisplatin-resistant CCRF-CEM cells, while some sphingomyelins were up-represented in the cisplatin-resistant A2780 cells. In both the resistant cell lines, dihydroxyacetone phosphate was found to be more up-represented. Considering that the different composition of the cell membranes could be related to cisplatin resistance, the presence of some lipids as "markers" for cisplatin-resistance cells could help to

clarify the mechanisms underlying the development of the resistance. Moreover, these "markers" could be used for a possible clinical application, as for example monitoring the onset of the resistance during cisplatin treatment by detecting those specific lipids.

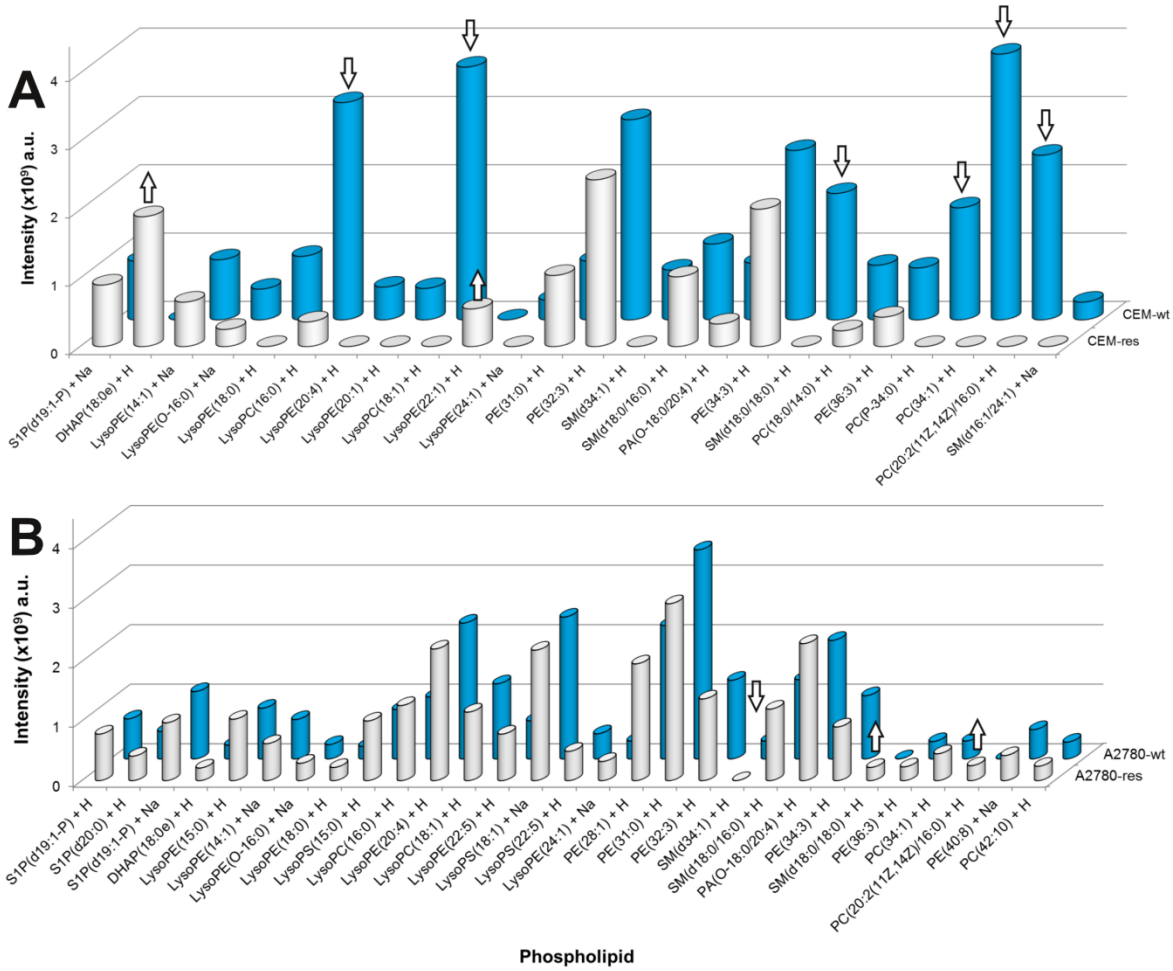

Figure 19. Phospholipids identified with ESI(+) in the lysate extract of CCRF-CEM wild type (CEM-wt) and cisplatin-resistant (CEM-res) cells (**A**), and A2780 wild type (A2780-wt) and cisplatin-resistant (A2780-res) cells (**B**). The phospholipids that are up-represented (⇧) or down-represented (⇩) in the cisplatin-resistant cells with respect to the wild type ones, are marked.

Submitted manuscript I

Identification of specific phospholipids to differentiate cisplatin-resistant and wild type cells in leukemic (CCRF-CEM) and ovarian cancer (A2780)

Elisa Valletta, Elisabetta Pinna, Sarah Vascellari, Graziano Caddeo, Enzo Cadoni, Francesco Isaia, Alessandra Pani, Tiziana Pivetta

Submitted - PLoS ONE

IDENTIFICATION OF SPECIFIC PHOSPHOLIPIDS TO DIFFERENTIATE CISPLATIN-RESISTANT AND WILD TYPE CELLS IN LEUKEMIC (CCRF-CEM) AND OVARIAN CANCER (A2780).

*Elisa Valletta[a], Elisabetta Pinna[b], Sarah Vascellari[b], Graziano Caddeo[a], Enzo Cadoni[a], Francesco Isaia[a], Alessandra Pani[b], Tiziana Pivetta[a]**

[a]*Dipartimento di Scienze Chimiche e Geologiche,* [b]*Dipartimento di Scienze Biomediche, University of Cagliari, Cittadella Universitaria, 09042 Monserrato (CA) – Italy*

* Corresponding author: Tiziana Pivetta, tpivetta@unica.it, 0039 070 675 44 73, fax 0039 070 584597.

Keywords: CCRF-CEM cells, A2780 cells, cisplatin resistance, phospholipids, ESI-MS, solid phase extraction.

Abstract

Changes in lipid distribution and composition of the cellular membranes have been observed in cancer and several other pathologies. The conformation of the cell membrane could directly or indirectly be related with the cisplatin resistance. With the aim to highlight possible differences between wild type and cisplatin-resistant cells and to identify some specific phospholipids, we studied the phospholipid profile of wild type and cisplatin-resistant cells of two kinds of tumours, acute T-lymphoblastic leukaemia (CCRF-CEM) and ovarian carcinoma (A2780).The analytical procedure proposed in this work, based on solid phase extraction and mass spectrometry, allowed to identify specific components of the cisplatin-resistant cells. With respect to their wild type counterparts, it was found that some glycerophosphocholines were strongly down-represented in the cisplatin-resistant CCRF-CEM cells, while some sphingomyelins were up-represented in the cisplatin-resistant A2780 cells. In both the resistant cell lines, dihydroxyacetone phosphate was found to be more up-represented. The evidenced phospholipid changes play a key role in the detection of the transformation from wild type to cisplatin-resistance cells and can help to clarify the mechanisms underlying the development of the resistance. Moreover, the potential use of some lipids as “markers” for resistant cells could be important for a possible clinical application. In fact, the onset of the resistance during cisplatin treatment could be monitored by detecting those specific lipids. Under this perspective, the obtained findings represent an advancement of knowledge and can be exploited for the design of new strategies in cancer treatment.

Introduction

Cell membranes consist of a lipid bilayer with inserted proteins, whose content depends both on the cell type and on the cell compartment of the membrane itself. In the plasma membrane, for example, lipids and proteins are almost equally distributed, whereas in the inner membrane of mitochondria, a higher proportion of proteins is present (about 75%) [1]. Membranes can be considered as fluids in which lipids and proteins are free to rotate and shift laterally. The fluidity of the membranes depends principally on the lipid composition. Regions of membrane with long fatty acid residues are more rigid, since the interactions among long acyl chains are stronger than those among short ones, while the degree of unsaturation of the fatty acids increases the membrane fluidity as folds in the chains decrease interactions among them. The asymmetric distribution of lipids between the inner and the outer leaflets defines the characteristics of the cell membranes [1,2]. Three classes of lipids constitute the cell membrane: phospholipids (PLs), glycolipids and sterols. PLs are commonly present in the highest concentration and are considered the fundamental components of all the cell membranes. PLs are amphipathic molecules, consisting of two hydrophobic fatty acid chains linked to a hydrophilic phosphate-containing head group. The

principal PLs present in the membranes are glycerophospholipids (GPLs), which contain a glycerol backbone with a fatty acyl or alkyl group at the *sn*-1 position, a fatty acyl group at the *sn*-2 position, and a phosphodiester moiety linked to a polar head-group at the *sn*-3 position [3]. GPLs are classified on the basis of the polar head: glycerophosphocholine (PC), glycerophosphoserine (PS), glycerophosphoethanolamine (PE), and glycerophosphoinositol (PI), in the presence of choline, serine, ethanolamine and inositol, respectively. PC derivatives represent more than 50% of the PLs in most eukaryotic membranes [4]. The second important family of structural polar lipids is represented by the sphingolipids (SLs), which consist of a ceramide unit with phosphocholine or phosphoethanolamine as a head group. In Fig. 1, the most important PLs are depicted.

Changes in lipid distribution and composition of the cellular membranes have been observed in several pathologies and in cancer [5–8]. In neoplastic cells, alterations of the PL's composition, [6] increases in the concentration of PI, PS, PE and PC derivatives, as well as increases in the level of esterified cholesterol were observed [6,9]. Moreover, considering that the mechanisms of transport through the plasma membrane depends on its assembly, particularly on its rigidity and permeability, and that these characteristics are determined by composition and structure of the membrane constituents, an alteration of the physiological membrane condition could readily affect drug influx and efflux across cell membrane. The conformation of the cell membrane could be then directly or indirectly also be related to the undesirable phenomena of drug resistance, such as cisplatin resistance. Cisplatin (CDDP) is used for the treatment of breast, ovarian [10], prostate [11], testes [12], and non-small cell lung cancer [13]. However, the administration of CDDP is limited by its side effects and the onset of inherited or acquired resistance.

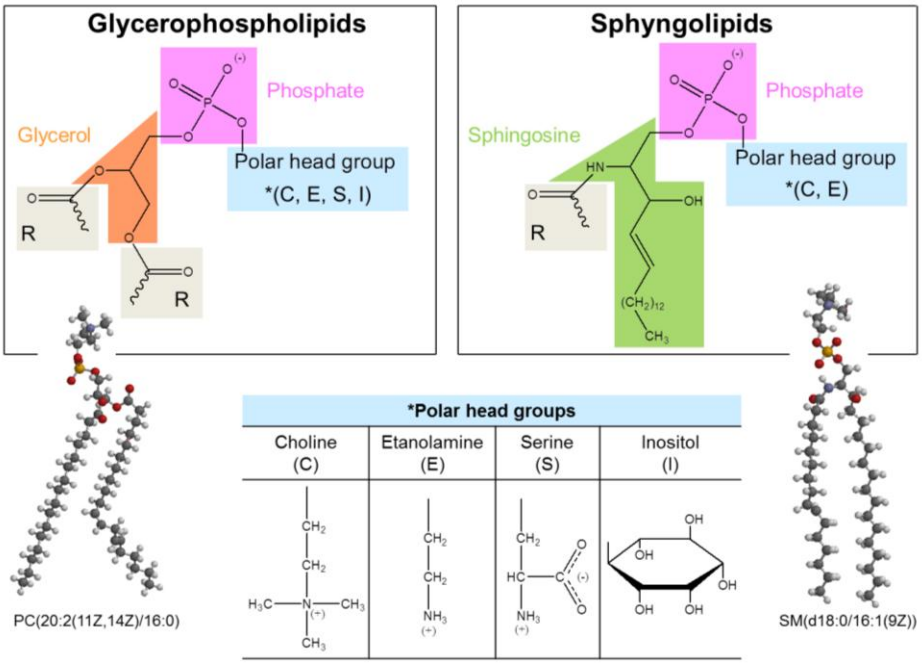

Fig. 1 Principal phospholipids contained in the cell membranes. For a complete description of the nomenclature of the phospholipids see ref. [1] and [14].

Cisplatin resistance is supposed to be related to its mechanism of action. Briefly, cisplatin enters the cells by passive diffusion or by active protein-mediated transport systems, i.e. human organic cation transporter (hOCT2) and copper transport protein (Ctr1). Once in cytoplasm, one of the two chloride ligands of CDDP is displaced by a water molecule to form the complex $[PtCl(H_2O)(NH_3)_2]^+$. This species binds DNA bases, mainly in the N7 position of guanine and adenine, and the N3 of cytosine, to form the monofunctional adduct $[PtCl(DNA)(NH_3)_2]^+$. Also the second chloride ion can be displaced by a water molecule to form $[Pt(H_2O)(DNA)(NH_3)_2]^{2+}$. This last may bind DNA by crosslinking to form a bifunctional adduct that is responsible of the triggering of cell death [15–21]. The influx of the drug inside the cell and/or drug efflux outside the cell represent possible mechanisms for the onset of cisplatin resistance [22]. On the basis of these considerations, we decided to study the qualitative PL profile of two cancer cell lines and of their corresponding cisplatin-resistant sublines, to highlight possible differences and identify some cell-line specific PLs. With this aim, we set up a procedure to analyse the PL content of the cell lysate sample in a fast, routine, accurate, and reproducible method, based on the solid phase extraction (SPE) and electrospray ionisation mass spectrometry (ESI-MS) and tandem mass spectrometry (MS-MS). In particular, the proposed method allows one to obtain mass spectra with high signal to noise ratio, preventing the interference of peptides that act as ionic suppressors and removing the metabolites that can be recovered for other uses. Moreover, we analysed both the supernatants and pellet of each cell lysate, finding interesting differences between the two lysate fractions. We studied the PL composition of *i*) the acute T-lymphoblastic leukaemia derived CCRF-CEM cell line (CCRF-CEM-wt), *ii*) the ovarian carcinoma derived A2780 cell line (A2780-wt), *iii*) the cisplatin-resistant subline of acute T-lymphoblastic leukaemia cells (CCRF-CEM-res), and *iv*) the cisplatin-resistant subline of ovarian carcinoma cells (A2780-res). The leukemic CCRF-CEM cells were selected since they represent a classical model widely used for studies in biochemistry and biomedicine, while the A2780 cells were selected because ovarian cancer is actually treated with cisplatin.

Experimental

Reagents

Acetonitrile (CH_3CN), ammonium hydroxide (NH_4OH), formic acid (HCOOH), methanol (CH_3OH), and trifluoroacetic acid (HTFA) were purchased from Sigma-Aldrich (Milan, Italy). Cisplatin was purchased from Alfa Aesar (Karlsruhe, Germany). Fetal Bovine Serum, Kanamycin, L-Glutamine medium, and RPMI medium were purchased from Euroclone (Milan, Italy). The

commercial reagents were used as received. Ultra-pure water obtained with MilliQ Millipore was used for all the experiments.

Cell culture

The human acute T-lymphoblastic leukaemia cell line (CCRF-CEM-wt) was purchased from the American Type Culture Collection (ATCC, USA), whereas a subline cisplatin-resistant cells (CCRF-CEM-res), was obtained by us via serial passages of the CCRF-CEM cell line in the presence of increasing concentrations of cisplatin. The CCRF-CEM-res subline was stabilized at 5 μM cisplatin (for details see ref. [23]). The human ovarian carcinoma cell line (A2780-wt) and the cisplatin-resistant subline (A2780-res), were a generous gift by Dr. Eva Fischer (Tumor Biology Laboratory, The Ion Chiricuta Oncology Institute, Cluj-Napoca, Romania). CCRF-CEM cell lines were maintained in culture between 1×10^5 cells/ml and 2×10^6 cells/ml, in RPMI medium with stable L-Glutamine medium supplemented with 10% Fetal Bovine Serum and 1% Kanamycin (growth medium). A2780 cell lines were maintained in culture between 1.5×10^5 cells/ml and 3×10^6 cells/ml (~70% confluency) in the same medium. Mycoplasma contamination was periodically monitored. All cell lines were replaced every 3 months with cells freshly thawed from liquid nitrogen. In addition, CCRF-CEM-res and A2780-res were treated with 5 μM (every passage) and 1 μM (every two or three splits) cisplatin, respectively, in order to maintain the drug resistance. Cisplatin resistance was checked every month. All experiments with cisplatin-resistant sublines were performed using cell populations that were grown for one passage without cisplatin.

Cell lysates

Exponentially growing CCRF-CEM-wt/CCRF-CEM-res (2×10^7 total) and A2780-wt/A2780-res (4×10^6 total) cells were centrifuged at 1500 rpm for 5 minutes. Pellets were resuspended in 1 ml of deionized H_2O. Cell lysates were obtained by using a 2 ml dounce tissue grinder set (Sigma Aldrich) followed by centrifugation at 4600 rpm for 2 minutes. PLs were extracted from supernatants and pellets and analysed by ESI-MS, immediately after the lysis in order to minimize the enzymatic activity. During manipulation, the samples were kept on ice.

Extraction of phospholipids

The SPE of PLs from the crude cell lysate was performed with the Visiprep^{TM} Solid Phase Extraction Vacuum Manifolds 12-Port Model and the SPE HybridSPE-Phospholipid Ultra Cartridge (Supelco). The cartridges were conditioned with 1 ml of CH_3CN containing 1% of HCOOH, followed by 1 ml of water. The lysate pellets or 200 μl of each cell lysate supernatants, was put into a cartridge with 600 μl of CH_3CN containing 1% of HCOOH. To facilitate the protein

precipitation, the mixture was mixed by repeated pipetting with a micropipette. The solution, containing almost metabolites, was extracted under vacuum and stored in freezer for other uses. The cartridge was washed with 1 ml of CH_3CN containing 1% of HCOOH and afterwards the phospholipids were extracted with 1 ml of CH_3OH containing 5% of NH_4OH. The resulting solution was divided in two fractions: one was immediately used for negative ESI-MS spectrometry, the other one was evaporated under vacuum and the solid residue was dissolved in 1 ml of H_2O containing 0.5% HTFA and CH_3OH (1:1) for positive ESI-MS. Five different lysate samples of each cell line were analysed and every extraction was repeated six times from every sample. The error percentage of the repeated measurements was always lower than 1%.

Mass spectrometry

Mass spectra were collected on a triple quadrupole QqQ Varian 310-MS mass spectrometer using the atmospheric-pressure ESI technique.

The sample solutions were infused directly into the ESI source using a programmable syringe pump at a flow rate of 0.70 ml/h. A dwell time of 14 s was used and the spectra were accumulated for at least 10 minutes in order to increase the signal-to-noise ratio. Mass spectra were recorded in the *m/z* 50–1000 range. The experimental conditions for positive- and negative-ion mode were: needle voltage 4500 V and −5500 V, shield voltage 600 V and −600 V, housing temperature 60 °C, drying gas temperature 100 °C and 120 °C, nebuliser gas pressure 40 PSI, drying gas pressure 20 PSI, and detector voltage 1600 V and −1800 V. Tandem MS-MS experiments were performed with argon as the collision gas (1.8 PSI). The collision energy was varied from 2 to 45 V. The isotopic patterns of the measured peaks in the mass spectra were analysed using mMass 5.5.0 software package [24–26]. The assignment of the PLs to the spectral peaks was performed by using the human metabolite database HMDB (www.hmdb.ca) [27–29], on the basis of the MS-MS spectra. In case of ambiguity the human biofluid location of the chosen PL was also considered. Only peaks with intensities higher than 2×10^7a.u. were considered. In some cases, due to the simultaneous presence of PLs with similar masses, convoluted signals were observed. In these cases, the experimental pattern was attributed to a weighted combination of the isotopic pattern of the different molecules [23]. The weights, that represent the percentage in which each molecule was present, were obtained by multivariate regression analysis of the experimental data.

Results and discussion

Sample preparation for ESI-MS spectrometry

The PLs of the cellular lysate samples were extracted in a fast, routine, accurate, and reproducible method based on the solid phase extraction and analysed by mass spectrometry (Fig. 2).

The mass spectrum of the cell lysate analysed without any pre-treatment is characterised by a high number of overlapped peaks of low intensity and a baseline with poor quality (Fig. 3A). The low intensity of the signals (10^8 a.u.) is mainly due to the presence of proteins that act as ionic suppressors [30]. Following the procedure reported in Fig. 2, a reliable spectrum is instead obtained. Proteins are precipitated inside a cartridge (HybridSPE-Phospholipid Ultra Cartridge, Supelco, HybridSPE is a registered trademark of Sigma-Aldrich Co. LLC.) by addition of CH_3CN and HCOOH. The resulting mixture is passed, under vacuum, through the cartridge to remove the liquid phase containing almost metabolites, while the precipitated proteins are retained in the upper frit of the cartridge. PLs are retained by the cartridge via a selective Lewis acid-base interaction between the proprietary zirconia ions, functionally bonded to the stationary phase, and the phosphate moiety of the PLs [31]. The PLs are then recovered by extraction with NH_4OH in CH_3OH. The resulting solution is divided in two fractions: one is used for negative ESI-MS spectrometry, the other one is evaporated under vacuum and the solid residue is dissolved in a proper amount of 1:1 H_2O (0.5% HTFA) and CH_3OH for positive ESI-MS spectrometry. The proposed procedure was followed for lysate samples of the four cell lines. Sixteen replicates for each cell line were analysed to check the reproducibility of the results and the robustness of the method.

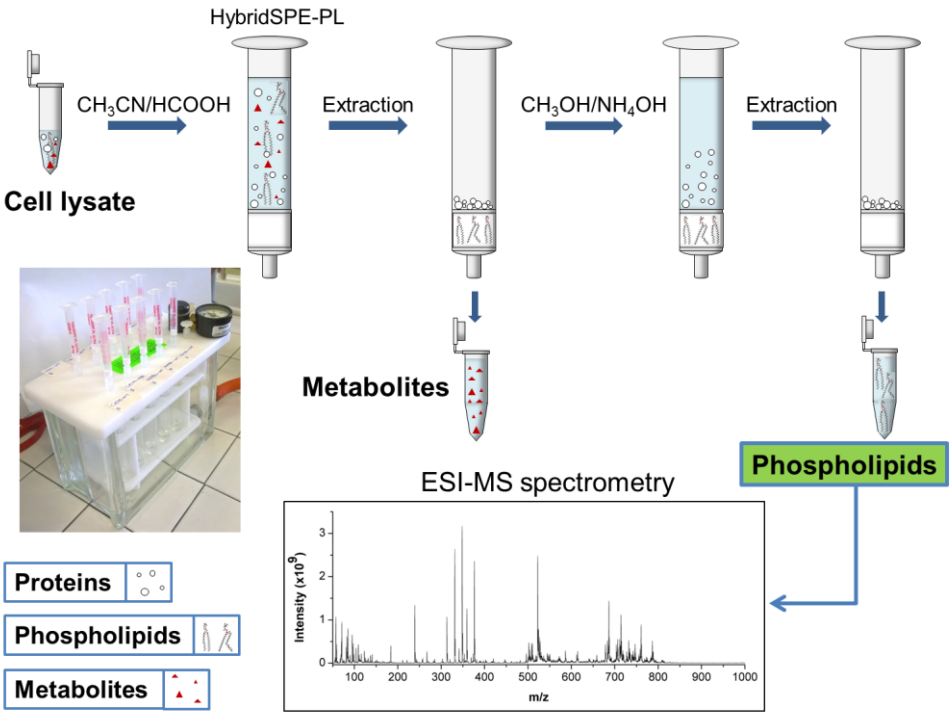

Fig. 2 Experimental procedure followed in this work to extract the phospholipids from the cell lysate. In the picture, the SPE extractor is shown (Visiprep Solid Phase Extraction Manifold - 12 Port Model).

Mass spectrometry

Cell lysates were obtained by a mechanical method using a dounce homogenizer without detergents. The supernatant solutions containing cytoplasmic extracts and the respective pellets having nuclei and cell debris of the cell lysates were analysed by ESI-MS and different results were obtained for the two lysate fractions. The spectra recorded in positive ion mode for supernatant and pellet fractions and untreated lysate of CCRF-CEM-wt cells are reported in Fig. 3. The mass spectra recorded in positive, ESI(+), and negative, ESI(-), ion mode for all the samples are reported in the Supporting Information (Fig. S1-S4).

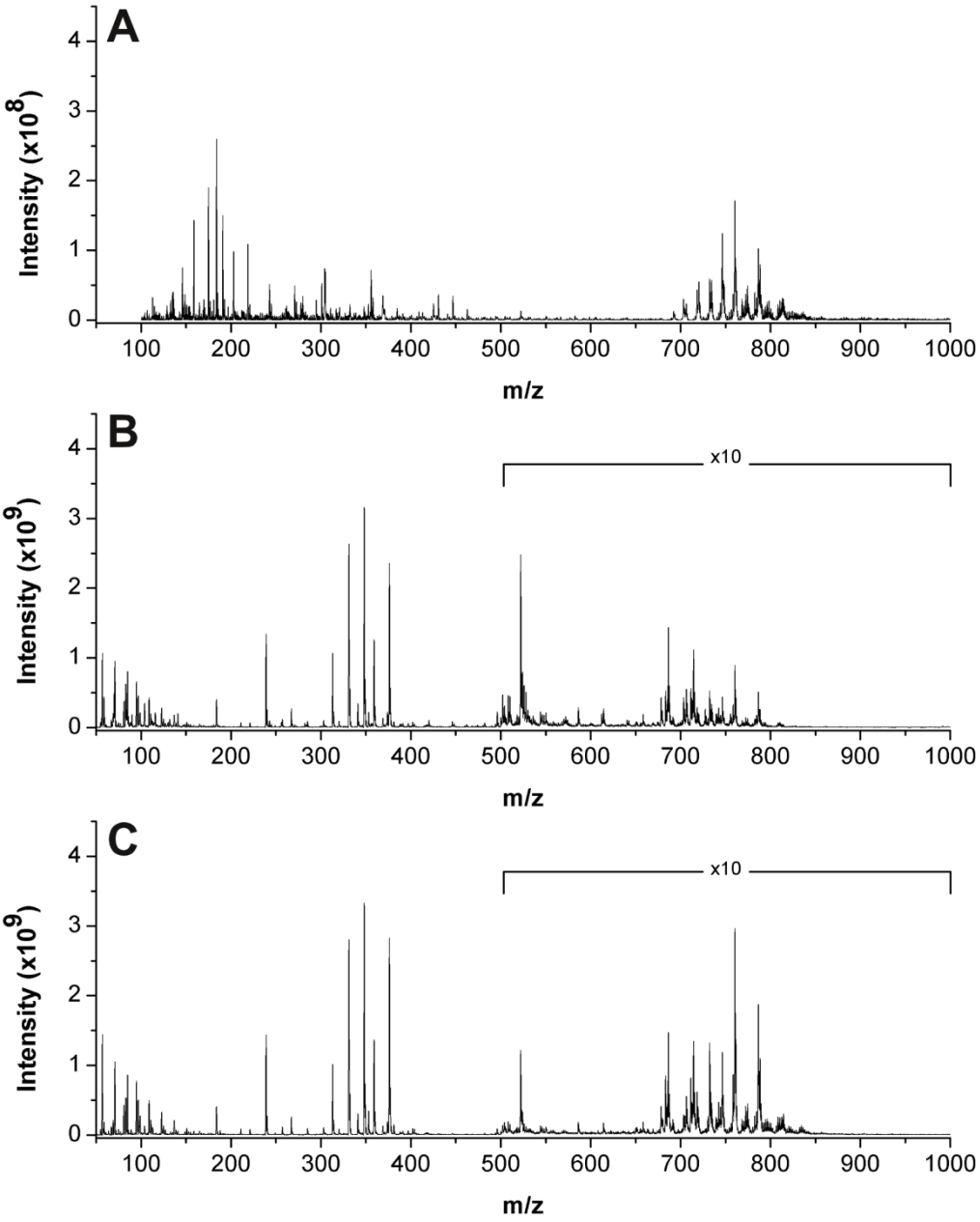

Fig. 3 ESI(+) mass spectra of the lysate solutions of CCRF-CEM wild type cells without any pretreatment (**A**), after SPE extraction from the supernatant fraction (**B**), and from the pellet fraction (**C**). The intensities are reported in different scales; the intensity of the signals in the *m/z* 500–1000 range was multiplied by a factor of 10 in **B** and **C**.

The spectrum of the untreated lysate (Fig. 3A) is characterised by a very low intensity (10^8 vs 10^9 a.u. of 3B and 3C) and by the presence of many broad peaks due most probably to multi-charged protonated peptides. Comparing the spectrum of the lysate with those of the supernatant and pellet, it appears evident that the SPE treatment produces higher quality spectra. Signals of the PLs fall in the mass/charge ratio (*m/z*) 500–1000 range, while signals falling in the *m/z* 50–400 range are principally due to their fragment products, as confirmed by the MS-MS experiments.

The PL peaks observed in the spectra were identified on the basis of the masses, isotopic distribution patterns and the structural information obtained from tandem MS-MS. PLs were assigned to a given family on the basis of characteristic peaks in the tandem MS-MS spectra and by precursor/product ion scan and neutral loss scan experiments. For example, the *m/z* 184 precursor ion scan gives the possibility to detect all the lipids containing the phosphocholine ion, while the neutral loss of phosphoethanolamine (*m/*z 141) helps in the identification of PEs. The collision-induced fragmentation experiments were carried out varying the collision energy, in order to observe partial and complete fragmentation of the parent peaks. Considering the specific fragments and the common rules of fragmentation, in some cases it is possible to determine precisely the fatty-acyl group and the structure of the long-chain base (number and position of the double bonds). Some MS-MS spectra of PLs with the corresponding assignment are reported in the Supporting Information (Fig. S5-S10).

Phospholipid content

The height of a mass peak is proportional to the concentration of the species that originated that signal but depends also on its ionisation efficacy. Therefore, the intensity of two or more signals originated by different species cannot be directly compared. Instead, providing that the experimental conditions are kept constant, the intensity of signals arising from the same species can be compared each other. The heights of the mass peaks for the studied samples, recorded in ESI(+) and ESI(-), are reported in Fig. 4-7

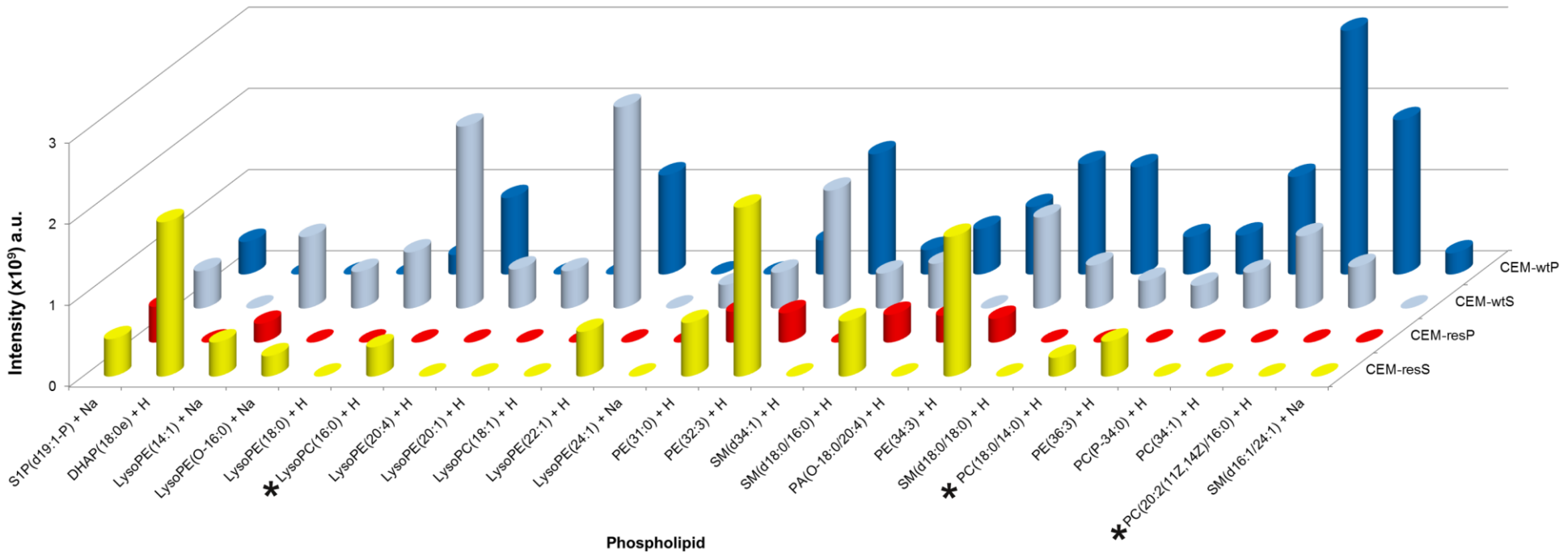

Fig. 4 Phospholipids identified with ESI(+) in the lysate fractions of supernatant (S) and pellet (P) for the CCRF-CEM wild type (CEM-wt) and cisplatin-resistant (CEM-res) cells (charges of proton and sodium ions are omitted for clarity), the MS-MS spectra of the marked (*) PLs are presented and discussed in the supporting (Fig. S5-S7). The error percentage in intensity for repeated measurements was always lower than 1%.

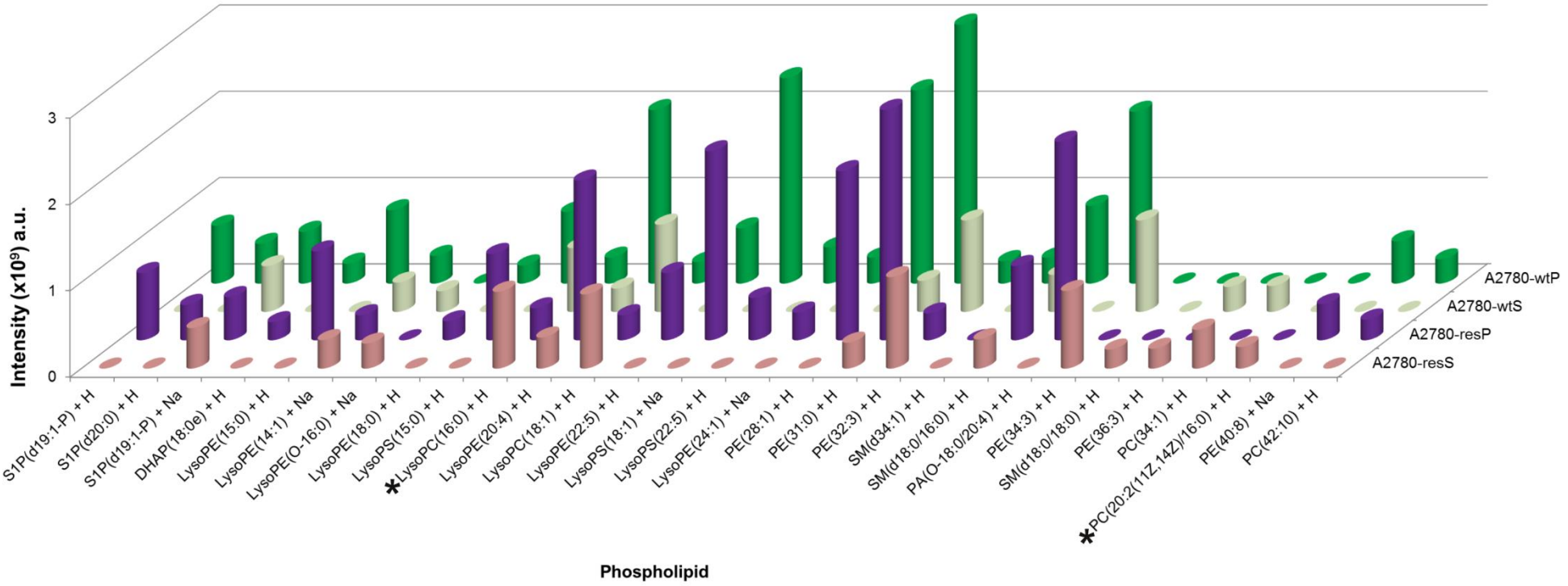

Fig. 5 Phospholipids identified with ESI(+) in the lysate fractions of supernatant (S) and pellet (P) for A2780 wild type (A2780-wt) and cisplatin-resistant (A2780-res) cells (charges of proton and sodium ions are omitted for clarity), the MS-MS spectra of the marked (∗) PLs are presented and discussed in the supporting (Fig. S5 and S7). The error percentage in intensity of the repeated measurements was always lower than 1%.

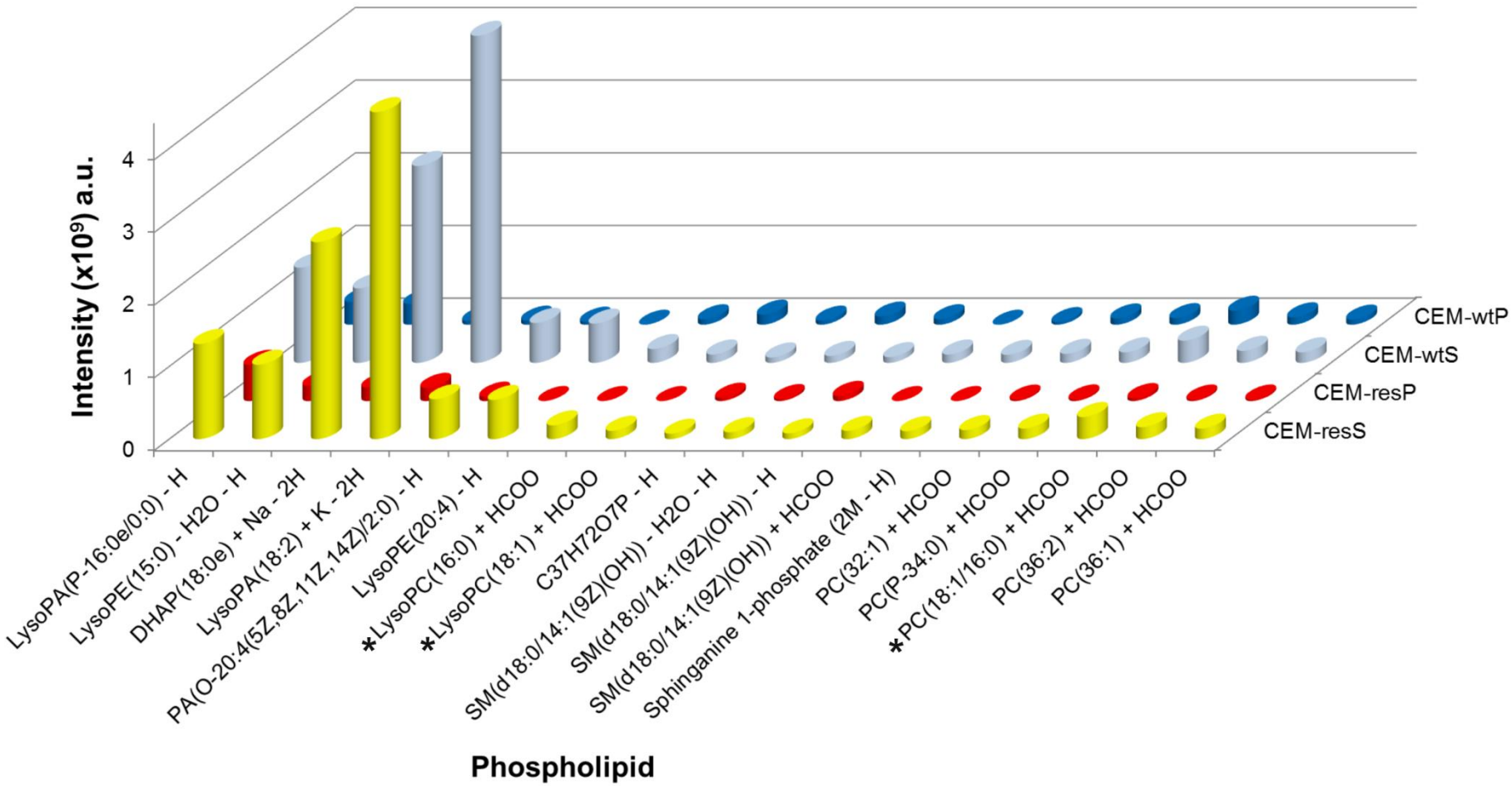

Fig. 6 Phospholipids identified with ESI(-) in the lysate fractions of supernatant (S) and pellet (P) for the CCRF-CEM wild type (CEM-wt) and cisplatin-resistant (CEM-res) cells (charges of proton, sodium, potassium and formate ions are omitted for clarity), the MS-MS spectra of the marked (*) PLs are presented and discussed in the supporting (Fig. S8-S10). The species $C_{37}H_{72}O_7P$ was not distinguishable between PA(P-34:0) and PA(O-34:1). The error percentage in intensity of the repeated measurements was always lower than 1%.

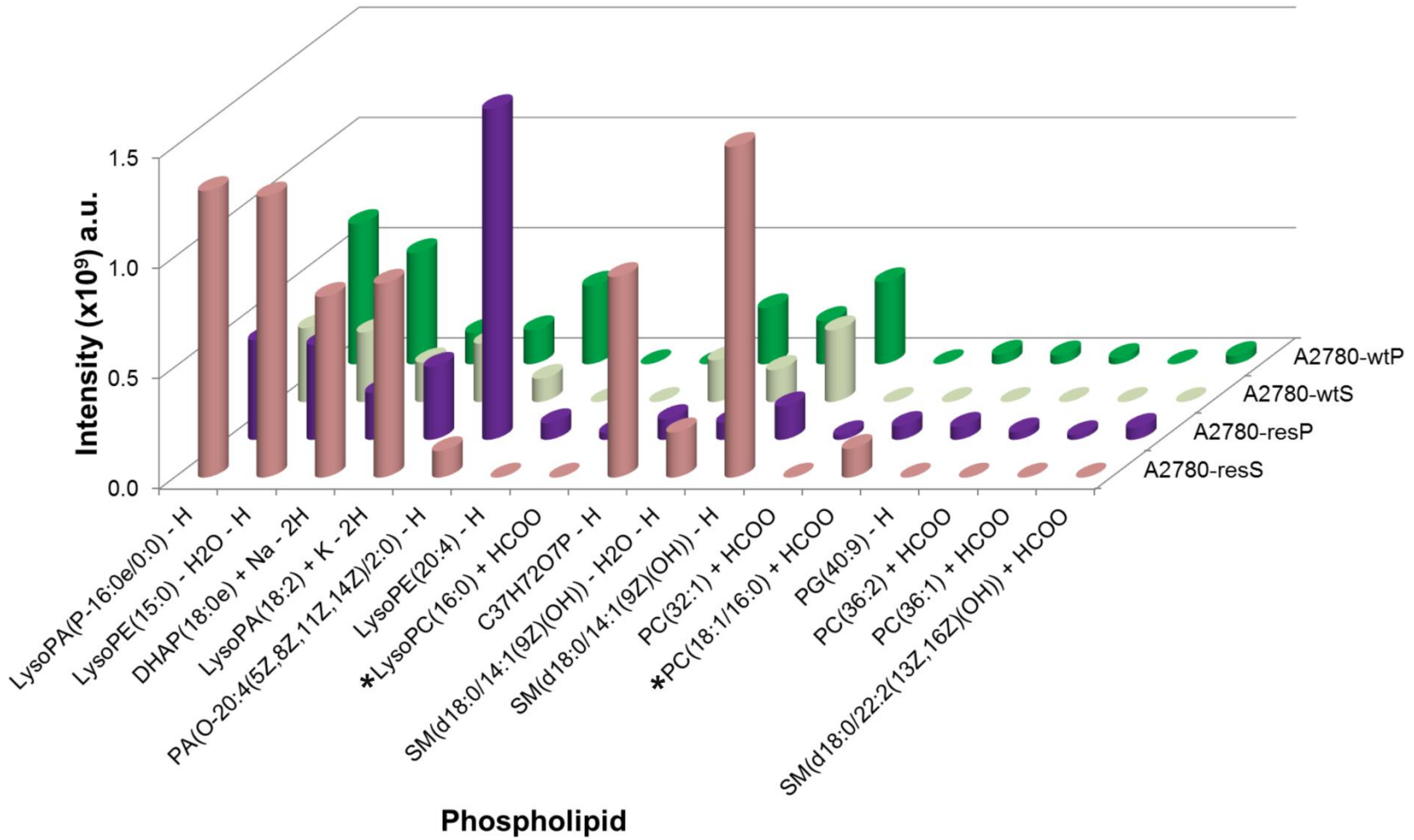

Fig. 7 Phospholipids identified with ESI(-) in the lysate fractions of supernatant (S) and pellet (P) for the CCRF-CEM wild type (CEM-wt) and cisplatin-resistant (CEM-res) cells (charges of proton, sodium, potassium and formate ions are omitted for clarity), the MS-MS spectra of the marked (*) PLs are presented and discussed in the supporting (Fig. S9 and S10). The species $C_{37}H_{72}O_7P$ was not distinguishable between PA(P-34:0) and PA(O-34:1). The error percentage in intensity of the repeated measurements was always lower than 1%.

The number of PLs detected in supernatant (S) and pellet (P) is different for each studied cell lines, as reported in Table 1.

Table 1. Number of PLs detected in ESI(+) and ESI(-) in supernatant and pellet fractions of lysates of CCRF-CEM and A2780 cell lines in the chosen experimental conditions.

Cell Line	Number of detected phospholipids			
	ESI(+)		ESI(-)	
	supernatant	pellet	supernatant	pellet
CCRF-CEM-wt	21	17	18	15
CCRF-CEM-res	12	7	18	8
A2780-wt	12	23	8	12
A2780-res	14	22	9	15

In ESI(+), the number of PLs detected in the supernatant fraction is higher than that of the pellet fraction in the CCRF-CEM lysate and lower in the A2780 lysate. In ESI(-), the number of PLs detected in the supernatant or pellet fractions is almost identical in the CCRF-CEM lysate, while is higher in the pellet fraction of A2780 lysate compared to the supernatant. Some PLs were detected only in one of the two fractions of the cell lysates.

The intensities of the peaks recorded in ESI(+) are generally higher than those recorded in ESI(-), except for the signals of (DHAP+Na) and (LysoPA(18:2)+K-2H), where the presence of the metal ion increases the ionisation efficacy and originates a very high response. Regards the ESI(+) experiments, the PLs SM(d16:1/24:1), PC(P-34:0), PC(18:0/14:0), LysoPE(22:1), and LysoPE(20:1) are present only in the CCRF-CEM cells, in particular LysoPE(22:1) is present only in the CEM-resS, LysoPE(20:1) only in CEM-wtS, and SM(d16:1/24:1) only in CEM-wtP. The PLs PC(42:10), PE(40:8), PE(28:1), LysoPS(22:5), LysoPS(18:1), LysoPS(15:0), LysoPE(22:5), LysoPE(15:0) and S1P(d20:0) are detected only in A2780 cells. Regards the ESI(-) experiments, the PLs sphinganine 1-phosphate, LysoPC(18:1) and PC(P-34:0) are present only in the CEM cell lysate. PG(40:9) and SM(d18:0/22:2(13Z,16Z)(OH)) are present only in A2780 cell lysate.

From the MS-MS experiments (precursor ion mode and parent ion mode), lysophospholipids were found to be present in the lysate but also formed by collision-induced fragmentation of PLs or by decomposition of precursor ions in ESI phase. LysoPE(15:0), for example, was derived from PE(36:3), PE(34:3) and PE(32:3).

Considering the different results obtained for surpernatant and pellets, it follows that in the study of cell lysates, it is important to analyse both supernatant and pellet fractions and consider the total PL content.

CCRF-CEM wild type and cisplatin-resistant cell lines

The total PL content for CCRF-CEM-wt and CCRF-CEM-res is reported in Fig. 8. Intense changes between cisplatin-resistant and wild type cells are observable in the PL abundances and kinds. In particular, from ESI(+) results, in the resistant cells it appears that i) PC(20:2), PC(34:1), PC(P-34:0), SM(d18:0/18:0), LysoPC(18:1), and LysoPC(16:0) are strongly down-represented, while ii) LysoPE(22:1) and DHAP(18:0e) are moderately up-represented. From ESI(-) results, it appears that i) PC(36:1), PC(18:1/16:0), PC(P-34:0), PC(32:1), LysoPC(18:1), LysoPC(16:0), LysoPA(18:2), DHAP(18:0e) are down-represented, while ii) SM(d18:0/14:1(9Z)(OH)), PA(O-20:4(5Z,8Z,11Z,14Z)/2:0), LysoPE(15:0), LysoPA(P-16:0e/0:0) are up-represented. The PLs S1P(d19:1-P), LysoPE(14:1), LysoPE(O-16:0), PE(31:0), SM(d18:0/16:0), PE(34:3), PE(36:3) are almost retained from wild type to cisplatin-resistant cells.

From the reported results, the principal outcome is that the PC content is strongly reduced in the cisplatin-resistant CCRF-CEM cells, with respect to the wild type ones. This could be due to increased PC catabolism or decreased PC biosynthesis. The biological turnover of PCs produces phosphatidic acid (PA) and choline, by the action of phospholipase D, and arachidonic acid and LysoPC, by the action of phospholipase A2. PA can be then converted in LysoPA, while arachidonic acid can be converted in prostaglandins and leukotriens. LysoPCs play an important role in lipid signaling by acting on the LysoPLs receptors**.** LysoPA stimulates proliferation, decreases apoptosis, platelet aggregation, smooth muscle contraction, and tumour cell invasion. PC biosynthesis is regulated by the cytidine 5'-diphosphocholine (CDP-choline), involved in the modulation of choline-phosphate cytidylyltransferase binding to membranes [32]. The CDP-choline reduces phospholipase A2 activity, increases the synthesis of S-Adenosyl methionine and glutathione, stimulates the glutathione reductase activity, and fixes the level of arachidonic acid [33–36]. DHAP(18:0e), moderately up-represented in the resistant cells, is the octadecanoyl derivative of the dihydroxyacetone phosphate (DHAP). DHAP is involved in the glycolysis metabolic pathway and it is produced by dehydrogenation of L-glycerol-3-phosphate (glycolytic pathway). DHAP(18:0e) or 1-octadecyl-glycerone-3-phosphate is converted from 1-octadecanoyl-glycerone-3-phosphate via alkylglycerone phosphate synthase [37]. The alkyl derivatives of DHAPs are intermediates in the synthesis of ether phospholipids, molecules with one or more carbon atoms on a glycerol moiety bonded to the alkyl chain via ether linkage. If a vinyl ether group is present in the first position of the glycerol chain, these lipids are called plasmalogens (1-O-1'-alkenyl-2-acylglycerophospholipids) [38].

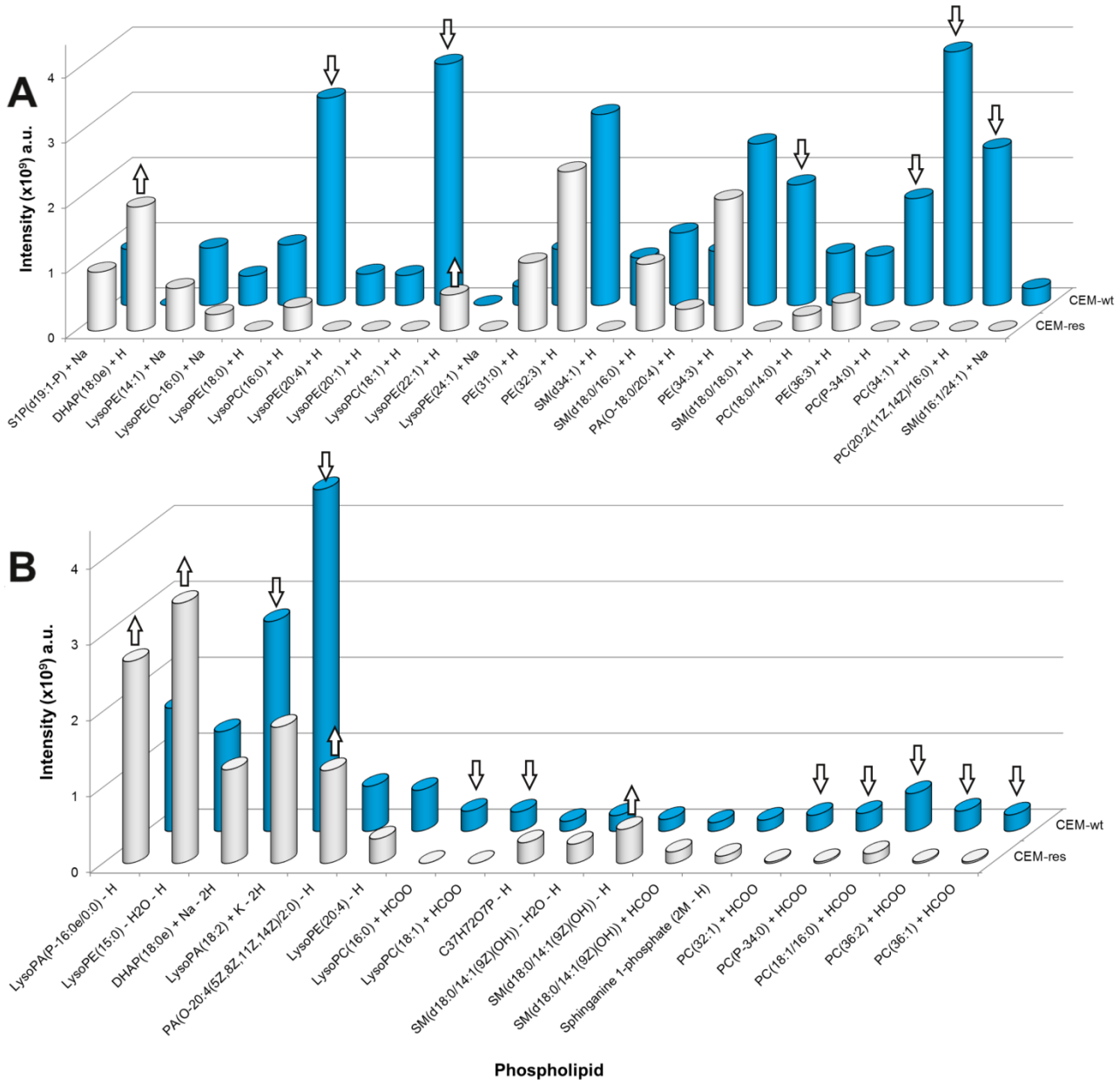

Fig. 8 Phospholipids identified with ESI(+) (**A**) and ESI(-) (**B**) in the lysate extract of CCRF-CEM wild type (CEM-wt) and cisplatin-resistant (CEM-res) cells (charges of proton, sodium, potassium and formate ions are omitted for clarity). The species $C_{37}H_{72}O_7P$ was not distinguishable between PA(P-34:0) and PA(O-34:1). The phospholipids that are up-represented (⇧) or down-represented (⇩) in the cisplatin-resistant cells with respect to the wild type ones, are marked.

A2780 wild type and cisplatin-resistant cell lines

As shown in Fig. 9, from ESI(+) measurements, almost all the PLs are present to the same extent in the wild type and cisplatin-resistant cells, except SM(d34:1) which is slightly down-represented, and SM(d18:0/18:0) and PC(20:2(11Z,14Z)/16:0), which are slightly up-represented. On the contrary, the PLs detected in ESI(-) are all up-represented in resistant cells, and some of them are strongly up-represented. In particular, SM(d18:0/14:1(9Z)(OH)), $C_{37}H_{72}O_7P$, PA(O-

20:4(5Z,8Z,11Z,14Z)/2:0), LysoPA(18:2), DHAP(18:0e) and LysoPA(P-16:0e/0:0) are up-represented.

SM(d18:0/14:1(9Z)) is a sphingolipid found in the membranous myelin sheath. The plasma membrane of cells is rich in sphingomyelin, in particular in the exoplasmic leaflet. Sphingomyelins (SMs) are important for signal transduction and are synthesized by the transfer of phosphorylcholine from phosphatidylcholine to a ceramide in a reaction catalyzed by sphingomyelin synthase. Sphingolipids are involved in the formation of rafts and caveolae (lipid raft of 50–100 nm in size), which are cellular domains involved in the regulation of cell function, transporters and proteins, and in the skin barrier permeability. Sphingomyelin turnover alters the structure of membrane domains [39,40].

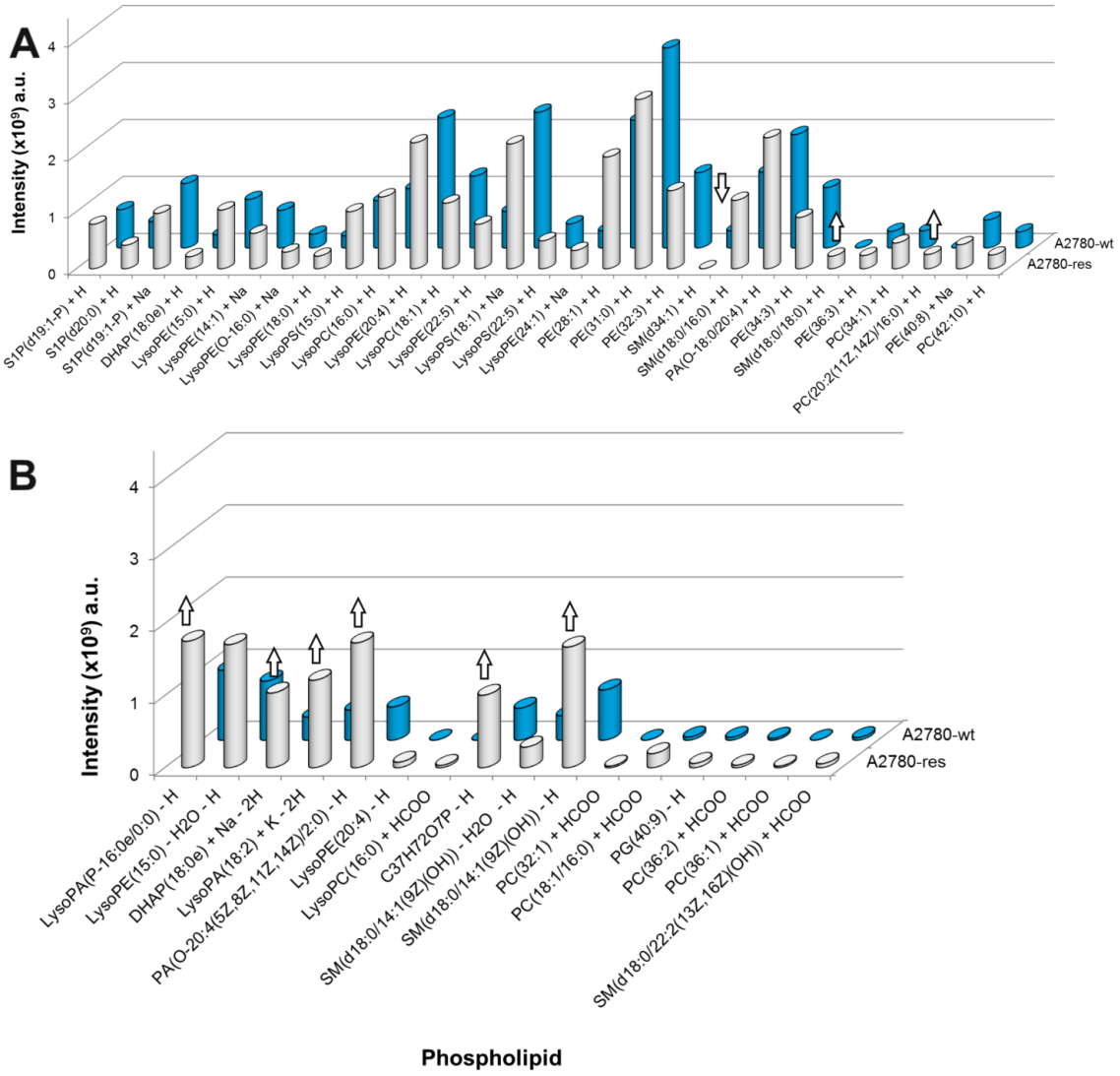

Fig. 9 Phospholipids identified with ESI(+) (**A**) and ESI(-) (**B**) in the lysate extract of A2780 wild type (A2780-wt) and cisplatin-resistant cells (A2780-res) (charges of proton, sodium, potassium and formate ions are omitted for clarity). The species $C_{37}H_{72}O_7P$ was not distinguishable between PA(P-34:0) and PA(O-34:1). The phospholipids that are up-represented (⇧) or down-represented (⇩) in the cisplatin-resistant cells with respect to the wild type ones, are marked.

Conclusions

We studied the phospholipid profile of wild type and cisplatin-resistant cells of two kinds of tumour, T-lymphoblastic leukaemia (CCRF-CEM) and ovarian carcinoma (A2780), with the aim to highlight possible differences and identify some specific phospholipids between wild type and cisplatin-resistant cells.

The analytical method proposed in this work is based on solid phase extraction and mass spectrometry and allowed us to study the phospholipidic (PL) profile of cell lysates, obtaining reliable and reproducible results and preventing peptide and metabolite interferences. A different phospholipidic profile was detected in supernatant and pellet fractions of the cell lysates, suggesting that these two fractions have to be taken into account simultaneously for a correct interpretation and a complete characterization of the phospholipidic profile.

Comparing the PL profiles of wild type and cisplatin-resistant cells, the absence of PC(34:1), LysoPC(18:1), PC(20:2(11Z,14Z)/16:0) and PC(P-34:0) was observed as specific for cisplatin-resistant CCRF-CEM cells, whereas the presence of PC(20:2(11Z,14Z)/16:0) and SM(d18:0/18:0) and the absence of SM(d34:1) were observed as specific for cisplatin-resistant A2780 cells. These lipids can be considered, within a specific line, as “markers” to distinguish between wild type and cisplatin-resistant cells.

Considering that the PL composition influences the transport of drugs across the membrane, affects the activity of the drug transporters and the ability of the cells to load and accumulate drugs, it is evident that a change of the PL content is connected with the development of the resistance. However, from the obtained results, it is not possible to define if these changes are the cause or the consequence of the cisplatin-resistance occurrence. Nevertheless, the potential use of some lipids as “markers” for resistant cells could be important for a possible clinical application. In fact, the onset of the resistance during cisplatin treatment could be monitored by detecting those specific lipids. Under this perspective, the obtained findings represent an advancement of knowledge and can be exploited for the design of new strategies in cancer treatment.

Abbreviations used

A2780-res, cisplatin resistant sub-line of ovarian carcinoma cells; A2780-wt, wild type ovarian carcinoma cells; CCRF-CEM-res, cisplatin resistant sub line of acute T-lymphoblastic leukaemia cells; CCRF-CEM-wt, wild type acute T-lymphoblastic leukaemia cells; CDP-choline, cytidine 5'-diphosphocholine; CID, collision-induced decomposition; DHAP, dihydroxyacetone phosphate; ESI(+), electrospray ionisation positive ion mode; ESI(-), electrospray ionisation negative ion mode; ESI-MS, electrospray ionisation mass spectrometry; FBS, foetal bovine serum; GPLs, glycerophospholipids; HTFA, trifluoroacetic acid; MS-MS, tandem mass spectrometry; P, pellet

fraction; PA, phosphatidic acid; PC, glycerophosphocholine; PE, glycerophosphoethanolamine; PI, glycerophosphoinositol; PS, glycerophosphoserine; PLs, phospholipids; RPMI medium, Roswell Park Memorial Institute medium; S, supernatant fraction; SLs, sphingolipids; SMs, sphingomyelins; SPE, solid phase extraction; TFA, trifluoroacetate.

References

1. Cooper GM. The Cell: A Molecular Approach. 2nd ed. Associates S, editor. Sunderland (MA); 2000.
2. van Meer G, de Kroon AIPM. Lipid map of the mammalian cell. J Cell Sci. 2011;124: 5–8. doi:10.1242/jcs.071233
3. Pulfer M, Murphy RC. Electrospray mass spectrometry of phospholipids. Mass Spectrom Rev. 2003;22: 332–364. doi:10.1002/mas.10061
4. van Meer G, R. Voelker D, W. Feigenson G. Membrane lipids - where they are and how they behave.pdf. Nat Rev Mol Cell Biol. 2009;9: 112–124. doi:10.1038/nrm2330.Membrane
5. Riboni L, Campanella R, Bassi R, Villani R, Gaini SM, Martinelli-Boneschi F, et al. Ceramide levels are inversely associated with malignant progression of human glial tumors. Glia. 2002;39: 105–113. doi:10.1002/glia.10087
6. Lladó V, López DJ, Ibarguren M, Alonso M, Soriano JB, Escribá P V., et al. Regulation of the cancer cell membrane lipid composition by NaCHOleate: Effects on cell signaling and therapeutical relevance in glioma. Biochim Biophys Acta - Biomembr. Elsevier B.V.; 2014;1838: 1619–1627. doi:10.1016/j.bbamem.2014.01.027
7. Kojima K. Molecular aspects of the plasma membrane in tumor cells. Nagoya J Med Sci. 1993; 1–18.
8. Naleskina LA, Todor IN, Nosko MM, Lukianova NY, Pivnyuk VM, Chekhun VF. Alteration In Lipid Composition Of Plasma Membranes Of Sensitive And Resistant Guerin Carcinoma Cells Due To The Action Of Free And Liposomal Form Of Cisplatin. 2013;2013: 192–197.
9. Szachowicz-Petelska B, Dobrzynska I, Sulkowski S, Figaszewski Z. Characterization of the cell membrane during cancer transformation. J Environ Biol. 2010;31: 845–850. doi:10.5772/29559
10. Eckstein N. Platinum resistance in breast and ovarian cancer cell lines. J Exp Clin Cancer Res. BioMed Central Ltd; 2011;30: 91–102. doi:10.1186/1756-9966-30-91
11. Dhar S, Gu FX, Langer R, Farokhzad OC, Lippard SJ. Targeted delivery of cisplatin to prostate cancer cells by aptamer functionalized Pt(IV) prodrug-PLGA-PEG nanoparticles. Proc Natl Acad Sci U S A. 2008;105: 17356–17361. doi:10.1073/pnas.0809154105
12. Rixe O, Ortuzar W, Alvarez M, Parker R, Reed E, Paull K, et al. Carboplatin : Spectrum of Activity in Drug-Resistant Cell Lines and in the Cell Lines of the National Cancer Institute's Anticancer Drug Screen Panel. Biochem Pharmacol. 1996;52: 1855–1865.
13. Michels J, Vitale I, Galluzzi L, Adam J, Olaussen KA, Kepp O, et al. Cisplatin Resistance Associated with PARP Hyperactivation. Cancer Res . 2013;73 : 2271–2280.
14. Cox MM, Nelson DL. Lehninger Principles of Biochemistry. 5th ed. Freeman WH, editor. 2008.

15. Burger H, Zoumaro-Djayoon A, Boersma AWM, Helleman J, Berns EMJJ, Mathijssen RHJ, et al. Differential transport of platinum compounds by the human organic cation transporter hOCT2 (hSLC22A2). Br J Pharmacol. 2010;159: 898–908. doi:10.1111/j.1476-5381.2009.00569.x

16. Ishida S, Lee J, Thiele DJ, Herskowitz I. Uptake of the anticancer drug cisplatin mediated by the copper transporter Ctr1 in yeast and mammals. Proc Natl Acad Sci U S A. 2002;99: 14298–14302. doi:10.1073/pnas.162491399

17. Song I, Savaraj N, Siddik ZH, Liu P, Wei Y, Wu CJ, et al. Role of human copper transporter Ctr1 in the transport of platinum-based antitumor agents in cisplatin-sensitive and cisplatin-resistant cells. Mol Cancer Ther. 2005;3: 1543–1549.

18. Alderden RA, Hall MD, Hambley TW. The Discovery and Development of Cisplatin. J Chem Educ. 2006;83: 728–734.

19. Trzaska S. Cisplatin. Chem Eng News. 2005;83.

20. Jamieson ER, Lippard SJ. Structure, Recognition, and Processing of Cisplatin-DNA Adducts. Chem Rev. 1999;99: 2467–2498.

21. Todd RC, Lippard SJ. Inhibition of transcription by platinum antitumor compounds. Metallomics. 2009;1: 280–291. doi:10.1039/b907567d

22. Trudu F, Amato F, Vaňhara P, Pivetta T, Peña-Méndez EM, Havel J. Coordination compounds in cancer: Past, present and perspectives. J Appl Biomed. 2015; doi:10.1016/j.jab.2015.03.003

23. Pivetta T, Lallai V, Valletta E, Trudu F, Isaia F, Perra D, et al. Mixed copper–platinum complex formation could explain synergistic antiproliferative effect exhibited by binary mixtures of cisplatin and copper-1,10-phenanthroline compounds: An ESI–MS study. J Inorg Biochem. Elsevier Inc.; 2015; doi:10.1016/j.jinorgbio.2015.05.004

24. Niedermeyer THJ, Strohalm M. mMass as a software tool for the annotation of cyclic peptide tandem mass spectra. PLoS One. 2012;7: e44913. doi:10.1371/journal.pone.0044913

25. Strohalm M, Kavan D, Nova P, Volny M. mMass 3 : A Cross-Platform Software Environment for Precise Analysis of Mass Spectrometric Data. Anal Chem. 2010;82: 4648–4651.

26. Strohalm M, Hassman M, Kosata B, Kodicek M. RCM Letter to the Editor. Rapid Commun Mass Spectrom. 2008;22: 905–908. doi:10.1002/rcm

27. Wishart DS, Tzur D, Knox C, Eisner R, Guo AC, Young N, et al. HMDB: the Human Metabolome Database. Nucleic Acids Res. 2007;35: D521–6. doi:10.1093/nar/gkl923

28. Wishart DS, Knox C, Guo AC, Eisner R, Young N, Gautam B, et al. HMDB: a knowledgebase for the human metabolome. Nucleic Acids Res. 2009;37: D603–10. doi:10.1093/nar/gkn810

29. Wishart DS, Jewison T, Guo AC, Wilson M, Knox C, Liu Y, et al. HMDB 3.0--The Human Metabolome Database in 2013. Nucleic Acids Res. 2013;41: D801–7. doi:10.1093/nar/gks1065

30. Henderson W, McIndoe JS. Mass Spectrometry of Inorganic, Coordination and Organometallic Compounds [Internet]. Chichester, UK: John Wiley & Sons, Ltd; 2005. doi:10.1002/0470014318

31. http://www.sigmaaldrich.com/content/dam/sigma-aldrich/docs/Supelco/Product_Information_Sheet/t708008.pdf.

32. Vance DE, Vance JE. Biochemistry of Lipds, Lipoproteins and Membranes. 4th ed. Bernardi G, editor. Elsevier; 2002.

33. Adibhatla RM, Hatcher JF, Dempsey RJ. Citicoline: Neuroprotective mechanisms in cerebral ischemia. J Neurochem. 2002;80: 12–23. doi:10.1046/j.0022-3042.2001.00697.x

34. López-Coviella I, Agut J, Savci V, Ortiz JA, Wurtman RJ. Evidence that 5′-Cytidinediphosphocholine Can Affect Brain Phospholipid Composition by Increasing Choline and Cytidine Plasma Levels. J Neurochem. Blackwell Science Ltd; 1995;65: 889–894. doi:10.1046/j.1471-4159.1995.65020889.x

35. Conant R, Schauss AG. Therapeutic Applications of Citicoline for Stroke and Cognitive Dysfunction in the Elderly: A Review of the Literature. Altern Med Rev. 2004;9: 17–31.

36. Babb S, Wald L, Cohen B, Villafuerte R, Gruber S, Yurgelun-Todd D, et al. Chronic citicoline increases phosphodiesters in the brains of healthy older subjects: an in vivo phosphorus magnetic resonance spectroscopy study. Psychopharmacology (Berl). Springer-Verlag; 2002;161: 248–254. doi:10.1007/s00213-002-1045-y

37. Chanda B, Xia Y, Mandal MK, Yu K, Sekine K-T, Gao Q, et al. Glycerol-3-phosphate is a critical mobile inducer of systemic immunity in plants. Nat Genet. 2011;43: 421–427. doi:10.1038/ng.798

38. Agranoff B, Benjamins J, Hajra A. Basic Neurochemistry: Molecular, Cellular and Medical Aspects. In: Siegel GJ, Agranoff BW, Albers RW et al., editor. 6th editio. Philadelphia: Lippincott-Raven; 1999.

39. Brown D a., London E. Structure and function of sphingolipid- and cholesterol-rich membrane rafts. J Biol Chem. 2000;275: 17221–17224. doi:10.1074/jbc.R000005200

40. Venkataraman K, Futerman AH. Ceramide as a second messenger: Sticky solutions to sticky problems. Trends Cell Biol. 2000;10: 408–412. doi:10.1016/S0962-8924(00)01830-4

41. Voinov VG, Claeys M. Charge-remote fragmentation of fatty acid molecular anions: Examination by using resonance electron capture mass spectrometry. Int J Mass Spectrom. 2000;198: 23–32. doi:10.1016/S1387-3806(99)00267-5

42. Hsu F-F, Turk J. Electrospray ionization/tandem quadrupole mass spectrometric studies on phosphatidylcholines: The fragmentation processes. J Am Soc Mass Spectrom. 2003;14: 352–363. doi:10.1016/S1044-0305(03)00064-3

43. Smith PB, Snyder a P, Harden CS. Characterization of bacterial phospholipids by electrospray ionization tandem mass spectrometry. Anal Chem. 1995;67: 1824–1830.

Supporting Information.

IDENTIFICATION OF SPECIFIC PHOSPHOLIPIDS TO DIFFERENTIATE CISPLATIN-RESISTANT AND WILD TYPE CELLS IN LEUKEMIC (CCRF-CEM) AND OVARIAN CANCER (A2780).

Elisa Valletta[a], Elisabetta Pinna[b], Sarah Vascellari[b], Graziano Caddeo[a], Enzo Cadoni[a], Francesco Isaia[a], Alessandra Pani[b], Tiziana Pivetta[a*]

[a]Dipartimento di Scienze Chimiche e Geologiche, [b] Dipartimento di Scienze Biomediche, University of Cagliari, Cittadella Universitaria, 09042 Monserrato (CA) – Italy

* Corresponding author

Tiziana Pivetta, tpivetta@unica.it, 0039 070 675 44 73, fax 0039 070 584597.

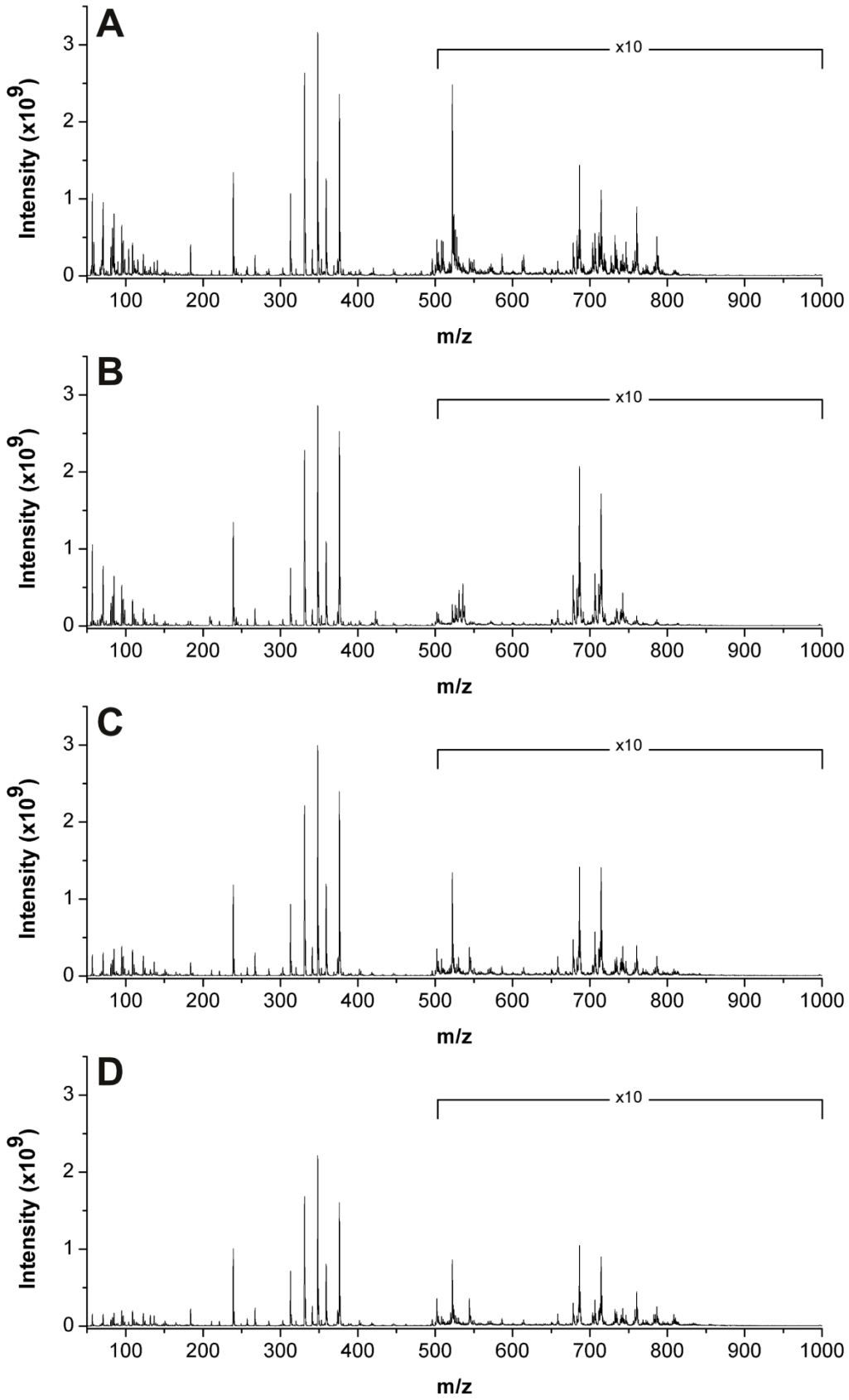

Fig. S1 ESI(+) mass spectra of the solution extracted from the supernatant fraction of CCRF-CEM-wt (**A**), CCRF-CEM-res (**B**), A2780-wt (**C**) and A2780-res (**D**) in the *m/z* 50–1000 range. The intensity of the signals in the *m/z* 500–1000 range was multiplied by a factor of 10 for clarity.

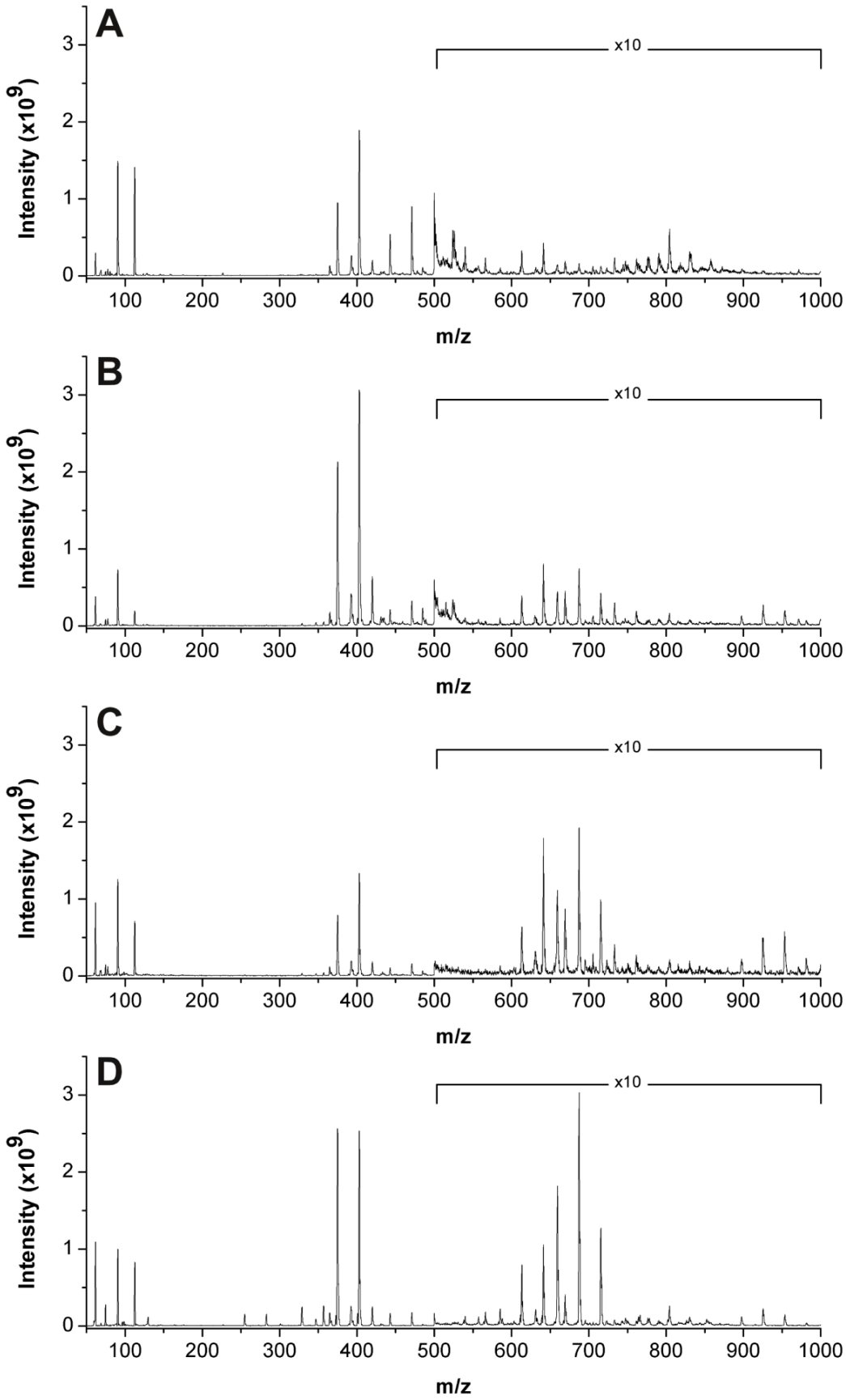

Fig. S2 ESI(-) mass spectra of the solution extracted from the supernatant fraction of CCRF CEM-wt (**A**), CCRF-CEM-res (**B**), A2780-wt (**C**) and A2780-res (**D**) in the *m/z* 50–1000 range. The intensity of the signals in the *m/z* 500–1000 range was multiplied by a factor of 10 for clarity.

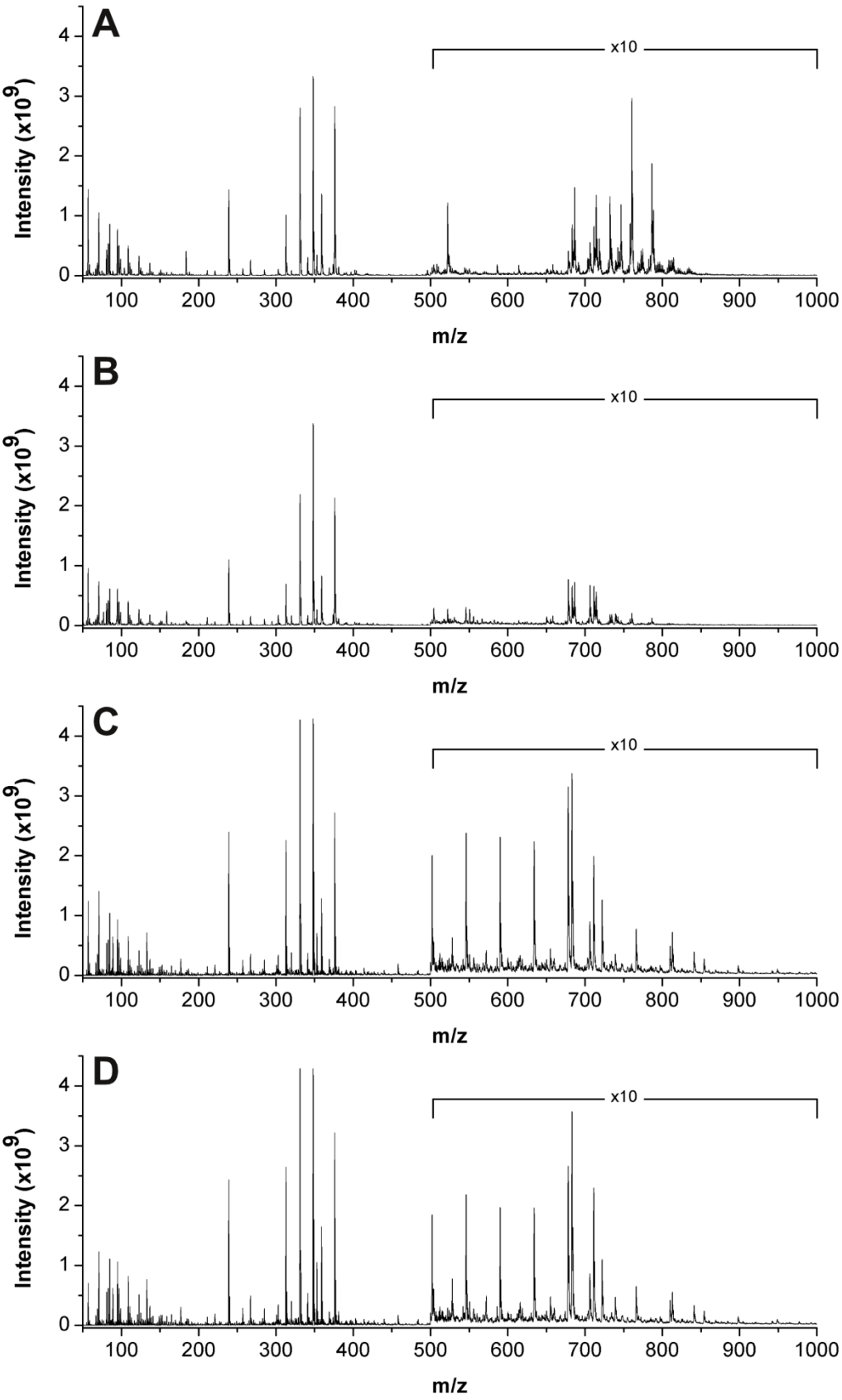

Fig. S3 ESI(+) mass spectra of the solution extracted from the pellet fraction of CCRF-CEM-wt (**A**), CCRF-CEM-res (**B**), A2780-wt (**C**) and A2780-res **(D)** in the *m/z* 50–1000 range. The intensity of the signals in the *m/z* 500–1000 range was multiplied by a factor of 10 for clarity.

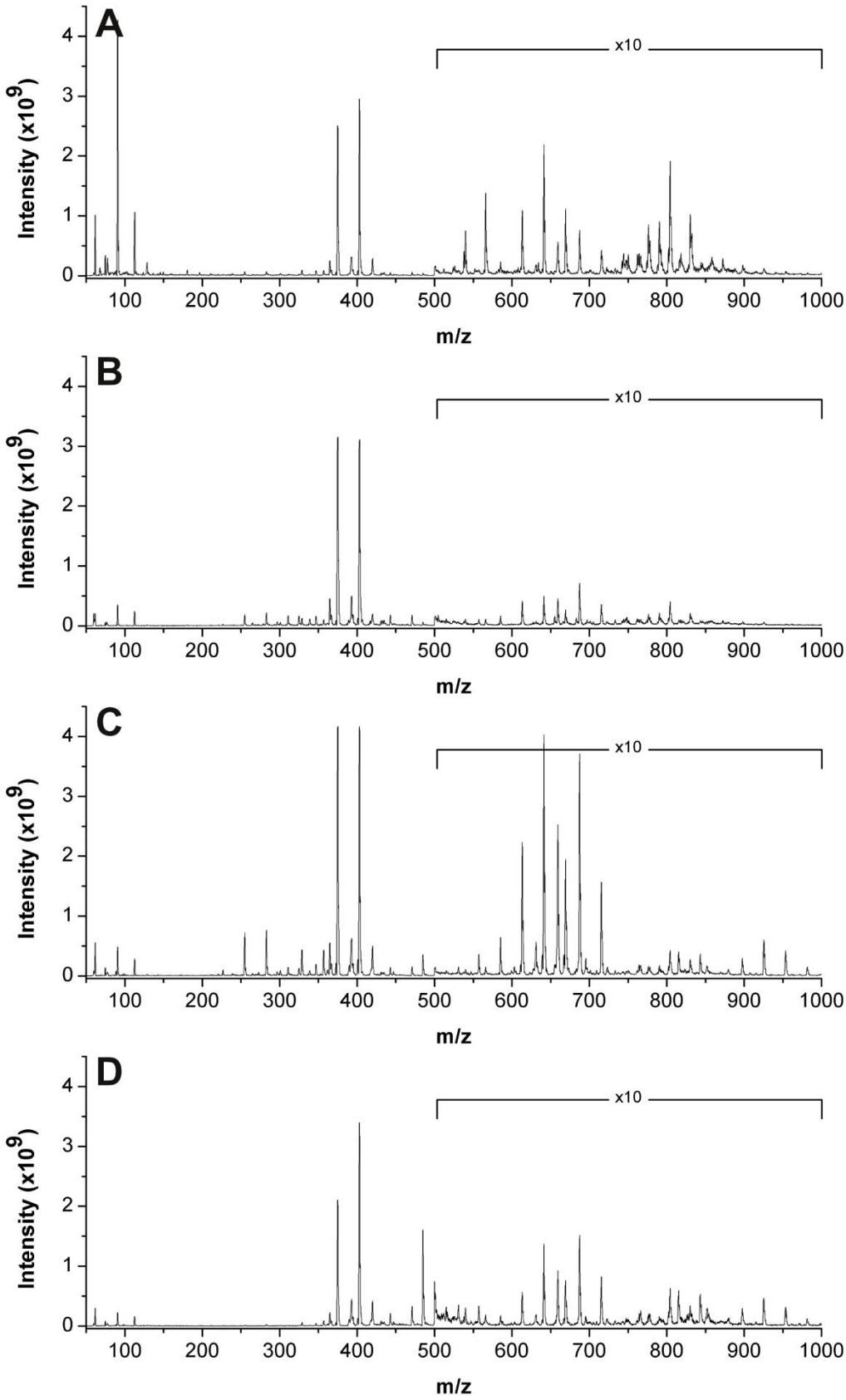

Fig. S4 ESI(-) mass spectra of the solution extracted from the pellet fraction of CCRF-CEM-wt (**A**), CCRF-CCRF-res (**B**), A2780-wt (**C**) and A2780-res (**D**) in the *m/z* 50–1000 range. The intensity of the signals in the *m/z* 500–1000 range was multiplied by a factor of 10 for clarity.

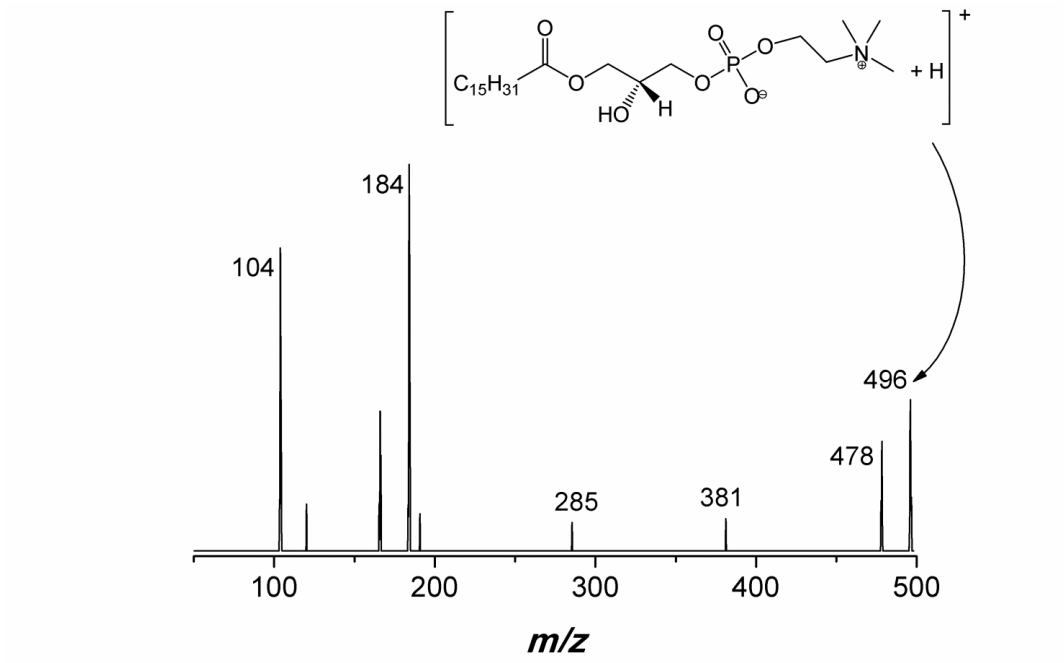

Fig. S5 Tandem MS-MS (+) spectrum of the *m/z* 496 peak. The structure of LysoPC(16:0) has been assigned based on the following considerations: *i*) correspondence between the molecular ion and the lipid present in the database; *ii*) loss of a water molecule resulting from the elimination of the free OH of the glycerol moiety and one of OH β protons; *iii*) presence of phosphocholinic ion at *m/z* 184 and cholinic ion at *m/z* 104 characteristicof this class of compounds; *iv*) the ions at *m/z* 381and *m/z* 285 generated by the loss of alkyl radicals are justified by the theory of charge-remote fragmentation [41]. The most probable structures of the fragments are reported in the Table S1.

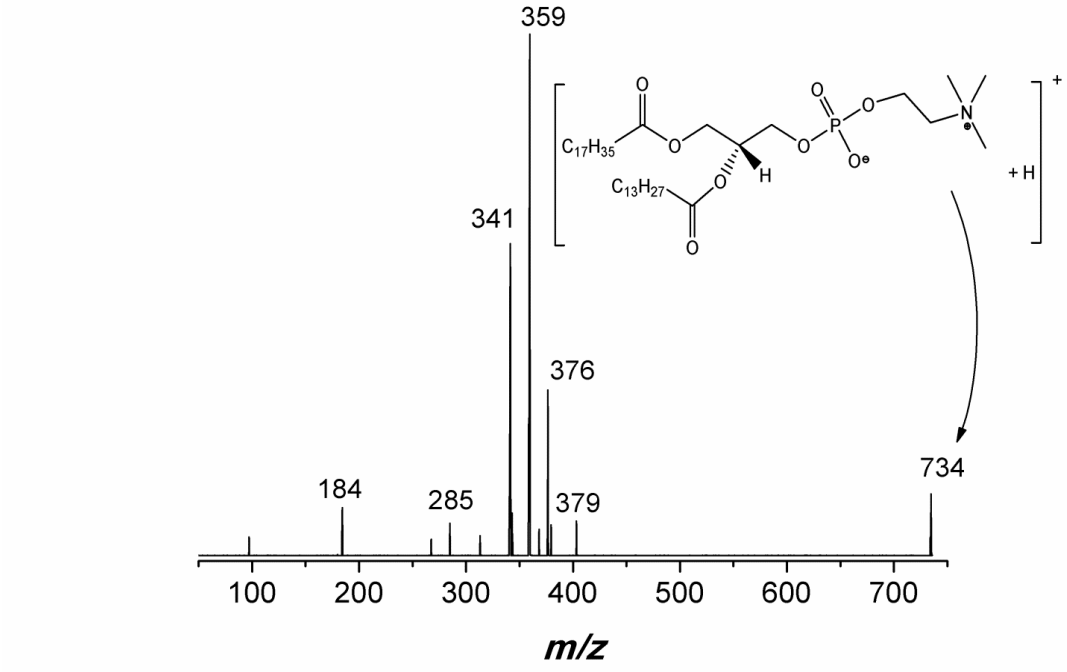

Fig. S6 Tandem MS-MS (+) spectrum of *m/z* 734 peak. Structure of PC(18:0/14:0) has been assigned based on the following considerations: *i*) correspondence among the molecular ion of the compound and those present in the database www.hmdb.ca; *ii*) peaks at *m/z* 379, 359, and 341 indicate the presence of the carboxylic chain with 18 carbon atoms, therefore, according to the data

base, this excludes the PC structure (16:0/16:0); *iii*) the peak at *m/z* 359 exclusively indicates the loss of the chain with 14 carbon atoms in the form of ketene, which is then eliminated more easily if it is in the *sn*-2 position [42]; *iv*) the presence of a phosphocholinic ion at *m/z* 184 is characteristic of this class of compounds. The most probable structures of the fragments are reported in the Table S3.

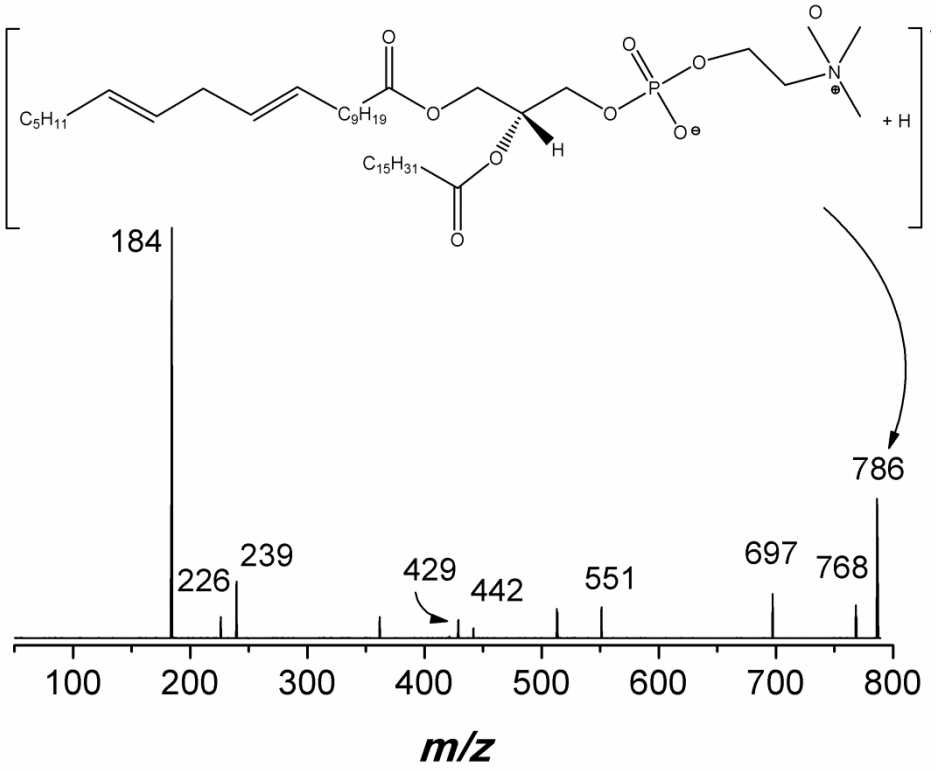

Fig. S7 Tandem MS-MS (+) spectrum of *m/z* 786 peak. A structure of PC(20:2(11Z,14Z)/16:0) has been assigned on the basis of the following considerations: *i*) correspondence among the molecular ion of the compound and those present in the database www.hmdb.ca; *ii*) loss of a water molecule resulting from the elimination of the OH arising from the enolic form of carboxylic acid moiety and one of OH β protons. The abundance of this ion is lower than the corresponding one found in the fragmentation of the LysoPC(16:0), where the free OH alcoholic group is present; *iii*) the peak at *m/z* 697 is originated by the loss of the ethanol-aminic group after transposition of a methyl of the amino group on an oxygen phosphate group; *iv*) the ion at *m/z* 551 could be tilting the balance towards the assignment of this spectrum at one of the two PC(18-18) present in the data base, but the peaks at *m/z* 442 and 429 clearly indicate the presence of fatty acids with 16 and 20 carbon atoms, respectively. Furthermore, the ion at *m/z* 239 can be assigned to the group with 16 carbon atoms rather than to the less stable saturated alkyl ion with 18 carbon atoms; *v*) presence of phosphocholinic ion at *m/z* 184 characteristic of this class of compounds; *vi*) the ion at *m/z* 514 generated by the loss of alkyl radicals from the ion at *m/z* 697 is justified by the presence of the chain with 16 atoms rather than 18 atoms due to the nearest charge being at the fragmentation point. The most probable structures of the fragments are reported in the Table S4.

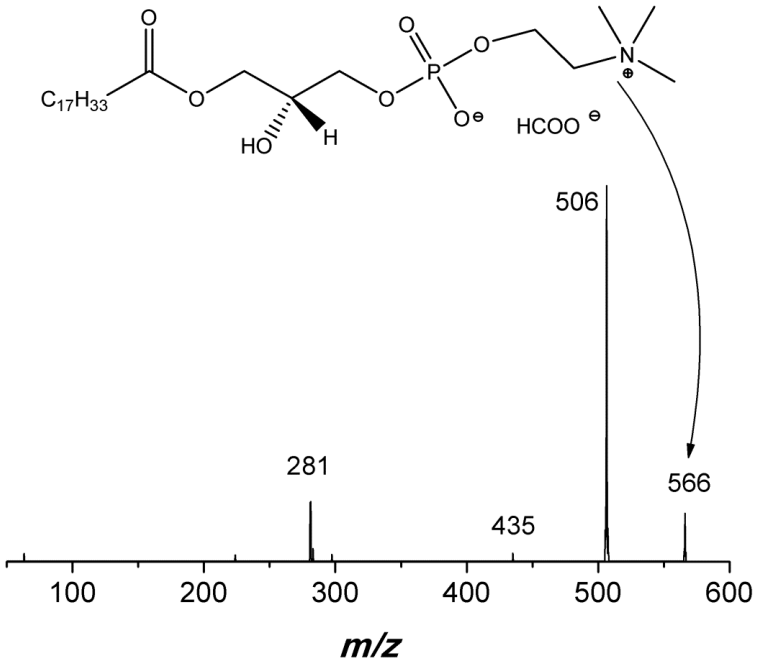

Fig. S8 Tandem MS-MS (-) spectrum of *m/z* 566 peak (LysoPC(18:1)+HCOO$^-$). The peak at *m/z* 506 allows us to identify the class of the lysoPC, while the peak at *m/z* 281 confirms the presence of the unsaturated acyl chain with 18 carbon atoms. The spectrum does not allow us to establish the position of the double bond. The most probable structures of the fragments are reported in the Table S2.

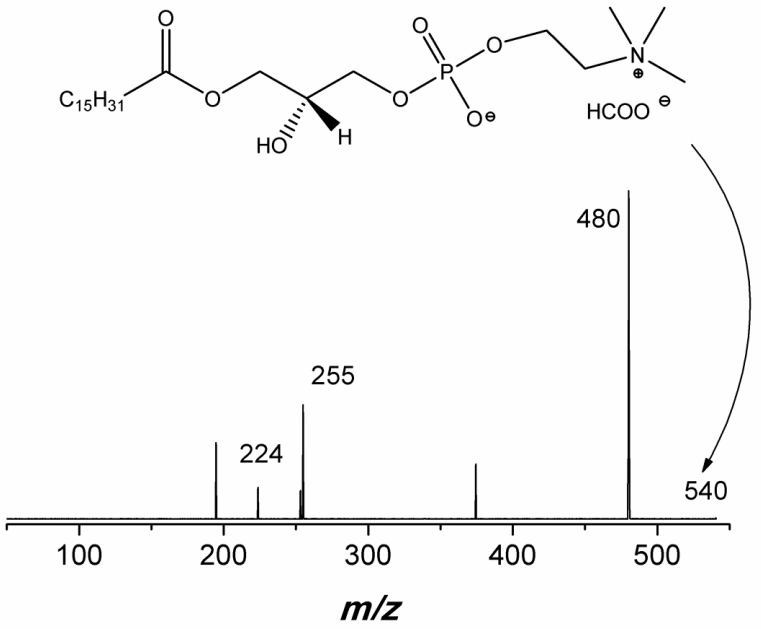

Fig. S9 Tandem MS-MS (-) spectrum of *m/z* 540 peak (LysoPC(16:0)+HCOO$^-$). The peak at *m/z* 480 allows us to identify the class of the lysoPC, while the peak at *m/z* 255 confirms the presence of the saturated acyl chain of 16 carbon atoms. The most probable structures of the fragments are reported in the Table S5.

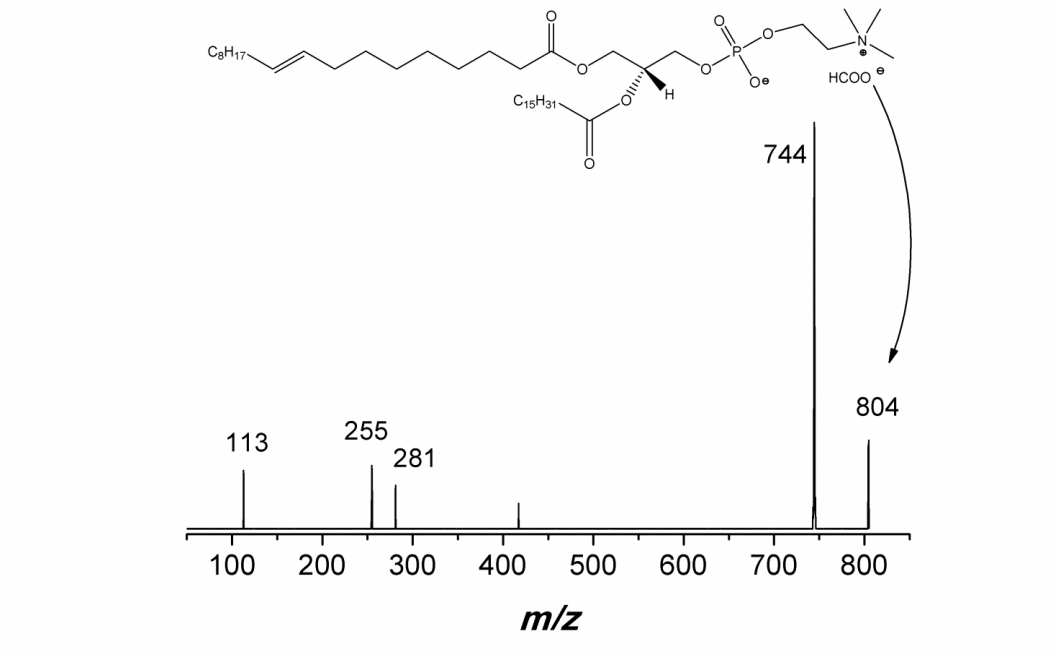

Fig. S10 Tandem MS-MS (-) spectrum of *m/z* 804 peak (PC(18:1/16:0)+HCOO$^-$). All the PC compounds in negative ionization mode and in the presence of formic acid exhibit the loss of 60 due to the methyl formiate. This peak allows us to identify the phospholipid as PC(34:1). The peaks at *m/z* 281 and 255 allow us to identify acyl chains with 18 and 16 carbon atoms, the latter with an unsaturation. The greater abundance of the peak at *m/z* 255, assigned to the chain with 16 carbon atoms, allows us to put this chain in the *sn*-2 position of the glycerol units [43]. The peak at *m/z* 113 allows us to tentatively assign the double bond position in the chain with 18 carbon atoms. In fact, its presence at position 9 favors the break between carbon atoms 6 and 7 due to the remote charge fragmentation. The most probable structures of the fragments are reported in the Table S6.

Table S1. Most probable structures of the fragments originated by the parent peak at *m/z* 496.

Ion	Ion mass	lose	lost mass
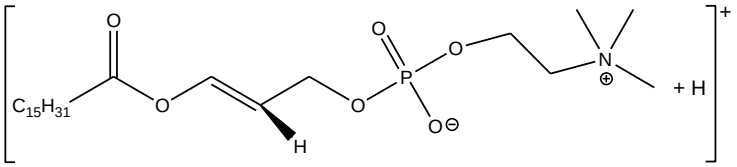	478	H_2O	18
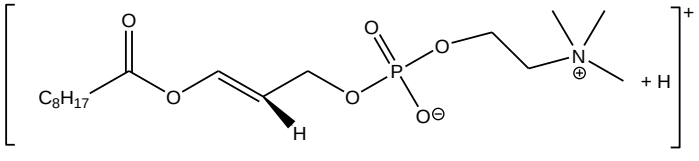	381	$CH_3(CH_2)_6 + H_2O$	115

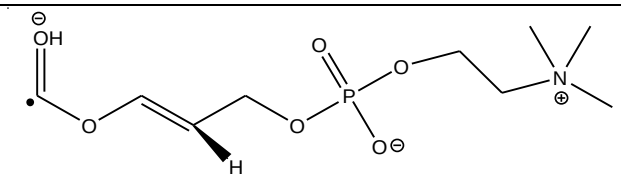	285	$CH_3(CH_2)_{14}$	211
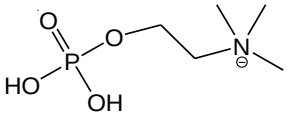	184	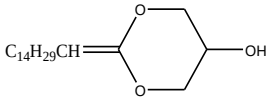	312
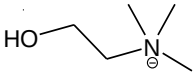	104	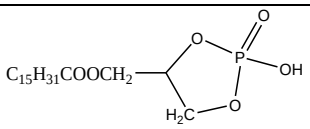	392

Table S2. Most probable structures of the fragments originated by the parent peak at *m/z* 560.

Ion	Ion mass	Lose	Lost mass
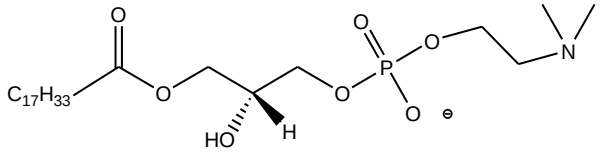	506	$HCOOCH_3$	60
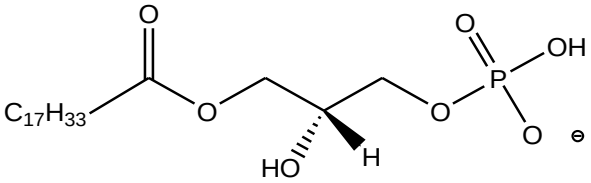	435	$HCOOCH_3$ + $CH_2CHN(CH_3)_2$	131
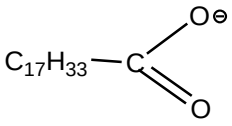	281	$HCOOCH_3$ + 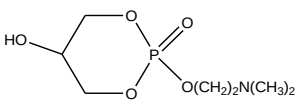	285

Table S3. Most probable structures of the fragments originated by the parent peak at *m/z* 734.

Ion	Ion mass	Lose	Lost mass
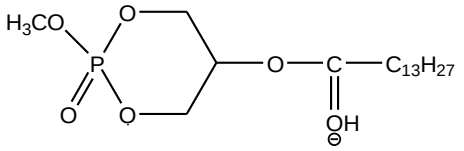	379	$C_{16}H_{33}CHCO$ + $N(CH_3)_2(CH_2)_2OH$	355
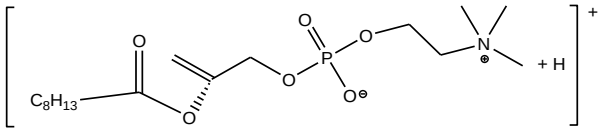	376	$C_{18}H_{35}COOH + C_5H_{12}$ + H_2	358
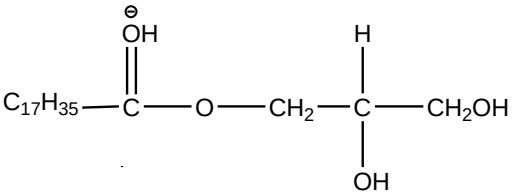	359	$C_{12}H_{25}CHCO$ + CH_3OPO_2 + $CH_2CHN(CH_3)_2$	375
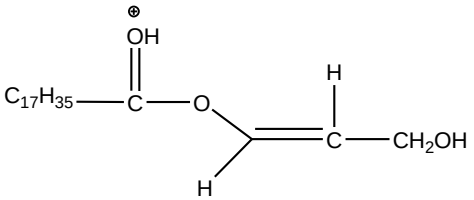	341	$C_{12}H_{25}CHCO$ + CH_3OPO_2 + $CH_2CHN(CH_3)_2$ + H_2O	393
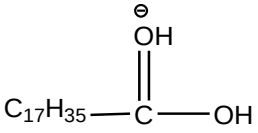	285		
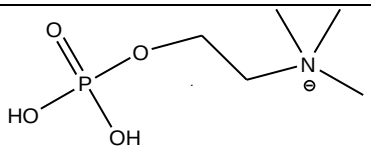	184		

Table S4. Most probable structures of the fragments originated by the parent peak at *m/z* 786.

Ion	Ion mass	Lose	Lost mass
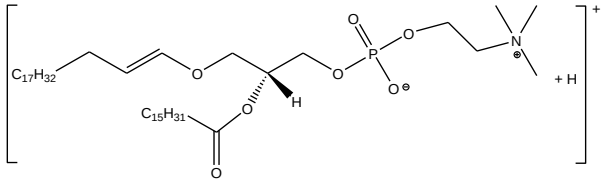	768	H_2O	18
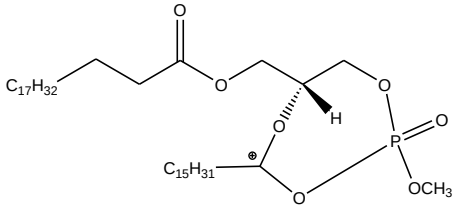	697	$N(CH_3)_2CH_2CH_2OH$	89
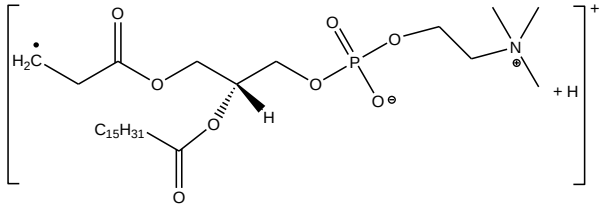	551	$C_{17}H_{31}$	235
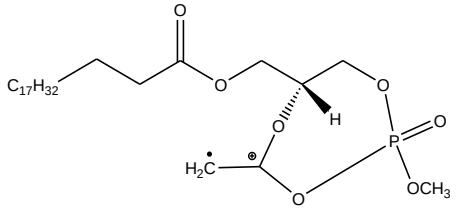	514	$N(CH_3)_2(CH_2)_2OH$ + $C_{13}H_{27}$	272
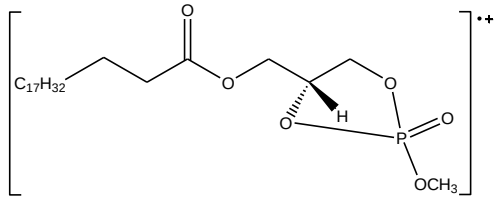	442	$N(CH_3)_2(CH_2)_2OH$ + $C_{15}H_{31}CO_2$	312
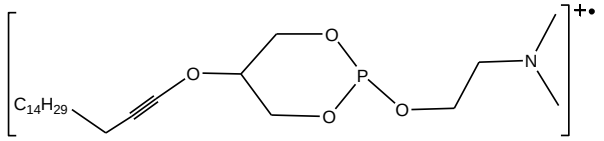	429	$H_2O + CH_3O$ + $C_{19}H_{35}CO_2H$	357
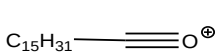	239	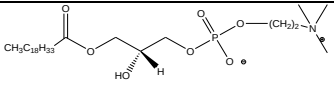	547

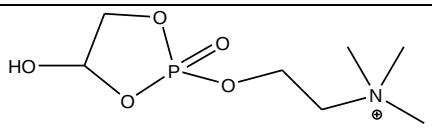	226
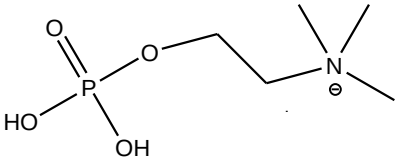	184

Table S5. Most probable structures of the fragments originated by the parent peak at *m/z* 540.

Ion	Ion mass	Lose	Lost mass
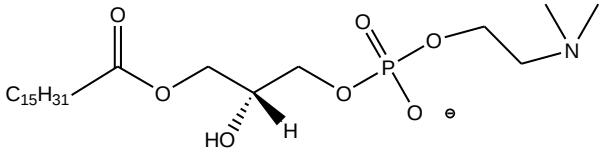	480	$HCOOCH_3$	60
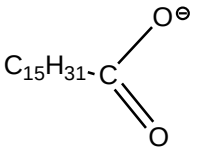	255	$HCOOCH_3$ + 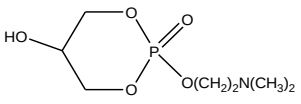	285
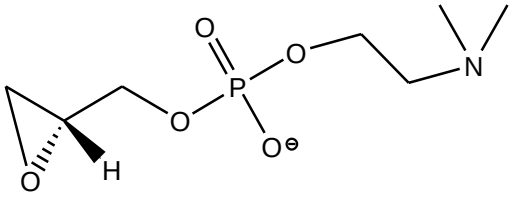	224		

Table S6. Most probable structures of the fragments originated by the parent peak at *m/z* 804.

Ion	Ion mass	Lose	Lost mass
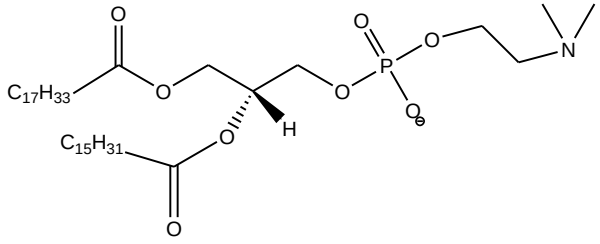	744	$HCOOCH_3$	60
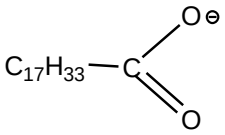	281	$HCOOCH_3$ + 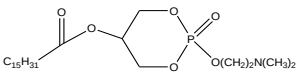	523
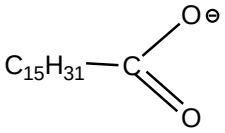	255	$HCOOCH_3$	549
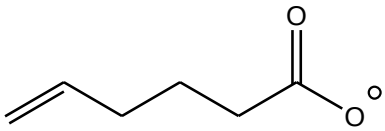	113	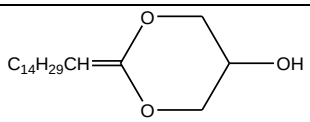	312

Chapter 6

Multivariate calibration approach for quantitative determination of cell-line cross contamination by intact cell mass spectrometry and artificial neural networks

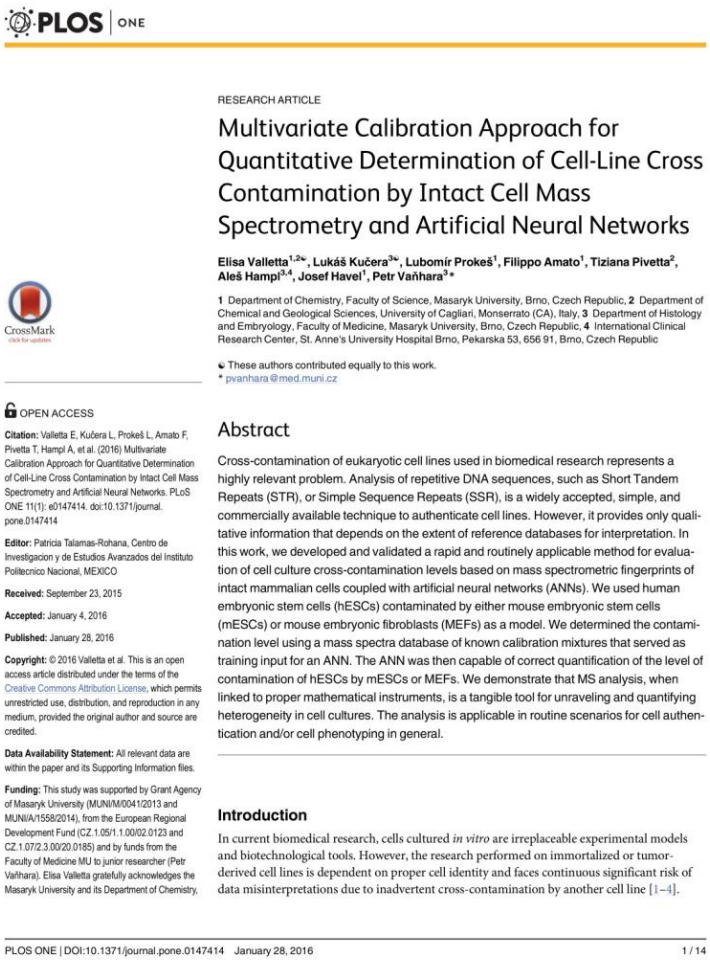

PLOS ONE

RESEARCH ARTICLE

Multivariate Calibration Approach for Quantitative Determination of Cell-Line Cross Contamination by Intact Cell Mass Spectrometry and Artificial Neural Networks

Elisa Valletta[1,2☯], Lukáš Kučera[3☯], Lubomír Prokeš[1], Filippo Amato[1], Tiziana Pivetta[2], Aleš Hampl[3,4], Josef Havel[1], Petr Vaňhara[3]*

1 Department of Chemistry, Faculty of Science, Masaryk University, Brno, Czech Republic, **2** Department of Chemical and Geological Sciences, University of Cagliari, Monserrato (CA), Italy, **3** Department of Histology and Embryology, Faculty of Medicine, Masaryk University, Brno, Czech Republic, **4** International Clinical Research Center, St. Anne's University Hospital Brno, Pekarska 53, 656 91, Brno, Czech Republic

☯ These authors contributed equally to this work.
* pvanhara@med.muni.cz

OPEN ACCESS

Citation: Valletta E, Kučera L, Prokeš L, Amato F, Pivetta T, Hampl A, et al. (2016) Multivariate Calibration Approach for Quantitative Determination of Cell-Line Cross Contamination by Intact Cell Mass Spectrometry and Artificial Neural Networks. PLoS ONE 11(1): e0147414. doi:10.1371/journal.pone.0147414

Editor: Patricia Talamas-Rohana, Centro de Investigacion y de Estudios Avanzados del Instituto Politecnico Nacional, MEXICO

Received: September 23, 2015

Accepted: January 4, 2016

Published: January 28, 2016

Data Availability Statement: All relevant data are within the paper and its Supporting Information files.

Funding: This study was supported by Grant Agency of Masaryk University (MUNI/M/0041/2013 and MUNI/A/1558/2014), from the European Regional Development Fund (CZ.1.05/1.1.00/02.0123 and CZ.1.07/2.3.00/20.0185) and by funds from the Faculty of Medicine MU to junior researcher (Petr Vaňhara). Elisa Valletta gratefully acknowledges the Masaryk University and its Department of Chemistry,

Abstract

Cross-contamination of eukaryotic cell lines used in biomedical research represents a highly relevant problem. Analysis of repetitive DNA sequences, such as Short Tandem Repeats (STR), or Simple Sequence Repeats (SSR), is a widely accepted, simple, and commercially available technique to authenticate cell lines. However, it provides only qualitative information that depends on the extent of reference databases for interpretation. In this work, we developed and validated a rapid and routinely applicable method for evaluation of cell culture cross-contamination levels based on mass spectrometric fingerprints of intact mammalian cells coupled with artificial neural networks (ANNs). We used human embryonic stem cells (hESCs) contaminated by either mouse embryonic stem cells (mESCs) or mouse embryonic fibroblasts (MEFs) as a model. We determined the contamination level using a mass spectra database of known calibration mixtures that served as training input for an ANN. The ANN was then capable of correct quantification of the level of contamination of hESCs by mESCs or MEFs. We demonstrate that MS analysis, when linked to proper mathematical instruments, is a tangible tool for unraveling and quantifying heterogeneity in cell cultures. The analysis is applicable in routine scenarios for cell authentication and/or cell phenotyping in general.

Introduction

In current biomedical research, cells cultured *in vitro* are irreplaceable experimental models and biotechnological tools. However, the research performed on immortalized or tumor-derived cell lines is dependent on proper cell identity and faces continuous significant risk of data misinterpretations due to inadvertent cross-contamination by another cell line [1–4].

Abstract

The *in vitro* cultured cell lines are widely used as models in biomedical research. However, the research performed on cultured cell is dependent on proper cell identity and continuously faces to significant risk of misinterpretations due to cross contamination. The cell-line cross contamination consists in the inadvertent inoculation of the desired cell line with another one, arising from improper handling during cellular splitting, medium sharing for multiple cell lines, and also in storage. Mouse embryonic fibroblasts cells (mEFs) are often used as feeder cells for the culture of human embryonic stem cells (hESCs) and can accidentally contaminate them. For over 50 years the problem of the cell-line cross-contamination has been underestimated and erroneous results and conclusions have been published. The ex-post discovery of such erroneous findings led to paper retraction, compromising both author's and journal's credibility. Although the issue of cell line misidentification is known for years in the scientific community, it is still a present matter. Nowadays, many high-impact journals started to adopt a zero-tolerance policy, requiring confirmation of cell line identity as prerequisite for publication. To check identity and cross-contamination of cell lines, methods such as DNA fingerprint analysis, karyotyping, isoenzyme analysis, immunotyping, human leukocyte antigen (HLA)-typing, and short tandem repeat (STR) profiling (this last accepted as international reference standard and used in the forensic field), are commonly used. However, all these methods do not allow the detection of interspecies contamination with a single technique able to provide all the information needed to completely identify a cell line. On the base of these considerations, a rapid and routinely applicable method for evaluation of cell culture cross contamination

levels, based on mass spectrometric fingerprints of intact mammalian cells coupled with artificial neural networks (ANNs), has been developed and validated (Figure 20) (Chapter 6 – Article III).

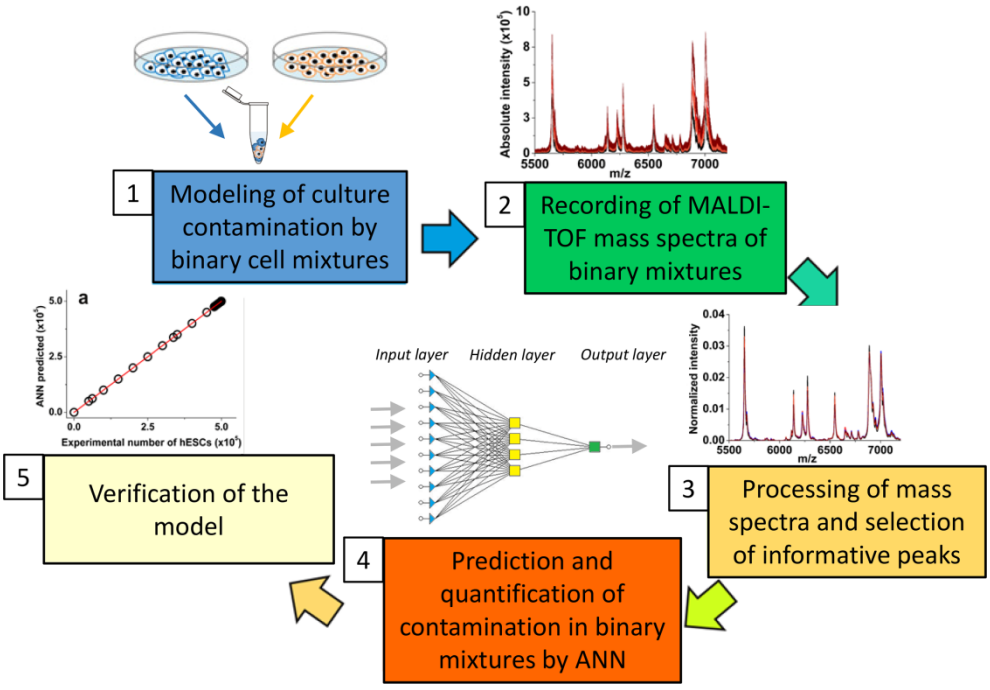

Figure 20. The development and validation of a method for the evaluation of the cell culture cross-contamination levels based on mass spectrometric fingerprints of intact mammalian cells coupled with artificial neural networks.

Human embryonic stem cells (hESCs) contaminated by either mouse embryonic stem cells (mESCs) or mouse embryonic fibroblasts (MEFs) have been used as a model. The contamination level has been determined using a mass spectra database of prepared calibration mixtures. The ANN was able to correct quantify the level of contamination of hESCs by mESCs or MEFs.

Article III

Multivariate calibration approach for quantitative determination of cell-line cross contamination by intact cell mass spectrometry and artificial neural networks

Elisa Valletta, Lukáš Kučera, Lubomír Prokeš, Filippo Amato, Tiziana Pivetta, Aleš Hampl, Josef Havel, Petr Vaňhara

Citation: PLoS ONE 11(1): e0147414

Cite this: DOI: 10.1371/journal.pone.0147414

Published by Public Library of Science

PLOS ONE

RESEARCH ARTICLE

Multivariate Calibration Approach for Quantitative Determination of Cell-Line Cross Contamination by Intact Cell Mass Spectrometry and Artificial Neural Networks

Elisa Valletta[1,2☯], Lukáš Kučera[3☯], Lubomír Prokeš[1], Filippo Amato[1], Tiziana Pivetta[2], Aleš Hampl[3,4], Josef Havel[1], Petr Vaňhara[3]*

1 Department of Chemistry, Faculty of Science, Masaryk University, Brno, Czech Republic, **2** Department of Chemical and Geological Sciences, University of Cagliari, Monserrato (CA), Italy, **3** Department of Histology and Embryology, Faculty of Medicine, Masaryk University, Brno, Czech Republic, **4** International Clinical Research Center, St. Anne's University Hospital Brno, Pekarska 53, 656 91, Brno, Czech Republic

☯ These authors contributed equally to this work.
* pvanhara@med.muni.cz

OPEN ACCESS

Citation: Valletta E, Kučera L, Prokeš L, Amato F, Pivetta T, Hampl A, et al. (2016) Multivariate Calibration Approach for Quantitative Determination of Cell-Line Cross Contamination by Intact Cell Mass Spectrometry and Artificial Neural Networks. PLoS ONE 11(1): e0147414. doi:10.1371/journal.pone.0147414

Editor: Patricia Talamas-Rohana, Centro de Investigacion y de Estudios Avanzados del Instituto Politecnico Nacional, MEXICO

Received: September 23, 2015

Accepted: January 4, 2016

Published: January 28, 2016

Data Availability Statement: All relevant data are within the paper and its Supporting Information files.

Funding: This study was supported by Grant Agency of Masaryk University (MUNI/M/0041/2013 and MUNI/A/1558/2014), from the European Regional Development Fund (CZ.1.05/1.1.00/02.0123 and CZ.1.07/2.3.00/20.0185) and by funds from the Faculty of Medicine MU to junior researcher (Petr Vaňhara). Elisa Valletta gratefully acknowledges the Masaryk University and its Department of Chemistry,

Abstract

Cross-contamination of eukaryotic cell lines used in biomedical research represents a highly relevant problem. Analysis of repetitive DNA sequences, such as Short Tandem Repeats (STR), or Simple Sequence Repeats (SSR), is a widely accepted, simple, and commercially available technique to authenticate cell lines. However, it provides only qualitative information that depends on the extent of reference databases for interpretation. In this work, we developed and validated a rapid and routinely applicable method for evaluation of cell culture cross-contamination levels based on mass spectrometric fingerprints of intact mammalian cells coupled with artificial neural networks (ANNs). We used human embryonic stem cells (hESCs) contaminated by either mouse embryonic stem cells (mESCs) or mouse embryonic fibroblasts (MEFs) as a model. We determined the contamination level using a mass spectra database of known calibration mixtures that served as training input for an ANN. The ANN was then capable of correct quantification of the level of contamination of hESCs by mESCs or MEFs. We demonstrate that MS analysis, when linked to proper mathematical instruments, is a tangible tool for unraveling and quantifying heterogeneity in cell cultures. The analysis is applicable in routine scenarios for cell authentication and/or cell phenotyping in general.

Introduction

In current biomedical research, cells cultured *in vitro* are irreplaceable experimental models and biotechnological tools. However, the research performed on immortalized or tumor-derived cell lines is dependent on proper cell identity and faces continuous significant risk of data misinterpretations due to inadvertent cross-contamination by another cell line [1–4].

for the kind hospitality and for funding her stay in Brno. The funders had no role in study design, data collection and analysis, decision to publish, or preparation of the manuscript.

Competing Interests: The authors have declared that no competing interests exist.

Contamination can easily occur by improper passaging, sharing of culture media for multiple cell lines, or inaccurate labeling and storage. Indeed, sophisticated techniques of cell culture and tissue engineering, such as high-throughput reactors, microfluidics, and stem cell or tissue cultures, require stringent monitoring of cell identity and phenotype stability [5–7]. The current gold standard for authentication of individual cell lines is analysis of Short Tandem Repeat sequences (STR) or Simple Sequence Repeats (SSR) widespread throughout the genome, since each cell line theoretically has a unique STR-profile [1,2]. In specific scenarios, such as co-culture setups of two cell lines, use of various cell populations derived from a single individual or from inbred strains, or the occurrence of phenotypic changes within STR- or otherwise stable cell lines, STR analysis cannot provide sufficient discrimination. Furthermore, in cases of intrinsic heterogeneity or impurity of cell cultures, co-culture setups, microsatellite instability, phenotype shifts, or viral or mycoplasma infections, STR analysis can provide ambiguous results, or, in the best case, allow only a qualitative assessment of cell identity without any information on the extent of contamination or heterogeneity in cell populations. Techniques that can complement STR authentication, such as identification of phenotype- or genotype-related markers, e.g. karyotype, isoenzymes, surface markers, or single nucleotide polymorphisms (SNPs) [8,9], are nevertheless dependent on preceding knowledge of the biological background of the model system used. Optimization of high-resolution methods common in physical and analytical chemistry and advanced mathematical modeling can circumvent the need for specific markers by analysis of global cellular or tissue patterns. Spectral techniques, such as Raman near-infrared or mass spectrometry were recently demonstrated to provide global fingerprints with sufficient capacity to distinguish diseased and normal tissues in models of metabolic disorders, or even individual states of cell differentiation or metabolism [10–13].

Matrix-assisted laser desorption/ionization–time of flight mass spectrometry (MALDI-TOF MS) has recently been used in fields beyond analytical and structural chemistry, such as biomedical research or clinical practice, and has been adapted for characterization of complex biological samples by peptide-mass-fingerprinting or peptide sequence tagging. Biotyping of non-fractioned intact microorganisms by MS is now a fast, routine, and cheap technique in clinical microbiology. Similarly, the concept of biotyping eukaryotic cells by intact cell (IC) MALDI-TOF MS has been suggested to allow identification of cell lines [13–18] or to characterize of physiological events occurring in the cells, such as terminal differentiation or programmed cell death [19]. The IC MALDI-TOF MS technique allows for recording the characteristic profiles of eukaryotic cells in quality sufficient for detailed analyses ranging from ultrastructural molecular cytology, to deep cell phenotyping and tissue analyses [13,15,18–22], to species recognition [23] and ecotoxicology [24,25].

However, a simple visual inspection of mass spectra is often not sufficient to establish an unambiguous cell line-specific set of biomarker peaks. Moreover, specific signal intensity and analytic concentration are not linear except in a narrow concentration range due to various stochastic "MALDI effects," such as variability in matrix/analyte interactions and energy dissipation or quenching or enhancing of ionization [26]. Mathematical methods that are successfully used in chemometrics, such as bivariate regression, polynomial fitting, multiple linear regression, partial least squares, and artificial intelligence, must therefore be applied in MS analysis of complex biological samples [27–29]. Artificial neural networks (ANNs) represent a robust and versatile mathematical tool for many applications in various fields [30]. ANNs mimic the "*learning*" and "*generalization*" abilities of human neural structures. ANNs are able to model highly complex non-linear systems and are used for classification, pattern recognition, modeling, and multivariate data analysis [31]. The basic units of ANNs are "*nodes*" or "*neurons*." They are organized in one "*input*" layer, in one or more "*hidden*" layers, and in one "*output*" layer. Each of the i-th neurons in a layer is linked to all the j-th neurons in the next layer. Each

connection is weighted with a weight w_{ij}. The role of the neurons in the input layer is to receive input data and transfer it to the neurons in the hidden layer through the weighted connections. The neurons in the hidden layer(s) perform mathematical operations on the incoming data (summation, addition of a "*bias*" term, and transformation by a suitable mathematical function). The result is then transferred to the neurons in the output layer where the ANN output is calculated.

Here we study the possibility of using ANNs to determine a quantity of cells of a particular cell line and/or type in two-component mixtures, mimicking a scenario of cell line cross-contamination. To create such situations, we used: a) line CCTL14 of human embryonic stem cells (hESCs), b) mouse embryonic fibroblasts (MEFs), and c) line R1 of mouse embryonic stem cell (mESCs). The cells were arranged into two-component calibration mixtures of hESCs + MEFs and hESCs + mESCs in various ratios. Line CCTL14 of hESCs has previously been thoroughly characterized [32]. MEFs freshly isolated from connective tissue of 11.5 days old mouse embryos are commonly used as a supportive feeder layer for hESCs in a routine co-culture mode. Mouse ESCs [33] represent pluripotent and self-renewing cells that are developmentally and functionally similar to hESCs.

The two-component cell suspensions were analyzed by ANN-coupled IC MALDI-TOF MS in a multivariate calibration approach. We demonstrate that mass spectra contain sufficient information to identify the presence of individual cell types in mixtures, and we report for the first time that ANN analysis of mass spectra from two-component mixtures can correctly predict the level of cell cross-contamination in very complex microenvironment.

Material and Methods

Chemicals

Knockout Dulbecco's modified Eagle's medium (DMEM), DMEM/F12, knockout serum replacement, fetal bovine serum, L-glutamine, minimum essential medium non-essential amino acids, penicillin-streptomycin, and TrypLE™ Select were purchased from Gibco, Life Technologies Czech Republic Ltd. (Prague, Czech Republic). Ammonium bicarbonate, sinapinic acid, trifluoroacetic acid, DMEM, 2-mercaptoethanol, phosphate buffered saline (PBS), and gelatin were purchased from Sigma-Aldrich Ltd. (Prague, Czech Republic). Matrigel™ was purchased from BD Bioscience, I.T.A.-Intertact Ltd. (Prague, Czech Republic). Fibroblast growth factor-2 was purchased from PeproTech, Baria Ltd. (Prague, Czech Republic). Leukemia Inhibitory Factor Protein was purchased from Chemicon, Merck Millipore (Prague, Czech Republic). Acetonitrile was purchased from J.T. Baker, VWR International Ltd. (Prague, Czech Republic). PepMix standard was purchased from Laser BioLabs (Sophia-Antipolis, France). Tissue culture dishes were purchased from TPP (Trasadingen, Switzerland).

Cell cultures

Mouse embryonic fibroblasts derived from CF1-mouse embryos were cultured in tissue culture dishes in medium consisting of Knockout DMEM supplemented with 10% fetal bovine serum, 2 mM L-glutamine, 1% minimum essential medium non-essential amino acids, 1% penicillin-streptomycin, and 0.1 mM 2-mercaptoethanol as described previously [34,35]. Human embryonic stem cells [36,37] were cultured in the undifferentiated state in tissue culture dishes coated with Matrigel™ in culture media conditioned by MEFs consisting of DMEM/F12 supplemented with 15% knockout serum replacement, 2 mM L-glutamine, 1% minimum essential medium non-essential amino acids, 0.5% penicillin-streptomycin, 0.1 mM 2-mercaptoethanol, and 4 ng/ml fibroblast growth factor-2. Mouse embryonic stem cells [33] were cultured in tissue culture dishes coated with 0.1% gelatin in medium consisting of DMEM supplemented

with 20% fetal bovine serum, 1% minimum essential medium non-essential amino acids, 1% penicillin-streptomycin, 1 mM 2-mercaptoethanol and 5.5 μg/ml leukemia inhibitory factor (LIF). All cell lines were maintained in an incubator at 37°C with a humidified atmosphere containing 5% CO_2, with daily media exchange.

Sample preparation

Cultured cells were washed with 1×PBS and enzymatically disaggregated to single cell suspension using TrypLE™ Select. After 2 min, the enzymatic activity was stopped by the respective culture medium. Detached cells were pelleted by centrifugation at 200 g for 5 min and washed once again with 1×PBS. Cell number was determined by CEDEX XS cell counter operated with CEDEX Control Center software v. 1.0.3. from Innovatis AG, Roche Life Sciences (Prague, Czech Republic).

Preparation of cell mixtures for MS analysis

hESCs + MEFs mixture. Cell suspensions containing a total of 1×10^6 hESCs and MEFs in 1×PBS in defined ratios were pelleted by centrifugation at 200 g for 5 min at 4°C and washed three times with an aqueous solution of 150 mM ammonium bicarbonate. Then, the cell pellets were resuspended in 10 μl of 150 mM ammonium bicarbonate and mixed with 5 μl of freshly prepared sinapinic acid matrix (30 mg/ml in 70% acetonitrile and 7.5% trifluoroacetic acid). Two microliters of sample/matrix mixture were immediately spotted in pentaplicates onto the MALDI target and dried at room temperature.

hESCs + mESCs mixture. Aliquots of 1×10^6 mESCs or hESCs in 1×PBS were pelleted by centrifugation at 200 g for 5 min at 4°C. Supernatant was discarded and pelleted cells were washed three times with 150 mM ammonium bicarbonate solution. Resulting cell pellets were then snap-frozen and stored until further processing. At the time of analysis, both mESCs and hESCs aliquots were quickly thawed and reconstituted in 20 μl of 150 mM ammonium bicarbonate solution and sonicated briefly in a water ultrasound bath. Then, MEFs and hESCs were mixed in given ratios to a total of 0.5×10^6 cells per sample and total volume was adjusted to 15 μl with 150 mM ammonium bicarbonate. Each cell suspension was mixed with 7.5 μl of freshly prepared sinapinic acid matrix solution. Two microliters of sample/matrix mixture were immediately spotted onto the MALDI target and dried at room temperature. Each sample was spotted in five technical replicates.

Mass spectrometry

Mass spectra were recorded on an AXIMA CFR mass spectrometer from Kratos Analytical (Manchester, UK) in linear positive ion mode. The instrument was equipped with a nitrogen laser (337 nm) and delayed extraction was used. The laser energy was expressed in arbitrary units from 0 to 180 a.u. The power of the laser at 180 a.u. was 6 mW, while the irradiated spot size was approximately 150 μm in diameter. External mass calibration was done using the Pep-Mix4 standard. The laser repetition rate was 5 Hz with a pulse time width of 3 ns. Each mass spectrum was obtained by the accumulation of at least 5000 shots. In order to decrease the contribution of chemical noise and possible errors on the baseline and in calibration, the raw mass spectra were pre-processed, cleaned, transformed, and reduced in dimensionality before the data analysis, as described elsewhere [38].

Mass spectra were analyzed using Launchpad Software (Kompact version 2.9.3, 2011) from Kratos Analytical Ltd. Pre-processing of mass spectra and ANN computation were performed using MATLAB 8.6. 2015 from The MathWorks Inc. (Natick, Massachusetts, USA) and Trajan Neural Network Simulator, Release 3.0 D 1996–1998, from Trajan Software Ltd. (Durham, U.

K.). Partial least squares projection to latent structures regression was performed with "leave-one-out" cross-validated prediction in program R (www.r-project.org) using the external *pls* library [39].

Artificial neural networks

We constructed an artificial neural network containing four neurons in one hidden layer. The intensities of processed mass spectra served as the input, while the number of contaminating cells in the two-component mixtures was the output. The "*learning*" of the ANN was performed using the back-propagation training algorithm as described elsewhere [40,41]. The back-propagation was achieved by iteratively adjusting the values of connection weights in order to minimize the difference between the ANN calculated output value (o^*_{pk}) and the experimental one (o_{pk}). After each iteration, the root mean square of the sum of $(o_{pk} - o^*_{pk})^2$ residuals (RMS) was calculated according to Eq 1:

$$\mathrm{RMS} = \sqrt{\frac{\sum_{p=1}^{N}\sum_{k=1}^{M}\left(o_{pk} - o^*_{pk}\right)^2}{N \times M}} \quad (1)$$

where N is the number of mass spectra, M is the number of outputs, o^*_{pk} is the ANN calculated, and o_{pk} is the experimental output value. The optimal ANN architecture was confirmed by plotting the RMS value against the number of neurons in the hidden layer(s) and number of training cycles (epochs).

Results And Discussion

Preparation of two-component mixtures of different cell types and intact cell MALDI-TOF mass spectrometry

We prepared calibration datasets consisting of twenty-eight defined two-component mixtures of hESCs + MEFs, thirty-four mixtures of hESCs + mESCs (**Fig 1A and 1D**), and pure cell populations, with total cell numbers of 1×10^6 (**Fig 1B and 1E**). We then recorded the mass spectra of two-component cell mixtures and pure cell populations in the 2000–20000 m/z range without previous fractionation or extraction. We pre-processed the mass spectra by *(i)* resampling to 30000 m/z values (homogenizing in a chosen range and reducing the number of m/z values), *(ii)* aligning (removing the systematic shifts in mass spectra of repeated experiments), *(iii)* baseline subtraction, *(iv)* smoothing, and *(v)* normalization to a vector of unit length ($\mathbf{\Sigma X_i = 1}$), where X_i are the intensities of the peaks of the mass spectrum) [42] (**Fig 1C and 1F**, **S1 Fig**). Next, we organized the spectral data into a matrix with dimensions $m \times n$, where m represents the number of the mass spectrum of the particular cell mixture and n are the m/z values. The *i-th* row of the matrix represents the mass spectrometric fingerprint of the *i-th* mixture. In order to decrease the latent noise in pre-processed mass spectra, we selected only the peaks with intensity higher than an arbitrarily set threshold (1×10^{-3}) for further analysis. Thus, the data matrices of hESCs + MEFs and hESCs + mESCs were reduced from the original $n \times 30000$ to $n \times 84$ and $n \times 122$, respectively. Next, we identified peaks with the highest intrinsic variability in the datasets, as described elsewhere [43–46]. In brief, we selected informative peaks by comparative determination of standard deviations of individual peaks normalized to the total variance of the dataset, Lasso regression, and sparse partial least squares regression. The informative peaks are visualized in **S3 Fig**. That allowed us to finally reduce the data matrices of hESCs + MEFs and hESCs + mESCs to $n \times 10$ and $n \times 30$, respectively (**S1 Table**).

Then, we used these datasets to perform principal component analysis aiming to discriminate the pure hESC and MEF cell populations and the cell mixtures containing 50% of each cell

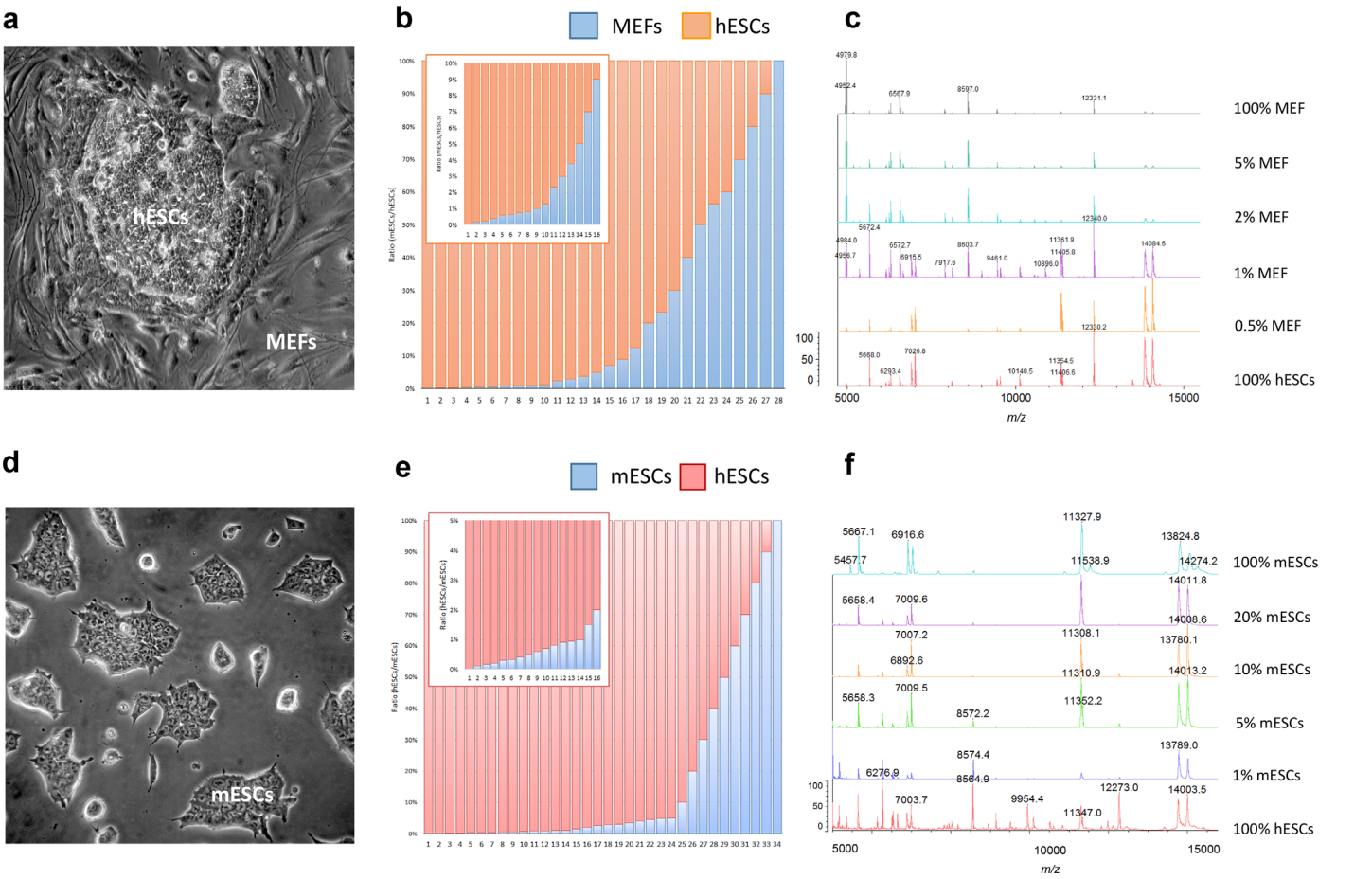

Fig 1. (A) Colony of human embryonic stem cells (hESCs) cultured on a feeder layer of mouse embryonic fibroblasts. (B) Experimental ratios of two-component mixtures of hESCs + MEFs. (C) Representative mass spectra of selected two-component mixtures of hESCs + MEFs. (D) Colony of mouse embryonic stem cells (mESCs) in a feeder-free culture. (E) Experimental ratios of two-component mixtures of hESCs + mESCs. (F) Representative mass spectra of selected two-component mixtures of hESCs + mESCs.

doi:10.1371/journal.pone.0147414.g001

type. Eigenvalue analysis showed the presence of three factors contributing up to 94% of the overall variability. Plotting the principal components revealed three clearly separated clusters and provided proof of principle for the discriminative information of the MEF and hESC mass spectra (Fig 2A and 2B). Similar discrimination was achieved for mESCs and hESCs (data not shown).

Next, we visually compared mass spectra obtained from the pure hESCs and MEFs, and their two-component mixtures. Despite the high similarity of the mass spectra, we identified peaks unique to hESCs and MEFs (m/z 3992 and 9908) (Fig 2C) appearing reproducibly over various mixtures. We presumed that if these two marker peaks are informative for MEFs, their intensities should be proportional to the content of MEFs in the two-component mixtures. However, we did not identify any linear trend between the normalized intensities of these two marker peaks and the percentage of MEFs, especially in two-component mixtures with low concentrations of MEFs (Fig 2D). In the case of highly similar pluripotent cell types, the mass spectra of hESCs + mESCs mixtures lacked any spectral patterns specific for individual pure cell lines (Fig 1F). Therefore, assessment of the individual biomarker peaks was not suitable for precise and unambiguous quantification.

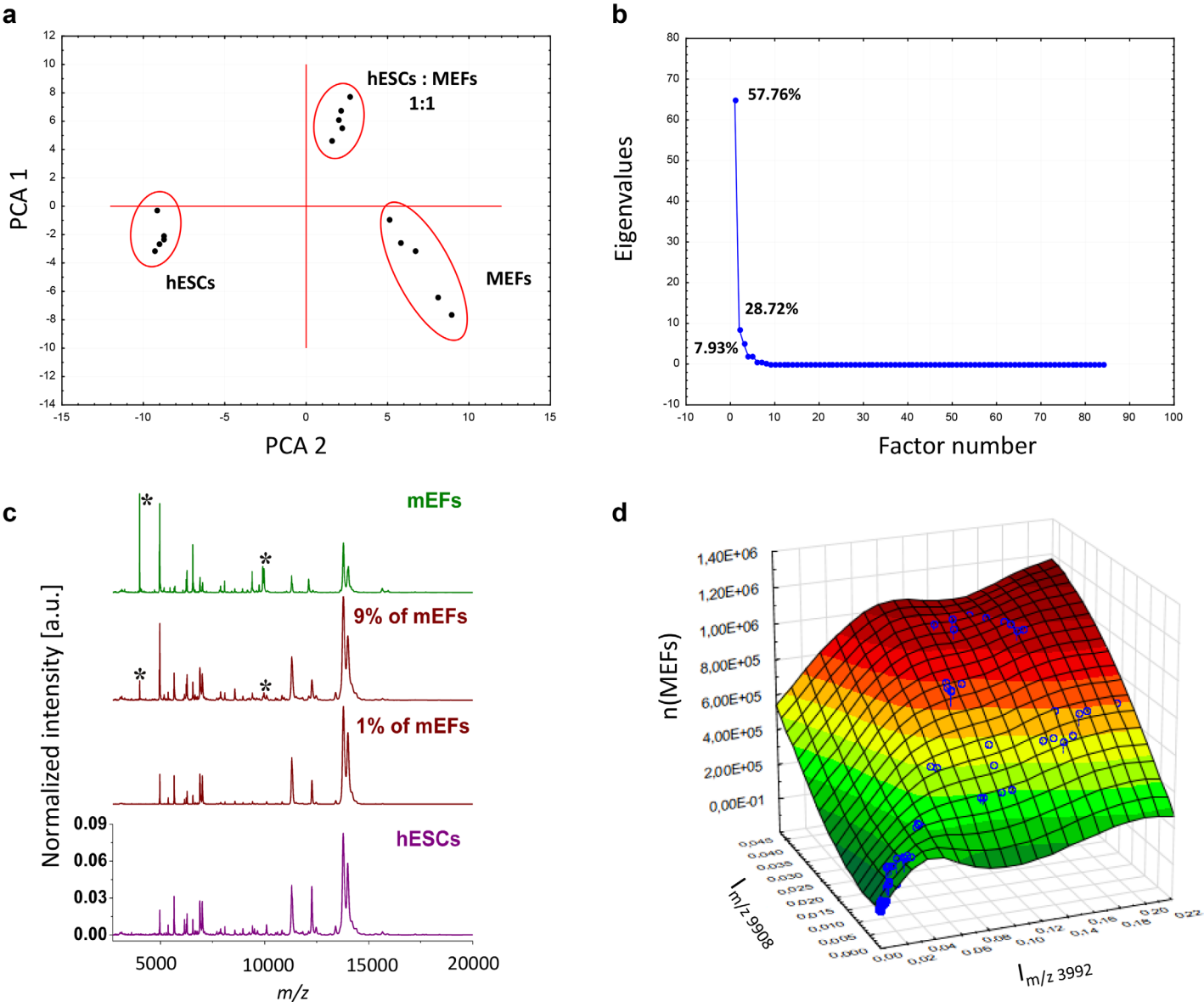

Fig 2. (A) Principal component analysis of mass spectra dataset containing intensities of 84 m/z for pure MEF and hESC populations and their 1:1 mixture. (B) Scree plot documenting the presence of three factors contributing predominantly to the overall variability in the analyzed dataset. (C) Pre-processed MALDI-TOF mass spectra for pure hESCs and MEFs and a hESCs + MEFs two-component mixture containing 99% hESCs and 1% MEFs. The spectra were normalized to vector of unit length (a.u.). Asterisks indicate peaks at m/z 3992 and 9908. (D) Surface plot of intensities of peaks at m/z 3992 and 9908 versus the number of MEFs in hESCs + MEFs two-component mixtures.

doi:10.1371/journal.pone.0147414.g002

Quantitative determination of contamination levels

Because of the data complexity, it was difficult to handle the mass spectral datasets by simple linear analyses. We first examined the data by a method of partial least squares with projection to latent structures regression (PLS) on the full data matrix of the complete mass spectra. PLS has been developed and extended by Herman and Svante Wold, respectively, [47] for quantitative analysis of highly complex multivariate data and is used preferentially in chemometrics. Despite a correlation between predicted and actual cell percentages in the two-component mixtures, the prediction precision by PLS was rather low, with substantial root mean square error

Table 1. Values of RMS calculated as differences between predicted and observed values, *k* (regression coefficients), and R^2 (determination coefficient).

	hESCs: MEFs		hESCs: mESCs	
	PLS	ANN	PLS	ANN
RMS	51.7×10^3	3.16×10^3	96.6×10^3	7.1×10^3
k	0.976	0.996	0.601	0.975
R^2	0.9759	0.9992	0.6010	0.9822

doi:10.1371/journal.pone.0147414.t001

(RMS) showing signs of systematic trends (Table 1, S3 Fig). Therefore, we asked whether non-linear approaches and artificial intelligence methods, such as ANNs, could make predictions with more precision. ANNs were previously reported to provide effective analysis and classification of biological, clinical or bioanalytical, and chemometric non-linear data (for review see [30]), and were found particularly suitable for analysis of MS data [28].

In our analysis the intensities of the selected peaks comprised the ANN-input data and the number of MEFs and/or mESCs cells in the hESC calibration mixtures was the ANN-output data. For the training step of the ANN, we tested several algorithms and found the back-propagation algorithm to be the most suitable (data not shown). We determined the optimal architecture containing four neurons in one hidden layer (Fig 3A) by plotting the RMS against the number of nodes (data not shown) and we validated over 100000 training cycles (epochs), without overfitting the model (Fig 3B). We used the leave-one-out cross-validation method to test the "*generalization*" ability of the designed network to predict the single cases excluded

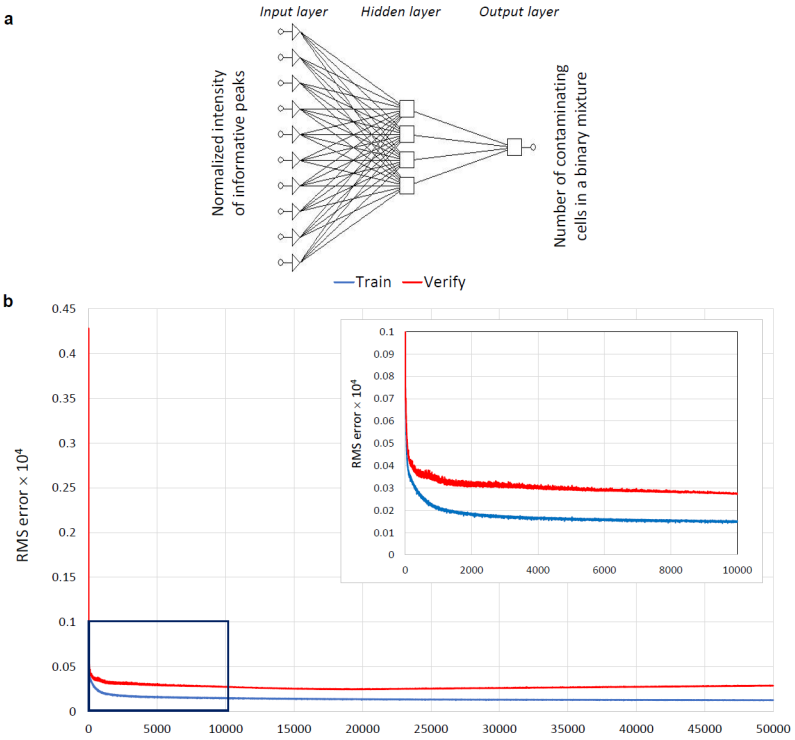

Fig 3. (A) Optimal ANN architecture (one Input layer, one Hidden layer with four neurons, and one Output layer). (B) Training and leave-one-out verification plot of the RMS versus the number of training cycles (epochs). First 50 000 iterations are shown. The inset shows a detailed plot for the first 10 000 training cycles.

doi:10.1371/journal.pone.0147414.g003

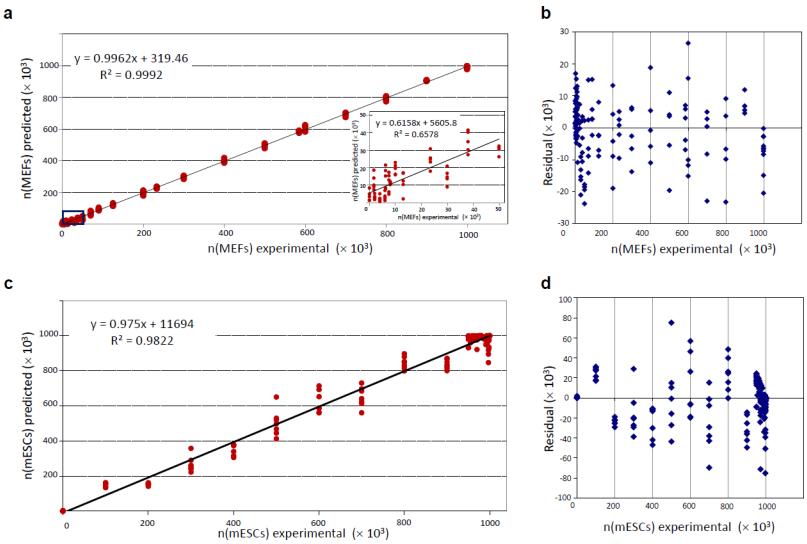

Fig 4. (A) Correlation between ANN-predicted number of cells and the experimental number of MEFs in two-component mixtures of hESCs + MEFs. The inset shows the correlation between experimental and predicted values in low concentration ranges of MEFs up to the $50{\times}10^3$ cells in the two-component mixtures. (B) Overview of Residuals (difference between ANN-predicted number of cells and the experimental values) versus the experimental number of MEF cells in two-component mixtures of hESCs + MEFs. (C) Correlation between ANN-predicted number of cells and the experimental number of mESCs in two-component mixtures of hESCs + mESCs. (D) Overview of Residuals (difference between ANN-predicted number of cells and the experimental values) versus the experimental number of mESC cells in the two-component mixtures of hESCs + mESCs.

doi:10.1371/journal.pone.0147414.g004

from the training data set. We used the RMS as a measure of the prediction accuracy. The network was able to evaluate the input data and correctly predict the number of MEFs (Fig 4A) and mESCs (Fig 4C) in the hESC suspensions over the whole range of evaluated ratios. Prediction by ANN was correct even at low percentages of contaminating cells in suspension. To validate the model, the RMS was calculated as the differences between the predicted and experimental values. The residuals reached significantly lower values than in PLS predictions (Table 1). Moreover, the residual values were randomly distributed, and the absence of any systematic error or trend in residuals demonstrated correctness of the model (Fig 4B and 4D). To perform further validation of the method, we analyzed an independent dataset of fifty hESCs + MEFs mixtures. Using a training set described above, the ANN correctly determined the numbers of MEFs in hESCs suspension with high correlation between predicted and experimental values (S4 Fig). In summary, multivariate calibration coupled with a correctly trained ANN was able to determine the ratio of cell numbers in two-component mixtures.

We have identified the conditions and developed a step-by-step protocol for successful quantitation of two distinct cell types in a single two-component mixture by a multivariate calibration approach based on an ANN-coupled IC MALDI-TOF MS analysis. The major steps of the method include:

1. *a priori* knowledge or identification of the contaminating cell line
2. construction of two-component calibration mixtures of the given cell lines
3. mass spectra pre-processing and m/z selection
4. parallel recording of mass spectra of pure cell populations and calibration mixtures and building a library of spectral datasets for multivariate calibration

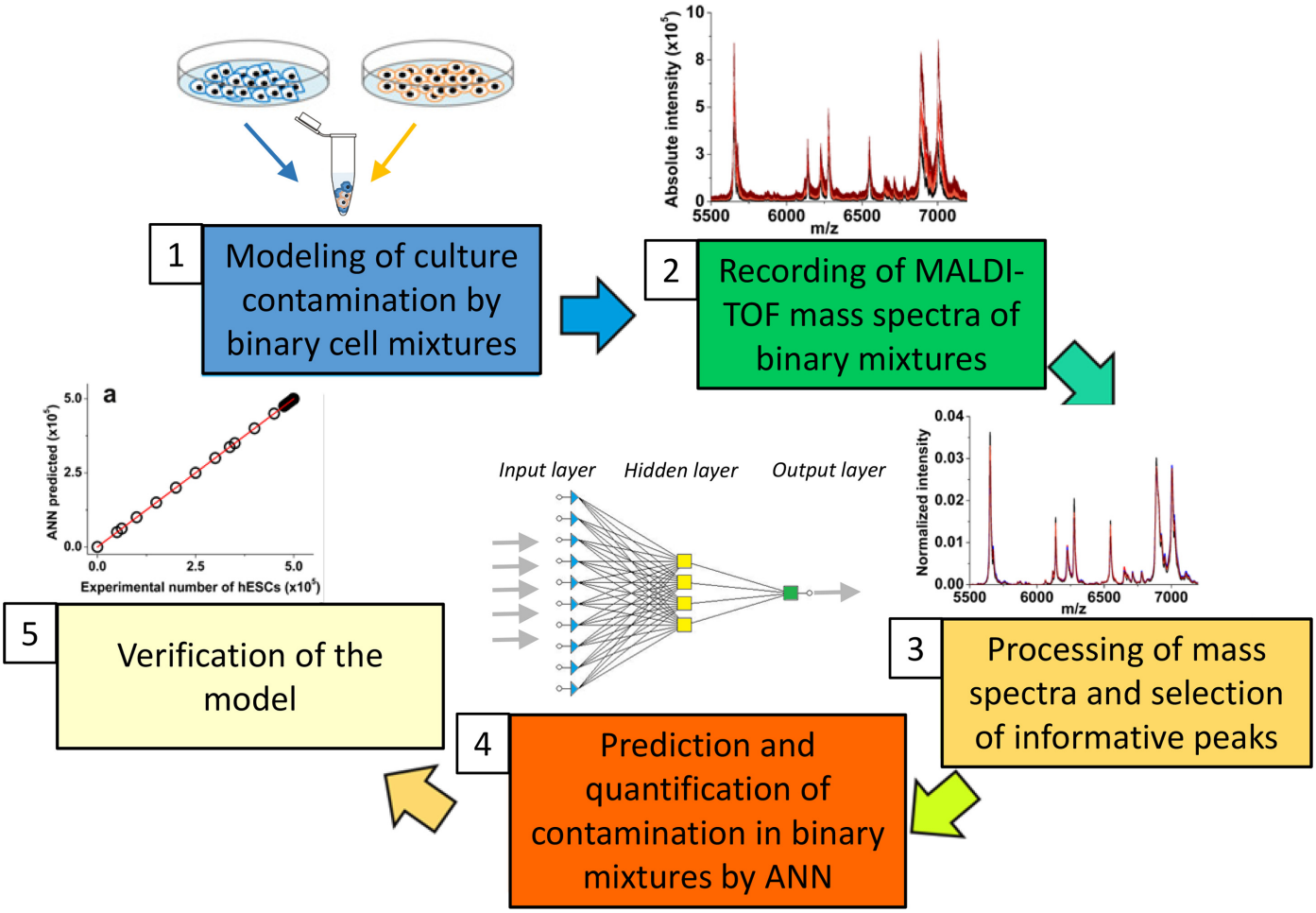

Fig 5. Overview for quantitative ANN-coupled MS-based analysis of cross-contamination.

doi:10.1371/journal.pone.0147414.g005

5. estimation of the contamination levels in unknown samples using an ANN model trained on the calibration datasets

The application of ANNs allowed us to overcome the unwanted inconsistency and non-linearity of IC MALDI-TOF MS spectra and reveal hidden patterns in mass spectra to unambiguously identify and quantify MEFs or mESCs in the hESC culture. However, *a priori* knowledge of the contaminating cell line is a prerequisite for correct prediction and selection of the training dataset. The multivariate calibration-based ANN approach can be easily adapted to routine protocols for quantitative determination of cell culture homogeneity and consistency and for thorough MS analyses of cell parameters in various culture platforms, with all steps adaptable for any experimental, routine, or high-throughput culture setup [48,49] (**Figs 5 and 6**). Currently, methods involving assessment of cell quality in clinical grade cultures, biomedical research or bio-industry involve either genetic authentication confirming the cell identity or functional assays documenting the phenotype. The intact cell mass spectrometry coupled with ANN can reveal inconsistencies occurring in high-throughput or long-term cultures or co-cultures, by monitoring spectral patterns and their alterations.

In conclusion, we demonstrated for the first time that the multivariate calibration approach based on ANN-coupled IC MALDI-TOF MS analysis can provide quantitative information on

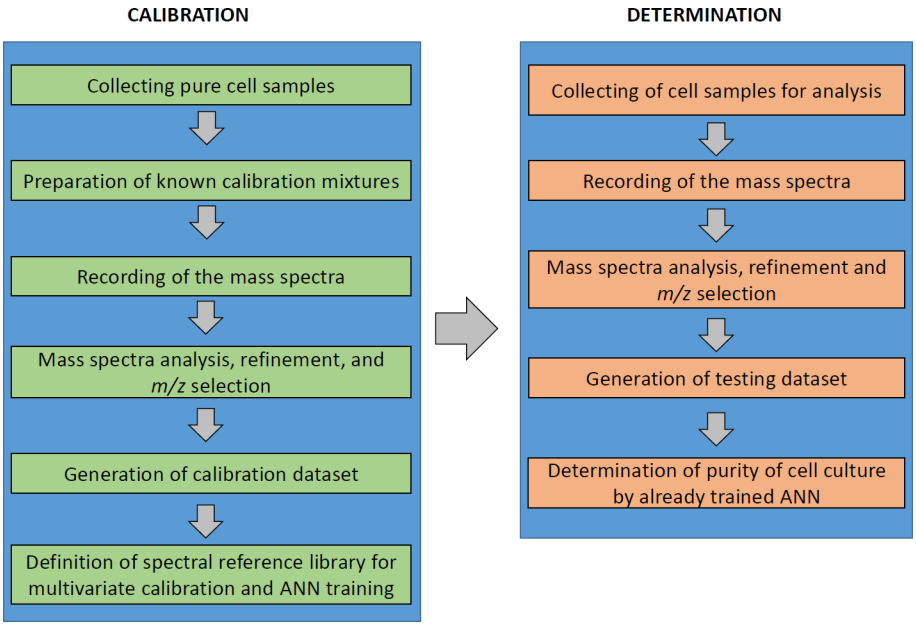

Fig 6. Experimental schematic of the multivariate calibration-based ANN spectral analysis.

doi:10.1371/journal.pone.0147414.g006

cell culture heterogeneity and authenticity and thus complement the portfolio of techniques that are available for characterization of mammalian cell cultures.

Supporting Information

S1 Fig. Comparison of raw (a) and pre-processed (b) mass spectra (five replicates) characterizing human embryonic stem cells (hESCs). The pre-processed mass spectra were normalized to a vector of unit length ($\Sigma X_i = 1$), where X_i are the intensities of the peaks of the mass spectrum).
(TIF)

S2 Fig. Standard deviations of the mean intensity of peaks of the particular m/z in the dataset normalized to the standard deviation of the mean intensity of the hESCs + MEFs (a) and hESCs + mESCs dataset (b). Peaks used in the further analyses are indicated by respective m/z values.
(TIF)

S3 Fig. Correlation between PLS-predicted number of cells and the experimental number of MEFs in two-component mixtures of (a) hESCs + MEFs and (b) hESCs + mESCs. Overview of Residuals (difference between PLS-predicted number of cells and the experimental values) versus the experimental number of cells in the two-component mixtures of (c) hESCs + MEFs and (d) hESCs + mESCs.
(TIF)

S4 Fig. Training and verification plot for an independent dataset of 50 cases of hESCs + MEFs mixtures (a). Correlation between experimental and ANN-predicted numbers of MEFs in hESCs suspension.
(TIF)

S1 Table. Overview of normalized mass-to-charge ratios (m/z) of informative peaks used for analysis.
(TIF)

Acknowledgments

We thank Dr. Jiří Pacherník from the Department of Experimental Biology, Faculty of Science, Masaryk University for the kind provision of mouse embryonic stem cell line R1.

Author Contributions

Conceived and designed the experiments: TP JH AH PV. Performed the experiments: EV LK FA. Analyzed the data: LK LP JH PV. Contributed reagents/materials/analysis tools: TP JH AH PV. Wrote the paper: AH JH PV.

References

1. Capes-Davis A, Theodosopoulos G, Atkin I, Drexler HG, Kohara A, MacLeod RAF, et al. (2010) Check your cultures! A list of cross-contaminated or misidentified cell lines. International Journal of Cancer 127: 1–8.
2. Marx V (2014) Cell-line authentication demystified. Nature Methods 11: 483–+.
3. Masters JRW (2010) Cell line misidentification: the beginning of the end. Nature Reviews Cancer 10: 441–448. doi: 10.1038/nrc2852 PMID: 20448633
4. Nardone RM (2007) Eradication of cross-contaminated cell lines: A call for action. Cell Biology and Toxicology 23: 367–372. PMID: 17522957
5. Hynds RE, Giangreco A (2013) Concise Review: The Relevance of Human Stem Cell-Derived Organoid Models for Epithelial Translational Medicine. Stem Cells 31: 417–422. doi: 10.1002/stem.1290 PMID: 23203919
6. Mehling M, Tay S (2014) Microfluidic cell culture. Current Opinion in Biotechnology 25: 95–102. doi: 10.1016/j.copbio.2013.10.005 PMID: 24484886
7. Nienow AW (2006) Reactor engineering in large scale animal cell culture. Cytotechnology 50: 9–33. doi: 10.1007/s10616-006-9005-8 PMID: 19003068
8. Baradez MO, Lekishvili T, Marshall D (2015) Rapid phenotypic fingerprinting of cell products by robust measurement of ubiquitous surface markers. Cytometry Part A 87A: 624–635.
9. Didion JP, Buus RJ, Naghashfar Z, Threadgill DW, Morse HC 3rd, de Villena FP (2014) SNP array profiling of mouse cell lines identifies their strains of origin and reveals cross-contamination and widespread aneuploidy. BMC Genomics 15: 847. doi: 10.1186/1471-2164-15-847 PMID: 25277546
10. Brougham DF, Ivanova G, Gottschalk M, Collins DM, Eustace AJ, O'Connor R, et al. (2011) Artificial neural networks for classification in metabolomic studies of whole cells using 1H nuclear magnetic resonance. J Biomed Biotechnol 2011: 158094. doi: 10.1155/2011/158094 PMID: 20886062
11. Houska J, Pena-Mendez EM, Hernandez-Fernaud JR, Salido E, Hampl A, Havel J, et al. (2014) Tissue profiling by nanogold-mediated mass spectrometry and artificial neural networks in the mouse model of human primary hyperoxaluria 1. Journal of Applied Biomedicine 12: 119–125.
12. Lui H, Zhao JH, McLean D, Zeng HS (2012) Real-time Raman Spectroscopy for In Vivo Skin Cancer Diagnosis. Cancer Research 72: 2491–2500. doi: 10.1158/0008-5472.CAN-11-4061 PMID: 22434431
13. Munteanu B, von Reitzenstein C, Hansch GM, Meyer B, Hopf C (2012) Sensitive, robust and automated protein analysis of cell differentiation and of primary human blood cells by intact cell MALDI mass spectrometry biotyping. Analytical and Bioanalytical Chemistry 404: 2277–2286. doi: 10.1007/s00216-012-6357-0 PMID: 22955673
14. Buchanan CM, Malik AS, Cooper GJS (2007) Direct visualisation of peptide hormones in cultured pancreatic islet alpha- and beta-cells by intact-cell mass spectrometry. Rapid Communications in Mass Spectrometry 21: 3452–3458. PMID: 17918213
15. Lokhov P, Balashova E, Dashtiev M (2009) Cell proteomic footprint. Rapid Communications in Mass Spectrometry 23: 680–682. doi: 10.1002/rcm.3928 PMID: 19184978
16. Maurer K, Eschrich K, Schellenberger W, Bertolini J, Rupf S, Remmerbach TW (2013) Oral brush biopsy analysis by MALDI-ToF Mass Spectrometry for early cancer diagnosis. Oral Oncology 49: 152–156. doi: 10.1016/j.oraloncology.2012.08.012 PMID: 23000400

17. Munteanu B, Hopf C (2013) Emergence of whole-cell MALDI-MS biotyping for high-throughput bioanalysis of mammalian cells? Bioanalysis 5: 885–893. doi: 10.4155/bio.13.47 PMID: 23590472
18. Zhang X, Scalf M, Berggren TW, Westphall MS, Smith LM (2006) Identification of mammalian cell lines using MALDI-TOF and LC-ESI-MS/MS mass spectrometry. Journal of the American Society for Mass Spectrometry 17: 490–499. PMID: 16488154
19. Dong HJ, Shen W, Cheung MTW, Liang YM, Cheung HY, Allmaier G, et al. (2011) Rapid detection of apoptosis in mammalian cells by using intact cell MALDI mass spectrometry. Analyst 136: 5181–5189. doi: 10.1039/c1an15750g PMID: 22059228
20. Hanrieder J, Wicher G, Bergquist J, Andersson M, Fex-Svenningsen A (2011) MALDI mass spectrometry based molecular phenotyping of CNS glial cells for prediction in mammalian brain tissue. Analytical and Bioanalytical Chemistry 401: 135–147. doi: 10.1007/s00216-011-5043-y PMID: 21553124
21. Munteanu B, Meyer B, von Reitzenstein C, Burgermeister E, Bog S, Pahl A, et al. (2014) Label-Free in Situ Monitoring of Histone Deacetylase Drug Target Engagement by Matrix-Assisted Laser Desorption Ionization-Mass Spectrometry Biotyping and Imaging. Analytical Chemistry 86: 4642–4647. doi: 10.1021/ac500038j PMID: 24559101
22. Povey JF, O'Malley CJ, Root T, Martin EB, Montague GA, Feary M, et al. (2014) Rapid high-throughput characterisation, classification and selection of recombinant mammalian cell line phenotypes using intact cell MALDI-ToF mass spectrometry fingerprinting and PLS-DA modelling. Journal of Biotechnology 184: 84–93. doi: 10.1016/j.jbiotec.2014.04.028 PMID: 24858576
23. Volta P, Riccardi N, Lauceri R, Tonolla M (2012) Discrimination of freshwater fish species by Matrix-Assisted Laser Desorption/Ionization-Time Of Flight Mass Spectrometry (MALDI-TOF MS): a pilot study. Journal of Limnology 71: 164–169.
24. Chiu NH, Jia Z, Diaz R, Wright P (2015) Rapid differentiation of in vitro cellular responses to toxic chemicals by using matrix-assisted laser desorption/ionization time-of-flight mass spectrometry. Environ Toxicol Chem 34: 161–166. doi: 10.1002/etc.2774 PMID: 25319019
25. Kober SL, Meyer-Alert H, Grienitz D, Hollert H, Frohme M (2015) Intact cell mass spectrometry as a rapid and specific tool for the differentiation of toxic effects in cell-based ecotoxicological test systems. Anal Bioanal Chem.
26. Asakawa D, Sakakura M, Takayama M (2012) Matrix effect on in-source decay products of peptides in matrix-assisted laser desorption/ionization. Mass Spectrom (Tokyo) 1: A0002.
27. Bas D, Boyaci IH (2007) Modeling and optimization I: Usability of response surface methodology. Journal of Food Engineering 78: 836–845.
28. Goodacre R, Neal MJ, Kell DB (1996) Quantitative analysis of multivariate data using artificial neural networks: A tutorial review and applications to the deconvolution of pyrolysis mass spectra. Zentralblatt Fur Bakteriologie-International Journal of Medical Microbiology Virology Parasitology and Infectious Diseases 284: 516–539.
29. Li H, Zhang YX, Polaskova P, Havel J (2002) Enhancement of precision in the analysis of medicines by capillary electrophoresis using artificial neural networks. Acta Chimica Sinica 60: 1264–1268.
30. Amato F, Lopez A, Pena-Mendez EM, Vanhara P, Hampl A, Havel J (2013) Artificial neural networks in medical diagnosis. Journal of Applied Biomedicine 11: 47–58.
31. Basheer IA, Hajmeer M (2000) Artificial neural networks: fundamentals, computing, design, and application. Journal of Microbiological Methods 43: 3–31. PMID: 11084225
32. International Stem Cell Initiative, Adewumi O, Aflatoonian B, Ahrlund-Richter L, Amit M, Andrews PW, et al. (2007) Characterization of human embryonic stem cell lines by the International Stem Cell Initiative. Nat Biotechnol 25: 803–816. PMID: 17572666
33. Kotasova H, Vesela I, Kucera J, Houdek Z, Prochazkova J, Kralickova M, et al. (2012) Phosphoinositide 3-kinase inhibition enables retinoic acid-induced neurogenesis in monolayer culture of embryonic stem cells. Journal of Cellular Biochemistry 113: 563–570. doi: 10.1002/jcb.23380 PMID: 21948563
34. Barta T, Vinarsky V, Holubcova Z, Dolezalova D, Verner J, Pospisilova S, et al. (2010) Human embryonic stem cells are capable of executing G1/S checkpoint activation. Stem Cells 28: 1143–1152. doi: 10.1002/stem.451 PMID: 20518019
35. Holubcova Z, Matula P, Sedlackova M, Vinarsky V, Dolezalova D, Barta T, et al. (2011) Human embryonic stem cells suffer from centrosomal amplification. Stem Cells 29: 46–56. doi: 10.1002/stem.549 PMID: 20960514
36. Adewumi O, Aflatoonian B, Ahrlund-Richter L, Amit M, Andrews PW, Beighton G, et al. (2007) Characterization of human embryonic stem cell lines by the International Stem Cell Initiative. Nature Biotechnology 25: 803–816. PMID: 17572666

37. Amps K, Andrews PW, Anyfantis G, Armstrong L, Avery S, Baharvand H, et al. (2011) Screening ethnically diverse human embryonic stem cells identifies a chromosome 20 minimal amplicon conferring growth advantage. Nature Biotechnology 29: 1132–U1113. doi: 10.1038/nbt.2051 PMID: 22119741

38. Hilario M, Kalousis A, Pellegrini C, Muller M (2006) Processing and classification of protein mass spectra. Mass Spectrometry Reviews 25: 409–449. PMID: 16463283

39. Mevik B-H, Wehrens R (2007) The pls Package: Principal Component and Partial Least Squares Regression in R. Journal of Statistical Software, 18: 1–24.

40. Amato F, Gonzalez-Hernandez JL, Havel J (2012) Artificial neural networks combined with experimental design: a "soft" approach for chemical kinetics. Talanta 93: 72–78. doi: 10.1016/j.talanta.2012.01.044 PMID: 22483879

41. Pivetta T, Isaia F, Trudu F, Pani A, Manca M, Perra D, et al. (2013) Development and validation of a general approach to predict and quantify the synergism of anti-cancer drugs using experimental design and artificial neural networks. Talanta 115: 84–93. doi: 10.1016/j.talanta.2013.04.031 PMID: 24054565

42. Alfassi ZB (2004) On the normalization of a mass spectrum for comparison of two spectra. Journal of the American Society for Mass Spectrometry 15: 385–387. PMID: 14998540

43. Filzmoser P, Gschwandtner M, Todorov V (2012) Review of sparse methods in regression and classification with application to chemometrics. Journal of Chemometrics 26: 42–51.

44. Friedman J, Hastie T, Tibshirani R (2010) Regularization Paths for Generalized Linear Models via Coordinate Descent. Journal of Statistical Software 33: 1–22. PMID: 20808728

45. Chun H, Keles S (2010) Sparse partial least squares regression for simultaneous dimension reduction and variable selection. Journal of the Royal Statistical Society Series B-Statistical Methodology 72: 3–25.

46. Rasmussen MA, Bro R (2012) A tutorial on the Lasso approach to sparse modeling. Chemometrics and Intelligent Laboratory Systems 119: 21–31.

47. Wold S, Sjöström M, Eriksson L (2001) PLS-regression: a basic tool of chemometrics. Chemometrics and Intelligent Laboratory Systems 58: 109–130.

48. Dittrich P, Ibanez AJ (2015) Analysis of metabolites in single cells-what is the best micro-platform? Electrophoresis.

49. Xie W, Gao D, Jin F, Jiang Y, Liu H (2015) Study of Phospholipids in Single Cells Using an Integrated Microfluidic Device Combined with Matrix-Assisted Laser Desorption/Ionization Mass Spectrometry. Anal Chem 87: 7052–7059. doi: 10.1021/acs.analchem.5b00010 PMID: 26110742

S1 Fig.

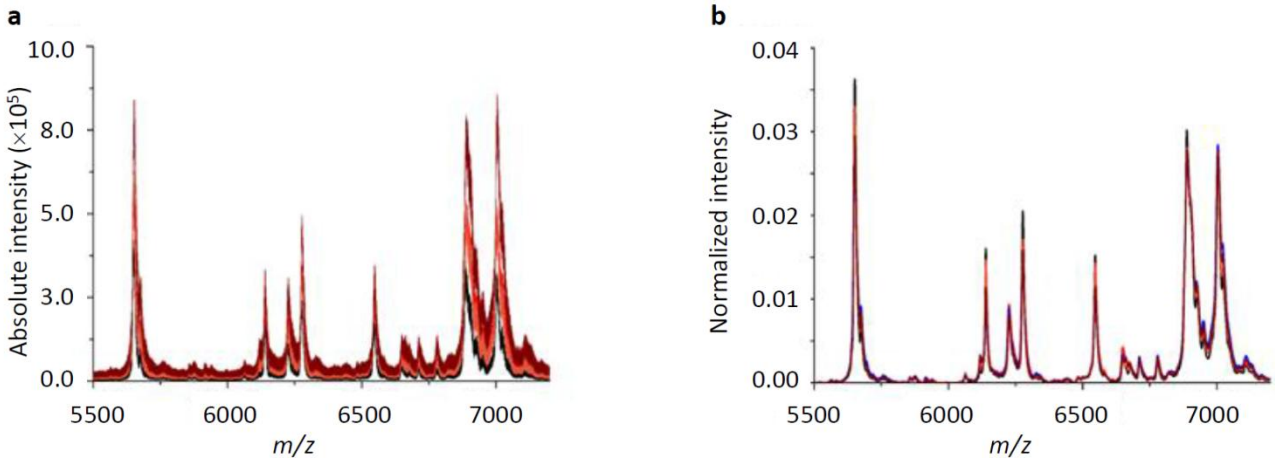
a
Absolute intensity (×10^5)
10.0
8.0
5.0
3.0
0.0
5500
6000
6500
7000
m/z
b
Normalized intensity
0.04
0.03
0.02
0.01
0.00
5500
6000
6500
7000
m/z

S2 Fig.

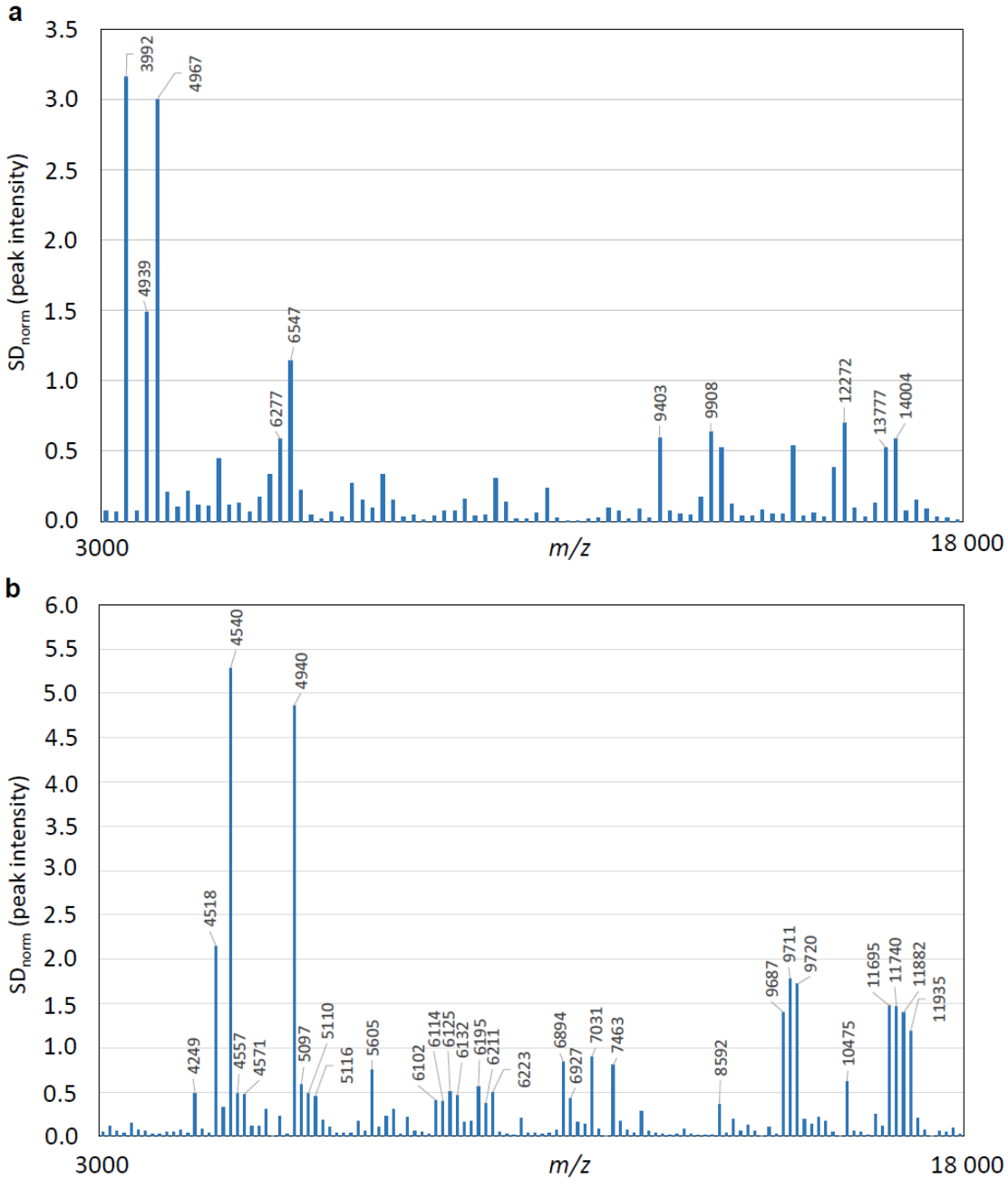
a
SDnorm (peak intensity)
3992
4967
4939
6547
6277
9403
9908
12272
13777
14004
3000
m/z
18 000
b
SDnorm (peak intensity)
4540
4940
4518
4249
4557
4571
5097
5110
5116
5605
6102
6114
6125
6132
6195
6211
6223
6894
6927
7031
7463
8592
9687
9711
9720
10475
11695
11740
11882
11935
3000
m/z
18 000

S3 Fig.

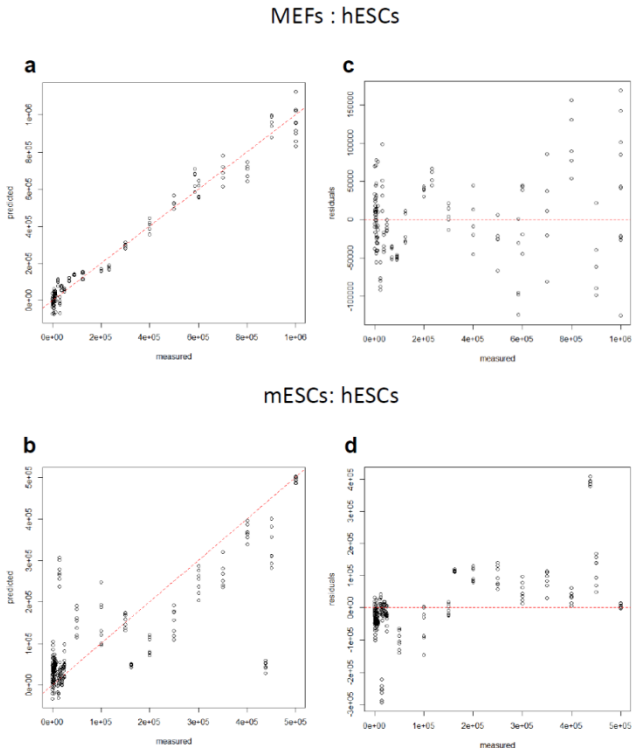
MEFs : hESCs
a
c
predicted
residuals
measured
mESCs: hESCs
b
d

S3 Fig.

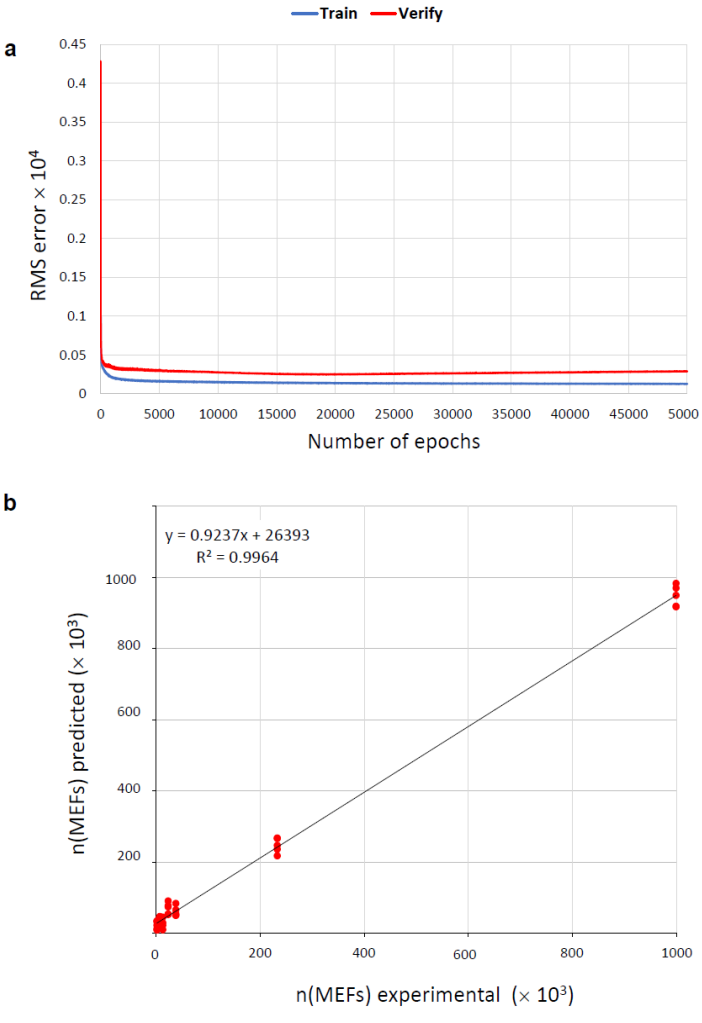
Train
Verify
a
RMS error × 10^4
Number of epochs
b
y = 0.9237x + 26393
R² = 0.9964
n(MEFs) predicted (× 10³)
n(MEFs) experimental (× 10³)

S1 Table.

m/z		
MEFs : hESCs	mESCs : hESCs	
3992.5	4248.9	6210.7
4938.9	4518.2	6222.9
4966.9	4540.1	6894.1
6277.3	4557.4	6927.0
6547.2	4571.3	7031.3
9403.2	4940.4	7463.3
9908.3	5097.2	8592.4
12271.5	5110.5	9686.9
13776.8	5116.2	9711.1
14004.2	5605.3	9720.3
	6102.3	10475.2
	6113.9	11694.9
	6125.4	11740.4
	6131.7	11881.7
	6195.2	11934.7

Chapter 7

Zinc(II)-methimazole complexes: synthesis and reactivity

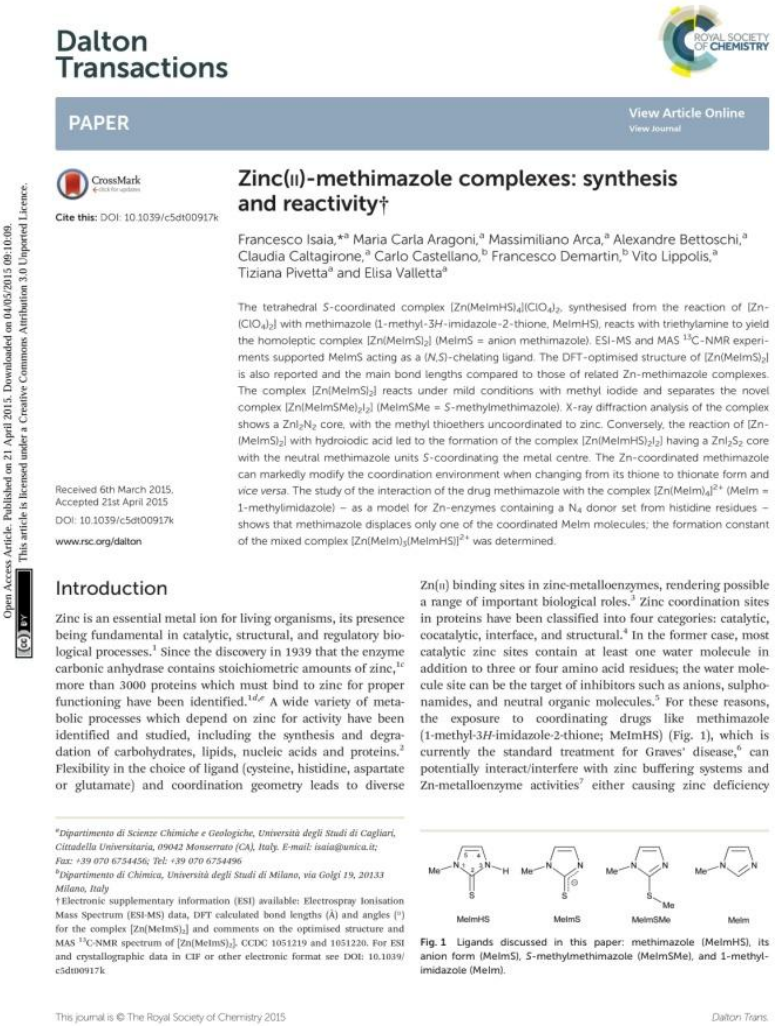

Dalton Transactions

PAPER

View Article Online
View Journal

CrossMark

Cite this: DOI: 10.1039/c5dt00917k

Zinc(II)-methimazole complexes: synthesis and reactivity†

Francesco Isaia,*[a] Maria Carla Aragoni,[a] Massimiliano Arca,[a] Alexandre Bettoschi,[a] Claudia Caltagirone,[a] Carlo Castellano,[b] Francesco Demartin,[b] Vito Lippolis,[a] Tiziana Pivetta[a] and Elisa Valletta[a]

The tetrahedral *S*-coordinated complex $[Zn(MeImHS)_4](ClO_4)_2$, synthesised from the reaction of $[Zn(ClO_4)_2]$ with methimazole (1-methyl-3*H*-imidazole-2-thione, MeImHS), reacts with triethylamine to yield the homoleptic complex $[Zn(MeImS)_2]$ (MeImS = anion methimazole). ESI-MS and MAS ^{13}C-NMR experiments supported MeImS acting as a (*N*,*S*)-chelating ligand. The DFT-optimised structure of $[Zn(MeImS)_2]$ is also reported and the main bond lengths compared to those of related Zn-methimazole complexes. The complex $[Zn(MeImS)_2]$ reacts under mild conditions with methyl iodide and separates the novel complex $[Zn(MeImSMe)_2I_2]$ (MeImSMe = *S*-methylmethimazole). X-ray diffraction analysis of the complex shows a ZnI_2N_2 core, with the methyl thioethers uncoordinated to zinc. Conversely, the reaction of $[Zn(MeImS)_2]$ with hydroiodic acid led to the formation of the complex $[Zn(MeImHS)_2I_2]$ having a ZnI_2S_2 core with the neutral methimazole units *S*-coordinating the metal centre. The Zn-coordinated methimazole can markedly modify the coordination environment when changing from its thione to thionate form and *vice versa*. The study of the interaction of the drug methimazole with the complex $[Zn(MeIm)_4]^{2+}$ (MeIm = 1-methylimidazole) – as a model for Zn-enzymes containing a N_4 donor set from histidine residues – shows that methimazole displaces only one of the coordinated MeIm molecules; the formation constant of the mixed complex $[Zn(MeIm)_3(MeImHS)]^{2+}$ was determined.

Received 6th March 2015,
Accepted 21st April 2015
DOI: 10.1039/c5dt00917k
www.rsc.org/dalton

Introduction

Zinc is an essential metal ion for living organisms, its presence being fundamental in catalytic, structural, and regulatory biological processes.[1] Since the discovery in 1939 that the enzyme carbonic anhydrase contains stoichiometric amounts of zinc,[1c] more than 3000 proteins which must bind to zinc for proper functioning have been identified.[1d,f] A wide variety of metabolic processes which depend on zinc for activity have been identified and studied, including the synthesis and degradation of carbohydrates, lipids, nucleic acids and proteins.[2] Flexibility in the choice of ligand (cysteine, histidine, aspartate or glutamate) and coordination geometry leads to diverse Zn(II) binding sites in zinc-metalloenzymes, rendering possible a range of important biological roles.[3] Zinc coordination sites in proteins have been classified into four categories: catalytic, cocatalytic, interface, and structural.[4] In the former case, most catalytic zinc sites contain at least one water molecule in addition to three or four amino acid residues; the water molecule site can be the target of inhibitors such as anions, sulphonamides, and neutral organic molecules.[5] For these reasons, the exposure to coordinating drugs like methimazole (1-methyl-3*H*-imidazole-2-thione; MeImHS) (Fig. 1), which is currently the standard treatment for Graves' disease,[6] can potentially interact/interfere with zinc buffering systems and Zn-metalloenzyme activities[7] either causing zinc deficiency

[a]*Dipartimento di Scienze Chimiche e Geologiche, Università degli Studi di Cagliari, Cittadella Universitaria, 09042 Monserrato (CA), Italy. E-mail: isaia@unica.it; Fax: +39 070 6754456; Tel: +39 070 6754496*
[b]*Dipartimento di Chimica, Università degli Studi di Milano, via Golgi 19, 20133 Milano, Italy*

†Electronic supplementary information (ESI) available: Electrospray Ionisation Mass Spectrum (ESI-MS) data, DFT calculated bond lengths (Å) and angles (°) for the complex $[Zn(MeImS)_2]$ and comments on the optimised structure and MAS ^{13}C-NMR spectrum of $[Zn(MeImS)_2]$. CCDC 1051219 and 1051220. For ESI and crystallographic data in CIF or other electronic format see DOI: 10.1039/c5dt00917k

Fig. 1 Ligands discussed in this paper: methimazole (MeImHS), its anion form (MeImS), *S*-methylmethimazole (MeImSMe), and 1-methylimidazole (MeIm).

Abstract

Zinc is an essential metal ion for living organisms, involved in a wide variety of metabolic processes, several proteins needs zinc for their proper functioning. A large number of structurally characterised Zn-catalytic sites are four-coordinated tetrahedra, where the zinc is bound to three histidine nitrogen atoms and to a water molecule, as found, for example, in carbonic anhydrases or phosphate esterases. The site occupied by the water molecule can be the target of anions, sulphonamides, and neutral organic molecules, that act as inhibitors. For these reasons, the exposure to coordinating drugs like methimazole (1-methyl-3H-imidazole-2-thione, **MeImHS**) (Figure 21) can potentially interact/interfere with zinc buffering systems and Zn-metalloenzyme activities, either causing zinc deficiency and/or potentially reducing the efficacy of the drug. MeImHS is currently the standard treatment for Graves' disease, which is an autoimmune disease that affects the thyroid.

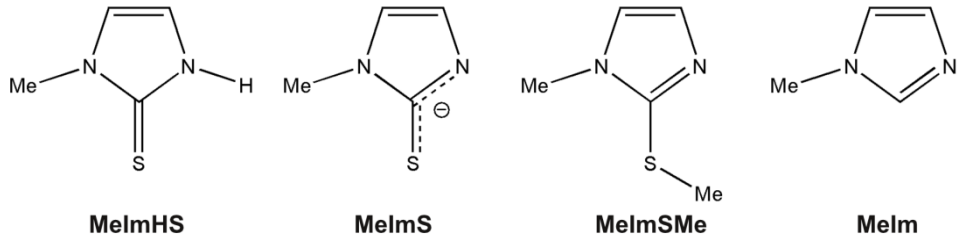

Figure 21. Formulas and acronyms of studied ligands: methimazole (**MeImHS**), its anionic form (**MeImS**), S-methylmethimazole (**MeImSMe**), and 1-methylimidazole (**MeIm**).

I synthesized and characterized zinc complexes with (N,S)-donor molecules to provide information about the coordination mode and reactivity of Zn-metalloproteins and -metalloenzymes (Chapter 7 - Article IV). In particular, zinc complexes of the drug methimazole (**MeImHS**) and its

anion (**MeImS**) have been synthesized, and structurally characterized[1]. The structures of the complexes have been optimized using DFT calculations.

The complex $[Zn(MeImS)_2]$ has been studied also using Electro-Spray Ionisation at Atmospheric-Pressure Mass Spectrometry (Figure 22) and tandem MS-MS.

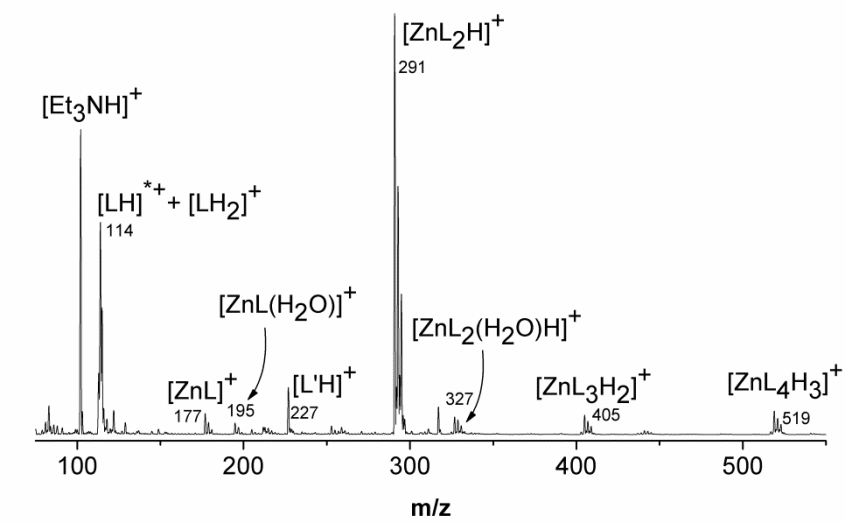

Figure 22. Positive ion ESI-MS spectrum of $[Zn(MeImS)_2]$; L = **MeImS**, L' = methimazole-disulfide ($C_8H_{10}N_4S_2$).

A mononuclear ZnN_4 model complex with the 1-methylimidazole (**MeIm**) ligands representing the histidine (His) amino acid residues has been selected to study the interaction of methimazole with a ZnN_4 coordination sphere. The model complex $[Zn(MeIm)_4](ClO_4)_2$ represents $[Zn(His)_4]^{2+}$ and $[Zn(His)_3(H_2O)]^{2+}$ protein sites. Spectrophotometric titrations showed methimazole displacing only one of the coordinated **MeIm** molecules (Figure 23). This evidence supports the possibility that methimazole, by blocking a histidine/water binding site, could interfere with the multifunctional roles of zinc atoms in proteins (e.g. the enzymatic activity of carbonic anhydrases).

[1] In collaboration with professor Francesco Demartin (Dipartimento di Chimica, Università degli Studi di Milano).

The anionic methimazole can effectively act as a (N,S)-bridging/chelating ligand to a variety of metal ions due to its N–C–S functional group.

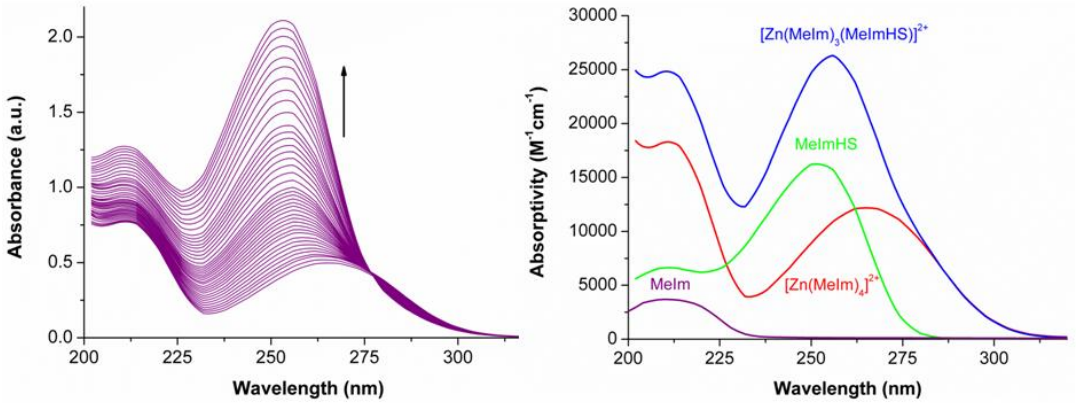

[Zn(MeIm)$_4$]$^{2+}$ = model for Zn-enzymes containing a N_4 donor set from histidine residues ([Zn(His)$_4$]$^{2+}$ and [Zn(His)$_3$(H$_2$O)]$^{2+}$ protein sites)

$$[Zn(MeIm)_4]^{2+} + MeImHS \rightleftarrows [Zn(MeIm)_3(MeImHS)]^{2+} + MeIm$$

Figure 23. Selected spectra collected during the titration of [Zn(MeIm)$_4$]$^{2+}$ with **MeImHS** (left) and pure spectra of **MeIm**, **MeImHS**, [Zn(MeIm)$_4$]$^{2+}$, and [Zn(MeIm)$_3$(MeImHS)]$^{2+}$ (right).

The synthesized complex [Zn(MeImS)$_2$] featuring a ZnN_2S_2 core is of interest in the study of S-alkylation of zinc-thiolates in biological processes. This complex reveals a different reactivity towards the electrophilic addition of CH_3^+ and H^+. The **MeImS** moieties are N-protonated by HI to form the neutral complex [Zn(MeImHS)$_2$I$_2$]; conversely, the reaction of [Zn(MeImS)$_2$] with methyl iodide leads to the formation of the complex [Zn(MeImSMe)$_2$I$_2$]. This evidence shows that Zn-coordinated methimazole can markedly modify the coordination environment when changing from its thione to thionate form, and vice versa.

Within the scope of the study on the interaction of molecules of pharmacological interest with zinc, these results underline that methimazole shows a reactivity and a variety of coordinating modes that may alter the biological processes that are based on the zinc ion.

Article IV

Zinc(II)-methimazole complexes: synthesis and reactivity

Francesco Isaia, Maria Carla Aragoni, Massimiliano Arca, Alexandre Bettoschi, Claudia Caltagirone, Carlo Castellano, Francesco Demartin, Vito Lippolis, Tiziana Pivetta and Elisa Valletta

Citation: Dalton Trans., 44 (2015) 9805-9814

Cite this: DOI: 10.1039/c5dt00917k

Published by The Royal Society of Chemistry

Dalton Transactions

PAPER

View Article Online
View Journal

Cite this: DOI: 10.1039/c5dt00917k

Zinc(II)-methimazole complexes: synthesis and reactivity†

Francesco Isaia,*[a] Maria Carla Aragoni,[a] Massimiliano Arca,[a] Alexandre Bettoschi,[a] Claudia Caltagirone,[a] Carlo Castellano,[b] Francesco Demartin,[b] Vito Lippolis,[a] Tiziana Pivetta[a] and Elisa Valletta[a]

Received 6th March 2015,
Accepted 21st April 2015

DOI: 10.1039/c5dt00917k

www.rsc.org/dalton

The tetrahedral *S*-coordinated complex $[Zn(MeImHS)_4](ClO_4)_2$, synthesised from the reaction of $[Zn(ClO_4)_2]$ with methimazole (1-methyl-3*H*-imidazole-2-thione, MeImHS), reacts with triethylamine to yield the homoleptic complex $[Zn(MeImS)_2]$ (MeImS = anion methimazole). ESI-MS and MAS ^{13}C-NMR experiments supported MeImS acting as a (*N*,*S*)-chelating ligand. The DFT-optimised structure of $[Zn(MeImS)_2]$ is also reported and the main bond lengths compared to those of related Zn-methimazole complexes. The complex $[Zn(MeImS)_2]$ reacts under mild conditions with methyl iodide and separates the novel complex $[Zn(MeImSMe)_2I_2]$ (MeImSMe = *S*-methylmethimazole). X-ray diffraction analysis of the complex shows a ZnI_2N_2 core, with the methyl thioethers uncoordinated to zinc. Conversely, the reaction of $[Zn(MeImS)_2]$ with hydroiodic acid led to the formation of the complex $[Zn(MeImHS)_2I_2]$ having a ZnI_2S_2 core with the neutral methimazole units *S*-coordinating the metal centre. The Zn-coordinated methimazole can markedly modify the coordination environment when changing from its thione to thionate form and *vice versa*. The study of the interaction of the drug methimazole with the complex $[Zn(MeIm)_4]^{2+}$ (MeIm = 1-methylimidazole) – as a model for Zn-enzymes containing a N_4 donor set from histidine residues – shows that methimazole displaces only one of the coordinated MeIm molecules; the formation constant of the mixed complex $[Zn(MeIm)_3(MeImHS)]^{2+}$ was determined.

Introduction

Zinc is an essential metal ion for living organisms, its presence being fundamental in catalytic, structural, and regulatory biological processes.[1] Since the discovery in 1939 that the enzyme carbonic anhydrase contains stoichiometric amounts of zinc,[1c] more than 3000 proteins which must bind to zinc for proper functioning have been identified.[1d,e] A wide variety of metabolic processes which depend on zinc for activity have been identified and studied, including the synthesis and degradation of carbohydrates, lipids, nucleic acids and proteins.[2] Flexibility in the choice of ligand (cysteine, histidine, aspartate or glutamate) and coordination geometry leads to diverse Zn(II) binding sites in zinc-metalloenzymes, rendering possible a range of important biological roles.[3] Zinc coordination sites in proteins have been classified into four categories: catalytic, cocatalytic, interface, and structural.[4] In the former case, most catalytic zinc sites contain at least one water molecule in addition to three or four amino acid residues; the water molecule site can be the target of inhibitors such as anions, sulphonamides, and neutral organic molecules.[5] For these reasons, the exposure to coordinating drugs like methimazole (1-methyl-3*H*-imidazole-2-thione; MeImHS) (Fig. 1), which is currently the standard treatment for Graves' disease,[6] can potentially interact/interfere with zinc buffering systems and Zn-metalloenzyme activities[7] either causing zinc deficiency

[a]*Dipartimento di Scienze Chimiche e Geologiche, Università degli Studi di Cagliari, Cittadella Universitaria, 09042 Monserrato (CA), Italy. E-mail: isaia@unica.it; Fax: +39 070 6754456; Tel: +39 070 6754496*

[b]*Dipartimento di Chimica, Università degli Studi di Milano, via Golgi 19, 20133 Milano, Italy*

†Electronic supplementary information (ESI) available: Electrospray Ionisation Mass Spectrum (ESI-MS) data, DFT calculated bond lengths (Å) and angles (°) for the complex $[Zn(MeImS)_2]$ and comments on the optimised structure and MAS ^{13}C-NMR spectrum of $[Zn(MeImS)_2]$. CCDC 1051219 and 1051220. For ESI and crystallographic data in CIF or other electronic format see DOI: 10.1039/c5dt00917k

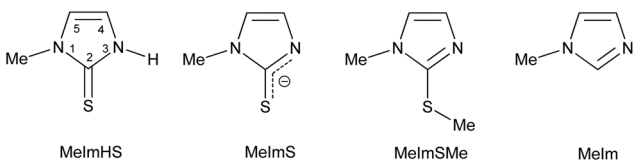

Fig. 1 Ligands discussed in this paper: methimazole (MeImHS), its anion form (MeImS), *S*-methylmethimazole (MeImSMe), and 1-methylimidazole (MeIm).

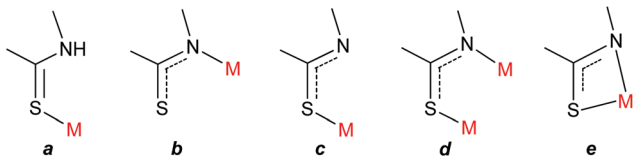

Fig. 2 Main coordination mode of neutral MeImHS: (a) η^1-S and of anion MeImS: (b) η^1-N; (c) η^1-S; (d) μ-N,S (η^1-N, η^1-S); (e) η^2-N,S.

and/or potentially reducing the efficacy of the drug.[7] The rich coordination chemistry of methimazole with transition metals has previously been investigated in detail.[8–10] Methimazole can bind a metal ion as a neutral species (*via* the thione sulphur atom) or in its anionic form (as a monodentate species *via* either the thionate sulphur atom, the thioamido nitrogen atom, or as an ambidentate ligand *via* a variety of bonding modes) (Fig. 2).

In previous studies, we investigated the reactivity of methimazole with liquid mercury and zinc powder obtaining complexes of stoichiometry $[Hg_2(MeImHS)_2I_4]$ and $[Zn(MeImHS)_2I_2]$ whose X-ray crystal structures show the neutral methimazole *S*-binding the metal centre and the formation of intermolecular hydrogen bonding *via* C(4)H, N–H, and N–Me groups.[11]

Although the drug methimazole has been marketed since 1950, its interaction with zinc ions has received little attention to date. In this context, the synthesis and characterisation of zinc complexes with (*N*,*S*)-donor molecules provide information for the structure prediction and reactivity of Zn-metalloproteins and -metalloenzymes. In this study, the X-ray crystal structures of the complexes $[Zn(MeImHS)_4](ClO_4)_2$ and $[Zn(MeImSMe)_2I_2]$ are reported; the optimised structure of the complex $[Zn(MeImS)_2]$ has been proposed on the basis of density functional theory (DFT) calculations. The complex $[Zn(MeImS)_2]$ featuring a ZnN_2S_2 core is of interest in the study of *S*-alkylation of zinc-thiolates in biological processes: the electrophilic addition of CH_3^+ and H^+ to the coordinated MeImS anions is discussed. Moreover, the system methimazole-$[Zn(MeIm)_4](ClO_4)_2$ (MeIm = 1-methylimidazole), where the Zn-complex acts as a model for Zn-enzymes containing a N_4 donor set from histidine residues, has been investigated.

Results and discussion

Synthesis, structure characterization and reactivity of the complexes $[Zn(MeImHS)_4](ClO_4)_2$ and $[Zn(MeImS)_2]$

A search in the Cambridge Structural Database shows that only a limited number of zinc-methimazole complexes have been structurally characterised to date (Table 1). In all of the reported complexes but one, the methimazole acts as a neutral ligand binding to the Zn(II) ion *via* the sulphur atom, whereas in the case of the complex $[Zn_4O(MeImS)_6]$ each anionic methimazole ligand bridges two zinc ions *via* the sulphur atom and the nitrogen atom. Metal complexes with MeImS in (*N*,*S*)-bridging/chelating mode are quite scarce in the literature.[8,9] Bell *et al.* reported on the synthesis of the complex $[Hg(MeImS)_2]$,[15] failing, however, to obtain a crystalline sample. For the synthesis of the homoleptic complex $[Zn(MeImS)_2]$ we further simplified the synthetic procedure proposed by Bell[15] for the mercury analogue by reacting the cationic complex $[Zn(MeImHS)_4]^{2+}$ with a base.

The synthesis of the complex $[Zn(MeImHS)_4](ClO_4)_2$ was accomplished by reacting $Zn(ClO_4)_2{\cdot}6H_2O$ with MeImHS (1 : 4 molar ratio) in EtOH/H_2O. X-ray diffraction analysis was performed on a single crystal and data collection and refinement parameters are summarised in Table 2. The Zn atom of the $[Zn(MeImHS)_4]^{2+}$ cation is located on a four-fold rotoinversion axis whereas the chlorine atom of the perchlorate anion is on a two-fold axis. The perchlorate oxygens are disordered over two very close positions (see the Experimental section). Fig. 3 shows the structure of the complex $[Zn(MeImHS)_4]$-$(ClO_4)_2$ with the expected four-coordinate tetrahedral geometry around the zinc ion. It is quite evident from the bond angle values S–Zn–S^{i} of 103.47(1)° and S–Zn–S^{ii} 122.28(3)° (^{i} 0.75 + *y*, 1.25 − *x*, 0.25 − *z*; ^{ii} 2 − *x*, 0.5 − *y*, *z*) that deviation from the expected 109.5° is related to a compression along one of the S_4 improper rotation axes of the tetrahedron. Thus the coordination sphere around zinc may be described as a flattened tetrahedron with two longer non-bonding edges (S···Si^{ii} and S^{i}···S^{iii} distances equal to 4.076(1) Å) and four shorter edges (3.655(1) Å). Ligand bond distances and angles are comparable to those previously observed for related compounds (see Table 1), and to those observed in similar 1,3-dialkyl-imidazole-thione Zn complexes.[16] Each MeImHS molecule is involved in a N–H···O

Table 1 Structurally characterised metal complexes of methimazole with a zinc(II) ion

Complex	Mean *d*(Zn–S) (Å)	Geometry/core	Reaction/solvent	Ref.
$[Zn(MeImHS)_2Cl_2]$	2.3405(2)	T_d/ZnS_2Cl_2	$ZnCl_2$ + MeImHS/MeOH	12
$[Zn(MeImHS)_2Br_2]$	2.340(2)	T_d/ZnS_2Br_2	$ZnBr_2$ + MeImHS/MeOH	12
$[Zn(MeImHS)_2I_2]$	2.3581(5)	T_d/ZnS_2I_2	Zn + MeImHS + I_2/CH_2Cl_2	11*b*
$[Zn(MeImHS)_3I]I$	2.3746(3)	T_d/ZnS_3I	ZnI_2 + MeImHS/MeOH	12
$[Zn(MeImHS)_4](NO_3)]{\cdot}H_2O$	2.3385(2)	T_d/ZnS_4	$Zn(NO_3)_2$ + MeImHS/EtOH	13
$[Zn(MeImHS)_4](ClO_4)_2$	2.3273(4)	T_d/ZnS_4	$Zn(ClO_4)_2$ + MeImHS/EtOH-H_2O	*a*
$[Zn_4O(MeImS)_6]{\cdot}CHCl_3{\cdot}3H_2O^b$	2.3375(3)	T_d/ZnN_2OS–$ZnOS_3$	Electrochemical oxidation of the zinc anode in the presence of MeImHS/CH_3CN	14

[a] This work. [b] *d*(Zn–N) = 2.003(10) Å.

Table 2 Crystal data collection and refinement parameters for the compounds $[Zn(MeImHS)_4](ClO_4)_2$ and $[Zn(MeImSMe)_2I_2]$

	$[Zn(MeImHS)_4](ClO_4)_2$	$[Zn(MeImSMe)_2I_2]$
Empirical formula	$C_{16}H_{24}Cl_2N_8O_8S_4Zn$	$C_{10}H_{16}I_2N_4S_2Zn$
M	720.94	575.56
Crystal system	Tetragonal	Triclinic
Space group	$I4_1/a$ (no. 88)	$P\bar{1}$ (no. 2)
a, b, c (Å)	12.3057(4), 12.3057(4), 20.5539(7)	8.9185(11), 9.1511(11), 11.8137(15)
α, β, γ (°)	90, 90, 90	88.66(2), 86.89(2), 71.16(2)
Volume (Å^3)	3112.5(2)	911.2(2)
Z	4	2
Temperature (K)	294(2)	294(2)
D_{calc} (Mg m^{-3})	1.539	2.098
μ (mm^{-1})	1.280	4.958
θ min-max (°)	1.93–31.70	2.35–31.67
Refl. collected/ unique	16 439/2546 (R_{int} = 0.023)	9676/5494 (R_{int} = 0.016)
Data/restraints/ parameters	2546/0/89	5494/0/172
Refl. obs. ($I > 2\sigma I$)	2085	4482
Final R indices [$I > 2\sigma(I)$]	R_1 = 0.0341, wR_2 = 0.1022	R_1 = 0.0245, wR_2 = 0.0669
R indices (all data)	R_1 = 0.0434, wR_2 = 0.1090	R_1 = 0.0324, wR_2 = 0.0702
Goodness-of-fit on F^2	1.066	1.050
Largest diff. peak, hole (e Å^{-3})	0.42, −0.41	0.89, −0.66

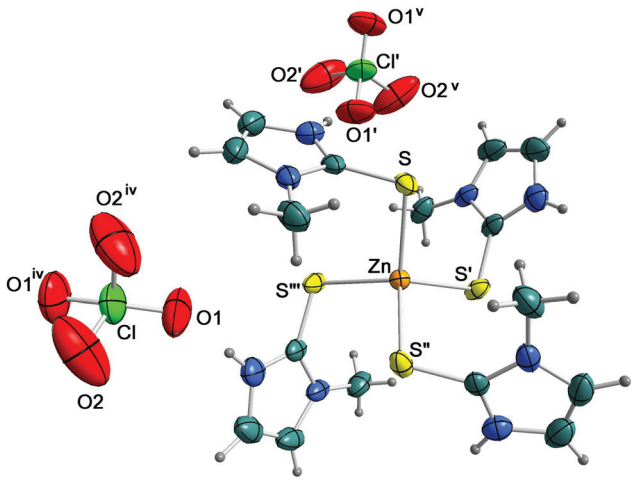

Fig. 3 Displacement ellipsoid model (obtained by Diamond 3.2k) of the complex $[Zn(MeImHS)_4](ClO_4)_2$ at the 20% probability level with the numbering scheme. Only one of the two positions of the disordered perchlorate anion (see the Experimental section) is shown for clarity. Symmetry codes: [i] 0.75 + y, 1.25 − x, 0.25 − z; [ii] 2 − x, 0.5 − y, z; [iii] 1.25 − y, −0.75 + x, 0.25 − z; [iv] 2 − x, −0.5 − y, z; [v] 0.25 − y, −0.75 + x, 0.25 − z. Selected coordination-sphere bond distances (Å) and angles (°): Zn–S 2.3273(4), S–C1 1.712(2); S–Zn–S′ 103.47(1), S–Zn–S″ 122.28(3); N1–H1···O1′: H1···O1′ 2.100(8) Å, N1···O1′ 2.940(8) Å, N1–H1···O1′ 165.1(3)°.

bond (interaction **a** in Fig. 4a) with perchlorate anions, thus generating a highly symmetric network constructed by identical $C_2^2(12)$ chains running along both the [100] and [010] directions (Fig. 4a). Fig. 4b shows a lateral view of this network (highlighted in red) sited in the crystal with a packing resembling a bubble pack foil.

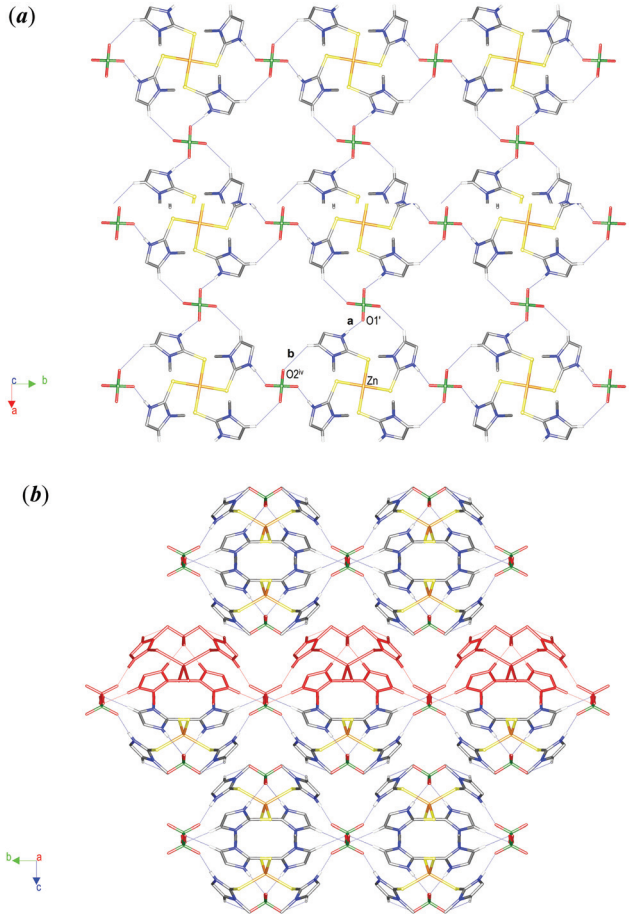

Fig. 4 Packing views of the complex showing (a) identical $C_2^2(12)$ chains running along both the [100] and [010] directions; (b) a 3D packing view evidencing (red) the network depicted in (a). H-atoms have been omitted for clarity reasons except for those involved in the interactions shown: **a**, N1–H1···O1′: H1···O1′ 2.100(8) Å, N1···O1′ 2.940(8) Å, N1–H1···O1′ 165.1(3)°; **b**, C3–H3···O2[iv] 2.82(1) Å, 3.54(1) Å, 135.9(3)°. Symmetry codes: [i] 0.75 + y, 1.25 − x, 0.25 − z; [iv] 2 − x, −0.5 − y, z.

Despite the low solubility in water of the complex $[Zn(MeImHS)_4](ClO_4)_2$, it readily reacts in the heterogeneous phase with a diluted aqueous solution of triethylamine to form an insoluble powder which we failed to crystallise.

The ESI-MS spectrum of the isolated complex and the peak assignments are shown in ESI-Fig. S1.† The characteristic isotopic peaks for zinc-containing ions are clearly identifiable in the spectrum. The calculated and experimental isotopic patterns for selected peaks are reported in ESI-Fig. S2.† The signal with the highest intensity at m/z 291 is due to the expected $[Zn(MeImS)_2H]^+$ ion. Moreover, as shown by the signals at m/z 405 and m/z 519, traces of complexes $[Zn(MeImS)_3H_2]^+$ and $[Zn(MeImS)_4H_3]^+$, respectively, were found. Fragmentation of the main species $[Zn(MeImS)_2H]^+$

gives, besides the ligand, the $[Zn(MeImS)(H_2O)]^+$ (*m*/*z* 195) and $[Zn(MeImS)]^+$ (*m*/*z* 177) species.

Useful information on the nature of the complex $[Zn(MeImS)_2]$ was also obtained from solid-state MAS ^{13}C-NMR spectroscopy (ESI-Fig. S3†). Deprotonation of the Zn-bound methimazole produces the corresponding thionate species in which the anionic charge is mainly localised on the N–C–S thioamide fragment (see below). The spectrum of the complex shows only four resonances showing the equivalence of the MeImS molecules. As a consequence of (*N*,*S*)-coordination to the Zn-centre, the thioamido carbon C(2) (δ = 145.6) proves to be the most sensitive to complexation as confirmed by the significantly high field shift observed (≈18 ppm) relative to that of the free ligand. Conversely, carbons C(4) and C(5) are slightly deshielded (3.1 and 1.0 ppm, respectively) compared to free MeImHS (δ_C, 25 °C, MeImHS: *C*S 163.5, *C*5 120.0, *C*4 114.2, NMe 34.0, $CHCl_3$/MeCN 4 : 1 v/v).[11] On the basis of experimental evidence, it is therefore reasonable to hypothesise for the homoleptic complex $[Zn(MeImS)_2]$ that each MeImS unit binds the metal ion forming a four-membered (*N*,*S*)-chelate.

Theoretical calculations

In recent years, theoretical calculations carried out at the density functional theory (DFT)[17,18] level have been widely recognised as a reliable tool capable of providing very accurate information at an acceptable computational cost. In particular, some authors have exploited DFT calculations to investigate the nature of different Zn^{II} complexes[19] and the reactivity of several systems based on imidazole-2-chalcogenone derivatives.[11a,20] Encouraged by these results, we have investigated the donor properties of the anionic species MeImS by adopting the well-known B3LYP[21] functional along with the 6-31G* all-electron basis set. Kohn–Sham (KS) HOMO calculated for the donor is a π-orbital largely localised on the S and N atoms, antibonding with respect to the C═S bond. KS-HOMO−1 and HOMO−3 feature the largest contributions from the lone pairs localised on the sulphur and nitrogen atoms, respectively (ESI-Fig. S4†). An examination of the natural charges calculated for MeImS at the optimised geometry reveals that the nitrogen atom in the 3-position and the exocyclic sulphur atom display similar negative charges (−0.565 and −0.536 *e*, respectively). The Kohn–Sham MO composition and the charge distribution support the capability of both atoms to behave as donors, as hypothesised for the complex $[Zn(MeImS)_2]$ (see above). A view of the optimised complex $[Zn(MeImS)_2]$ is presented in ESI-Fig. S5† (see ESI-Table S1† for a list of selected bond lengths and angles). The zinc atom adopts a distorted tetrahedral geometry with both anions (*N*,*S*)-chelating.

The presented data suggest that the strained four-membered ring in Zn/MeImS affects the electronic-donation from the imido and thiocarbonyl groups to the hybrid orbitals of the zinc ion, thus causing a lower orbital overlap.

The complex $[Zn(MeImS)_2]$: reactivity at the zinc-coordinated methimazole anion

Picot *et al.*[22a] recently reported biomimetics complex-models featuring different cores and charges to study the alkylation reactions that occur at zinc-bound thiolate in a variety of zinc sites of enzymes. The reactions of these biomimetic complexes with methyl iodide led to the formation of thioethers and zinc complexes containing iodide, allowing the authors to investigate the mechanism of zinc-mediated alkyl group transfer to thiols.[22b–d]

In this context, we have investigated the reactivity of the complex $[Zn(MeImS)_2]$ with methyl iodide as the alkylating agent. The $[Zn(MeImS)_2]$ complex may be subject to reactions that can occur both at the coordinated methimazole and at the metal centre. As zinc(II) is an ion of borderline hardness, nitrogen, sulphur, halogen, and oxygen donor atoms can all be involved in coordination at the metal centre, with a coordination number of four, five, or six depending on the ligand size and charge-transfer ability.[8–11,22] Moreover, the lack in d^{10} metal ions of crystal field stabilisation energy (CFSE) enables a facile change of the coordination sphere in a reaction.

The reaction between the complex $[Zn(MeImS)_2]$ and CH_3I (1 : 2 molar ratio) was carried out in a water/MeOH mixture for five days. During this time, the suspended complex dissolved completely with the formation of a clear solution by slow evaporation, allowing crystals of stoichiometry $[Zn(MeImSMe)_2I_2]$ to form. X-ray diffraction analysis was performed on a single crystal; a displacement ellipsoid model view of the complex is shown in Fig. 5 and data collection and refinement parameters are summarised in Table 2.

The zinc(II) centre of the complex is coordinated by two MeImSMe molecules acting as monodentate *N*-ligands and two iodides in a slightly distorted tetrahedral geometry. The Zn–N and Zn–I bond distances are similar to those in other zinc complexes reported in the literature.[23]

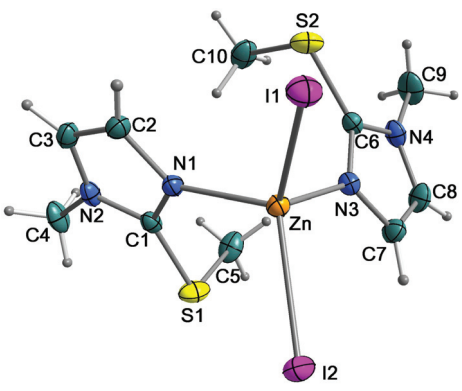

Fig. 5 Displacement ellipsoid model (obtained by Diamond 3.2k) of the complex $[Zn(MeImSMe)_2I_2]$ at the 20% probability level with the numbering scheme. H-atoms are omitted for clarity reasons. Selected coordination sphere bond distances (Å) and angles (°): Zn–I1 2.5822(5), Zn–I2 2.5852(7), Zn–N1 2.018(2), Zn–N3 2.028(2), S1–C1 1.738(3); S2–C6 1.742(3); I1–Zn–I2 109.75(2), I1–Zn–N1 109.61(6), I1–Zn–N3 112.17(6), N1–Zn–N3 103.14(8).

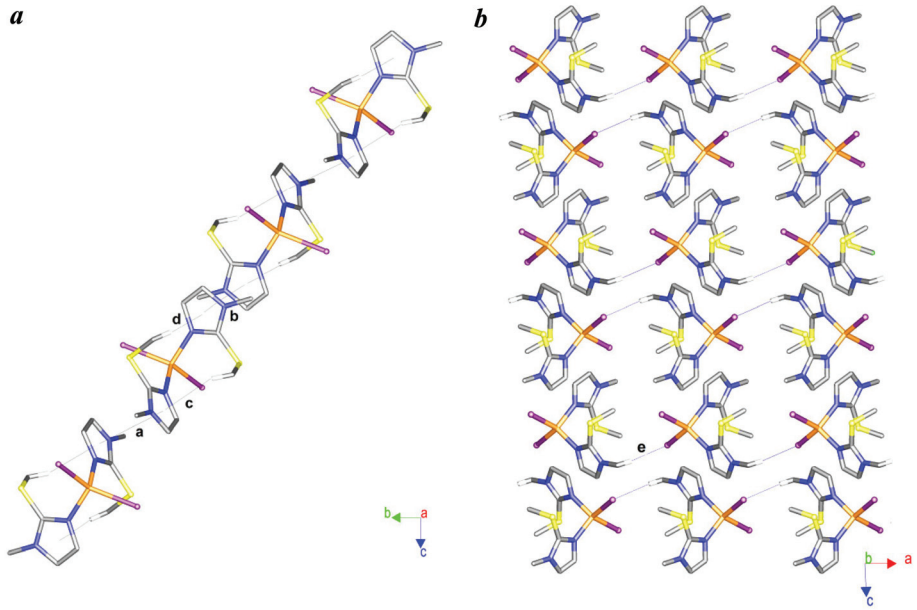

Fig. 6 Packing views of the complex showing (a) pillars running along the [011] built up through **a** and **b** inter-molecular π···π interactions; (b) aligned pillars interacting along the [100] direction. H-atoms have been omitted for clarity reasons except for those involved in the illustrated interactions: **a**, $Cnt_{Im(N1-N2)}$···$Cnt_{Im(N1-N2)}^{i}$, 3.50 Å, 0°; **b**, $Cnt_{Im(N3-N4)}$···$Cnt_{Im(N3-N4)}^{ii}$, 3.61 Å, 0°; **c**, C5–H5c···$Cnt_{Im(N3-N4)}$ 2.88 Å; **d**, C10–H10c···$Cnt_{Im(N1-N2)}$ 2.92 Å; **e**, C4–H4a···I1^{iii} 3.13 Å. Symmetry codes: ^{i} $-x, 1-y, 2-z$; ^{ii} $-x, 1-y, 1-z$; ^{iii} $-1-x, -y, 1-z$.

The imidazole rings are planar and the S-Me groups are oriented through the centre of opposite imidazole rings with C–H···Cnt_{Im} distances of 2.88 and 2.92 Å for C5–H5c···$Cnt_{Im(N3-N4)}$ and C10–H10c···$Cnt_{Im(N1-N2)}$, respectively (**c** and **d** interactions in Fig. 6a). Inter-molecular π···π interactions between parallel facing Im rings pile up the molecules in pillars developing along the [011] direction (Fig. 6a). Parallel pillars weakly interact with each other through C–H···I contacts as shown in Fig. 6b.

The interesting reactivity shown by the system $[Zn(MeImS)_2]/CH_3I$ led us to test the reaction of the complex $[Zn(MeImS)_2]$ towards hydriodic acid (HI) with the aim of verifying the site of protonation.

The complex $[Zn(MeImS)_2]$ was suspended in a water/MeOH mixture with HI in a 1 : 2 molar ratio. The reaction proceeded with the complete dissolution of the powder and the formation of a clear pale yellow solution. After slow evaporation of the solution, white crystals of the complex $[Zn(MeImHS)_2I_2]$ were isolated. The X-ray crystal structure which we recently reported[11b] features a tetrahedral zinc(II) centre coordinated by two neutral methimazole units and two iodides. Since the four-membered ring formed by (*N*,*S*)-chelating thionates is inherently strained,[8,9] it is not surprising that the products separated no longer feature the ZnNCS four-atom ring. In the case of the reaction with HI we observe the protonation of the imido-nitrogen atom along with the formation of a Zn–S(thione) bond, leading to the formation of the neutral complex $[Zn(MeImHS)_2I_2]$. In the case of the reaction with MeI, the methylation reaction occurs on the thionate leading to the formation of the organic moiety *S*-methylmethimazole that binds the Zn centre *via* the imido-nitrogen atom only. Being a neutral organic moiety, the charge is balanced by two coordinating iodides. It is interesting to observe that the thioether group is uncoordinated to zinc. On this matter, previous studies[22,24,25] have shown that factors such as the charge and structure at the Zn centre play an important role in driving the coordinating ability of thioether groups; when thioethers are part of neutral chelates they result in tetrahedral complexes which are invariably uncoordinated since a negatively charged ligand (*i.e.* I^-) transfers more charge to Zn^{2+} than a neutral one.

Reactivity of methimazole towards the ZnN_4 core

A large number of structurally characterised Zn-catalytic sites are four-coordinated tetrahedra, with the zinc bound to three histidine nitrogens and the fourth site occupied by a water molecule, as found, for example, in carbonic anhydrases or phosphate esterases.[5c,d] To study the interaction of methimazole with a ZnN_4 coordination sphere, we selected a simple mononuclear ZnN_4 model complex with the 1-methylimidazole (MeIm) ligands representing the histidine (His) amino acid residues.[26] The complex $[Zn(MeIm)_4](ClO_4)_2$ was synthesised according to Chen *et al.*[27] The X-ray crystal structure of this complex consists of tetrahedral monomeric $[Zn(MeIm)_4]^{2+}$ cations and the Zn–N_{MeIm} bond lengths (1.991(2) Å) are comparable to the Zn–N(His) average bond length found in Zn proteins as determined by NMR spectroscopy[28] (2.09 ± 0.14 Å). The complex $[Zn(MeIm)_4](ClO_4)_2$ shows good stability in water since no relevant changes in its absorption spectrum were found after 6 h at 25 °C. MeIm in aqueous solution shows a

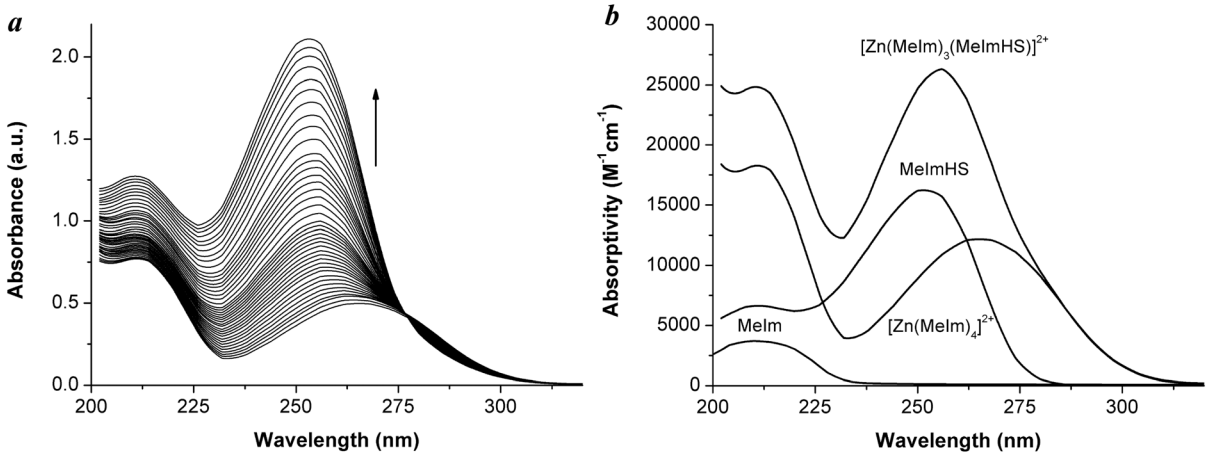

Fig. 7 (a) Selected spectra collected during the titration of $[Zn(MeIm)_4]^{2+}$ (8.53×10^{-5} M) with MeImHS (3.50×10^{-4} M) from 0 to 4 MeImHS/$[Zn(MeIm)_4]^{2+}$ molar ratio; (b) pure spectra of MeIm, MeImHS, $[Zn(MeIm)_4]^{2+}$, and $[Zn(MeIm)_3(MeImHS)]^{2+}$; [$T$ = 25 °C, 0.1 M buffer solution pH 9 (borax/hydrochloric acid), 1 cm optical path length].

broad absorption band located at 210 nm due to π–π* transitions of the imidazole ring (Fig. 7b).[29] In the absorption spectrum of $[Zn(MeIm)_4]^{2+}$ the π–π* transitions are almost unshifted (band at 212 nm), and a new band at 266 nm due to the MeIm → Zn ligand-to-metal charge-transfer transition is observed.[31] The complex shows no appreciable absorption in the region above 400 nm in water, in accord with the d^{10} electronic configuration of the zinc(II) ion.

The interaction of methimazole with the cationic complex $[Zn(MeIm)_4]^{2+}$ was assessed by spectrophotometric titration. By adding increasing amounts of MeImHS, the band at 266 nm related to $[Zn(MeIm)_4]^{2+}$ shifts towards a shorter wavelength, increasing its absorbance intensity (Fig. 7a), a feature consistent with an interaction altering the ZnN_4 core. An isosbestic point is present at 277 nm, providing evidence for at least one equilibrium. From eigenvalue analysis of the spectrophotometric data in the 230–300 nm range, three significant eigenvalues were found, indicating that in solution three linearly independent absorbing species were present (in the 230–300 nm range the absorption of MeIm is negligible), namely $[Zn(MeIm)_4]^{2+}$, MeImHS and a newly formed species identified as the complex $[Zn(MeIm)_3(MeImHS)]^{2+}$. By fitting the experimental data considering the equilibrium as in eqn (1),

$$[Zn(MeIm)_4]^{2+} + MeImHS \rightleftharpoons [Zn(MeIm)_3(MeImHS)_1]^{2+} + MeIm \quad (1)$$

the complex formation constant of $[Zn(MeIm)_3(MeImHS)]^{2+}$ was calculated (K_f = 5.82 ± 0.02 M^{-1}). Any attempt to fit the experimental data considering zinc complexes with more than one MeImHS ligand led to unreliable results. The pure spectra of MeIm, MeImHS, $[Zn(MeIm)_4]^{2+}$, and $[Zn(MeIm)_3(MeImHS)]^{2+}$ are reported in Fig. 7b and the spectral parameters of all the absorbing species are reported in Table 3. These results suggest that the electron-accepting ability of Zn in the complex[29] depends on the set of coordinating ligands. In this case, the formation of $[Zn(MeIm)_3(MeImHS)]^{2+}$ species forecloses the entry of another unit of MeImHS.

Table 3 Summary of UV/vis maximum absorption wavelength and molar absorptivity values for ligands and complexes (aqueous solution, 25 °C, 0.1 M buffer solution, pH 9 (borax/hydrochloric acid), 1.0 cm optical path length)

	λ_{max}/nm	ε (M^{-1} cm^{-1})
MeIm	210	3691
MeImHS	252	16 300
	210	6600
$[Zn(MeIm)_4]^{2+}$	266	12 200
	212	18 400
$[Zn(MeIm)_3(MeImHS)]^{2+}$	256	26 300
	210	25 000

Lim pointed out that the catalytic activity of the Zn-His_3-OH_2 site is mainly due to the water ligand that transfers the least charge to the zinc ion and is less bulky compared to the protein residues.[30] In this context, the marked difference in charge-transfer ability between MeImHS and water supports the possibility that MeImHS can interfere with the catalytic activity of Zn-His_3-OH_2 metalloenzymes[31] by displacing the Zn-bound water molecule from the active site.[30] The promising results obtained are a stimulus for further investigations (beyond the scope of the present study) of the interaction of methimazole, or of thioamide containing drugs in general, with mononuclear models representative of [Zn-(XYZ)-(OH_2)] enzymes (where X, Y, Z = His, Asp, Cys, Glu).

Conclusions

New stable complexes of the drug methimazole (MeImHS) and its anion (MeImS) with zinc ions have been separated and

structurally characterised. In the case of $[Zn(MeImHS)_4](ClO_4)_2$, four neutral ligands are *S*-coordinated in a distorted tetrahedral coordination geometry; the Zn–S bond distances are comparable to the average Zn–S(cysteine) bond lengths (2.32 Å) found in zinc proteins. Solution studies on the reaction of methimazole with $[Zn(MeIm)_4](ClO_4)_2$, selected as a model compound representing $[Zn(His)_4]^{2+}$ and $[Zn(His)_3(H_2O)]^{2+}$ protein sites, show methimazole displacing only one of the coordinated MeIm molecules. This evidence supports the possibility that methimazole, by blocking a histidine/water binding site, could interfere with the multifunctional roles of zinc atoms in proteins (*e.g.* the enzymatic activity of carbonic anhydrases).[5c] The anion methimazole can effectively act as a (*N*,*S*)-bridging/chelating ligand to a variety of metal ions due to its N–C–S functional group. The synthesised homoleptic complex $[Zn(MeImS)_2]$ reveals a different reactivity towards the electrophilic addition of H^+ and CH_3^+. The MeImS moieties are *N*-protonated by HI to form the neutral complex $[Zn(MeImHS)_2I_2]$; conversely, the reaction of $[Zn(MeImS)_2]$ with methyl iodide leads to the formation of the complex $[Zn(MeImSMe)_2I_2]$. This evidence shows that Zn-coordinated methimazole can markedly modify the coordination environment when changing from its thione to thionate form, and *vice versa*. Within the scope of the study on the interaction of molecules of pharmacological interest with zinc, these results underline that methimazole shows a reactivity and a variety of coordinating modes that may in some way alter the biological processes that are based on the zinc ion.

Experimental

Materials and instrumentation

Reagents were used as purchased from Aldrich or Fluka. Elemental analyses were performed using a Fisons Instruments 1108 CHNS elemental analyser. FT-infrared spectra of powdered samples were recorded with a Thermo-Nicolet 5700 spectrometer from 4000 to 400 cm^{-1} in the form of pressed KBr pellets. UV-vis spectrophotometric measurements were carried out with a Varian Cary 50 spectrophotometer equipped with a fiber optic dip probe (1 cm optical path length). ^{13}C-NMR spectra were recorded on a Varian 400 MHz spectrometer. Chemical shifts are reported in ppm (δ) downfield from TMS using the same solvent as the internal reference. The MAS ^{13}C-NMR spectrum was calibrated such that the observed upfield peak in the spectrum of adamantane is set to δ = 31.47. Mass spectra were obtained on a QqQ triple quadrupole Varian 310-MS LC/MS mass spectrometer, with electrospray ionisation at atmospheric pressure. The complex tetrakis(1-methylimidazole-N^3)zinc(II) diperchlorate $[Zn(MeIm)_4](ClO_4)_2$ was synthesised according to ref. 27.

Synthesis of complexes

Synthesis of complex $[Zn(MeImHS)_4](ClO_4)_2$. A mixture of methimazole (0.100 g, 0.88 mmol) dissolved in 5 mL of ethyl alcohol and $Zn(ClO_4)_2$ hexahydrate (0.082 g, 0.22 mmol) dissolved in 5 mL of water was slightly heated for 10 min and then stirred for 12 h. A white solid powder was separated from the solution, washed with an ethyl alcohol/*n*-hexane mixture (v/v 1 : 1) and dried in an oven at 50 °C. The filtered solution was slowly concentrated, and cooled at 10 °C for two days to separate crystals of the title compound. Yield $C_{16}H_{24}Cl_2N_8O_8S_4Zn$ (720.94): calcd C 26.67, H 3.36, N 15.55, S 17.75; found: C 27.0, H 3.4, N 15.6, S 17.7. δ_C (100.5 MHz, $CDCl_3$-CH_3CN 4 : 1 v/v) 150.7 (*C*S), 122.4 (*C*5), 118.0 (*C*4) 32.5 (N-*C*H_3). IR (KBr, ν/cm^{-1}): 3127m, 1548m, 1532m, 1420w, 1289w, 1252w, 1235m, 1094s, 957w, 937m, 846w, 828w, 767m, 744m, 674w, 658m, 624m.

Synthesis of complex $[Zn(MeImS)_2]$. The complex $[Zn(MeImHS)_4](ClO_4)_2$ (0.200 g, 0.277 mmol) in 50 mL of water was reacted with triethylamine (0.39 mL, 2.770 mmol) for 2 h at room temperature. The solid powder was filtered and washed several times with ethyl alcohol/water (1 : 1 v/v) to eliminate the triethylamine and then dried in an oven at 50 °C. Yield: 0.066 g, 75%; $C_8H_{10}N_4S_2Zn$ (291.53): calcd C 32.96, H 3.46, N 19.21, S 21.93; found: C 33.2, H 3.5, N 19.3, S 21.8. δ_C (100.5 MHz, solid state) 145.6 (*C*S), 123.1 (*C*5), 17.7 (*C*4), 31.4 (N-*C*H_3). IR (KBr, ν/cm^{-1}): 3118w, 2940 m, 1536 m, 1456vs, 1414s, 1372vs, 1315s, 1284s, 1144s, 1084 m, 954 m, 732s, 697s, 688s, 517s.

Synthesis of the complex $[Zn(MeImSMe)_2I_2]$. The complex $Zn(MeImS)_2$ (0.100 g, 0.344 mmol) suspended in 20 mL of a water/MeOH mixture (1/1 v/v) and methyl iodide (0.098 g, 0.688 mmol) were reacted at room temperature for five days with continuous stirring. In the course of the reaction the suspended complex dissolved with the formation of a clear solution. It was filtered to remove traces of solids and allowed to stand at 5° C. After two days white crystals were collected and washed with *n*-hexane. Yield: 0.148 g, 75%; $C_{10}H_{16}I_2N_4S_2Zn$ (575.41): calcd C 20.87, H 2.80, N 9.73, S 11.37; found: C 21.0, H 2.9, N 9.9, S 11.4. δ_C (100.5 MHz, $CDCl_3$–CH_3CN 4 : 1 v/v) 160.9 (*C*2S), 121.8 (*C*5), 128.5 (*C*4), 33.5 (N–*C*H_3), 15.6(S–*C*H_3). IR (KBr, ν/cm^{-1}): 3119w, 2919w, 1529w, 1462s, 1410s, 1338w, 1283s, 1148vs, 1080w, 970w, 953w, 764vs, 692vs.

Synthesis of the complex $[Zn(MeImHS)_2I_2]$. The complex $Zn(MeImS)_2$ (0.100 g, 0.344 mmol) suspended in 20 mL of a water/MeOH mixture (1/1 v/v) and hydriodic acid (55 wt% in water) (0.160 g, 0.688 mmol) dissolved in 5 mL of water were reacted for two days at r.t. The clear pale yellow solution was filtered and allowed to stand at 5 °C for three days. A pale yellow powder was collected and washed with a 1 : 1 (v/v) mixture of CH_2Cl_2/*n*-hexane and then dried *in vacuo*. Yield: 0.169 g, 90%; $C_8H_{12}I_2N_4S_2Zn$ (547.36): calcd C 17.54, H 2.21, N 10.23, S 11.68; found: C 17.3, H 2.1, N 10.2, S 11.6. δ_C (100.5 MHz, $CDCl_3$–CH_3CN 4 : 1 v/v) 152.5 (*C*S), 120.6 (*C*5), 115.4 (*C*4) 34.1 (N-*C*H_3). IR (KBr, ν/cm^{-1}): 3287br, 3163m, 3133m, 1683w, 1573s, 1468s, 1450s, 1404 m, 1280 m, 1155m, 1086 m, 1015w, 920w, 733s, 685m, 667s, 627s, 595m, 510m.

Spectrophotometric measurements

The complex formation constant of $[Zn(MeIm)_3(MeImHS)]^{2+}$ was determined at 25 °C by spectrophotometric titration of $[Zn(MeIm)_4]^{2+}$ (8.53×10^{-5} mmoles) with MeImHS (3.50×10^{-4} M) in 0.1 M buffer solution, pH 9 (borax/hydrochloric acid). The number of linearly independent absorbing species was obtained by applying eigenvalues analysis on the absorbance data matrix.[32] The complex formation constant was obtained using the Hyperquad 2003 program.[33]

Mass spectrometry

Sample solutions (10 mg L^{-1}) were prepared in CH_3CN and infused directly into the ESI source using a programmable syringe pump, with a flow rate of 1.50 mL h^{-1}. Needle, shield and detector voltages were kept at 4500, 800 and 1450 V, respectively. Pressures of nebulising and drying gas were both 15 psi, and housing and drying gas temperatures were 60 and 50 °C, respectively. The isotopic patterns of the signals in the mass spectra were analysed using the mMass 5.5.0 software package.[34]

X-ray structure determination of $[Zn(MeImHS)_4](ClO_4)_2$ and $[Zn(MeImSMe)_2I_2]$

A summary of the crystal data and refinement details is given in Table 2. Intensity data were collected at room temperature on a Bruker Smart CCD diffractometer using graphite-monochromatised Mo-Kα radiation (λ = 0.71073 Å). Datasets were corrected for Lorentz-polarisation effects and for absorption (SADABS[35]). All structures were solved by direct methods (SIR-97[36]) and completed by iterative cycles of full-matrix least-squares refinement on F_o^2 and ΔF synthesis using the SHELXL-97[37] program (WinGX suite).[38] Hydrogen atoms located on the ΔF maps were allowed to ride on their carbon or nitrogen atoms. In $[Zn(MeImHS)_4](ClO_4)_2$, the perchlorate showed high anisotropic displacement parameters for the oxygen atoms, thus indicating a situation of disorder, which was subsequently modelled by spitting each oxygen atom over two close positions, and refining them with an occupancy factor of 0.5 each. Crystallographic data have been deposited with the Cambridge Crystallographic Data Centre as supplementary publication no. CCDC-1051219 and CCDC-1051220.

Computational studies

Theoretical calculations were carried out at the DFT level on MeImS and $Zn(MeImS)_2$ using the software Spartan '10 v. 1.1.0 for Linux (parallel 64-bit version) with the B3LYP hybrid functional.[39] The all-electron 6-31G* was adopted for all atomic species.

Acknowledgements

We would like to thank Regione Autonoma della Sardegna for financial support (grant number CRP-59699).

Notes and references

1 (*a*) W. N. Lipscomb and N. Sträter, *Chem. Rev.*, 1996, **96**, 2375–2433; (*b*) D. R. Williams, *Coord. Chem. Rev.*, 1999, **186**, 177–188; (*c*) D. S. Auld, *Biometals*, 2001, **14**, 271–273; (*d*) S. Hughes and S. Saran, *J. Am. Coll. Nutr.*, 2006, **25**, 285–291; (*e*) W. Maret, *Adv. Nutr.*, 2013, **4**, 82–91; (*f*) M. Laitaoja, J. Valjakka and J. Jänis, *Inorg. Chem.*, 2013, **52**, 10983–10991; (*g*) T. Kochańczyk, A. Drozd and A. Krężel, *Metallomics*, 2015, **7**, 244–257. and references therein.

2 (*a*) G. Parkin, *Chem. Rev.*, 2004, **104**, 699–767; (*b*) W. Maret, *Biometals*, 2011, **24**, 411–418; (*c*) D. S. Auld, *Biometals*, 2009, **22**, 141–148.

3 D. W. Christianson, *Adv. Protein Chem.*, 1991, **42**, 281–355.

4 (*a*) I. L. Alberts, K. Nadassy and S. J. Wodak, *Protein Sci.*, 1998, **7**, 1700–1716; (*b*) A. J. Turner, *Biochem. Soc. Trans.*, 2003, **31**, 723–727.

5 (*a*) M. Laitaoja, J. Valjakka and J. Jänis, *Inorg. Chem.*, 2013, **52**, 10983–10991; (*b*) K. A. McCall, C.-C. Huang and C. A. Fierke, *J. Nutr.*, 2000, **130**, 1437S–1446S; (*c*) B. L. Vallee and D. S. Auld, *Acc. Chem. Res.*, 1993, **26**, 543–551; (*d*) W. N. Lipscomb and N. Strater, *Chem. Rev.*, 1996, **96**, 2375–2433.

6 The antithyroid drug methimazole is currently the mainstay of pharmacological treatment for Graves' disease in Europe, Japan and the United States having become the most frequently prescribed antithyroid drug in the last 20 years. The primary effect of methimazole is to inhibit thyroid hormone precursor synthesis by competing with the tyrosine residues of the enzyme thyroperoxidase (TPO) for an oxidised form of iodine. (*a*) A. B. Emiliano, L. Governale, M. Parks and D. S. Cooper, *J. Clin. Endocrinol. Metab.*, 2010, **5**(5), 2227–2233; (*b*) D. S. Cooper, *N. Engl. J. Med.*, 2005, **352**, 905–917.

7 (*a*) A. A. Alturfan, E. Zengin, N. Dariyerli, E. E. Alturfan, M. K. Gumustas, E. Aytac, M. Aslan, N. Balkis, A. Aksu, G. Yigit, E. Uslu and E. Kokoglu, *Folia Biol.*, 2007, **53**, 183–188; (*b*) N. M. Urquiza, S. G. Manca, M. A. Moyano, R. A. Dellmans, L. Lezama, T. Rojo, L. G. Naso, P. A. M. Williams and E. G. Ferrer, *Biometals*, 2010, **23**, 255–264.

8 E. S. Raper, *Coord. Chem. Rev.*, 1996, **153**, 199–255.

9 (*a*) E. S. Raper, *Coord. Chem. Rev.*, 1997, **165**, 475–567; (*b*) E. S. Raper, J. R. Creighton, R. E. Oughtred and I. W. Nowell, *Acta Crystallogr., Sect. B: Struct. Sci.*, 1983, **39**, 355–360.

10 P. D. Akrivos, *Coord. Chem. Rev.*, 2001, **213**, 181–210.

11 (*a*) F. Isaia, M. C. Aragoni, M. Arca, C. Caltagirone, C. Castellano, F. Demartin, A. Garau, V. Lippolis and A. Pintus, *Dalton Trans.*, 2011, **40**, 4505–4513; (*b*) F. Isaia, M. C. Aragoni, M. Arca, C. Caltagirone, A. Garau, P. G. Jones, V. Lippolis and R. Montis, *CrystEngComm*, 2014, **16**, 3613–3623.

12 Y. Matsunaga, K. Fujisawa, N. Amir, Y. Miyashita and K.-I. Okamoto, *J. Coord. Chem.*, 2005, **58**, 1047–1061.

13 I. W. Nowell, A. G. Cox and E. S. Raper, *Acta Crystallogr., Sect. B: Struct. Crystallogr. Cryst. Chem.*, 1979, **35**, 3047–3050.

14 R. Castro, J. A. Garcia-Vasquez, J. Romero, A. Sousa, Y. D. Chang and J. Zubieta, *Inorg. Chim. Acta*, 1995, **237**, 143–146.

15 Bell *et al.* reported on the synthesis of the homoleptic complex $[Hg(MeImS)_2]$ obtained from the reaction of mercury(II) acetate with MeImHS in a water/triethylamine solution. N. A. Bell, W. Clegg, J. R. Creighton and E. S. Raper, *Inorg. Chim. Acta*, 2000, **303**, 12–16.

16 (*a*) D. J. Williams, K. A. Arrowood, L. M. Bloodworth, A. L. Carmack, D. Gulla, M. W. Gray, I. Maasen, F. Rizvi, S. L. Rosenbaum, K. P. Gwaltney and D. VanDerveer, *J. Chem. Crystallogr.*, 2010, **40**(12), 1074–1077; (*b*) D. J. Williams, J. J. Concepcion, M. C. Koether, K. A. Arrowood, A. L. Carmack, T. G. Hamilton, S. M. Luck, M. Ndomo, C. R. Teel and D. VanDerveer, *J. Chem. Crystallogr.*, 2006, **36**(8), 453–457.

17 W. Koch and M. C. Holthausen, Front Matter and Index, in *A Chemist's Guide to Density Functional Theory*, Wiley-VCH Verlag GmbH, Weinheim, FRG, 2nd edn, 2001, pp. 1–13.

18 (*a*) C. J. Cramer and D. G. Truhlar, *Phys. Chem. Chem. Phys.*, 2009, **11**, 10757–10816; (*b*) E. R. Davidson, *Chem. Rev.*, 2000, **100**, 351–352.

19 (*a*) M. C. Aragoni, M. Arca, A. Bencini, C. Caltagirone, A. Garau, F. Isaia, M. E. Light, V. Lippolis, C. Lodeiro, M. Mameli, R. Montis, M. C. Mostallino, A. Pintus and S. Puccioni, *Dalton Trans.*, 2013, **42**, 14516–14530; (*b*) V. M. Nurchi, G. Crisponi, M. Arca, M. Crespo-Alonso, J. I. Lachowicz, D. Mansoori, L. Toso, G. Pichiri, M. A. Santos, S. M. Marques, J. Niclos-Gutierrez, J. M. Gonzales-Perez, A. Dominguez-Martin, D. Choquesillo-Lazarte, Z. Szewczuk, M. A. Zoroddu and M. Peana, *J. Inorg. Biochem.*, 2014, **141**, 132–143.

20 (*a*) A. Mancini, M. C. Aragoni, N. Bricklebank, V. Lippolis, A. Pintus and M. Arca, *Chem. – Asian J.*, 2013, **8**, 639–647; (*b*) E. J. Juarez-Perez, M. C. Aragoni, M. Arca, A. J. Blake, F. A. Devillanova, A. Garau, F. Isaia, V. Lippolis, R. Nuñez, A. Pintus and C. Wilson, *Chem. – Eur. J.*, 2011, **17**, 11497–11514.

21 (*a*) A. D. Becke, *J. Chem. Phys.*, 1993, **98**, 5648–5652; (*b*) C. Lee, W. Yang and R. G. Parr, *Phys. Rev.*, 1988, **B37**, 785–789; (*c*) S. H. Vosko, L. Wilk and M. Nusair, *Can. J. Phys.*, 1980, **58**, 1200–1211; (*d*) P. J. Stephens, F. J. Devlin, C. F. Chabalowski and M. J. Frisch, *J. Phys. Chem.*, 1994, **98**, 11623–11627.

22 (*a*) D. Picot, G. Ohanessian and G. Frison, *Inorg. Chem.*, 2008, **47**, 8167–8178; (*b*) J. Penner-Hahn, *Curr. Opin. Chem. Biol.*, 2007, **11**, 166–171; (*c*) C. R. Warthen, B. S. Hammes, C. J. Carrano and D. C. Crans, *J. Biol. Inorg. Chem.*, 2001, **6**, 82–90; (*d*) B. S. Hammes and C. J. Carrano, *Chem. Commun.*, 2000, 1635–1636; (*e*) H. Vahrenkamp, *Dalton Trans.*, 2007, 4751–4759., and references therein.

23 A search in the CDS showed similar $[Zn(Im)_2X_2]$ zinc complexes featuring two halides (X^-) and differently substituted imidazole moieties (Im) showing the following mean values referred to 54 structures and 62 fragments: Zn–N 2.021(7) Å, N–Zn–N 106(1)°. Among these structures, only three feature the iodide halogen showing the following mean values: Zn–I 2.600(1) Å, N–Zn–N 110(2)°.

24 B. S. Hammes and C. J. Carrano, *Inorg. Chem.*, 2001, **40**, 919–927.

25 M. Gennari, M. Retegan, S. DeBeer, J. Pecaut, F. Neese, M.-N. Collomb and C. Duboc, *Inorg. Chem.*, 2011, **50**, 10047–10055.

26 (*a*) D. T. Corwin Jr. and S. A. Koch, *Inorg. Chem.*, 1988, **27**, 493–496; (*b*) D. T. Corwin Jr., E. S. Gruff and S. A. Koch, *Chem. Commun.*, 1987, 966–967; (*c*) J. Otto, I. Jolk, T. Viland, R. Wonnemann and B. Krebs, *Inorg. Chim. Acta*, 1999, **285**, 262–268; (*d*) J. J. Wilker and S. J. Lippard, *Inorg. Chem.*, 1997, **36**, 969–978., and references therein.

27 X.-M. Chen, X.-C. Huang, Z.-T. Xu and X.-Y. Huang, *Acta Crystallogr., Sect. C: Cryst. Struct. Commun.*, 1996, **C52**, 2482–2484.

28 M. Laitaoja, J. Valjakka and J. Jänis, *Inorg. Chem.*, 2013, **52**, 10983–10991.

29 E. Bernarducci, P. K. Bharadwqj, K. Krogh-Jespersen, J. A. Potenza and H. J. Schugar, *J. Am. Chem. Soc.*, 1983, **105**, 3860–3866.

30 (*a*) Y.-M. Lee and C. Lim, *J. Mol. Biol.*, 2008, **379**, 545–553; (*b*) Y.-M. Lee and C. Lim, *J. Am. Chem. Soc.*, 2011, **133**, 8691–8703.

31 An example of a Zn-His_3-OH_2 coordination core is to be found in the carbonic anhydrase family of enzymes. Carbonic anhydrases catalyse the reversible reaction between carbon dioxide hydration and bicarbonate dehydration. They have essential roles in facilitating the transport of carbon dioxide and protons in the intracellular space, across biological membranes. S. Lindskog, *Pharmacol. Ther.*, 1997, **74**, 1–20.

32 (*a*) M. Meloun, J. Čapek, P. Mikšík and R. G. Brereton, *Anal. Chim. Acta*, 2000, **423**, 51–68; (*b*) E. R. Malinowski, in *Factor Analysis in Chemistry*, Wiley-Interscience, New York, 3rd edn, 2002.

33 P. Gans, A. Sabatini and A. Vacca, *Talanta*, 1996, **43**, 1739–1753.

34 (*a*) T. H. J. Niedermeyer and M. Strohalm, *PLoS One*, 2012, **7**(9), e44913; (*b*) M. Strohalm, D. Kavan, P. Nova and M. Volny, *Anal. Chem.*, 2010, **82**, 4648–4651; (*c*) M. Strohalm, M. Hassman, B. Kosata and M. Kodicek, RCM Letter to the Editor, *Rapid Commun. Mass Spectrom*, 2008, 22, 905–908.

35 *SADABS Area-Detector Absorption Correction Program*, Bruker AXS Inc., Madison, WI, USA, 2000.

36 A. Altomare, M. C. Burla, M. Camalli, G. L. Cascarano, C. Giacovazzo, A. Guagliardi, A. G. G. Moliterni, G. Polidori and R. Spagna R, *J. Appl. Crystallogr.*, 1999, **32**, 115–119.

37 G. M. Sheldrick, *Acta Crystallogr., Sect. A: Fundam. Crystallogr.*, 2008, **64**, 112–122.

38 L. J. Farrugia, *J. Appl. Crystallogr.*, 1999, **32**, 837–838.

39 Y. Shao, L. F. Molnar, Y. Jung, J. Kussmann, C. Ochsenfeld, S. T. Brown, A. T. B. Gilbert, L. V. Slipchenko, S. V. Levchenko, D. P. O'Neill, R. A. DiStasio Jr., R. C. Lochan, T. Wang, G. J. O. Beran, N. A. Besley, J. M. Herbert, C. Y. Lin, T. Van Voorhis, S. H. Chien, A. Sodt, R. P. Steele, V. A. Rassolov, P. E. Maslen, P. P. Korambath, R. D. Adamson, B. Austin, J. Baker, E. F. C. Byrd, H. Dachsel, R. J. Doerksen, A. Dreuw, B. D. Dunietz, A. D. Dutoi, T. R. Furlani, S. R. Gwaltney, A. Heyden, S. Hirata, C.-P. Hsu, G. Kedziora, R. Z. Khalliulin, P. Klunzinger, A. M. Lee, M. S. Lee, W. Z. Liang, I. Lotan, N. Nair, B. Peters, E. I. Proynov, P. A. Pieniazek, Y. M. Rhee, J. Ritchie, E. Rosta, C. D. Sherrill, A. C. Simmonett, J. E. Subotnik, H. L. Woodcock III, W. Zhang, A. T. Bell, A. K. Chakraborty, D. M. Chipman, F. J. Keil, A. Warshel, W. J. Hehre, H. F. Schaefer, J. Kong, A. I. Krylov, P. M. W. Gill and M. Head-Gordon, *Phys. Chem. Chem. Phys.*, 2006, **8**, 3172–3191.

ELECTRONIC SUPPLEMENTARY INFORMATION

Zinc(II)-methimazole complexes: synthesis and reactivity

Francesco Isaia,*[†] Maria Carla Aragoni,[†] Massimiliano Arca,[†] Alexandre Bettoschi,[†] Claudia Caltagirone,[†] Carlo Castellano,[‡] Francesco Demartin,[‡] Vito Lippolis,[†] Tiziana Pivetta[†] and Elisa Valletta[†]

[†]Dipartimento di Scienze Chimiche e Geologiche, Università degli Studi di Cagliari, Cittadella Universitaria, 09042 Monserrato (CA), Italy. Fax: +39 070 6754456; Tel: +39 070 6754496. E-mail: isaia@unica.it

[‡]Dipartimento di Chimica, Università degli Studi di Milano, via Golgi 19, 20133 Milano. Italy.

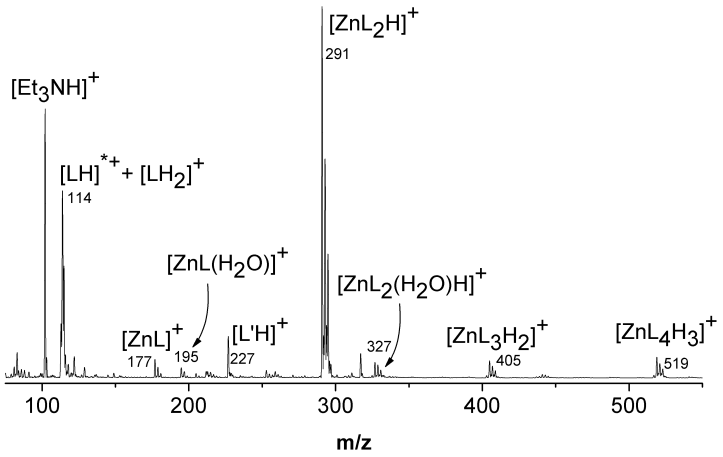

Fig. S1 Positive ion ESI-MS spectrum of $[Zn(MeImS)_2]$, ($3.45x10^{-5}$ M, CH_3CN); L = MeImS, L' = methimazole-disulfide ($C_8H_{10}N_4S_2$) (part of the released ligand from $[ZnL_2H]^+$, undergoes oxidation and formation of protonated methimazole-disulfide $[(C_4H_5N_2S)_2H]^+$ (*m/z* 227). The signal at m/z 114 corresponds to a convoluted signals of the radical $[MeImSH]^{*+}$ (86%) and the $[MeImHS+H^+]^+$ (14%) species. In fact, the experimental pattern is due to a weighted combination of the isotopic pattern of the two molecules. The weights, namely the percentage in which each molecule is present, was obtained by multivariate regression analysis of the experimental data.

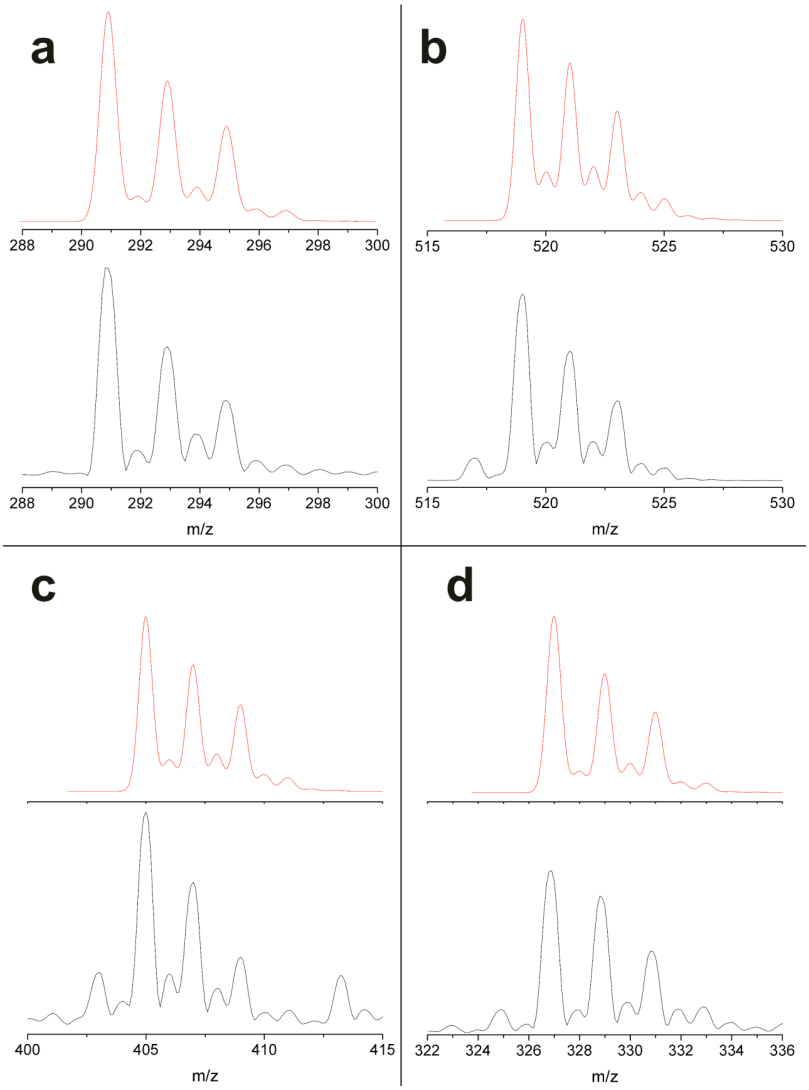

Fig. S2 Calculated (red) and experimental (black) isotopic patterns for $[ZnL_2H]^+$ (**a**), $[ZnL_4H_3]$ (**b**), $[ZnL_3H_2]^+$ (**c**), $[ZnL_2(H_2O)_2H_2]^+$ (**d**) ions, (L = MeImS).

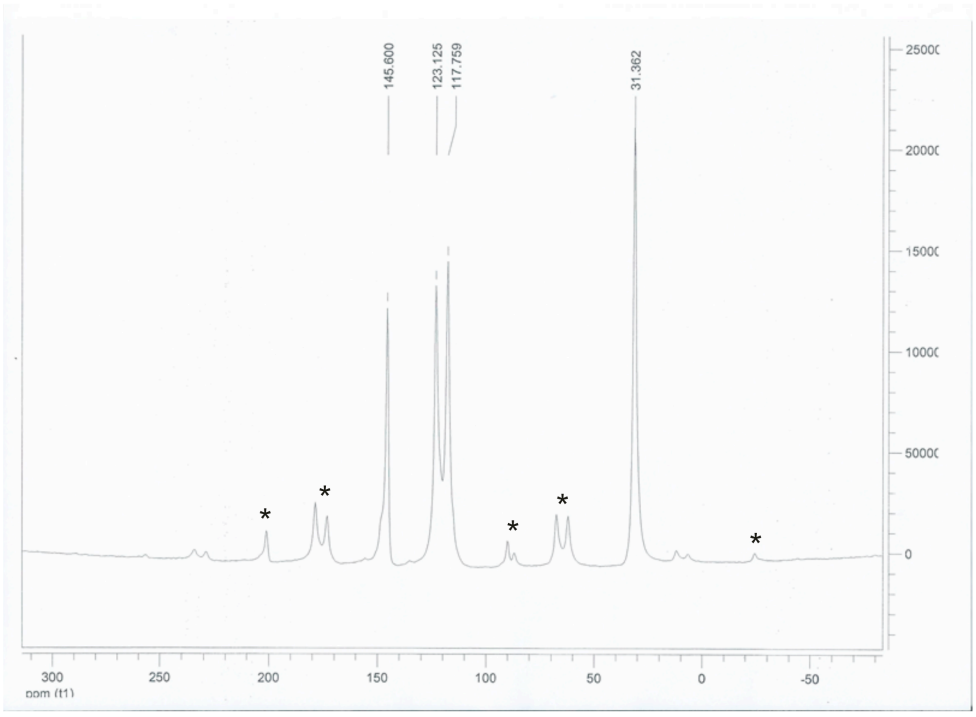

Fig. S3 MAS ^{13}C-NMR of complex [Zn(MeImS)$_2$].[1]

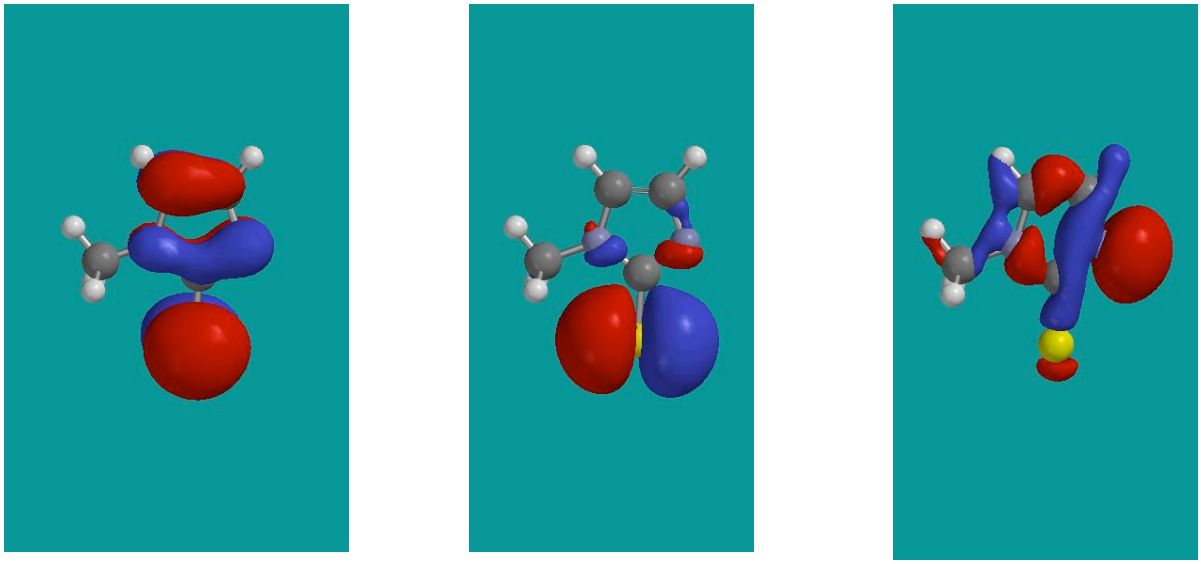

Fig. S4 Iso-surface drawings of Kohn–Sham HOMO (left), HOMO–1 (centre), and HOMO–3 (right) calculated for anion methimazole (MeImS).

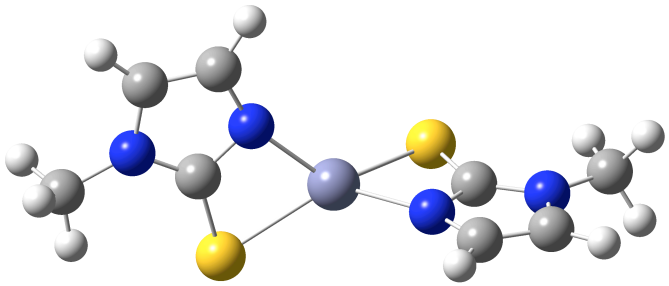

Fig. S5 Ball and stick representation of the structure of [Zn(MeImS)$_2$] optimised at DFT level.

Table S1 DFT calculated bond lengths (Å) and angles (°) for complex [Zn(MeImS)$_2$]; schematic structure and atom numbering of complex [Zn(MeImS)$_2$].

Bond		Angle	
N1-C2	1.358	N1-C2-S	130.98
N3-C2	1.345	N3-C2-S	119.34
N1-C5	1.390	N1-C2-N3	109.69
N2-C4	1.379	C5-N1-C2	107.58
C4-C5	1.364	C4-N3-C2	107.27
C2-S	1.746	N1-C5-C4	106.61
N1-C5	1.390	N3-C4-C5	108.90

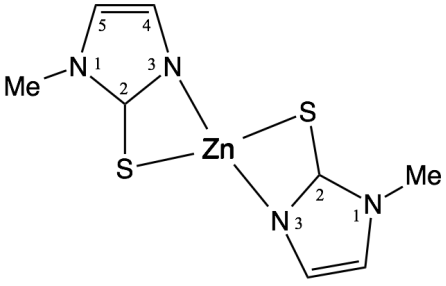

Comments on the optimized structure of complex [Zn(MeImS)$_2$].

The zinc atom adopts a distorted tetrahedral geometry with both anions (*N,S*)-chelating. An examination of the metric parameters at the Zn centre provide evidence for a strain in the metallacycle formed under coordination [Zn-N(3)-C and N(3)-C-S = 94.68° and 119.34°, respectively; Zn-S-C = 72.69°]. Due to the S-C-N(3) narrow bite, the calculated S-Zn-N(3) angle

(73.24°) shows a great departure from ideal tetrahedral coordination geometry; however, a similar extent of distortion was also found in the (*N,S*)-chelating pyridine-2-thionate (py2S) complexes [MeHg(py2S)],[2a] [$Me_2Sn(py2S)_2$],[2b] and [$Me_2Tl(py2S)$],[2b] with thioamide angles of 58.5, 60.5, and 54.2°, respectively.

The calculated values of the bond lengths: *d*(Zn-N) 2.035 and *d*(Zn-S) 2.421 Å are consistent with those found in complex [$Zn_4O(MeImS)_6$],[3] which features MeImS acting as a (*N,S*)-bridging ligand that binds pairs of non-interacting zinc atoms [average *d*(Zn-N) 2.003(10), *d*(Zn-S) 2.337(3) Å]. Moreover, a comparison of the Zn-N_{MeImS} bond distance with those reported for tetrahedral Zn-pyridine complexes[2c,d] (2.063-2.060 Å) shows that it is markedly shorter. Conversely, the calculated Zn-S_{MeImS} bond distance is about 3% longer than the mean Zn-S bond distances reported for the neutral complexes listed in Table 1 [*d*(Zn-S_{thione}) in the range 2.340–2.3581 Å], possibly due to the overestimation of the metal-sulphur bond lengths previously observed for the B3LYP functional.[4]

References and notes

1. MAS ^{13}C-NMR spectrum was recorded on a Varian 400 MHz spectrometer. The spectrum was calibrated such that the observed up field peak in the spectrum of adamantane is set to $\delta = 31.47$. The MAS rate was 5500 Hz. Acquisition was performed with standard MAS pulsing sequence using a 2.0 s delay between repetition, number of scans completed: 32000; $T = 23$ °C. Starred peaks are spinning side bands.
2. (*a*) H. Lynton, M. C. Sears, *Can. J. Chem.,* 1971, **49**, 3418–3424; (*b*) W. L. Steffen, G. J. Palenik, *Acta Crystallogr., Sect. B,* 1976, **32**, 298–300; (*c*) A. Castineiras, W. Hiller, J. Strahle, J. Bravo, J. Casa, M. Gayoso, J. Sordo, *J. Chem. Soc. Dalton Trans*., 1986, 1945–1948, (*d*) M. V. castano, A. Macias, A. Castineiras, A. S. Gonzales, E. G. Martinez, J. S. Casas, J. Sordo, W. Hiller, E. E. Castellano, *J. Chem. Soc. Dalton Trans*., 1990, 10011005.
3. R. Castro, J. A. Garcia-Vasquez, J. Romero, A. Sousa, Y. D. Chang, J. Zubieta, *Inorg. Chim. Acta*, 1995, **237**, 143–146.
4. M. Elstner, Q. Cui, P. Munih, E. Kaxiras, T. Frauenheim, M. Karplus, *J. Comp. Chem*., 2003, **24**, 565–581.

Chapter 8

Speciation of the potential anti-tumor agent vanadocene dichloride in the blood plasma and model systems

Inorganic Chemistry

Article

pubs.acs.org/IC

Speciation of the Potential Antitumor Agent Vanadocene Dichloride in the Blood Plasma and Model Systems

Daniele Sanna,[†] Valeria Ugone,[§] Giovanni Micera,[§] Tiziana Pivetta,[#] Elisa Valletta,[#] and Eugenio Garribba*[,§]

[†]Istituto CNR di Chimica Biomolecolare, Trav. La Crucca 3, I-07040 Sassari, Italy

[§]Dipartimento di Chimica e Farmacia and Centro Interdisciplinare per lo Sviluppo della Ricerca Biotecnologica e per lo Studio della Biodiversità della Sardegna, Università di Sassari, Via Vienna 2, I-07100 Sassari, Italy

[#]Dipartimento di Scienze Chimiche e Geologiche, Università di Cagliari, Cittadella Universitaria, I-09042 Monserrato, Cagliari, Italy

Supporting Information

ABSTRACT: The speciation of the potential antitumor agent vanadocene dichloride ($[Cp_2VCl_2]$, abbreviated with VDC) in the blood plasma was studied by instrumental (EPR, ESI-MS, MS-MS, and electronic absorption spectroscopy) and computational (DFT) methods. The behavior of VDC at pH 7.4 in aqueous solution, the interaction with the most important bioligands of the plasma (oxalate, carbonate, phosphate, lactate, citrate, histidine, and glycine among those with low molecular mass and transferrin and albumin between the proteins) was evaluated. The results suggest that $[Cp_2VCl_2]$ transforms at physiological pH to $[Cp_2V(OH)_2]$ and that only oxalate, carbonate, phosphate, and lactate are able to displace the two OH^- ions to yield $[Cp_2V(ox)]$, $[Cp_2V(CO_3)]$, $[Cp_2V(lactH_{-1})]$, and $[Cp_2V(HPO_4)]$. The formation of the adducts with oxalate, carbonate, lactate, and hydrogen phosphate was confirmed also by ESI-MS and MS-MS spectra. The stability order is $[Cp_2V(ox)] \gg [Cp_2V(CO_3)] > [Cp_2V(lactH_{-1})] > [Cp_2V(HPO_4)]$. No interaction between VDC and plasma proteins was detected under our experimental conditions. Several model systems containing the bioligands (bL) in the same relative ratio as in the blood samples were also examined. Finally, the speciation of VDC in the plasma was studied. The results obtained show that the model systems behave as the blood plasma and indicate that when V concentration is low (10 μM) VDC is transported in the bloodstream as $[Cp_2V(ox)]$; when V concentration is high (100 μM) oxalate binds only 9.2 μM of $[Cp_2V]^{2+}$, whereas the remaining part distributes between $[Cp_2V(CO_3)]$ (main species) and $[Cp_2V(lactH_{-1})]$ (minor species); and when V concentration is in the range 10−100 μM $[Cp_2V]^{2+}$ distributes between $[Cp_2V(ox)]$ and $[Cp_2V(CO_3)]$.

INTRODUCTION

Vanadium plays a number of roles in biological systems and has been found in many naturally occurring compounds.[1] In humans, vanadium compounds exhibit a wide variety of pharmacological properties. In particular, the antidiabetic activity has been extensively studied during the last 20 years;[2] bis(maltolato)oxidovanadium(IV) (or BMOV) became the benchmark complex for the new molecules with antidiabetic action,[3] and its derivative bis(ethylmaltolato)oxidovanadium(IV) (or BEOV) arrived to phase IIa of the clinical trials,[4] even if these have provisionally been abandoned due to renal problems arising with several patients.[5,6] Furthermore, vanadium complexes have been tested as antiparasitic, spermicidal, antiviral, anti-HIV, and antituberculosis agents.[5,7]

The first report on the potential anticancer action of a vanadium compound, bis(cyclopentadienyl)vanadium(IV) dichloride or vanadocene dichloride ($[Cp_2VCl_2]$ abbreviated to VDC, Scheme 1a), active in the treatment of Ehrlich ascites tumor, dates back to 1983.[8] Subsequently, VDC underwent the same extensive preclinical testing against both animal and human cell lines alongside the parent compound $[Cp_2TiCl_2]$ (TDC).[9] The clinical test on TDC stopped at phase II of the clinical trials, due to the low efficacy in patients with metastatic renal cell carcinoma or metastatic breast cancer.[10] However, in all the studies in vitro $[Cp_2VCl_2]$ was found to be more active than $[Cp_2TiCl_2]$; in particular, in a systematic study on the activity of several metallocenes on the human testicular cancer cell lines Tera-2 and Ntera-2, only vanadocene derivatives exhibited significant cytotoxicity leading the tumor cells to apoptosis within 24 h.[9a] A very active derivative of VDC is bis-[(*p*-methoxybenzyl)cyclopentadienyl]vanadium(IV) dichloride (vanadocene **Y**, Scheme 1b), which exhibits an IC_{50} value of 3.0 μM against the LLC-PK (pig kidney epithelial) cell line (in contrast, the value of titanocene **Y** is significantly higher, 21 μM).[11] This is a particularly encouraging datum, since

Received: March 18, 2015

DOI: 10.1021/acs.inorgchem.5b01277
Inorg. Chem. XXXX, XXX, XXX−XXX

Abstract

Vanadium plays a number of roles in biological systems and has been found in many naturally occurring compounds. Vanadium compounds exhibit a wide variety of pharmacological properties. The first vanadium species that shown anticancer activity was vanadocene dichloride ([Cp_2VCl_2] or **VDC**), proposed in 1983 for the treatment of Ehrlich ascites tumour. Considering that the mechanism of action of **VDC** is closely related to the biotransformation in the blood plasma, I decided to study the speciation of VDC in the plasma under physiological conditions (Chapter 8 - Article V).

The speciation of the potential antitumor agent **VDC** in the blood plasma was studied by instrumental (EPR, ESI-MS, MS-MS, and UV-vis spectroscopy) and computational (DFT) methods[1]. The complex **VDC** transforms at physiological pH to [$Cp_2V(OH)_2$] and only the bio-ligands oxalate, carbonate, hydrogen phosphate, and lactate are able to displace the two oxydrilic ions to yield [$Cp_2V(ox)$], [$Cp_2V(CO_3)$], [Cp2V($lactH_{-1}$)], and [$Cp_2V(HPO_4)$] (Figure 24).

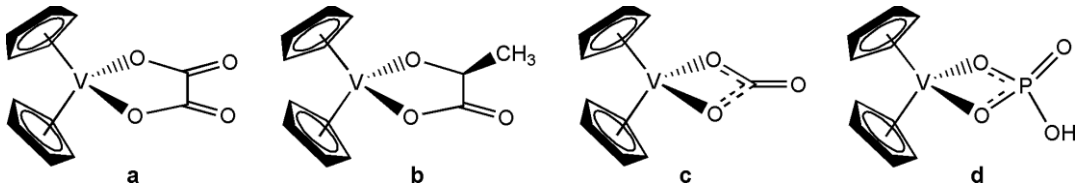

Figure 24. Structure of [$Cp_2V(ox)$] (**a**), [$Cp_2V(lactH_{-1})$] (**b**), [$Cp_2V(CO_3)$] (**c**), and [$Cp_2V(HPO_4)$] (**d**).

The formation of the complexes with oxalate, carbonate, lactate, and hydrogen phosphate was confirmed by ESI-MS and MS-MS spectra.

[1] In collaboration with professor Eugenio Garribba (Dipartimento di Chimica e Farmacia and Centro Interdisciplinare per lo Sviluppo della Ricerca Biotecnologica e per lo studio della Biodiversità della Sardegna, Università di Sassari).

It has been found that the affinity order of the four strongest bio-ligands is $ox^{2-} \gg CO_3^{2-} > lactH_{-1}^{2-} > HPO_4^{2-}$. The complex $[Cp_2V(OH)_2]$ does not interact with the plasma proteins transferrin and albumin under my experimental conditions (Figure 25).

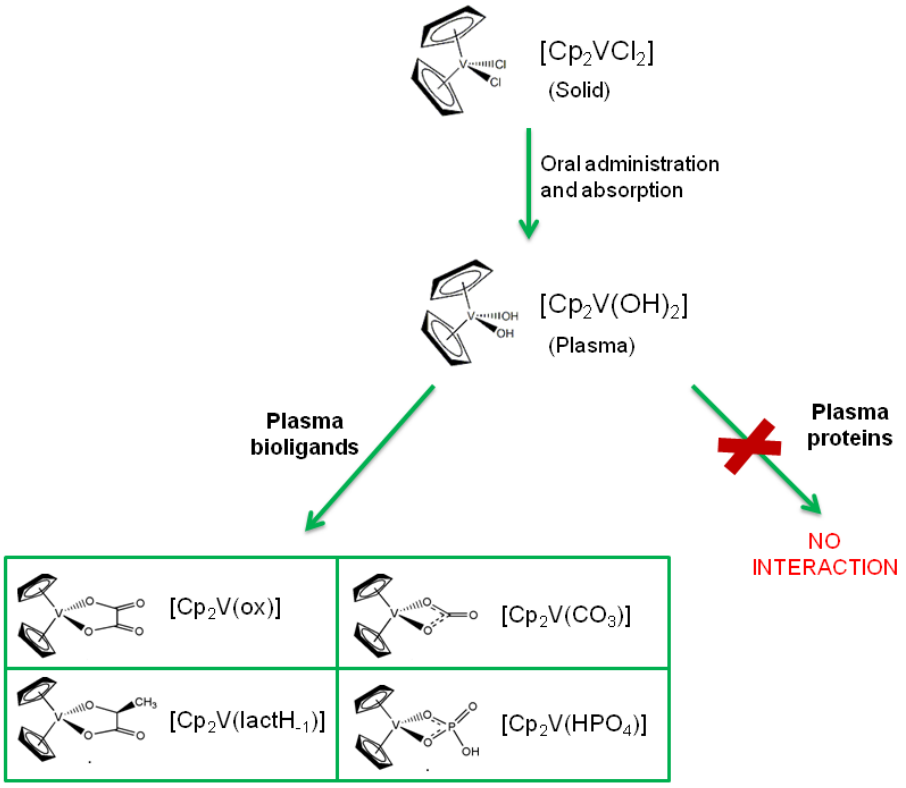

Figure 25. Scheme of interaction of the **VDC** with bioligands (oxalate, carbonate, phosphate, lactate, citrate, histidine, glycine, and trasferrrin and albumin) of the plasma.

The **VDC**, after the oral administration, enters in the stomach, arrives in the small intestine and then in the bloodstream where reacts with the bio-ligands of the plasma. The concentration of **VDC** in the plasma does not correspond to the administered dose, but depends mainly on the gastrointestinal absorption. The speciation of **VDC** at the physiological conditions has been examined studying several model systems containing the bio-ligands in the same relative ratio as in the blood and, subsequently, carrying out experiments with plasma samples (Table 2).

V concentration in plasma		
< 10 μM	10-100 μM	> 100 μM
$[Cp_2V(ox)]$ **(main species)**	$[Cp_2V(ox)]$ **(main species)**	$[Cp_2V(CO_3)]$ **(main species)**
$[Cp_2V(CO_3)]$ **(minor species)**	$[Cp_2V(CO_3)]$ **(main species)**	$[Cp_2V(ox)]$ **(minor species)**
	$[Cp_2V(lactH_{-1})]$ **(minor species)**	$[Cp_2V(lactH_{-1})]$ **(minor species)**

Table 2. Speciation of **VDC** in the blood plasma as a function of its concentration.

The obtained results show that the model systems behave in the same way as the blood plasma and if vanadium concentration is ≈ 10 μM, most of **VDC** administered is transported in the organism as $[Cp_2V(ox)]$, in fact the strongest bio-ligand, oxalate, binds the $[Cp_2V]^{2+}$ moiety. In contrast, if vanadium concentration is higher than 100 μM, **VDC** is complexed mainly by carbonate ($[Cp_2V(CO_3)]$ is the main species), and in minor quantity by oxalate and lactate ($[Cp_2V(ox)]$ and $[Cp_2V(lactH_{-1})]$ are the minor species). Finally, if vanadium concentration is in the range 10−100 μM, $[Cp_2V]^{2+}$ distributes among the oxalate and carbonate (main species), and lactate (minor species).

Article V

Speciation of the potential anti-tumor agent vanadocene dichloride in the blood plasma and model systems

Daniele Sanna, Valeria Ugone, Giovanni Micera, Tiziana Pivetta, Elisa Valletta, Eugenio Garribba

Citation: *Inorg.chem.*, 2015, *54* (17), 8237–8250

Cite this: DOI: 10.1021/acs.inorgchem.5b01277

Published by American Chemical Society

Inorganic Chemistry

Article

pubs.acs.org/IC

Speciation of the Potential Antitumor Agent Vanadocene Dichloride in the Blood Plasma and Model Systems

Daniele Sanna,[†] Valeria Ugone,[§] Giovanni Micera,[§] Tiziana Pivetta,[#] Elisa Valletta,[#] and Eugenio Garribba*[,§]

[†]Istituto CNR di Chimica Biomolecolare, Trav. La Crucca 3, I-07040 Sassari, Italy

[§]Dipartimento di Chimica e Farmacia and Centro Interdisciplinare per lo Sviluppo della Ricerca Biotecnologica e per lo Studio della Biodiversità della Sardegna, Università di Sassari, Via Vienna 2, I-07100 Sassari, Italy

[#]Dipartimento di Scienze Chimiche e Geologiche, Università di Cagliari, Cittadella Universitaria, I-09042 Monserrato, Cagliari, Italy

Supporting Information

ABSTRACT: The speciation of the potential antitumor agent vanadocene dichloride ($[Cp_2VCl_2]$, abbreviated with VDC) in the blood plasma was studied by instrumental (EPR, ESI-MS, MS-MS, and electronic absorption spectroscopy) and computational (DFT) methods. The behavior of VDC at pH 7.4 in aqueous solution, the interaction with the most important bioligands of the plasma (oxalate, carbonate, phosphate, lactate, citrate, histidine, and glycine among those with low molecular mass and transferrin and albumin between the proteins) was evaluated. The results suggest that $[Cp_2VCl_2]$ transforms at physiological pH to $[Cp_2V(OH)_2]$ and that only oxalate, carbonate, phosphate, and lactate are able to displace the two OH^- ions to yield $[Cp_2V(ox)]$, $[Cp_2V(CO_3)]$, $[Cp_2V(lactH_{-1})]$, and $[Cp_2V(HPO_4)]$. The formation of the adducts with oxalate, carbonate, lactate, and hydrogen phosphate was confirmed also by ESI-MS and MS-MS spectra. The stability order is $[Cp_2V(ox)] \gg [Cp_2V(CO_3)] > [Cp_2V(lactH_{-1})] > [Cp_2V(HPO_4)]$. No interaction between VDC and plasma proteins was detected under our experimental conditions. Several model systems containing the bioligands (bL) in the same relative ratio as in the blood samples were also examined. Finally, the speciation of VDC in the plasma was studied. The results obtained show that the model systems behave as the blood plasma and indicate that when V concentration is low (10 μM) VDC is transported in the bloodstream as $[Cp_2V(ox)]$; when V concentration is high (100 μM) oxalate binds only 9.2 μM of $[Cp_2V]^{2+}$, whereas the remaining part distributes between $[Cp_2V(CO_3)]$ (main species) and $[Cp_2V(lactH_{-1})]$ (minor species); and when V concentration is in the range 10−100 μM $[Cp_2V]^{2+}$ distributes between $[Cp_2V(ox)]$ and $[Cp_2V(CO_3)]$.

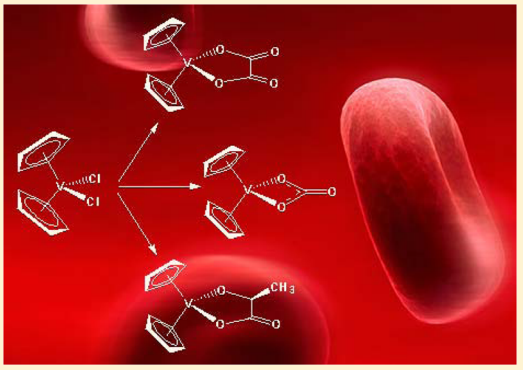

INTRODUCTION

Vanadium plays a number of roles in biological systems and has been found in many naturally occurring compounds.[1] In humans, vanadium compounds exhibit a wide variety of pharmacological properties. In particular, the antidiabetic activity has been extensively studied during the last 20 years;[2] bis(maltolato)oxidovanadium(IV) (or BMOV) became the benchmark complex for the new molecules with antidiabetic action,[3] and its derivative bis(ethylmaltolato)oxidovanadium(IV) (or BEOV) arrived to phase IIa of the clinical trials,[4] even if these have provisionally been abandoned due to renal problems arising with several patients.[5,6] Furthermore, vanadium complexes have been tested as antiparasitic, spermicidal, antiviral, anti-HIV, and antituberculosis agents.[5,7]

The first report on the potential anticancer action of a vanadium compound, bis(cyclopentadienyl)vanadium(IV) dichloride or vanadocene dichloride ($[Cp_2VCl_2]$ abbreviated to VDC, Scheme 1a), active in the treatment of Ehrlich ascites tumor, dates back to 1983.[8] Subsequently, VDC underwent the same extensive preclinical testing against both animal and human cell lines alongside the parent compound $[Cp_2TiCl_2]$ (TDC).[9] The clinical test on TDC stopped at phase II of the clinical trials, due to the low efficacy in patients with metastatic renal cell carcinoma or metastatic breast cancer.[10] However, in all the studies in vitro $[Cp_2VCl_2]$ was found to be more active than $[Cp_2TiCl_2]$; in particular, in a systematic study on the activity of several metallocenes on the human testicular cancer cell lines Tera-2 and Ntera-2, only vanadocene derivatives exhibited significant cytotoxicity leading the tumor cells to apoptosis within 24 h.[9a] A very active derivative of VDC is bis[(*p*-methoxybenzyl)cyclopentadienyl]vanadium(IV) dichloride (vanadocene **Y**, Scheme 1b), which exhibits an IC_{50} value of 3.0 μM against the LLC-PK (pig kidney epithelial) cell line (in contrast, the value of titanocene **Y** is significantly higher, 21 μM).[11] This is a particularly encouraging datum, since

Received: March 18, 2015

DOI: 10.1021/acs.inorgchem.5b01277
Inorg. Chem. XXXX, XXX, XXX−XXX

Scheme 1. Structure of Vanadocene Dichloride (VDC) (a) and Its Derivatives Vanadocene Y (b) and Diisoselenocyanate Vanadocene Y (c)

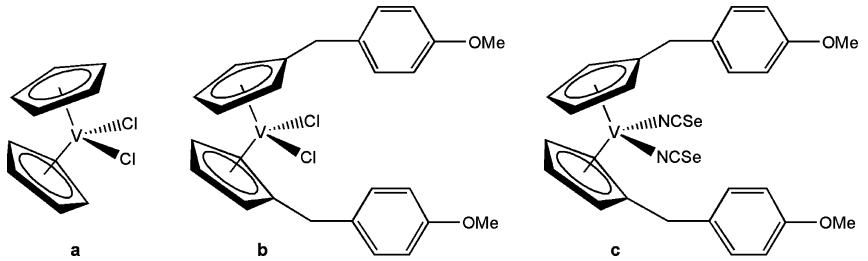

vanadocene **Y** is slightly more active against this cell line than the "classic" cisplatin, which shows an IC_{50} value of 3.3 μM.[11] Recently, in vitro experiments on modified vanadocene **Y** (diisoselenocyanate vanadocene **Y**, Scheme 1c) have shown impressive cytotoxic effects against the human renal cancer cells CAKI-1, with an IC_{50} value reaching for the first time the nanomolar range for metallocene anticancer potential drugs.[12] A comprehensive study of the cytotoxic activity of methyl- and methoxy-substituted VDC toward T-lymphocytic leukemia cells MOLT-4 has been recently reported.[13] Under the physiological conditions, the $[Cp_2V]^{2+}$ moiety remains essentially intact, while the auxiliary X ligand, chloride or isoselenocyanate, is subject to substitution by H_2O/OH^- that can further be exchanged for functions provided by DNA. However, in contrast with Pt(II), V(IV) is a particularly hard metal center and thus should preferentially bind to phosphate residues of DNA rather than N bases of guanosine.[7a]

The speciation of an active metal complex in the blood is an important aspect of the drug metabolism, and the form transported to the target organs significantly affects its efficiency and mechanism of action. The assumption that the V complexes (and metal complexes, in general) reach the target cells in the same form as they are administrated can be considered an oversimplification.[14] Indeed, in the blood ligand exchange and complexation reactions by the components of the plasma are possible; moreover, a V compound can distribute between plasma and erythrocytes.[15] All of the main proteins of the plasma, such as transferrin (hTf), albumin (HSA), and immunoglobulin G (IgG), and the low molecular mass (*l.m.m.*) bioligands, such as oxalate, lactate, phosphate, citrate, and amino acids, can interact with the V compound administered and partly or fully displace the organic ligands.[16,17] For example, it has been recently demonstrated through an X-ray determination that lysozyme replaces the water molecule equatorially coordinated in the insulin-mimetic agent $[VO(pic)_2(H_2O)]$ through the COO^- group of the Asp-52 residue.[18] Unfortunately, the study of the speciation of a metal complex in a complicated system such as the blood plasma is not an easy task because plasma contains many bioligands with very different concentration and molecular mass[19] and many chemical reactions—as mentioned above—are possible. For this reason, in many cases model systems have been investigated to infer indirect information on the biological system.[20] However, very often the results obtained in the models are not fully in agreement with those observed in the real systems and give only partial information.

In this work, the speciation of VDC in several model systems and in blood plasma was studied and compared. It has been noted recently that the paramagnetic nature of the V(IV) center (electronic configuration $3d^1$), which precludes the use of classical NMR tools, makes the characterization of these complexes and their biologically active species more difficult than the parent titanocene derivatives, and this slowed down their analysis and the advances in this topic.[21] However, EPR spectroscopy is a valid tool to characterize V(IV) in solution;[22] for example, nonoxido V(IV) complexes display distinctive spectroscopic features, in particular, hyperfine coupling constants A much smaller than those observed for V(IV)O species.[23] Herein, EPR characterization was supported by electronic absorption spectroscopy[24] and electrospray ionization mass spectrometry (ESI-MS), which allows the detection of metal complexes and adducts that readily fragment.[25,26] Tandem mass spectrometry (MS-MS) was used to confirm the stoichiometry of the species. Computational methods based on DFT (density functional theory) provide other valuable information on the coordination mode of the bioligands on and the environment of V(IV) species.[27]

The results reported in this study on the model systems perfectly coincide with those observed in a complex real system such as the plasma and allow the prediction of the speciation of VDC in the blood as a function of the vanadium concentration in the organism.

EXPERIMENTAL AND COMPUTATIONAL SECTION

Chemicals. Water was deionized prior to use through the purification system Millipore Milli-Q Academic. Vanadocene dichloride was a Sigma-Aldrich product. 4-(2-Hydroxyethyl)-1-piperazineethanesulfonic acid (HEPES), sodium hydrogen carbonate ($NaHCO_3$), sodium hydrogen phosphate (Na_2HPO_4), citric acid (H_3citr), lactic acid (Hlact), oxalic acid (H_2ox), histidine (His), and glycine (Gly) were Sigma-Aldrich, Merck, or Carlo Erba products of the highest grade available and used as received. Human serum apotransferrin (98%, T4283) and human serum albumin (97−99%, A9511) were purchased from Sigma-Aldrich with a molecular mass of 76−81 and 66 kDa, respectively.

Methanol (CH_3OH) for LC-MS and trifluoroacetic acid (TFA) used in the ESI-MS and MS-MS experiments were purchased from Sigma-Aldrich.

Preparation of the Solutions for Spectroscopic Measurements. The solutions were prepared by dissolving in ultrapure water, obtained through the purification system Millipore Milli-Q Academic, weighted amounts of VDC and bioligands.

In the binary systems VDC concentration was 1.0×10^{-3} M, and the VDC to bioligand ($NaHCO_3$, Na_2HPO_4, oxalic acid, lactic acid, citric acid, histidine, glycine) molar ratio was 1/10 (Figures S5−S9 of Supporting Information). In all systems the pH was adjusted to 7.4, and spectra were immediately recorded. Argon was bubbled through the solutions during their preparation to ensure the absence of oxygen and avoid oxidation of the V(IV) ion. The eventual oxidation of V(IV) to V(V), therefore, could start only during the spectroscopic measurements.

In the multicomponent systems containing VDC and the bioligands ($NaHCO_3$, Na_2HPO_4, oxalic acid, lactic acid) three types of

DOI: 10.1021/acs.inorgchem.5b01277
Inorg. Chem. XXXX, XXX, XXX−XXX

experiments were carried out: (i) in the first experiment the VDC and bioligands concentration was 1.0×10^{-3} M and 1.0×10^{-2} M and the molar ratio VDC/bL was 1/10 (Figures 3 and S11 and S12 of the Supporting Information); (ii) in the second one VDC concentration was 4.0×10^{-4} M and the ratio VDC/ox/$NaHCO_3$/lact/Na_2HPO_4 1/1/2706.5/164.1/119.6 (Figures 4–6); (iii) in the third one VDC concentration was 4.0×10^{-4} M and the ratio VDC/ox/$NaHCO_3$/lact/Na_2HPO_4 1/0.1/270.7/16.4/12.0 (Figures 5, 7, and S13 of the Supporting Information). In all experiments the pH was brought to 7.4 and argon was bubbled through the solutions to avoid oxidation of the V(IV) ion.

EPR spectra with the physiological concentrations of the bioligands (and metal ion) cannot be measured because very low intensity signals would be detected. To overcome this problem we used higher concentrations of the metal ion (4.0×10^{-4} M) and bioligands but maintaining the same ratio as in a blood plasma. The same strategy was previously used when studying the distribution of insulin-enhancing $V(IV)O^{2+}$ complexes between the high and low molecular mass components of the plasma, with the extrapolation to low concentrations being a normal procedure used in the literature.[17c,20,28,29]

In the experiments involving apo-hTf a concentration of VDC of 5.0×10^{-4} M was used. The pH was raised to ca. 4.0, and $NaHCO_3$ and HEPES were added in appropriate amounts in order to have a concentration of 2.5×10^{-2} and 1.0×10^{-1} M, respectively. Subsequently, pH was brought to ca. 5.0, and apo-hTf was added to the solution to obtain a final concentration of 2.5×10^{-4} M. Finally, pH was increased to 7.40. In the experiments involving HSA the concentration of VDC was 1.0×10^{-3} M. The pH was raised to ca. 5.0, and HEPES and HSA were added to have a concentration of 1.0×10^{-1} and 2.5×10^{-4} M. Then the pH was brought to 7.40. In all systems, the spectra were immediately measured to minimize the possible oxidation of V(IV) to V(V).

Experiments with Blood Plasma. Blood samples were obtained from Servizio Trasfusionale Aziendale (ASL of Sassari). Blood samples were centrifuged for 10 min at 3000 rpm, and the plasma was separated from buffy coat and red blood cells. The plasma was subsequently incubated for 30 min at 37 °C with a solution of VDC to have a final concentration of 4.5×10^{-5} M. The EPR spectrum was immediately measured.

Spectroscopic Measurements. EPR spectra were recorded at room temperature (298 K) or on frozen solutions (120 K) using an X-band (9.4 GHz) Bruker EMX spectrometer equipped with an HP 53150A microwave frequency counter. When the signal-to-noise ratio was low due to the low V(IV) concentration, signal averaging was used.[30] Electronic absorption spectra were obtained with a PerkinElmer Lambda 35 spectrophotometer.

Mass Spectrometry. The aqueous sample solutions containing VDC or the adducts with oxalate, lactate, carbonate, and hydrogen phosphate were prepared in ultrapure water obtained with Milli-Q Millipore. To improve the quality of the spectra, all solutions were mixed in a 1:1 v/v ratio with methanol containing 1% of TFA. These solutions were infused in the ESI chamber immediately after their preparation in order not to modify the aqueous solution equilibria. Mass spectra in positive- and negative-ion mode were obtained on a triple-quadrupole QqQ Varian 310-MS mass spectrometer using the atmospheric-pressure technique. The sample solutions were infused into the ESI source using a programmable syringe pump at a flow rate of 1.00 mL/h. A dwell time of 14 s was used, and the spectra were accumulated for at least 10 min in order to increase the signal-to-noise ratio. Mass spectra were recorded in the m/z range 50–500 at a final concentration of 5.0×10^{-4} M. The experimental conditions used for the measurements were: needle voltage 4500 V, shield voltage 600 V, housing temperature 60 °C, drying gas temperature 100 °C, nebulizer gas pressure 40 PSI, drying gas pressure 20 PSI, and detector voltage 1450 V. MS-MS experiments were performed with argon as collision gas (1.8 PSI) using a needle voltage of 6000 V, shield voltage of 800 V, housing temperature of 60 °C, drying gas temperature of 120 °C, nebulizer gas pressure of 40 PSI, drying gas pressure of 20 PSI, and detector voltage of 2000 V. Collision energy was varied from 2 to 50 eV. The isotopic patterns of the experimental peaks were analyzed using the mMass 5.5.0 software package.[31]

DFT Calculations. DFT (density functional theory) calculations were performed with the software Gaussian 03 (revision C.01)[32] and ORCA.[33]

The geometry of V(IV) complexes was optimized with Gaussian at the B3P86/6-311g level of theory with the procedure reported in the literature.[34] This choice ensures a good degree of accuracy in the prediction of the structures of first-row transition metal complexes[35] and, in particular, of vanadium species.[34] For all structures, minima were verified through frequency calculations.

On the optimized structures, the ^{51}V hyperfine coupling tensor $\boldsymbol{A}$ was calculated with Gaussian software using the hybrid functional half-and-half BHandHLYP and the basis set 6-311g(d,p) and with ORCA software using the hybrid functional PBE0 and the basis set VTZ, according to the procedures previously published.[36] It must be taken into account that for a V(IV) species A is usually negative, but in the literature its absolute value is often reported; this formalism was also used in a number of points of this study. The ^{51}V $\boldsymbol{A}$ tensor has three contributions: the isotropic Fermi contact (A^{FC}), the anisotropic or dipolar hyperfine interaction ($\boldsymbol{A}^{D}$), and one second-order term that arises from spin–orbit (SO) coupling ($\boldsymbol{A}^{SO}$):[33b] $\boldsymbol{A} = A^{FC}\mathbf{1} + \boldsymbol{A}^{D} + \boldsymbol{A}^{SO}$, where $\mathbf{1}$ is the unit tensor. The values of the ^{51}V anisotropic hyperfine coupling constants along the x, y, and z axes are as follows: $A_x = A^{FC} + A_x^{D} + A_x^{SO}$, $A_y = A^{FC} + A_y^{D} + A_y^{SO}$, and $A_z = A^{FC} + A_z^{D} + A_z^{SO}$. From these equations, the value of A_{iso} is $A_{iso} = (1/3)(A_x + A_y + A_z) = A^{FC} + (1/3)(A_x^{SO} + A_y^{SO} + A_z^{SO}) = A^{FC} + A^{PC}$, where the term $(1/3)(A_x^{SO} + A_y^{SO} + A_z^{SO})$ is named isotropic pseudocontact, A^{PC}.[33b] Gaussian neglects the second-order term represented by $\boldsymbol{A}^{SO}$; thus, $A^{PC} = 0$ and $A_{iso} = A^{FC}$. The theory background was described in detail in ref 37. The percent deviation from the experimental value $|A_i|^{exptl}$, where i = iso, x, y, was calculated as $100 \times [(|A_i|^{calcd} - |A_i|^{exptl})/|A_i|^{exptl}]$.

RESULTS AND DISCUSSION

1. Behavior of VDC in Aqueous Solution. The behavior of VDC in aqueous solution has been investigated through the combined application of EPR, UV–vis spectroscopy, ESI-MS, MS-MS, and DFT methods. The structure of VDC has been already solved by X-ray diffraction analysis:[38] it is tetrahedral with two sites occupied by the cyclopentadienyl rings and the other two sites by the ions Cl^-. The geometry of VDC has been optimized with Gaussian 03 software through DFT methods, which give good results in the optimization of the structure of transition metal complexes[35] and of vanadium complexes in particular.[34] The structure of VDC is shown in Figure S1a of the Supporting Information, and a comparison between the bond distances and angles is given in Table S1.

The behavior of $[Cp_2VCl_2]$ in aqueous solution has been examined by Toney and Marks and, subsequently, by Pavlík and Vinklárek.[39–41] The results indicate that the two Cp–V bonds are more resistant to hydrolysis than the analogous compounds of titanium and zirconium, $[Cp_2TiCl_2]$ and $[Cp_2ZrCl_2]$, and the stability order is V > Ti > Zr. When $[Cp_2MCl_2]$ (M = V, Ti, Zr) are dissolved in water the dissociation of both the Cl^- ions is revealed, with the dissociation of the first chloride being too fast to be observed and the half-life time for the dissociation of the second one being 50 (M = Ti), 30 (M = Zr), and 24 min (M = V). The dissociation constant for the loss of the first Cl^- is very large and cannot be measured; that for the second Cl^- is 4.2×10^{-2} (M = Ti) and 2.7×10^{-3} M (M = V).[40] In the system with VDC, the species formed at acid pH is $[Cp_2V(H_2O)_2]^{2+}$, whose structure has been determined by X-ray diffraction analysis[39] and simulated in this study (Table S1 and Figure S1b of the Supporting Information). The two water molecules bound to vanadium(IV) in $[Cp_2V(H_2O)_2]^{2+}$ are strongly acid (pK_a =

DOI: 10.1021/acs.inorgchem.5b01277
Inorg. Chem. XXXX, XXX, XXX–XXX

4.73 and 5.15).[40] Pavlík and Vinklárek demonstrated that $[Cp_2V(H_2O)_2]^{2+}$ is stable in aqueous solution for several days. They also proved that at pH 7.4 the only species present in solution is $[Cp_2V(OH)_2]$, whose EPR signal disappears after exposition to air for 72 h.[41]

The behavior of VDC in aqueous solution has been re-examined in this work through EPR and UV−vis spectroscopy and the ESI-MS technique as the basis for the study of its speciation in the blood plasma under the physiological pH. EPR spectra recorded as a function of pH on a solution containing VDC 1.0×10^{-3} M (Figure S2 of Supporting Information) show, according to the results reported in the literature, the presence of $[Cp_2V(H_2O)_2]^{2+}$ in acid solution (pH < 4.0) and of $[Cp_2V(OH)_2]$ in neutral and basic solution (pH > 6.0). The intermediate species $[Cp_2V(H_2O)(OH)]^+$ is not observable because the two deprotonations of the water molecules overlap for the very close values of pK_a.[40] Room-temperature EPR spectra are characterized by a significant variation of g_{iso} and A_{iso} from $[Cp_2V(H_2O)_2]^{2+}$ (g_{iso} = 1.980 and A_{iso} = 73.5 × 10^{-4} cm^{-1}) to $[Cp_2V(OH)_2]$ (g_{iso} = 1.985 and A_{iso} = 58.4 × 10^{-4} cm^{-1}), see Figure S3 of the Supporting Information.

The mass spectrum of VDC (Figure 1) shows, in particular, the peaks of $[Cp_2VCl]^+$ (m/z 216) and $[Cp_2V(OH)]^+$ (m/z 198). Other peaks were also identified, such as those of $[Cp_2V(TFA)]^+$ (m/z 294), $[Cp_2VF]^+$ (m/z 200), $[2Cp+3H]^+$ (m/z 133), and $[Cp_2V]^{2+}$ (m/z 90), but they were recognized as products of the fragmentation−recombination reactions occurring in ESI phase. All identified signals are listed in Table 4, together with the fragmentation products of the most intense peaks. Calculated and experimental isotopic patterns for selected peaks are reported in Figure S4 of the Supporting Information. The stoichiometry of the hypothesized species was confirmed by MS-MS experiments.

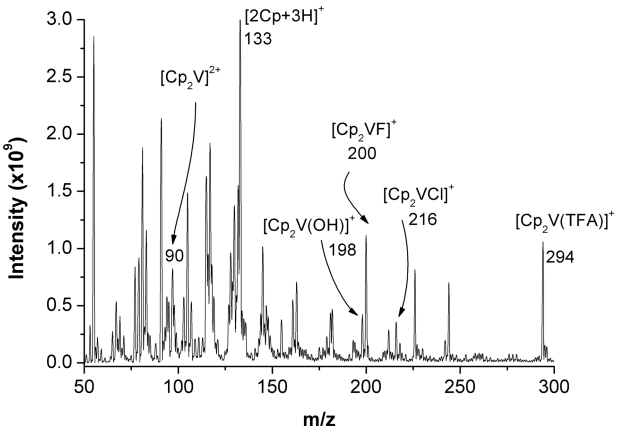

Figure 1. Positive ESI mass spectrum of VDC (5.0×10^{-4} M), recorded in H_2O/CH_3OH 1:1 v/v (1% TFA).

The A_{iso} values were calculated by DFT methods, which are a good tool to predict the hyperfine coupling constants between the unpaired electron with ^{51}V nucleus measured in an EPR spectrum.[42,43] According to the procedures established in the literature,[37c] the calculations were performed with Gaussian 03 (which does not include the spin−orbit coupling) using the half-and-half functional BHandHLYP and the basis set 6-311g(d,p) and ORCA (which takes into account the second-order spin−orbit contribution) with the functional PBE0 and the basis set VTZ. To the best of our knowledge, no systematic study on the prediction of the EPR parameters (tensors $\boldsymbol{g}$ and $\boldsymbol{A}$) for nonoxido vanadium(IV) complexes was published, but recent results indicate that ORCA performs slightly better than Gaussian because the percent contribution of the spin−orbit coupling to A_{iso} is larger than in the case of $V(IV)O^{2+}$ complexes,[44] i.e., the pseudocontact term $A^{PC} = (1/3)(A_x^{SO} + A_y^{SO} + A_z^{SO})$ is not negligible with respect to Fermi contact, A^{FC} (see Experimental and Computational Section). The results obtained for VDC and the V(IV) species formed in solution, including those with the bioligands, are listed in Table 1.

From the data reported in Table 1, it emerges that ORCA performs better than Gaussian in the prediction of A_{iso}. This difference can be attributed to the term A^{PC} (considered by ORCA and not by Gaussian), which contributes for 8−10% to A_{iso}. On the basis of the results, it can be argued that a DFT calculation with ORCA can be used to predict the A_{iso} value of a V(IV) complex; in particular, a calculation performed at the level of theory PBE0/VTZ allows one to predict A_{iso} with a mean deviation from the experimental value of 3.1% (Table 1).

2. Interaction of VDC with the l.m.m. Bioligands of the Blood Serum. Among the low molecular mass bioligands of the blood serum (bL), oxalate (ox), lactate (lact), citrate (citr), hydrogen phosphate (HPO_4^{2-}), glycine (Gly), histidine (His), and carbonate (CO_3^{2-}) are the most likely potential V(IV) binders.[16a,20] In this work, the systems VDC/bL were studied at the physiological pH using a ratio of 1/10 and VDC

Table 1. Experimental (exptl) and Calculated (calcd) Isotropic Hyperfine Coupling Constants (A_{iso}) for VDC, Its Hydrolytic Products, and Ternary Complexes[a]

	exptl		calcd (Gaussian)[b]		calcd (ORCA)[c]	
complex	g_{iso}	A_{iso}	A_{iso}	dev. %[d]	A_{iso}	dev. %[d]
$[Cp_2VCl_2]$	1.978	−69.1	−59.6	−13.7	−64.0	−7.4
$[Cp_2V(H_2O)_2]^{2+}$	1.980	−73.5	−71.6	−2.6	−78.3	6.5
$[Cp_2V(OH)_2]$	1.985	−58.4	−52.6	−9.9	−60.0	2.7
$[Cp_2V(ox)]$	1.983	−63.5	−56.1	−11.7	−63.8	0.5
$[Cp_2V(CO_3)]$	1.985	−58.3	−51.8	−11.1	−59.6	2.2
$[Cp_2V(lactH_{-1})]$	1.984	−63.6	−58.1	−8.6	−65.7	1.7
$[Cp_2V(citrH_{-1})]^{3-}$	1.987	−65.4	−62.8	−4.0	−67.2	2.8
$[Cp_2V(HPO_4)]$	1.993	−63.3	−55.9	−11.7	−63.4	0.2
MAD[e]				9.5		3.1

[a] A_{iso} value measured in 10^{-4} cm^{-1}. [b] Values calculated at the level of theory BHandHLYP/6-311g(d,p). [c] Values calculated at the level of theory PBE0/VTZ. [d] Percent deviation from the experimental value, $|A_{iso}|^{exptl}$, calculated as $100 \times [(|A_{iso}|^{calcd} - |A_{iso}|^{exptl})/|A_{iso}|^{exptl}]$. [e] Mean of the absolute percent deviations (MAD) from the experimental values.

DOI: 10.1021/acs.inorgchem.5b01277
Inorg. Chem. XXXX, XXX, XXX−XXX

Scheme 2. Structures of $[Cp_2V(ox)]$ (a), $[Cp_2V(lactH_{-1})]$ (b), $[Cp_2V(CO_3)]$ (c), and $[Cp_2V(HPO_4)]$ (d)

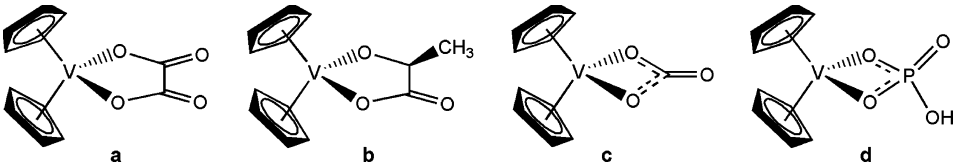

Table 2. Experimental (exptl) and Calculated (calcd) Anisotropic Hyperfine Coupling Constants (A_i) for Ternary Complexes Formed by VDC[a]

	calcd (Gaussian)[b]			calcd (ORCA)[c]			exptl[d]		% (Gaussian)		% (ORCA)	
	A_x	A_y	A_z	A_x	A_y	A_z	A_x	A_y	% $\lvert A_x\rvert^e$	% $\lvert A_y\rvert^e$	% $\lvert A_x\rvert^e$	% $\lvert A_y\rvert^e$
$[Cp_2V(ox)]$	−91.7	−74.9	−1.6	−98.4	−85.4	−7.5	−102.1	−77.9	−10.2	−3.9	−3.7	9.7
$[Cp_2V(CO_3)]$	−87.9	−70.8	3.3	−95.5	−79.9	−3.3	−94.5	−75.9	−7.0	−6.7	1.0	5.3
$[Cp_2V(lactH_{-1})]$	−94.9	−78.7	−0.7	−101.9	−88.0	−7.2	−101.7	−79.1	−6.7	−0.5	0.2	11.3
MAD[f]									8.0	3.7	1.6	8.8

[a]All values measured in 10^{-4} cm^{-1}. [b]Values calculated at the level of theory BHandHLYP/6-311g(d,p). [c]Values calculated at the level of theory PBE0/VTZ. [d]A_z not measurable. [e]Percent deviation from the experimental value, $\lvert A_i\rvert^{exptl}$ (i = x, y), calculated as $100 \times [(\lvert A_i\rvert^{calcd} - \lvert A_i\rvert^{exptl})/\lvert A_i\rvert^{exptl}]$. [f]Mean of the absolute percent deviations (MAD) from the experimental values.

Scheme 3. Possible Coordination Modes of Hydrogen Phosphate (a−c) and (bi)Carbonate (d−f) to the $[Cp_2V]^{2+}$ Moiety of VDC

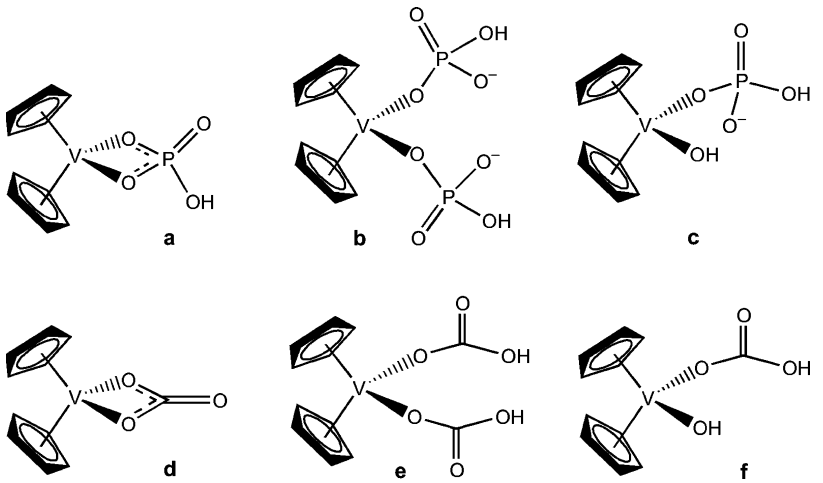

concentration of 1×10^{-3} M. EPR and UV−vis spectra were compared with those of $[Cp_2V(OH)_2]$, which—as mentioned above—is the only species existing at pH 7.4 when VDC is dissolved in aqueous solution. ESI-MS, MS-MS spectra, and DFT calculations were carried out to confirm the results (see below). The oxidation of V(IV) to V(V) is negligible at the experimental conditions used in this study, and EPR and UV−vis data support this conclusion: indeed, the spectroscopic signals of the main V(IV) species existing at pH 7.4 do not change significantly as a function of time.

The formation of the ternary species in the solid state between the moiety $[Cp_2V]^{2+}$ and mono- and bidentate ligands was demonstrated in the literature. In particular, Vinklárek and co-workers prepared solid samples upon reaction of VDC with amino acids with noncoordinating[45] and coordinating side-chain groups,[46] with phosphate,[47] oxalate,[48] and carbonate.[49] The results of the spectroscopic measurements revealed in this study on the systems VDC/oxalate, VDC/lactate, VDC/citrate, VDC/HCO_3^-, VDC/HPO_4^{2-}, VDC/Gly, and VDC/His showed that only oxalate, lactate, carbonate, and hydrogen phosphate are able to replace the two OH^- ions of $[Cp_2V(OH)_2]$ to yield mixed species (Figure S5 of Supporting Information). Glycine and histidine, in contrast with what was observed in the solid state, do not form ternary complexes in solution, whereas in the system with citrate the amount of mixed compound is significantly lower than that of $[Cp_2V(OH)_2]$ (Figure S6 of the Supporting Information).

In the system with oxalate, the formation of a neutral species $[Cp_2V(ox)]$ was detected. Oxalate binds vanadium(IV) with the two oxygen atoms of carboxylate groups forming a five-membered chelate ring (Scheme 2a). The concentration of this species is close to 100% (Figure S5, trace b). The structural details calculated by DFT methods for the species $[Cp_2V(ox)]$ are compared with those determined in the solid state through X-ray diffraction analysis by Honzíček et al. (Table S2 of the Supporting Information).[48] Another aspect to be noticed is the small line width of the eight resonances ($\Delta H_1 = 6.5 \times 10^{-1}$ mT and $\Delta H_8 = 9.3 \times 10^{-1}$ mT); here, we would like to stress that this observation will be very important when the distribution of $[Cp_2V]^{2+}$ between the bioligands of the blood serum will be discussed. The formation of $[Cp_2V(ox)]$ from $[Cp_2V(OH)_2]$ is also demonstrated by examination of the electronic absorption spectra reported in Figure S7 of the Supporting Information (traces black and red).

DOI: 10.1021/acs.inorgchem.5b01277
Inorg. Chem. XXXX, XXX, XXX−XXX

Table 3. Experimental (exptl) and Calculated (calcd) Isotropic Hyperfine Coupling Constants (A_{iso}) with the Nuclei of ^{51}V, ^{31}P, and ^{13}C for the Possible Ternary Complexes Formed by VDC with HPO_4^{2-} and CO_3^{2-} Anions[a]

	A_{iso} (^{51}V)[b]		A_{iso} (^{31}P)[c]		A_{iso} (^{13}C)[d]	
species	calcd (Gaussian)	calcd (ORCA)	calcd (Gaussian)	calcd (ORCA)	calcd (Gaussian)	calcd (ORCA)
$[Cp_2V(HPO_4)]$	−55.9	−63.4	33.2	45.3		
$[Cp_2V(HPO_4)_2]^{2-}$	−56.6	−64.7	1.5	2.6		
$[Cp_2V(HPO_4)(OH)]^-$	−55.7	−64.1	4.9	5.7		
$[Cp_2V(CO_3)]$	−51.8	−59.6			10.5	17.4
$[Cp_2V(HCO_3)_2]$	−64.3	−70.6			1.7	6.1
$[Cp_2V(HCO_3)(OH)]$	−60.6	−66.3			1.1	3.5

[a]All values measured in 10^{-4} cm^{-1}. [b]The experimental value of A_{iso} (^{51}V) for the ternary complex formed in the system VDC/HPO_4^{2-} is -63.3×10^{-4} cm^{-1}, while that for the ternary complex formed in the system VDC/HCO_3^- is -58.3×10^{-4} cm^{-1}. [c]The experimental value of A_{iso} (^{31}P) for the ternary complex formed in the system VDC/HPO_4^{2-} is 27.5×10^{-4} cm^{-1} (ref 47). [d]The experimental value of A_{iso} (^{13}C) for the ternary complex formed in the system VDC/HCO_3^- is 8.0×10^{-4} cm^{-1} (ref 49).

The frozen solution EPR spectrum of $[Cp_2V(ox)]$ is reported in trace a of Figure S8 of Supporting Information, whereas the values of A_x, A_y, and A_z calculated with Gaussian and ORCA are listed in Table 2. Also, in the case of the anisotropic hyperfine constants, the prediction of ORCA is slightly better than that of Gaussian.

To the best of our knowledge, the system VDC/lactate was never studied up to now. The room-temperature EPR spectrum recorded at pH 7.4 is shown in Figure S5, trace a, and the frozen solution spectrum in Figure S8, trace b. The spectroscopic data (Tables 1 and 2) show that a mixed species with composition $[Cp_2V(lactH_{-1})]$ is formed (the structure is represented Scheme 2b), in which lactate binds V(IV) with the donor set (COO^-, O^-). This species is present in solution with a small amount of the bis-chelated $V(IV)O^{2+}$ complex, $[VO(lactH_{-1})_2]^{2-}$, in which lactate in the doubly deprotonated form binds vanadium with the coordination mode 2 × (COO^-, O^-).[50] The line width of the eight resonances of the room-temperature spectrum ($\Delta H_1 = 8.1 \times 10^{-1}$ mT and $\Delta H_8 = 12.0 \times 10^{-1}$ mT) is larger than that of the analogous species of oxalate, $[Cp_2V(ox)]$. The electronic absorption spectrum of $[Cp_2V(lactH_{-1})]$ (Figure S7, green) differs significantly from that of $[Cp_2V(OH)_2]$ (Figure S7, black).

The room-temperature EPR spectrum recorded at the physiological pH in the system with hydrogen phosphate is reported in Figure S5, trace c. It is possible to observe that instead of the eight transitions expected for a mononuclear V(IV) species, 16 resonances are revealed. This is due to the coupling of the unpaired electron with the nucleus of ^{31}P (I = 1/2) and is in agreement with the results in the literature.[47] Concerning the species formed under these experimental conditions, three possibilities for coordination of the HPO_4^{2-} ion must be taken into account: in the first it is bidentate and forms a four-membered chelated cycle (Scheme 3a), in the second one it is monodentate and replaces only one OH^- ion (Scheme 3b), and in the third one two HPO_4^{2-} anions replace both OH^- ligands in $[Cp_2V(OH)_2]$ (Scheme 3c).

Some years ago, Vinklárek and co-workers demonstrated through the combined application of spectroscopic and computational methods that $[Cp_2V(HPO_4)]$ exists in solution.[47] Here, we repeated the DFT calculations: the values of A_{iso} for the coupling between the unpaired electron and the nuclei of ^{51}V and ^{31}P were calculated with the software Gaussian and ORCA for $[Cp_2V(HPO_4)]$, $[Cp_2V(HPO_4)_2]^{2-}$, and $[Cp_2V(HPO_4)(OH)]^-$ and are reported in Table 3. In agreement with the results reported,[47] the best agreement with the experimental data is obtained for $[Cp_2V(HPO_4)]$ with a bidentate coordination mode of hydrogen phosphate (Scheme 3a). In particular, the high value of A_{iso} (^{31}P) is compatible only with this species. The electronic spectrum of $[Cp_2V(HPO_4)]$ is represented in Figure S7, purple, and is different from those of the other mixed complexes and of $[Cp_2V(OH)_2]$.

In the system with the ion HCO_3^- the formation of only one species is observed in the room-temperature spectrum (Figure S5, trace d) with g_{iso} = 1.985 and $A_{iso} = 58.3 \times 10^{-4}$ cm^{-1}. These parameters are very similar to those of $[Cp_2V(OH)_2]$, in agreement with what is predicted by DFT calculations (Table 1). The anisotropic EPR spectrum recorded at 120 K in the system VDC/HCO_3^- at pH 7.4 with a ratio 1/10 is shown in Figure S9, trace b, and is compared with that expected for $[Cp_2V(CO_3)]$ on the basis of the calculations with ORCA software. From an examination of Figure S9, it can be observed that the agreement between the two spectra is rather good. The formation of $[Cp_2V(CO_3)]$ was demonstrated in the literature by Vinklárek et al.[45,49] Another confirmation of the formation of $[Cp_2V(CO_3)]$ is the significant difference in the electronic absorption spectra recorded at pH 7.4 in the systems containing only VDC and VDC/HCO_3^- (cfr. traces black and blue in Figure S7).

As for hydrogen phosphate, carbonate could bind to the unit $[Cp_2V]^{2+}$ in three different modes represented in Scheme 3d–f. In this case too, the comparison between the experimental values of A_{iso} (^{51}V) and A_{iso} (^{13}C) allowed us to demonstrate that the correct coordination mode for CO_3^{2-} ligand is the bidentate one. For example, the values of A_{iso} (^{51}V) predicted for structures d, e, and f of Scheme 3 are 59.6, 70.6, and 66.3 × 10^{-4} cm^{-1} (with ORCA), respectively, to be compared with 58.3×10^{-4} cm^{-1} experimentally measured. These results are in agreement with those obtained by Vinklárek and co-workers.[45,49]

The formation of the mixed species revealed by EPR and UV–vis spectroscopy and DFT calculations was confirmed by ESI-MS and MS-MS spectrometry preparing solutions containing VDC and the bioligand in 1/1–1/10 ratios. These two techniques are suitable tools for the study of metal complexes in solution.[25] Of course, in the transfer from solution to gas phase, two important phenomena may happen: (i) the redox reactions occurring at the capillary may alter the valence state of the metal ion inducing a coordination change and a structural rearrangement; (ii) the fragmentation products may themselves recombine forming new species. The mass spectra of solutions containing VDC and oxalate, lactate, or carbonate show the peaks of the corresponding adducts, i.e., $[Cp_2V(ox)+H]^+$ (m/z 270), $[Cp_2V(lactH_{-1})+H]^+$ (m/z 270),

DOI: 10.1021/acs.inorgchem.5b01277
Inorg. Chem. XXXX, XXX, XXX–XXX

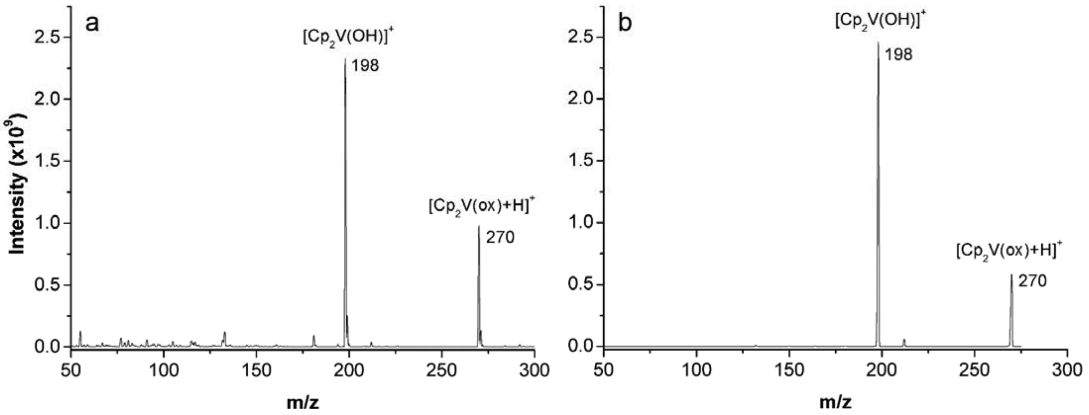

Figure 2. (a) Positive ESI mass and (b) tandem MS-MS spectrum of the solution containing VDC and oxalate (5.0×10^{-4} M, 1/1 molar ratio), recorded in H_2O/CH_3OH 1:1 v/v (1% TFA).

and $[Cp_2V(CO_3)+H]^+$ (m/z 242). In Figure 2a, the mass spectrum of the system VDC/oxalate is reported as an example. In the case of phosphate, due to the suppression effect of this ion,[51] a reliable spectrum was obtained only working with high voltages at needle (6000 V) and shield (800 V). At these conditions, a peak attributable to $[Cp_2V^V(PO_4)+Na]^+$ was found (m/z 299), together with peaks indicating the formation of polynuclear species. However, some of the detected species could have been formed in ESI phase for the severe experimental conditions used and then do not reflect the composition of the solution.

The stoichiometry hypothesized for the adducts formed with oxalate, lactate, and carbonate was confirmed by MS-MS experiments. The fragmentation profile obtained for the peak at m/z 270 for the system VDC/oxalate is reported in Figure 2b as an example. As it can be seen, the MS-MS is identical to the ESI-MS spectrum, indicating that the species with stoichiometry $[Cp_2V(OH)]^+$ (m/z 198) is a recombined fragment of the parent compound $[Cp_2V(ox)+H]^+$ (m/z 270). Therefore, the results confirm that $[Cp_2V(ox)]$ is the predominant species in solution. Analogous results were obtained in the systems with lactate and carbonate. The comparison between the calculated and the experimental isotopic pattern for $[Cp_2V(ox)+H]^+$, $[Cp_2V(lactH_{-1})+H]^+$, and $[Cp_2V^V(PO_4)+Na]^+$ is shown in Figure S4 of the Supporting Information. In Table 4 the experimental and calculated m/z values for the detected species are reported.

In contrast with the ligands discussed above, in the system with citrate $[Cp_2V(citrH_{-1})]^{2-}$ is a minor species (Figure S6 of Supporting Information, trace c). The major complex is $[Cp_2V(OH)_2]$, whereas the resonances of two $V(IV)O^{2+}$ species, $[VO(H_2O)_5]^{2+}$ (g_{iso} = 1.968 and A_{iso} = 106.9 × 10^{-4} cm^{-1}) and $[VO(citrH_{-1})]^{2-}$ (g_{iso} = 1.970 and A_{iso} = 98.0 × 10^{-4} cm^{-1}), in which citrate in the fully deprotonated form binds vanadium with the donor set (COO^-, O^-), are also detected.[50a,52]

Among the amino acids of the blood serum, in this study glycine (as an example of an amino acid without coordinating side-chain group) and histidine (as an example of an amino acid with coordinating side-chain group) were examined. The team of Vinklárek synthesized several complexes in the solid state formed by amino acids (a.a.) with structure $[Cp_2V(a.a.)]^+$.[45] When such species are dissolved in an organic solvent such as MeOH, the resonances of $[Cp_2V(a.a.)]^+$ can be revealed. The data obtained in this study indicate that the behavior in aqueous solution is different. In the system with glycine (Figure S6 of the Supporting Information, trace b) the only species is $[Cp_2V(OH)_2]$; the value of A_{iso} measured (58.3×10^{-4} cm^{-1}) is significantly different from that of the species formed by the amino acids, $[Cp_2V(a.a.)]^+$ ($62.2–62.9 \times 10^{-4}$ cm^{-1} [45]), and

Table 4. Species Identified from the ESI-MS Studies and MS-MS Fragmentation Products

	ion	composition	exptl m/z[a]	calcd m/z[a]
I	$[Cp_2V]^{2+}$ (originated from **XI** and **XIII**)	$C_{10}H_{10}V$	90.90	90.51
II	$[C_5H_6 + C_3H_3]^+$ (originated from **XIV**)	C_8H_9	104.92	105.07
III	$[CpV]^+$ (originated from **VIII** and **XVI**)	C_5H_5V	115.85	115.98
IV	$[2Cp + 3H]^+$ (originated from **IX**, **XIV** and **XVIII**)	$C_{10}H_{13}$	132.90	133.10
V	$[CpV^{III}F]^+$ (originated from **X**)	C_5H_5FV	134.91	134.98
VI	$[CpVN_2]^+$ (originated from **VIII**)	$C_5H_5N_2V$	143.87	143.98
VII	$[Cp_2V^{III}]^+$ (originated from **XI**, **XV** and **XVI**)	$C_{10}H_{10}V$	180.95	181.02
VIII	$[Cp_2VH]^+$ (MS-MS fragments: m/z 144, 116)	$C_{10}H_{11}V$	181.98	182.01
IX	$[Cp_2V(OH)]^+$ (MS-MS fragment: m/z 133)	$C_{10}H_{11}OV$	197.94	198.00
X	$[Cp_2VF]^+$ (MS-MS fragment: m/z 135)	$C_{10}H_{10}FV$	199.97	200.00
XI	$[Cp_2VCl]^+$ (MS-MS fragments: m/z 181, very low, 91)	$C_{10}H_{10}ClV$	215.98	216.00
XII	$[Cp_2V(OH)N_2]^+$ (originated from **XIV**)	$C_{10}H_{11}N_2OV$	225.94	226.03
XIII	$[Cp_2V(CO_3)+H]^+$ (MS-MS fragments: m/z 198, 91)	$C_{11}H_{11}O_3V$	242.03	242.00
XIV	$[Cp_2V(OH)(H_2O)N_2]^+$ (MS-MS fragments: m/z 226, 133, 105)	$C_{10}H_{13}N_2O_2V$	243.98	244.03
XV	$[Cp_2V(lactH_{-1})+H]^+$ (MS-MS fragments: m/z 198, 181)	$C_{13}H_{15}O_3V$	269.99	270.00
XVI	$[Cp_2V(ox)+H]^+$ (MS-MS fragments: m/z 198, 181, 116)	$C_{12}H_{11}O_4V$	270.01	270.00
XVII	$[Cp_2V(TFA)]^+$	$C_{12}H_{10}F_3O_2V$	294.04	294.00
XVIII	$[Cp_2V^V(PO_4)+Na]^+$ (MS-MS fragment: m/z 133)	$C_{10}H_{10}NaO_4PV$	299.00	299.00

[a]The experimental and calculated m/z values refer to the peak representative of the monoisotopic mass.

DOI: 10.1021/acs.inorgchem.5b01277
Inorg. Chem. XXXX, XXX, XXX−XXX

that calculated with ORCA for $[Cp_2V(Gly)]^+$ (62.8×10^{-4} cm^{-1}). In the system with histidine the major species is $[Cp_2V(OH)_2]$, whereas the resonances of $[Cp_2V(His)]^+$ (g_{iso} = 1.984 and A_{iso} = 62.4×10^{-4} cm^{-1}) are much less intense, suggesting that the mixed complex is present at the physiological pH in a very low amount. Therefore, at the experimental conditions of this study, it can be affirmed that the affinity of the amino acids for the moiety $[Cp_2V]^{2+}$ is much lower than that of other *l.m.m.* bL. This may be due to the low affinity of $[Cp_2V]^{2+}$ for the nitrogen with respect to that for the oxygen donors. A demonstration of this finding is the behavior of 1-methylimidazole (that has been used over the last years by our team as a model for the coordination of an imidazole nitrogen of a histidine residue to the insulin-mimetic $V(IV)O^{2+}$ complexes[16b−i]), which does not form mixed complexes and confirms the poor affinity of $[Cp_2V]^{2+}$ ion toward the nitrogen donors.

3. Interaction of VDC with Blood Serum Proteins. The interaction of the insulin-mimetic $V(IV)O^{2+}$ complexes with the blood serum proteins has been widely studied by our team.[16b−i] The results demonstrated that both hTf and HSA bind vanadium(IV) complexes with a nitrogen donor of an accessible histidine residue, probably exposed on the protein surface. Recently, it was proved that also carboxylate of an aspartate residue is able to coordinate $V(IV)O^{2+}$ ion.[18] Some years ago, the interaction of VDC with apo-transferrin (apo-hTf) has been studied through the combined application of EPR, electronic absorption, CD, and fluorescence spectroscopy.[53,54] In particular, Nishida et al. in the system VDC/apo-hTf observed two sets of isotropic resonances with g_{iso} = 1.985 and A_{iso} = 95.9×10^{-4} cm^{-1} (species a) and g_{iso} = 1.984 and A_{iso} = 58.0×10^{-4} cm^{-1} (species b). These two signals were incorrectly attributed to the species in which $V(IV)O^{2+}$ ion is bound to the Fe sites in the *N*- and *C*-terminal regions of the protein and to the species derived from VDC in which the two Cl^- ions are replaced by O and N donors of the side chains of transferrin.[54] It is well known that EPR spectra recorded at room temperature in the systems containing proteins can be characterized by two types of signals: isotropic signals belonging to species in which V(IV) is bound to the *l.m.m.* ligands and anisotropic signals for the binary or ternary species in which V(IV) is bound to the proteins.[16f,17d,28,55] The detection of anisotropic signals at room temperature is due to slow tumbling motion, in the time scale of an EPR experiment, of the complexes formed by the proteins which behave as a solid or a frozen solution. In contrast, the signals revealed by Nishida et al. are completely isotropic, and this induces us to believe that apo-transferrin did not interact with VDC under their experimental conditions. On the basis of the results discussed above, species b observed by Nishida et al. is the complex in which two OH^- ions bind $[Cp_2V]^{2+}$ forming $[Cp_2V(OH)_2]$ (A_{iso} = 58.0×10^{-4} cm^{-1}), whereas species a is, without any doubt for the large value of A_{iso} (95.9×10^{-4} cm^{-1}), a $V(IV)O^{2+}$ complex; in addition, the intensity of the signal of $[Cp_2V(OH)_2]$ decreases as a function of the time and that of $V(IV)O^{2+}$ species increases significantly, indicating a V(IV)−V(IV)O transformation. Du et al., instead, proposed that the interaction between $[Cp_2VCl_2]$ and apo-hTf is similar to $[Cp_2TiCl_2]$,[53] which loses the two cyclopentadienyl rings forming Ti_2(apo-Tf);[56] this result appears to be in contrast with the fact that the fragment $[Cp_2V]^{2+}$ is much more stable than $[Cp_2Ti]^{2+}$ and that EPR data do not show the formation of $(VO)_2$(apo-hTf), whose spectrum is well known.[17b,30,55,57,58]

In this study, the system VDC/apo-hTf has been re-examined and the EPR spectrum recorded at pH 7.4 is shown in Figure S10 of the Supporting Information, trace b. Our data are in agreement with those of Nishida et al., even if the interpretation of the data is different; in particular, it emerges that the spectrum at the physiological conditions is superimposable with that of $[Cp_2V(OH)_2]$ (see traces a and b of Figure S10).

Nishida et al. also examined the system VDC/HSA. EPR signals at room temperature are isotropic with g_{iso} = 1.984 and A_{iso} = 58.0×10^{-4} cm^{-1}.[54] On the basis of this result, the authors concluded that albumin interacts with $[Cp_2V]^{2+}$ through surface sites of the protein, analogously to what was observed for TDC.[59] Our data confirm what was detected by Nishida et al.,[54] but in this case too the detection of isotropic signals (Figure S10 of Supporting Information, trace c) allowed us to rule out that the albumin interacts with $[Cp_2V]^{2+}$ ion. The eight resonances (which do not change as a function of the time) and the spectral parameters (g_{iso} = 1.985 and A_{iso} = 58.3×10^{-4} cm^{-1}) can be attributed to $[Cp_2V(OH)_2]$ (spectrum shown in trace a of Figure S10 of Supporting Information). Moreover, in both systems with apo-hTf and HSA no decrease of the isotropic signals, attributable to an interaction with the proteins such as to broaden the resonances, is observed.

In conclusion it can be argued that, under the experimental conditions used in this study, the blood plasma proteins do not interact with VDC. At the moment the reasons of this behavior are not known, but it can be hypothesized that several factors contribute to disfavor the formation of the possible ternary species formed upon interaction of the moiety $[Cp_2V]^{2+}$ with the proteins: (i) as mentioned above, the affinity of $[Cp_2V]^{2+}$ toward the nitrogen donors is rather poor, and this would preclude the bonding with His-N, which instead appears to be very important for the insulin-mimetic $V(IV)O^{2+}$ complexes;[16b−i] (ii) the protein surface is rich of polar residues such as aspartate, glutamate, tyrosine, and threonine, and this could hinder their interaction with the $[Cp_2V]^{2+}$ moiety, in which the two cyclopentadienyl rings are strongly apolar; (iii) as noticed for citrate, the presence of the two bulky cyclopentadienyls may hinder the interaction with the side chains of the amino acids of apo-hTf and HSA.

4. Speciation of VDC in Blood Plasma Model Solutions. After the examination of the binary systems formed by VDC and the main blood plasma components (bL and proteins), in this section the behavior of several model systems of the blood plasma will be discussed. In particular, the multicomponent system formed by VDC and the bioligands with higher affinity for $[Cp_2V]^{2+}$ (i.e., oxalate, carbonate, lactate, and hydrogen phosphate, see above) was studied. For all systems, room-temperature and frozen solution EPR spectra and electronic absorption spectra were recorded at pH 7.4. Initially, the molar ratio between VDC and the bioligands bL was set at 1/10, whereas subsequently it was brought to the physiological value using the relative concentration of oxalate, carbonate, lactate, and hydrogen phosphate in the plasma as reported by Harris ([ox] = 9.2 μM, $[HCO_3^-]$ = 24.9 mM, [lact] = 1.51 mM, $[HPO_4^{2-}]$ = 1.10 mM);[19] in particular, the ratios $[HPO_4^{2-}]$/[ox], [lact]/[ox], and $[HCO_3^-]$/[ox] were 119.6, 164.1, and 2706.5, respectively.

The room-temperature EPR spectrum recorded at pH 7.4 in the system VDC/ox/$NaHCO_3$/lact with molar ratio 1/10/10/10 is shown in Figure 3b. It can be noticed that in the quaternary system the main species is $[Cp_2V(ox)]$ and

DOI: 10.1021/acs.inorgchem.5b01277
Inorg. Chem. XXXX, XXX, XXX−XXX

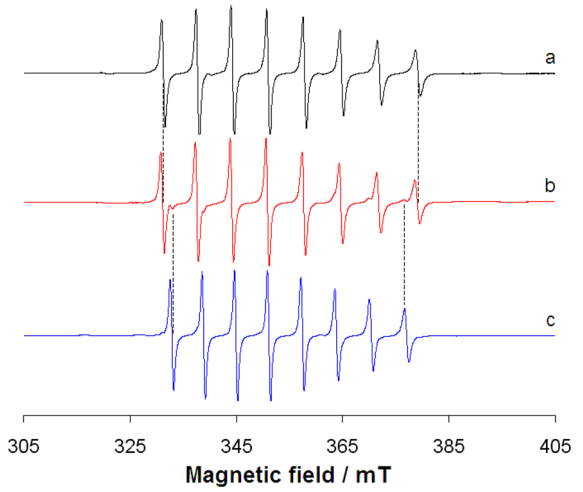

Figure 3. Room-temperature (298 K) EPR spectra recorded at pH 7.4 in aqueous solution in the systems containing (a) VDC/ox 1/10, (b) VDC/ox/$NaHCO_3$/lact 1/10/10/10, and (c) VDC/$NaHCO_3$ 1/10. VDC concentration was 1.0×10^{-3} M. With the dotted lines the resonances $M_I = -7/2, 7/2$ of the complexes $[Cp_2V(ox)]$ (trace a) and $[Cp_2V(CO_3)]$ (trace c) are shown.

$[Cp_2V(CO_3)]$ is a minor species. Even if $[Cp_2V(ox)]$ and $[Cp_2V(lactH_{-1})]$ are characterized by similar EPR parameters, the signals can be attributed without ambiguity to $[Cp_2V(ox)]$ for the small experimental line width ($\Delta H_1 = 6.2 \times 10^{-1}$ mT and $\Delta H_8 = 9.0 \times 10^{-1}$ mT, to be compared with $\Delta H_1 = 6.5 \times 10^{-1}$ mT and $\Delta H_8 = 9.3 \times 10^{-1}$ mT for $[Cp_2V(ox)]$ and $\Delta H_1 = 8.1 \times 10^{-1}$ mT and $\Delta H_8 = 12.0 \times 10^{-1}$ mT for $[Cp_2V(lactH_{-1})]$, see above). This result suggests that the affinity of $[Cp_2V]^{2+}$ for oxalate is much higher than that for carbonate and lactate.

In Figure S11 of the Supporting Information (trace b) the room-temperature EPR spectrum of the system VDC/$NaHCO_3$/lact/Na_2HPO_4 with ratio 1/10/10/10 and VDC concentration 1.0×10^{-3} M is reported. In this system the two species $[Cp_2V(CO_3)]$ (spectrum shown in trace a) and $[Cp_2V(lactH_{-1})]$ (spectrum in trace c) are formed in comparable amounts, with the concentration of the mixed complex with carbonate slightly larger than that with lactate. The possible formation of $[Cp_2V(HPO_4)]$ can be excluded because this species would be countersigned by the characteristic coupling between the unpaired electron and the ^{31}P nucleus (Figure S5, trace c).

The behavior of the ternary system VDC/lact/Na_2HPO_4 with molar ratio 1/10/10 is represented in Figure S12 of the Supporting Information (trace b). In such a system $[Cp_2V(lactH_{-1})]$ is the main species, and $[Cp_2V(HPO_4)]$ (which can be distinguished very well for the 16-line spectrum) is the minor species. This indicates that the affinity of lactate for $[Cp_2V]^{2+}$ ion is slightly higher than that of phosphate.

On the basis of these results, it can be affirmed that the affinity order of the four blood plasma bL ligands for the moiety $[Cp_2V]^{2+}$ is $ox^{2-} \gg CO_3^{2-} > lactH_{-1}^{2-} > HPO_4^{2-}$.

The systems discussed above (see Figure 3 and Figures S11 and S12 of Supporting Information), even if they allow us to demonstrate the relative strength of the bL bioligands for $[Cp_2V]^{2+}$, are not good models of the blood plasma because the relative concentrations of bL must be considered; for example, the higher affinity of oxalate may be compensated by the larger concentration of the other three components. To throw light on this point, the quinary system VDC/ox/$NaHCO_3$/lact/Na_2HPO_4 has been studied at pH 7.4 with the bioligands at the same concentration ratio as in the blood plasma. Concerning the concentration of VDC in the blood necessary to display a pharmacological effect, no decisive datum was published in the literature, but it seems to be reasonable assume that, analogously to what was reported for the insulin-mimetic vanadium compounds, the value must be in the range 10−100 μM.[1b,60] Therefore, the system VDC/ox/$NaHCO_3$/lact/Na_2HPO_4 was examined at molar ratio 1/1/2706.5/164.1/119.6 and 1/0.1/270.7/16.4/12.0 with a concentration of VDC of 4×10^{-4} M. The first model system "simulates" the situation in which the concentration in the plasma of the containing-V drug is close to that of oxalate (9.2 μM[19]), whereas in the second system the concentration is 10 times that of oxalate (92.0 μM). With this approach, the concentration range 9.2−92.0 μM of the pharmacologically active VDC can be explored.

The room-temperature spectrum recorded on the system VDC/ox/$NaHCO_3$/lact/Na_2HPO_4 with molar ratio 1/1/2706.5/164.1/119.6 is shown in Figure 4b. It can be observed that the main species is $[Cp_2V(ox)]$ (Figure 4a), whereas

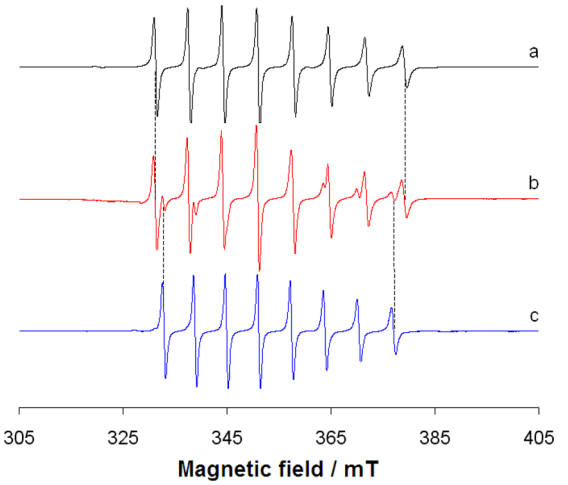

Figure 4. Room-temperature (298 K) EPR spectra recorded at pH 7.4 in aqueous solution in the systems containing (a) VDC/ox 1/10, (b) VDC/ox/$NaHCO_3$/lact/Na_2HPO_4 1/1/2706.5/164.1/119.6, and (c) VDC $NaHCO_3$ 1/10. The concentration of VDC was 4.0×10^{-4} M (b) or 1.0×10^{-3} M (a and c). With the dotted lines the resonances $M_I = -7/2, 7/2$ of the complexes $[Cp_2V(ox)]$ (trace a) and $[Cp_2V(CO_3)]$ (c) are shown.

$[Cp_2V(CO_3)]$ (Figure 4c) is formed only in a very small amount. Therefore, when the ratio VDC/ox is 1/1, almost all $[Cp_2V]^{2+}$ ion is bound by oxalate and the participation of the other bL is negligible. Analogous results are expected when the ratio VDC/ox is <1, i.e., when the concentration of VDC at physiological conditions is lower than 9.2 μM.

The behavior of the quinary system VDC/ox/$NaHCO_3$/lact/Na_2HPO_4 with ratio 1/0.1/270.7/16.4/12.0 is reported in Figure S13 of the Supporting Information, trace b. In such a system the main species is $[Cp_2V(CO_3)]$ (Figure S13, trace a), whereas two minor species are observable, $[Cp_2V(ox)]$ and probably $[Cp_2V(lactH_{-1})]$ (Figure S13, traces c and d). $[Cp_2V(HPO_4)]$, instead, is not formed. This behavior can be rationalized in the following way: when VDC is present in solution in excess with respect to oxalate (i.e., when it is present in the blood plasma with a concentration higher than 9.2 μM),

DOI: 10.1021/acs.inorgchem.5b01277
Inorg. Chem. XXXX, XXX, XXX−XXX

the latter binds the maximum possible amount of $[Cp_2V]^{2+}$, whereas the remaining part of VDC distributes between the carbonate ion (mainly) and lactate (in much smaller concentration). The exact amount of the mixed complex with lactate cannot be determined because the resonances of $[Cp_2V(ox)]$ and $[Cp_2V(lactH_{-1})]$ fall in the same region of the EPR spectrum.

The electronic absorption spectra recorded in the two quinary systems VDC/ox/$NaHCO_3$/lact/Na_2HPO_4 with ratio 1/1/2706.5/164.1/119.6 and 1/0.1/270.7/16.4/12.0 (Figure 5) allowed us to confirm this finding. It can be noticed that in

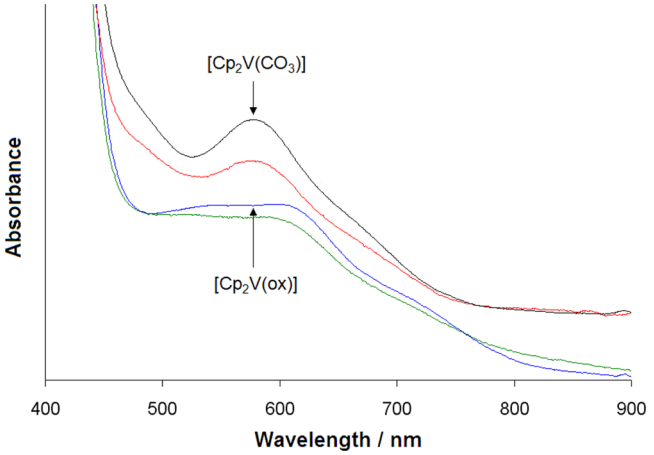

Figure 5. Electronic absorption spectra recorded in aqueous solution at pH 7.4 in the systems containing VDC/ox/$NaHCO_3$/lact/Na_2HPO_4 1/1/2706.5/164.1/119.6 (green), VDC/ox 1/10 (blue), VDC/ox/$NaHCO_3$/lact/Na_2HPO_4 1/0.1/270.7/16.4/12.0 (red), and VDC/$NaHCO_3$ 1/10 (black). VDC concentration was 4.0×10^{-4} (green and red) and 1.0×10^{-3} M (blue and black). Spectra of $[Cp_2V(CO_3)]$ and $[Cp_2V(ox)]$ are indicated by the two arrows.

the first case (VDC and oxalate at the equimolar ratio) the electronic absorption spectrum is comparable to that of $[Cp_2V(ox)]$ (in blue in Figure 5), whereas when an excess of VDC is present (for example, when it is 10 times more concentrated than oxalate) the spectrum closely resembles that of $[Cp_2V(CO_3)]$ (in black in Figure 5) with an absorption band at 575 nm.

The behavior at low temperature of the two systems VDC/ox/$NaHCO_3$/lact/Na_2HPO_4 at molar ratio 1/1/2706.5/164.1/119.6 and 1/0.1/270.7/16.4/12.0 is the same as described at room temperature. Frozen solutions EPR spectra are reported in Figures 6 and 7 and, as usual, are better resolved than the room-temperature ones. It can be observed that when the ratio VDC/ox is 1/1, the main species is $[Cp_2V(ox)]$, whereas $[Cp_2V(CO_3)]$ is the minor species; the spectrum recorded in the system with ratio 1/1/2706.5/164.1/119.6 can be reproduced postulating 70% of $[Cp_2V(ox)]$ and 30% of $[Cp_2V(CO_3)]$ in aqueous solution (Figure 6c). When the ratio VDC/ox is 10/1, instead, the main species is $[Cp_2V(CO_3)]$, whereas $[Cp_2V(ox)]$ and $[Cp_2V(lactH_{-1})]$ are the minor species; in this case the spectrum was simulated considering in aqueous solution 80% of $[Cp_2V(CO_3)]$, 10% of $[Cp_2V(ox)]$, and 10% of $[Cp_2V(lactH_{-1})]$ (Figure S14 of the Supporting Information).

5. Speciation of VDC in the Blood Plasma. After the investigation of the behavior of VDC in the blood model solutions, the speciation in the plasma was evaluated. To carry

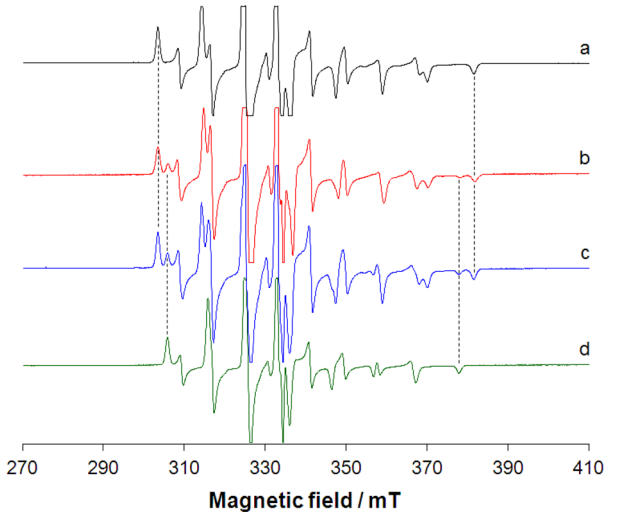

Figure 6. EPR spectra recorded at 120 K and pH 7.4 in aqueous solution in the systems containing (a) VDC/ox 1/10, (b) VDC/ox/$NaHCO_3$/lact/Na_2HPO_4 1/1/2706.5/164.1/119.6, (c) spectrum obtained in aqueous solution 70% of $[Cp_2V(ox)]$ (trace a) and 30% of $[Cp_2V(CO_3)]$ (trace d) and (d) VDC/$NaHCO_3$ 1/10. The concentration of VDC was 4.0×10^{-4} (b) and 1.0×10^{-3} M (a and c). With the dotted lines the resonances $M_I = -7/2, 7/2$ of the complexes $[Cp_2V(ox)]$ (a) and $[Cp_2V(CO_3)]$ (d) are shown.

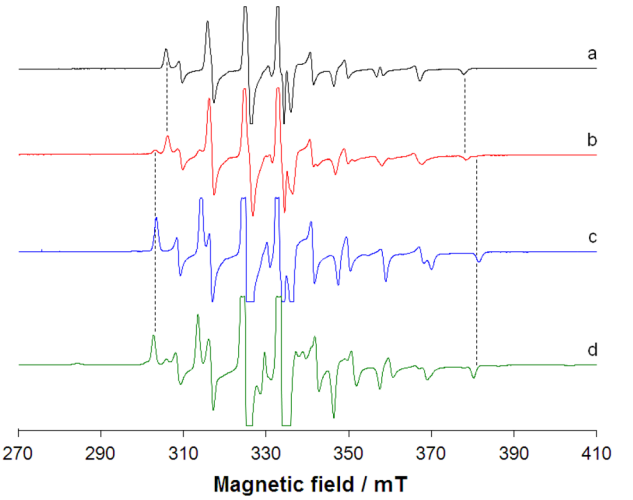

Figure 7. EPR spectra recorded at 120 K in aqueous solution at pH 7.4 in the systems containing (a) VDC/$NaHCO_3$ 1/10, (b) VDC/ox/$NaHCO_3$/lact/Na_2HPO_4 1/0.1/270.7/16.4/12.0, (c) VDC/ox 1/10, and (d) VDC/lact 1/10. The concentration of VDC was 4.0×10^{-4} M (b) and 1.0×10^{-3} M (a, c, and d). With the dotted lines the resonances $M_I = -7/2, 7/2$ of the complexes $[Cp_2V(CO_3)]$ (a), $[Cp_2V(ox)]$ (c), and $[Cp_2V(lactH_{-1})]$ (d) are shown.

out these experiments, a blood sample was centrifuged to separate plasma from buffy coat and red blood cells (see Experimental and Computational Section). The plasma was subsequently incubated for 30 min at 37 °C with a solution of VDC with a concentration of 4.5×10^{-5} M, and the EPR spectrum at 120 K was immediately measured. As pointed out in the literature,[37b] the analysis of a frozen solution EPR spectrum is preferred to that of room-temperature one because it allows one to get more detailed information on (i) the type of V(IV) species (nonoxido or oxido), (ii) the coordination mode, geometry, and distortion of V(IV) species, since the values of A_i

DOI: 10.1021/acs.inorgchem.5b01277
Inorg. Chem. XXXX, XXX, XXX−XXX

(i = *x*, *y*, *z*) are more sensitive to the identity of the donors than A_{iso}, and (iii) the presence of minor species in solution, which usually are not detectable from the examination of a room-temperature spectrum. The EPR spectrum recorded in the blood plasma is shown in Figure 8a, together with the spectra of

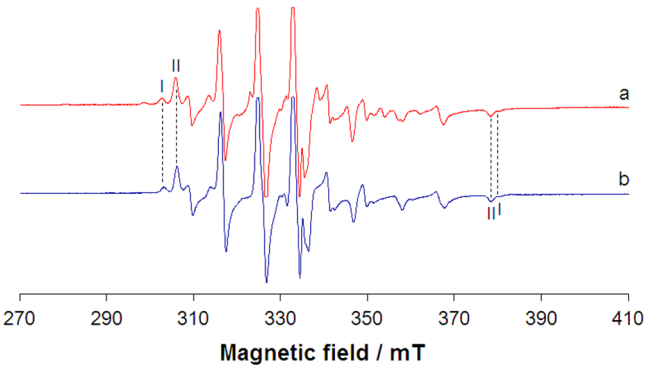

Figure 8. EPR spectra recorded at 120 K at pH 7.4 in the systems containing (a) blood plasma incubated with VDC for 30 min and (b) VDC/ox/$NaHCO_3$/lact/Na_2HPO_4 1/0.1/270.7/16.4/12.0. The concentration of VDC was 4.5×10^{-5} M (a) and 4.0×10^{-4} M (b). With the dotted lines the resonances $M_I = -7/2, 7/2$ of the complexes $[Cp_2V(ox)]$ (**I**) and $[Cp_2V(CO_3)]$ (**II**) are indicated.

the system VDC/ox/$NaHCO_3$/lact/Na_2HPO_4 at ratio 1/0.1/270.7/16.4/12.0 (Figure 8b). The results are very surprising: the behavior revealed in the blood plasma is perfectly superimposable to that observed in the model system, demonstrating that the study of a good model can give valuable information on the behavior of a more complicated system such as a biological one. From an examination of Figure 8, it can be observed that V(IV) distributes between oxalate and carbonate ion: in particular, the strongest ligand, oxalate (9.2 μM), binds 9.2 μM of VDC to form $[Cp_2V(ox)]$, whereas the remaining part of $[Cp_2V]^{2+}$ (35.8 μM) is complexed by carbonate as $[Cp_2V(CO_3)]$. The predicted ratio between the amounts of $[Cp_2V(CO_3)]$ and $[Cp_2V(ox)]$ should be ca. 4:1, in very good agreement with what was observed in the spectrum reported in Figure 8a.

Some years ago, Vinklárek and co-workers dissolved VDC in the blood plasma and recorded room-temperature EPR spectra; they found two sets of isotropic signals attributed to $[Cp_2V(CO_3)]$ and an unspecified species with an amino acid, $[Cp_2V(a.a.)]$.[45] The results of this study indicate that their results are partially correct: whereas $[Cp_2V(CO_3)]$ is—without any doubt—formed, the other species was confused with $[Cp_2V(a.a.)]$ (not formed) because its spectrum is characterized by an A_{iso} value similar to that of $[Cp_2V(ox)]$.

On the basis of the results discussed in this study, the speciation of $[Cp_2VCl_2]$ in the blood plasma can be illustrated in Scheme 4. After the oral administration VDC passes in solution at the acid pH of the stomach (where the two Cl^- ions are probably replaced by two H_2O ligands). When $[Cp_2V(H_2O)_2]^{2+}$ arrives in the small intestine and then in the bloodstream at pH 7.4, $[Cp_2V(OH)_2]$ is formed and can react with the bioligands of the plasma (in particular, oxalate, carbonate, and lactate, see above). The concentration of VDC in the plasma does not correspond to the administered dose; in fact, usually only 1−10% of orally ingested V compound is absorbed in the gastrointestinal tract, the real percent amount being influenced by several factors such as the chemical form

Scheme 4. Speciation of VDC in the Blood Plasma as a Function of Its Concentration[a]

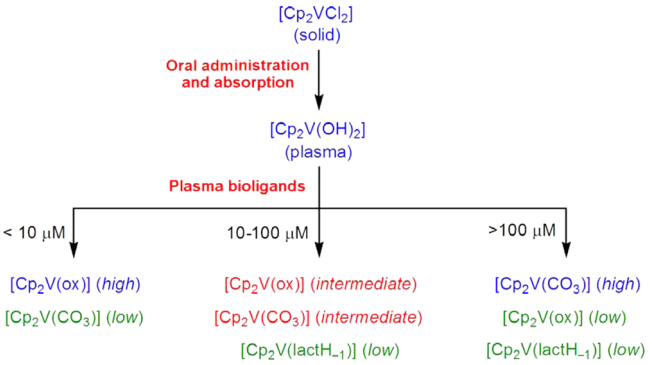

[a]With high, intermediate, and low the relative amount of each species is shown.

(inorganic salt or complex), the charge, and the polarity of the species.[61] A total concentration in the range 10−100 μM is plausible for an orally administered active V compound,[1b,60] the exact value depending mainly on the gastrointestinal tract absorption. If V concentration is around 10 μM, most of VDC administered is transported to the target organs in the organism as $[Cp_2V(ox)]$, i.e., the moiety $[Cp_2V]^{2+}$ is bound by the strongest bL bioligand, oxalate. If V concentration is 10 times higher, 100 μM, only 9.2 μM of $[Cp_2V]^{2+}$ is complexed by oxalate, whereas the remaining part distributes between carbonate which forms the main species $[Cp_2V(CO_3)]$ and lactate which forms the minor species $[Cp_2V(lactH_{-1})]$. When V concentration is in the intermediate concentration range, 10−100 μM, $[Cp_2V]^{2+}$ distributes between oxalate and carbonate, with the role of the latter being more important with increasing concentration with respect to the lowest limit of 10 μM.

CONCLUSIONS

It is now demonstrated that many vanadium compounds have antitumor activity. $[Cp_2VCl_2]$ or VDC has been the first V species with anticancer activity and has been proposed in 1983 in the treatment of Ehrlich ascites tumor. All VDC derivatives studied subsequently induce apoptosis in human cancer cells, but their mode of action remains elusive. The mechanism of VDC is closely related to the biotransformation in the blood plasma because the latter determines which species arrives to the target cells in the organism.

Therefore, in this study the speciation of VDC in the plasma under physiological conditions was studied. The results indicate that in an aqueous solution the two Cp−V bonds are very resistant to the hydrolysis, whereas both Cl^- ions dissociate to form at acid pH of the stomach $[Cp_2V(H_2O)_2]^{2+}$, which at physiological pH deprotonates quantitatively to $[Cp_2V(OH)_2]$. In contrast with what was found for other pharmacologically active V compounds, such as antidiabetic $V(IV)O^{2+}$ species, $[Cp_2V(OH)_2]$ does not interact with the plasma proteins (transferrin and albumin) and undergoes displacement reactions with the low molecular mass bioligands. The bioligands with highest affinity for $[Cp_2V]^{2+}$ moiety are oxalate, carbonate, lactate, and hydrogen phosphate, whereas other candidates to V binding such as citrate and amino acids do not show any affinity for it. On the basis of EPR, UV−vis, ESI-MS, MS-MS, and DFT results, it has been found that the affinity

DOI: 10.1021/acs.inorgchem.5b01277
Inorg. Chem. XXXX, XXX, XXX−XXX

order of the four strongest bioligands is $ox^{2-} \gg CO_3^{2-} > lactH_{-1}^{2-} > HPO_4^{2-}$. The speciation of VDC at the physiological conditions has been examined studying several model systems containing the bioligands with the same relative amount as in the blood and, subsequently, carrying out experiments with plasma samples. The results obtained show that the model systems behave in the same way as the blood plasma, demonstrating that the choice of a good model is essential to get information on more complicated systems, such as the biological ones.

The speciation of VDC in the blood plasma can be summarized as follows: if V concentration is low (10 μM), most of VDC administered is transported in the organism as $[Cp_2V(ox)]$, i.e., the strongest bioligand, oxalate, binds the $[Cp_2V]^{2+}$ moiety. In contrast, if V concentration is high (100 μM) oxalate binds only 9.2 μM of $[Cp_2V]^{2+}$ (9.2 μM is the oxalate concentration in the plasma), whereas the remaining 90.8 μM of $[Cp_2V]^{2+}$ distributes between carbonate to form $[Cp_2V(CO_3)]$ (main species) and lactate to yield $[Cp_2V(lactH_{-1})]$ (minor species). Finally, if V concentration is in the range 10−100 μM, $[Cp_2V]^{2+}$ distributes between $[Cp_2V(ox)]$ and $[Cp_2V(CO_3)]$, with the role of carbonate being more and more important with increasing V concentration with respect to 10 μM.

■ ASSOCIATED CONTENT

Supporting Information

The Supporting Information is available free of charge on the ACS Publications website at DOI: 10.1021/acs.inorgchem.5b01277.

Tables and figures with the results of DFT calculations, figures with EPR spectra recorded at 298 and 120 K and pH 7.4 on VDC and its binary, ternary, quaternary and quinary systems, figure with electronic absorption spectra recorded at pH 7.4 on VDC and its binary systems, calculated and experimental isotopic pattern for the most intense peaks detected in the mass spectra (PDF)

■ AUTHOR INFORMATION

Corresponding Author

*E-mail: garribba@uniss.it.

Notes

The authors declare no competing financial interest.

■ ACKNOWLEDGMENTS

The authors thank Fondazione Banco di Sardegna for financial support (project Prot. U924.2014/AI.807.MGB; Prat. 2014.0443) and Servizio Trasfusionale Aziendale (ASL of Sassari).

■ REFERENCES

(1) (a) Crans, D. C.; Smee, J. J.; Gaidamauskas, E.; Yang, L. *Chem. Rev.* **2004**, *104*, 849−902. (b) Rehder, D. *Bioinorganic Vanadium Chemistry*; John Wiley & Sons, Ltd.: Chichester, 2008.

(2) (a) Thompson, K. H.; Orvig, C. *Coord. Chem. Rev.* **2001**, *219*−*221*, 1033−1053. (b) Shechter, Y.; Goldwaser, I.; Mironchik, M.; Fridkin, M.; Gefel, D. *Coord. Chem. Rev.* **2003**, *237*, 3−11. (c) Sakurai, H.; Yoshikawa, Y.; Yasui, H. *Chem. Soc. Rev.* **2008**, *37*, 2383−2392.

(3) (a) Thompson, K. H.; McNeill, J. H.; Orvig, C. *Chem. Rev.* **1999**, *99*, 2561−2572. (b) Thompson, K. H.; Orvig, C. In *Metal Ions in Biological Systems*; Sigel, H., Sigel, A., Eds.; Marcel Dekker: New York, 2004; Vol. *41*, pp 221−252. (c) Thompson, K. H.; Liboiron, B. D.; Hanson, G. R.; Orvig, C. In *Medicinal Inorganic Chemistry*; American Chemical Society: Washington, DC, 2005; Vol. *903*, pp 384−399. (d) Thompson, K. H.; Orvig, C. *J. Inorg. Biochem.* **2006**, *100*, 1925−1935.

(4) Thompson, K. H.; Lichter, J.; LeBel, C.; Scaife, M. C.; McNeill, J. H.; Orvig, C. *J. Inorg. Biochem.* **2009**, *103*, 554−558.

(5) Costa Pessoa, J.; Tomaz, I. *Curr. Med. Chem.* **2010**, *17*, 3701−3738.

(6) Carroll, J. http://www.fiercebiotech.com/story/akesis-shutters-program-files-chap-7/2009-01-22.

(7) (a) Rehder, D. *Future Med. Chem.* **2012**, *4*, 1823−1837. (b) Costa Pessoa, J.; Etcheverry, S.; Gambino, D. *Coord. Chem. Rev.* **2015**, 10.1016/j.ccr.2014.12.002.

(8) (a) Köpf-Maier, P.; Krahl, D. *Chem.-Biol. Interact.* **1983**, *44*, 317−328. (b) Köpf-Maier, P.; Köpf, H. *Chem. Rev.* **1987**, *87*, 1137−1152.

(9) (a) Ghosh, P.; D'Cruz, O. J.; Narla, R. K.; Uckun, F. M. *Clin. Cancer Res.* **2000**, *6*, 1536−1545. (b) Navara, C. S.; Benyumov, A.; Vassilev, A.; Narla, R. K.; Ghosh, P.; Uckun, F. M. *Anti-Cancer Drugs* **2001**, *12*, 369−376.

(10) (a) Lümmen, G.; Sperling, H.; Luboldt, H.; Otto, T.; Rübben, H. *Cancer Chemother. Pharmacol.* **1998**, *42*, 415−417. (b) Kröger, N.; Kleeberg, U. R.; Mross, K.; Edler, L.; Hossfeld, D. K. *Onkologie* **2000**, *23*, 60−62.

(11) Gleeson, B.; Claffey, J.; Hogan, M.; Müller-Bunz, H.; Wallis, D.; Tacke, M. *J. Organomet. Chem.* **2009**, *694*, 1369−1374.

(12) Gleeson, B.; Deally, A.; Müller-Bunz, H.; Patil, S.; Tacke, M. *Aust. J. Chem.* **2010**, *63*, 1514−1520.

(13) Honzíček, J.; Klepalová, I.; Vinklárek, J.; Padělková, Z.; Císařová, I.; Šiman, P.; Řezáčová, M. *Inorg. Chim. Acta* **2011**, *373*, 1−7.

(14) Yoshikawa, Y.; Sakurai, H.; Crans, D. C.; Micera, G.; Garribba, E. *Dalton Trans.* **2014**, *43*, 6965−6972.

(15) (a) Sanna, D.; Serra, M.; Micera, G.; Garribba, E. *Inorg. Chem.* **2014**, *53*, 1449−1464. (b) Sanna, D.; Serra, M.; Micera, G.; Garribba, E. *Inorg. Chim. Acta* **2014**, *420*, 75−84. (c) Sanna, D.; Fabbri, D.; Serra, M.; Buglyó, P.; Bíró, L.; Ugone, V.; Micera, G.; Garribba, E. *J. Inorg. Biochem.* **2015**, *147*, 71−84. (d) Levina, A.; McLeod, A. I.; Pulte, A.; Aitken, J. B.; Lay, P. A. *Inorg. Chem.* **2015**, *54*, 6707−6718. (e) Levina, A.; McLeod, A. I.; Gasparini, S. J.; Nguyen, A.; De Silva, W. G. M.; Aitken, J. B.; Harris, H. H.; Glover, C.; Johannessen, B.; Lay, P. A. *Inorg. Chem.* **2015**, *54*, 7753−7766.

(16) (a) Sanna, D.; Micera, G.; Garribba, E. *Inorg. Chem.* **2009**, *48*, 5747−5757. (b) Sanna, D.; Micera, G.; Garribba, E. *Inorg. Chem.* **2010**, *49*, 174−187. (c) Sanna, D.; Buglyó, P.; Micera, G.; Garribba, E. *JBIC, J. Biol. Inorg. Chem.* **2010**, *15*, 825−839. (d) Sanna, D.; Micera, G.; Garribba, E. *Inorg. Chem.* **2011**, *50*, 3717−3728. (e) Sanna, D.; Biro, L.; Buglyo, P.; Micera, G.; Garribba, E. *Metallomics* **2012**, *4*, 33−36. (f) Sanna, D.; Ugone, V.; Micera, G.; Garribba, E. *Dalton Trans.* **2012**, *41*, 7304−7318. (g) Sanna, D.; Bíró, L.; Buglyó, P.; Micera, G.; Garribba, E. *J. Inorg. Biochem.* **2012**, *115*, 87−99. (h) Sanna, D.; Micera, G.; Garribba, E. *Inorg. Chem.* **2013**, *52*, 11975−11985. (i) Koleša-Dobravc, T.; Lodyga-Chruscinska, E.; Symonowicz, M.; Sanna, D.; Meden, A.; Perdih, F.; Garribba, E. *Inorg. Chem.* **2014**, *53*, 7960−7976.

(17) (a) Willsky, G. R.; Goldfine, A. B.; Kostyniak, P. J.; McNeill, J. H.; Yang, L. Q.; Khan, H. R.; Crans, D. C. *J. Inorg. Biochem.* **2001**, *85*, 33−42. (b) Liboiron, B. D.; Thompson, K. H.; Hanson, G. R.; Lam, E.; Aebischer, N.; Orvig, C. *J. Am. Chem. Soc.* **2005**, *127*, 5104−5115. (c) Jakusch, T.; Costa Pessoa, J.; Kiss, T. *Coord. Chem. Rev.* **2011**, *255*, 2218−2226. (d) Correia, I.; Jakusch, T.; Cobbinna, E.; Mehtab, S.; Tomaz, I.; Nagy, N. V.; Rockenbauer, A.; Costa Pessoa, J.; Kiss, T. *Dalton Trans.* **2012**, *41*, 6477−6487. (e) Vincent, J. B.; Love, S. *Biochim. Biophys. Acta, Gen. Subj.* **2012**, *1820*, 362−378. (f) Mehtab, S.; Gonçalves, G.; Roy, S.; Tomaz, A. I.; Santos-Silva, T.; Santos, M. F. A.; Romão, M. J.; Jakusch, T.; Kiss, T.; Costa Pessoa, J. *J. Inorg. Biochem.* **2013**, *121*, 187−195. (g) Gonçalves, G.; Tomaz, A. I.; Correia, I.; Veiros, L. F.; Castro, M. M. C. A.; Avecilla, F.; Palacio, L.; Maestro, M.; Kiss, T.; Jakusch, T.; Garcia, M. H. V.; Costa Pessoa, J. *Dalton Trans.* **2013**, *42*, 11841−11861. (h) Costa Pessoa, J.; Garribba, E.; Santos, M. F. A.; Santos-Silva, T. *Coord. Chem. Rev.* **2015**, DOI: 10.1016/j.ccr.2015.03.016.

DOI: 10.1021/acs.inorgchem.5b01277
Inorg. Chem. XXXX, XXX, XXX−XXX

(18) Santos, M. F. A.; Correia, I.; Oliveira, A. R.; Garribba, E.; Costa Pessoa, J.; Santos-Silva, T. *Eur. J. Inorg. Chem.* **2014**, 3293−3297.
(19) Harris, W. R. *Clin. Chem.* **1992**, *38*, 1809−1818.
(20) Kiss, T.; Kiss, E.; Garribba, E.; Sakurai, H. *J. Inorg. Biochem.* **2000**, *80*, 65−73.
(21) Gómez-Ruiz, S.; Maksimović-Ivanić, D.; Mijatović, S.; Kaluđerović, G. N. *Bioinorg. Chem. Appl.* **2012**, 140248.
(22) Garner, C. D.; Collison, D.; Mabbs, F. E. In *Vanadium and its role in life*, Sigel, H., Sigel, A., Eds.; Marcel Dekker, Inc.: New York, 1995; Vol. *31*, pp 617−670.
(23) (a) Morgenstern, B.; Steinhauser, S.; Hegetschweiler, K.; Garribba, E.; Micera, G.; Sanna, D.; Nagy, L. *Inorg. Chem.* **2004**, *43*, 3116−3126. (b) Rangel, M.; Leite, A.; Amorim, M. J.; Garribba, E.; Micera, G.; Lodyga-Chruscinska, E. *Inorg. Chem.* **2006**, *45*, 8086−8097. (c) Morgenstern, B.; Kutzky, B.; Neis, C.; Stucky, S.; Hegetschweiler, K.; Garribba, E.; Micera, G. *Inorg. Chem.* **2007**, *46*, 3903−3915.
(24) Micera, G.; Sanna, D. In *Vanadium in the environment Part I: Chemistry and Biochemistry*; Nriagu, J. O., Ed.; Wiley: New York, 1998; pp 131−166.
(25) Henderson, W.; McIndoe, J. S. *Mass Spectrometry of Inorganic, Coordination and Organometallic Compounds*; John Wiley & Sons, Ltd.: Chichester, 2005.
(26) (a) Doležel, P.; Kubáň, V. *Chem. Pap.* **2002**, *56*, 236−240. (b) Di Marco, V. B.; Bombi, G. G. *Mass Spectrom. Rev.* **2006**, *25*, 347−379. (c) Esteban-Fernandez, D.; Canas, B.; Pizarro, I.; Palacios, M. A.; Gomez-Gomez, M. M. *J. Anal. At. Spectrom.* **2007**, *22*, 1113−1121. (d) Sekar, R.; Kailasa, S. K.; Abdelhamid, H. N.; Chen, Y.-C.; Wu, H.-F. *Int. J. Mass Spectrom.* **2013**, *338*, 23−29. (e) Sgarbossa, P.; Sbovata, S. M.; Bertani, R.; Mozzon, M.; Benetollo, F.; Marzano, C.; Gandin, V.; Michelin, R. A. *Inorg. Chem.* **2013**, *52*, 5729−5741. (f) Telpoukhovskaia, M. A.; Rodríguez-Rodríguez, C.; Scott, L. E.; Page, B. D. G.; Patrick, B. O.; Orvig, C. *J. Inorg. Biochem.* **2014**, *132*, 59−66. (g) Pivetta, T.; Lallai, V.; Valletta, E.; Trudu, F.; Isaia, F.; Perra, D.; Pinna, E.; Pani, A. *J. Inorg. Biochem.* **2015**, DOI: 10.1016/j.jinorgbio.2015.05.004.
(27) (a) Sanna, D.; Pecoraro, V.; Micera, G.; Garribba, E. *JBIC, J. Biol. Inorg. Chem.* **2012**, *17*, 773−790. (b) Justino, G. C.; Garribba, E.; Costa Pessoa, J. *JBIC, J. Biol. Inorg. Chem.* **2013**, *18*, 803−813.
(28) Jakusch, T.; Hollender, D.; Enyedy, E. A.; Gonzalez, C. S.; Montes-Bayon, M.; Sanz-Medel, A.; Costa Pessoa, J.; Tomaz, I.; Kiss, T. *Dalton Trans.* **2009**, 2428−2437.
(29) Kiss, T.; Jakusch, T.; Gyurcsik, B.; Lakatos, A.; Enyedy, É. A.; Sija, É. *Coord. Chem. Rev.* **2012**, *256*, 125−132.
(30) Sanna, D.; Garribba, E.; Micera, G. *J. Inorg. Biochem.* **2009**, *103*, 648−655.
(31) (a) Strohalm, M.; Hassman, M.; Košata, B.; Kodíček, M. *Rapid Commun. Mass Spectrom.* **2008**, *22*, 905−908. (b) Strohalm, M.; Kavan, D.; Novák, P.; Volný, M.; Havlíček, V. *Anal. Chem.* **2010**, *82*, 4648−4651. (c) Niedermeyer, T. H. J.; Strohalm, M. *PLoS One* **2012**, *7*, e44913.
(32) Frisch, M. J.; Trucks, G. W.; Schlegel, H. B.; Scuseria, G. E.; Robb, M. A.; Cheeseman, J. R.; Montgomery, J. A., Jr.; Vreven, T.; Kudin, K. N.; Burant, J. C.; Millam, J. M.; Iyengar, S. S.; Tomasi, J.; Barone, V.; Mennucci, B.; Cossi, M.; Scalmani, G.; Rega, N.; Petersson, G. A.; Nakatsuji, H.; Hada, M.; Ehara, M.; Toyota, K.; Fukuda, R.; Hasegawa, J.; Ishida, M.; Nakajima, T.; Honda, Y.; Kitao, O.; Nakai, H.; Klene, M.; Li, X.; Knox, J. E.; Hratchian, H. P.; Cross, J. B.; Adamo, C.; Jaramillo, J.; Gomperts, R.; Stratmann, R. E.; Yazyev, O.; Austin, A. J.; Cammi, R.; Pomelli, C.; Ochterski, J. W.; Ayala, P. Y.; Morokuma, K.; Voth, G. A.; Salvador, P.; Dannenberg, J. J.; Zakrzewski, V. G.; Dapprich, S.; Daniels, A. D.; Strain, M. C.; Farkas, O.; Malick, D. K.; Rabuck, A. D.; Raghavachari, K.; Foresman, J. B.; Ortiz, J. V.; Cui, Q.; Baboul, A. G.; Clifford, S.; Cioslowski, J.; Stefanov, B. B.; Liu, G.; Liashenko, A.; Piskorz, P.; Komaromi, I.; Martin, R. L.; Fox, D. J.; Keith, T.; Al-Laham, M. A.; Peng, C. Y.; Nanayakkara, A.; Challacombe, M.; Gill, P. M. W.; Johnson, B.; Chen, W.; Wong, M. W.; Gonzalez, C.; Pople, J. A. *Gaussian 03*, revision C.02; Gaussian, Inc.: Wallingford, CT, 2004.
(33) (a) Neese, F. *Wiley Interdiscip. Rev. Comput. Mol. Sci.* **2012**, *2*, 73−78. (b) Neese, F. *ORCA-An Ab Initio, DFT and Semiempirical Program Package*, Version 3.0; Max-Planck-Institute for Chemical Energy Conversion: Mülheim a. d. Ruhr, 2013.
(34) Micera, G.; Garribba, E. *Int. J. Quantum Chem.* **2012**, *112*, 2486−2498.
(35) (a) Bühl, M.; Kabrede, H. *J. Chem. Theory Comput.* **2006**, *2*, 1282−1290. (b) Bühl, M.; Reimann, C.; Pantazis, D. A.; Bredow, T.; Neese, F. *J. Chem. Theory Comput.* **2008**, *4*, 1449−1459.
(36) (a) Micera, G.; Pecoraro, V. L.; Garribba, E. *Inorg. Chem.* **2009**, *48*, 5790−5796. (b) Micera, G.; Garribba, E. *Eur. J. Inorg. Chem.* **2010**, 4697−4710. (c) Micera, G.; Garribba, E. *Eur. J. Inorg. Chem.* **2011**, 3768−3780. (d) Sanna, D.; Varnágy, K.; Timári, S.; Micera, G.; Garribba, E. *Inorg. Chem.* **2011**, *50*, 10328−10341. (e) Sanna, D.; Buglyo, P.; Biro, L.; Micera, G.; Garribba, E. *Eur. J. Inorg. Chem.* **2012**, 1079−1092. (f) Sanna, D.; Buglyo, P.; Tomaz, A. I.; Costa Pessoa, J.; Borovic, S.; Micera, G.; Garribba, E. *Dalton Trans.* **2012**, *41*, 12824−12838. (g) Justino, G.; Garribba, E.; Costa Pessoa, J. *JBIC, J. Biol. Inorg. Chem.* **2013**, *18*, 803−813.
(37) (a) Micera, G.; Garribba, E. *Dalton Trans.* **2009**, 1914−1918. (b) Gorelsky, S.; Micera, G.; Garribba, E. *Chem. - Eur. J.* **2010**, *16*, 8167−8180. (c) Micera, G.; Garribba, E. *J. Comput. Chem.* **2011**, *32*, 2822−2835.
(38) (a) Tzavellas, N.; Klouras, N.; Raptopoulou, C. P. *Z. Anorg. Allg. Chem.* **1996**, *622*, 898−902. (b) Honzíček, J.; Vinklárek, J.; Císařová, I.; Erben, M. *Inorg. Chim. Acta* **2009**, *362*, 83−88.
(39) Toney, J. H.; Brock, C. P.; Marks, T. J. *J. Am. Chem. Soc.* **1986**, *108*, 7263−7274.
(40) Toney, J. H.; Marks, T. J. *J. Am. Chem. Soc.* **1985**, *107*, 947−953.
(41) Pavlik, I.; Vinklárek, J. *Eur. J. Solid State Inorg. Chem.* **1991**, *28*, 815−827.
(42) (a) Munzarová, M. L. In *Calculation of NMR and EPR Parameters*; Kaupp, M., Bühl, M., Malkin, V. G., Eds.; Wiley-VCH Verlag GmbH & Co. KGaA: Weinheim, 2004; pp 461−482. (b) Neese, F. *Coord. Chem. Rev.* **2009**, *253*, 526−563.
(43) (a) Munzarová, M. L.; Kaupp, M. *J. Phys. Chem. B* **2001**, *105*, 12644−12652. (b) Neese, F. *J. Chem. Phys.* **2003**, *118*, 3939−3948. (c) Saladino, A. C.; Larsen, S. C. *J. Phys. Chem. A* **2003**, *107*, 1872−1878. (d) Aznar, C. P.; Deligiannakis, Y.; Tolis, E. J.; Kabanos, T.; Brynda, M.; Britt, R. D. *J. Phys. Chem. A* **2004**, *108*, 4310−4321. (e) Saladino, A. C.; Larsen, S. C. *Catal. Today* **2005**, *105*, 122−133. (f) King, A. E.; Nippe, M.; Atanasov, M.; Chantarojsiri, T.; Wray, C. A.; Bill, E.; Neese, F.; Long, J. R.; Chang, C. J. *Inorg. Chem.* **2014**, *53*, 11388−11395.
(44) (a) Pisano, L.; Varnagy, K.; Timari, S.; Hegetschweiler, K.; Micera, G.; Garribba, E. *Inorg. Chem.* **2013**, *52*, 5260−5272. (b) Sanna, D.; Varnagy, K.; Lihi, N.; Micera, G.; Garribba, E. *Inorg. Chem.* **2013**, *52*, 8202−8213. (c) Lodyga-Chruscinska, E.; Szebesczyk, A.; Sanna, D.; Hegetschweiler, K.; Micera, G.; Garribba, E. *Dalton Trans.* **2013**, *42*, 13404−13416.
(45) Vinklárek, J.; Paláčková, H.; Honzíček, J.; Holubová, J.; Holčapek, M.; Císařová, I. *Inorg. Chem.* **2006**, *45*, 2156−2162.
(46) (a) Vinklárek, J.; Dědourková, T.; Honzíček, J.; Růžička, A. *J. Inorg. Biochem.* **2010**, *104*, 936−943. (b) Vinklárek, J.; Honzíček, J.; Erben, M.; Klepalová, I.; Eisner, A.; Růžička, A. *Inorg. Chim. Acta* **2013**, *405*, 121−127.
(47) Vinklárek, J.; Honzíček, J.; Holubová, J. *Inorg. Chim. Acta* **2004**, *357*, 3765−3769.
(48) Honzíček, J.; Nachtigall, P.; Císařová, I.; Vinklárek, J. *J. Organomet. Chem.* **2004**, *689*, 1180−1187.
(49) Vinklárek, J.; Honzíček, J.; Holubová, J. *Magn. Reson. Chem.* **2004**, *42*, 870−874.
(50) (a) Micera, G.; Sanna, D.; Dessì, A.; Kiss, T.; Buglyó, P. *Gazz. Chim. Ital.* **1993**, *123*, 573−577. (b) Garribba, E.; Micera, G.; Panzanelli, A.; Sanna, D. *Inorg. Chem.* **2003**, *42*, 3981−3987.
(51) Bakhtiar, R.; Tse, F. L. S. *Mutagenesis* **2000**, *15*, 415−430.
(52) Lodyga-Chruscinska, E.; Sanna, D.; Garribba, E.; Micera, G. *Dalton Trans.* **2008**, 4903−4916.

DOI: 10.1021/acs.inorgchem.5b01277
Inorg. Chem. XXXX, XXX, XXX−XXX

(53) Du, H.; Xiang, J.; Zhang, Y.; Tang, Y.; Xu, G. *J. Inorg. Biochem.* **2008**, *102*, 146−149.
(54) Nishida, Y.; Niinuma, A.; Abe, K. *Inorg. Chem. Commun.* **2009**, *12*, 198−200.
(55) Kiss, T.; Jakusch, T.; Bouhsina, S.; Sakurai, H.; Enyedy, É. A. *Eur. J. Inorg. Chem.* **2006**, 3607−3613.
(56) Guo, M.; Sun, H.; McArdle, H. J.; Gambling, L.; Sadler, P. J. *Biochemistry* **2000**, *39*, 10023−10033.
(57) Chasteen, D. N. *Coord. Chem. Rev.* **1977**, *22*, 1−36.
(58) White, L. K.; Chasteen, N. D. *J. Phys. Chem.* **1979**, *83*, 279−284.
(59) Tinoco, A. D.; Eames, E. V.; Valentine, A. M. *J. Am. Chem. Soc.* **2008**, *130*, 2262−2270.
(60) (a) Thompson, K. H.; Battell, M.; McNeill, J. H. In *Vanadium in the Environment, Part 2: Health Effects: Toxycology of Vanadium in Mammals*; Nriagu, J. O., Ed.; Wiley: New York, 1998; pp 21−37. (b) Rehder, D.; Costa Pessoa, J.; Geraldes, C.; Castro, M.; Kabanos, T.; Kiss, T.; Meier, B.; Micera, G.; Pettersson, L.; Rangel, M.; Salifoglou, A.; Turel, I.; Wang, D. *JBIC, J. Biol. Inorg. Chem.* **2002**, *7*, 384−396. (c) Sakurai, H.; Fugono, J.; Yasui, H. *Mini-Rev. Med. Chem.* **2004**, *4*, 41−48. (d) Zhang, S.-Q.; Zhong, X.-Y.; Chen, G.-H.; Lu, W.-L.; Zhang, Q. *J. Pharm. Pharmacol.* **2008**, *60*, 99−105.
(61) (a) Nielsen, F. H. In *Metal ions in biological systems*; Sigel, H., Sigel, A., Eds.; Marcel Dekker: New York, 1995; Vol. *31*, pp 543−573. (b) Nielsen, F. H. In *Vanadium Compounds. Chemistry, Biochemistry, and Therapeutic Applications*; American Chemical Society: Washington DC, 1998; Vol. *711*, pp 297−307.

DOI: 10.1021/acs.inorgchem.5b01277
Inorg. Chem. XXXX, XXX, XXX−XXX

SUPPORTING INFORMATION

Speciation of the potential antitumor agent vanadocene dichloride in the blood plasma and model systems

Daniele Sanna,[†] Valeria Ugone,[§] Giovanni Micera,[§] Tiziana Pivetta,[#] Elisa Valletta,[#] Eugenio Garribba,*[,§]

[†] Istituto CNR di Chimica Biomolecolare, Trav. La Crucca 3, I-07040 Sassari, Italy

[§] Dipartimento di Chimica e Centro Interdisciplinare per lo Sviluppo della Ricerca Biotecnologica e per lo Studio della Biodiversità della Sardegna, Università di Sassari, Via Vienna 2, I-07100 Sassari, Italy

[#] Dipartimento di Scienze Chimiche e Geologiche, Università di Cagliari, Cittadella Universitaria, I-09042 Monserrato (CA), Italy

* Corresponding author. E-mail: garribba@uniss.it.

Table S1. Experimental (exptl.) and calculated (calcd.) structural parameters for VDC and its hydrolysis products in aqueous solution.[a]

	Exptl.[b]	Calcd.[c]	Exptl.[d]	Calcd.[c]	Calcd.[c]
Distance or angle[e]	$[Cp_2VCl_2]$		$[Cp_2V(H_2O)_2]^{2+}$		$[Cp_2V(OH)_2]$
V–Cl or V–O	2.408	2.410	2.056	2.109	1.874
V–Cl or V–O	2.411	2.410	2.070	2.109	1.874
V–Cg	1.968	1.980	1.963	1.978	2.071
V–Cg	1.977	1.983	1.964	1.978	2.071
Cl–V–Cl or O–V–O	87.2	88.9	83.9	79.9	84.9
Cl–V–Cg or O–V–Cg	107.2[f]	105.9[f]	107.1	107.8	108.0
Cg–V–Cg	131.9	134.8	133.3	133.0	130.4

[a] Distances in Å and angles in degrees (°). [b] Experimental structure reported in ref. 1. [c] Structure calculated at the level of theory B3P86/6-311g. [d] Experimental structure reported in ref. 2. [e] Cg indicates the centroid of the cyclopentadienyl ring. [f] Mean values.

Table S2. Structural parameters calculated by DFT methods for the mixed complexes formed by VDC.[a]

Distance or angle[d]	Exptl.[b]	Calcd.[c]	Calcd.[c]		
	$[Cp_2V(ox)]$		$[Cp_2V(lactH_{-1})]$	$[Cp_2V(CO_3)]$	$[Cp_2V(HPO_4)]$
V–O	2.021	1.950	1.878	1.973	1.986
V–O	2.038	1.950	1.953	1.974	1.988
V–Cg	1.959	1.998	2.021	1.986	1.989
V–Cg	1.961	1.998	2.038	1.989	1.993
O–V–O	78.6	79.4	80.5	67.2	72.7
O–V–Cg [e]	107.8	107.2	107.6	108.2	107.9
Cg–V–Cg	133.5	134.8	133.3	136.0	135.2

[a] Distances in Å and angles in degrees (°). [b] Experimental structure reported in ref. 3. [c] Structures calculated with Gaussian at the level of theory B3P86/6-311g. [d] Cg indicates the centroid of cyclopentadienyl ring. [e] Mean values.

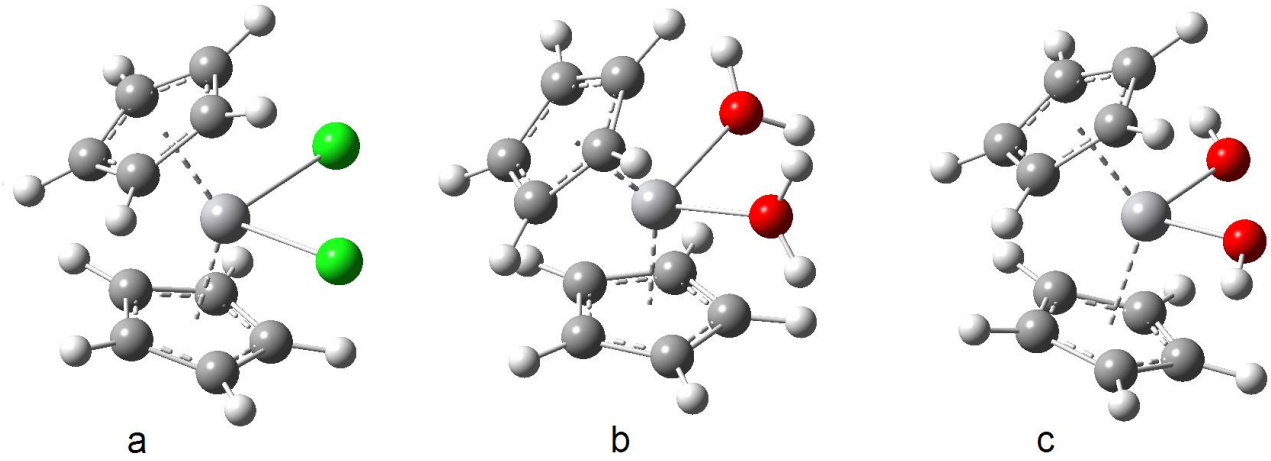

Figure S1. Structure of the complexes $[Cp_2VCl_2]$ (a), $[Cp_2V(H_2O)_2]^{2+}$ (b) and $[Cp_2V(OH)_2]$ (c) optimized by DFT methods at the level of theory B3P86/6-311g.

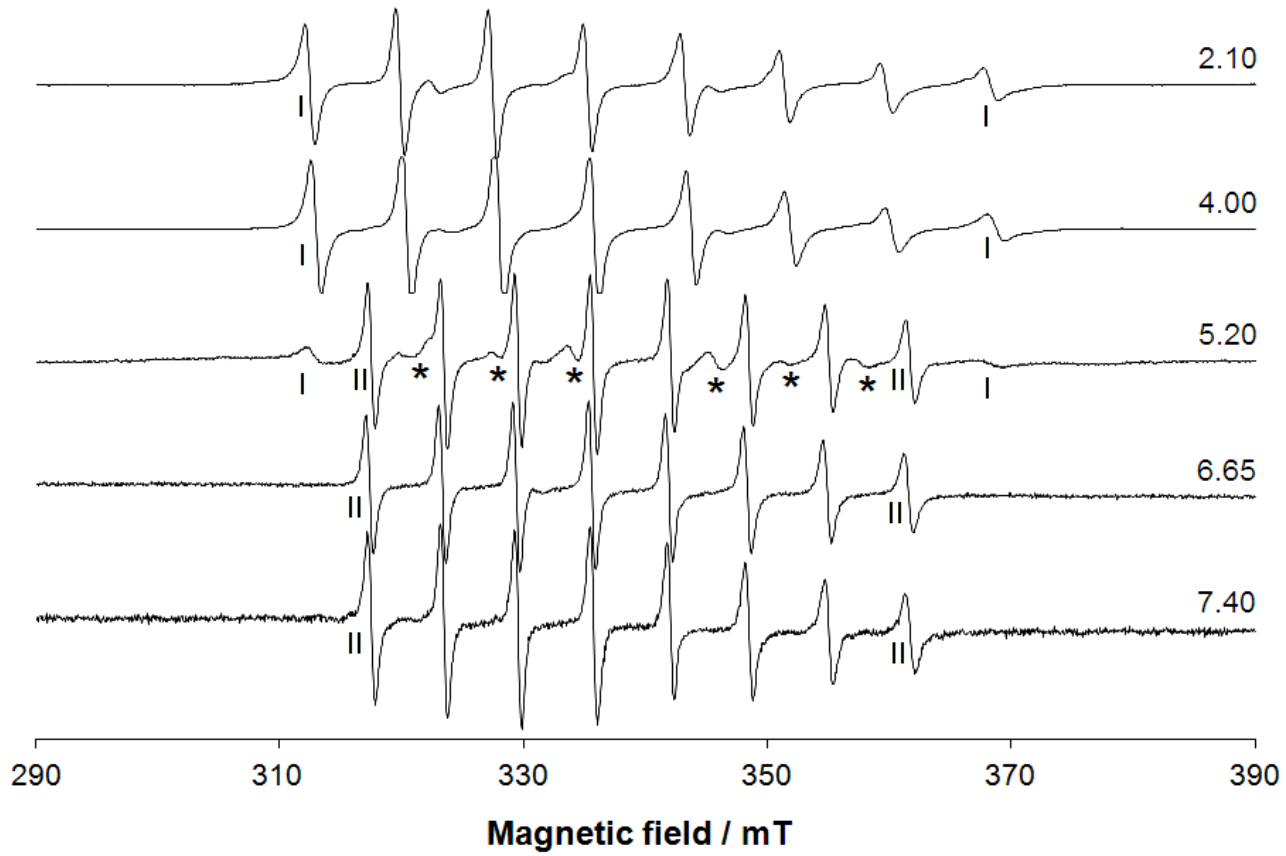

Figure S2. Room temperature (298 K) EPR spectra recorded as a function of pH dissolving VDC (1.0×10^{-3} M) in water. With **I** and **II** $[Cp_2V(H_2O)_2]^{2+}$ and $[Cp_2V(OH)_2]$ are indicated. The asterisks denote the resonances of the species $[Cp_2V(H_2O)(OH)]^{+}$, present in a small amount around pH 5.

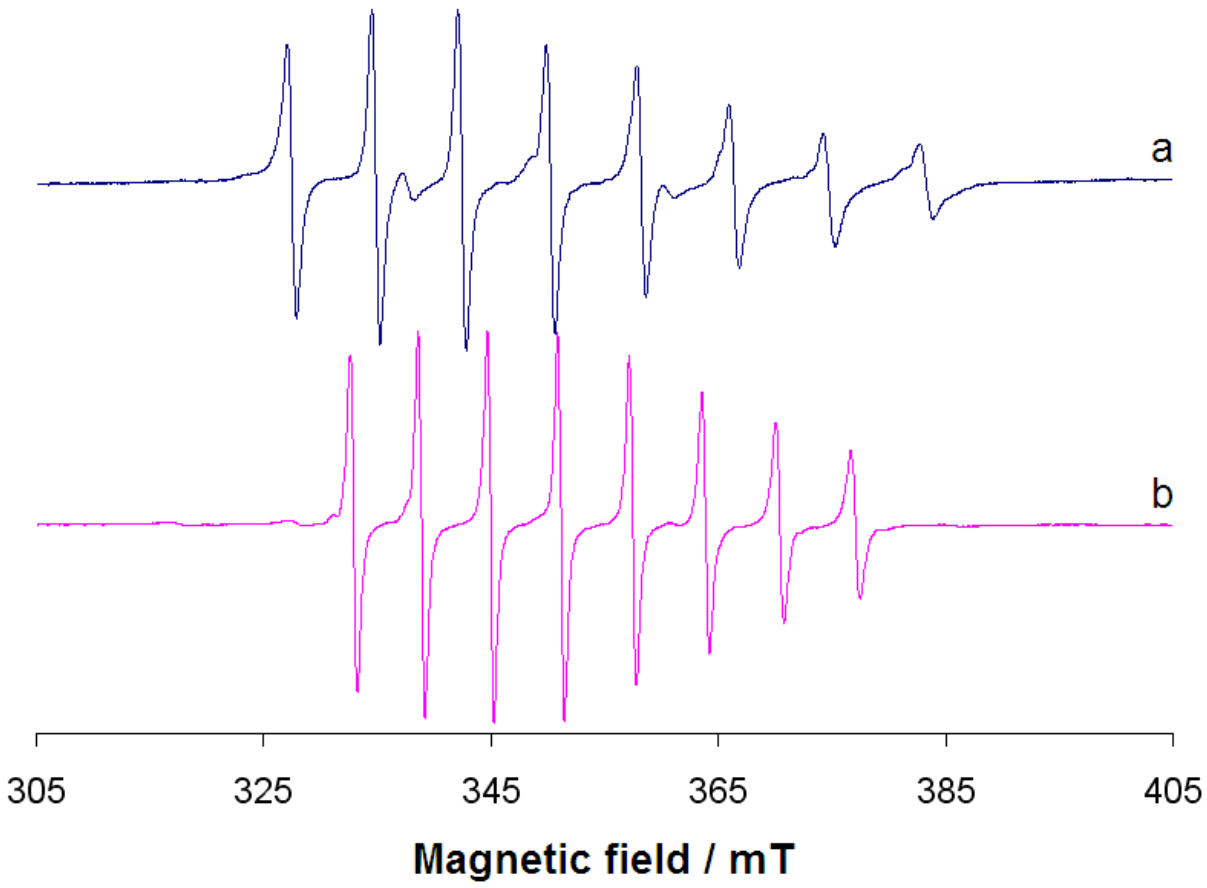

Figure S3. Room temperature (298 K) EPR spectra obtained dissolving VDC (1.0×10^{-3} M) in water: (a) spectrum of $[Cp_2V(H_2O)_2]^{2+}$ (pH 2.10) and (b) spectrum of $[Cp_2V(OH)_2]$ (pH 7.40).

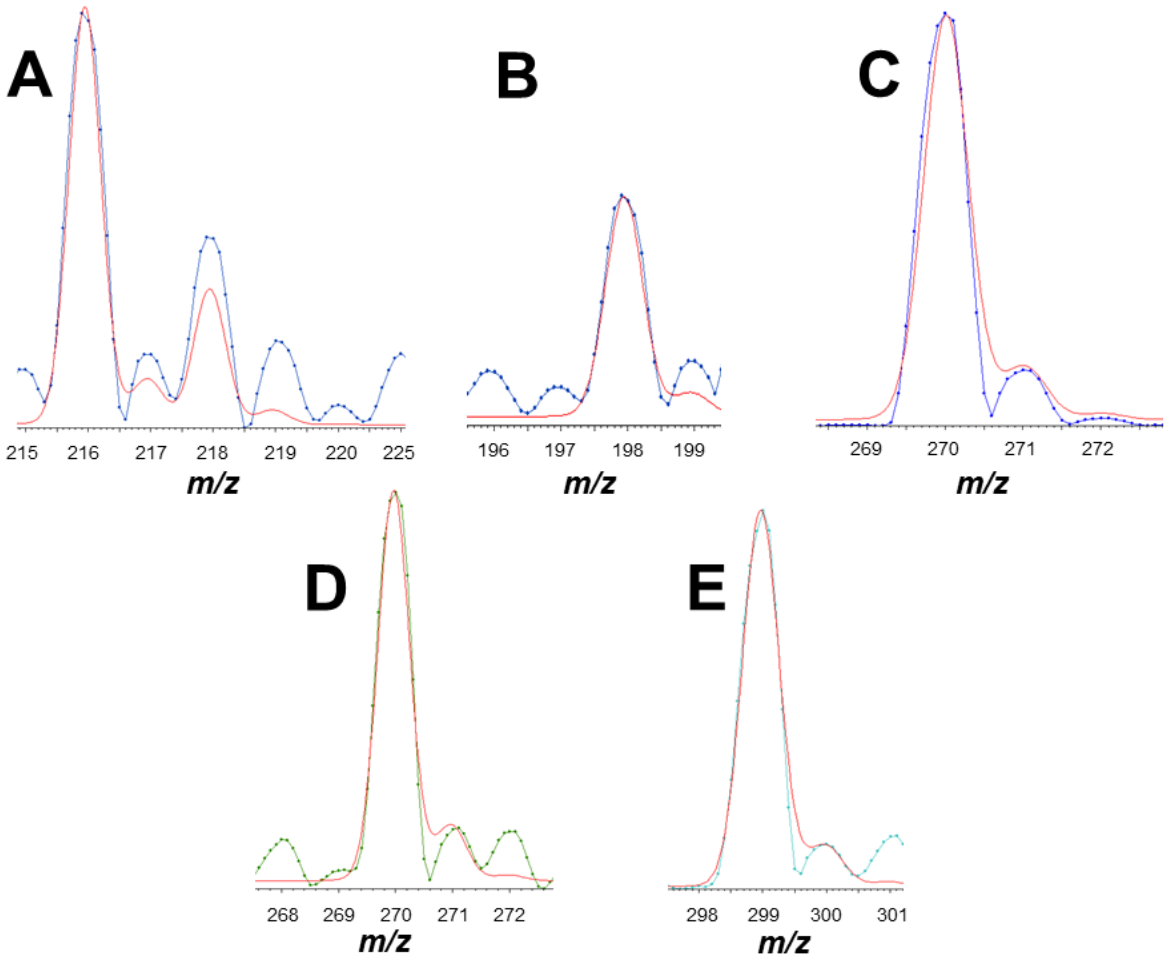

Figure S4. Calculated (red line) and experimental (blue line) isotopic pattern for (A) $[Cp_2VCl]^+$ (*m/z* 216); (B) $[Cp_2V(OH)]^+$ (*m/z* 198); (C) $[Cp_2V(lactH_{-1})+H]^+$ (*m/z* 270); (D) $[Cp_2V(ox)+H]^+$ (*m/z* 270) and (E) $[Cp_2V^V(PO_4)+Na]^+$ (*m/z* 299).

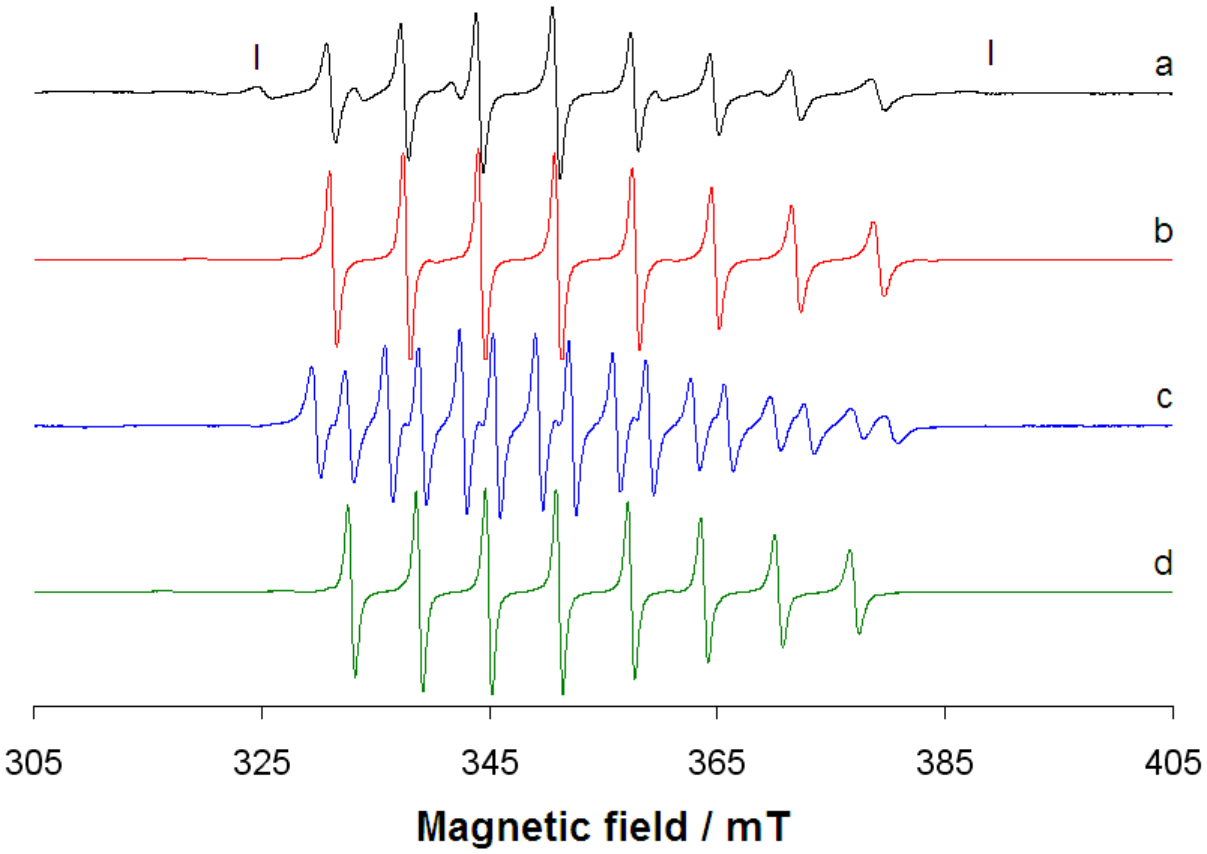

Figure S5. Room temperature (298 K) EPR spectra recorded in aqueous solution at pH 7.4 in the systems containing: (a) VDC/lactate 1/10 (spectrum of $[Cp_2V(lactH_{-1})]$); VDC/oxalate system 1/10 (spectrum of $[Cp_2V(ox)]$); (c) VDC/HPO_4^{2-} 1/10 (spectrum of $[Cp_2V(HPO_4)]$) and (d) VDC/HCO_3^- 1/10 (spectrum of $[Cp_2V(CO_3)]$). VDC concentration was 1.0×10^{-3} M. With **I** the species $[VO(lactH_{-1})_2]^{2-}$ is indicated.

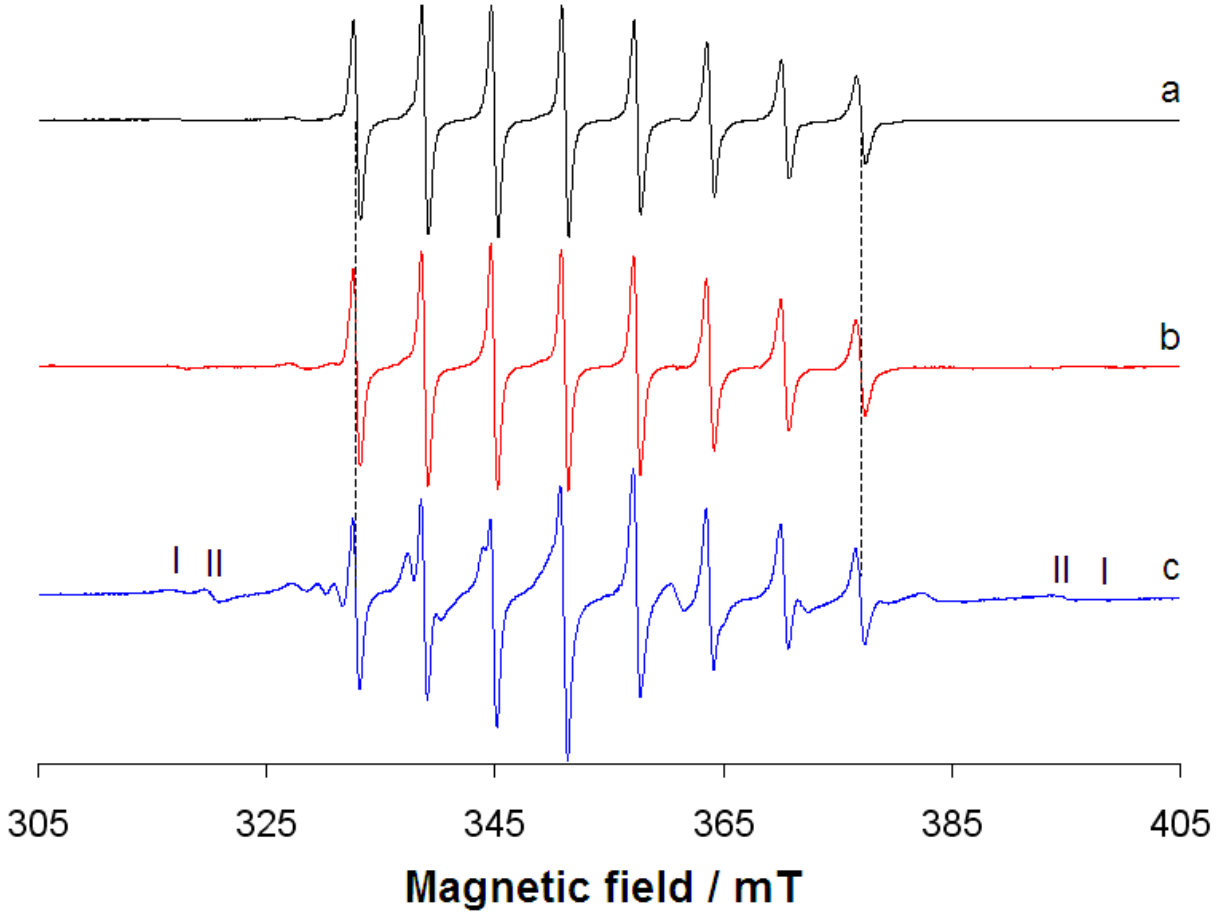

Figure S6. Room temperature (298 K) EPR spectra recorded in aqueous solution at pH 7.4 in the systems containing: (a) VDC; (b) VDC/glycine 1/10 and (c) VDC/citrate 1/10. VDC concentration was 1.0×10^{-3} M. The M_I = -7/2, 7/2 resonances of $[Cp_2V(OH)_2]$ are shown with a dotted line. With **I** and **II** the species $[VO(H_2O)_5]^{2+}$ and $[VO(citrH_{-1})]^{2-}$ are indicated.

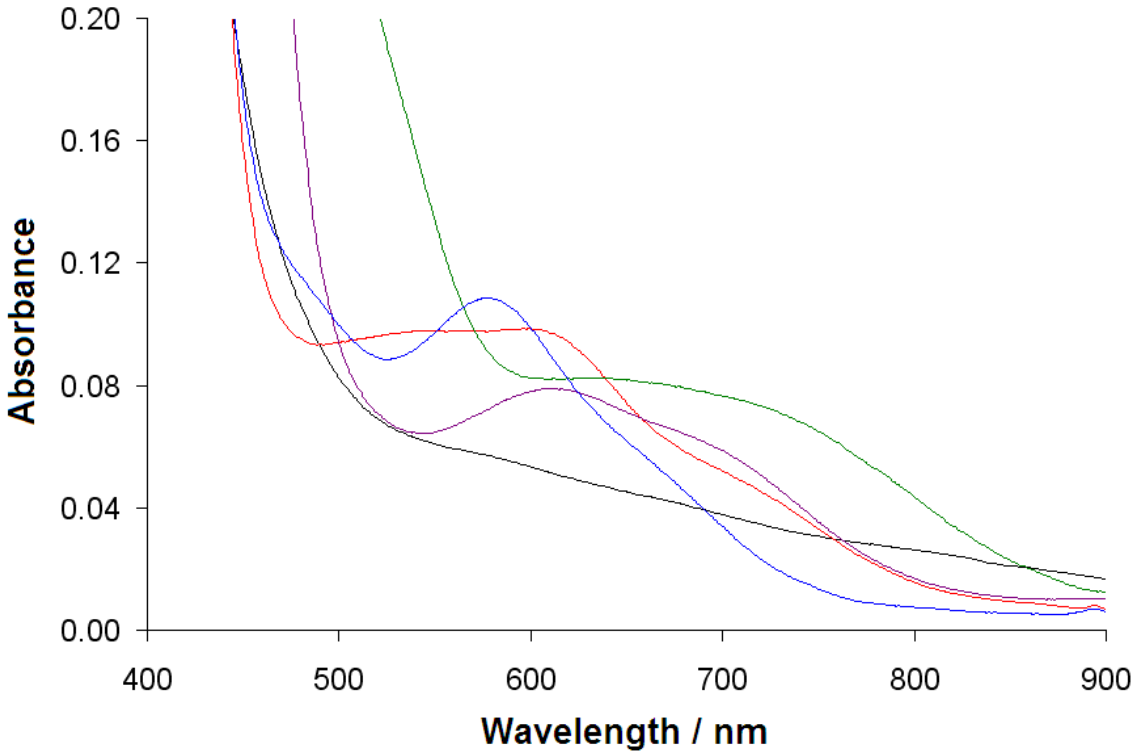

Figure S7. Electronic absorption spectra recorded in aqueous solution at pH 7.4 in the systems containing: (trace black) VDC (spectrum of $[Cp_2V(OH)_2]$); (trace red) VDC/oxalate 1/10 (spectrum of $[Cp_2V(ox)]$; (trace blue) 1/10 VDC/HCO_3^- (spectrum of $[Cp_2V(CO_3)]$); (trace green) VDC/lactate 1/10 (spectrum of $[Cp_2V(lactH_{-1})]$) and (trace purple) VDC/HPO_4^{2-} 1/10 (spectrum of $[Cp_2V(HPO_4)]$). VDC concentration was 1.0×10^{-3} M.

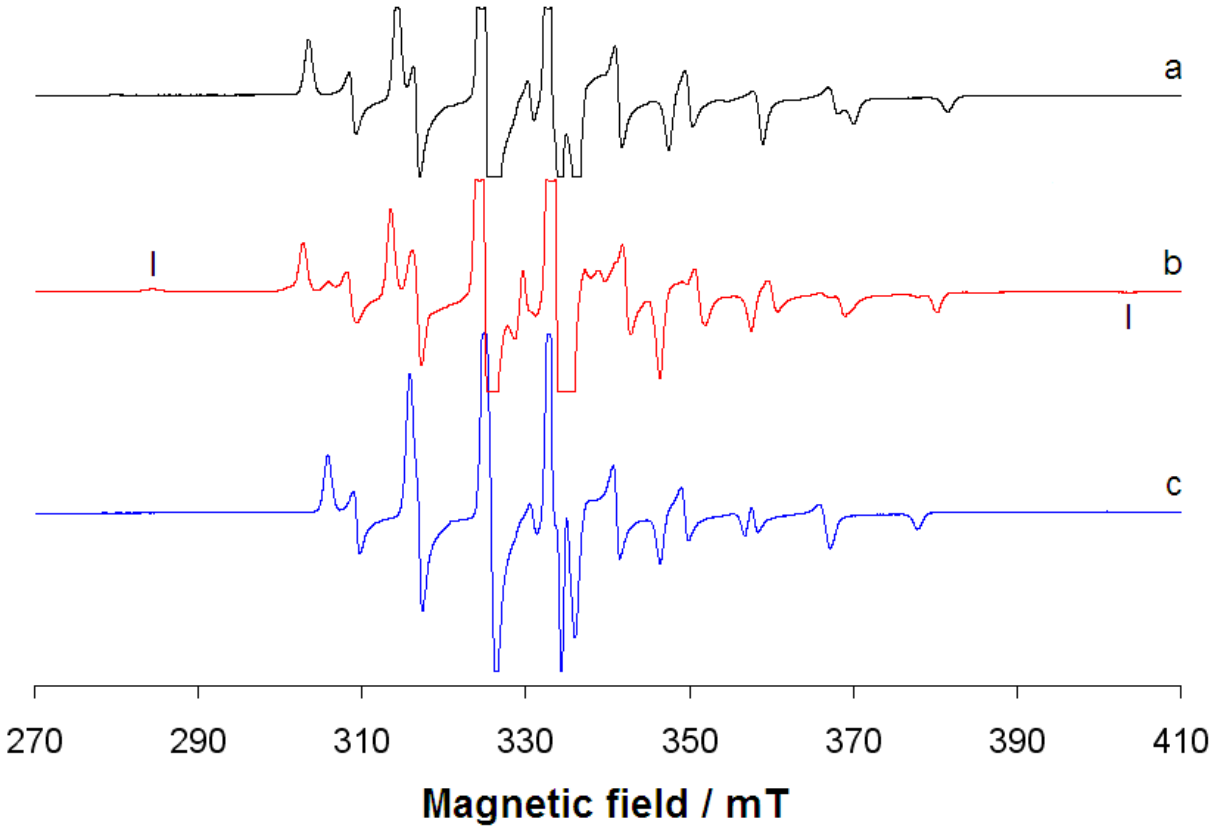

Figure S8. EPR spectra recorded at 120 K and pH 7.4 in aqueous solution in the systems containing: (a) VDC/oxalate 1/10 (spectrum of [$Cp_2V(ox)$]); (b) VDC/lactate 1/10 (spectrum of [$Cp_2V(lactH_{-1})$]) and (c) VDC/HCO_3^- 1/10 (spectrum of [$Cp_2V(CO_3)$]). VDC concentration was 1.0×10^{-3} M. With **I** the species $[VO(lactH_{-1})_2]^{2-}$ is indicated.

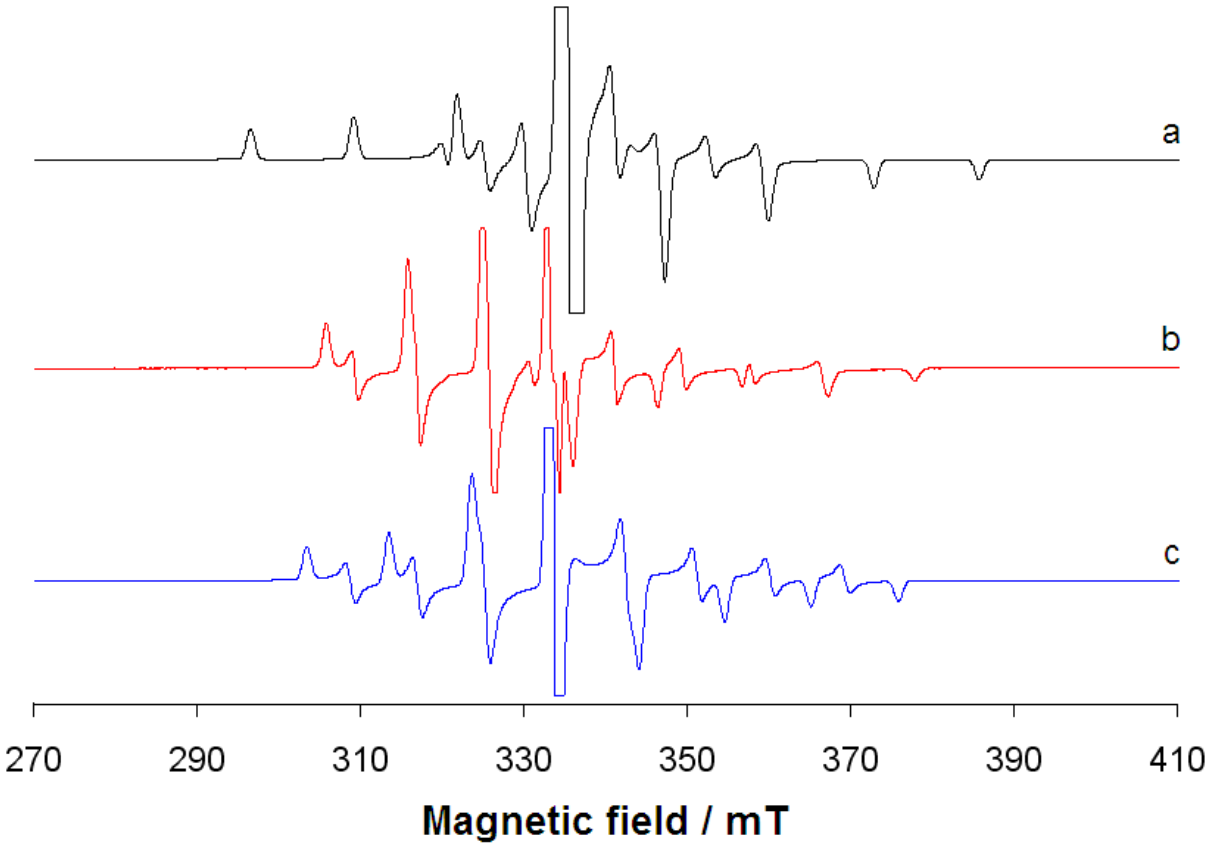

Figure S9. Experimental EPR spectrum recorded at 120 K and pH 7.4 in aqueous solution in the system VDC/HCO_3^- with VDC concentration of 1.0×10^{-3} and ratio 1/10 (b) and comparison with those calculated by ORCA software for $[Cp_2V(OH)_2]$ (a) and $[Cp_2V(CO_3)]$ (c). For $[Cp_2V(OH)_2]$ were used $g_x = 1.968$, $g_y = 1.975$, $g_z = 1.981$, $A_x = -117.1\times10^{-4}$ cm^{-1}, $A_y = -50.9\times10^{-4}$ cm^{-1}, $A_z = -12.1\times10^{-4}$ cm^{-1} and for $[Cp_2V(CO_3)]$ $g_x = 1.976$, $g_y = 1.979$, $g_z = 1.997$, $A_x = -95.5\times10^{-4}$ cm^{-1}, $A_y = -79.9\times10^{-4}$ cm^{-1}, $A_z = -3.3\times10^{-4}$ cm^{-1}.

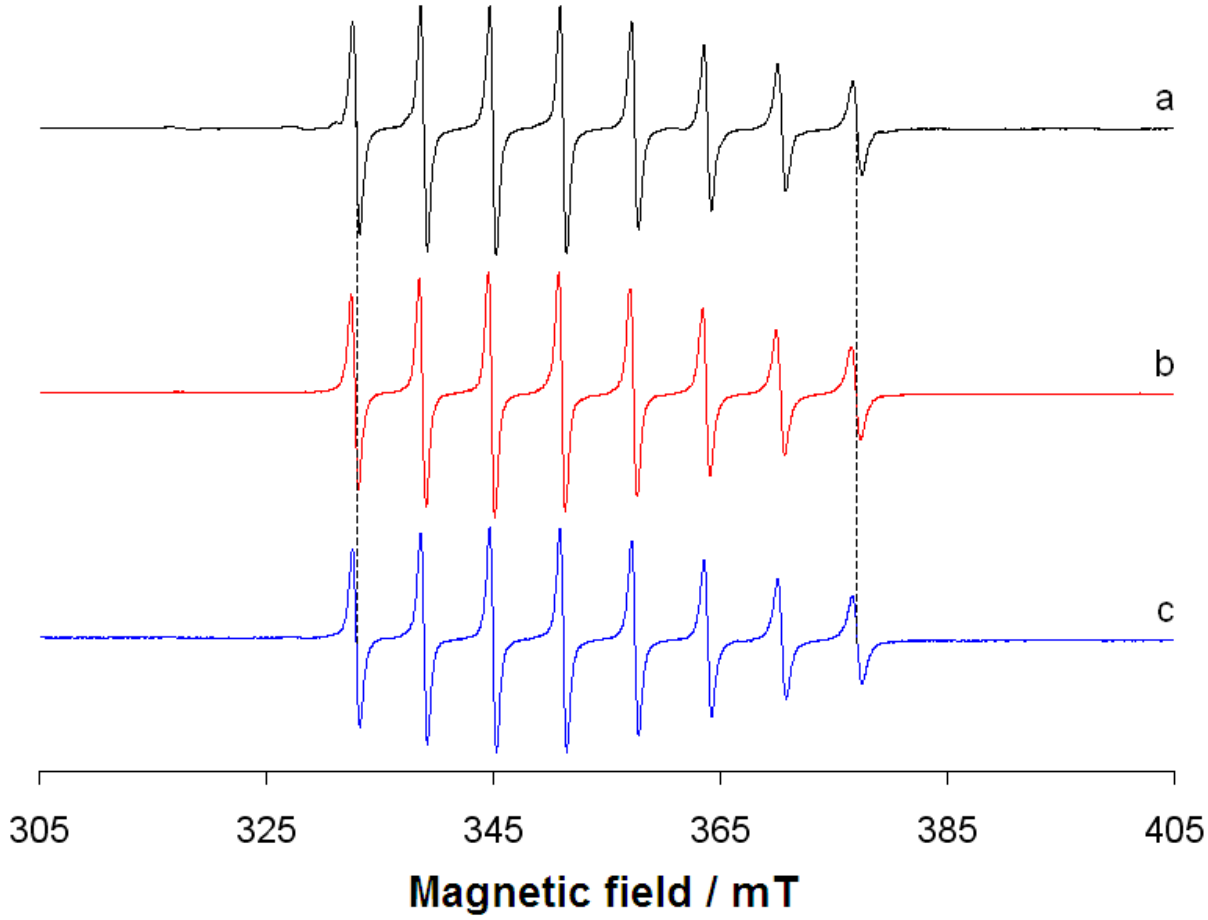

Figure S10. Room temperature (298 K) EPR spectra recorded in aqueous solution at pH 7.4 in the systems containing: (a) VDC; (b) VDC/apo-hTf 2/1 and (c) VDC/HSA 4/1 (c). VDC concentration was 1.0×10^{-3} (traces a and c) and 5.0×10^{-4} (trace b). The M_I = -7/2, 7/2 resonances of $[Cp_2V(OH)_2]$ are shown with a dotted line.

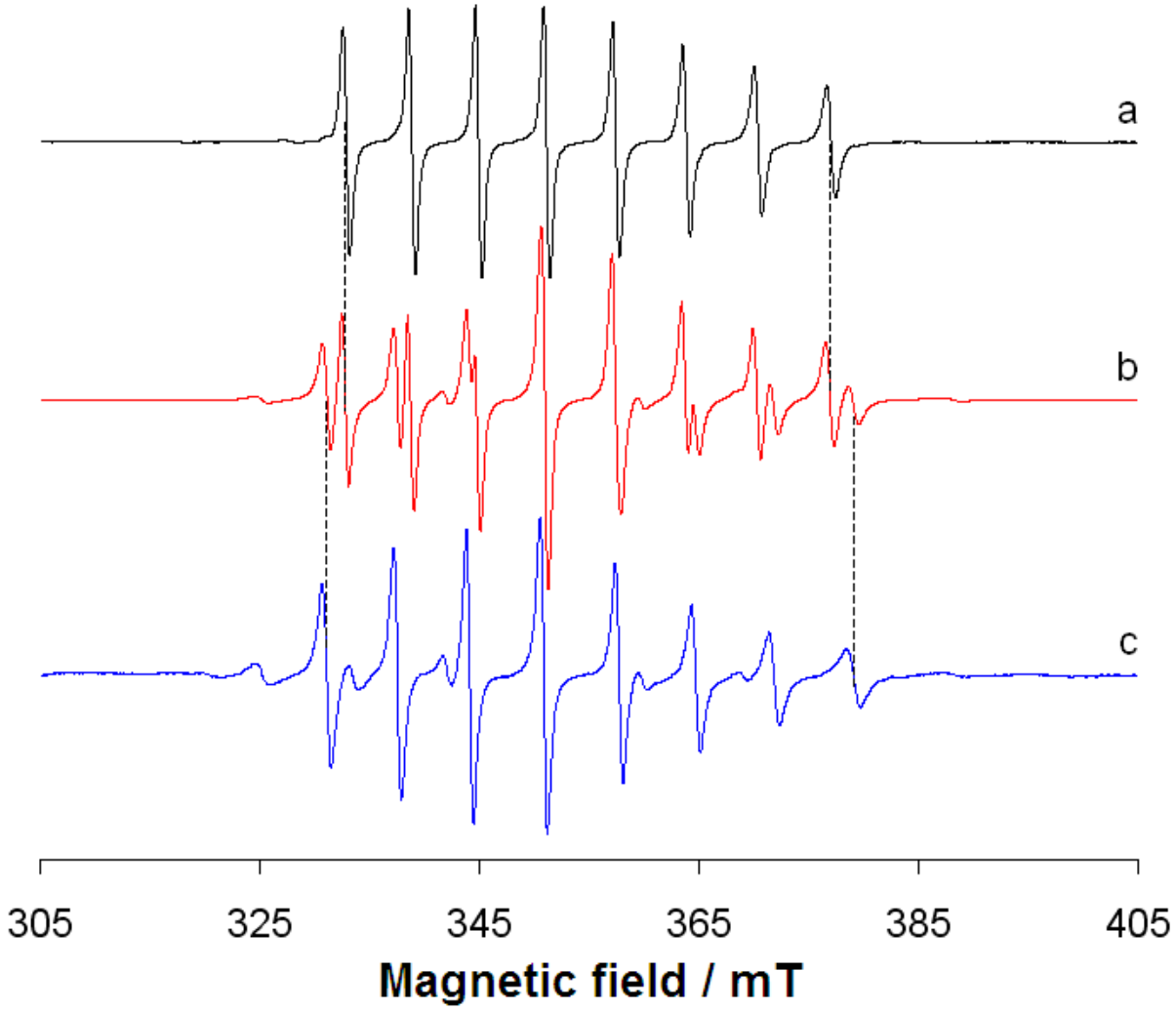

Figure S11. Room temperature (298 K) EPR spectra recorded in aqueous solution at pH 7.4 in the systems containing: (a) VDC/$NaHCO_3$ 1/10; (b) VDC/$NaHCO_3$/lact/Na_2HPO_4 1/10/10/10 and (c) VDC/lact 1/10. VDC concentration was 1.0×10^{-3} M. With the dotted lines the resonances M_I = -7/2, 7/2 of the complexes [$Cp_2V(CO_3)$] (trace a) and [$Cp_2V(lactH_{-1})$] (trace c) are shown.

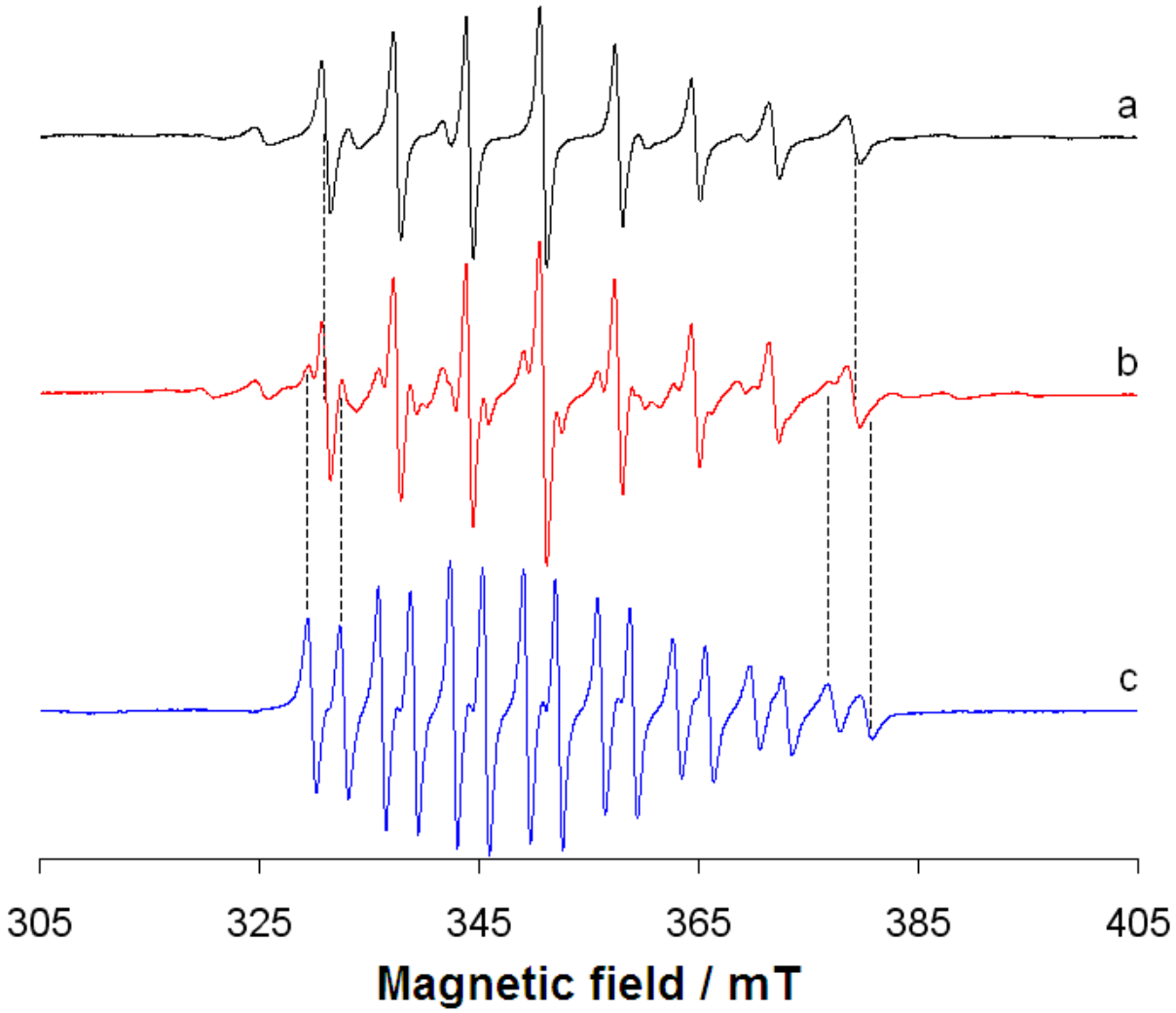

Figure S12. Room temperature (298 K) EPR spectra recorded in aqueous solution at pH 7.4 in the systems containing: (a) VDC/lact 1/10; (b) VDC/lact/Na_2HPO_4 1/10/10 and (c) VDC/Na_2HPO_4 1/10 (c). VDC concentration was 1.0×10^{-3} M. With the dotted lines the resonances M_I = -7/2, 7/2 of the complexes [$Cp_2V(lactH_{-1})$] (trace a) and [$Cp_2V(HPO_4)$] (trace c) are shown.

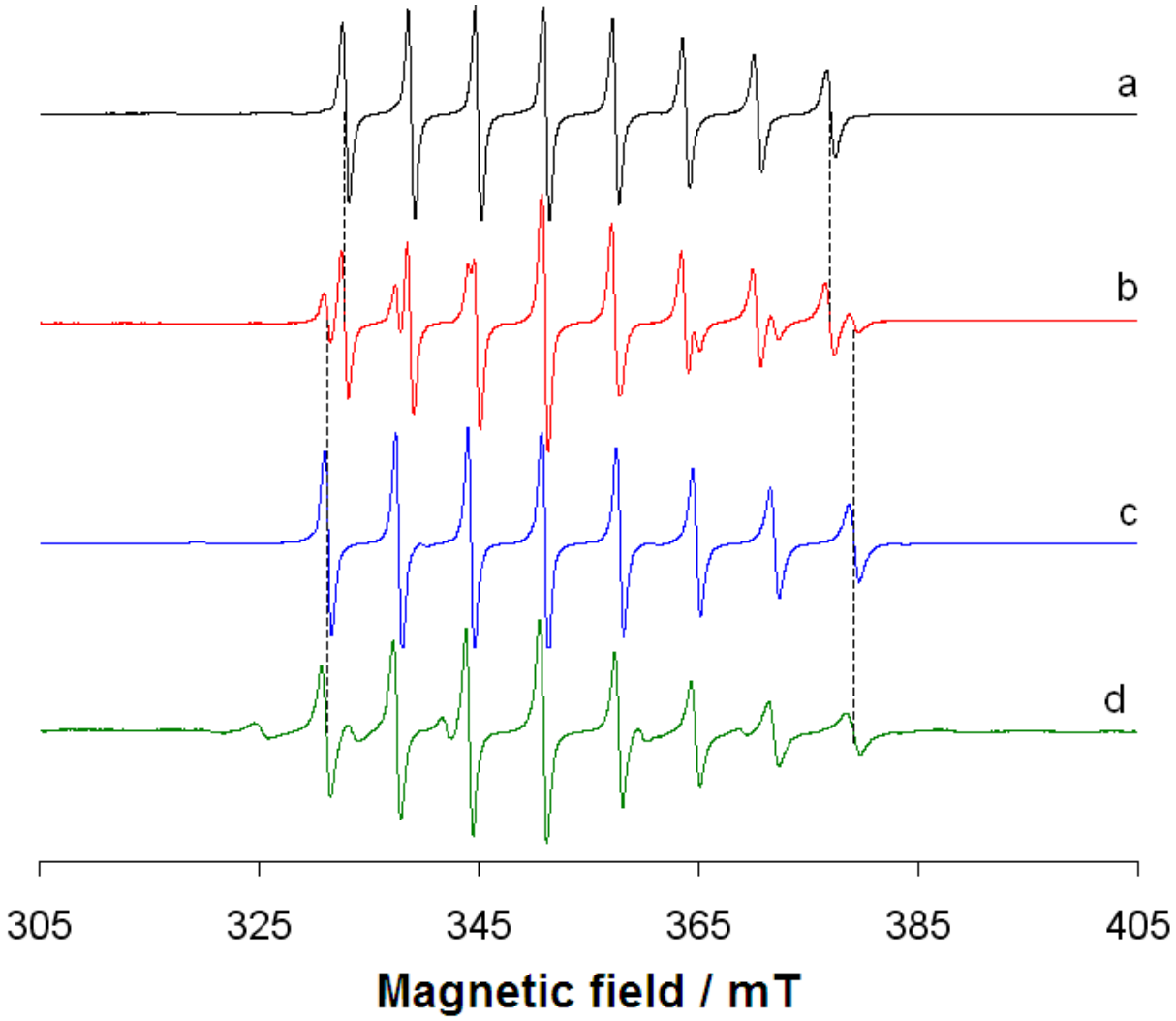

Figure S13. Room temperature (298 K) EPR spectra recorded in aqueous solution at pH 7.4 in the systems containing: (a) VDC/$NaHCO_3$ 1/10; (b) VDC/ox/$NaHCO_3$/lact/Na_2HPO_4 1/0.1/270.7/16.4/12.0; (c) VDC/ox 1/10 and (d) VDC/lact 1/10. The concentration of VDC was 4.0×10^{-4} M. With the dotted lines the resonances M_I = -7/2, 7/2 of the complexes [$Cp_2V(CO_3)$] (trace a) and [Cp_2V(ox)] (trace c) and [$Cp_2V(lactH_{-1})$] (trace d) are shown.

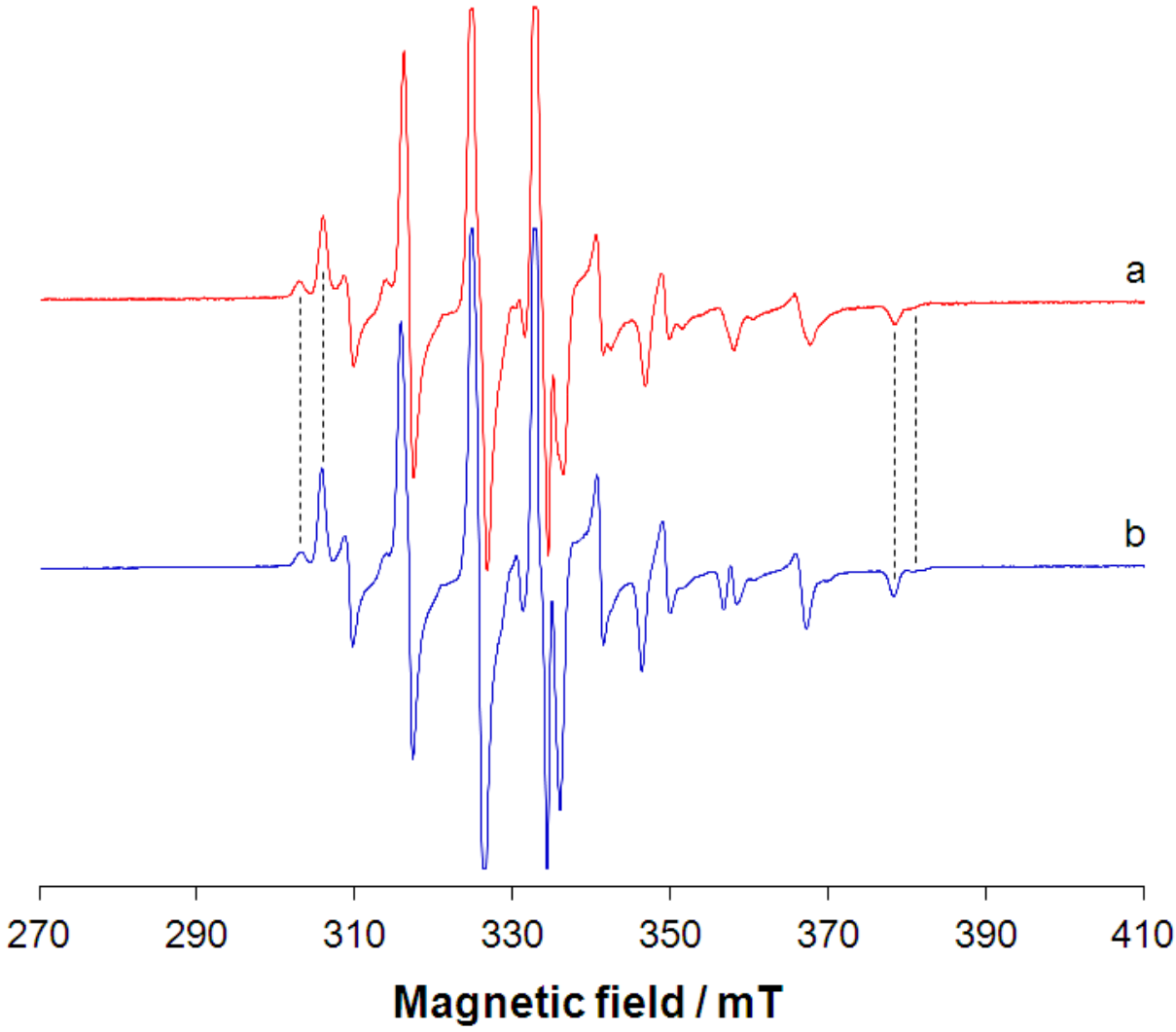

Figure S14. (a) EPR spectrum recorded at 120 K and at pH 7.4 in aqueous solution in the systems containing VDC/ox/$NaHCO_3$/lact/Na_2HPO_4 1/0.1/270.7/16.4/12.0 and (b) spectrum obtained considering in aqueous solution 80% of [$Cp_2V(CO_3)$] (trace a of Figure 7 of the main text), 10% of [$Cp_2V(ox)$] (trace c of Figure 7 of the main text) and 10% of [$Cp_2V(lactH_{-1})$] (trace d of Figure 7 of the main text). The concentration of VDC was 4.0×10^{-4} M. With the dotted lines the resonances M_I = -7/2, 7/2 of the complexes [$Cp_2V(ox)$] (external lines) and [$Cp_2V(CO_3)$] and [$Cp_2V(lactH_{-1})$] (internal lines) are shown.

References

1. Honzíček, J.; Vinklárek, J.; Císařová, I.; Erben, M. *Inorg. Chim. Acta* **2009**, *362*, 83-88.
2. Toney, J. H.; Brock, C. P.; Marks, T. J. *J. Am. Chem. Soc.* **1986**, *108*, 7263-7274.
3. Honzíček, J.; Nachtigall, P.; Císařová, I.; Vinklárek, J. *J. Organomet. Chem.* **2004**, *689*, 1180-1187.

Chapter 9

Synthesis, protonation constants, spectral characterization, biological activity and theoretical studies of salicylaldehyde-derived Schiff bases

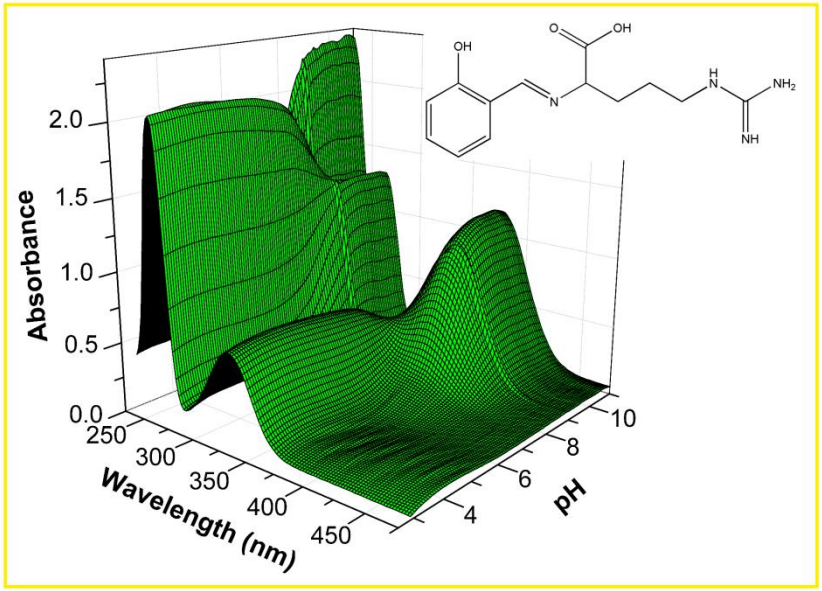

This chapter reports the synthesis, characterization, solution equilibria, antitumour activity, and DNA affinity of a group of Schiff bases ligands derived from salicyladehyde and six natural amino acids.

Abstract

Schiff bases represent a class of biological active molecules widely studied in organic synthesis, coordination and pharmaceutical chemistry. They are also used in the preparation of β-lactam family of antibiotics. Besides β-lactams, other Schiff bases show biological activity against fungi, bacteria and viruses. The potential development of pharmaceutical applications of these compounds, requires a proper knowledge of the chemical and biological reactions in which they are involved, and of their toxicological profiles. Despite the great amount of studies reported in literature on chemical and biological properties of the Schiff bases, the different experimental conditions often chosen, prevent a comparison to investigate the structure-activity correlation. This problem is relevant in particular for the solution equilibria study, since protonation constants of Schiff bases belonging to the same family are often determined in different solvents, temperatures, and ionic buffers. For these reasons, I decided to study a group of Schiff bases ligands derived from salicyladehyde and six natural amino acids, keeping constant the experimental conditions, in order to obtain comparable information and find useful insights about the relationship existing between their structure and their biological activity (Chapter 9 – Manuscript III).

The use of ATR-IR spectroscopy, together with NMR, UV-vis and potentiometric measurements, was investigated on the Schiff bases with the aim to collect useful information on the species actually formed. Theoretical studies were also performed. In particular, I studied the solution equilibria, the antiproliferative activity and the DNA-binding ability of L-Salicylidenealanine (**1**), L-Salicylidenevaline (**2**), L-Salicylidenecysteine (**3**), L-Salicylideneserine (**4**), L-Salicylidenearginine (**5**), and L-Salicylidenehistidine (**6**). The formulas, names and abbreviations of the studied molecules are reported in Figure 26.

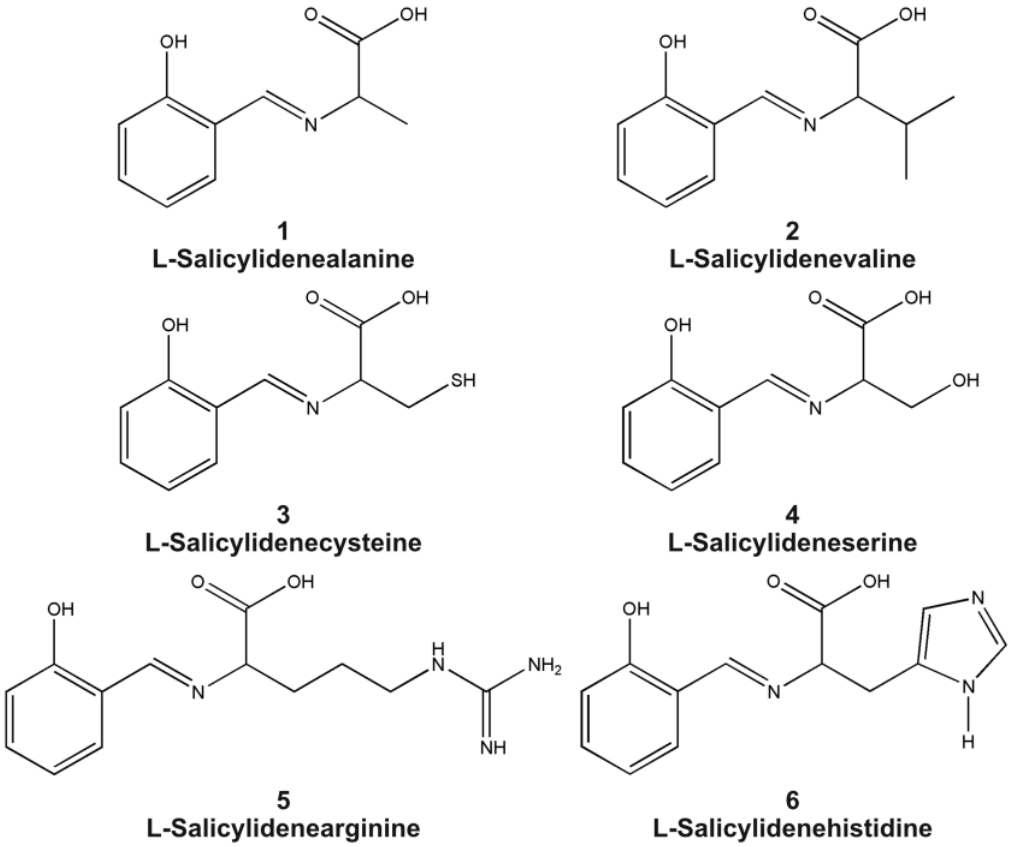

Figure 26. Formulas, names and abbreviations of the studied Schiff bases.

The chosen compounds have been synthesised[1] through optimization of previously reported methods, and they have been characterized by elemental analysis, Nuclear Magnetic Resonance (NMR) and Infrared (IR) Spectroscopy techniques.

The protonation constants of the studied compounds have been determined by potentiometric and spectrophotometric titrations carried out simultaneously in aqueous solution at 25 °C in 0.1 M ionic strength (NaCl). ATR-IR spectra at variable pH of the six Schiff bases were interpreted with the aid of simulated spectra obtained by quantum mechanical calculations.

The interaction of the six Schiff bases with calf thymus DNA (ct-DNA) and the cytotoxic activity against a panel of human tumour cell lines SK-MES-1 (squamous cell lung carcinoma),

[1] In collaboration with professor C. Fattuoni (Dipartimento di Scienze Chimiche e Geologiche, University of Cagliari).

DU-145 (prostate carcinoma), Hep-G2 (hepatocellular carcinoma), CCRF-CEM (acute T-lymphoblastic leukemia), CCRF-SB (acute B-lymphoblastic leukemia) have been also studied.

The studied ligands do not show cytotoxic activity, however they are able to interact with DNA, showing DNA binding constant in the 48–447 M^{-1} range. The absence of cytotoxicity and the poor reactivity with DNA, confirm the feasibility of these compounds for pharmaceutical applications, also in complexes with metal ions to exploit their unique properties. In fact, although the ligands are devoid of significant activity, it is not untypical that the derived complexes show antitumor activity.

Manuscript III

Synthesis, protonation constants, spectral characterization, biological activity and theoretical studies of salicylaldehyde-derived Schiff bases

Elisa Valletta, Claudia Fattuoni, Federica Trudu, Alessandra Pani, Sarah Vascellari, Tiziana Pivetta

To be submitted

Synthesis, protonation constants, spectral characterization, biological activity and theoretical studies of salicylaldehyde-derived Schiff bases

Elisa Valletta, [†] Claudia Fattuoni, [†] Federica Trudu, [†], Alessandra Pani,[§] Sarah Vascellari, [§] Tiziana Pivetta, [a †]

† Dipartimento di Scienze Chimiche e Geologiche, University of Cagliari, Cittadella Universitaria, 09042 Monserrato – CA (ITALY)

§ Dipartimento di Scienze Biomediche, University of Cagliari, Cittadella Universitaria, 09042 Monserrato – CA (ITALY)

[a]corresponding author:

Tiziana Pivetta

Dipartimento di Scienze Chimiche e Geologiche

University of Cagliari, Cittadella Universitaria, 09042 Monserrato – CA (ITALY)

Tel. +39 0706754473, mail: tpivetta@unica.it

ABSTRACT

Schiff bases represent a class of biological active molecules widely studied for their importance in organic and coordination chemistry. They are also used in the preparation of β-lactam family of antibiotics. Despite the great amount of studies on the chemical and biological properties of Schiff bases, the different experimental conditions prevent a useful comparison to investigate the structure-activity correlation. For this reason, we decided to study a group of Schiff bases derived from salicyladehyde and six natural amino acids, keeping constant the experimental conditions, in order to obtain comparable information and find useful insights about the relationship existing between their structure and activity. Interestingly, accurate NMR characterization for these compounds has not been yet reported. In particular, solution equilibria, antiproliferative activity and DNA-binding activity were studied. These compounds show DNA-binding constants in the 48-447 M^{-1} range, depending on the different amino acid side-chain, and exert no significant cytotoxic activity against the human tumour cell lines SK-MES-1, DU-145, Hep-G2, CCRF-CEM, CCRF-SB. Finally, the studied Schiff bases were synthesized through optimized methods, and all products were fully characterized by NMR spectroscopy.

KEYWORDS

Schiff bases; DNA binding; cytotoxicity; spectrophotometric titration

1. INTRODUCTION

Schiff bases, also known as imines or azomethines and named after their discoverer Hugo Schiff, are condensation products of primary amine and aldehydes or ketones. Schiff bases are represented by the general formula $R_1N=CR_2R_3$, where R_1, R_2 and R_3 may be alkyl, aryl or hydrogen [1]. Schiff bases are important intermediates in bio-processes such as the transamination reaction or the protein glycation, and are involved in racemization and decarboxylation reactions [2–4]. This class of compounds is important in organic synthesis and pharmaceutical chemistry. In organic synthesis, Schiff bases are used in nucleophilic addition, hetero Diels-Alder [5] and Staudinger [6] reactions. The latter process is widely used for the preparation of the β-lactams by reaction of a Schiff base with a ketene. The β-lactams constitute an important class of antibiotics such as penams, cephems, penems, monobactams, carbapenems, and trinems. The interest of pharmaceutical companies in the study of new derivatives of this family is kept alive by the onset of antibiotic resistance in some microorganisms such as Staphylococcus aureus, Streptococcus, Pseudomonas aeruginosa, and others. Besides β-lactams, other Schiff bases show biological activity against fungi, bacteria and

viruses [7–10]. In addition, some derivatives have been recently proposed for the treatment of Alzheimer's disease, as metal binding agents able to promote the disaggregation of β-amyloid plaques [11]. Thanks to their soft-hard donor character, Schiff bases are commonly used as ligands for several metal ions. They are used to recognize anions and cations and their application in biochemical and environmental fields has been proposed [12]. Moreover, complexes formed by Schiff bases with metals such as Cu(II) [13], Cd(II) [14], Ru(II) [15], Zn(II) [16], and lanthanides [17], show antitumor activity. The potential development of pharmaceutical applications of these compounds, requires a proper knowledge of the chemical and biological reactions in which they are involved, and their toxicological profile. Despite the high level of interest among the scientific community for these molecules, scientific literature highlights an overall lack of consistency. In fact, although Schiff bases are widely studied from different points of view, a direct comparison of the reported data is not possible because different experimental conditions have been used. This problem is relevant in particular for the solution equilibria study, since protonation constants of Schiff bases belonging to the same family are often determined in different solvents, temperatures, and ionic buffers [3,18–20]. Being the knowledge of the protonation constants fundamental for the study of the complex formation constants, it is suitable that the experiments are carried out in the same conditions at least for homologous series of compounds. For these reasons, we decided to study a group of Schiff bases derived from salicyladehyde and six natural amino acids, in the same experimental conditions in order to have comparable information on their chemical and biological behaviour. In particular, we studied the solution equilibria, the cytotoxic activity and the DNA binding ability of L-Salicylidenealanine (**1**), L-Salicylidenevaline (**2**), L-Salicylidenecysteine (**3**), L-Salicylideneserine (**4**), L-Salicylidenearginine (**5**), and L-Salicylidenehistidine (**6**). Formulas, names and abbreviations of the studied molecules are reported in Figure 1. The chosen compounds have been synthesised through optimization of previously reported methods, and they have been characterized by elemental analysis, Nuclear Magnetic Resonance (NMR) and Infrared (IR) Spectroscopy techniques. The protonation constants of the compounds have been determined by potentiometric and spectrophotometric titrations, carried out simultaneously in aqueous solution at 25 °C in 0.1 M ionic strength (NaCl). The interaction of the six Schiff bases with calf thymus DNA (ct-DNA) and the cytotoxic activity against a panel of human tumour cell lines (SK-MES-1, DU-145, Hep-G2, CCRF-CEM, CCRF-SB) have been also studied.

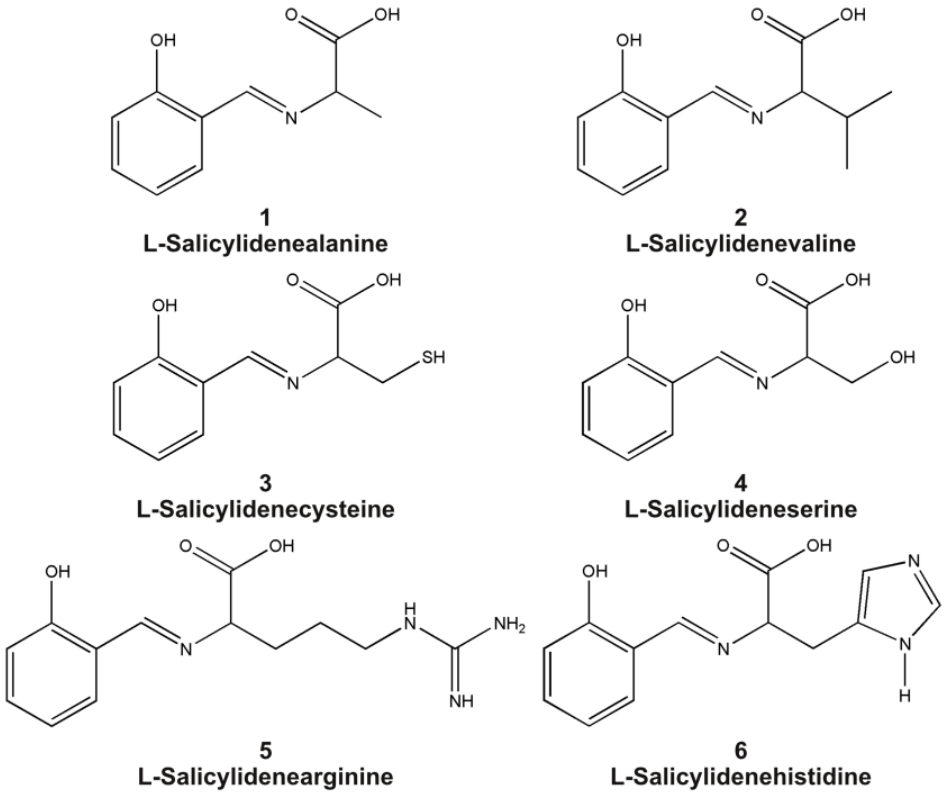

Figure 1. Formulas, names and abbreviations of the studied Schiff bases.

2. EXPERIMENTAL

2.1 Reagents

Calf thymus DNA sodium salt, hydrochloric acid standard solutions, diethyl ether, dimethylsulfoxide-d_6 (DMSO-d_6), ethanol, L-aniline, L-arginine, L-cysteine, L-histidine, L-serine, L-valine, methanol, 1,4-piperazinediethanesulfonic acid, potassium bromide, salicylaldehyde, sodium bromide, sodium chloride, sodium hydroxide pellets, sodium hydroxide standard solution, sodium sulfate were purchased from Sigma-Aldrich and used without any further purification.

2.2 Characterization

Infrared spectra were recorded using a Bruker Equinox 55 spectrophotometer, in KBr medium (pellets). ^{1}H and ^{13}C NMR spectra were recorded on Varian 400 and 500 spectrometers. Proton and carbon chemical shifts in DMSO-d_6 were referenced to the residual solvent signals (^{1}H NMR, δ = 2.60 ppm; ^{13}C NMR, δ = 39.6 ppm). Melting points (mp) were measured using a Kofler hot stage microscope and are uncorrected.

2.3 Synthesis

2.3.1 Synthesis of L-Salicylidenealanine (1)

Compound **1** was prepared according to the literature method [21]. A mixture of L-alanine (0.8 g, 9 mmol), salicylaldehyde (1 ml, 9 mmol) and Na_2SO_4 (4 g) in methanol (150 mL) was stirred under reflux for 12 h. The solid was filtered, the solvent was removed under reduced pressure to give 1.6 g (90% yield) of light brown solid, mp 138-142 °C (dec).^{1}H NMR (400 MHz, DMSO-d_6): δ 8.59 (s, 1H, CH=N), 7.46 (m, 1H, Ar-H), 7.35 (m, 1H, Ar-H), 6.90 (m, 2H, Ar-H), 4.21 (q, 1H, CH-CO_2H, J=6.7), 1.44 (d, 3H, CH_3, J=6.7). ^{13}C NMR (125 MHz, DMSO-d_6): δ 19.48, 64.79, 116.60, 117.36, 118.69, 131.93, 132.69, 160.62, 166.61, 173.29. IR (KBr): ν/cm^{-1} 3418, 3090, 2604, 1630, 1595, 1452, 1409, 1356, 1309, 1117, 853, 542. Elemental analysis found (calc. for $C_{10}H_{11}NO_3$): C% 61.80 (62.17), H% 5.64 (5.74), N% 7.21 (7.25).

2.3.2 Synthesis of L-Salicylidenevaline (2)

Compound **2** was prepared according to the literature method [21]. A mixture of L-valine (1.05 g, 9 mmol), salicylaldehyde (1 ml, 9 mmol) and Na_2SO_4 (4 g) in methanol (150 mL) was stirred under reflux for 12 h. The solid was filtered, the solvent was removed under reduced pressure to give 1.22 g (62% yield) of light yellow solid, mp 162-164 °C. ^{1}H NMR (500 MHz, DMSO-d_6): δ 0.89 (d, 3H, CH_3, J=4 Hz), 0.91 (d, 3H, CH_3, J=4.5 Hz), 2.26 (m, 1H, CH-CH_3), 3.82 (m, 1H, CH-CO_2H), 6.89 (m, 2H, Ar-H), 7.35 (t, 1H, Ar-H, J=7.6 Hz), 7.45 (d, 1H, Ar-H, J=7.6 Hz), 8.53 (s, 1H, CH=N). ^{13}C NMR (100 MHz, DMSO-d_6): δ 17.8, 19.3, 31.1, 75.9, 116.6, 118.6, 118.7, 132.0, 132.7, 160.8, 167.4, 172.4. IR (KBr): ν/cm^{-1} 3430, 2961, 2626, 1648, 1589, 1511, 1394, 1330, 757, 541. Elemental analysis found (calc. for $C_{12}H_{15}NO_3$): C% 64.98 (65.14), H% 6.84 (6.83), N%6.21 (6.33).

2.3.3 Synthesis of L-Salicylidenecysteine (3)

A mixture of L-cysteine (1.09 g, 9 mmol) and salicylaldehyde (1 ml, 9 mmol) in ethanol (50 mL) was stirred under reflux for 12h. The solid product was filtered, washed with ethanol and dried. The white solid obtained (1.75 g, 86% yield) resulted at the NMR analysis to be formed by two isomers (*E* and *Z*) of compound **3**, mp 166-167 °C. ^{1}H NMR (500 MHz, DMSO-d_6): δ (*E*) 2.97 (dd unresolved, 1H, CH_2, J= 9.5 Hz), 3.34 (dd, 1H, CH_2, J=7 and 9.5 Hz), 4.20 (m, 1H, C*H*-CO_2H), 5.65 (s, 1H, CH=N), 6.81 (t, 2H, Ar-H, J=7 Hz), 7.13 (t, 1H, Ar-H, J=7.5 Hz), 7.34 (d, 1H, Ar-H, J=7 Hz); δ (*Z*) 3.03 (dd, 1H, CH_2, J=5 and 10 Hz), 3.20 (dd, 1H, CH_2, J=7 and 10 Hz), 3.82 (m, 1H, C*H*-CO_2H), 5.85 (s, 1H, CH=N), 6.76 (m, 2H, Ar-H), 7.06 (t, 1H, Ar-H, J=7.5 Hz), 7.30 (d, 1H, Ar-H, J=7.5 Hz). ^{13}C NMR (100 MHz, DMSO-d_6): δ (*E*) 37.11 (CH_2), 64.85 (CH-C=O), 65.69 (CH=N), 115.15 (C_{Ar}-H), 118.81 (C_{Ar}-H), 127.67 (C_{Ar}-C), 126.16 (C_{Ar}-H), 128.16 (C_{Ar}-H), 155.23

(C_{Ar}-OH), 172.98 (C=O); δ (*Z*) 38.21 (CH_2), 65.26 (CH-C=O), 67.73 (CH=N), 115.74 (C_{Ar}-H), 119.10 (C_{Ar}-H), 124.30 (C_{Ar}-C), 127.94 (C_{Ar}-H), 129.09 (C_{Ar}-H),154.65 (C_{Ar}-OH),172.51 (C=O). IR (KBr): ν/cm^{-1} 3438, 3100, 2701, 2578, 1622, 1598, 1577, 1457, 1384, 1334, 1283, 760, 679. Elemental analysis found (calc. for $C_{10}H_{11}NO_3S$): C% 53.64 (53.32), H% 5.06 (4.92), N% 6.31 (6.22), S% 13.87 (14.23).

2.3.4 Synthesis of L-Salicylideneserine (4)

A mixture of L-serine (0.95 g, 9 mmol) and salicylaldehyde (1 ml, 9 mmol) in ethanol (50 mL) was stirred under reflux for 2.5 h, then kept in the refrigerator overnight. The solid product was filtered, washed with ethanol, and dried. Product **4** was obtained as a light brown solid (1.00 g, 53% yield), mp 220 °C (dec). ^{1}H NMR (500 MHz, DMSO-d_6): δ 3.69 (dd, 1H, CH_2, J=7.5 and 11 Hz), 3.86 (dd, 1H, CH_2, J=4 and 11 Hz), 4.09 (dd, 1H, C*H*-CO_2H, J=4 and 7.5 Hz), 6.90 (m, 2H, Ar-H), 7.35 (t, 1H, Ar-H, J=7.5 Hz), 7.46 (d, 1H, Ar-H, J=7.5 Hz), 8.53 (s, 1H, CH=N). ^{13}C NMR (125 MHz, DMSO-d_6): δ 62.7, 72.5, 116.7, 118.5, 118.7, 132.0, 132.7, 160.9, 167.6, 171.4. IR (KBr): ν/cm^{-1} 3444, 3054, 2947, 1635, 1618, 1603, 1507, 1472, 1416, 1348, 1313, 1125, 1015, 615, 527. Elemental analysis found (calc. for $C_{10}H_{11}NO_4$): C% 57.46 (57.41), H% 5.25 (5.30), N% 6.31 (6.70).

2.3.5 Synthesis of L-Salicylidenearginine (5)

A mixture of L-arginine (1.57 g, 9 mmol) and salicylaldehyde (1 ml, 9 mmol) in ethanol (50 mL) was stirred under reflux for 12 h. The solid product was filtered, washed with ethanol and dried. Product **5** was obtained as a bright yellow solid (2.45 g, 98% yield), mp 200-202 °C. ^{1}H NMR (500 MHz, DMSO-d_6): δ 1.58 (m, 2H, CH_2C*H*$_2$$CH_2$), 1.83 (m, 1H, CHC*H*$_2$), 2.01 (m, 1H, CHC*H*$_2$), 3.18 (m, 2H, C*H*$_2$-NH), 3.88 (m, 1H, C*H*-COOH), 6.86 (m, 2H, Ar-H), 7.36 (t, 1H, Ar-H, J=8 Hz), 7.45 (d, 1H, Ar-H, J=8 Hz), 8.52 (s, 1H, CH=N), 9.60 (s, broad, 1H, NH). ^{13}C NMR (100 MHz, DMSO-d_6): δ 26.0, 31.6, 41.4, 71.3, 117.4, 118.2, 119.4, 133.2, 134.5, 157.5 (NH_2-C=NH), 165.3, 166.8, 174.8. IR (KBr): ν/cm^{-1} 3407, 3315, 3078, 2965, 2865, 1662, 1650, 1634, 1591, 1474, 1377, 1343, 1192, 1149, 777, 536. Elemental analysis found (calc. for $C_{13}H_{18}N_4O_3$): C% 56.16 (56.10), H% 6.59 (6.52), N% 20.08 (20.13).

2.3.6 Synthesis of L-Salicylidenehistidine (6)

A mixture of L-histidine (0.7 g, 4.5 mmol) and salicylaldehyde (1 ml, 9 mmol) in ethanol (50 mL) was stirred under reflux for 24 h. The solid product was filtered, washed with ethanol and dried. Product **6** was obtained as a bright yellow solid (0.9 g, 77% yield), mp 174-180 °C. ^{1}H NMR (400MHz, DMSO-d_6): δ 3.00 (dd, 1H, CH_2, J=8.4 and 14.6 Hz), 3.18 (dd, 1H, CH_2, J=4.8 and 14.6 Hz), 4.32 (dd, 1H, CH-CO_2H, J=4.8 and 8.4 Hz), 6.77 (s, 1H, C=CH-N), 6.85 (m, 2H, Ar-H), 7.34

(m, 2H, Ar-H), 7.59 (s, 1H, NH-CH=N), 8.32 (s, 1H, CH=N). ^{13}C NMR (125 MHz, DMSO-d_6): δ 31.22, 70.19, 116.57, 118.59, 119.49, 129.28, 131.86, 132.63, 134.84, 136.46, 160.62, 166.93, 172.38. IR (KBr): ν/cm^{-1} 3422, 3122, 3018, 2879, 1638, 1531, 1470, 1416, 1341, 1267, 1149, 838, 624, 535. Elemental analysis found (calc. for $C_{13}H_{13}N_3O_3$): C% 60.19 (60.22), H% 4.97 (5.05), N% 16.24 (16.21).

2.4 Potentiometric and spectrophotometric titrations

Potentiometric titrations were performed in a thermostated vessel with a Mettler-Toledo Seven Compact pH/Ion-meter, equipped with a Mettler-Toledo InLab Micro Pro combined glass electrode with an integrated temperature probe. Potentiometric titrations were performed at 25 °C in 0.1 M ionic strength (NaCl) under N_2 atmosphere. The glass electrode was calibrated daily by titration of a known amount of HCl with carbonate-free NaOH standard solution. Electrode standard potential (E^0), water ionic product (pK_w), electrode response and carbonate content of the titrant solution were checked with Gran's procedure [22] using the Glee software [23]. The UV-visible (UV–vis) measurements were carried out with a Varian Cary 60 spectrometer equipped with an optical fiber dip probe with a 1 cm optical path length.

2.5 Protonation constants

Protonation constants of compounds **1**-**6** were determined by spectrophotometric and potentiometric titrations, at 25 °C in 0.1 M ionic strength (NaCl), following the spectral variations due to the additions of the titrant. Solutions of ligand were prepared daily by dissolving the proper amount of the compound in freshly distilled water. Concentrations of compounds **1**-**6** ranged from 2.8 x 10^{-4} M to 1.0 x 10^{-3} M, according to their absorptivity and solubility. Solutions containing a known amount of compound and HCl (necessary to fully protonate the molecule) were titrated with NaOH standard solution. The reversibility of the involved equilibria was checked by back-titration with standard HCl. The overall stability constants were determined with the Hyperquad 2003 software [24].

2.6 DNA binding

The binding constants (K_b) between ct-DNA and compounds **1**-**6** were determined at 25 °C by spectrophotometric titrations in PIPES buffer 0.01 M at pH 7.0. A stock solution of ct-DNA in 0.01 M PIPES buffer at pH 7.0 was prepared and stored at 4 °C. This solution was used within four days. The concentration of DNA per nucleotide was determined by UV absorption at 260 nm using its molar absorption coefficient (6600 M^{-1}cm^{-1}) [25]. The purity of the DNA was checked by monitoring the ratio of the absorbance at 260 nm to that at 280 nm. A ratio higher than 1.8 indicates a DNA sufficiently protein-free [26]. Twenty solutions containing a fixed amount of the compounds (ranging from ≈ 2.03 x 10^{-4} to ≈ 6.07 x 10^{-4} mmol, according to the absorptivity) and variable

amounts of DNA (ranging from 6.09 x 10^{-4} to 1.82 x 10^{-3} mmol) were prepared. The stock solution of **3** was prepared at least 39 h before the experiment due to its slow hydrolysis in PIPES. Since the interactions between DNA and compounds **1-6** are slow processes, spectra in the 200–500 nm range were recorded when equilibration was reached (15 h). All the solutions were stored meanwhile in the dark at room temperature. The DNA binding constants were obtained by using the Hyperquad 2003 software [24].

2.7 Cell lines

Cell lines were purchased from the American Type Culture Collection (ATCC) and were derived from: lung squamous carcinoma (SK-MES-1); prostate carcinoma (DU-145); hepatocellular carcinoma (Hep-G2); acute T-lymphoblastic leukaemia (CCRF-CEM); acute B-lymphoblastic leukaemia (CCRF-SB). All cell lines were grown at 37 °C in a 5% CO_2 atmosphere, in their specific media according to ATCC instructions, in presence of 5–10% foetal bovine serum (FBS), antibiotic and, unless otherwise indicated, sodium pyruvate. All cell cultures were maintained in exponential growth by periodically splitting high density suspension cultures (i.e. 10^6 cell/mL) or when cell monolayers reached sub-confluence. The absence of mycoplasma contamination was checked periodically by the Hoechst staining method [27].

2.8 Cytotoxic assays

The cytotoxic effect of the compounds **1-6** was evaluated in cell lines during exponential growth stage. Stock solutions of compounds were stored at 4 °C in the dark. For the evaluation of cytotoxicity, solutions of compounds **1-6** were serially diluted in growth medium specific for the different cell lines. Suspension cell lines were seeded in 96-well plates at an initial density of 1 x 10^5 cells/mL in specific growth medium, with or without serial dilutions of each compound. Adherent cell lines were seeded at an initial density of 1 x 10^4 cells per well and incubated overnight before adding serial dilutions of the test compound. Cell viability was determined after 96 h at 37 °C, 5% CO_2, by the 3-(4,5-dimethylthiazol-2-yl)-2,5-diphenyl-tetrazolium bromide (MTT) method as previously described [28]. Cell growth at each drug concentration was expressed as the percentage of untreated controls. The results were expressed as IC_{50}, i.e. the concentration of compound required to reduce the viability of the tested cells by 50%.

3. RESULTS AND DISCUSSION

3.1. Synthesis

Literature reports many different synthetic methods to prepare amino acid-derived Schiff bases [29–32]. The classic method to synthetize Schiff bases consists of simple mixing equimolar amounts of amine and aldehyde in ethanol, and refluxing the mixture for some hour: the readily formed product can be filtered and isolated. When the amine role is played by an α-amino acid, the synthetic procedure may not be so straightforward: the amino acid zwitterionic character is responsible for a weaker nucleophilic amino-group. Several modifications of the classic method are then reported. For example, potassium [33] or sodium hydroxide [34] is added to an aqueous or methanolic solution of the amino acid to enhance its nucleophilic character. An analogous effect is obtained with a bicarbonate buffer [30]. On the other hand, the effect of the added base is also to promote the aldehyde self-reaction, leading to lower yield of the desired Schiff base. We found that the simple mixing-reflux method works well only for cysteine and arginine derivatives. To obtain a satisfactory yield for the other four amino acid based compounds, the classic method has been modified as follows: i) for histidine derivative, a double amount of aldehyde was used; ii) for alanine and valine derivatives, anhydrous sodium sulfate was added to the reaction mixture (as also reported by Hsieh [21]) to obtain the two Schiff-bases in satisfactory yield; iii) for serine derivative, an equimolar mixture of amino acid and aldehyde was refluxed in ethanol for 2 h and the resulting solution was kept in the refrigerator overnight. It is noteworthy the high reactivity of cysteine in the reported condition: in fact, after only an hour at the reflux temperature a thick white precipitate was formed. The NMR analysis revealed it was constituted by the two geometric isomers E and Z. The E isomer, which was found as the most abundant, was identified due to the correspondence of the CH=N chemical shift value with those reported [35]. All attempts to prepare only one isomer, as lowering the reaction temperature or increasing the solvent amount, were unsuccessful.

3.2 Protonation constants

The protonation constants of the studied Schiff bases were determined by a basic titration, measuring simultaneously the electrochemical potential and the UV-vis absorption. The absorbance values measured during the potentiometric titrations of the six Schiff bases are reported as a function of wavelength and pH, in Figure 2. The functional groups involved in the protonation and the protonation sequence were determined by comparing the pure UV-vis spectra of the formed species and ATR-IR spectra at variable pH of the studied compounds. No reliable NMR spectra in water solution were obtained due to the low water solubility of the compounds (<1 mM).

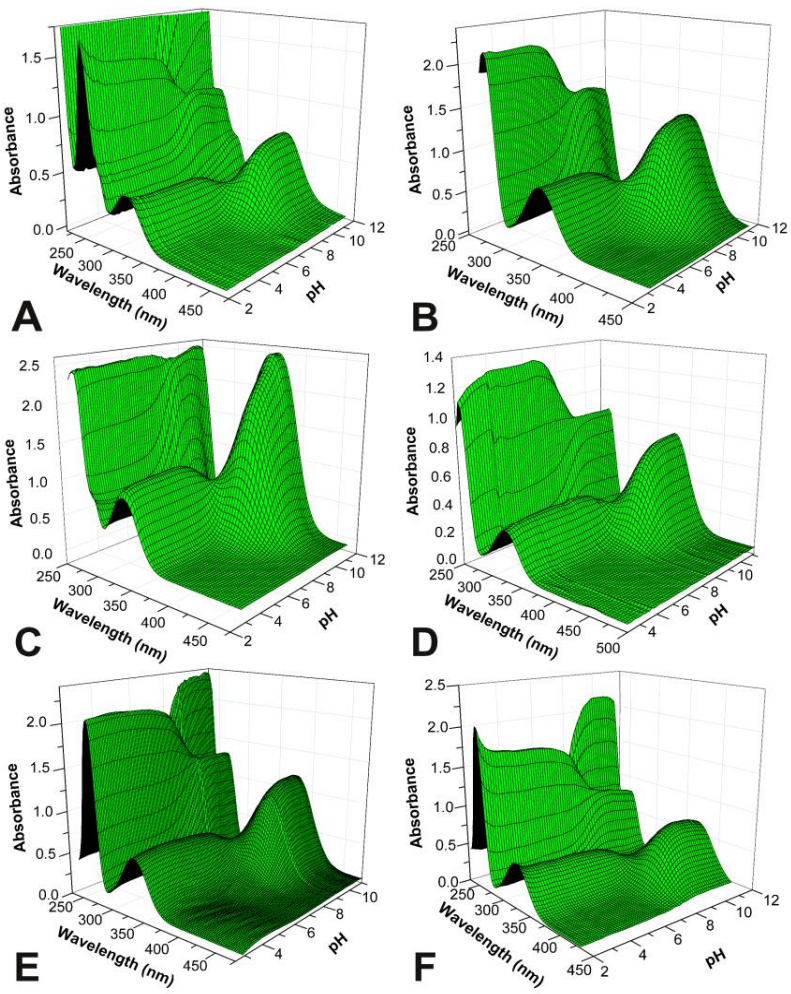

Figure 2. Absorbance as a function of wavelength and pH measured during the titrations of 0.0240 mmol of **1** (**A**), 0.0178 mmol of **2** (**B**), 0.0141 mmol of **3** (**C**), 0.00058 mmol of **4** (**D**), 0.00401 mmol of **5** (**E**) and 0.00061 mmol of **6** (**F**); 25 °C, 0.1 M NaCl ionic buffer, 1 cm optic path length.

3.2.1 Spectral evidences

Compound 1

During the titration of compound **1** with NaOH, three equilibria are spectrally evidenced in the pH range 2-11.4 (Figure 3A). At pH 2, two peaks and a shoulder are present at 325, 257 and ≈ 280 nm, respectively. Increasing the pH, the absorbance of the peaks slightly decreases, not for the dilution as it can be seen in the inset of the Figure 3B, where the absorbance at 325 nm is corrected for the dilution. The observed spectral variation is caused by the deprotonation of the H_3L^+ species to form the H_2L one. These two species appear spectrally not well distinguishable. Increasing the pH value to 8.8, the intensity of the peaks at 325 and 257 nm decreases, while two new peaks appear at 378 nm and 266 nm due to the formation of the HL^- species (Figure 3C). Four isosbestic points are present at 340, 300, 265 and 247 nm. At pH higher than 8.8, the intensity of the peak at

378 raises while that of the peak at 265 diminishes, and a shoulder is observed at ≈ 300 nm because of the formation of the L^{2-} species (Figure 3D). Two isosbestic point are present at 283 and 259 nm.

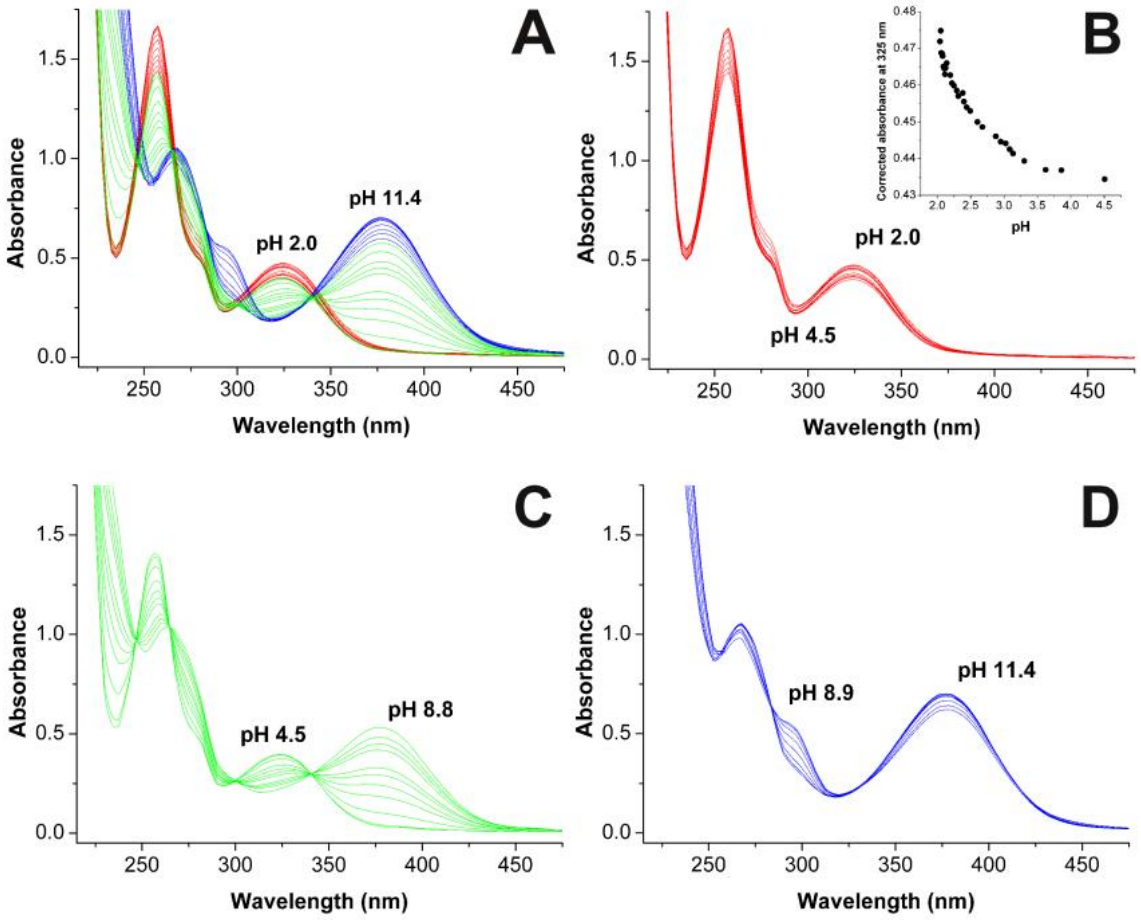

Figure 3. Selected spectra recorded during the potentiometric titration of **1** (9.01×10^{-4} M, 25 °C, 0.1 M NaCl, 1 cm optical path length) from pH 2.0 to 11.4 (**A**), from pH 2.0 to 4.5 (**B**), from pH 4.5 to 8.8 (**C**) and from pH 8.9 to 11.4 (**D**).

*Compound **2***

The analysis of the spectra recorded during the titration of **2** gives evidence of three equilibria (Figure 4A). At acidic pH two peaks are present at 252 and 325 nm. Increasing the pH till 8, the intensity of these two peaks decreases, while two new peaks appear at 264 and 378 nm (Figure 4B). Four isosbestic points are present at 342, 292, 265 and 245 nm. After pH 8, the maximum of intensity shifts at 380 nm and three isosbestic points are present at 342, 292 and 265 nm (Figure 4C). After pH 9, the peaks shifts at 374 nm with larger width, a poor resolved isosbestic point is present at 332 nm (Figure 4D).

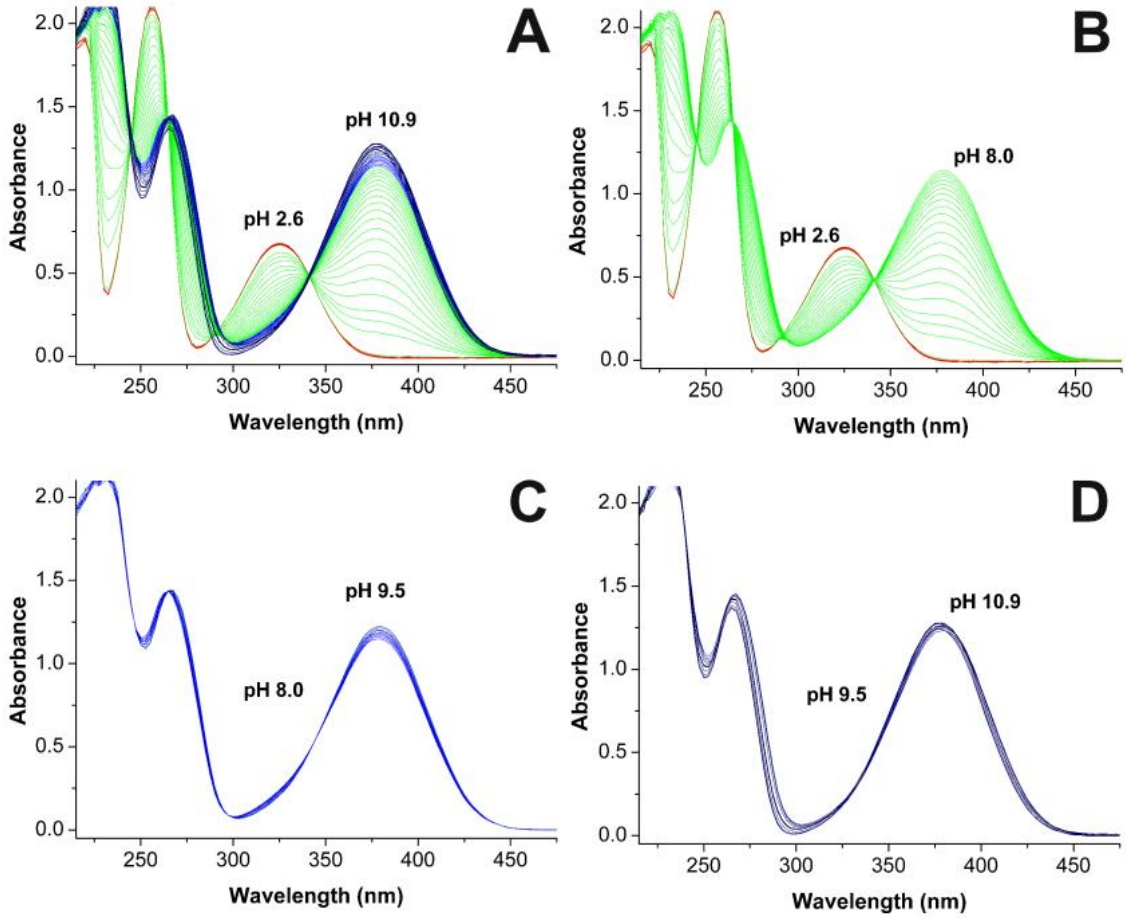

Figure 4. Selected spectra recorded during the potentiometric titration of **2** (9.32×10^{-4} M, 25 °C, 0.1 M NaCl, 1 cm optical path length) from pH 2.6 to 10.9 (**A**), from pH 2.6 to 8.0 (**B**), from pH 8.0 to 9.5 (**C**) and from pH 9.5 to 10.9 (**D**).

*Compound **3***

The analysis of the spectra recorded during the titration of **3**, gives evidence of four equilibria (Figure 5A). At pH 2.7 two bands at 324 and ≈ 260 nm and a shoulder at 280 nm are present. Increasing the pH, the intensity of the band centered at 324 nm rises while that of the shoulder at 280 nm decreases (Figure 5B). An isosbestic point is present at 290 nm. At pH values higher than 5.9, a new band forms at 378 nm, while the intensity of the band at 324 nm decreases (Figure 5C). An isosbestic point is present at 339 nm. At pH higher than 8, the band at 378 nm grows with a different shape while the shoulder at ≈ 300 nm decreases. An isosbestic point is present at 326 nm (Figure 5D). At pH > 9.5, the width of the band centered at 378 nm continues to increase.

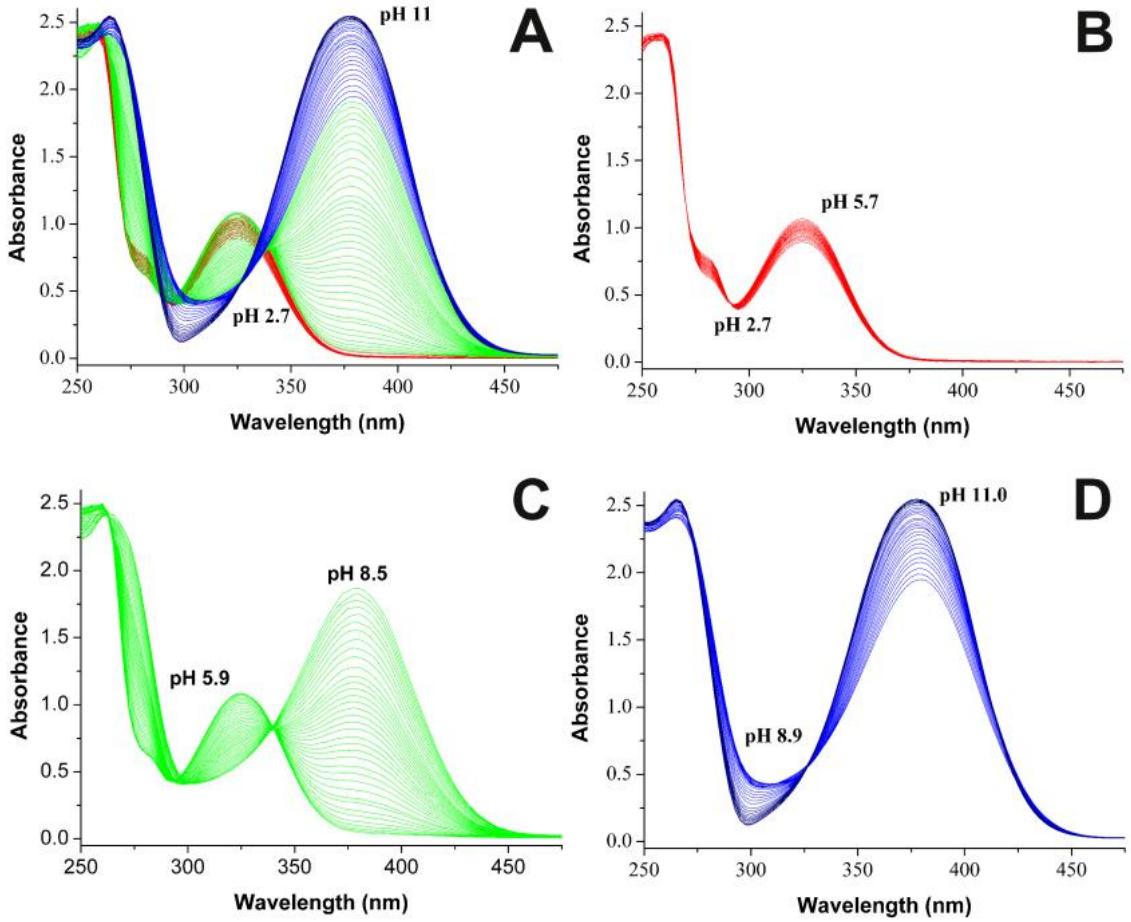

Figure 5. Some spectra recorded during the potentiometric titration of **3** (7.07×10^{-4} M, 25 °C, 0.1 M NaCl, 1 cm optical path length) from pH 2.7 to 11 (**A**), from pH 2.7 to 5.7 (**B**), from pH 5.9 to 8.5 (**C**) and from pH 8.9 to 11.0 (**D**).

*Compound **4***

As for **3**, during the titration of **4**, four protonation equilibria are evidenced by spectral variations (Figure 6A). At acidic pH, two peaks at 256 and 325 nm are present, which absorbance rises till pH 6.1 (Figure 6B). At pH > 6.1, the intensity of these two peaks decreases while two new peaks are formed at 263 and 377 nm (Figure 6C). Three isosbestic points are present at 264, 289 and 340 nm. At pH > 9, the peak at 377 nm increases in intensity but with different shape, while that at 265 nm does not vary significantly (Figure 6D). Two isosbestic points are present at 336 and 264 nm.

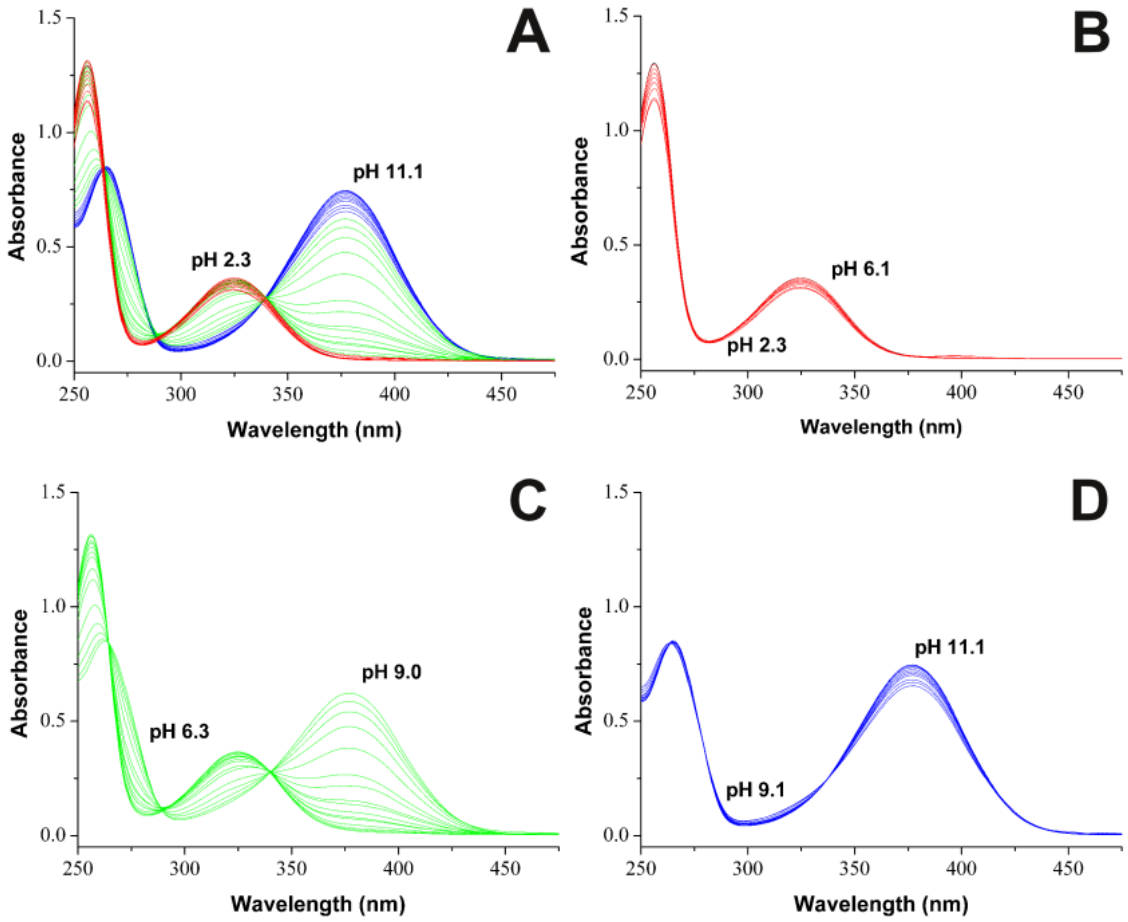

Figure 6. Some spectra recorded during the potentiometric titration of **4** (2.9×10^{-4} M, 25 °C, 0.1 M NaCl, 1 cm optical path length) from pH 2.3 to 11.1 (**A**), from pH 2.3 to 6.1 (**B**), from pH 6.3 to 9.0 (**C**) and from pH 9.1 to 11.1 (**D**).

*Compound **5***

The analysis of the spectra recorded during the titration of **5**, gives evidence of four equilibria (Figure 7A). At pH 3, two absorption peaks, at 255 and 325 nm, are present. Increasing the pH till 3.3, the intensity of these peaks increases slightly (Figure 7B). At pH > 3.3, the intensity of the peaks at 255 and 325 nm decreases while two peaks at 265 and 377 nm appear (Figure 7C). Four isosbestic points are present at 244, 264, 290 and 340 nm. At pH > 8, the intensity of the peak at 265 nm increases while that of the peak at 377 nm decreases (Figure 7D). An isosbestic point is present at 344 nm. At pH values higher than 9, the width of the peak centred at 377 nm continues to increase.

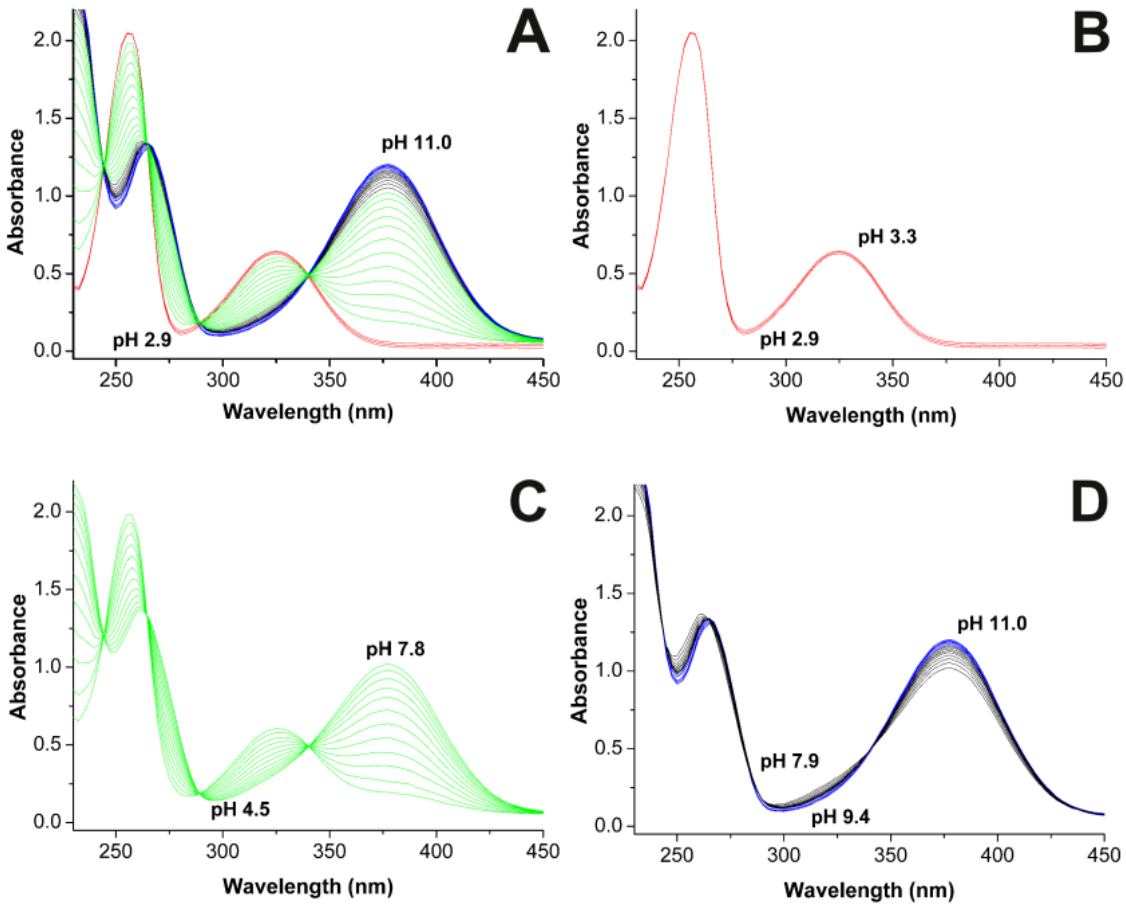

Figure 7. Some spectra recorded during the potentiometric titration of **5** (2.01×10^{-4} M, 25 °C, 0.1 M NaCl, 1 cm optical path length) from pH 2.9 to 11.0 (**A**), from pH 2.9 to 3.3 (**B**), from pH 4.5 to 7.8 (**C**) and from pH 7.9 to 11.0 (**D**).

*Compound **6***

During the titration of **6**, three protonation equilibria are evidenced by the spectral variations (Figure 8A). At acidic pH, two peaks are present at 256 and 325 nm. Increasing the pH to the value of 6.1, the intensity of both the peaks decreases while a shoulder is form at ≈ 280 nm (Figure 8B). Two isosbestic points are present at 270 and 291 nm. At pH > 6.1 two peaks at 265 and 377 nm are formed (Figure 8C). Four isosbestic points are present at 244, 265, 289 and 341 nm. At pH > 9.4, the peaks at 265 and 377 nm decrease in intensity, while a little band appear at ≈ 300 nm (Figure 8D). Two isosbestic points are present at 286 and 309 nm.

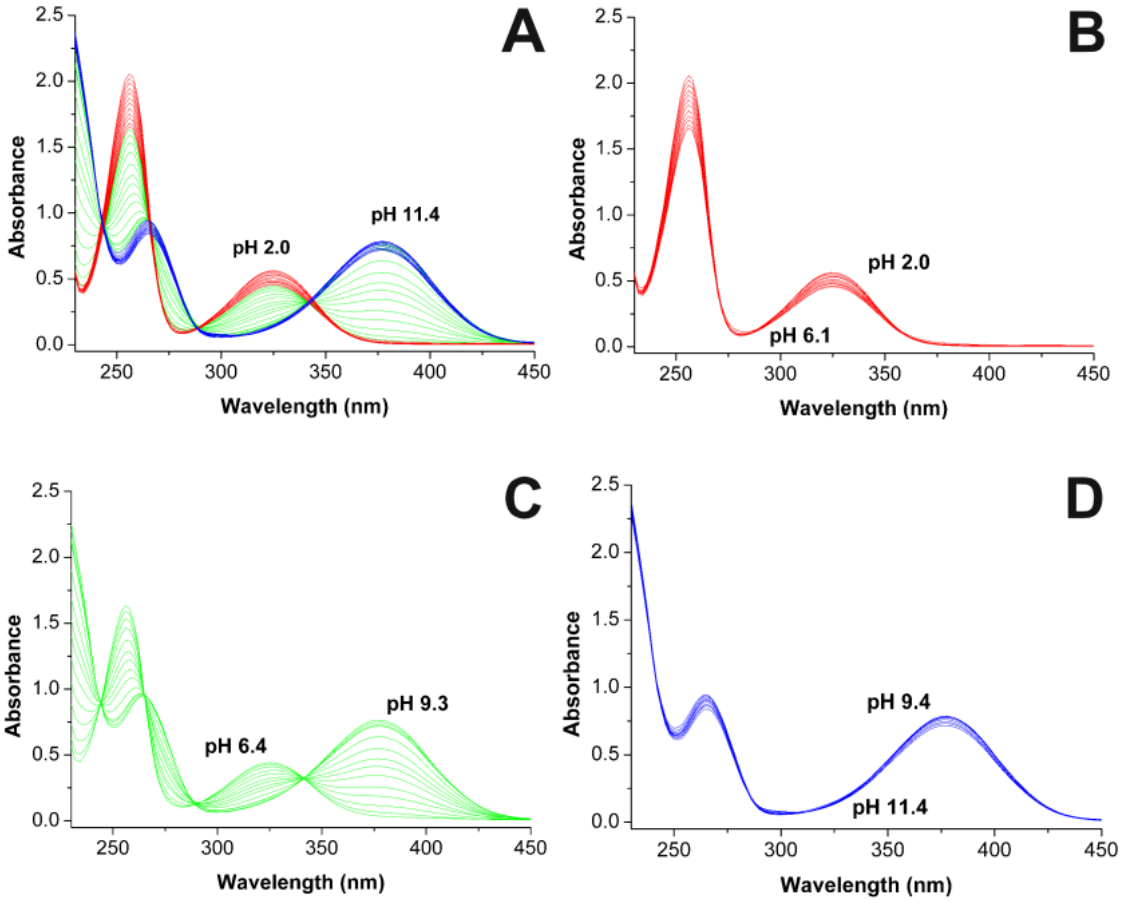

Figure 8. Some spectra recorded during the potentiometric titration of **6** (2.78×10^{-4} M, 25 °C, 0.1 M NaCl, 1 cm optical path length) from pH 2.0 to 11.4 (**A**), from pH 2.0 to 6.1 (**B**), from pH 6.4 to 9.3 (**C**) and from pH 9.4 to 11.4 (**D**).

3.2.2 Calculation of the protonation constants

From the eigenvalue analysis of the spectrophotometric data, the significant eigenvalues, interpreted as the number of linearly independent absorbing species, were found.[1] The concentration profile as a function of pH, and the pure UV-vis spectra of all the absorbing species were then calculated without model assumptions. The results are shown in Figures 9-10 for all the studied compounds.

Three significant eigenvalues were found for **1**, four for **2**, **4** and **6**, and five for **3** and **5**. Four eigenvalues were expected for **1** and **2** and five for the other compounds. Any attempt to fit the experimental data taking into account four eigenvalues for **1** or five for **4** and **6** led to negative calculated pure spectra. These results show that H_3L^+ and H_2L species for **1,** and H_4L^+ and H_3L species for **4** and **6** were not spectrally distinguishable. The potentiometric and spectrophotometric data were fitted simultaneously supposing a model considering three protonation equilibria (from L^{2-} to H_3L^+) for **1** and **2**, and four protonation equilibria (from L^{3-} to H_4L^+) for **3**, **4**, **5**, and **6**. The protonation constants and the refined pure spectra were calculated. The protonation constants are

reported in Table 1. The pK values related to the formation of the H_3L^+, H_4L^+, and H_4L^{2+} species for **1**, **4** and **6**, respectively, are outside the experimental pH range.

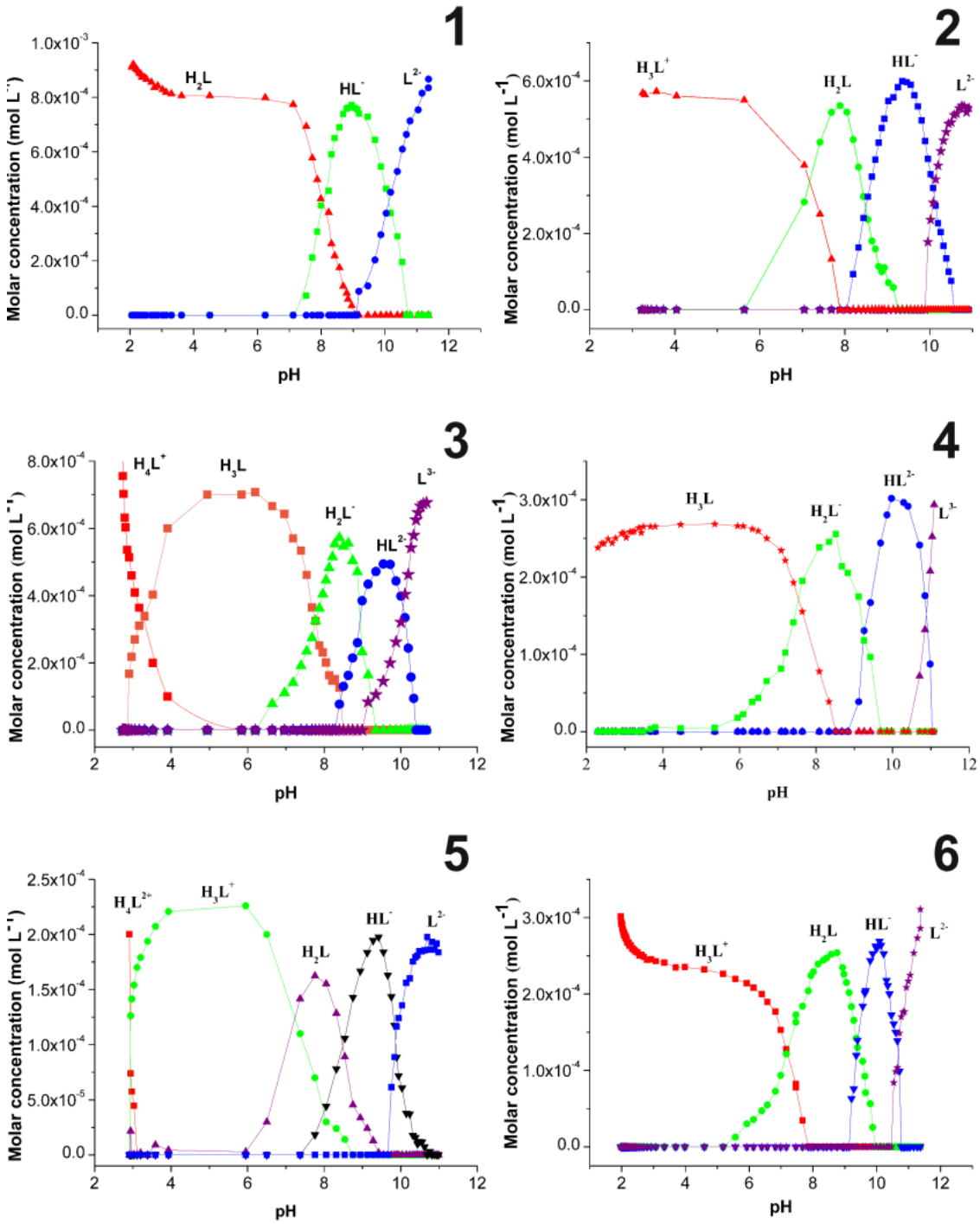

Figure 9. Model free concentration profile calculated with eigenvalues analysis of the spectrophotometric data collected during the potentiometric titration of **1**-**6** (**1** 9.01 × 10^{-4} M, **2** 9.32 × 10^{-4} M, **3** 7.07 × 10^{-4} M, **4** 2.9 × 10^{-4} M, **5** 2.01 × 10^{-4} M, **6** 2.78 × 10^{-4} M) at 25 °C, 0.1 M NaCl, 1 cm optical path length.

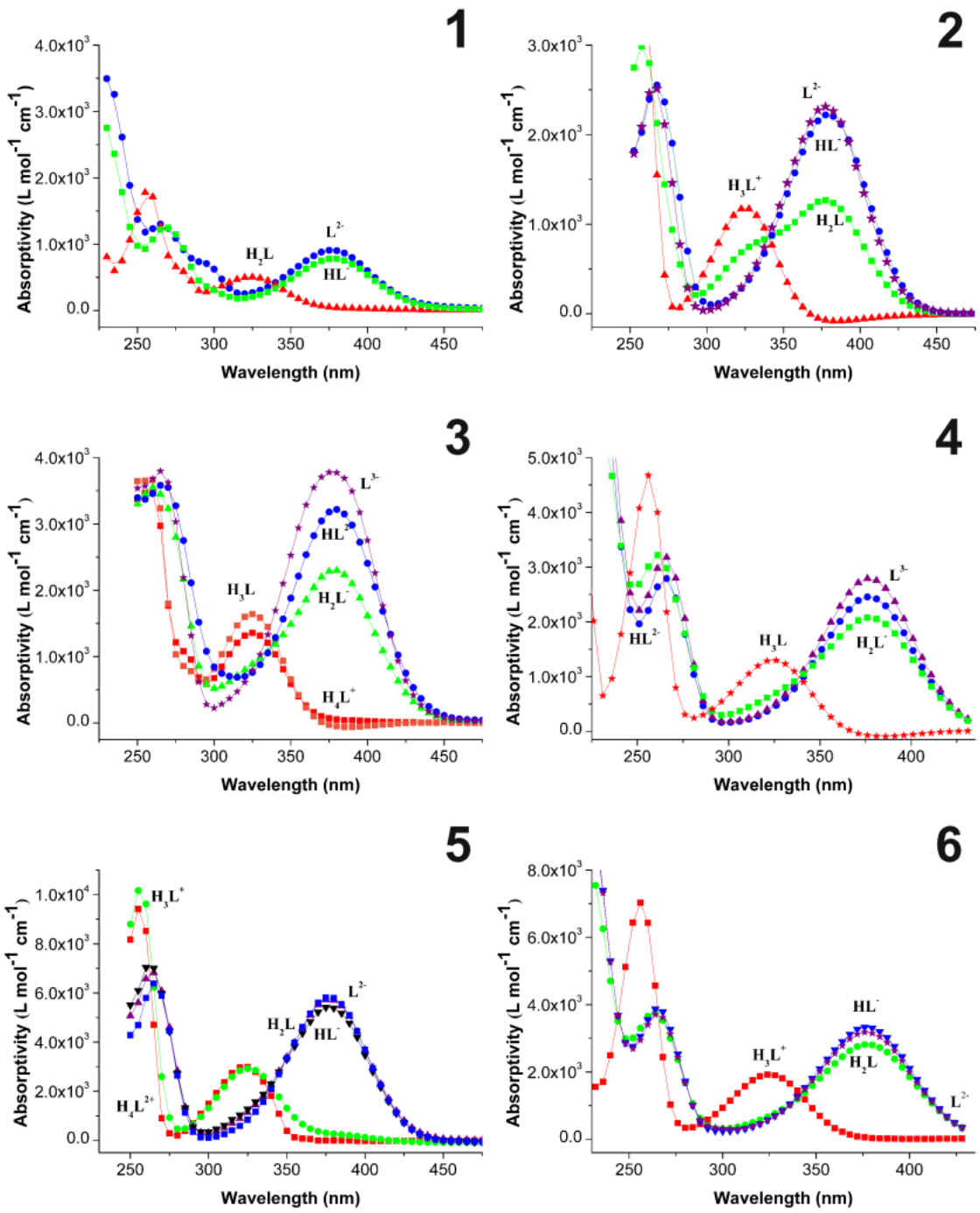

Figure 10. Pure spectra calculated with eigenvalues analysis of the spectrophotometric data collected during the potentiometric titration of **1-6** (**1** 9.01 × 10^{-4} M, **2** 9.32 × 10^{-4} M, **3** 7.07 × 10^{-4} M, **4** 2.9 × 10^{-4} M, **5** 2.01 × 10^{-4} M, **6** 2.78 × 10^{-4} M) at 25 °C, 0.1 M NaCl, 1 cm optical path length.

Overall Stability Constants			
Compound	**Species**	**Log β**	**pK**
	HL^-	10.2(1)	10.2
1	H_2L	18.30(5)	8.1
	H_3L^+	19.8(2)	< 2

2	HL^-	9.40(2)	9.4
	H_2L	18.2(1)	8.8
	H_3L^+	21.5(1)	3.3
3	HL^{2-}	10.14(1)	10.14
	H_2L^-	18.72(1)	8.58
	H_3L	26.72(1)	8.00
	H_4L^+	29.80(4)	3.08
4	HL^{2-}	11.0(5)	11.0
	H_2L^-	20.3(1)	9.3
	H_3L	27.8(1)	7.5
	H_4L^+	28.5(5)	< 2
5	HL^-	9.81(3)	9.81
	H_2L	18.52(3)	8.71
	H_3L^+	26.09(4)	7.57
	H_4L^{2+}	28.2(4)	≈ 2
6	HL^-	10.7(2)	10.7
	H_2L	20.15(2)	9.45
	H_3L^+	27.33(2)	7.18
	H_4L^{2+}	29.3(3)	< 2

Table 1. Protonation constants of the compounds **1**-**6** at 25 °C and 0.1 M NaCl ionic strength.

3.2.1 Protonation sequence

The assignment of the protonation sequence is straightforward for compounds **1** and **2**. In fact, the first pK is related to the protonation of the oxygen atom of the ring, the second one to the iminic nitrogen, and the third one to the carboxylate group. Protonation sequence for compounds **1** and **2** is reported in Scheme 1.

To define the order in which the functional groups of **3** are protonated, the absorptivity spectra of the different species of **3** were compared with those of **1**. The spectra of the HL species (charges are omitted for simplicity) of **1** and **3** are similar for position and absorptivity ratio of the bands. This suggests that the same group is protonated in both the species, i.e. the oxygen atom on the aromatic ring. The spectrum of the H_2L species of **3** is different from that of the H_2L species of **1**, where the iminic group is protonated, and is similar to that of the HL species of **1**, where the iminic group is still not protonated. Then the second protonation in **3** involves the sulphur atom. Being the spectra of the H_3L species of **3** and that of the H_2L species of **1** similar, it can be deduced that the third

protonation in **3** involves the nitrogen atom. Finally, the fourth protonation occurs on the carboxylate group of **3** (see Scheme 2).

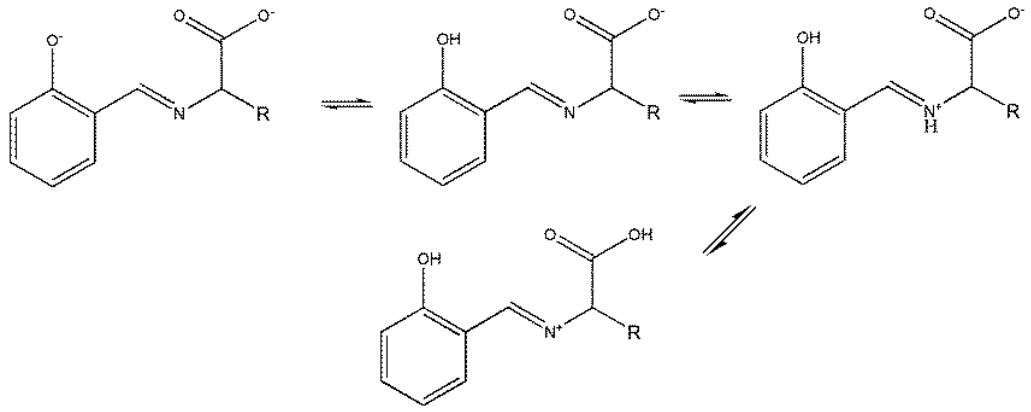

Scheme 1. Protonation sequence for compound **1** and **2**.

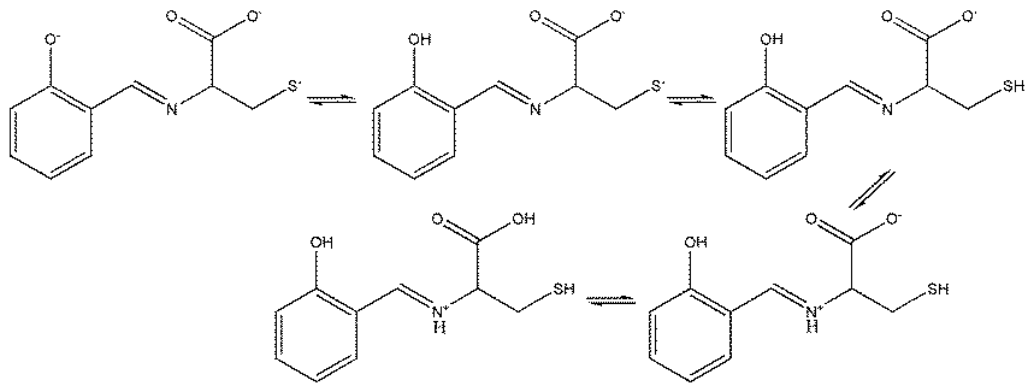

Scheme 2. Protonation sequence for compound **3**.

For the compound **4**, by comparison of the pure spectra of all the species formed by the studied compounds, it follows that the protonations occurs in the order: the oxygen of the side chain, the oxygen of the ring, the iminic group, and the carboxylate group (Scheme 3).

For compound **5**, considering the absorptivity spectra of the formed species and the pK 12.48 of the $–NH_2$ group in the arginine side chain[2], the first protonation appears to involve the $–NH_2$ group. The second protonation involves the oxygen atom of the aromatic ring, the third one the –C=N group and the last one the carboxylate group (Scheme 4).

Regarding compound **6**, comparing the spectra of the absorbing species of all the studied compounds, and taking into account the protonation constants of histidine[3], the protonations occur in the order: the oxygen of the ring, the nitrogen atom of the histidine residue, the iminic group and finally the carboxylate group (Scheme 5).

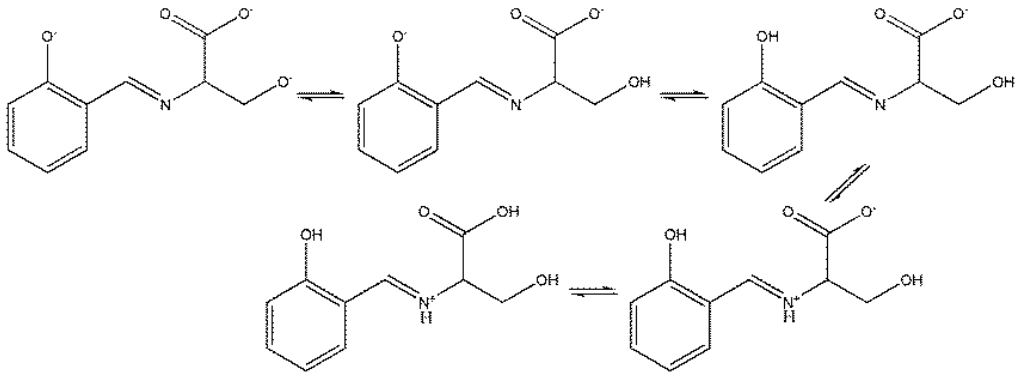

Scheme 3. Protonation sequence for compound **4**.

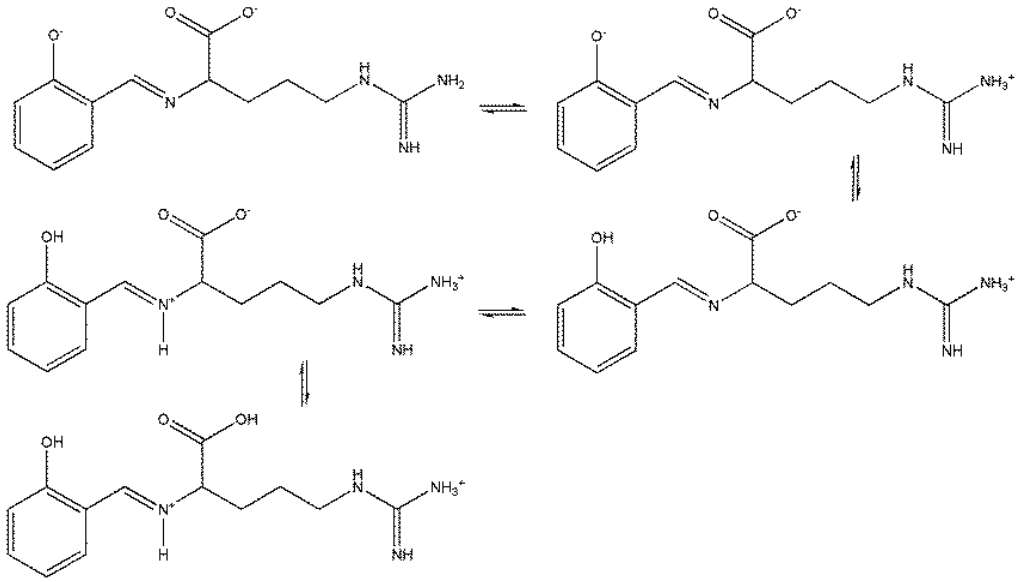

Scheme 4. Protonation sequence for compound **5**.

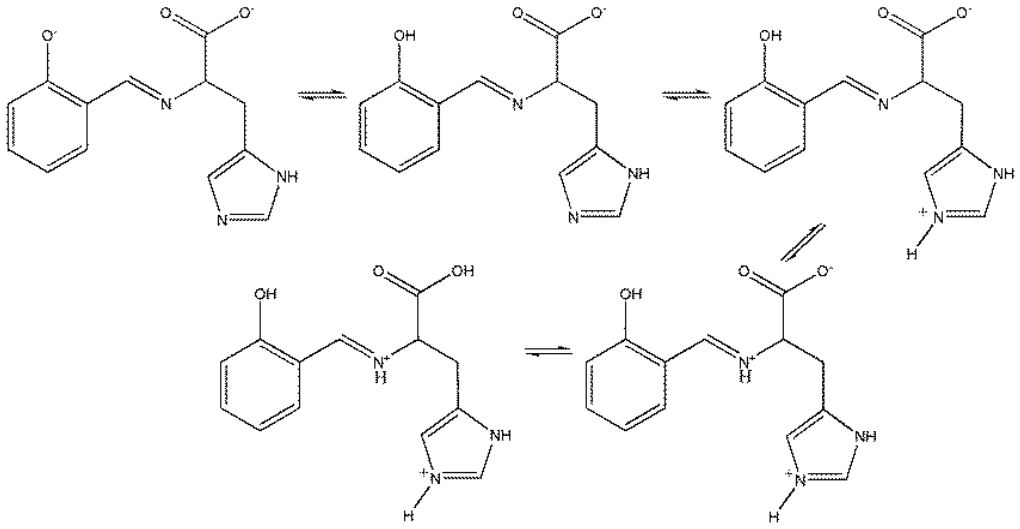

Scheme 5. Protonation sequence for compound **6**.

All the proposed protonation sequences have been confirmed by the ATR-IR spectra at variable pH of the studied compounds. For each sample, the transition from the aqueous phase to the solid film was followed. In Figure 11, ATR-IR spectra of **2** recorded at a different time period are reported as example.

The spectra show changes due to water evaporation and once the solid film is formed, sharp and distinguishable vibration bands are visible. During the evaporation, the shape of the vibration bands changes, but the peak positions remain constant.[4] This means that the same species in aqueous phase are found in the solid film.

All the attributions of the peaks were based on quantomechanical calculations. In Figures 12-13, the spectra of the compounds **1** and **3** and relative attribution are reported as example.

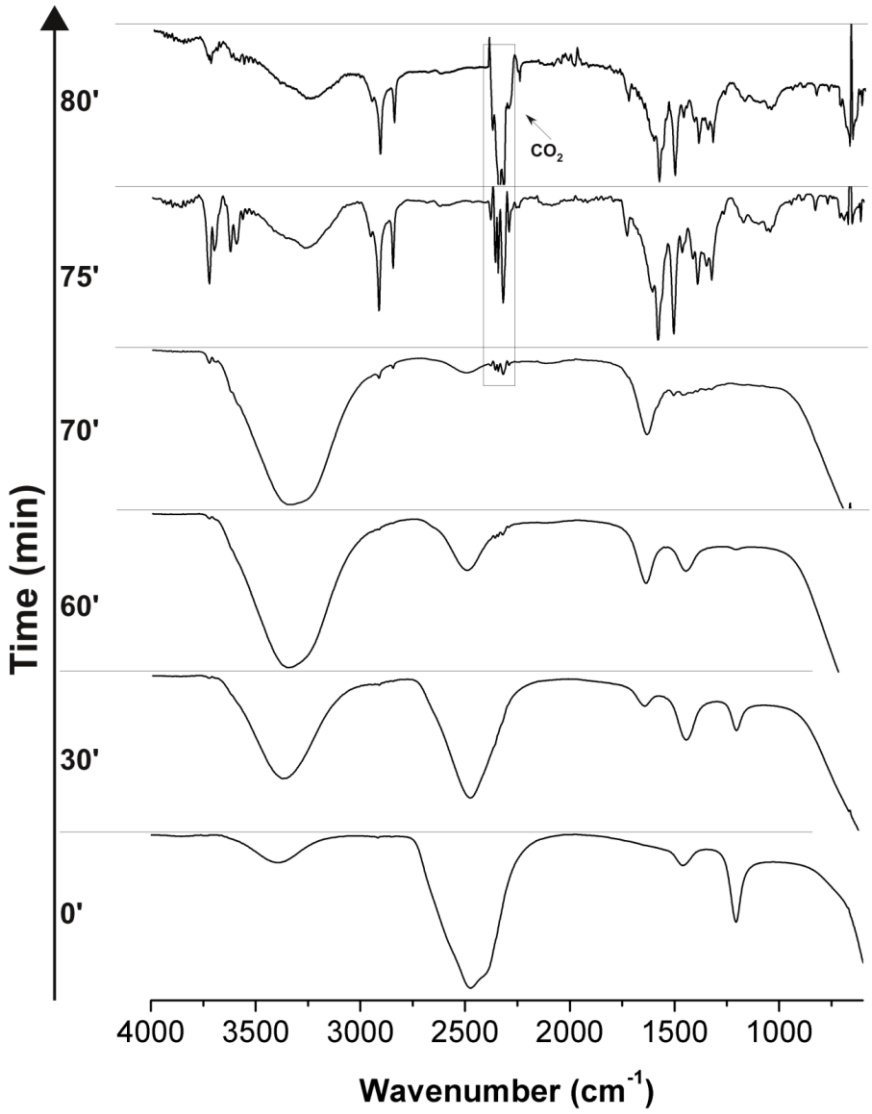

Figure 11. ATR-IR spectra of **2**. Each spectrum was collected at a different time period after depositing the solution on the ATR crystal, showing changes due to water evaporation. Concentration of the compounds **2** was 1.108×10^{-3} M, according to its solubility.

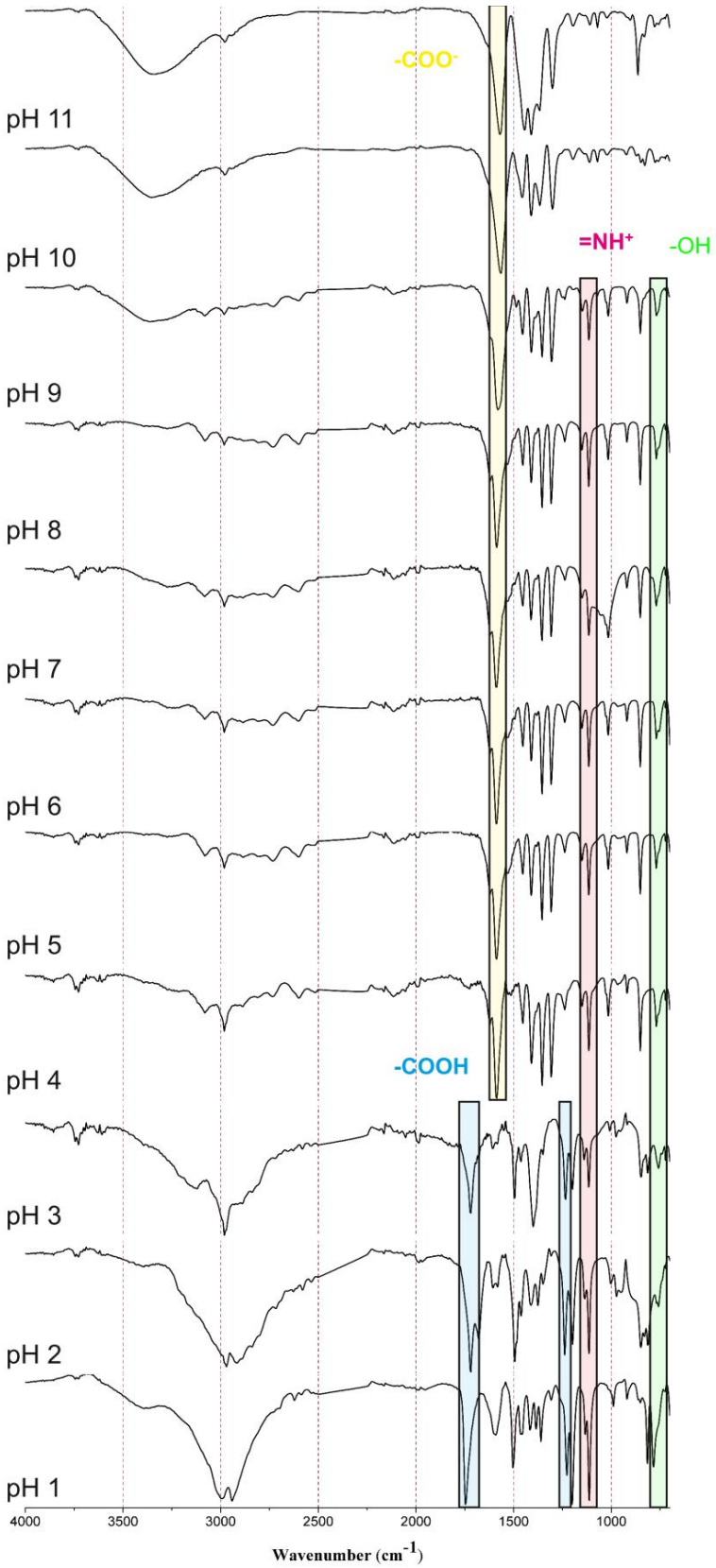

Figure 12. ATR-IR spectra of **1** at different pH ranging from pH 1 to 11. Concentration of the compounds **1** in each sample was 5.072×10^{-4} M, according to its solubility.

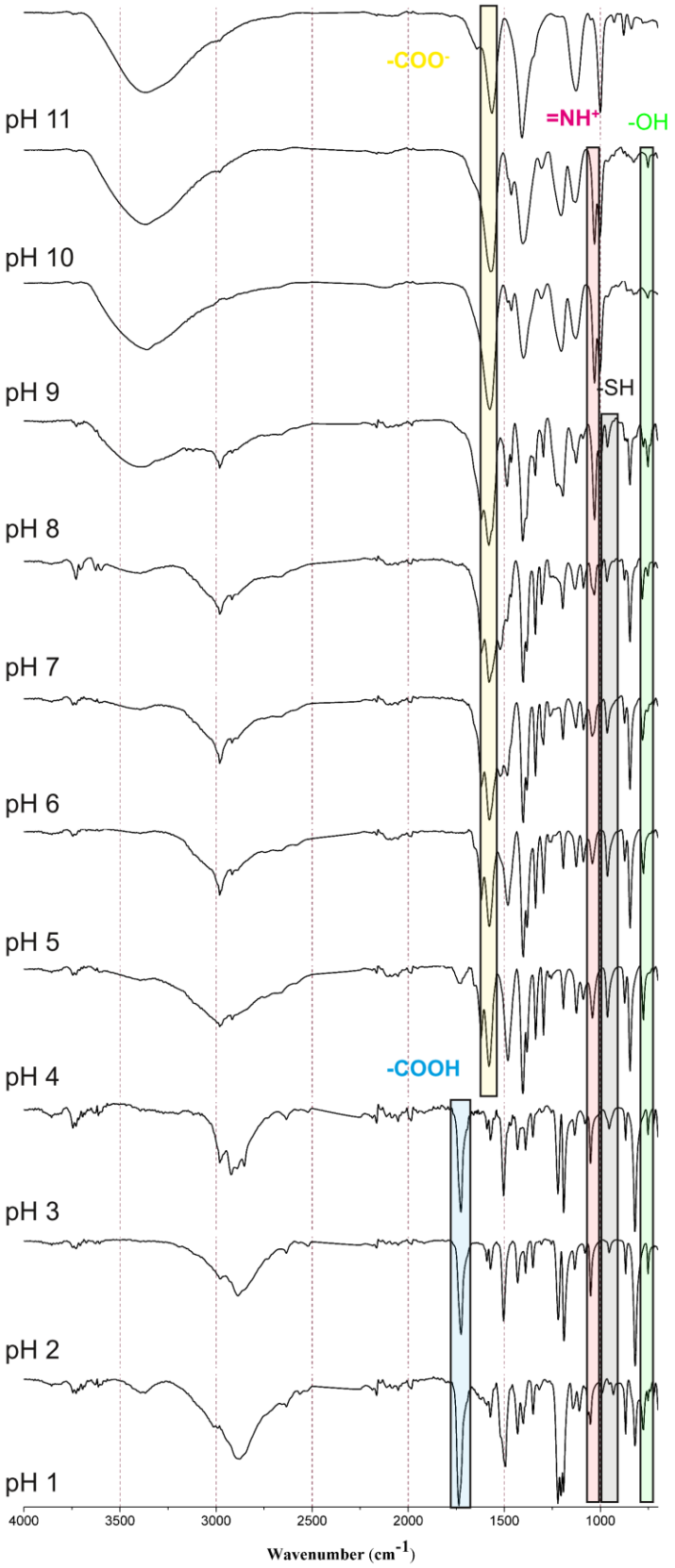

Figure 13. ATR-IR spectra of **3** at different pH ranging from pH 1 to 11. Concentration of the compounds **3** in each sample was 1.021×10^{-3} M, according to its solubility.

3.3. DNA-binding study

The ability of the compounds **1**-**6** to bind DNA has been studied by UV-vis titration with ct-DNA. The interaction of a molecule with DNA is known to result in a modification of its UV-vis spectrum. The type of changes (red or blue shift, and hyper- or hypochromism) gives information on the binding mode.[5] All the studied compounds show, in the chosen experimental conditions, a peak at ≈ 325 nm. After each addition of DNA, the band decreases in intensity for compounds **2**-**6** whereas for the compound **1** only slight variations of the absorbance are present. No significant shift of the maximum is observed. The formation of another small band around 400 nm is also observed for all the compounds. Selected spectra collected during the titrations with ct-DNA are reported in Figure 14 for all the compounds. The spectral evidences suggest that compounds **2**-**6** slightly interact with DNA thorough intercalation between base pairs.

The equilibrium reaction involved in DNA binding is described by the equation ($L + D \leftrightarrow LD$), where L is a generic molecule interacting with DNA, D is the DNA and LD is the formed adduct. The DNA binding constants, defined as $K_b=[LD]/[L][D]$, have been calculated by fitting the experimental absorbance data supposing the formation of the 1:1 compound-DNA adduct, according to [6]. The K_b values range from 48 to 447 (Table 2), and vary along the series **6** > **3** > **5** > **4** > **2** > **1**.

The affinity with the DNA appears related to the substituents present in the side chain. In fact, the lowest values (48 and 69 M^{-1}) are observed for **1** and **2**, that have a methyl and a *iso*-propyl as substituents. The presence in the side-chain of the imidazole or of the thiolic group increases the K_b by ≈ 10 and ≈ 5 times, respectively, with respect to the compound **1**. Our K_b values are lower to those reported in literature for similar Schiff bases.[7],[8] The difference is probably due to the presence of other substituents that can participate to the DNA interaction. The experimental evidences show that the amino acid moiety present in our compounds contributes, but not heavily, to the DNA binding.

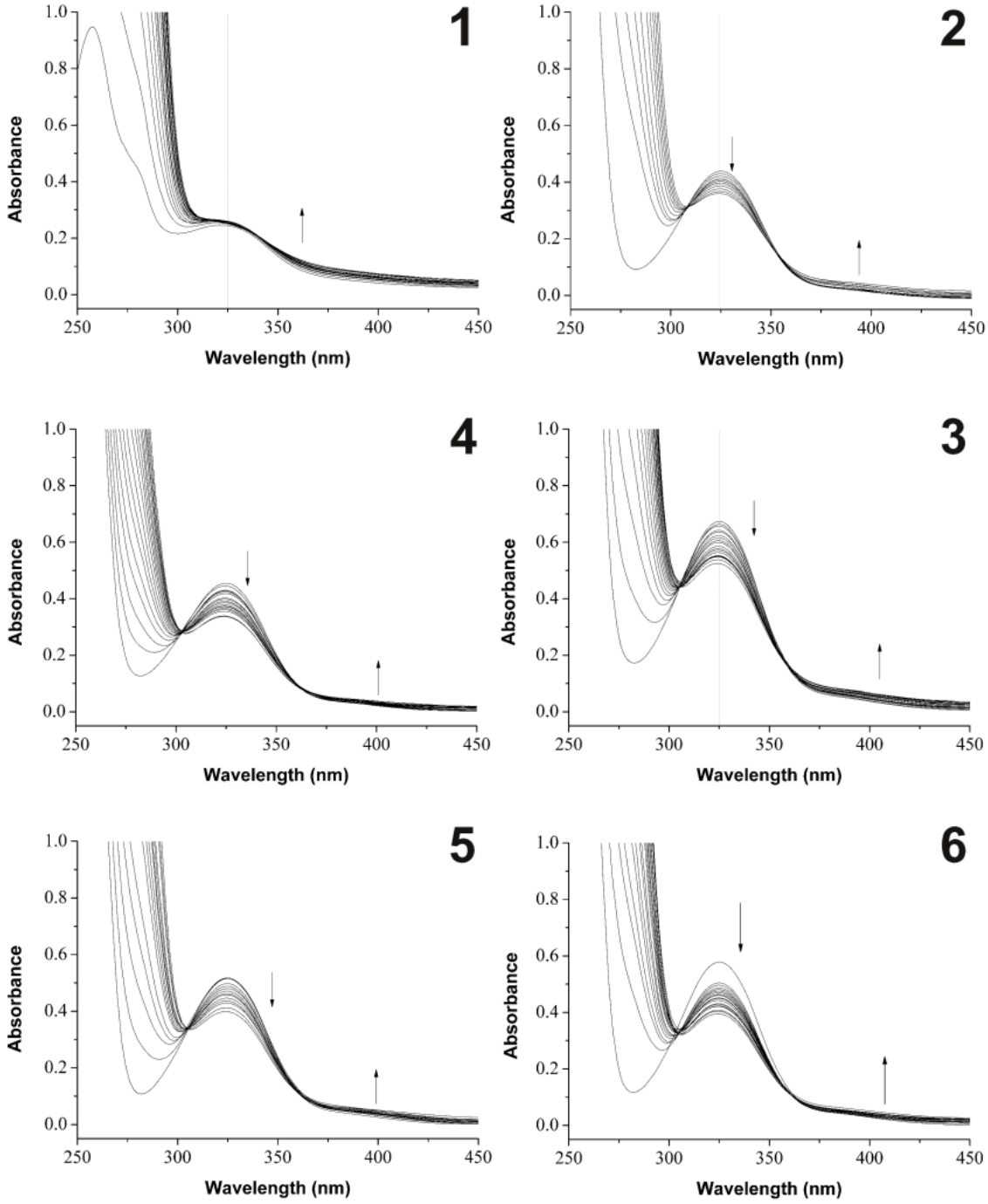

Figure 14. Selected UV-vis spectra collected during the titration of **1**-**6** with ct-DNA (5.02×10^{-4} mmol of **1** with DNA 3.44×10^{-3} M; 4.88×10^{-4} mmol of **2** with DNA 3.10×10^{-3} M; 2.10×10^{-4} mmol of **3** with DNA 1.24×10^{-3} M; 6.07×10^{-4} mmol of **4** with DNA 3.32×10^{-3} M; 2.03×10^{-4} mmol of **5** with DNA 2.07×10^{-3} M; 3.03×10^{-4} mmol of **6** with DNA 1.95×10^{-3} M) in PIPES buffer 0.01 M at pH 7.0, 1 cm optical path length, 25 °C. The arrows show the change in absorbance due to the DNA addition.

Compound	K_b (M^{-1})
1	48
2	69
3	229
4	110
5	148
6	447

Table 2. DNA-binding constants of the studied Schiff bases.

3.3 Cytotoxicity

An evaluation of the cytotoxic activity of the synthetized compounds has been carried out in order to study the influence of the introduction of the phenolic ring on the cytotoxicity of the amino acids. In fact, phenolic compounds are known to be toxic due to ROS formation.[9] The antiproliferative activities of the six studied compounds have been tested against three human solid tumour cell lines (SK-MES-1, DU-145, and Hep-G2), and two human haematological tumour cell lines (CCRF-CEM, and CCRF-SB). All the studied compounds show IC_{50} values higher than 100 μM against all the tested tumour cell lines, and are then devoid of a significant cytotoxic activity.

4. Conclusions

The compounds L-Salicylidenealanine, L-Salicylidenevaline, L-Salicylidenecysteine, L-Salicylideneserine, L-Salicylidenearginine, and L-Salicylidenehistidine have been synthesized through optimization of previously reported methods: reduced reaction time (for L-Salicylidenecysteine and L-Salicylideneserine), doubled amount of salicyladehyde (for L-Salicylidenehistidine) and sodium sulphate addition (for L-Salicylidenealanine and L-Salicylidenevaline) were needed for the synthesis of the compounds according to the different reactivity of amino acids. The synthesized Schiff bases were characterized by means of elemental analysis, NMR and IR spectroscopy. The protonation and DNA-binding constants and the cytotoxic activity have been determined. The protonation of the carboxylate group occurs at around pH 3 for compounds L-Salicylidenevaline and L-Salicylidenecysteine whereas for all the other compounds around 2 or lower. The protonation of the iminic group occurs between pH 7.2 and 8.8, while that of the oxygen of the phenolic group between pH 8.7 and 10.7. The protonation of the amino acid side chain occurs before the protonation of the phenolic oxygen only for compounds L-Salicylideneserine and L-Salicylidenearginine. Afterwards, in all the compounds the iminic group is protonated after the carboxylic group. The studied compounds do not show cytotoxic activity,

however they are able to interact with DNA, showing DNA binding constant in the 48–447 M^{-1} range. The absence of cytotoxicity and the poor reactivity with DNA, confirm the feasibility of these compounds for pharmaceutical applications, also in complexes with metal ions to exploit their unique properties. In fact, although the ligands are devoid of significant activity, it is not untypical that the derived complexes show antitumor activity.

References

[1] W. Qin, S. Long, M. Panunzio, S. Biondi, Schiff bases: a short survey on an evergreen chemistry tool, Molecules. 18 (2013) 12264–12289. doi:10.3390/molecules181012264.

[2] B. Vilanova, J. Gallardo, C. Caldés, M. Adrover, J. Ortega-Castro, F. Muñoz, et al., Formation of Schiff Bases of O-Phosphorylethanolamine and O-Phospho-d,l-serine with Pyridoxal 5′-Phosphate. Experimental and Theoretical Studies, J. Phys. Chem. A. 116 (2012) 1897–1905.

[3] A.A. El-Sherif, M.S. Aljahdali, Review: protonation, complex-formation equilibria, and metal–ligand interaction of salicylaldehyde Schiff bases, J. Coord. Chem. 66 (2013) 3423–3468. doi:10.1080/00958972.2013.839027.

[4] C.M. Rajesh, M. Ray, Characterization of a meso-chiral isomer of a hexanuclear Cu(II) cage from racemization of the L-alanine Schiff base, Dalton Trans. 43 (2014) 12952–12960. doi:10.1039/c4dt01443j.

[5] A.G. Dossetter, T.F. Jamison, E.N. Jacobsen, Highly Enantio- and Diastereoselective Hetero-Diels-Alder Reactions Catalyzed by New Chiral Tridentate Chromium(III) Catalysts, Angew. Chem. Int. Ed. Engl. 38 (1999) 2398–2400.

[6] C. Palomo, J.M. Aizpurua, I. Ganboa, M. Oiarbide, Asymmetric Synthesis of β -Lactams by Staudinger Ketene-Imine Cycloaddition Reaction, European J. Org. Chem. 1999 (1999) 3223–3235.

[7] K. Sundaram, R. Subban, SYNTHESIS AND BIOLOGICAL ACTIVITIES OF SCHIFF BASES OF 2, 5–DIMERCAPTO 1, 3, 4-THIADIAZOLE DERIVATIVES, Indo Am. J. Pharm. …. 4 (2014) 1–7.

[8] W. Zishen, L. Zhiping, Y. Zhenhuan, Synthesis, characterization and antifungal activity of glycylglycine Schiff base complexes of 3d transition metal ions, Transit. Met. Chem. 18 (1993) 291–294. doi:10.1007/BF00207949.

[9] L. Shi, H.-M. Ge, S.-H. Tan, H.-Q. Li, Y.-C. Song, H.-L. Zhu, et al., Synthesis and antimicrobial activities of Schiff bases derived from 5-chloro-salicylaldehyde, Eur. J. Med. Chem. 42 (2007) 558–564. doi:10.1016/j.ejmech.2006.11.010.

[10] Z. Guo, R. Xing, S. Liu, Z. Zhong, X. Ji, L. Wang, et al., Antifungal properties of Schiff bases of chitosan, N-substituted chitosan and quaternized chitosan, Carbohydr. Res. 342 (2007) 1329–1332. doi:10.1016/j.carres.2007.04.006.

[11] L.M.F. Gomes, R.P. Vieira, M.R. Jones, M.C.P. Wang, C. Dyrager, E.M. Souza-Fagundes, et al., 8-Hydroxyquinoline Schiff-base compounds as antioxidants and modulators of copper-mediated Aβ peptide aggregation, J. Inorg. Biochem. 139 (2014) 106–116. doi:10.1016/j.jinorgbio.2014.04.011.

[12] S. Dalapati, S. Jana, N. Guchhait, Anion recognition by simple chromogenic and chromo-fluorogenic salicylidene Schiff base or reduced-Schiff base receptors, Spectrochim. Acta Part A Mol. Biomol. Spectrosc. 129 (2014) 499–508. doi:10.1016/j.saa.2014.03.090.

[13] X. Qiao, Z.-Y. Ma, C.-Z. Xie, F. Xue, Y.-W. Zhang, J.-Y. Xu, et al., Study on potential antitumor mechanism of a novel Schiff base copper(II) complex: synthesis, crystal structure, DNA binding, cytotoxicity and apoptosis induction activity., J. Inorg. Biochem. 105 (2011) 728–37. doi:10.1016/j.jinorgbio.2011.01.004.

[14] N. Zhang, Y. Fan, Z. Zhang, J. Zuo, P. Zhang, Q. Wang, et al., Syntheses, crystal structures and anticancer activities of three novel transition metal complexes with Schiff base derived from 2-

acetylpyridine and l-tryptophan, Inorg. Chem. Commun. 22 (2012) 68–72. doi:10.1016/j.inoche.2012.05.022.

[15] M.J. Chow, C. Licona, D.Y.Q. Wong, G. Pastorin, C. Gaiddon, W.H. Ang, Discovery and Investigation of Anticancer Ruthenium–Arene Schiff-Base Complexes via Water-Promoted Combinatorial Three-Component Assembly, J. Med. Chem. 57 (2014) 6043–6059. doi:10.1021/jm500455p.

[16] X. Zhong, J. Yi, J. Sun, H.-L. Wei, W.-S. Liu, K.-B. Yu, Synthesis and crystal structure of some transition metal complexes with a novel bis-Schiff base ligand and their antitumor activities, Eur. J. Med. Chem. 41 (2006) 1090–1092. doi:10.1016/j.ejmech.2006.05.009.

[17] Z.-Y. Yang, R.-D. Yang, F.-S. Li, K.-B. Yu, Crystal structure and antitumor activity of some rare earth metal complexes with Schiff base, Polyhedron. 19 (2000) 2599–2604. doi:10.1016/S0277-5387(00)00562-3.

[18] N. Galić, Z. Cimerman, V. Tomišić, Tautomeric and protonation equilibria of Schiff bases of salicylaldehyde with aminopyridines, Anal. Chim. Acta. 343 (1997) 135–143.

[19] C.M. Metzler, A. Cahill, D.E. Metzler, Equilibria and Absorption Spectra of Schiff Bases, J. Am. Chem. Soc. 102 (1980) 6075–6082.

[20] G. Türkoğlu, H. Berber, H. Dal, C. Öğretir, Synthesis, characterization, tautomerism and theoretical study of some new Schiff base derivatives, Spectrochim. Acta. A. Mol. Biomol. Spectrosc. 79 (2011) 1573–83. doi:10.1016/j.saa.2011.04.089.

[21] S.-H. Hsieh, Y.-P. Kuo, H.-M. Gau, Synthesis, characterization, and structures of oxovanadium(V) complexes of Schiff bases of beta-amino alcohols as tunable catalysts for the asymmetric oxidation of organic sulfides and asymmetric alkynylation of aldehydes, Dalton Trans. (2007) 97–106. doi:10.1039/b613212j.

[22] G. Gran, Determination of the equivalence point in potentiometric titrations—Part II, Analyst. 77 (1952) 771–671.

[23] P. Gans, B. O'Sullivan, GLEE, a new computer program for glass electrode calibration, Talanta. 51 (2000) 33–7.

[24] P. Gans, A. Sabatini, A. Vacca, Investigation of equilibria in solution. Determination ofequilibrium constants with the hyperquad suite of programs, Talanta. (1996) 1739–1753.

[25] M.E. Reichmann, S.A. Rice, C.A. Thomas, P. Doty, A Further Examination of the Molecular Weight and Size of Desoxypentose Nucleic Acid, J. Am. Chem. Soc. 76 (1954) 3047–3053. doi:10.1021/ja01640a067.

[26] J. Murmur, A procedure for the isolation of deoxyribonucleic acid from micro-organisms, J. Mol. Biol. 3 (1961) 208–218.

[27] S.A. Latt, G. Stetten, L.A. Juergens, H.F. Willard, C.D. Scher, Recent developments in the detection of deoxyribonucleic acid synthesis by 33258 Hoechst fluorescence, J. Histochem. Cytochem. 23 (1975) 493–505. doi:10.1177/23.7.1095650.

[28] R. Pauwels, J. Balzarini, M. Baba, R. Snoeck, D. Schols, P. Herdewijn, et al., Rapid and automated tetrazolium-based colorimetric assay for the detection of anti-HIV compounds, J. Virol. Methods. 20 (1988) 309–321.

[29] H.E. Smith, E.P. Burrows, M.J. Marks, R.D. Lynch, F.-M. Chen, Optically Active Amines. 22. Application of the Salicylidenimino Chirality Rule to α-Amino Acids, J. Am. Chem. Soc. 2 (1977) 707–713.

[30] G. Rao, M. Philipp, Boronic acid catalyzed hydrolyses of salicylaldehyde imines, J. Org. Chem. 56 (1991) 1505–1512. doi:10.1021/jo00004a031.

[31] H. Saleem, Y. Erdogdu, S. Subashchandrabose, V. Thanikachalam, J. Jayabharathi, N. Ramesh Babu, Structural and vibrational studies on (E)-2-(2-hydroxy benzyliden amino)-3-phenyl propionic acid using experimental and DFT methods, J. Mol. Struct. 1030 (2012) 157–167. doi:10.1016/j.molstruc.2012.04.011.

[32] D.G. Nasledov, K. V Nasonova, K. V Sezyavina, T. V Susarova, I. V Lagoda, V. V Shamanin, et al., Ring-chain tautomerism of 2-aryl-6-oxohexahydropyrimidine-4-carboxylic acid sodium salts, 49 (2013) 640–645.

[33] S. Liu, J. Peng, H. Yang, Y. Bai, J. Li, G. Lai, Highly efficient and convenient asymmetric hydrosilylation of ketones catalyzed with zinc Schiff base complexes, Tetrahedron. 68 (2012) 1371–1375. doi:10.1016/j.tet.2011.12.054.

[34] R.G. Hiskey, J. M, Azomethine Chemistry. II. Formation of Peptides from Oxazolidine-5-ones, J. Am. Chem. Soc. 85 (1963) 578–582. doi:10.1021/ja00888a021.

[35] M.R. Maurya, U. Kumar, I. Correia, P. Adão, J. Costa Pessoa, A Polymer-Bound Oxidovanadium(IV) Complex Prepared from anL-Cysteine-Derived Ligand for the Oxidative Amination of Styrene, Eur. J. Inorg. Chem. (2008) 577–587. doi:10.1002/ejic.200700662.

[36] E.R. Malinowski, Factor Analysis in Chemistry, third edit, New York, 2002.

[37] J. Yoo, Q. Cui, Does arginine remain protonated in the lipid membrane? Insights from microscopic pKa calculations, Biophys. J. Biophys. Lett. 94 (2008) L61–63. doi:10.1529/biophysj.107.122945.

[38] E. Canel, A. Gültepe, A. Doğan, E. Kılıç, The Determination of Protonation Constants of Some Amino Acids and Their Esters by Potentiometry in Different Media, J. Solution Chem. 35 (2006) 5–19. doi:10.1007/s10953-006-8934-3.

[39] M.S.S. Babu, K.H. Reddy, P.G. Krishna, Synthesis, characterization, DNA interaction and cleavage activity of new mixed ligand copper(II) complexes with heterocyclic bases, Polyhedron. 26 (2007) 572–580. doi:http://dx.doi.org/10.1016/j.poly.2006.08.026.

[40] T. Pivetta, F. Trudu, E. Valletta, F. Isaia, C. Castellano, F. Demartin, et al., Novel copper(II) complexes as new promising antitumour agents. A crystal structure of [Cu(1,10-phenanthroline-5,6-dione)2(OH2)(OClO3)](ClO4), J. Inorg. Biochem. 141 (2014) 103–113. doi:http://dx.doi.org/10.1016/j.jinorgbio.2014.08.011.

[41] A.Q. Ali, S.G. Teoh, A. Salhin, N.E. Eltayeb, M.B. Khadeer Ahamed, A.M.S. Abdul Majid, Synthesis of isatin thiosemicarbazones derivatives: in vitro anti-cancer, DNA binding and cleavage activities, Spectrochim. Acta. A. Mol. Biomol. Spectrosc. 125 (2014) 440–448. doi:10.1016/j.saa.2014.01.086.

[42] M. Gowri, C. Jayabalakrishnan, DNA binding and cytotoxicity of newly synthesized Schiff base (Z)-4-(((2-hydroxy phenyl) amino)(phenyl)methylene)-3-methyl-1-phenyl-1H-pyrazol-5(4H)one and its analogues, Int. J. Appl. Biol. Pharm. Technol. 3 (2012) 327–337.

[43] N. Arshad, M. Ahmad, M.Z. Ashraf, H. Nadeem, Spectroscopic, electrochemical DNA binding and in vivo anti-inflammatory studies on newly synthesized Schiff bases of 4-aminophenazone, J. Photochem. Photobiol. B Biol. 138 (2014) 331–346. doi:10.1016/j.jphotobiol.2014.06.014.

[44] J. Michałowicz, W. Duda, Phenols – Sources and Toxicity, Polish J. Environ. Stud. 16 (2007) 347–362.

Part III

Conclusions and perspectives

Conclusions

In this work my attention was focused on the study of copper, zinc and vanadium complexes with biological activity and on the application of experimental design and artificial neural networks to the collected biochemical data. Moreover, I used the artificial neural networks to evaluate the cell culture cross-contamination.

A new family of copper(II) complexes with **phen**, **phendione**, and **phendiol** was prepared and studied towards the HEP-G2, SK-MES-1, CCRF-CEM, and CCRF-SB human tumour cell lines. This family presents an antiproliferative effect higher than that of cisplatin. In particular, [Cu(**phen**)$_2$(OH_2)](ClO_4)$_2$ and [Cu(**phendione**)$_2$(OH_2)($OClO_3$)](ClO_4) are promising for the treatment of SK-MES-1 and HEP-G2 cell lines, respectively. These two compounds, in fact, show an IC_{50} value 37 and 18 times lower than that of cisplatin.

The cytotoxic activity of the ligands was found to be correlated to the cellular microenvironment. Compound **phendiol**, the less lipophilic compound, appears as the most active ligand on cells surrounded by a hydrophilic environment, while **phendione**, the most lipophilic, is more effective against cells in a lipophilic environment.

The studied copper(II) complexes interact with DNA mainly by groove binding or electrostatic interactions. The DNA binding constants resulted directly correlated with the IC_{50} values and then inversely correlated with the antitumour activity, in fact, the complexes with the highest DNA affinity show the lowest cytotoxicity. This behavior can be explained assuming that the copper complexes exhibit their antiproliferative activity with mechanisms different from the DNA binding.

Binary combinations of cisplatin and the copper complex [Cu(**phen**)$_2$(OH_2)](ClO_4)$_2$ were tested and resulted to present a synergistic antiproliferative effect against the cisplatin-resistant sublines of leukemic (CCRF-CEM) and ovarian (A2780) cancer cells *in vitro*. A mixed complex containing

copper and platinum with a stoichiometry of $[Cu(\mathbf{phen})(OH)\mu\text{-}(Cl)_2Pt(NH_3)(H_2O)]^+$ was detected, and, considering that this complex is able to hydrolyze to form $[Cu(\mathbf{phen})(OH)\mu\text{-}(Cl)_2Pt(H_2O)_2]^+$ species, this complex could be responsible of the synergistic effect shown by the studied mixtures and it is likely to interfere with one or more of the mechanisms that lead to cisplatin resistance. Given that the determining step in the interaction of cisplatin with DNA are the slow hydrolysis processes and considering that the hydrolyzed complexes $[Cu(\mathbf{phen})(OH)\mu\text{-}(Cl)_2Pt(NH_3)(H_2O)]^+$ and $[Cu(\mathbf{phen})(OH)\mu\text{-}(Cl)_2Pt(H_2O)_2]^+$ are formed within a few minutes, this mixed copper-platinum complex is supposed to be able to react with DNA more readily than cisplatin.

I tested the cytotoxicity activity of binary mixtures of GSH with $[Cu(\mathbf{phen})_2(OH_2)](ClO_4)_2$ or cisplatin and ternary mixtures of GSH with $[Cu(\mathbf{phen})_2(OH_2)](ClO_4)_2$ and cisplatin against the wild type CCRF-CEM cancer cell line and its cisplatin-resistant subline, finding a synergistic effect between $[Cu(\mathbf{phen})_2(OH_2)](ClO_4)_2$ and cisplatin or GSH, and an antagonistic effect between cisplatin and GSH. In particular, in the ternary systems, in absence of $[Cu(\mathbf{phen})_2(OH_2)](ClO_4)_2$ there is antagonism between cisplatin and GSH, while at increasing concentrations of $[Cu(\mathbf{phen})_2(OH_2)](ClO_4)_2$ the antagonism between cisplatin and GSH disappears. The ternary combination shows a selective cytotoxic effect for T-leukemia CEM cells with respect to proliferating normal T-cells.

Cisplatin reacts with GSH to form the complex $[Pt(NH_3)_2Cl_2(GSH+H)]^+$, but with GSSG it forms the adduct $[Pt(NH_3)_2Cl_2+GSSG+H]^+$. Even in excess of thionic ligands, only a 1:1 cisplatin:ligand adduct was detected in the chosen experimental conditions. The copper complexes $[Cu(\mathbf{phen})_2(H_2O)](ClO_4)_2$ and $[Cu(\mathbf{phen})(H_2O)_2(ClO_4)_2]$ react with GSH or GSSG to form complexes such as $[Cu(\mathbf{phen})(GSH)\text{-}H]^+$ and $[Cu(\mathbf{phen})(GSSG)(ClO_4)]^+$. The copper complexes form with cisplatin mixed complexes where the two metal centers are linked by two bridging chloride. When the copper complexes were mixed with cisplatin and the thionic ligands, only

copper-glutathione complexes were detected. No platinum-glutathione adducts or copper-platinum complexes were found. Given that the antiproliferative activity of cisplatin in presence of $[Cu(\mathbf{phen})_2(OH_2)](ClO_4)_2$ against cisplatin-resistant cells was restored, $[Cu(\mathbf{phen})_2(OH_2)](ClO_4)_2$ can be supposed to bind glutathione preventing in this way the deactivation of cispaltin as anticancer agent.

Regarding the study of the phospholipid profile of wild type and cisplatin-resistant cells of CCRF-CEM and A2780, some phospholipids were identified to be specific components, and can be considered as "markers" to distinguish between wild type and cisplatin-resistant cells. Considering that the PL composition influences the transport of drugs across the membrane, affects the activity of the drug transporters and the ability of the cells to load and accumulate drugs, it is evident that a change of the PL content is connected with the development of the resistance. However, from the obtained results, it is not possible to define if these changes are the cause or the consequence of the cisplatin-resistance occurrence. Nevertheless, the potential use of some lipids as "markers" for resistant cells could be important for a possible clinical application. In fact, the onset of the resistance during cisplatin treatment could be monitored by detecting those specific lipids.

A step-by-step protocol for successful quantitation of two distinct cell types in a single two-component mixture by a multivariate calibration approach based on an ANN-coupled IC MALDI-TOF MS analysis has been developed and tested.

Solution studies on the reaction of the drug methimazole with $[Zn(\mathbf{MeIm})_4](ClO_4)_2$, selected as a model compound representing $[Zn(His)_4]^{2+}$ and $[Zn(His)_3(H_2O)]^{2+}$ protein sites, show that methimazole displaces only one of the coordinated **MeIm** molecules. This evidence supports the possibility that methimazole, by blocking a histidine/water binding site, could interfere with the multifunctional roles of zinc atoms in proteins (e.g. the enzymatic activity of carbonic anhydrases). The anion methimazole can effectively act as a (N,S)-bridging/chelating ligand to a variety of metal

ions due to its N–C–S functional group. Moreover, Zn-coordinated methimazole can markedly modify the coordination environment when changing from its thione to thionate form, and vice versa.

The vanadocene dichloride, $[Cp_2VCl_2]$, transforms at physiological pH to $[Cp_2V(OH)_2]$ and only the bio-ligands oxalate, carbonate, hydrogen phosphate, and lactate are able to displace the two oxydrilic ions to yield $[Cp_2V(ox)]$, $[Cp_2V(CO_3)]$, $[Cp_2V(lactH_{-1})]$, and $[Cp_2V(HPO_4)]$. The complex $[Cp_2VCl_2]$ does not interact with the plasma proteins transferrin and albumin under my experimental conditions.

The Schiff bases ligands **L-Salicylidenealanine**, **L-Salicylidenevaline**, **L-Salicylidenecysteine**, **L-Salicylideneserine**, **L-Salicylidenearginine**, and **L-Salicylidenehistidine**, do not show cytotoxic activity towards SK-MES-1, DU-145, Hep-G2, CCRF-CEM and CCRF-SB human tumour cell lines, however they are able to interact with DNA, showing DNA binding constant in the 48–447 M^{-1} range. The absence of cytotoxicity and the poor reactivity with DNA, confirm the feasibility of these compounds for pharmaceutical applications, also in complexes with metal ions to exploit their unique properties. In fact, although the ligands are devoid of significant activity, it is not untypical that the derived complexes show antitumor activity.

Perspectives

On the basis of the obtained results, it would be interesting to continue the study of copper complexes and to test *in vivo* the most effective combinations of drugs.

Given the importance to monitor the onset of the resistance during cisplatin treatment, the extension of the study of the phospholipid markers to other cell lines, could be important for a possible clinical application.

In order to complete the study on the Schiff base ligands, it would be necessary to synthesize complexes with different metal ions.

Acknowledgments

I would like to express my gratitude and my warm thanks to my supervisor Dr. Tiziana Pivetta for her precious guide, for her helpful teaching and comments and the continuous support during these years.

Special thanks go to Prof. Francesco Isaia for the synthesis of zinc complexes and the time spent in fruitful discussions on several issues related to this work.

I would also like to thank Prof. Josef Havel, the Masaryk University and its Department of Chemistry, for the kind hospitality and for funding my stay in Brno (Grant Agency of Masaryk University (MUNI/M/0041/2013 and MUNI/A/1014/2013), European Regional Development Fund (CZ.1.05/1.1.00/02.0123 and CZ.1.07/2.3.00/20.0185), Faculty of Medicine MU to junior researcher).

Thanks to Prof. Alessandra Pani and all her research group for the measurements of cytotoxicity.

Thanks to Prof. Enzo Cadoni for the assistance in performing MS analysis and for the fruitful and helpful suggestions in the interpretation of MS spectra.

Thanks to Prof. Claudia Fattuoni for the synthesis of Schiff bases ligands and NMR experiments.